FINAL REPORT

HINDCAST STUDY OF WIND WAVE AND CURRENT FIELDS IN HURRICANE ANDREW - GULF OF MEXICO

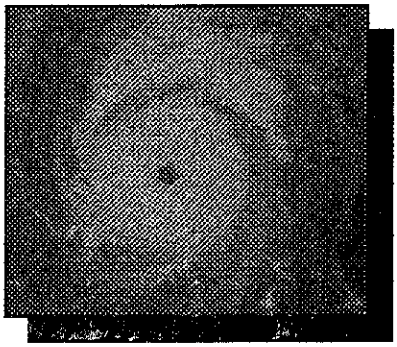

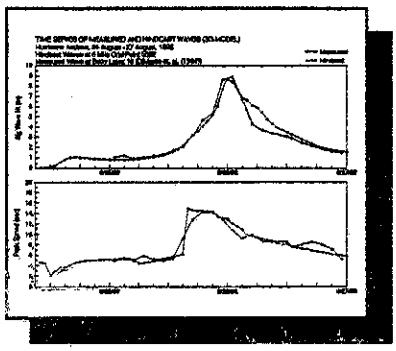

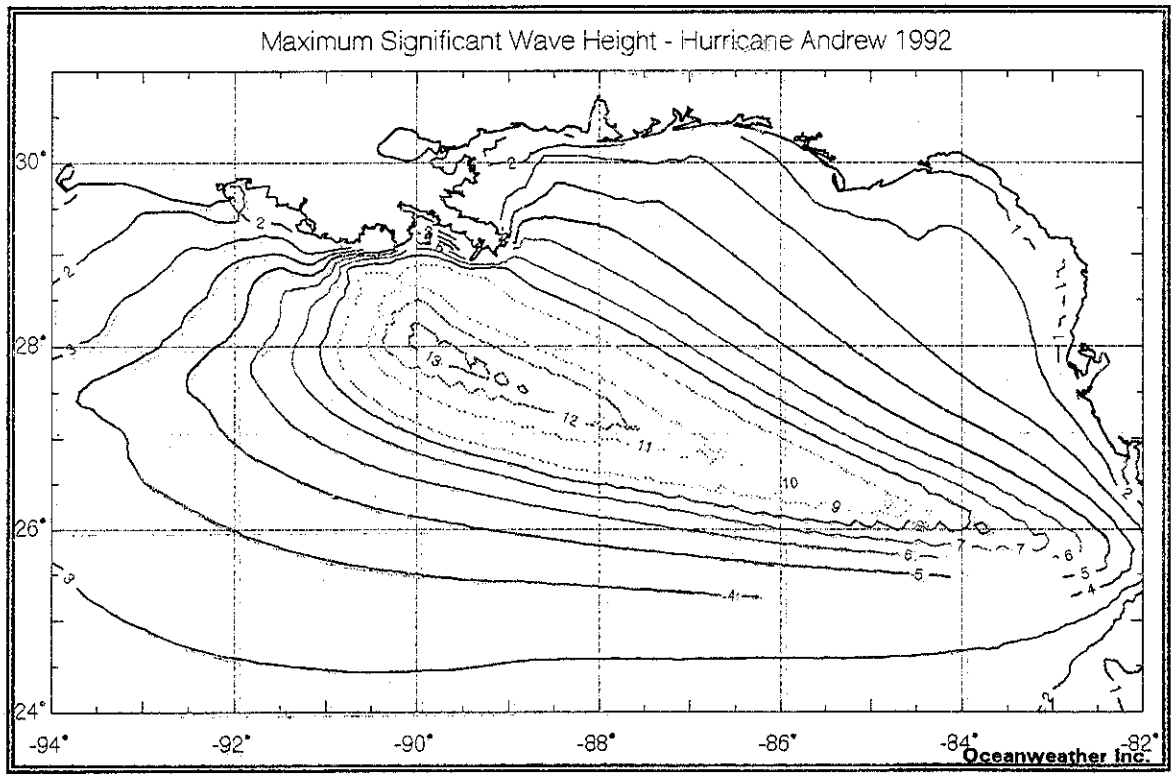

About the Cover

The upper left panel shows a GOES satellite visible image of Andrew in the Gulf of Mexico near maximum intensity (936 mb). The upper right panel shows the comparisons of hindcast (dashed) and measured (solid line) time series of significant wave height (upper graph) and spectral peak period (lower graph) at LATEX Station 16, located in 19 meters water depth at 28 degrees 52.024 minutes North latitude, 90 degrees 29.572 West longitude. The lower panel shows the envelope of maximum hindcast significant wave height (contours at 1 meter intervals). The wave hindcast was made with Oceanweather's third-generation spectral wave model.

FINAL REPORT

HINDCAST STUDY OF WIND WAVE AND CURRENT FIELDS IN HURRICANE ANDREW - GULF OF MEXICO

by

Vincent J. Cardone, Andrew T. Cox and J. A. Greenwood
Oceanweather Inc
Cos Cob, CT

Douglas J. Evans and Harriett Feldman
Evans - Hamilton Inc
Rockville, Maryland

Scott. M. Glenn
Rutgers University
New Brunswick, New Jersey

Timothy R. Keen
Naval Naval Research Laboratory
Stennis Space Center, MS

submitted to

Minerals Management Service
Department of Interior
Procurement Operations Branch, MS 2510
381 Elden Street
Herndon, VA 22070-4817
Contracting Officer: James E. MacKay

November, 1994

Acknowledgements

The project team would like to acknowledge the LATEX Shelf Program Office at Texas A&M University for providing the meteorological and oceanographic data from the LATEX met buoys and wave and current meter moorings and from the hydrographic survey coincident with Hurricane Andrew. Their study was funded by the U. S. Minerals Management Service under Contract No. 14-35-0001-30509. Also, the U. S. Army Corps of Engineer's Waterways Experiment Station provided the measured water level data at two shallow water platforms in the Gulf. Shell Development Company provided the wave measurements from their deep water Bullwinkle platform. Other data were obtained from published or to be published sources as cited.

Abstract

The evolution of the surface wind field and ocean response in the northern Gulf of Mexico in hurricane Andrew (1992) is described through the application of advanced numerical wind, ocean surface wave and three-dimensional current hindcast models adapted to the basin at high spatial resolution (grid spacing of 10 km). The models adopted have been previously applied to model historical Gulf of Mexico hurricanes; in this study, the models were carefully validated against all available data acquired in Andrew.

The study included a substantial data assembly and processing component to ensure that all public domain measurements from government, institutional and offshore industry sources of surface wind, surface waves, storm surge and currents were identified, acquired and made available in forms most useful for model calibration and validation.

Surface wind fields were developed using an improved version of a numerical model of the vortex planetary boundary layer model. The parameters of the model relied heavily on the extensive suite of meteorological data acquired by US Air Force and NOAA reconnaissance aircraft. Surface waves were modeled using a third-generation model which included shallow water physics. Surface and sub-surface currents were modelled using a three-dimensional hydrodynamic model which resolves the vertical coordinate in 13 layers and includes prognostic equations for temperature, salinity and turbulent energy as well as surface height and velocity.

The study provides a data base not only of scientific interest, but also of use in engineering studies, such as analyses of post-mortem platform response and failure, investigations of pipeline failure modes, and assessment of various types of environmental loading on offshore structures. The modeling capability demonstrated and validated through this study establishes an analysis tool for reassessment of extreme environmental criteria especially for water depths in which alternative existing criteria may conflict (approximately the range 15-50 m).

Table of Contents

1. INTRODUCTION

Hurricane Andrew is the costliest natural disaster in United States history. While much of the cost was incurred in South Florida, this study is prompted in part by the striking impact of this storm in the Gulf of Mexico. At least 36 major oil production platforms and 145 satellite wells were damaged including 35 structures completely toppled (Daniels, 1994). A reported 454 pipeline segments were damaged resulting in an estimated total spill of oil of 2,500 barrels. There was no loss of life offshore.

The experience of Hurricane Andrew provides an opportunity to quantitatively evaluate and gain better understanding of the structural response of offshore platforms to environmental loading. Such studies will be severely hampered, however, without reliable data on environmental conditions (sustained wind speed and peak gust, significant wave height, maximum wave height, maximum wave crest heights, storm surge and storm driven ocean currents) at each site affected. Unfortunately, there were few instrumental measurements made offshore of surface winds, waves, currents or surge within about 80 miles of the track of the center of Hurricane Andrew. The most critical requirement is for data in shallow water inside depths of about 60 meters. The objective of this study is to provide a comprehensive and reliable data base of environmental data in areas affected by Andrew, through the application of hindcast models which have not only been previously calibrated and validated against historical Gulf of Mexico hurricanes but which in this study are validated and, if necessary, recalibrated against all available data acquired in Andrew.

The study includes a substantial data assembly effort to ensure that all public domain measurements of surface wind, surface waves, storm surge and currents are identified and a data analysis effort to make those data sets deemed of value to the model calibration and validation available to the modelers in useable form.

The hindcasts were carried out basically by applying three numerical models. The first is a model of the wind field in the planetary boundary layer of a translating vortex embedded in a background flow (Cardone et al., 1976). This model has been used successfully to model historical tropical cyclones in prior studies (e.g. Forristall, Hamilton and Cardone, 1977) and has been recently substantially updated to allow the modeling of more complex storm wind field patterns (Thompson and Cardone, 1994). The second model is a third-generation (3G) spectral ocean wave model adapted to the Gulf of Mexico on a grid of 10 km spacing. Since the introduction of the 3-G WAM

model (WAMDI Group, 1988) 3-G type models have been adopted at several centers (e.g. ECMWF, FNOC, NMC) for global wave analysis and forecasting. The 3-G model applied here (Khandekar, Lalbeharry and Cardone, 1994) is Oceanweather's adaptation of WAM, which was tuned and validated in part against wave measurements in historical Gulf of Mexico hurricanes Camille (1969) and Frederic (1979). The third model applied is a three-dimensional hydrodynamic model (Keen and Slingerland, 1993a) which has also been previously applied to Gulf of Mexico hurricanes.

This report is organized as follows. Section 2 gives a general summary of the data collection and analysis effort. A complete report on this phase of the study is included as Appendix A. Section 3 describes the methodology used to specify the time history of the surface wind field in Andrew on the grid system used for the wave and hydrodynamic models and gives an overview of the wind field itself. The wave hindcast is described in Section 4 and the current modeling results are given in Section 5. In each of the above sections, comparisons between measured data and hindcasts are also given. Hindcast results are also provided in computer readable form. Section 6 contains the study summary and conclusions.

2. Data

2.1 Introduction

This section provides a summary of the data sources available during Andrew in the northern Gulf of Mexico and the data acquired and processed for this study. A complete data report is included as Appendix A, which includes many plots of time histories of measured winds, sea states and currents at various sites. The measured data files themselves for the 10-day window encompassing Hurricane Andrew are included on the CD-ROM provided with this report.

The hindcast analysis of Hurricane Andrew is dependent on the acquisition and subsequent analysis of measured meteorological and oceanographic data in basically two ways. First, the data are used to provide initial and/or boundary conditions for the models themselves. For example, the meteorological data are used to specify the storm track and the time history of the parameters needed to drive the wind field model. The hydrographic data help specify the initial distributions of temperature and salinity in the hindcast area. Second, measured data are used to either validate the results of the model or to fine tune parameters or physical mechanisms, usually those which model the frictional stresses at the sea surface and along the bottom or the turbulent structure of the water column.

Several reports documenting Andrew's meteorological and oceanographic conditions have been published using data readily available from coastal measurement sites and/or transmitting buoys or oil platforms. These include studies by Breaker et al. (1994), Stone et al. (1994) and DiMarco et al. (1994) which have concentrated on the surface observations. The present study concentrates primarily on the analysis of both the surface and subsurface parameters. These parameters are used in the development of the extreme wind, wave, storm tide and current velocity over the entire region affected by Andrew through the use of the hindcast models. Selected data sets from the earlier studies have been incorporated herein when they have provided useful results for the above objective.

Due to the considerable marine activity in the Gulf of Mexico, various government and industry data collection programs were in progress during Andrew's transit. The Minerals Management Service's LATEX Physical Oceanographic program was by far the most extensive of these measurement programs and has provided considerable data which can be used in the hindcast analysis of the wind, wave, storm tide and current velocity as well as for the

initial hydrographic conditions. Other data acquisition programs include the National Data Buoy Center's (NDBC) C-MAN measurements both on the coast and on oil platforms, the National Ocean Service's coastal tide gauge installations, the Army Corps of Engineers' (WES/COE) coastal wave measurement program on oil platforms, the National Hurricane Center's (NHC) and the Reserve Air Force's reconnaissance aircraft flights, the oil industry's measurements on selected platforms, especially Shell's Bullwinkle structure. These measurement sites are shown in Figure 2.1 which also shows Andrew's track.

2.2 Meteorological Data

Table 2.1 summarizes the locations, sensor elevations and averaging intervals at the measurement sites described in the following sections. In addition to these fixed sites, daily reconnaissance flights were made into and around Hurricane Andrew as it crossed the Gulf of Mexico collecting pressure, temperature and upper level wind data as well as eye shape and diameter observations by Air Force and NOAA personnel. These data have been collated at the National Hurricane Center in Coral Gables and at the National Hurricane Research Division of the Atlantic Meteorological and Oceanographic Laboratory of NOAA, and were obtained on magnetic tape for this study (these data are not contained on the CD). The use of the aircraft data is described in more detail in Section 3.

2.2.1 NDBC Buoy, Oil Platforms and C-MAN

Wind velocity and barometric pressure data were observed at NDBC buoys, oil production platforms, and C-MAN stations along the coast. Air and sea temperature were also recorded at the buoys and C-MAN locations. The location of these measurement sites are given in Figure 2.1 and Table 2.1 Some parameters are missing due to sensor failure and some records are truncated due to system failure. A description of the NDBC buoys used in this study is given in Gilhousen et. al. (1990). The data for Hurricane Andrew were obtained from the National Oceanographic Data Center in Washington, D.C.

The C-MAN data are also acquired by NDBC and the instrumentation systems are described in detail in Coastal-Marine Automated Network (C-MAN) Users Guide (NDBC, 1992). C-MAN stations are generally located in relatively shallow water near the coast located on aids-to-navigation structures or other existing platforms. Instrumented oil platforms are usually privately installed and maintained on existing platforms in deeper water than the C-MAN stations, but much shallower water than the NDBC buoys.

Meteorological and oceanographic data were also acquired during Hurricane Andrew from two oil platforms which were part of a joint oil industry and NDBC project called the Meteorological and Oceanographic Measurement System (MOMS). Shell's Bullwinkle platform (40 nm southwest) and Exxon's Lena platform (60 nm northeast) were the two closest MOMS structures to Andrew (see Figure 2.1). Only barometric pressure and wind speed were reported at the Lena platform. Meteorological data was also reported for Chevron's Garden Bank 236A platform, considerably west (125 nm) of the hurricane track. The measurements are useful for peripheral values of wind barometric pressure and wind speed which are used in the formulation of the model hurricane wind field. These data were reported as part of the C-MAN program in near real time during the hurricane. All platforms were just beyond the edge of the continental shelf. Meteorological data were also acquired at the Grand Isle C-MAN station as reported by Breaker et. al. (1994, in progress). Locations are given in Table 2.1. The reported minimum pressure and maximum wind speed and associated direction are given in Table 2.2. In this table all wind speeds are reduced to 10 m height using a 1/7th power law.

2.2.2 MMS/LATEX

There were three LATEX meteorological buoy mooring sites (17, 19 and 53) located in the path of Hurricane Andrew as shown in Figure 2.1. However, the meteorological buoy at mooring 53 and three others in the western Gulf were removed to decrease the possibility of considerable mooring losses during the hurricane season. The hurricane eye passed over mooring 53's normal location. The hurricane passed very close to the met buoy at LATEX mooring 17 where both wind velocity, barometric pressure and temperature data were recorded. The anemometer on mooring 17, located 30 nm to the west of the track, was lost prior to Andrew's arrival; however sea level pressure was recorded. At mooring 19, located 55 nm to the west of the track, both wind velocity and pressure were recorded. Storm peak data for moorings 17 and 19 are included in Table 2.2.

2.2.3 Other Measurements

Maximum 1-minute average and peak surface wind speeds were recorded at Ship Shoal 198G, East Cameron 83H and 42B and South Marsh Island 136B (Rappaport, 1992) and pressure and wind speed at Grand Isle Coast Guard Station (Breaker et al., 1994). Time histories of these data were not obtained. Maximum wind speeds are included in Table 2.2.

2.3 Hydrographic Data

The water mass distribution in that part of the Gulf where Andrew crossed the continental was sampled in a LATEX hydrographic cruise several weeks earlier. Both ADCP and CTD data had been acquired. The locations of the hydrographic stations are shown in Figure 2.2. The potential temperature and salinity data were acquired in both synoptic and time series measurements. The effect of the hurricane was to mix the water column, thereby reducing the surface potential temperature and increasing the salinity. At the bottom over the shelf, the mixing process was reversed, although the change in these two parameters was considerably less. At mooring 13, which was very close to the hurricane track, inertial oscillations were set-up at both the middle (100 m) and bottom (190 m) meter depths. These oscillations started a day after the hurricane passed through the site and lasted for 5 to 6 days. These oscillations were not as developed in shallower water (47 m) at mooring 14 and lasted only 1 to 2 days.

The synoptic hydrographic data, acquired about a week before Andrew's transit were used to initialize the boundary conditions in the current velocity model. Figure 2.3, for example, indicates the cross-shelf temperature distribution. The time series measurements were used to verify the temperature and salinity changes at discrete locations and depths.

2.4 Water Elevation

Storm water elevations over the continental shelf and along the coast are used to assist in the verification/calibration of the numerical-hydrodynamic current and storm tide model as well as in the computation of the hindcast wave parameters in shallow water. The NOS gauges along the coast acquired these data; however, offshore measurements are more suitable to the verification of the model as applied to the continental shelf.

2.4.1 Corps of Engineers

Three U. S. Army Corps of Engineers' wave pressure gauges were installed in water depths from 11.3 to 12.2 meters. These gauges sites and data status are shown in Table 2.3. Only the Eugene Island 100 data were processed in this project as the other gauges were either too far away or too much data was missing. The pressure gauge records from Eugene Island 100 were analyzed to determine the mean water elevation every three hours. As Hurricane Andrew approached the measurement site, the gauge began to malfunction intermittently, missing the more intense part of the hurricane which passed

through the area at about 0600 GMT on August 26th. There is a 12-hour data gap from 0220 GMT to 1420 GMT, thus the observations missed the peak water elevation. Due the gaps in the record, the water elevations were not detided. Note that the initial drop in storm water elevation below mean sea level is most likely due to the offshore winds before the hurricane approached the site plus the relatively shallow water depths.

2.4.2 NDBC Buoy and C-MAN

There are obviously no water elevations from the buoys. For the coastal C-MAN and NOS stations, the water elevation records were analyzed by Breaker et. al., (1994) and shown here as Figure 2.4. At Grand Isle the maximum storm surge was 1.11 m above MLLW and the maximum water elevation was 1.16 m. These were the largest measured values reported west of the Mississippi Delta.

2.4.3 MMS/LATEX

Water elevation data was available from the LATEX pressure gauge at mooring 16 which was located near the hurricane track. Although the pressure gauge tipped over during the hurricane, it was possible to account for this depth change and to use the entire record. The location of mooring 16 is shown in Figure 2.2. Note that other water level data was measured at LATEX sites (20, 23 and 1) further west; however, these were too far away to provide useful information for the hurricane model calibration.

LATEX mooring 16 pressure gauge operated throughout the hurricane including the period when the Minispec frame turned on its side. The change in the water depth was easily determined by comparing the mean depth of the gauge before the hurricane with the mean depth after the hurricane. Using a period of record of 60 days, a harmonic analysis was performed on the measured data to determine the tidal constituents. These constituents were then used to determine the tidal heights relative to mean sea level for the 10-day period centered on the storm. The tidal heights were then subtracted from the measured water elevations to give the peak storm water elevation or storm tide which was 68.5 cm. Time histories of the measured, tidal and detided water levels are shown in Figure 2.5.

2.5 Wave Measurements

2.5.1 NDBC Buoy and C-MAN

The NDBC buoys 42001 and 42003 provided complete wave time series but

were located on the weaker side of the hurricane (south of the hurricane track) . Buoy 42001 was considerably south of the hurricane track (125 nm) and the wave heights were dominated by the long period swell which arrived before the hurricanes had generated the maximum local sea conditions. The largest significant height was 4.4 m with a 10.9 sec spectral period. The significant wave heights were computed from the wave spectra. Buoy 42003 was considerably closer to the hurricane track (25 nm) and the maximum significant wave height was 6.2 m with a spectral period of 9.0 sec. The wave direction was from the east-northeast and rapidly shifted to the northwest as the hurricane passed by.

Of the two C-MAN stations located on oil platforms, the Bullwinkle location was relatively close to the hurricane track (45 nm southwest of the track) and thus provided good wave measurements. At the Shell Bullwinkle platform the wave heights increased to 7.9 m and wave period was 9.8 sec.

2.5.2 Corps of Engineers

Wave data were also recorded at the three instrumented platforms where water levels were measured (Table 2.3). However, the only nearly complete data set is at Eugene Island 100, which was located a few miles in the lee of a relatively shallow shoal (3 to 4 m deep) to the east through southeast, thereby limiting the wave heights by the breaking wave criteria. The pressure gauge provided intermittent data during the peak of Hurricane Andrew's transit through this area; therefore, the maximum significant wave height of 3.0 m at may not be the highest that occurred.

2.5.3 MMS/LATEX

Measured wave height data were obtained from LATEX mooring 16 which was about 20 nm northeast of the track at the closest point. A Coastal Leasing Inc. MimiSpec PUV type gauge was installed at this location. The mean water depth of the pressure gauge was 17.63 m before the pressure gauge housing turned over and 18.81 m thereafter. The pressure and current velocity data were used to obtain the directional wave spectra until it was overturned by Andrew. However, the pressure gauge continued to operate correctly thereafter and the non-directional wave spectra could be obtained from these data. Mooring 17, about 25 miles west of the hurricane track was not installed at this time.

LATEX mooring 16 was potentially in the direct path of the largest waves associated with Hurricane Andrew at the water depth of the site, since the

station is located just beyond the radius of maximum wind speed. Subsequent to the measurement of the waves in Hurricane Andrew, the MiniSpec was determined to have a number of problems including electronic noise, signal clipping, warm-up transients, and the lack of calibration for temperature effects. These problems were addressed by LATEX personnel (Kelly et. al., 1993) to reconstruct the wave measurements during Andrew as best possible. The tide mode (averaged) data remains questionable. The pressure data during Andrew has been corrected for these problems and verified by computing the wave heights using independent means, using both the pressure spectrum and the velocity spectrum. The overturning problem did not appear to present a problem to the wave analysis, except that the wave heights could no longer be constructed using the velocity spectrum after that event, just from the pressure spectrum.

The results of the wave data analysis are provided in Figure 2.6 for the 48-period encompassing the maximum wave height at mooring 16. These results were produced by the LATEX Data Management Office (DiMarco et. al., 1994, in progress) after the measured data had been thought to have been corrected for the above problems. The details of the analysis are contained in that study. The surface directional wave spectra were developed using linear wave theory to convert the pressure measurements to a surface wave spectrum. DiMarco et al. (1994) qualified the results in Figure 2.6 noting that the "energy seen in the 5-7 second period band can be attributed to nonlinear wave-wave interaction of the longer wave periods of 10-14 seconds" and that the "measurements should be regarded only as a first approximation". According to their analysis the maximum significant wave occurred at 0100 GMT on August 26th had a height of 8.9 m and a peak period of 10.7 seconds. Several hours earlier, a peak period of 14.2 sec was observed with lower wave heights. These are the largest measured wave heights in Hurricane Andrew. Additional work is underway at Texas A & M (personal communication) to determine the correct wave energy in the high frequency end of the spectrum.

2.5 LATEX Current Velocity Data

The measured current velocity data represent the greatest source of information due to the extensive installation of the LATEX program. Only one current meter was lost during Andrew (at mooring 16) as the largest waves passed through this location and several other nearby meters were damaged or tangled with debris at some point in the hurricane. A total of 7 moorings (16 meters) were selected from the available data set of 31 moorings as having potentially useful current velocities for model calibration. These moorings are shown in Figure 2.2 and are also listed in Table 2.4. The dates were

selected in order to obtain 90-day records for tidal analysis. These LATEX moorings contained two meters in shallow water and three meters in water depths greater than 45 m. Vector averaging meters were used at the surface and in shallow water where wave contamination would be a problem.

The current meter measurements contain both wind-driven and tidal components in the records. These components must be separated into tidal and non-tidal components so that the non-tidal (wind plus inertial) can be quantitatively compared to the wind-driven current velocity model results.

There are two indigenous problems in analyzing the tidal signal in the northern Gulf of Mexico. First, the tidal currents are relatively weak compared to the mean, inertial and wind-driven currents. Second, the O_1 component of the tidal current has a period (25.8194 hrs) which is very close to the inertial period at the latitudes of the northern Gulf of Mexico. Table 2.5 shows how the period of the O_1 constituent compares to the inertial periods at selected latitudes and also the synodic time require to be able to separate these constituents.

Theoretically, with nearly all moorings being located south of 29 deg-N for record lengths greater than 42 days, the inertial currents should not be a problem. However, it appears that the wind currents rotate at periods near the inertial period which overlap the O_1 and K_1 constituent's period. Therefore a sufficiently long record is needed to minimize the influence of the inertial current.

In order to evaluate the interference of the inertial currents on the tidal current analysis, an 180-day record was analyzed using mooring 12 day in deep water at 28 deg-N. The record was broken into two subsets of 90-day intervals and the latter subset broken into two subsets of 45-day intervals. Hurricane Andrew measurements were in the second 90-day subset and then in the first of the 45-day subsets. The results are given in Table 2.6 for both the current velocity amplitude (speed) and phase (degrees) for the east-west and north-south components for the 5 largest constituents. The mean current over the record length and the fractional residual variance are also given, the latter being a measure of the current velocity attributed to non-tidal sources. A least-square, best-fit type of tidal analysis program was used to determine the tidal amplitudes and phase angles from the measurements.

The results in Table 2.6 show that the tidal current velocity is relatively very weak. Assuming that the 180-day record starting on 15 April,

1992 was sufficiently long that any inertial current would not be significant, then the fractional residual variance attributed to the non-tidal component is .99 and .98 for the E-W and N-S components, respectively (or .01 and .02 for the tidal components, respectively). For the two 90-day records starting 15 April, 1992 and 22 July, 1992 the same tidal current fractional residual variances have increased very slightly to .02 and .03 -.04, respectively. The increase in amplitude of the O_1 component occurred mainly in the record which included Hurricane Andrew. When this latter 90-day record starting on 22 July, 1992 was divided into two 45-day records, the presence of the inertial currents in Andrew was observed in the record containing Andrew, as it strongly increased the amplitudes of both the K_1 and O_1 components and thereby increased the fractional residual variance to .10 for both the E-W and N-S tidal current components. The 45-day record which did not contain Andrew was relatively unchanged.

The conclusion from the above analysis was that a 180-record (or longer) would probably be the best for the tidal analysis to minimize the influence of the inertial currents on the diurnal tidal components. However, in practice, this is very hard to obtain due to mooring/instrument malfunctions. A continuous 90-day record for the period encompassing Hurricane Andrew was found to be available for all but two meters (14 middle and 19 middle) and this period was used in the subsequent current velocity analysis to detide the measured current velocity record.

The results of the current velocity analysis at mooring 12 (surface meter) also show that the mean current varied considerable depending on the period of observation. For example, the 180-day record shows a very weak mean current. When broken into the two 90-day components, the mean current is shown to consist of a moderate current to the northeast for the first 90-days followed by an equally strong current to the west-southwest for 90-days. Finally, when this latter 90-day current was divided into two-45 day periods, the mean current in both records was still west-southwest, but with considerably different velocities. Therefore, the mean current is quite variable with time in response to external forcing. No seasonal patterns were investigated.

The results of the measured current velocity analysis are summarized in Table 2.7 by mooring with the order given by north to south orientation and in Table 2.8 by meter position on the mooring (top, middle and bottom). The surface tidal currents in shallow water have increased speeds relative to the deep water surface current meters as expected. Also, the moorings further to

the west (18 and 19) have stronger semi-diurnal components, especially in the north-south direction. Finally, the maximum values of the total, the tidal and the non-tidal currents have been summarized in Table 2.9.

3. Surface Wind Field Specification

3.1 Definition

The reference height and temporal average of the wind fields required to drive sophisticated wave and hydrodynamic models must be precisely defined. Most such models are forced by winds referred to an elevation of 10-m or 20-m above mean sea level. Unlike measured winds or estimated winds, which are subject to considerable variability depending on the time interval over which the observation is made (for example, gust, 1-minute sustained winds etc.), a wind field used to force an ocean response model is the equivalent of an averaging process taken over a time interval sufficiently long to include all temporal and spatial variations induced by turbulence, whether mechanically or convectively produced. Usually, 30-minutes to 1-hour is a sufficiently long interval to produce a stable average from an anemometer trace, and the analysis winds therefore are usually referred to as 30-minute or 1-hour average winds. In other words, as far as turbulent fluctuations are concerned, there should be no significant difference between these two averaging intervals, though in practice, because of secular changes in the wind field due to motion or intensity changes of weather systems, it is often difficult to recover a stationary 1-hour average wind from an anemometer at a fixed site.

Constant gust factors are usually invoked to transform the model based extremes of the 1-hour average wind to shorter averaging intervals, though more complicated gust factor models have been introduced in recent years. For tropical cyclone dominated wind regimes the following gust factors (Black, 1994) are recommended:

3-second/1-hour	1.50
1-minute/1-hour	1.25
10-minute/1-hour	1.09

3.2 Wind Field Analysis Methodology

The analysis method adopted recognizes and responds to the following special difficulties of the problem of specifying surface winds in tropical cyclones.

1. Actual measurements of surface winds over water in tropical cyclones, especially their inner cores, are rare, so analysis schemes based mainly on the synthesis and objective analysis of measured wind data (such as used

generally in extratropical regimes) are of limited value. Some progress has been made in synthesizing wind data from different sources such as coastal stations, buoys, C-MAN stations and aircraft into a kinematic analysis (e.g. Powell and Houston, 1993) but a critical data set is usually produced by compositing data acquired over many hours (6-12 hours) and usually is only possible when the storm is near a coast. For this study, wind fields are required at regular half-hourly time intervals throughout the northern half of the Gulf of Mexico and throughout its life history in the Gulf.

2. Because of 1, standard sources such as the wind field analyses produced in real-time at NWP centers or storm reports produced at forecast centers such as NHC cannot be relied upon to provide the required surface winds, though the later source provides useful data on storm track, eye pressure and overall storm structure as revealed by radar and satellite composites.

3. Simple parametric models of the surface wind field in tropical cyclones, which have been used for many years for research and forecasting, impose a relatively simple axially symmetric radial wind speed and inflow angle profile shape to all storms and model storm motion and asymmetry effects in very simple ways. However, real storms may depart considerably from the assumed parametric shapes and exhibit considerable variability in structure from storm to storm and even within the evolution of single storm.

The method used in this study has been applied in over three dozen studies involving almost all basins on the globe within which tropical cyclones can occur. The method starts from raw data whenever possible and includes an intensive reanalysis of traditional cyclone parameters such as track and intensity (in terms of pressure) and then develops new estimates of the more difficult storm parameters, such as the shape of the radial pressure profile and the ambient pressure field within which the cyclone is embedded. The time histories of all of these parameters are specified within the entire period to be hindcast. Storm track and storm parameters are then used to drive a numerical primitive equation model of the cyclone boundary layer to generate a complete picture of the time-varying wind field associated with the cyclone circulation itself. That solution is then compared to time histories of accurately measured surface winds (reduced to standard height) at available measurement sites, and if necessary the storm parameters are varied and the model iterated until good agreement is obtained between the modeled wind field and the discrete high-quality wind observations available.

3.2.1 Numerical Vortex PBL Model

This model, first developed into a practical tool in the Ocean Data Gathering Program (ODGP) (Cardone et al. 1976), was first developed to provide a complete description of the surface winds in the boundary layer of a tropical cyclone from the simple model parameters available in historical storms. The model is an application of a theoretical model of the horizontal air flow in the boundary layer of a moving vortex. That model solves, by numerical integration, the vertically averaged equations of motion that govern a boundary layer subject to horizontal and vertical shear stresses. The equations are resolved in a Cartesian coordinate system whose origin translates at constant velocity with the storm center of the pressure field associated with the cyclone. Variations in storm intensity and motion are represented by a series of quasi-steady state solutions. In the original practical implementation the model, the vertically integrated boundary layer wind was related to the surface wind using an empirical scaling law.

The original theoretical formulation of the model is given by Chow (1971). A similar model was described more recently in the open literature by Shapiro (1983). The version of the model applied is this study is the result two major upgrades, one described by Cardone et al., (1992) and the second by Cardone et al. (1994). The first upgrade involved mainly replacement of the empirical scaling law by a similarity boundary layer formulation to link the surface drag, surface wind and the model vertically averaged velocity components.

The second upgrade added spatial resolution and generalized the pressure field specification. A concise description of the theoretical formulation of the model and of its practical implementation in upgraded form is given by Thompson and Cardone (1994).

The model pressure field is described as the sum of an axially symmetric part, and a large-scale pressure field of constant gradient. The symmetric part is described in terms of an exponential pressure profile

$$\tilde{p} = p_0 + \Delta p \exp(-r_a/r)^{\mathrm{b}}$$

where p_0 is central pressure, Δp is storm anomaly and r_a is a scaling

radius nearly equivalent to the radius of maximum wind and b is an additional scaling parameter shown by Holland (1980) to be necessary to match a wide range of storm types.

The model is driven from parameters that are derived from data in historical meteorological records and the ambient pressure field, which is prescribed in terms of an equivalent geostrophic "steering" current. The entire wind field history is computed from knowledge of the variation of those parameters along the storm track by computing solutions, or so-called "snapshots", on the nested grid as often as is necessary to describe different stages of intensity, and then interpolating the entire time history from the snapshots.

The model was validated originally against winds measured in several ODGP storms (i.e. Gulf of Mexico storms Camille, 1969, Felice, 1970, Edith, 1971). It has since been applied to nearly every recent hurricane to affect the United States coast. Comparisons with over-water measurements from buoys and rigs support an accuracy specification (rms) of about ± 20 degrees in direction and about ± 2 meters/second in wind speed (1-hour average at 20-meter elevation) with most of these model verifications published in the open literature (see e. g., Ross and Cardone, 1978; Cardone and Ross, 1979; Forristall et al., 1977; 1978; 1980; Cardone et al., 1992).

As presently formulated, the wind model is free of arbitrary calibration constants which might link the model to a particular storm type or region. For example, differences in latitude are handled properly in the primitive equation formulation through the Coriolis parameter. The variations in structure between tropical storm types manifest themselves basically in the characteristics of the pressure field of the vortex itself and of the surrounding region. The interaction of a hurricane and its environment, therefore, (except near mountainous terrain and large discontinuities in surface roughness) can be accounted for by a proper specification of the input parameters. The assignable parameters of the planetary boundary layer (PBL) formulation such as planetary boundary layer depth and stability are functions mainly of air-sea temperature difference. The sea surface roughness formulation is taken from a standard over-water drag law.

3.2.2 Determination of Hurricane Andrew Model Parameter

Storm Track. The track of Andrew must be determined as precisely as possible for most applications because. Given the very small spatial scale of the wind field, errors of the order of the radius of maximum wind (as small as

7 miles in Andrew) induce large errors in the modeled winds, sea states and currents at specific locations of interest (e.g. measurement sites, damaged or toppled platforms etc.) even if the numerical models have modelled the distributions of wind, sea state and currents relative to the center perfectly. The most important data sources for track specification are aircraft, satellite and radar center fixes. Figure 3.1 shows the data gathering flight tracks through the circulation of Andrew and the center penetrations available from the many reconnaissance missions flown by US Air Force and NOAA aircraft into Andrew in the Gulf of Mexico. Figure 3.2 is an example of the flight level winds acquired in one US Air Force flight. Synoptic data from surface stations (ships, buoys, C-MAN and coastal stations) are of less use because the eye of the storm rarely passes over such sites. For example, Figure 3.3 shows the synoptic reports of surface wind and pressure measured from platforms, buoys, C-MAN stations and merchant ships data available as Andrew approached the continental shelf at 1200 UT 25 August. Note that there are no surface observations within 200 km of the center at this time. A complete set of plots is included in Appendix B.

The track of Andrew was determined subjectively using fix information from aircraft, satellite, radar (including on-board radar and National Weather Service radar sites at Slidel, Baton Rouge, Lake Charles, LA. and Houston, TX.), and synoptic fixes. The best track (6 hourly) as determined by the National Hurricane Center (NHC) was also used as a guide. Figure 3.4 shows these fixes and the NHC track. The fix data show a wide scatter about the NHC best track, with differences of up to 50 km in the waters just off the Louisiana coast. To reduce this scatter, the fix data were ranked in the following order: aircraft fixes, radar, satellite, then synoptic fixes. Aircraft fixes were further ranked by the accuracy of the fix as given in the flight report (detailed vortex message). Radar sites were also further ranked by distance from the site to the storm (closer sites were given a higher rank) and by the quality of the fix (poor, fair, good) as determined by the radar operator. All fix data were reported to the nearest tenth of a degree, except aircraft fixes, which are reported to the nearest minute. Satellite and synoptic fixes generally were not used over water due to their large scatter, but were used over land when aircraft fixes were not available.

Ranked fix data led to a greatly reduced scatter in the apparent track of Andrew. Figure 3.5 shows the adopted track. The amount of data available just off the Louisiana coast (from 25/18Z to 26/12Z) was sufficiently fine to determine an hourly track, as shown in Figure 3.6. A 3-hourly track was used for the rest of the hindcast period. The track just east of and over Florida was not given as rigorous treatment since this part of the storm history is

used mainly for model spin-up. The adopted track is very close to the 3-hourly track adopted in a preliminary hindcast study of Andrew carried out by Oceanweather in 1992 with small differences confined to the area of greater resolution in the hourly section of the new track.

Model Parameters. The vortex model is initialized for each solution or "snapshot" from the following parameters: latitude, forward storm motion (speed and direction), central pressure, scale radius of the exponential pressure profile, Holland's B parameter, the far-field pressure and magnitude and direction of the geostrophic wind associated with the ambient pressure field in which the storm is embedded. Table 3.1 shows the inputs ultimately adopted. During the period modeled, 12 snapshots were generated by the model, with intermediate windfields interpolated between the model solutions.

The forward motion of Andrew was calculated using the best track with no smoothing. Central pressure was determined almost exclusively by the vortex messages filed by reconnaissance aircraft. Figure 3.7 shows the central pressures adopted for each snapshot vs. the aircraft dropsonde values and the NHC adopted 6-hourly pressures. Note that since the model calculated snapshots are linearly interpolated in time to provide snapshots at intermediate times, the snap times are deliberately chosen such that the interpolated snapshots and windfields correctly represent the changes in storm intensity. Central pressures over land were mainly determined by synoptic fixes and satellite interpretation of Andrew. The far-field pressure and the steering flow (speed and direction) are determined from reanalyzed isobaric analyses of the pressure field surrounding Andrew. These parameters were determined every 6 hours, then smoothed over the entire hindcast period.

The radius of maximum winds was estimated initially from the aircraft reconnaissance data (as estimated from both the reported the eye diameter and the radial distributions of flight level winds on eyewall penetration flight legs as shown for example in Figure 3.8) on the assumption that the radius does not vary significantly from flight level to the surface. As the center approached shore, radar fixes reporting eye diameter were also used. Given trial values for central pressure, the far-field pressure, and the radius of maximum winds, the pressure profile of the azimuthally averaged vortex was evaluated using Oceanweather's PC-based Tropical System Analysis interactive graphical system. Figure 3.9 shows a typical screen image. Time series of reconnaissance information from aircraft is converted from absolute latitude/longitude coordinates to coordinates relative to the translating center using the best track interpolated to 1-minute intervals. The repositioned data are composited within +/- 3 hours of standard synoptic

times so that comparisons to conventional data are possible. The data distribution is shown in the window at the upper right hand part of the screen of Figure 3.9. Winds are converted from flight level to surface 20 meter winds using a simple reduction factor (Powell and Black, 1991) and displayed in the window at the upper left of the screen. Surface pressures are calculated using Jordan's (1958) relationship between 700 mb height and sea level pressure in cyclones and are plotted relative to the center as shown in the window on the lower half of the screen. The analyst then iterates the parameters of the pressure profile to arrive at a best fit. The pressure profile determined by the central pressure, far-field pressure, radius of maximum winds and Holland's B can then be directly compared with the estimated surface pressures from aircraft. The best fit parameters determined for each composite in this manner are then smoothed over the entire hindcast period. All fits are included in Appendix C. Note that nominal central pressure used in the model does not always match the fitted central pressure due to the time differential and errors in the pressure reduction relationship.

3.3 Wind Field and Data Comparisons

The computed wind fields are shown in the form of wind barb plots at three hourly intervals in Appendix D. Andrew emerged off the west coast of south Florida as a small intense vortex, with central pressure of about 950 mb with radius of maximum winds of less than 10 miles. As Andrew moved toward the upper Gulf coast, the forward motion slowed from 18 knots to about 10 knots, eyewall radius expanded to about 16 nm and the central pressure lowered to 936 mb.

Figure 3.10 shows the wind field just before the center crossed the shelf break. The winds plotted are effective 1-hour average wind speeds at 20 m height. A finer view of the wind field at this time is given in Figure 3.11 (see Appendix E for additional plots at this resolution), which shows the winds plotted at 1/4th the resolution actually used for the ocean response hindcasts; that is, winds are plotted at every other row and column of the grid. The maximum surface winds at this time were close to 50 m/s in a small area of the front and right quadrants relative to storm motion.

The comparisons of the calculated wind fields and the modeled wind fields at high-quality measurement sites are shown in Figure 3.12 - 3.19. For these comparisons, wind speeds are reduced to 20 m height using the surface boundary layer model of Cardone et al. (1991) which uses a wind profile model consistent with that used in the vortex model. At buoy 42003, the time histories of wind speed and direction are generally well simulated. The

maximum model wind speed of 29 m/s is about 3 m/s greater than the maximum buoy wind speed though the buoy may have not sampled the absolute maximum wind speed at this site. At buoy 42001, which was further away from the center of Andrew, both buoy and model wind speeds peak at about 12 m/s with good agreement in wind direction. At buoy 42007 located far to the right of the track, the maximum wind speed of 16 m/s is well matched by the model with a slight lag. Model wind direction is turned clockwise by about 15 degrees from the buoy wind for most of the history. This may be attributable to the over-land trajectory of the air reaching the buoy for the indicated wind directions. The vortex model does not include a fetch-dependence in adjustment of the boundary layer flow downwind of the land-water discontinuity but instead adjusts the flow to over-water exposure immediately.

The comparisons of modelled and measured winds at Bullwinkle and Lena platforms show somewhat larger differences in wind speed near the times of closest storm approach than exhibited at the buoys. At Bullwinkle, which is located left of the track, the modeled winds are 2-4 m/s greater than the adjusted measured winds. At Lena, the model winds are 2-4 m/s lower than the measured winds within about 6 hours of the closest approach. It is difficult to judge to what extent these differences represent systematic effects in the modeled wind fields or to the platform winds which are also susceptible of systematic effects.

The measured winds at the C-MAN stations near the coast (BURL1, GDIL1, DPIA1) are probably affected by the upwind over-land trajectory of the air flow, especially at GDIL1 and BURL1. This is the most likely explanation for the tendency for the modelled wind speeds to average from 2-4 m/s greater than the measured wind speeds at the C-MAN stations while wind directions agree closely.

Overall, the agreement between measured and modeled winds in Andrew is comparable to that found in other Gulf of Mexico storms modeled this way. Taken over all sites (except the probably sheltered nearshore C-MAN stations) the mean and standard deviation of the wind speed differences are .22 m/s and 2.3 m/s respectively (see Figure 3.20). At least part of this difference may be attributable to small scale effects in the wind fields (e.g. rain band disturbances) not modelled and to systematic errors in the measurements themselves.

4. Wave Hindcast

4.1 Background

The wave hindcast model adapted for this study is a so-called fully-discrete spectral wave model. That is, the wave spectrum is resolved in discrete frequency-direction bins, a grid of points is laid out to represent the basin of interest, and a solution is obtained based upon integration of the spectral energy balance equation, a process which successively simulates, at each model grid point, and for each time step, the physical processes of wave growth and dissipation (through the source terms of the energy balance) and wave propagation.

Three classes of spectral models are generally recognized. First-generation models (1G), such as the ODGP model (Cardone, Pierson, and Ward, 1976), are part of the family of fully-discrete spectral models originally proposed by Pierson, Tick, and Baer (1966). This type of model is characterized by a source-term formulation which does not include an explicit representation of conservative transfers of energy between spectral components, believed to be associated with resonant non-linear wave-wave interactions. Second-generation models (2G) were introduced to include at least a parametric representation of a wave-wave interaction source term, while third-generation (3G) models, originally introduced as the WAM model (WAMDI Group, 1988) attempt to model the wave-wave interaction source term rigorously.

The formulation of the ODGP model, which we shall henceforth call OWI1G, has been described in detail in past studies. The skill of the model has also been documented in numerous studies, including Reece and Cardone (1982), Cardone and Greenwood (1987), and most recently in Cardone et al. (1994a) wherein the skill of the model in extreme events is compared to that of recent 2G and 3G models. This latter study (as well as a number of unpublished recent studies) suggest that the differences in skill between OWI1G and the WAM model are subtle in most wave regimes, and usually the differences are masked by wind errors. A 3G model requires about an order of magnitude more computer time than the 1G model for a given spectral and spatial resolution. OWI1G was in fact first developed for Gulf of Mexico hurricane modeling and has already been applied to hindcast hurricane Andrew in a previous study (Oceanweather, 1992). In this study Oceanweather's adaptation of the 3G model, henceforth OWI3G, is adapted to the Gulf of Mexico on a grid of about 10 km spacing.

4.2 Wave Model Specifications

Grid System

The grid system is a latitude-longitude array as shown in Figure 4.1, with the southwest corner of the grid at 23.938N, 94.940W, with spacing of 0.1022 deg in latitude and 0.1150 in longitude.

Spectral Resolution

Direction: 24 bands. Band 1 is centered 7.5° clockwise from true north, the width of each band is 15°

Frequency: Band 1 is centered on 0.039 hz; the bands increase in geometric progression (ratio = 1.10064) to band 23, .32157 hz. This binning is negligibly coarser than used in WAM (ratio = 1.100).

Propagation Scheme

The downstream interpolation scheme described by Greenwood et al.(1985) is used throughout. Propagation over a time step at a grid point is implemented within the alternate growth-propagation cycle in the model integration by forming linear combinations of spectral variances at neighboring points. The weights used are extracted from a precomputed table of propagation coefficients, which vary by latitude only in deep water, and are specific to each grid point in shallow water. The table of interpolation coefficients is calculated based upon great circle wave ray paths in deep water; in shallow water the weights are calculated following a ray tracing study through a digital bathymetry resolved on the wave model grid.

The water depth at each grid point was computed as a simple average of all depths at 5-minute intervals within the grid domain contained in the U. S. National Geophysical Data Center (NGDC) ETOPO5 global topographic-bathymetric digital data base. The version of ETOPO5 obtained by Oceanweather (circa 1988) contained erroneous data in areas of steep gradients and has been corrected in previous studies by reading off depths at 5-minute intervals directly from hydrographic charts covering the areas affected. Figure 4.2 shows the depth field over the whole domain of the model, and Figures 4.3-4.5 show the depth field contours for specific regions.

The limiting water depth for shallow propagation and growth processes is taken according to the conventional definition:

$kd > \pi$, where k = .006123 m^{-1} for the .039 hz frequency bin. Thus, propagation by depth-dependent ray tracing is executed at points within 20 km in any direction of points with depths 513 m or less.

OWI3G Spectral Growth/Dissipation Algorithm.

The theoretical basis of the spectral growth algorithm used in OWI3G follows closely that of the first 3G model developed during the 1980's through the efforts of an international panel of wave modelers, (including Cardone and Greenwood of Oceanweather) known as the WAM group. The WAM model was originally described by WAMDI Group (1988). In WAM, separate source terms for the physical mechanisms of atmospheric input, S_{in}, wave-wave interaction, S_{nl}, and dissipation by whitecapping, S_{ds}, (and in shallow water dissipation by bottom friction, S_b) are specified explicitly and the source term balance is integrated to yield the net development of the spectrum over a time step of integration without arbitrarily forcing of spectral shape or specification of an external limit to growth. However, in the original development of the model, considerable experimentation with and tuning of the input and dissipation source terms was carried out to achieve growth rates and asymptotic behavior under constant winds in agreement with field data. The wave-wave interaction "apparent" source term, S_{nl}, is not considered tunable and is a parameterization of the exact nonlinear interactions as proposed (see e.g. Hasselmann and Hasselmann, 1985). This so-called Discrete Interaction Approximation (DIA) is also described in WAMDI Group (1988).

OWI3G combines a source term representation and integration scheme based upon WAM with the propagation scheme used in OWI1G. The source terms follow the theoretical forms used in WAM but with different numerics and code and with the following modifications. First, a linear excitation source term is added to S_{in}, taken as a downscaled variant of the term used in ODGP. This allows the sea to grow from a flat calm initial condition in OWI3G, unlike all cycles of WAM which require an artificial warm start from a prescribed initial spectrum. The exponential input term is the empirical form of Snyder et al. (1981) in which S_{in} is taken as a linear function of friction velocity U_*. However, unlike WAM in which U_* is computed from the 10 meter wind speed U_{10} following the drag law of Wu (1982), in OWI3G, a different drag law is used developed in the model tuning stage. That drag law follows Wu closely up to about 20 m/sec then becomes asymptotic to a constant at hurricane wind speeds. The dissipation source term, S_{ds} is also taken from WAM except that the dependence on frequency is cubic rather than quadratic. Finally, for S_{nl}, the DIA is adopted except that two modes of interaction are included (in WAMDI the

second mode is ignored).

Oceanweather's version of 3G as just described was developed based upon tuning runs against the fetch-limited growth benchmark for 20 m/s wind speeds under constant winds used to tune WAMDI initially, as well as in repeated trial hindcasts of a well-documented moderate extratropical cyclone (SWADE IOP-1, see Cardone et al., 1994b) and two intense Gulf of Mexico hurricanes (Camille, 1969; Frederic, 1979). The bottom friction source term is a simple quadratic law with a specified tunable friction factor. OWI3G uses the same friction factor found in the North Sea version of WAM (NEDWAM) to yield skillful shallow water predictions. That factor, .076, is exactly twice the value originally proposed for WAM, which was based upon studies of pure swell attenuation in the North Sea JONSWAP experiment. An interesting comparison of the performance of OWI1G and OWI3G in an extratropical setting is given by Khandekar, Lalbeharry and Cardone (1994) which also further documents OWI3G.

4.3 Prior Validation of OWI3G Wave Model

The wave model selected for this study is relatively new and the relatively few wave measurements available near the center of Andrew provide only limited opportunity to validate the Andrew OWI3G hindcast. Therefore, it is useful to summmarize in this section several recent studies, some as yet unpublished, in which OWI3G has been validated, especially studies involving extreme wind forcing.

It is difficult to separate the validation of a wave model from the validation of the underlying wind fields. While the differential properties of alternative wave hindcasts driven by a common wind field reflect mainly differences in the wave model growth/dissipation physics, the absolute level of the skill in the wave hindcasts with OWI's family of models appears to be mainly determined by errors in the wind fields (e.g. Cardone and Szabo, 1985; Cardone et al., 1994b).

The OWI family of wave models have already undergone extensive previous validation with far more validation for OWI1G than OWI3G. For example, in the original ODGP program, OWI1G hindcasts of significant wave height, HS, spectral peak period, TP, and frequency spectra, were compared to measurements acquired at offshore platforms in five Gulf of Mexico hurricanes, including hurricane Camille. Since then, the model has been applied to many storms to affect the U.S. Gulf and East Coast coasts including Eloise and Belle (Cardone and Ross, 1979). Hindcast and measured directional spectra were evaluated in Eloise and Delia by Forristall et. al (1978, 1980). The model

skill in specification of peak storm HS and associated TP at a site in a storm was evaluated by Reece and Cardone (1982) for hindcasts made in four different types of meteorological systems (including tropical and extratropical systems) in three different basins. In over 60 individual comparisons in 19 different storms, the model hindcasts exhibited negligible bias (less than 0.5 m in HS), and rms errors of less than 1 meter in HS and 1 second in TP.

A popular index of skill used by wave modelers is the scatter index, which is defined as the rms error (or alternatively by the standard deviation of the model-measured differences) divided by the mean of the data in the measurement data set used for the validation, expressed in percent. For the data of Reece and Cardone the scatter index in HS is 11.8%. OWI1G has been shown, with a stable calibration (unlike many models which are retuned with each application) to consistently provide a scatter index in storm peak HS and TP in the range of 10-15%, wherever applied, as long as wind fields are accurately specified. For example, Swail et. al (1991) report a scatter index of 12.1% in HS and 11.3% in TP for hindcasts of severe storms off the west coast of Canada. Cardone and Ewans (1992) report scatter index of only 9% in HS and TP in hindcasts of severe storms off the west coast of New Zealand. Comparable skill has been demonstrated in major validation studies conducted in recent years as part of proprietary industry sponsored studies of tropical cyclone generated waves in the Gulf of Mexico, the Taiwan Straits, and parts of the South China Sea.

OWI3G, and the WAMDI model upon which it is based, have also been applied in a number of recent model validation studies specifically involving Gulf of Mexico hurricanes. In WAMDI Group (1988), for example, the WAM model was tested against hurricanes Camille (1969), Anita (1975) and Frederic (1979) and was found to be essentially as skillful as OWI1G in specification of HS, TP and frequency spectra. OWI3G was also applied to Camille and Frederic, which formed part of the model tuning set of test cases. Figure 4.6 compares the hindcast and measured time histories of HS in Camille at ODGP stations 1 and 2 offshore Louisiana. Figure 4.7 compares the hindcast and measured peak frequency spectra. These latter comparisons suggest slightly greater skill for OWI3G than OWI1G in specification of the TP and spectral shape. Figure 4.8 compares hindcast and measured HS time histories in hurricane Frederic at buoy 42003 and at the deep water Cognac platform offshore Mississippi. Directional wave measurements were also available at Cognac. Figure 4.9 compares the hindcast and measured frequency spectra and frequency distribution of mean wave direction. Agreement is excellent and significantly improved over the agreement achieved with OWI1G and early cycles of WAM in this case (WAMDI Group, 1988). Figure 4.10 shows a comparison of frequency spectra at 42003 in

Frederic for a time step when the total variances match closely.

OWI3G has also been applied to extratropical storms. The most indicative case of wave model skill is SWADE IOP-1 (Cardone et al., 1994b), because the wind field was specified in that case with unprecedented accuracy for an open sea scenario. During SWADE-IOP1, a series of moderately intense storms moved off the US East Coast and were sampled in a greatly enhanced array of moored buoys. Figures 4.11 - 4.14 compare OWI3G hindcast and buoy HS and TP at deep water buoys (OWI3G was run in a deep water mode for the SWADE IOP-1 hindcast). After a 72-hour period of model spinup the hindcast is exceptionally skillful and exhibits scatter indices in HS and TP which varies between 10-15% over the buoys shown.

OWI3G has been recently applied to two extreme US East Coast storms (Cardone et al., 1994a), namely the Halloween Storm of October 31, 1991 and the "Storm of the Century" of March 13, 1993. The scatter index in storm peak HS for OWI3G averaged over 9 buoys was 14% in the first storm and 10% in the second storm. The corresponding statistics for OWI1G, also applied in that study, were 14% and 15% respectively. Khandekar et al. (1994) investigated skill in OWI1G and OWI3G (as adapted in the Canadian CSOWM wave model) in a much gentler wave regime over a two week period and find the two models to be skillful and virtually comparable in performance with rms errors in time series of HS of .6 m and in TP of about 2 seconds. The scatter index is 19% in HS, higher than reported above for peak-peak comparisons because the mean of the measured data for time series (about 3 m) is less than half the level of data of storm peaks.

4.4 Andrew Wave Hindcast

4.4.1 Wave Model Input and Output

Input. OWI3G is driven by the time history of surface wind speed and direction (1-hour average at 20 m) at 30-minute intervals. The calculation of friction velocity, U_*, from U_{20} uses an empirical drag law reached by tuning OWI3G as noted above. The hindcast duration depends upon where the storm enters the grid, and the storm speed of propagation. The duration is long enough to ensure that the wave (and current) response is fully spun-up (i.e. lost memory of the cold model start) before peak conditions are specified in all areas of interest in the basin, and also spun-up in source regions of swell which eventually propagate to areas of interest. The hindcast began at 0900 UT August 24, 1992 as Andrew was entering the east coast of South Florida, and continued to 0000 UT August 27, 1992 about 12 hours after the

center crossed the Louisiana coast. A total of 128 wind field were supplied to the model for the hindcast.

Output. There are three output files of a hindcast run.

1. 1-line Summary Print File. This is a printable-only file of summary output at selected grid points (1-line per point per time step) at either 30-minute or hourly intervals. This file was used mainly to print results at a few points for quick-look and checking purposes.

2. Fields File. This is a permanent archive digital file of the 17 wave "fields" variables listed in Table 4.1 saved at 30-minute intervals. This file contains results at all grid points.

3. Spectra. This file contains the full two-dimensional spectrum at hourly intervals. Since this is by far the most voluminous data file, it was typically restricted to a relatively small subset of points.

These files are made as follows within the fractional growth and propagation steps which comprise the numerical solution:

15 minutes growth
30 minutes propagation
15 minutes growth
intermediate print of 1-line summary
15 minutes growth
30 minutes propagation
15 minutes growth
print 1-line summary
archive fields
archive spectra

4.4.2 Evolution of the Wave Field

The general evolution of the wave field is shown in the series of plots at three-hourly intervals which display contours of HS and unit length vectors in the direction of the vector mean wave direction, VMD. Figure 4.15 shows the HS/VMD pattern as Andrew's crossed the shelf break. The complete set of plots is included in Appendix F. As Andrew entered the Gulf from Florida, HS increased rapidly near the center to about 8 m within the first 9 hours in the Gulf at around 2100 UT 24 August. By 0600 UT, 25 August, peak HS had increased to 10 m and a pattern of radiated swell to the left and rear

quadrants was established in the VMD pattern. Between 1500 UT 25 August and 2000 UT August 25, the wave height pattern about the storm expanded and the peak hindcast HS exceeded 13 m, reaching an absolute peak of 13.47 m at grid point 4494 at 2000 UT 25 August, with associated TP of 14.12 seconds and associated wind speed of 47.5 m/s. The maximum HS hindcast just to the right of the eye began to decrease fairly rapidly after 2100 UT 25 August in response both to the filling of the storm even before the eye reached land (see Figure 3.7) and the effects of shallow water.

4.4.3 Model - Data Comparisons.

There are only four sites at which meaningful comparisons of hindcast and measured sea states are possible: buoys 42003 and 42001, Bullwinkle platform and LATEX station 16. Other available sites were either too far away from the storm or so close to the coast as to be within 1 model grid spacing of land. The comparisons between hindcast and measured HS and TP at these stations are shown in Figures 4.16 - 4.19. For these comparisons the hindcast series were taken from the grid point nearest the measurement site.

At buoy 42003, the first site to encounter the storm, the buildup and decay of HS are very well simulated and the peak hindcast and measured HS differ by less than 0.5 m. The TP series agree well overall, except for the single buoy estimate near the peak HS of 17 seconds, at which time the hindcast TP is about 12 seconds. It is quite possible that because the hindcast only had about 24 hours of spin-up time at the time of closest storm approach to 42003, that the hindcast spectrum is still deficient in low frequency energy but only slightly so, because the agreement in total energy is quite good. Another factor contributing to the difference may be the relatively low resolution of TP in the buoy spectra. At buoy 42001, as shown in Figure 4.17, the peak hindcast and measured HS agree closely though there is a lag of three hours in the hindcast time of occurrence of the peak. This peak is contributed mainly by swell emanating from the central part of the storm, as indicated by the very long period associated the peak. The arrival of this swell energy is indicated in both the hindcast and measured time series as the abrupt increase of TP at around 0900 UT August 25.

At Bullwinkle, as shown in Figure 4.18, the hindcast time series agrees well with the measurements except that the hindcast HS is between 0.5 and 1.0 m higher than the measured HS within about 6 hours of the occurrence of the peak energy. Only zero-crossing energy, TZ, is available at Bullwinkle. The model derived TZ, which is computed from the zeroth and second spectral moments, are at times up to 1.7 seconds lower than measured, suggesting again

that there may be a small deficiency of low frequency energy in the hindcast spectra in the southwest quadrant of the storm.

LATEX station 16 potentially is the most interesting and valuable comparison site because the eye passed very close to this station, and the water depth is in a range where shallow water physics plays a significant role. Unfortunately, there is as yet no definitive analysis of the measured data from the bottom mounted pressure transducer, and estimates of wave height and period published to date have varied widely, as discussed in Section 2. Figure 4.19 compares the hindcast with the latest LATEX analysis (DiMarco et al, 1994) which gives a peak HS of 8.9 m, in close agreement with the hindcast peak HS of 8.7 m. The time histories of hindcast and estimated TP also agree quite well. The difficulty with the data at this station however, is indicated in the frequency spectrum associated with the peak sea state at station 16. The analysis indicates a double-peaked spectrum with one peak at around 10-12 seconds, and a second peak around 5-7 seconds with a peak density there nearly half the density of the main peak. The hindcast spectra do not support a double peaked frequency spectrum, and it is indeed difficult physically to explain such a significant perturbation in the tail of an active storm spectrum. Additional analyses of the data which consider possible strong non-linearity in the sea state are underway at Texas A&M and the early indication is that the reanalysis will result in lower wave heights (personal communication). Of course, there is also the possibility that the overturning and partial burial of the transducer just before the peak sea state was encountered at this site have caused errors which are not correctable in a post-analysis and that the true condition at this site may never be known. It is interesting to note that the 3G model hindcast is very skillful at this site right up until the time of instrument overturning and disagrees only thereafter, suggesting the possibility that the hindcast is quite accurate throughout the time history, and that the deviation thereafter is due to instrument and analysis problems. On the other hand if wave heights were truly lower than hindcast right at and after the storm peak, this could be attributed to an additional attenuation mechanism which is not included in the model physics such as enhanced bottom attenuation due to a sudden change in bottom sediment characteristics (e.g. an invasion of mud) or to wave-current interactions.

Taken over all the available measurement sites, the agreement between hindcast and measured time histories of HS is shown in Figure 4.20a in the form of a scatter plot and difference statistics. The mean difference is just .05 m and the standard deviation of the differences is .69 m, with almost half (the ideal) of the points on the plot above the 45 degree line of perfect fit

(ratio = 0.47). These differences also appear to characterize the storm peak sea states and are consistent with accuracy achieved in prior studies with the modeling technology applied here. Figure 4.20b shows the same type of comparsion for spectral peak period. The Bullwinkle comparisons are omitted from this plot because only zero-crossing period was available there. The mean and rms diferences are .07 sec and .67 sec respectively and the ratio of points is exactly 0.50. This skill was achieved without any additional tuning of OWI3G.

5. Current Hindcast

5.1 Background

Previous efforts to simulate circulation during tropical cyclones have suffered from a lack of ocean data for model verification. The passage of Tropical Storm Delia in 1973 has been reproduced by Forristall et al. (1977), Spaulding and Isaji (1985), and Keen and Slingerland (1993a). All three studies reasonably reproduced the flow measured at a single location, the Buccaneer Platform. However, this mooring was located directly along the storm path. Until now, no current data has been reported for locations near the storm but not along its path.

For Tropical Storm Delia, Keen and Slingerland (1993a) discussed not only the local flow field, but also that for the entire NW Gulf. The model predicted an evolving circulation pattern that swept across the shelf from New Orleans to Galveston, where the eye made landfall. Currents were shoreward to the right of the eye and generally offshore to the left (looking along the storm path). Strong currents continued to flow offshore and southwestward after landfall because of the ebbing storm surge. The peak of this coastal trapped wave was where the eye made landfall, Galveston. This pattern of coastal surface heights relative to the storm track is supported by tidal station data from historical storms. Results for several historical hurricanes in the western Gulf of Mexico (Keen and Slingerland, 1993b) support the conclusions of the Delia study. However, this work also highlighted the importance of coastal geometry in determining the flow pattern, with distinctive patterns for broad, straight coasts, curved coasts, and narrow coasts. This previous work suggests that the flow field within the present study area, the Louisiana shelf, should consist of onshore flow to the west near New Orleans and offshore flow near Galveston. However, the presence of the Birdfoot Delta immediately east of the storm track will significantly alter this pattern. The previous work neglected stratification in studying tropical storm circulation because of the generally well-mixed nature of the water column during turbulent events. However, more recent work (Keen and Glenn, 1994a,b; Keen et al., 1994) has demonstrated the importance of stratification in controlling flow directions within the water column. This is especially true away from the radius of maximum winds. Downwelling flows will likely develop within 100 km of the eye. Thus, it is useful to include stratification in a model of regional flow during tropical cyclones.

5.2 Hindcast Method

With previous results in mind, this simulation study uses the hydrodynamic model described by Keen and Slingerland (1993a). Equations for temperature and salinity are also included in the model used in this study. The horizontal grid size is 10 Km as used in the wind and wave modeling. The grid used for the wind and wave hindcast covers the eastern Gulf and stops at 94.5 W longitude. Although this size covers the study area fully, it does not allow sufficient down-coast space for development of the storm surge. This trapped coastal wave can extend for hundreds of kilometers along the coast to the west. This problem was alleviated by using a different grid with the same horizontal resolution. This grid is centered on the mooring arrays and significantly improves the modeled circulation in the west.

The large size of the resulting grid (Grid A), 139x44, requires significant computation time and is prohibitive for evaluating turbulent mixing parameterizations. Therefore, a grid (Grid B) of dimensions 41x29 was introduced as well. These grids are shown in Figure 5.1. Several different choices of vertical resolution were used, with the greatest density of levels concentrated in the upper 100 m of the water column. Grid A used 13 model levels with the following thicknesses: Levels 1 to 10 are 10 m thick; Levels 11 and 12 are each 50 m in thickness; and Level 13 is 300 m in thickness. The total depth of the model grid is 500 m. This depth is used to increase the time step for integrating the model equations and it has been shown to be acceptable for studies focusing on the shelf (Keen, 1992). Grid B uses 11 levels: Levels 1 through 6 are 5 m thick; Levels 7 and 8 are each 10 m; Level 9 is 50 m; Level 10 is 100 m; and Level 11 is 300 m in thickness. The total depth is the same as for Grid A. Grid B requires approximately 1/12 the computation time as Grid A. In order to improve the barotropic response of Grid B it was fit with an Orlansky boundary condition on the west for all prognostic variables (i.e., currents, temperature, salinity, surface height, and turbulent energy). This results in no gradient and permits mass and energy to leave the model domain. The losses, however, were not significant for the short duration of the simulations. Either of these model grids gives a reasonable fit to the depths of the current meters during Hurricane Andrew.

Bottom friction is parameterized using a quadratic stress formulation with a constant drag coefficient Cb. In these simulations Cb = 0.001. This value is representative of the muddy bottom found throughout much of the region. The quadratic wind stress was parameterized using a drag coefficient Cs dependent on wind speed W.

For W < 6 m/s Cs = 0.0011

For 6 < W < 22 Cs = (.61+.063*W)*.001

For W > 22 Cs = (1.0+.07*W)*.001

5.3 Regional Results.

The storm surge, the evolution of which is shown in Figure 5.2 (a-f), developed first along the eastern Gulf, with heights less than 10 cm at 1500 GMT August 25. However, coastal water level was rising even along the Texas coast. As the eye approached Louisiana the surge began to build west of the birdfoot delta and trailed to the east. When the eye made landfall (about 0900 GMT, August 26), a peak of about 2 m occurred west of New Orleans. The wave was trapped by the wind pattern associated with landfall. After landfall the wave relaxed and propagated to the west as far as Galveston before being damped. By 2100 GMT August 26 coastal water levels were slightly elevated from Florida to Louisiana and a trough was located at Galveston. Similar responses have been noted in previous modeling studies.

The evolution of the surface current field is shown in Figure 5.3 (a-f). Because of the short spinup used in this simulation, surface currents were quite low throughout the Gulf at 1500 GMT August 25. Longshore currents south of New Orleans attained speeds of about 50 cm/s and were also present all along the Florida coast. The weakening of currents to the west is partly a function of the wind field which was not intended to capture synoptic processes, rather than the primary storm forcing itself. Also, the wind field was not extended to the western limit of this grid because its purpose was only to permit a barotropic wave to propagate. Most currents were located near the storm center and thus moved in a pattern across the open Gulf. Storm currents greater than 1 m/s reached the mooring array by about 2100 GMT August 25. When the eye made landfall the strongest currents were located at the coast east of the storm track. Currents of about 40 cm/s were generated by the passage of the Kelvin wave to the west. After landfall the storm surge relaxed and currents in excess of 1 m/s flowed seaward and to the west along western Louisiana. Coastal flow had reversed direction and was to the east at this time.

Surface temperature is a good indicator of both turbulent mixing and upwelling associated with storm passage. At 1500 GMT August 25 (Figure 5.4) turbulent mixing has resulted in a general decrease in temperature towards the storm, with a strong gradient to the right of the path where divergence (and

thus upwelling) is greatest. The pattern at 0900 GMT August 26 (Figure 5.5) reveals even greater upwelling and mixing up to the coast, as well as onshore transport of colder upwelled water from the slope. However, because of the generally high temperatures on the shelf the temperature did not change much near the coast. Near the outer moorings, however, a significant temperature decrease occurred in the model. The lack of mixing in the west is because of the much lower wind stresses away from the storm track.

The performance of the model based on Grid B (Figure 5.6 a-c) can be evaluated during the storm peak using surface currents. At 2100 GMT August 25 currents near the coast are larger than for Grid A and they are more evenly distributed away from the storm. Magnitudes are about the same at the eastern mooring array. The smaller grid also produces more offshore flow along eastern Louisiana at landfall (about 0300 GMT August 26) while predicting somewhat weaker flow to the east. However, because of the weakness of western boundary, despite the Orlansky boundary condition, flow is opposite after landfall. This reflects the fact that the wave cannot propagate fast enough to the west. The smaller grid is primarily able to reproduce the wind-driven response.

5.4 Model-Data Comparisons

Data Preparation

Hindcast currents were compared to observations in two sets of plots. The first set contains standard time series comparisons of the hindcast and observed current speeds at the location and depth of each current meter. The second set compares the spatial distribution of the hindcast and observed surface current vectors as the hurricane crosses the continental slope and shelf in the vicinity of the moorings. These charts are important for understanding how the observations at the different moorings are related.

The time series plots were easily constructed using the detided current meter records, but the spatial distribution charts required additional work. The charts focus on the continental slope and shelf south of the Mississippi Delta. For an initial view of their spatial distribution, observed current charts were prepared at half hourly intervals for the 48 hour time period spanning August 25-26. They are labeled by frame numbers 0 through 96 in the Appendix E. The current meter locations are marked with diamonds. Detided surface current vectors are plotted for each current meter on a scale equivalent to the distance traveled in 1/2 day at the reported speed. The hurricane track is included for reference. The interpolated hurricane eye locations (heavy cross) and radius to maximum winds (heavy circles) are

included on each plot for reference.

The observed current charts can be summarized at six hourly intervals beginning with Frame 6 GMT on August 25 at 0300 GMT (Figure 5.7 a-h). To aid in their interpretation, the wind vectors have been superimposed. The hurricane is far to the southeast and currents on the slope/shelf initially are running between 10-30 cm/sec to the west or southwest with the weak winds. Six hours later in Frame 18, the hurricane is located just outside of the southeast corner of the plot. Observed current speeds and directions are nearly unchanged. In Frame 30, the hurricane has just crossed the 2000 m isobath. Surface currents over the shelf (200 m water depth or less) are beginning to increase, but currents at the deepwater mooring appear unaffected. The hurricane just hits the 200 m isobath in Frame 42. Current speeds along the eastern cross-shelf transect are clearly responding to the hurricane wind field. Current directions are deflected to the right of the winds. Along the western transect, the flow remains to the west and southwest with slight increases in speed. By Frame 54, the hurricane is half way across the continental shelf. The inshore surface current meter (19t) on the eastern transect has failed. Strong currents at the shallowest working current meter are directed to the northwest, perpendicular to the wind field.

Currents at the two deepest moorings along this transect oppose the wind field and increase offshore. To the west, both current meters report flow to the southwest. The hurricane has just made landfall in Frame 66. Strong currents in the direction of the wind are experienced at the shallowest meter on the western transect. Currents at the deep shelf mooring remain to the south. Along the eastern transect, flows at the remaining shelf (14) and the shelf break (13) moorings rotate clockwise to the northeast or east, while flow at the deepwater station remains generally to the south. Moving from Frame 66 to Frame 78 as the hurricane continues inland, the flow along the western mooring is similar but the current direction has rotated to the east at the deep station. Along the eastern transect, strong currents at the two shelf moorings continue to rotate clockwise, while currents at the deep mooring rotate counterclockwise. Continuing on to Frame 90, strong currents along the entire eastern array continue to rotate clockwise until they are all lined up with flow to the southwest against the weak winds. Flows at the shallow western array sites remain to the southeast.

Time Series Plots

As of August, 1994, our best overall current hindcast is Run 26 in Grid A of Figure 5.1, so the comparison with observations will focus on this run. The

time series plots shown in Figure 5.8 a-m are considered first. In these plots, the full 10 days of observed current speeds are shown. The hindcast interval designated by the dashed lines runs from 0900 GMT on August 24 (day 237) through midnight GMT on August 26 (day 239).

Starting offshore and moving in along the eastern array, data is available for the top and middle current meters of Mooring 12. The modeled surface currents respond to the initial wind forcing near the correct time on day 238, but the peak response of about 100 cm/sec is below that of the observed 140 cm/sec currents. Modeled currents at mid depth exhibit very little response to the direct wind forcing on day 238. The observed mid-depth currents exhibit an approximately constant speed near 20 cm/sec for several days before and during the hurricane. Since the model does not contain the forcing for the 20 cm/sec steady current before and during the storm, this response is absent in the model results. The initial storm peak is followed in the observations by a strong, surface intensified hurricane wake response. The model also responds with a hurricane wake, but the surface intensification is much less.

Mooring 13 has current meters at three depths. The top meter responds to the direct wind forcing on day 238, followed by five peaks associated with the hurricane wake. The modeled and observed surface currents respond quickly to the wind and agree well with the observations in terms of timing and height of the peak. Modeled and surface currents decay just as quickly as the hurricane passes. The current meters then observe the strong currents associated with the hurricane wake, but the model wake response in this case is much lower in speed. At depth, the wake response after the hindcast produces the strongest observed currents. Modeled currents at depth respond after the storm peak with currents of similar 5-20 cm/sec magnitude, but the approach of the wake peak at the end of the hindcast interval is not seen.

At Mooring 14, top and bottom current meters are available. In contrast to Mooring 13, both current meters exhibit a strong direct wind driven response as the hurricane passes on day 238. Current magnitudes at the surface are slightly overpredicted and at the bottom are slightly underpredicted. (This may be a result of insufficent vertical mixing.) The timing of the modeled surface current response is correct, with the observed strong currents beginning a few hours early and persisting for a few hours later in the observations. At depth, the increasing current side of the peak is matched better, but the currents decrease too soon. In both cases, the wake response is evident in the model, but it is much weaker.

At the shallowest mooring on the eastern array, Mooring 15, the surface current meter failed near the peak of the storm, so the exact value of the peak currents is unknown. The wind driven peak is strong in the bottom meter and occurs several hours after the surface current meter failed. The wake response is clearly present in the bottom current meter. The timing, height and width of the current peak in the bottom current meter is nearly perfect. The response to the wake is also present, but as before is smaller than the observations. The response of the top current meter is well matched by the model until the current meter failed. Although the exact height of the peak is unknown, the model peak currents appear to be high at the surface.

The western array is located well to the left of the storm track. The observed response to the storm along this array has been the hardest to capture, requiring us to extend the hindcast grid to the west. At Mooring 18, the shallower mooring along this array, the model clearly is responding with three peaks at the surface, but the last peak does not persist as long as observed. The bottom current meter is clearly responding to the direct wind forcing on day 239, but the response appears to be delayed.

At Mooring 19, the deep shelf mooring on the western array, the model wind driven response is again noted, and appears to be in good agreement with the top and bottom observations. Again, three peaks are noted in both the surface observations and the model results.

Spatial Distribution Charts

The surface current spatial distribution charts (Figure 5.9 a-h) were prepared from the model output every six hours and plotted over the observed currents. Again starting with Frame 6 at 0300 GMT on August 25, the hurricane center is well off the chart to the southeast. The initial response of the model is a slow, broad surface flow to the southwest in agreement with the current meters and a narrow coastal jet along the Mississippi Delta shoreward of the array. Six hours later in Frame 18, the hurricane is centered just outside the southwest corner of the chart. The deepwater response of the current model to the approaching hurricane is observed in the southwest corner. The coastal jet along the Mississippi Delta remains inshore of the array. The slow, broad southwest flow continues to influence most of the moorings.

By Frame 30, the hurricane has entered the grid and has crossed the 2000 m isobath. The deepwater response of the current model is an elliptical cyclonic flow with the hurricane eye at the leading focus and the most intense

currents to the right of the track. The coastal jet along with the broad southwestward flow between the hurricane and the coastal jet are beginning to intensify. The coastal jet is approaching the inshore current meter on the eastern array, and the observed currents are more intense at this location.

As the hurricane crosses the 200 m isobath in Frame 42, the leading edge of the strong cyclonic wind driven flow is directly over the eastern array, reaching northward to the previously discussed coastal jet. The modeled hurricane current directions are in good agreement with the observations, but their magnitudes are somewhat smaller. Currents of the same magnitude as the observations are confined to a smaller region near the radius of maximum winds. This explains the narrower current peaks observed in the time series plots. The highest currents appear to be confined to a smaller region in the model results. Current speeds near the western array remain smaller than observed. Directions at the onshore station remain westerly, and farther offshore, the currents are beginning to rotate counterclockwise in response to the wind, both in agreement with the observations.

In Frame 54, the hurricane has propagated half way across the continental shelf. Very strong flows are predicted between the eye and the coast, but much weaker flows are hindcast near the moorings. Hindcast current directions are in good agreement with the observations. At Mooring 15 along the eastern array, strong currents are observed flowing to the northwest, toward the eye. Similar current speeds and directions are observed one row north on this grid. Moving counterclockwise around the storm from Mooring 15, the hindcast currents increase between the eye and the coast, then rapidly decelerate on the western side, with southwestward flow near the shallow mooring and offshore flow near the deeper mooring. The flow continues around the eye then turns offshore into the hurricane wake just before it reaches the western array.

By Frame 66, the hurricane has made landfall. The direct wind forcing results in an onshore flow to the right of the track and an offshore flow to the left. Strong alongshore currents to the west are experienced along the coastline surrounding the landfall location. The observed strong eastward currents at the shallow mooring along the western array are hindcast several grid points to the east. After passing the shallow mooring, the offshore flow weakens and rotates counterclockwise to east. The hindcast currents near the deep mooring are of similar magnitude, but the directions 3 grid points north are in much better agreement. Along the eastern array, the current is to the northeast over the remaining shallow water mooring, but the flow is turning offshore near the two deeper moorings as the currents respond to the incoming

hurricane wake.

The hurricane has moved inland by Frame 78. Currents on the back side of the hurricane are now along-coast to the east and are intensified shoreward, in good agreement with observations along the western array. The eastern array is coming under the cyclonic influence of the hurricane wake, but the observed current response is stronger.

Finally, in Frame 90, the well developed cyclonic wake is hindcast to be approaching the eastern array. Observed currents are stronger, indicating that the actual wake is more intense and may be larger or arrive sooner. To the west, the eastward alongshore flow persists in the hindcast and in the observations.

5.5 Discussion of Current Hindcast

The shallow water current model appears to do best in intermediate water depths. At this time it appears to slightly underpredict in very deepwater, slightly overpredict in very shallow water. It also appears to have a smaller hurricane wake response. Some of the observations indicate that more mixing may be required in shallow water. This may be achieved with the inclusion of wave enhanced bottom stresses. Although the model captured the large scale variability of the storm wind field, it can be improved by placing more effort on the initial distribution of currents and density over the shelf. Assuming that this is not feasible it is reasonable to expect discrepancies as seen at the deep moorings pre-storm.

6. Summary and Conclusions

This study may be viewed within the context of a series of industry and government sponsored measurement programs conducted within the past 20 years or so in the Gulf of Mexico to study the ocean response to the passage of hurricanes, including the Ocean Data Gathering Program (ODGP) for winds and waves, the Ocean Current Measurement Program (OCMP) for continental shelf currents, the Ocean Test Structure (OTS) program for platform response, and a number of Ocean Response to a Hurricane (ORH) programs which utilized air-dropped current meters to measure mixed-layer storm driven currents. Data acquired in these programs have been used extensively to develop, refine and validate numerical models. The data acquired in the ODGP provided a basis for the development and calibration of numerical models for the accurate specification of surface wind and wave fields in historical Gulf of Mexico hurricanes (Cardone et al., 1976). The ocean current data acquired in the OCMP and ORH have used by several current modelers to adapt and calibrate current response models (e.g. Forristall et al, 1977, Keen and Slingerland, 1993a).

The models applied in this study may be considered logical evolutions and refinements of the these modeling capabilities. The surface wind field was specified with an improved version of the method and model used in the ODGP to specify surface winds. The almost continuous monitoring of Hurricane Andrew by aircraft, satellite and shore based radars allowed the specification of storm track to the maximum possible accuracy, within about +/- 10 km, or about one grid spacing of the grids used for ocean response models applied. The hindcast windfields are compared to available measurements sites, none of which experienced hurricane force winds because the eye of the storm passed more than 50 km from the closest measurement site. Based upon these data comparisons and prior validation studies carried out with the same hindcast methodology we estimate that the wind fields are specified to an accuracy within +/- 2.5 m/s in wind speed and +/-25 degrees in wind direction (rms). However, we can not state unequivocally that these errors are randomly distributed about negligible means. If they are not, then the systematic part of the error is probably distributed by storm quadrant (e.g. wind speeds slightly too high with too much inflow in one quadrant and vice versa in another). We estimate the magnitude of systematic errors to be less than half the magnitude of the errors quoted above.

The hindcast wave fields are verified against waves which in deep water were measured at sites which again were never closer than about 50 km from the storm center. The maximum waves in deep water were measured at Bullwinkle

platform, which was located 74 km southwest of the center at closest approach. The maximum measured HS at this site was 7.9 m, which may be compared to the maximum hindcast HS of 8.7 m at the model grid point closest to the platform. The peak hindcast HS was within 1 m of the peak measured HS at the other deep water sites as well. At the shallow water site, LATEX station 16, the most recent analysis of the measured data yields a peak HS of 8.9 m in 20 m water depth, compared to the hindcast peak of 8.7 m. This excellent agreement, however, must be conditioned on the continuing investigation of the validity of the measurements at this site after the instrument mount overturned just before peak conditions were experienced.

The maximum hindcast HS in deep water of 13.5 m ranks Hurricane Andrew very highly in terms of wave generation. If we use the ODGP suite of historical hindcasts as a reference (Ward et al., 1979) the maximum deep water hindcast HS in Andrew at the shelf break south of the Mississippi Delta of 13.5 m (44.3 ft) was exceeded in only 6 storms this century anywhere in the Gulf. This ranking is consistent with the basic meteorological characteristics of Andrew in the Gulf. Only four hurricanes this century attained central pressure of lower than 936 mb in the Gulf. In the absence of any compelling evidence to the contrary we estimate that the hindcast of peak HS and associated TP has achieved an accuracy consistent with a scatter index of about 10%.

The hydrodynamic modeling of Andrew was most successful at simulating the spatial distribution and magnitude of the primary forced ocean response at intermediate water depths. Runs completed to date appear to slightly underpredict peak currents in very deep water and to slightly overpredict peak current speeds in very shallow water. These "asymptotic" response regimes are often modeled fairly accurately with simpler mixed-layer (deep water) and barotropic vertically integrated formulations (shallow water), but such models can not provide a complete three-dimensional picture of the ocean current response on the whole of the continental shelf. It is expected that with some further refinement and tuning of the vertical mixing parameterization of the model and inclusion of wave enhanced bottom stresses, better absolute agreement between the modeled and measured peak currents may be achieved. Additional improvement in the overall time history of agreement would appear to benefit from a more complete specification of the initial current and density distributions throughout the model domain than was possible in this study.

REFERENCES

Breaker, L.C., L.D. Burroughs, Y.Y. Chao, J.F Culp, N.L Guinasso, Jr., R.L Teboulle and C.R. Wong, 1994: The Impact of Hurricane Andrew on the Near-Surface Marine Environment in the Bahamas and the Gulf of Mexico. OPC Technical Note/NMC Office, Washington, D.C.,1994 (in progress).

Black, P. 1993. Evolution of maximum wind estimates in typhoons. In Tropical Cyclone Disasters, ed. J. L. Lighthill, Zheng Zhemin, G. Holland and K. Emmanuel. Peking University Press, Bejing, China, 104-115.

Cardone, V. J., W. J. Pierson, and E. G. Ward, 1976. Hindcasting the directional spectra of hurricane generated waves. J. of Petrol. Technol., 28, 385-395.

Cardone, V. J. and D. B. Ross, 1979. State-of-the-art wave prediction methods and data requirements. Ocean Wave Climate ed. M. D. Earle and A. Malahoff. Plenum Publishing Corp., 1979, 61-91.

Cardone, V. J. and D. Szabo, 1985. Impact of uncertainty in specification of offshore wind on accuracy of wave hindcasts and forecasts. Proc. Int. Workshop on Offshore Winds and Icing, Nova Scotia, 7-11 October, 1985. Publ. Environment Canada, Downsview, Ontario.

Cardone, V. J. and J. A. Greenwood, 1987. A sensitivity study of spectral growth algorithm. Proc. of Int'l Workshop on Wave Hindcasting and Forecasting, 23-26 September, 1986 (ESRF Report 65), 133-143

Cardone, V. J., J. G. Greenwood and M. A. Cane, 1990. On trends in historical marine wind data. J. of Climate. 3, 113-127.

Cardone, V. J., C. V. Greenwood, and J. A. Greenwood, 1992. Unified program for the specification of hurricane boundary layer winds over surfaces of specified roughness. Final Report. Contract Report CERC-92-1. Dept. of the Army, Waterways Experiment Station, Vicksburg, MS.

Cardone, V. J. and K. C. Ewans. 1992. Validation of the hindcast approach to the specification of wave conditions at the Maui location off the west coast of New Zealand. Preprints of the Third International Workshop on Wave Hindcasting and Forecasting, May 19-22, 1992, Montreal, Quebec, 232-247.

Cardone, V. J., A. T. Cox, J. A. Greenwood and E. F. Thompson, 1994. Upgrade of tropical cyclone surface wind field model. CERC Miscellaneous Paper, February, 1994. Dept. of the Army, Waterways Experiment Station, Vicksburg, MS

Cardone, V. J., R. E. Jensen, D. T. Resio, V. R. Swail and A. T. Cox, 1994a. Evaluation of Contemporary Ocean Wave Models in Rare Extreme Events: "Halloween Storm" of October, 1991; "Storm of the Century" of March, 1993.

Cardone, V. J., H. C. Graber, R. E. Jensen, S. Hasselmann and M. J. Caruso, 1994: In search of the true surface wind field during SWADE IOP-1: ocean wave modelling perspective. Submitted to The Atmosphere-Ocean System.

Chow, S. H. 1971. A study of the wind field in the planetary boundary layer of a moving tropical cyclone. Master of Science Thesis in Meteorology, School of Engineering and Science, New York University, New York, N.Y.

Cooper, C. and J. D. Thompson. 1989. Hurricane-generated currents on the outer continental shelf, 1, model formulation and verification. J. Geophys. Res., 94, C9 (September 15), 12513-12540.

Daniels, G. R., 1994: Hurricane Andrew's Impact on Natural Gas and Oil Facilities on the Outer Continental Shelf. OCS Report MMS 94-0031. US Department of the Interior, Minerals Management Service, Engineering and Technology Division. 49 pp.

DiMarco, S.F., F.J. Kelly and N.L. Guinasso, Jr., 1994: Directional Wave Spectra on the Louisiana-Texas Shelf During Hurricane Andrew. Submitted to J. of Coastal Research.

Forristall, G.Z., R. C. Hamilton and V. J. Cardone. 1977. Continental shelf currents in tropical storm Delia: observations and theory. J. of Phys. Oceanog. 7, 532-546.

Forristall, G. Z., E. G. Ward, V. J. Cardone, and L. E. Borgman. 1978. The directional spectra and kinematics of surface waves in Tropical Storm Delia. J. of Phys. Oceanog., 8, 888-909.

Forristall, G. Z. 1980. A two-layer model for hurricane driven currents on an irregular grid. J. Phys. Oceanog., 10, 9, 1417-1438.

Forristall, G. Z., E. G. Ward and V. J. Cardone. 1980. Directional spectra and wave kinematics in hurricanes Carmen and Eloise. 17th International Conference on Coastal Engineering, Sydney, Australia.

Gilhousen, D.B., E.M. Meindl, M.J. Changery, P.L. Franks, M.G. Burgin and D.A. McKittrick, 1990: Climatic Summaries for NDBC Buoys and Stations Update 1. NOAA, NDBC.

Greenwood, J. A., V. J. Cardone, and L. M. Lawson, 1985. Intercomparison test version of the SAIL model. Ocean Wave Modeling. The SWAMP Group, Plenum Press, 221-234.

Hasselmann, S. and K. Hasselmann, 1985. Computations and parameterizations of the nonlinear energy transfer in gravity wave spectrum. Part I: A new method for efficient computations of the exact nonlinear transfer integral. J.Phys. Oceanogr., 12, 1369-1377.

Holland, G. J., 1980: An analytic model of the wind and pressure profiles in hurricanes. Mon. Wea. Rev., 108, 1212-1218.

Jordan, C. L., 1958. Estimation of surface central pressures in tropical cyclones from aircraft observations. Bull. Amer. Meteor. Soc., 39, 345-352.

Keen, T. R., A three-dimensional numerical investigation of storm event bed genesis on the Texas-Louisiana continental shelf. Ph.D. Thesis, Penn State, University Park, 1992.

Keen, T. R., and R. L. Slingerland, 1993a. A numerical study of sediment transport and event bed genesis during Tropical Storm Delia. J. Geophys. Res., 98, pp. 4775-4791..

Keen, T. R., and R. L. Slingerland, 1993b. Four storm-event beds and the tropical cyclones that produced them: a numerical hindcast. J. Sedimentary Petrology, 63, pp. 218-232.

Keen, T. R., and S. M. Glenn, 1994a. A coupled hydrodynamic-bottom boundary layer model of Ekman flow on stratified continental shelves. J. Phys. Oceanogr.,99, 1994a.

Keen, T. R., and S. M. Glenn, 1994b. A coupled hydrodynamic-bottom boundary layer model of storm and tidal flow in the Middle Atlantic Bight of

North America. J. Phys. Oceanogr., in press.

Keen, T. R., S. M. Glenn, and R. L. Slingerland, 1994. Coastal circulation and sedimentation during severe storms. Estuarine and Coastal Modeling III, Proceedings of the 3rd International Conference, ASCE, pp. 279-293.

Kelly, J.F., S.F. DiMarco, N.L. Guinasso, Jr., R.C. Hamilton and K.A. Kurrus, 1993: Calibration and Performance of the Pressure and Temperature Sensors in the Coastal Leasing, Inc., MiniSpec Directional Wave Gage. Texas A&M University, Dept. of Oceanography, Reference No. 93-07-T.

Khandekar, M. L., R. L. Lalbeharry and V. J. Cardone, 1994. The performance of the Canadian Spectral Ocean Wave Model (CSOWM) during the Grand Banks ERS1 SAR Wave Spectra Validation Experiment. Atmosphere-Ocean, 32, 31-60.

Pierson, W. J., L. J. Tick and L. Baer, 1966. Computer based procedures for preparing global wave forecasts and wind field analyses capable of using wave data obtained by a spacecraft. Sixth Naval Hydrodynamics Symposium, ACR-136, Office of Naval Research, Dept. of the Navy, Washington, D.C., 490-532.

Powell, M. D. and P. G. Black, 1989. The relationship of hurricane reconnaissance flight-level wind measurements to wionds measured by NOAA'a oceanic platforms. 6th U. S. Natioal Conference onWind Engineering. 7-10 March, Houston, Texas.

Powell, M. D. and S. Houston, 1993. Surface wind field analyses in Hurricane Andrew. 20th Conference on Hurricanes and Tropical Meteorology. San Antonio. 10-14 May, 1993.

Rappaport, E.: Hurricane Andrew - A Preliminary Look. Mariners Weather Log, Fall 1992.

Reece, A. M. and V. J. Cardone. 1982. Test of wave hindcast model results against measurements during four meteorological systems. Offshore Technology Conference. OTC 4323, 269- .

Ross, D. B. and V. J. Cardone. 1978. A comparison of parametric and spectral hurricane wave prediction products. Turbulent Fluxes through the Sea Surface, Wave Dynamics, and Prediction, A. Favre and K. Hasselmann, editors, 647-665.

Shapiro, L. J. 1983. The asymmetric boundary layer flow under a translating hurricane. J. of Atm. Sci., 39.

Snyder, R. L., F. W. Dobson, J. A. Elliot and R.B. Long, 1981. Array measurements of atmospheric pressure fluctuations above surface gravity waves. J. Fluid Mech., 102, 1-59.

Spaulding, M.L. and T. Isaji, 1985. Design flow conditions near bottom, phase II, coupling of a continental shelf hydrodynamics model to a bottom boundary layer model. Vol. 1, Theoretical development and application. Final Rep. to Pipeline Res. Comm., PRoject PR-169-1186, Amer. Gas. Assoc.

Stone, G.W., J.M. Grymes, III, K.D. Robbins, S.G. Underwood, G.D. Steyer, R.A. Muller, 1994, Shore and Beach, 61(2), 2-12.

Swail, V. R., V. J. Cardone, and B. Eid., 1991. An extremes wind and wave hindcast off the west coast of Canada. (Preprint Volume) Fifth Conference on Meteorology and Oceanography of the Coastal Zone, 6-9 May, 269-281.

Thompson, E. F. and V. J. Cardone. Practical modelling of hurricane surface wind fields. Submitted to J. of Waterway,Port, Coastal Engineering.

Tubb. M.: Industry Efforts Minimize Andrew's Destruction. Ocean Industry, October, 1992.

WAMD1 Group. 1988. The WAM model-a third generation ocean wave prediction model. J. Phys. Oceanog., 18, 1275-1810.

Ward, E. G., L. E. Borgman and V. J. Cardone, 1978. Statistics of hurricane waves in the Gulf of Mexico. OTC 3229. 10th Annual Offshore Technology Conference, 8-11 May, 1978, Houston, TX.

Wu, J. 1982. Wind-stress coefficients over the sea surface from breeze to hurricane. J. Geophys. Res., 87, 9704-9706.

Table 2.1

Platform Location and Meteorological Sensor Characteristics

Station	Latitude (deg N)	Longitude (deg W)	Barometer Elevation (m)	Anemometer Elevation (m)	Anemometer Duration (min)
42001	25.54	89.42	0.0	10.0	8
42003	25.90	85.90	0.0	10.0	8
Shell Bullwinkle	27.90	90.90	20.1	93.6	2/10
Exxon Lena	28.67	89.17	34.8	60.1	2/10
Grand Isle	29.27	89.96	9.1	15.8	2/10
Southwest Pass	28.90	89.43	33.2	33.8	2/10
LATEX Mooring 17	29.20	91.96	0.0	3.6	??
LATEX Mooring 19	28.47	92.03	0.0	3.6	??
Ship Shoal 198G	28.6	91.3	NA	NA	1
East Cameron 83H	29.3	93.0	NA	NA	1
East Cameron 42B	29.5	92.8	NA	NA	1
South Marsh Is. 136	28.3	92.1	NA	NA	1

Table 2.2

Minimum Observed Barometric Pressure and Maximum Wind Velocity

Station	Latitude (deg N)	Longitude (deg W)	Barometer Pressure (mbs)	Wind Velocity Speed (kt)	Direction (deg)
42001	25.54	89.42	-	12.3	235.0
42003	25.90	85.90	997.4	23.4	310.0
Shell Bullwinkle	27.90	90.90	998.5	26.6	277.0
Exxon Lena	28.67	89.17	1007.7	-	-
Grand Isle	29.27	89.96	1005.2	24.7	80.0
Southwest Pass	28.90	89.43	1006.1	25.1	67.0
LATEX Mooring 17	29.20	91.96	993.3	-	-
LATEX Mooring 19	28.47	92.03	1004.2	15.4	328.2
Ship Shoal 198G	28.6	91.3	-	40.0	-
East Cameron 83H	29.3	93.0	-	23.6	-
East Cameron 42B	29.5	92.8	-	19.5	-
South Marsh Is. 136	28.3	92.1	-	19.5	-

Table 2.3.

Corps of Engineers Pressure Gauges

MMS Block	Latitude (deg min N)	Longitude (deg min W)	Depth (m)	Data Status
Bay Marchand 20A	28 58.80	90 10.50	11.5	Large data gaps, not used
Eugene Island 100	29 04.03	91 26.70	11.3	Few data gaps, OK
West Cameron 178	29 34.00	93 16.00	12.2	Too far west of hurricane

Table 2.4

LATEX Measured Current Velocity Moorings
during Hurricane Andrew (1992)

Mooring No.	Water Depth (m)	Meter Depth (m)	Start Date	Stop Date	Latitude (deg min N)	Longitude (deg min W)
12	505	12	6/2	9/10	27 55.432	90 29.676
		100	6/8	9/11		
13	200	12	7/23	10/22	28 03.452	90 29.153
		100	7/23	10/22		
		190	7/23	10/22		
14	47	11	6/2	9/1	28 23.674	90 29.572
		26	6/2	9/2		
		37	-	-		
15	20	10	6/2	8/26	28 36.498	90 29.459
		17	6/2	9/2		
16	19	11[1]	-	-	28 52.024	90 29.451
		17	6/1	8/25		
17	7	3[2]	-	-	29 11.762	91 57.893
		5[3]	-	-		
18	22	10	6/1	9/2	28 57.764	91 58.963
		19	6/1	8/31		
19	51	3	7/24	10/20	28 27.910	92 02.088
		20	-	-		
		47	6/2	8/30		

1. Mooring and meter lost during Andrew
2. Meter impeller lost during Andrew
3. Minispec not installed during Andrew

Table 2.5

Comparison of O_1 and Inertial Periods in Northern Gulf of Mexico

Latitude (deg-N)	O1 Period (deg/hr)	Inertial Period (deg/hr)	Difference (deg/hr)	Synodic Period (days)
30	25.8194	25.9173	.0979	153.2
29	"	26.1754	.3560	42.1
28	"	26.4237	.6043	24.8

Table 2.6

Current Velocity Analysis at Site 12T
for Varying Durations (days)

Start Date	Duration in Days	Mean E-W cm/s	Mean N-S cm/s	C.V. E-W cm/s	C.V. N-S cm/s	East - West Amplitude M2 (cm/sec)	S2	N2	K1	O1	North - South Amplitude M2 (cm/s)	S2	N2	K1	O1
4-15[2]	180	-0.4	1.4	.99	.98	0.6	0.2	0.3	2.4	1.0	0.0	0.4	0.3	2.1	1.4
4-15	90	7.4	6.2	.98	.96	1.0	0.4	0.3	2.3	0.9	0.7	0.5	0.5	1.6	1.7
7-22[2]	90	-8.1	-3.3	.98	.97	0.4	0.4	0.6	2.6	1.6	0.6	0.4	0.2	2.7	1.7
7-22[2]	45	-4.2	-3.0	.90	.90	0.3	0.6	1.4	6.6	3.0	0.6	0.4	0.6	6.2	3.0
9-4	45	-12.0	-3.6	.97	.98	0.6	0.8	0.2	2.1	1.9	0.5	0.8	0.6	1.4	1.7

Start Date	Duration in Days	Mean E-W cm/s	Mean N-S cm/s	C.V. E-W cm/s	C.V. N-S cm/s	East - West Phases M2 (degrees)	S2	N2	K1	O1	North - South Phases M2 (degrees)	S2	N2	K1	O1
4-15[2]	180	-0.4	1.4	.99	.98	278	103	163	120	317	179	353	013	043	205
4-15	90	7.4	6.2	.98	.96	260	180	036	114	264	133	017	359	050	167
7-19[2]	90	-8.1	-3.3	.98	.97	326	051	178	124	343	313	334	020	039	247
7-19[2]	45	-4.2	-3.0	.90	.90	340	116	172	106	307	320	047	074	025	221
9-4	45	-12.0	-3.6	.97	.98	309	007	315	243	024	295	307	291	151	279

1. F.R.V. (Fractional Residual Variance - variance due to the non-tidal currents)
2. Period includes Hurricane Andrew

Table 2.7

Summary of Current Velocity Analysis by Mooring Location

Moor/ Meter	Depth: Meter/ Water	Mean C.V. E-W cm/s	N-S cm/s	F.R.V.[1] E-W cm/s	N-S cm/s	East - West Amplitude (cm/sec) M2	S2	N2	K1	O1	North - South Amplitude (cm/s) M2	S2	N2	K1	O1
16B	17/19	-2.1	0.0	.87	.93	2.1	0.7	0.8	0.7	0.3	0.4	0.5	0.4	0.9	1.3
15T	10/20	10.8	4.8	.78	.71	0.3	0.1	0.3	6.5	6.2	1.2	0.9	0.3	5.5	4.8
15B	17/20	0.1	-0.1	.94	.94	1.6	0.3	0.5	1.4	1.5	1.0	0.3	0.5	0.8	1.7
14T	11/47	6.2	2.2	.88	.89	1.3	0.7	0.9	5.3	6.6	0.4	0.9	0.7	4.0	5.3
14M	26/47														
14B	37/47	0.4	-0.2	.97	.98	1.1	0.6	0.2	1.6	0.4	0.4	0.4	0.3	1.0	0.3
13T	12/200	-3.4	-2.5	.98	.98	0.7	0.2	0.2	2.4	1.7	0.6	0.3	0.4	3.1	1.5
13M	100/200	-10.7	-1.5	.98	.95	0.7	0.5	0.8	0.6	2.1	0.3	0.4	0.5	1.2	2.2
13B	190/200	-6.5	-3.2	.98	.97	0.7	0.4	0.3	0.7	1.5	0.7	0.7	0.4	1.3	1.9
12T	12/505	-8.1	-3.3	.98	.97	0.4	0.4	0.6	2.6	1.6	0.5	0.4	0.2	2.7	1.7
12M	100/505	-1.1	3.4	.99	.99	0.6	0.5	0.4	0.3	0.7	0.1	0.3	0.4	0.5	0.5
18T	10/22	10.4	-2.5	.89	.64	1.9	0.8	1.2	3.0	4.7	3.7	1.8	0.8	4.8	5.3
18B	19/22	1.6	0.4	.94	.75	1.2	0.1	0.5	1.1	0.5	3.6	0.9	1.0	1.0	0.3
19T	4/51	-4.1	2.3	.96	.94	1.5	1.0	1.1	5.6	1.3	2.4	0.6	1.0	4.1	2.2
19M	20/51	(record too short for tidal analysis)													
19B	47/51	0.7	-0.4	.95	.77	0.7	0.3	0.4	1.2	0.4	2.6	1.2	1.0	1.6	1.2

1. F.R.V. (Fractional Residual Variance - variance due to the non-tidal currents)

Table 2.8

Summary of Current Velocity Analysis By Meter Depth

Moor/ Meter	Depth: Meter/ Water	Mean E-W cm/s	Mean N-S cm/s	C.V. E-W cm/s	C.V. N-S cm/s	East - West Amplitude M2 (cm/sec)	S2	N2	K1	O1	North - South Amplitude M2 (cm/s)	S2	N2	K1	O1
Top Meter															
15T	10/20	10.8	4.8	.78	.71	0.3	0.1	0.3	6.5	6.2	1.2	0.9	0.3	5.5	4.8
14T	11/47	6.2	2.2	.88	.89	1.3	0.7	0.9	5.3	6.6	0.4	0.9	0.7	4.0	5.3
13T	12/200	-3.4	-2.5	.98	.98	0.7	0.2	0.2	2.4	1.7	0.6	0.3	0.4	3.1	1.5
12T	12/505	-8.1	-3.3	.98	.97	0.4	0.4	0.6	2.6	1.6	0.5	0.4	0.2	2.7	1.7
18T	10/22	10.4	-2.5	.89	.64	1.9	0.8	1.2	3.0	4.7	3.7	1.8	0.8	4.8	5.3
19T	4/51	-4.1	2.3	.96	.94	1.5	1.0	1.1	5.6	1.3	2.4	0.6	1.0	4.1	2.2
Middle Meter															
14M	26/47	7.6	-1.1	(record too short for tidal analysis)											
13M	100/200	-10.7	-1.5	.98	.95	0.7	0.5	0.8	0.6	2.1	0.3	0.4	0.5	1.2	2.2
12M	100/505	-1.1	3.4	.99	.99	0.6	0.5	0.4	0.3	0.7	0.1	0.3	0.4	0.5	0.5
19M	20/51	4.1	-0.6	(record too short for tidal analysis)											
Bottom Meter															
16B	17/19	-2.1	0.0	.87	.93	2.1	0.7	0.8	0.7	0.3	0.4	0.5	0.4	0.9	1.3
15B	17/20	0.1	-0.1	.94	.94	1.6	0.3	0.5	1.4	1.5	1.0	0.3	0.5	0.8	1.7
14B	37/47	0.4	-0.2	.97	.98	1.1	0.6	0.2	1.6	0.4	0.4	0.4	0.3	1.0	0.3
13B	190/200	-6.5	-3.2	.98	.97	0.7	0.4	0.3	0.7	1.5	0.7	0.7	0.4	1.3	1.9
18B	19/22	1.6	0.4	.94	.75	1.2	0.1	0.5	1.1	0.5	3.6	0.9	1.0	1.0	0.3
19B	47/51	0.7	-0.4	.95	.77	0.7	0.3	0.4	1.2	0.4	2.6	1.2	1.0	1.6	1.2

1. F.R.V. (Fractional Residual Variance - variance due to the non-tidal currents)

Table 2.9

Maximum Values of Total, Tidal and Non-Tidal Current Velocity

Location	Day & Time	Maximum Vel.	Dir.
12T Total:	239.0000	138.6	204.0
12T Tidal:	240.5208	7.9	30.9
12T Non-Tidal:	239.0000	137.4	204.5
12M Total:	241.2917	69.7	276.9
12M Tidal:	238.6250	1.5	207.6
12M Non-Tidal:	241.2917	69.9	274.1
13T Total:	238.9375	163.5	198.0
13T Tidal:	239.9792	5.9	216.4
13T Non-Tidal:	238.9375	154.6	196.5
13M Total:	240.1042	111.2	274.9
13M Tidal:	242.2292	4.4	268.6
13M Non-Tidal:	239.9375	99.3	213.7
13B Total:	240.0000	126.9	182.0
13B Tidal:	243.8542	4.4	199.8
13B Non-Tidal:	240.0000	125.7	180.1
14T Total:	239.0000	133.9	241.0
14T Tidal:	238.0625	14.6	267.6
14T Non-Tidal:	239.0000	128.0	242.3
14B Total:	239.0694	139.2	266.9
14B Tidal:	242.1736	3.6	275.1
14B Non-Tidal:	239.0694	136.7	267.0
15T Total:	238.8750	116.0	243.0
15T Tidal:	237.0625	12.8	278.8
15T Non-Tidal:	238.8750	122.2	247.6
15B Total:	238.9583	114.4	253.0
15B Tidal:	242.4167	6.0	129.8
15B Non-Tidal:	238.9583	114.1	252.7
16B Total:	238.8958	96.0	254.0
16B Tidal:	236.6875	1.8	15.8
16B Non-Tidal:	238.8958	93.9	252.6
18T Total:	239.7083	87.7	111.0
18T Tidal:	238.1458	14.7	338.6
18T Non-Tidal:	239.7083	76.5	111.6
18B Total:	239.3542	61.4	36.0
18B Tidal:	241.7083	6.5	342.0
18B Non-Tidal:	239.3542	64.6	31.8
19T Total:	239.1625	54.0	202.0
19T Tidal:	237.8708	9.2	192.3
19T Non-Tidal:	239.1625	58.7	188.8
19B Total:	240.3958	32.8	199.0
19B Tidal:	239.3750	5.4	182.7
19B Non-Tidal:	240.7917	32.3	209.6

Table 3.1

Table . Storm parameters and track used for numerical model simulation of boundary wind field.

Snap	YYMMDDHH	Lat	Long	Speed	Direc	Eyepres	Radius	B	Pfar	Sgw	An1
1	92082409	25.50	-80.22	18	275	932	7	1.30	1017	8	90
	92082412	25.60	-81.20								
2	92082415	25.65	-82.20	18	275	951	8	1.25	1017	8	100
	92082418	25.78	-83.12								
	92082421	26.00	-84.12								
3	92082500	26.17	-85.07	16	285	943	8	1.25	1017	6	115
	92082503	26.37	-85.90								
	92082506	26.63	-86.80								
4	92082509	26.93	-87.68	14	295	949	14	1.25	1017	6	123
	92082512	27.22	-88.28								
5	92082515	27.47	-89.05	14	295	944	14	1.25	1017	6	128
	92082518	27.77	-89.73								
	92082519	27.90	-89.92								
6	92082520	28.05	-90.03	10	320	936	14	1.25	1017	5	133
	92082521	28.17	-90.15								
	92082522	28.32	-90.33								
	92082523	28.47	-90.52								
7	92082600	28.57	-90.67	10	325	941	16	1.20	1017	5	135
	92082601	28.67	-90.82								
8	92082602	28.73	-90.97	8	335	949	16	1.15	1017	5	137
	92082603	28.85	-91.05								
	92082604	28.88	-91.17								
	92082605	29.05	-91.22								
	92082606	29.17	-91.23								
	92082607	29.28	-91.42								
9	92082608	29.48	-91.43	9	345	957	16	1.15	1017	5	145
	92082609	29.63	-91.52								
	92082610	29.77	-91.57								
	92082611	29.88	-91.63								
10	92082612	30.05	-91.65	9	335	973	25	1.10	1017	5	150
	92082615	30.47	-91.67								
11	92082618	30.90	-91.60	8	020	991	25	1.10	1017	5	160
	92082621	31.20	-91.33								
12	92082700	31.50	-91.10	7	035	995	25	1.10	1017	5	175

Table 4.1 "Fields" variables archived.

Fields	
1	Wind Direction (deg from which)
2	Wind speed (m/s)
3	Total variance of total spectrum (i.e. 0th spectral moment)
4	Peak spectral period of total spectrum (sec)
5	Vector mean direction of total spectrum (deg to which)
6	Total variance of primary partition (i.e. sea)
7	Peak spectral period of primary partition (sec)
8	Vector mean direction of primary partition (deg to which)
9	Total variance of secondary partition (i.e. swell)
10	Peak spectral period of secondary partition (sec)
11	Vector mean direction of secondary partition (deg to which)
12	First spectral moment of total spectrum
13	Second spectral moment as computed by Haring & Hiedeman these moments use first & second powers of omega
14	Significant wave height (m)
15	Dominant direction (Haring and Heideman)
16	Angular spreading function, as defined by Gumbel, Greenwood & Durand 0.0 for equal energy in all directions; 1.0 for spike
17	In-line variance ratio (Haring & Heideman)

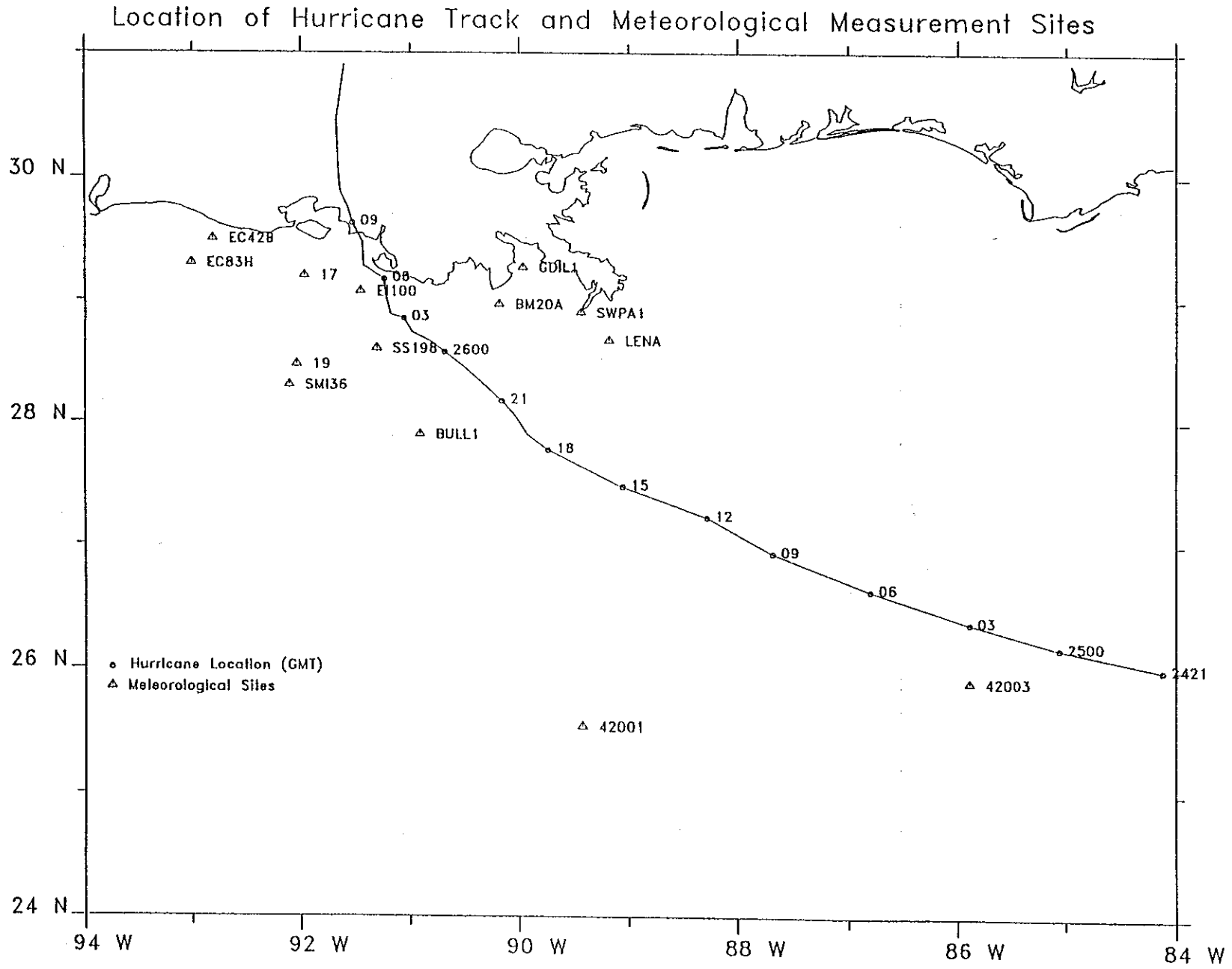

Figure 2.1. Hurricane track and location of meteorological measurement sites.

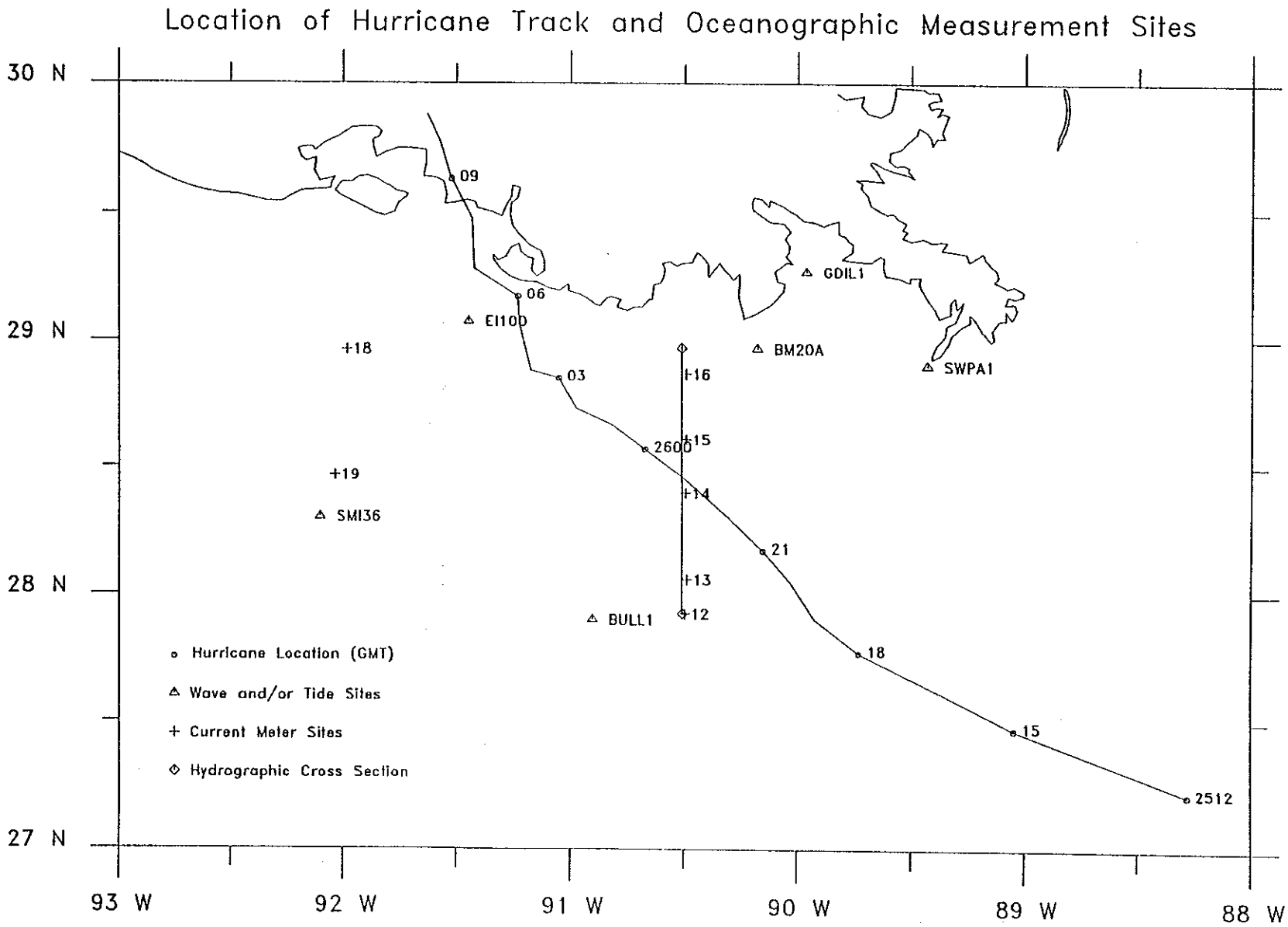

Figure 2.2 Hurricane track and location of oceanographic measurement sites.

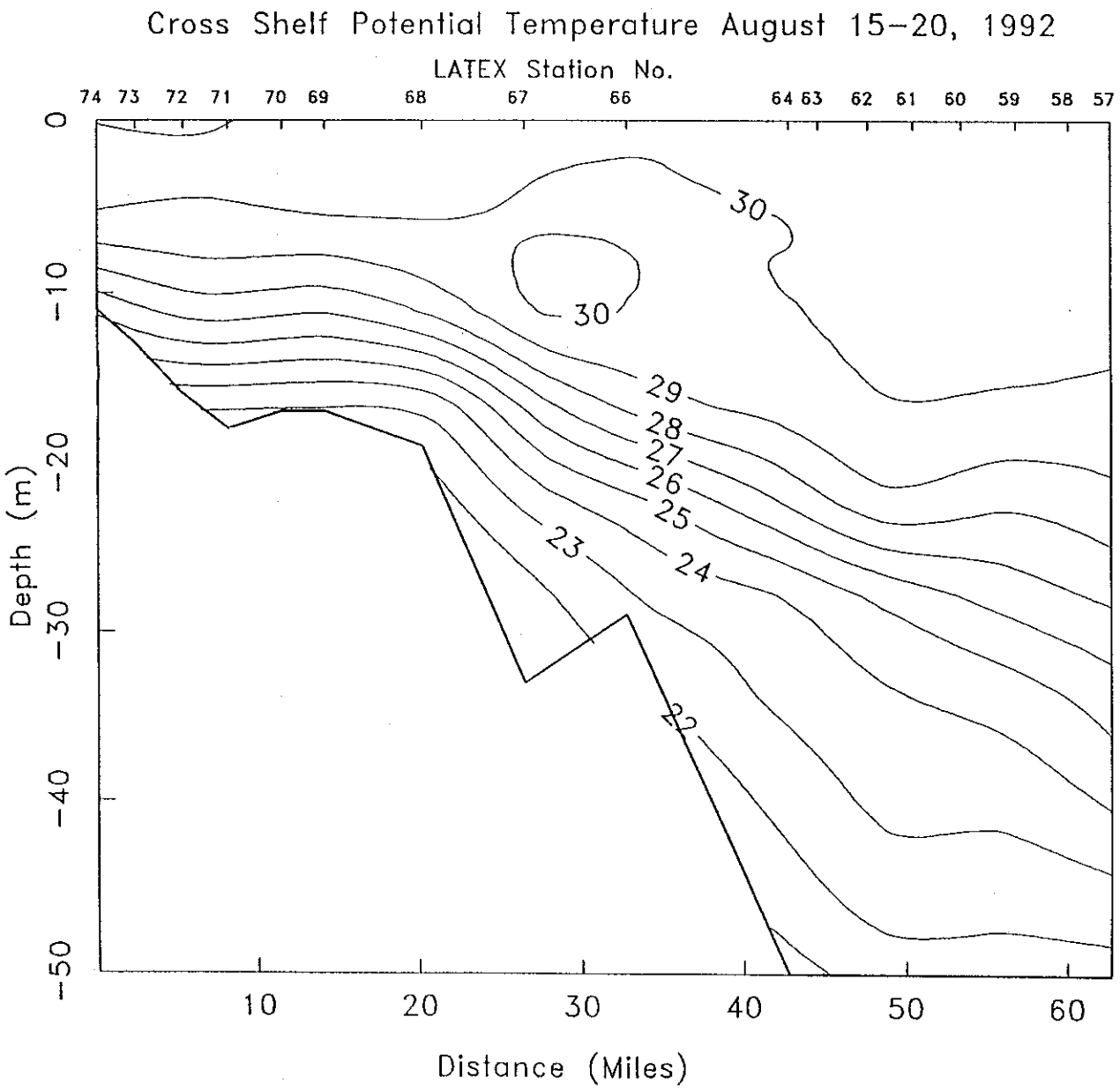

Figure 2.3 Cross-shelf potential temperature: August 15-20, 1992.

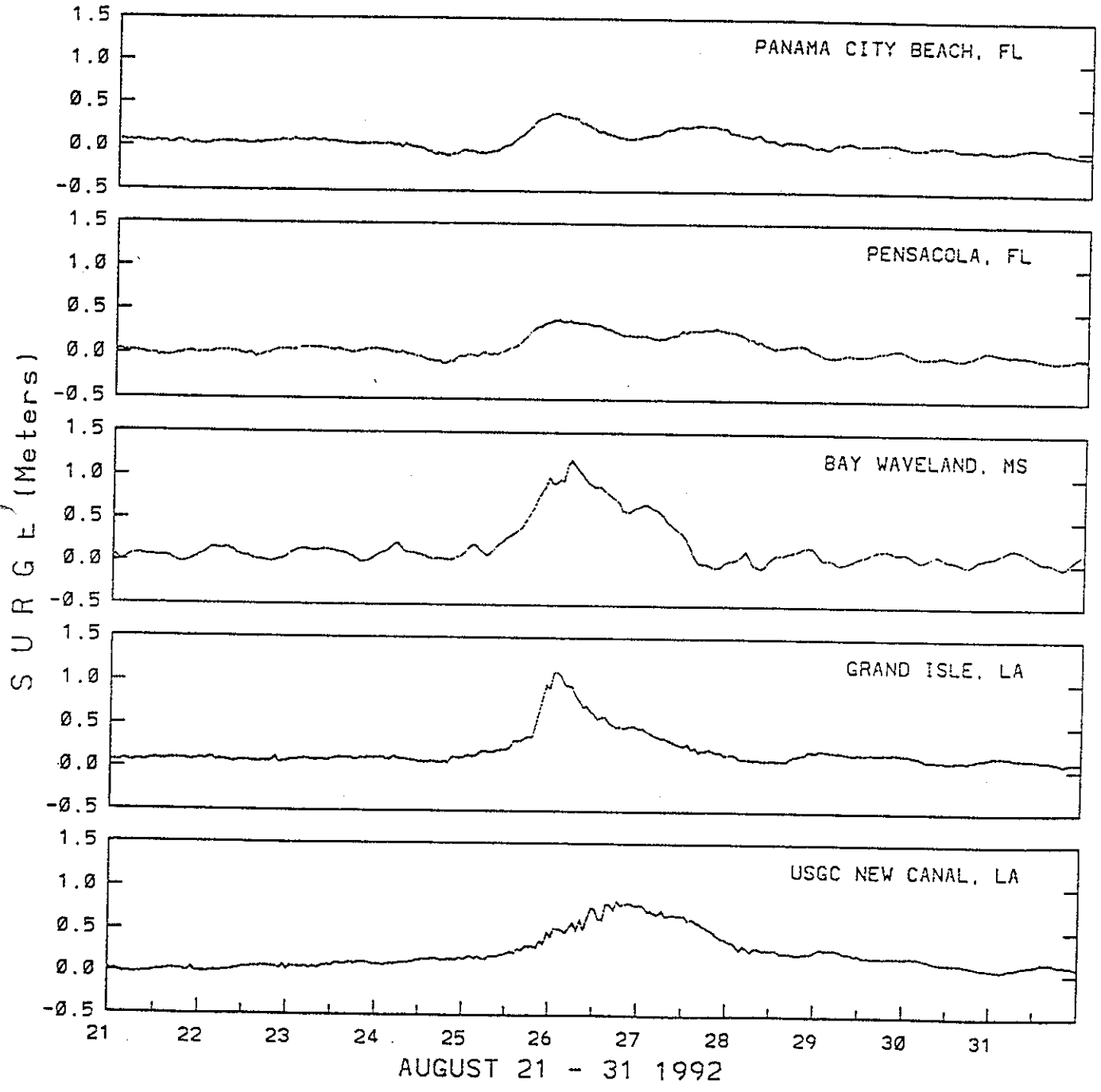

Figure 2.4 Measured water elevations from coastal C-MAN and NOS stations, from Breaker et al., 1994.

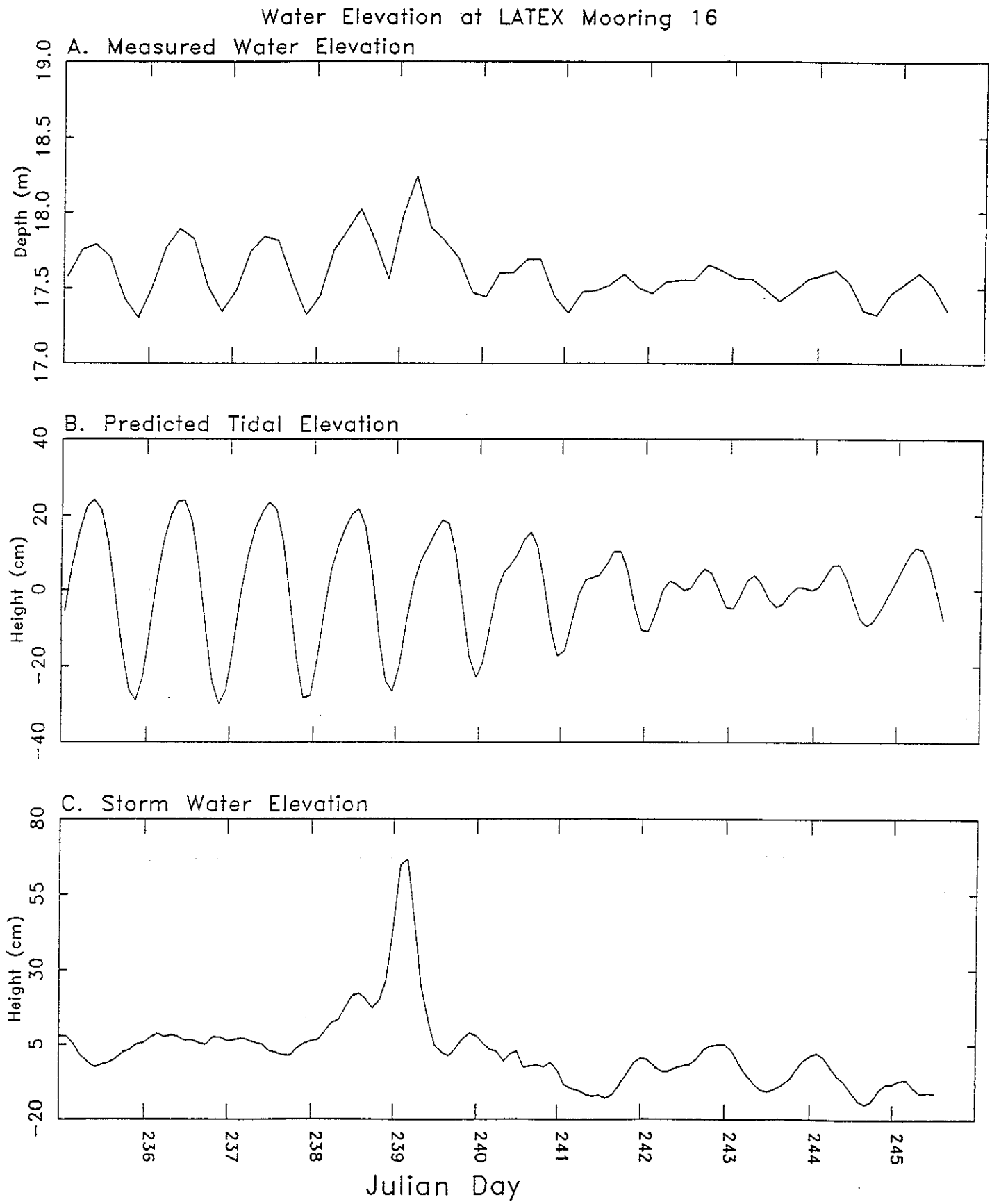

Figure 2.5 Water level elevation at LATEX mooring 16.

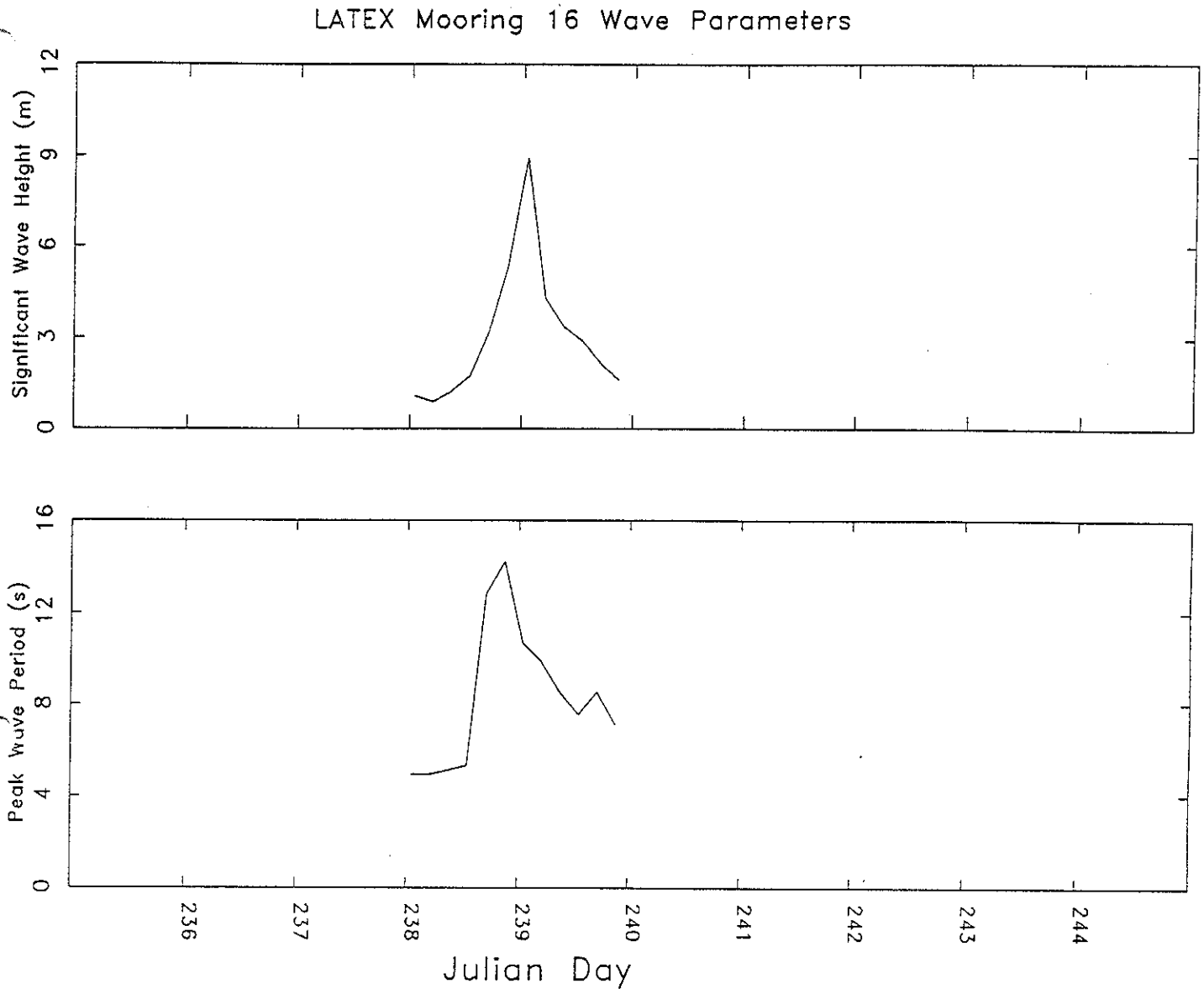

Figure 2.6 LATEX mooring 16 wave parameters.

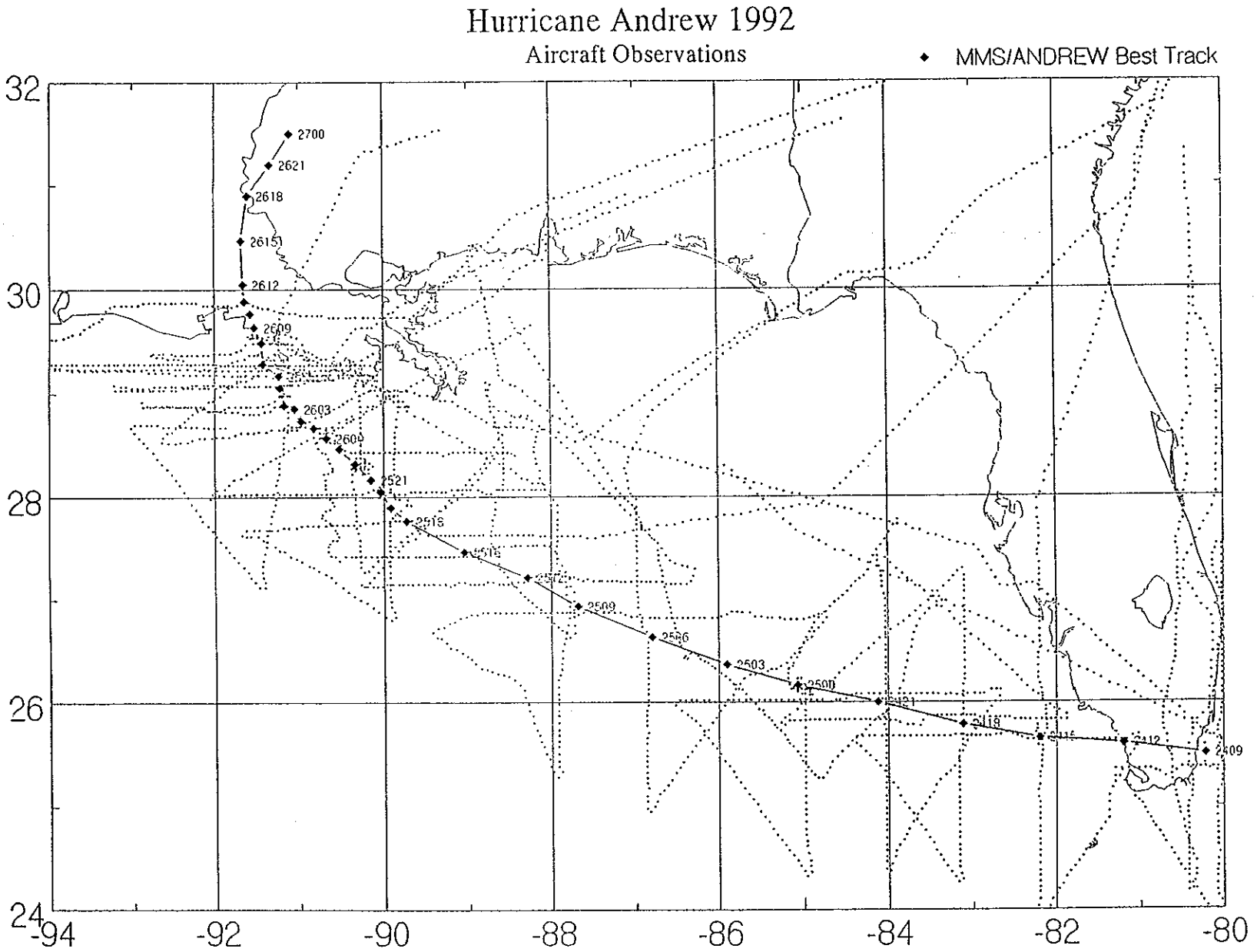

Figure 3.1 Hurricane Andrew aircraft reconnaissance observations.

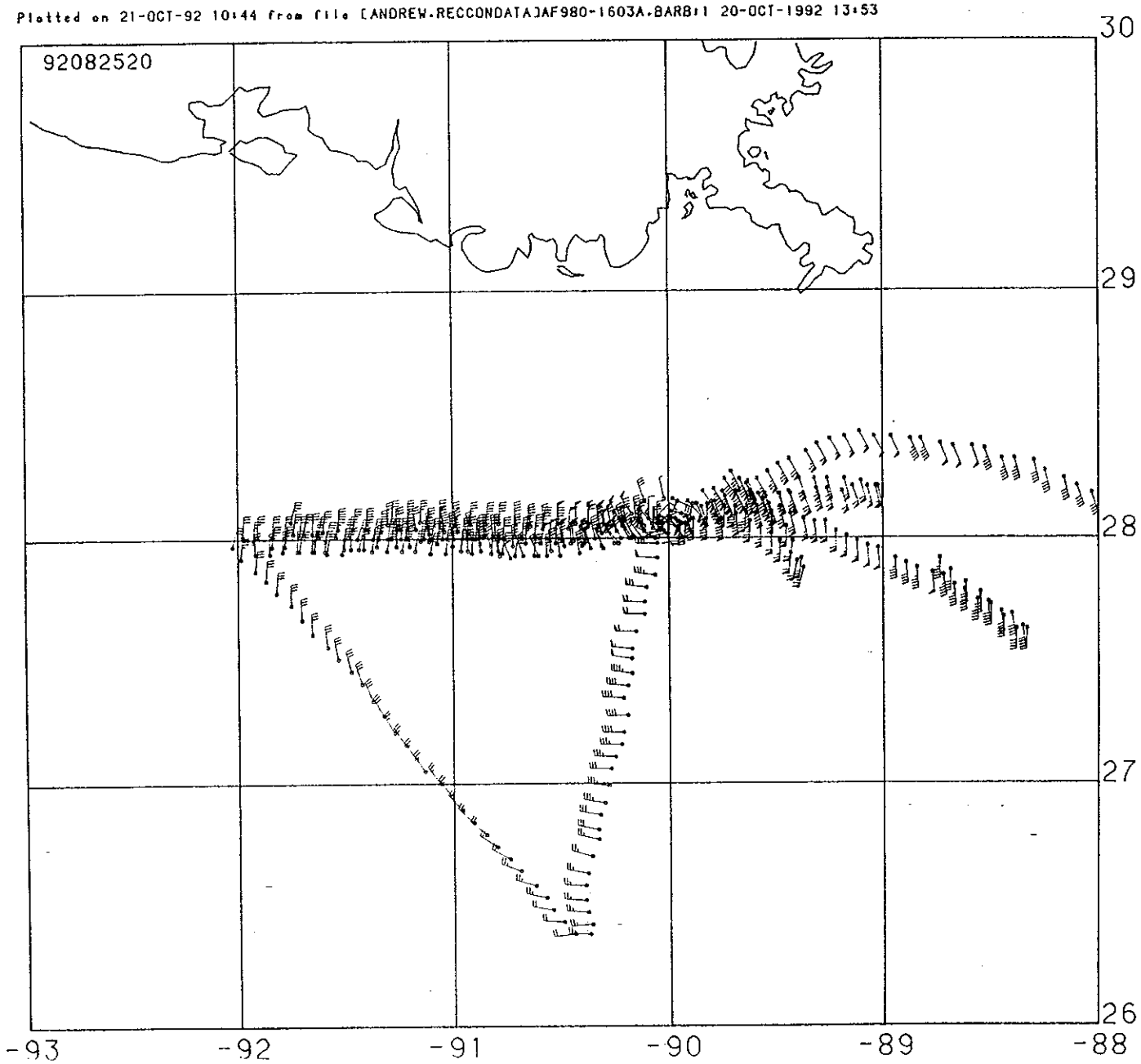

Figure 3.2 Sample of aircraft flight level winds in Andrew.

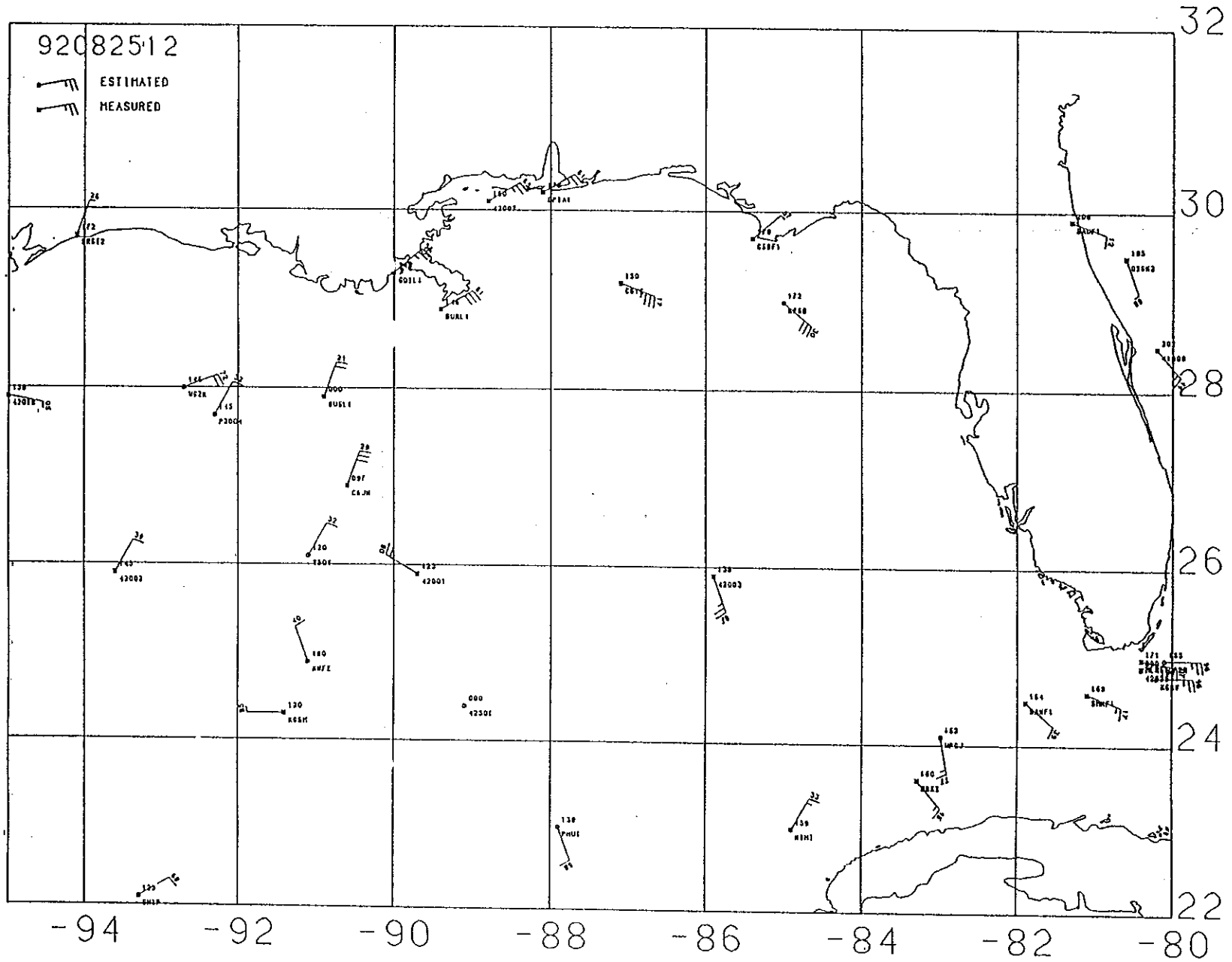

Figure 3.3 Sample plot of conventional surface observations of surface pressure and surface wind in Gulf of Mexico during Hurricane Andrew.

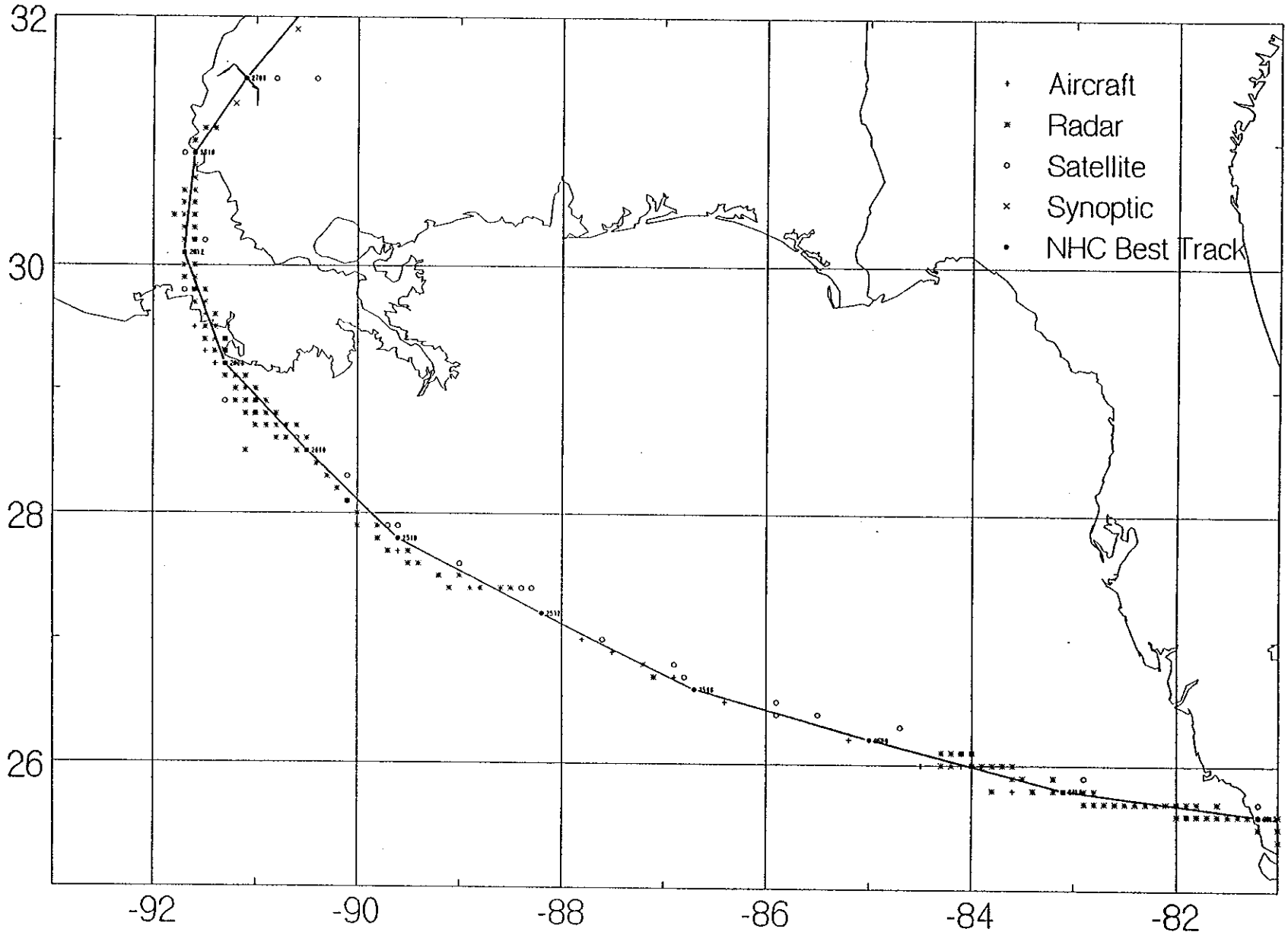

Figure 3.4 Hurricane Andrew fixes compared to "NHC Track".

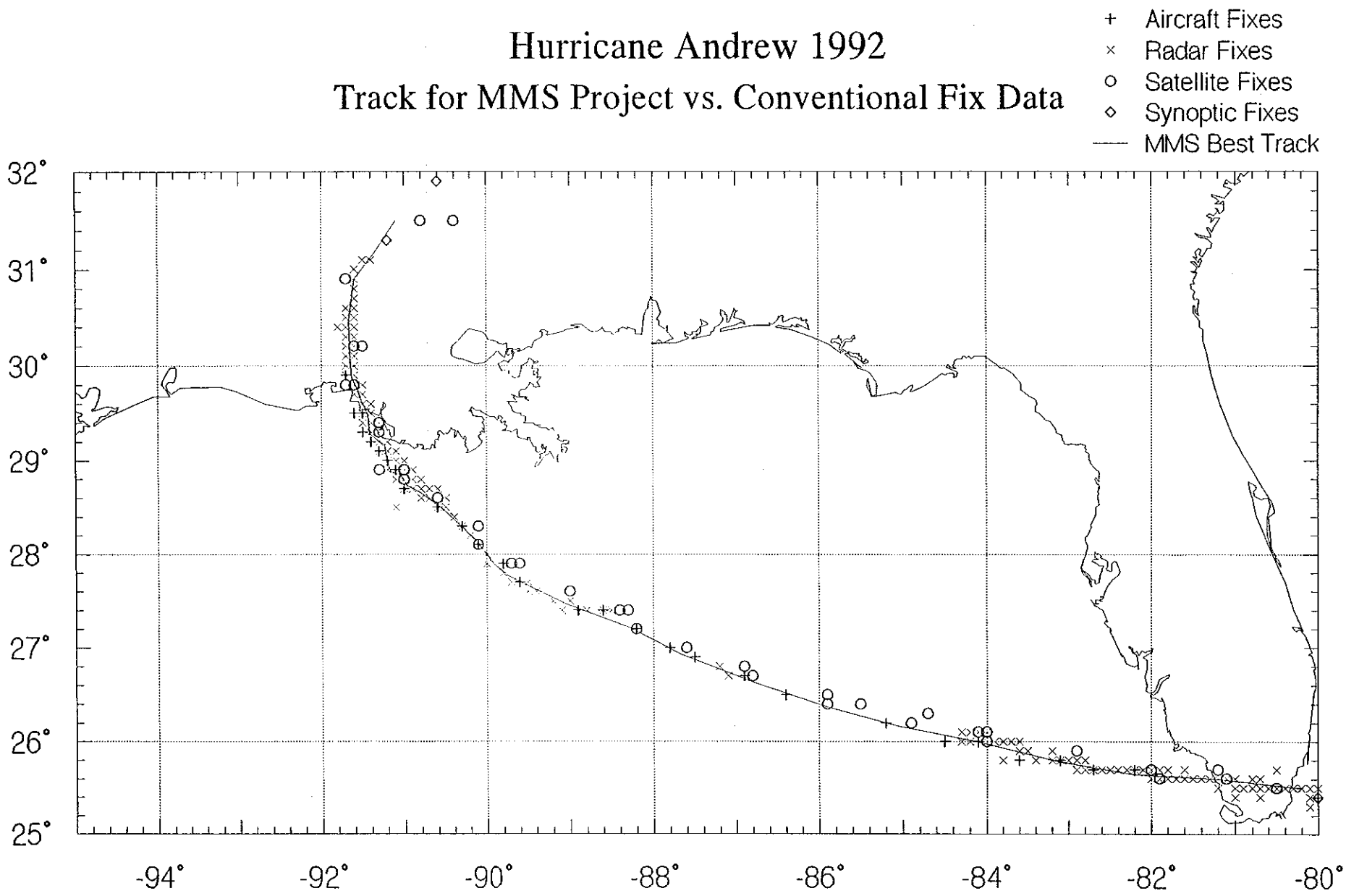

Figure 3.5 Hurricane Andrew fixes compared to best track used in this study.

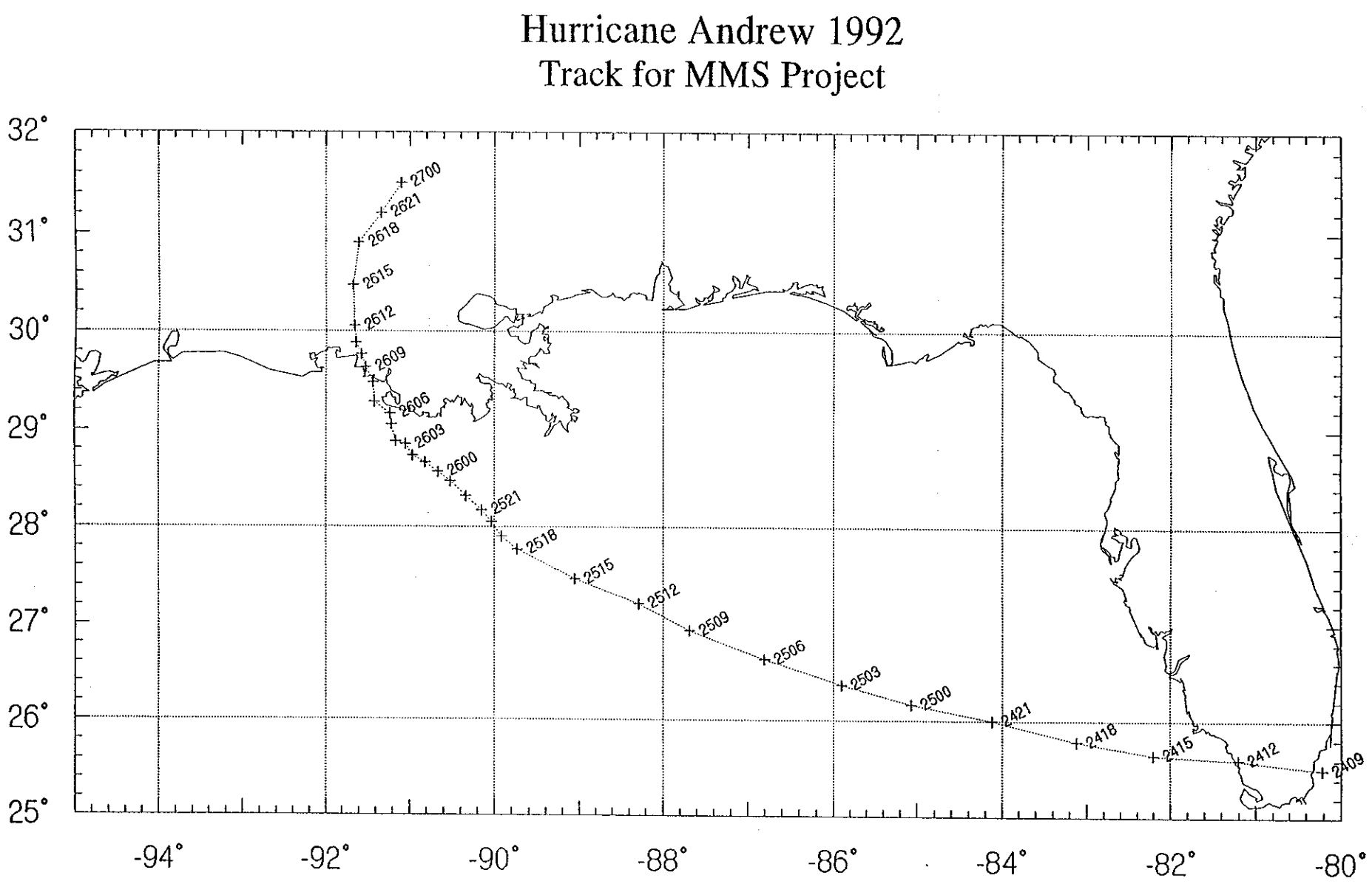

Figure 3.6 Hurricane Andrew best track with hourly and three-hourly positions.

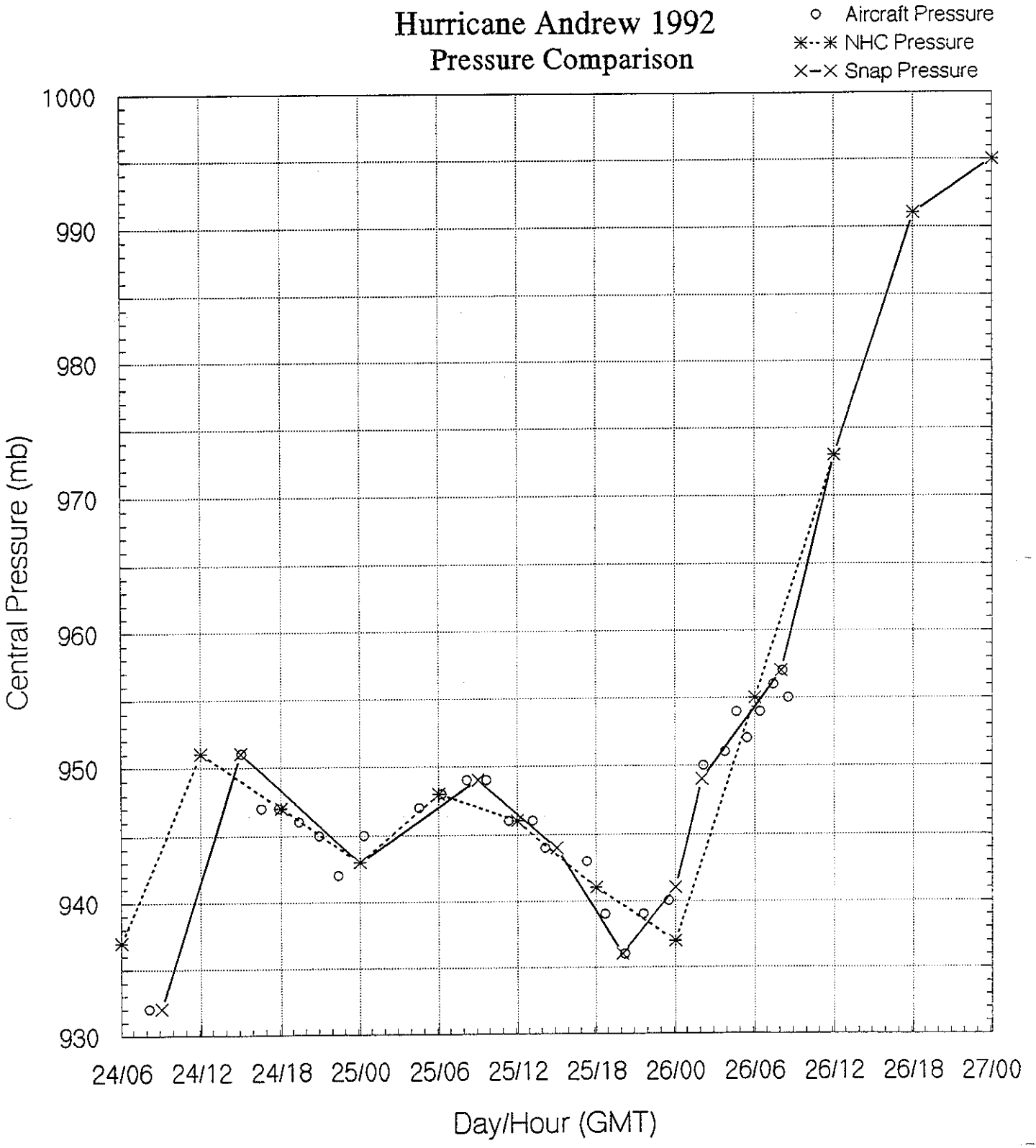

Figure 3.7 Minimum central pressure in Hurricane Andrew from aircraft observations and NHC and time history used in this study.

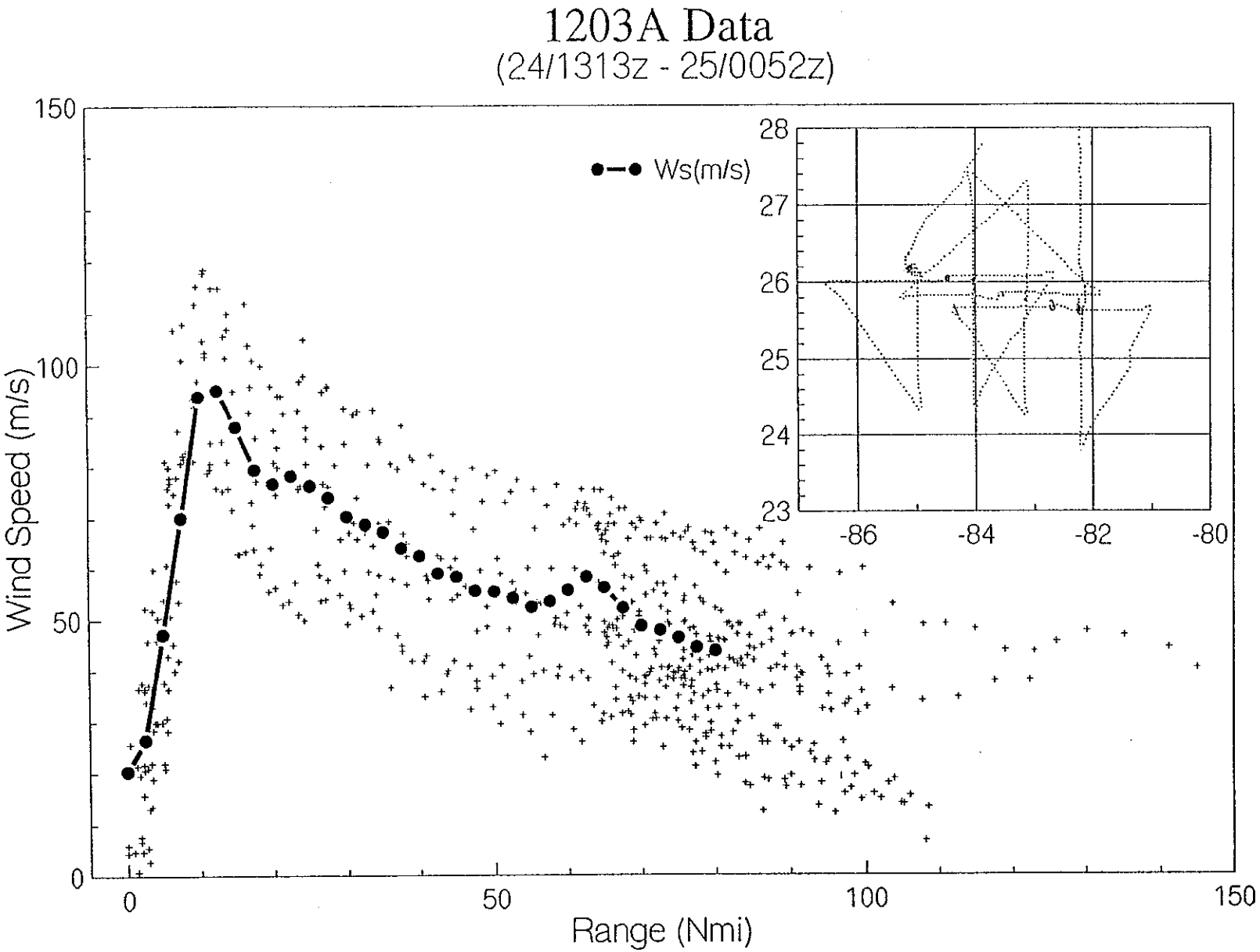

Figure 3.8 Sample of aircraft flight level winds (plus signs) reduced to 20 and azimuthal average (filled circles).

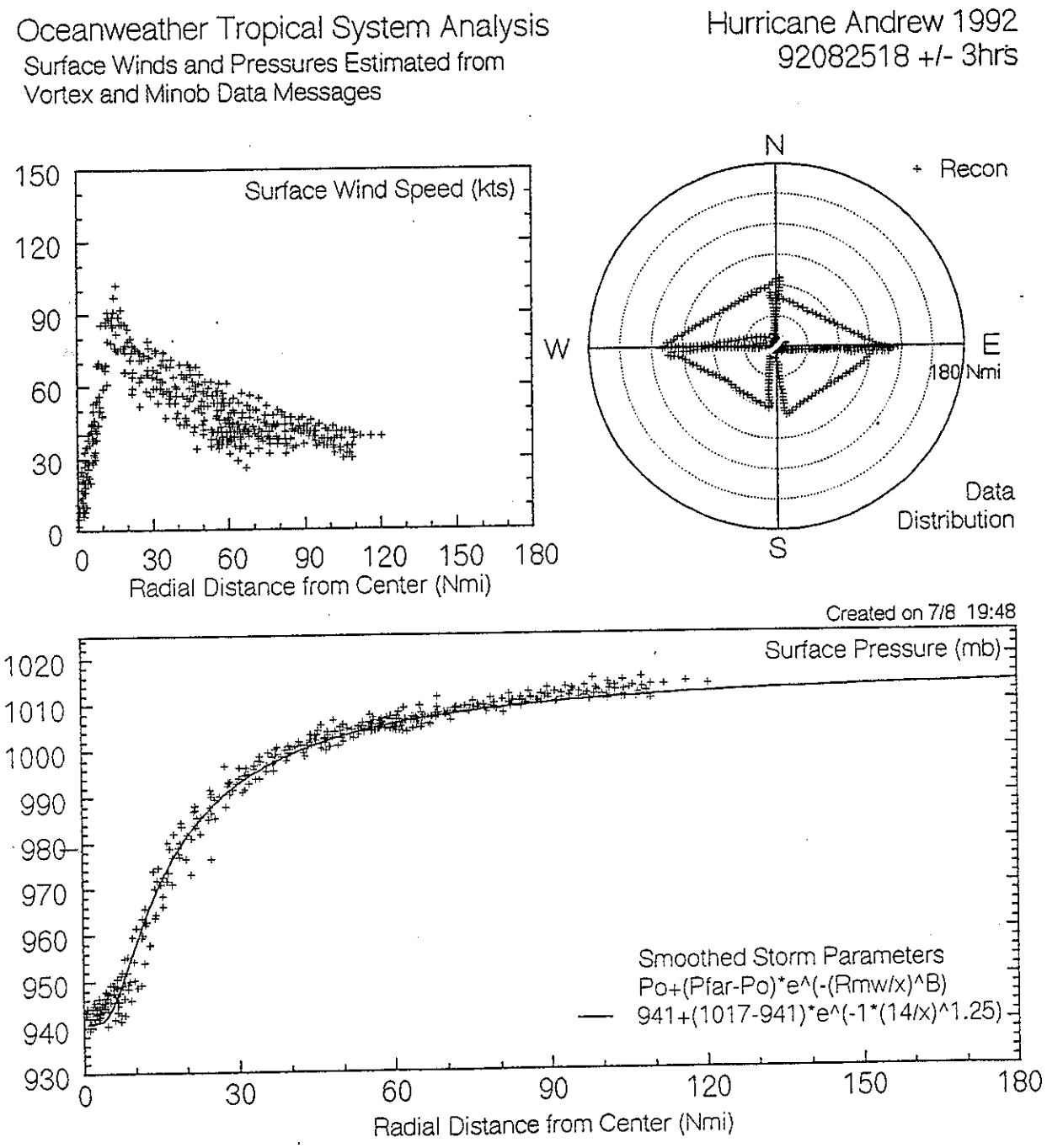

Figure 3.9 Screen display of workstation program used to fit radial pressure profile.

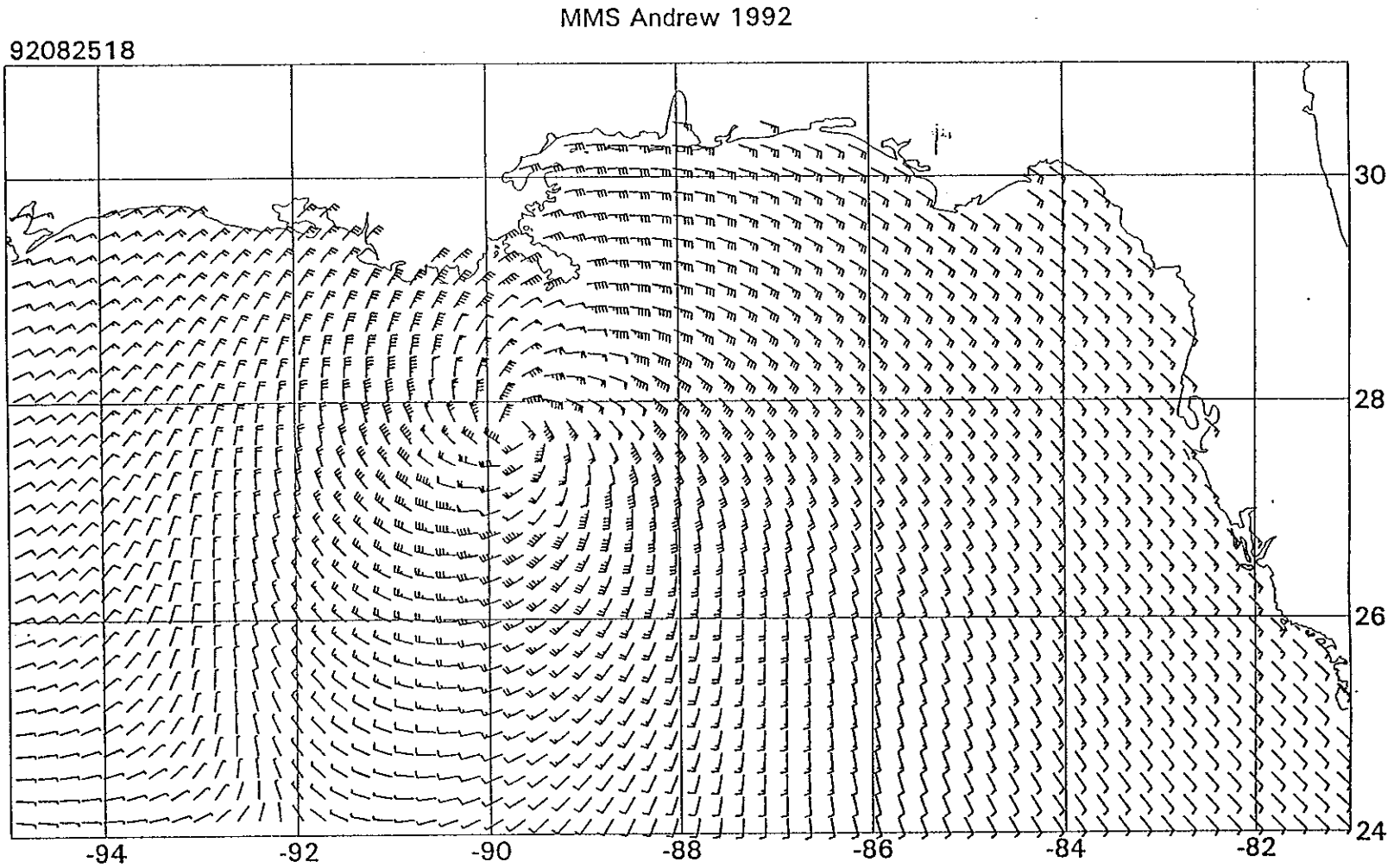

Figure 3.10 Sample wind barb plot of modeled 20-m level 1-hour average wind field in Hurricane Andrew (knots) over whole domain.

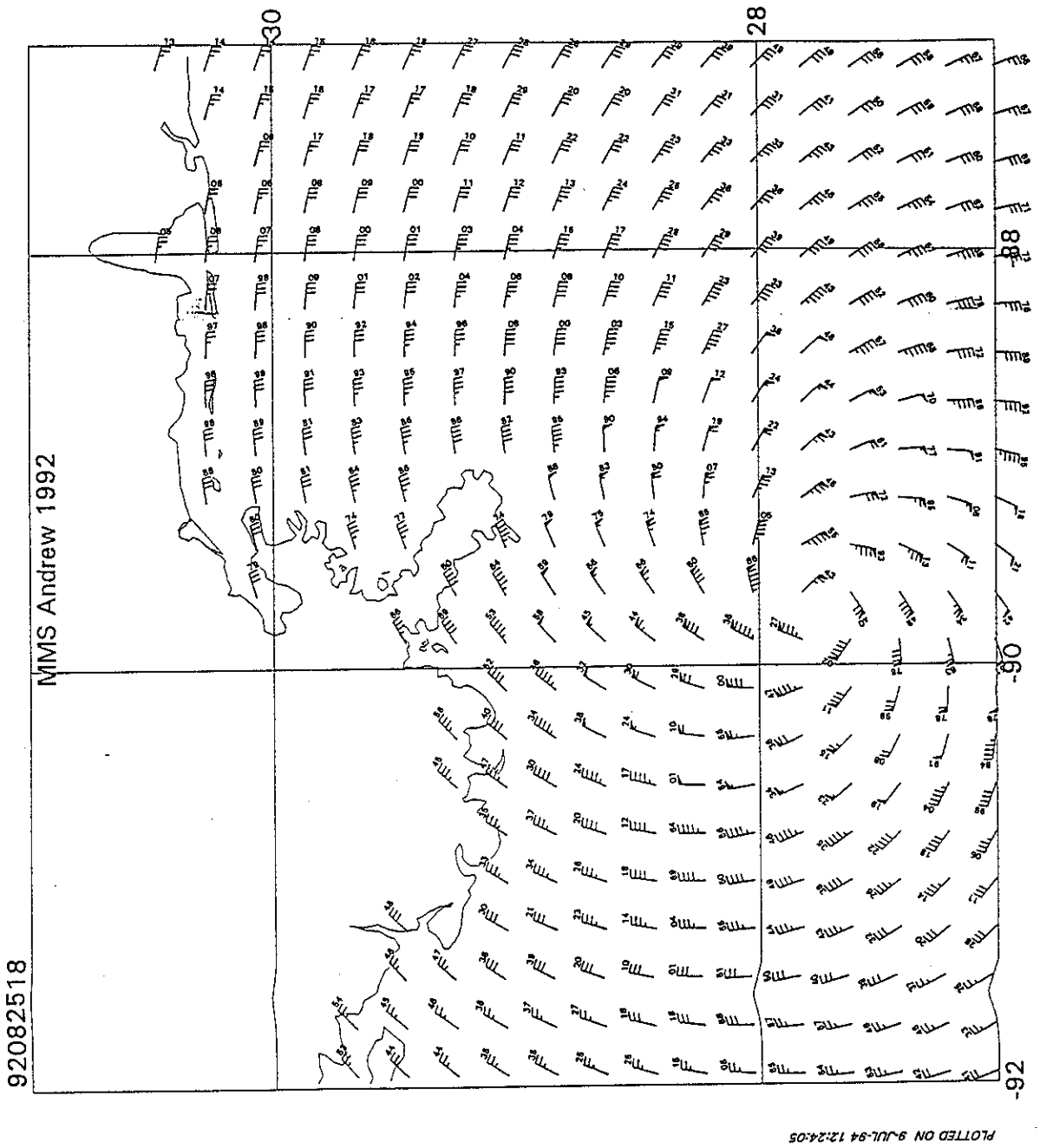

Figure 3.11 Sample wind barb plot of modeled 20-m level 1-hour average wind field in Hurricane Andrew (knots) over limited domain.

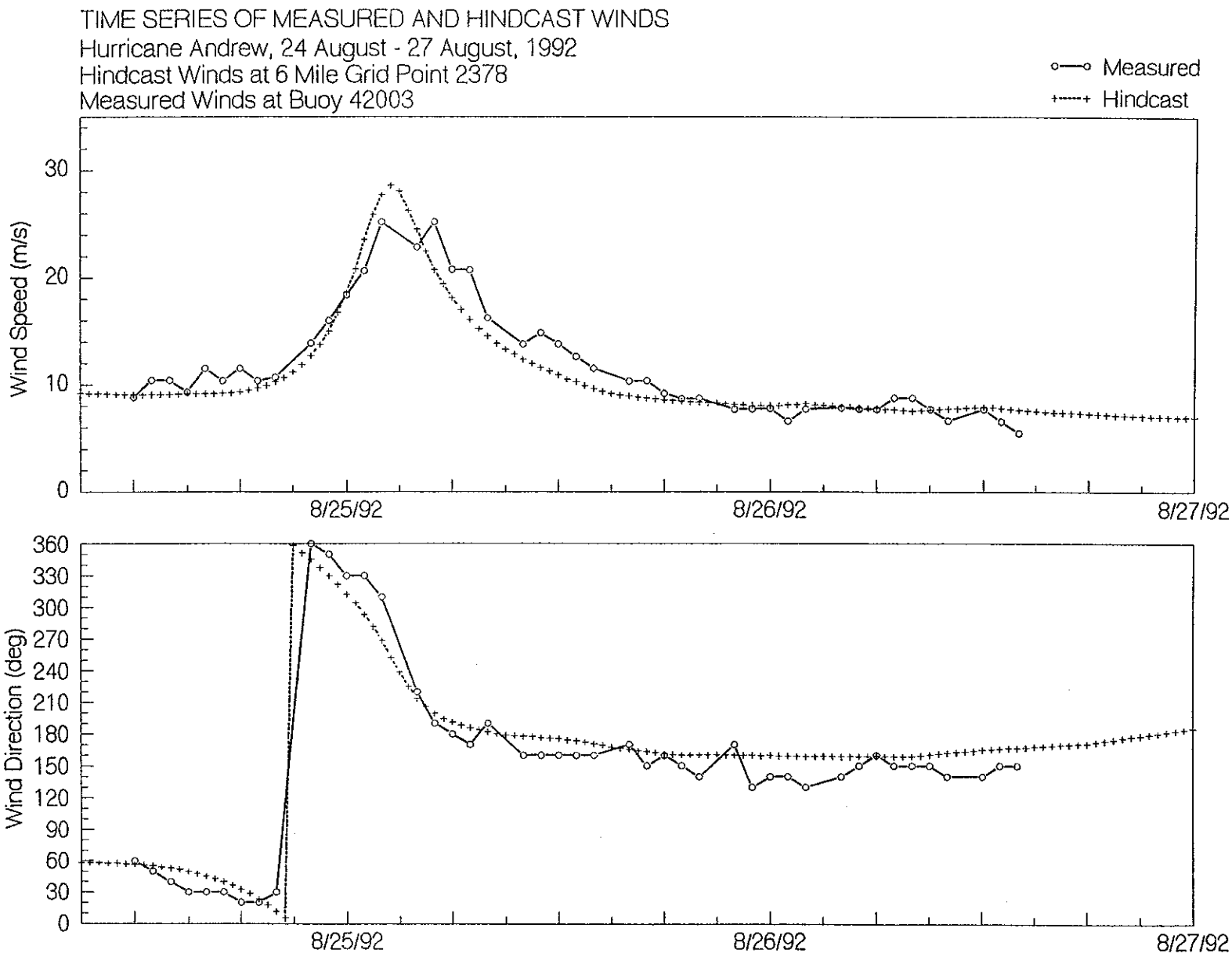

Figure 3.12 Modeled and measured wind speed and direction (at 20 meters) at buoy 42003.

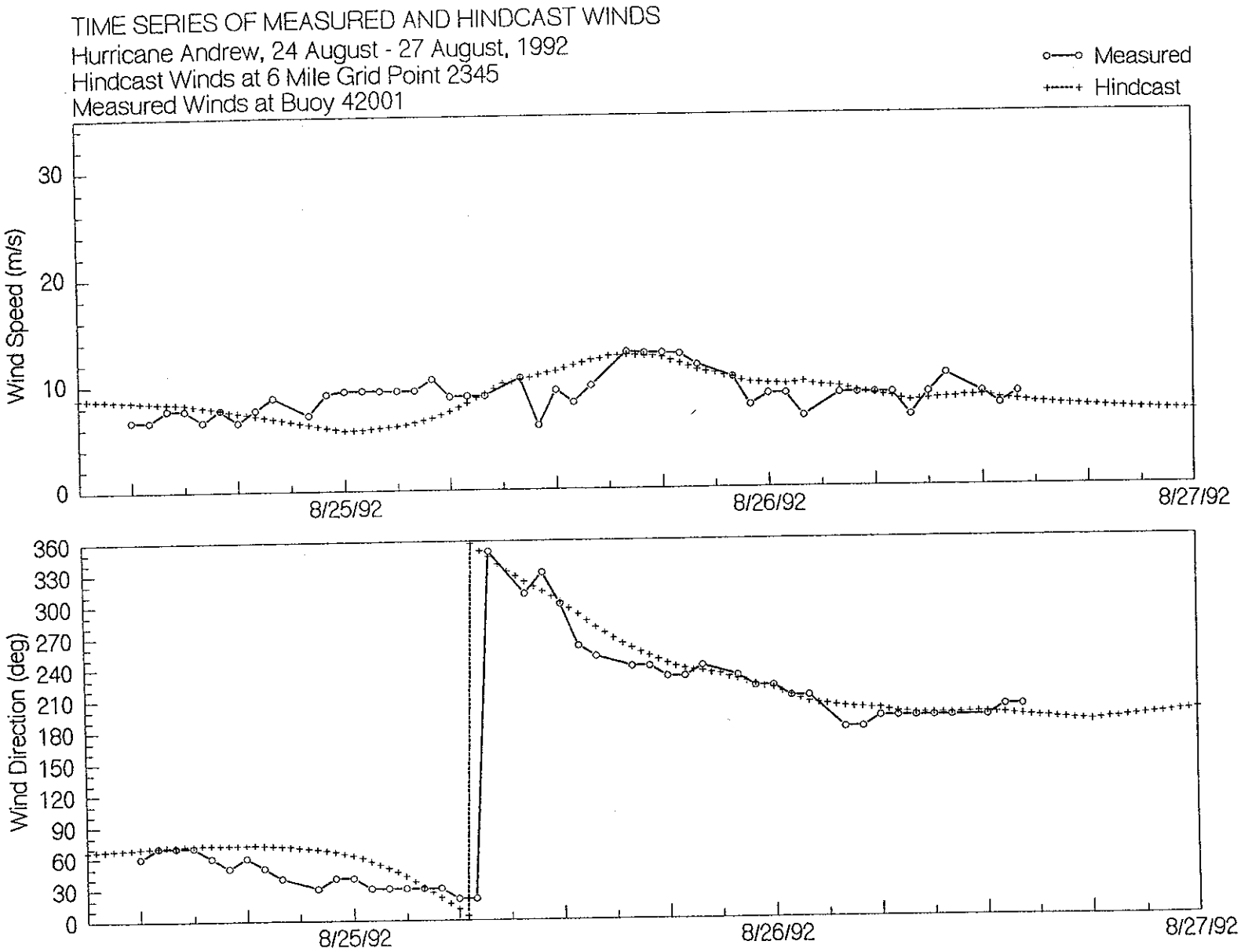

Figure 3.13 Modeled and measured wind speed and direction (at 20 meters) at buoy 42001.

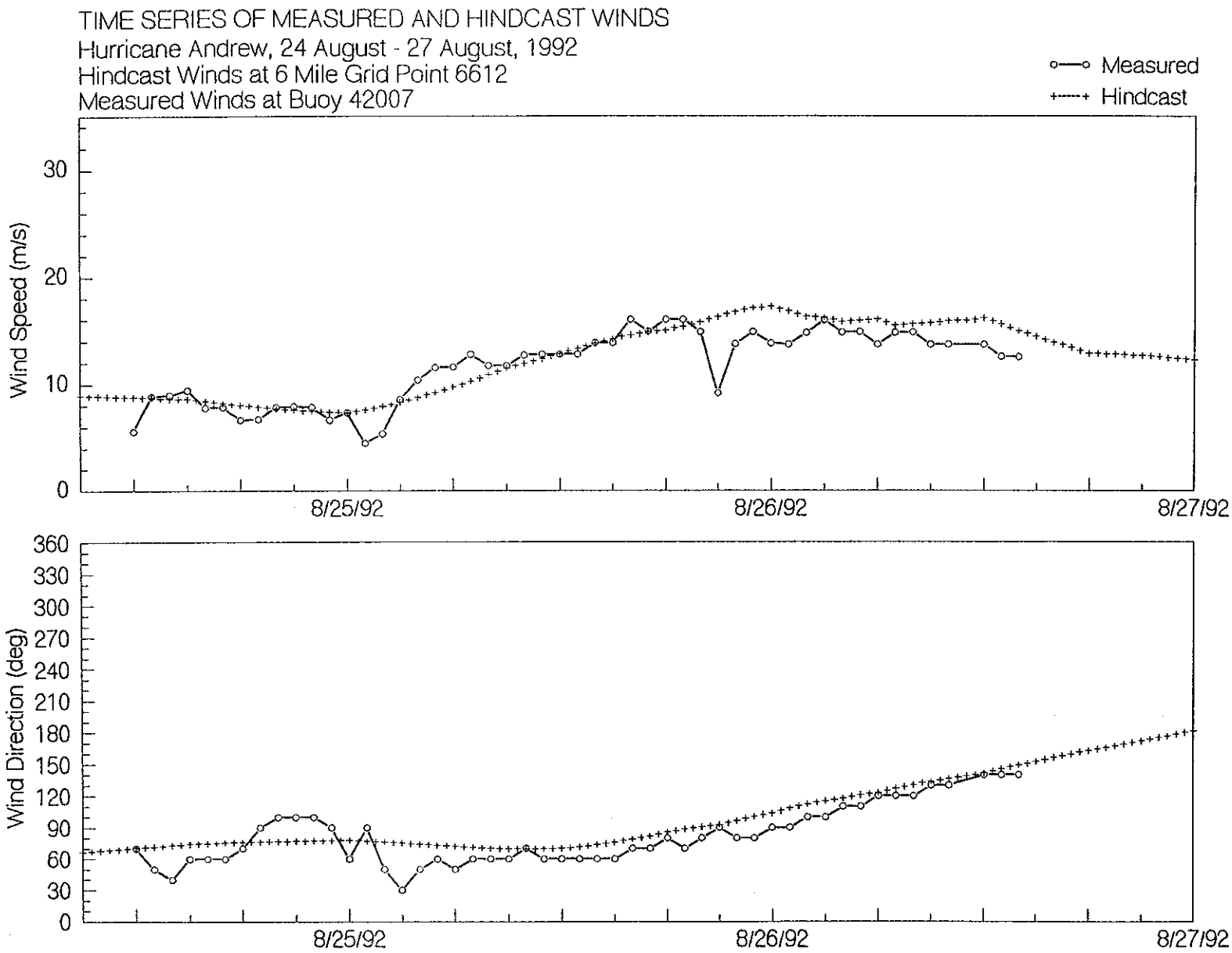

Figure 3.14 Modeled and measured wind speed and direction (at 20 meters) at buoy 42007

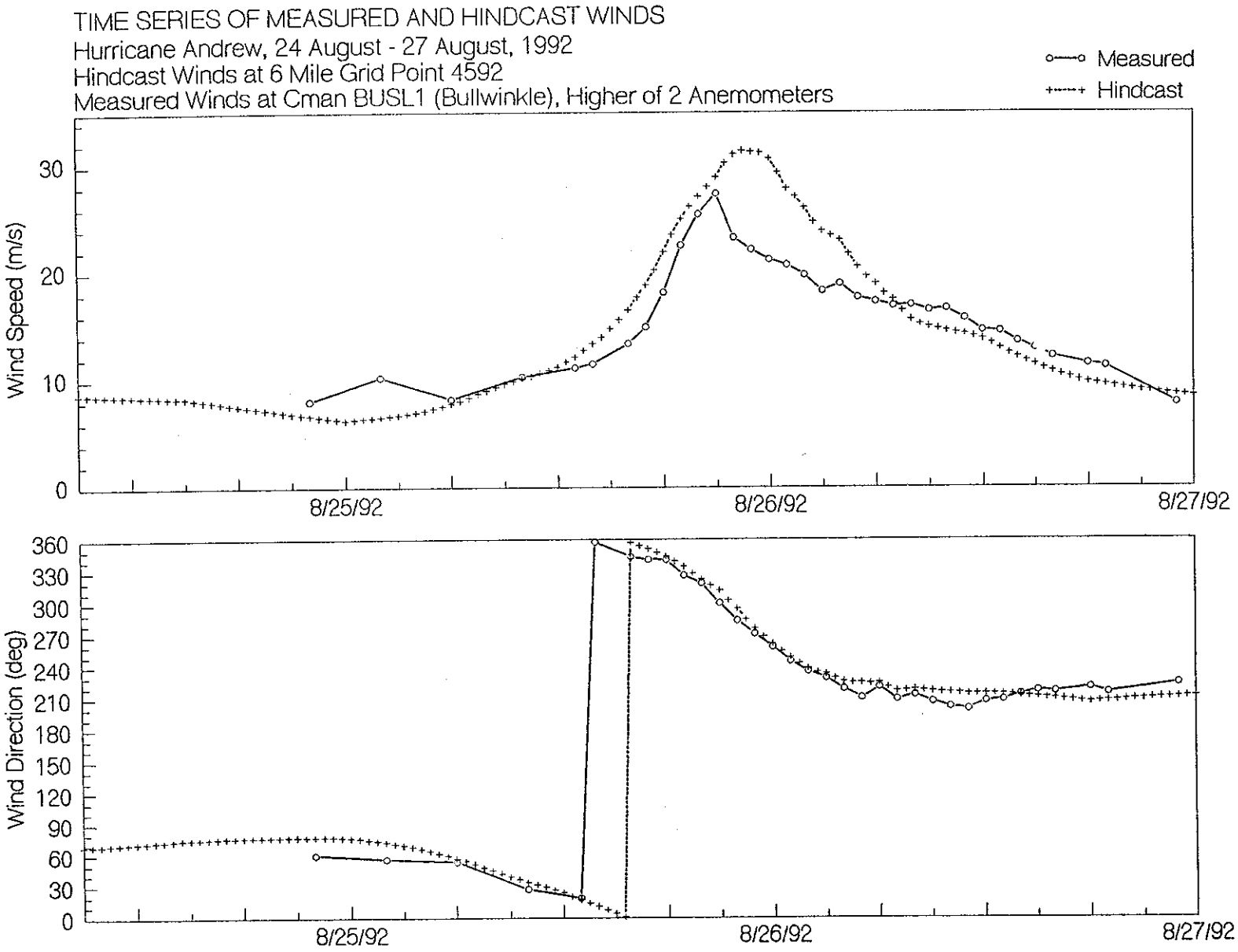

Figure 3.15 Modeled and measured wind speed and direction (at 20 meters) at Bullwinkle C-M

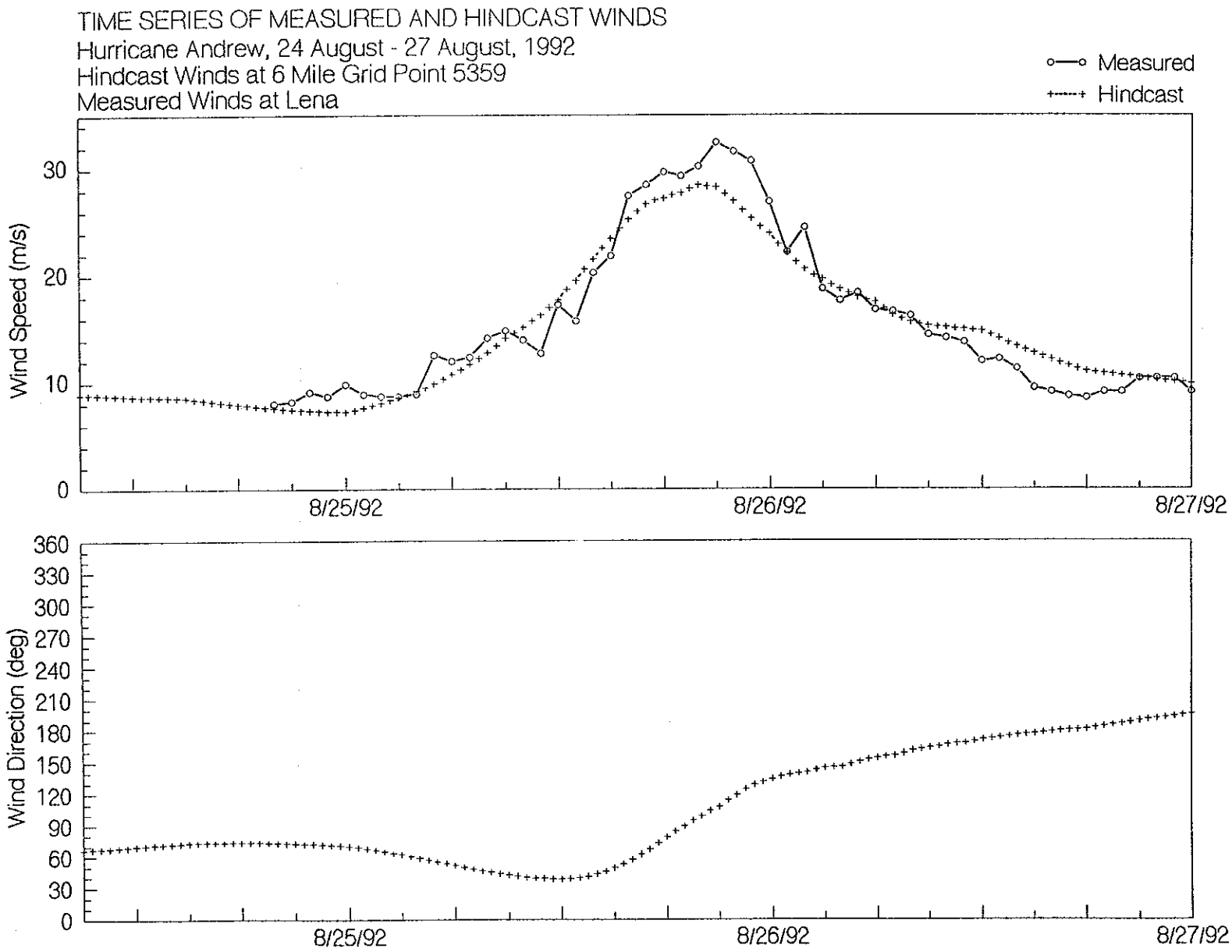

Figure 3.16 Modeled and measured wind speed and direction (at 20 meters) at LENA.

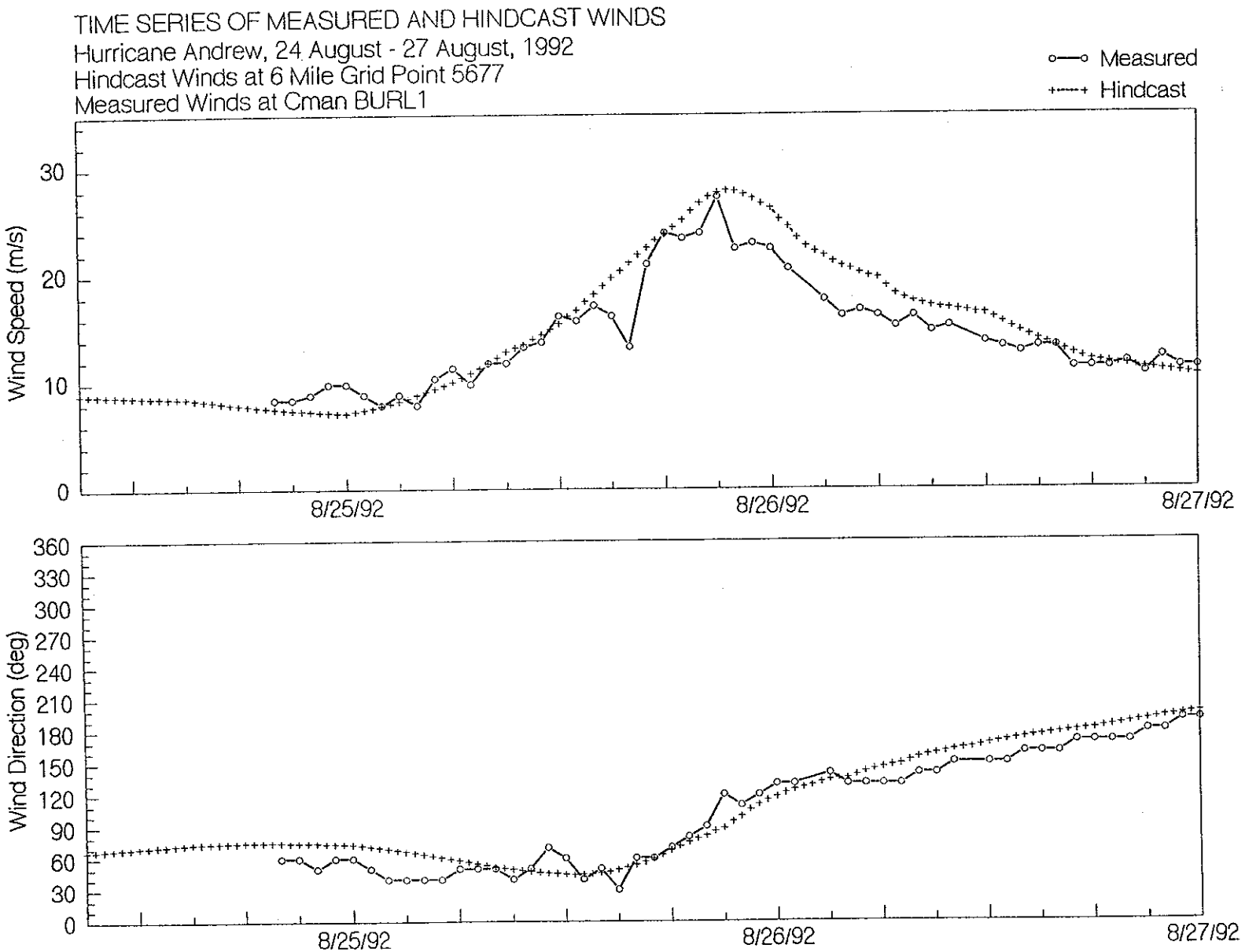

Figure 3.17 Modeled and measured wind speed and direction (at 20 meters) at BURL1 C-MAN.

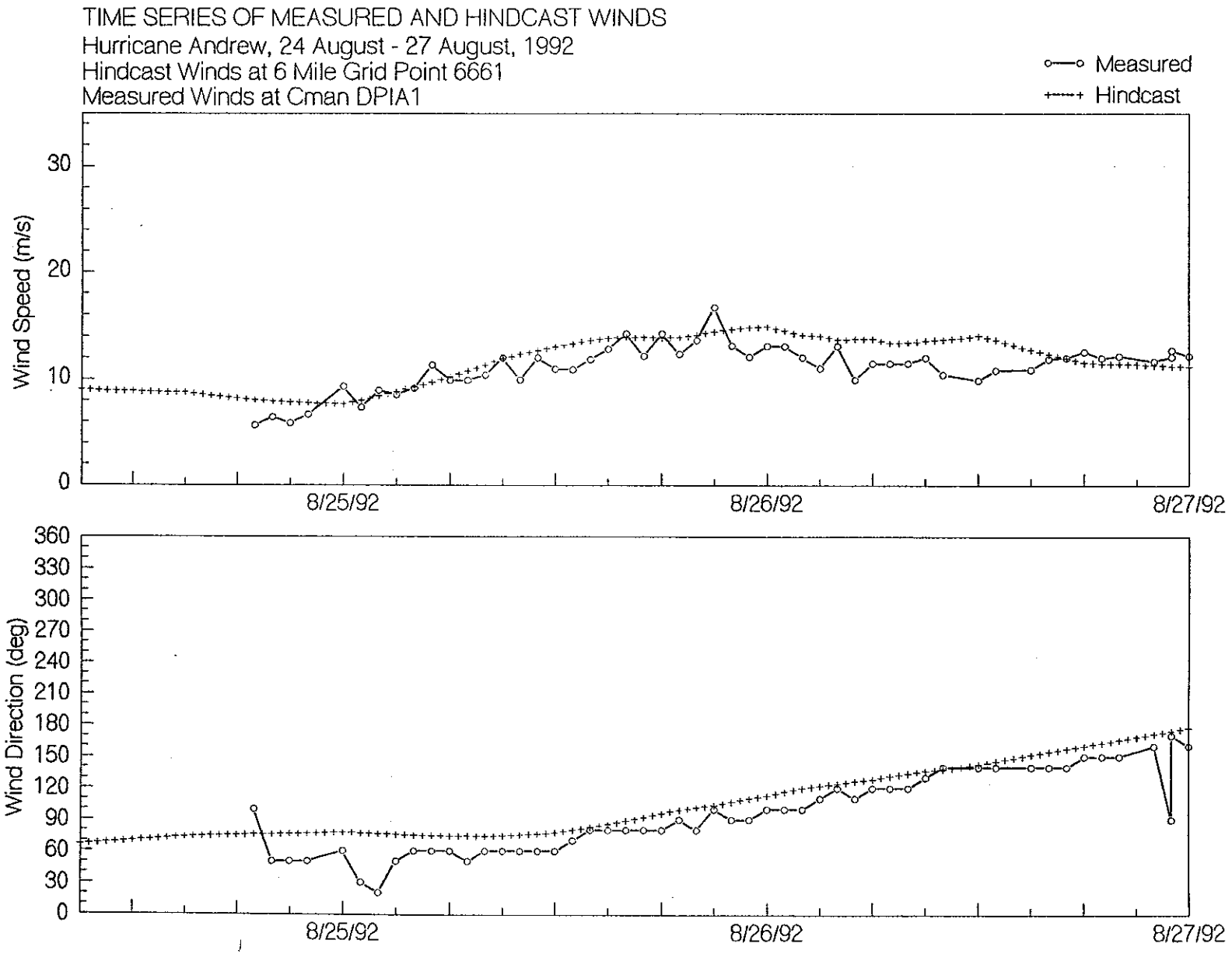

Figure 3.18 Modeled and measured wind speed and direction (at 20 meters) at DPIA C-MAN.

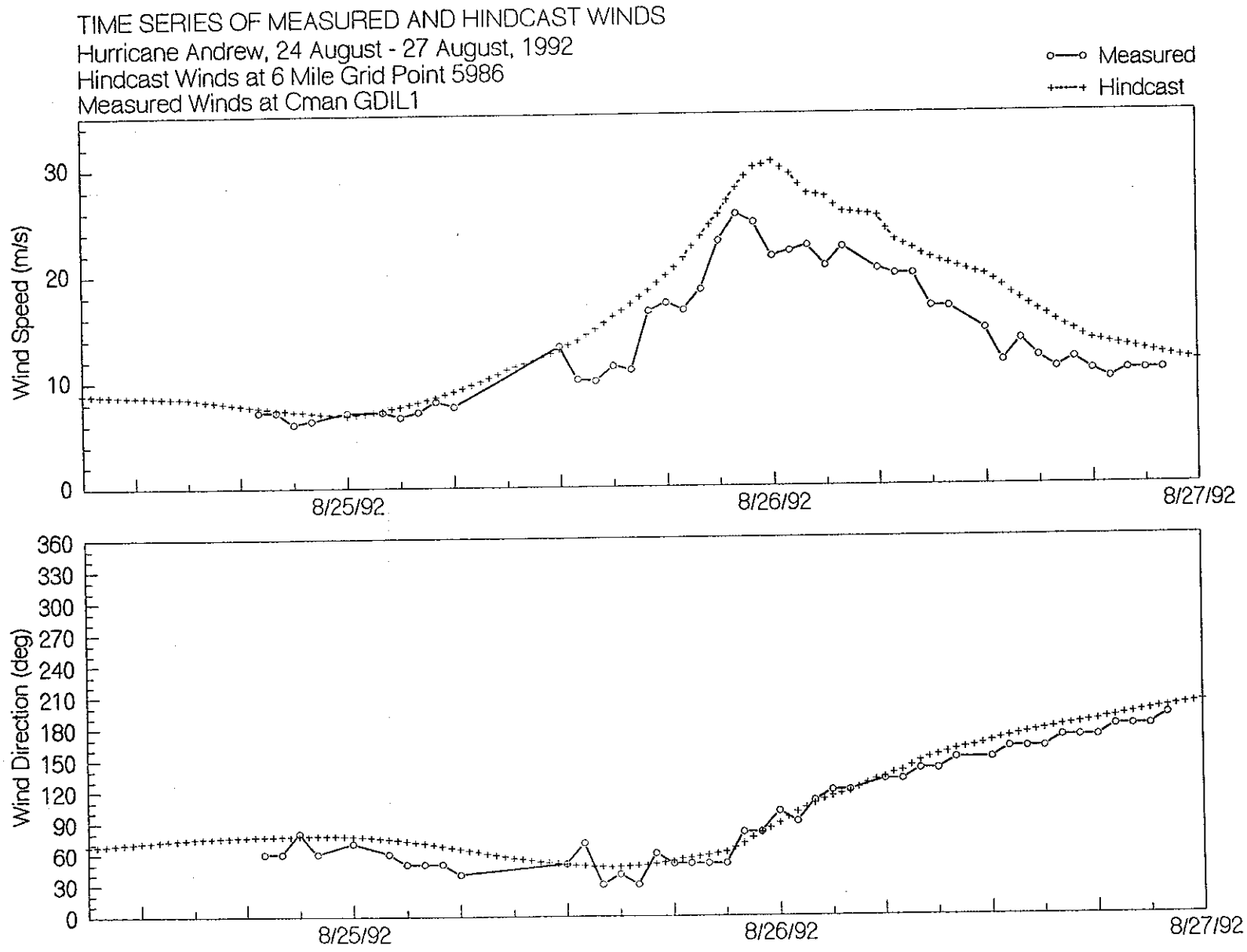

Figure 3.19 Modeled and measured wind speed and direction (at 20 meters) at GDIL C-MAN.

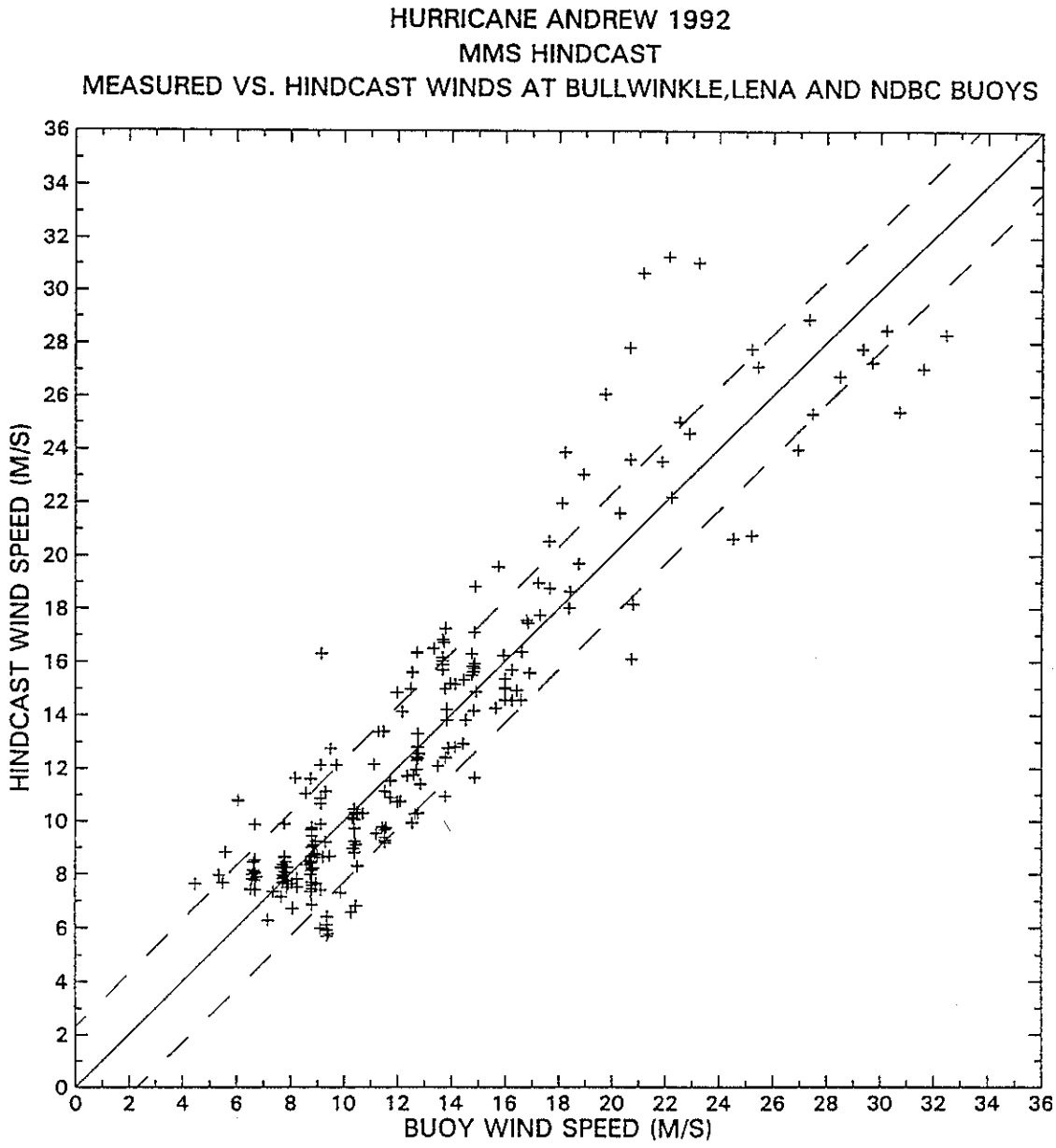

Number of points:	226
Mean Measurement:	12.74
Mean Hindcast:	12.96
Mean Difference:	.22
Root mean square:	2.30
Standard deviation:	2.29
Scatter index:	.18
Ratio:	.48
Correlation Coefficient:	.92

Figure 3.20 Scatter plot of measured and hindcast wind speed in Hurricane Andrew at offshore measurement sites.

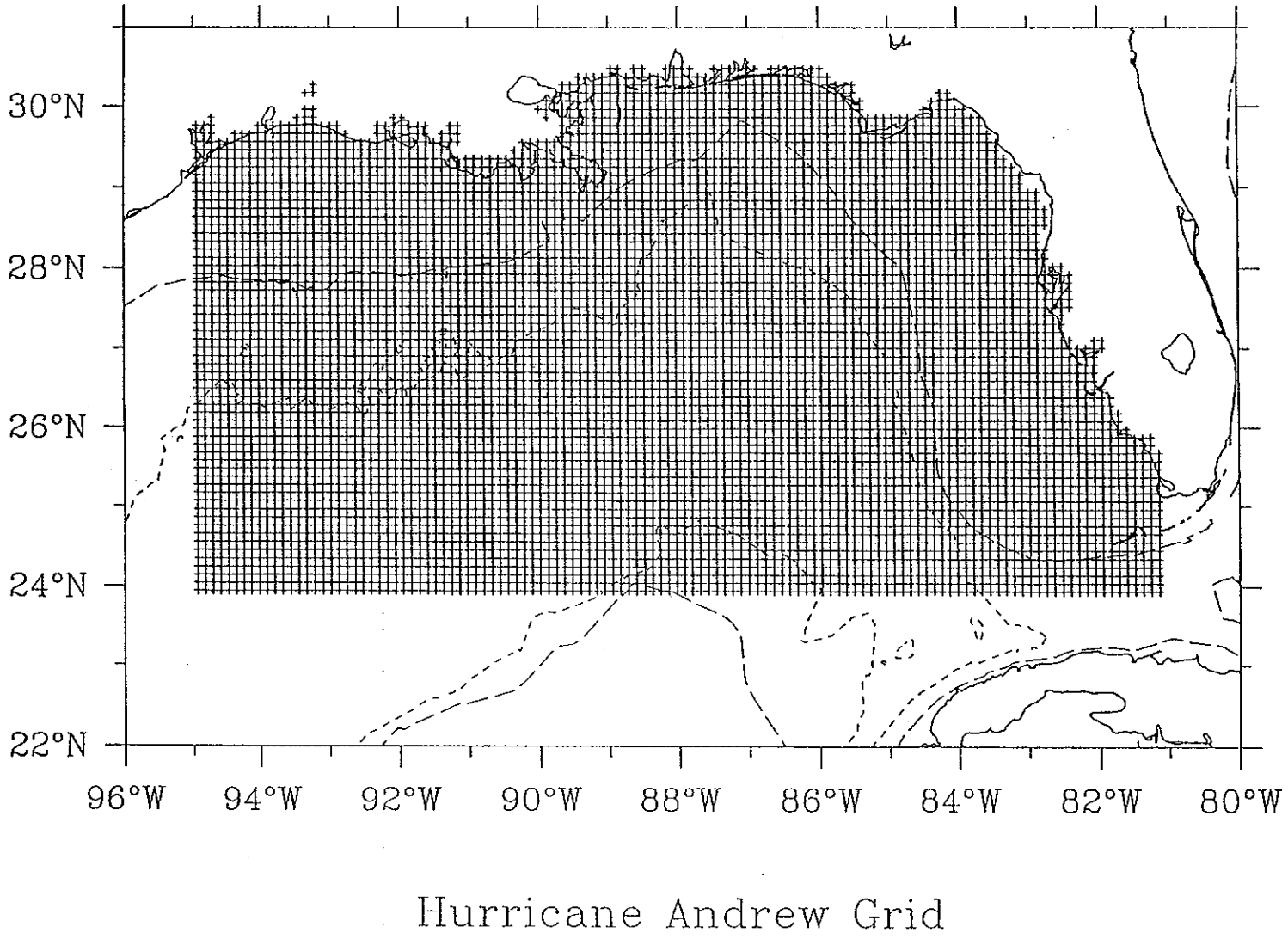

Figure 4.1 Grid system used for wave and hydrodynamic modeling.

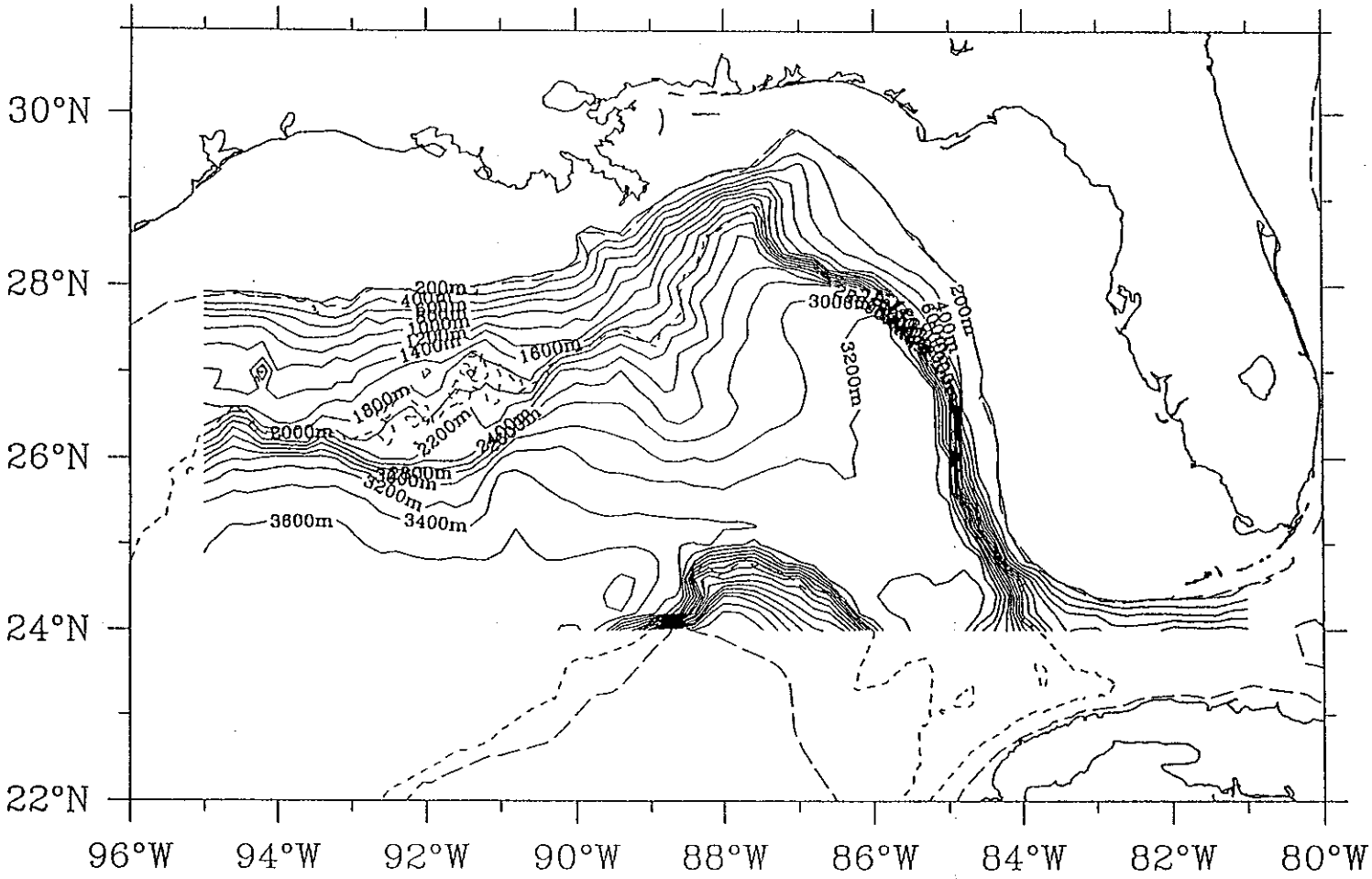

Figure 4.2 Depth field over model domain.

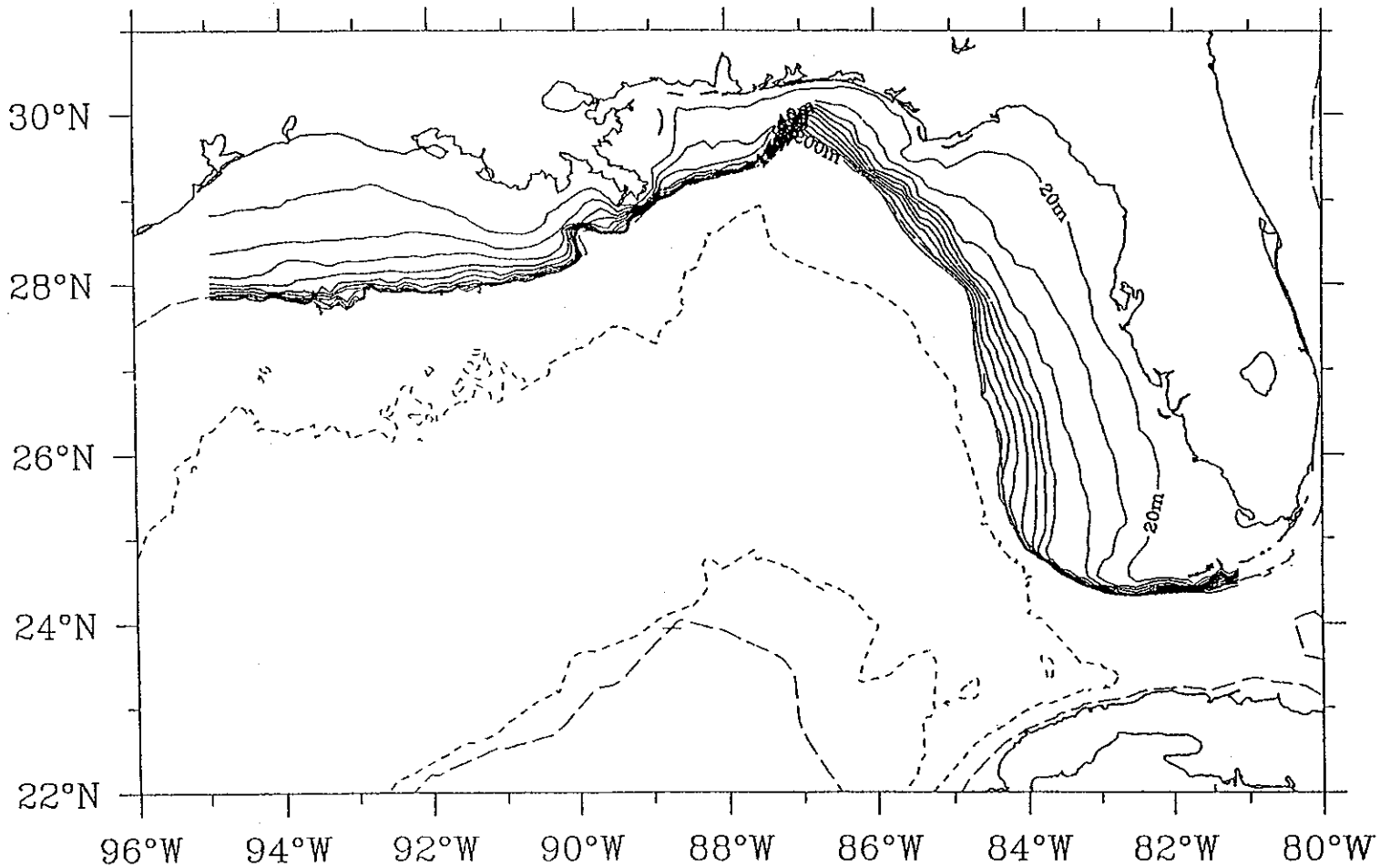

Figure 4.3 Depth field adopted over the continental shelf.

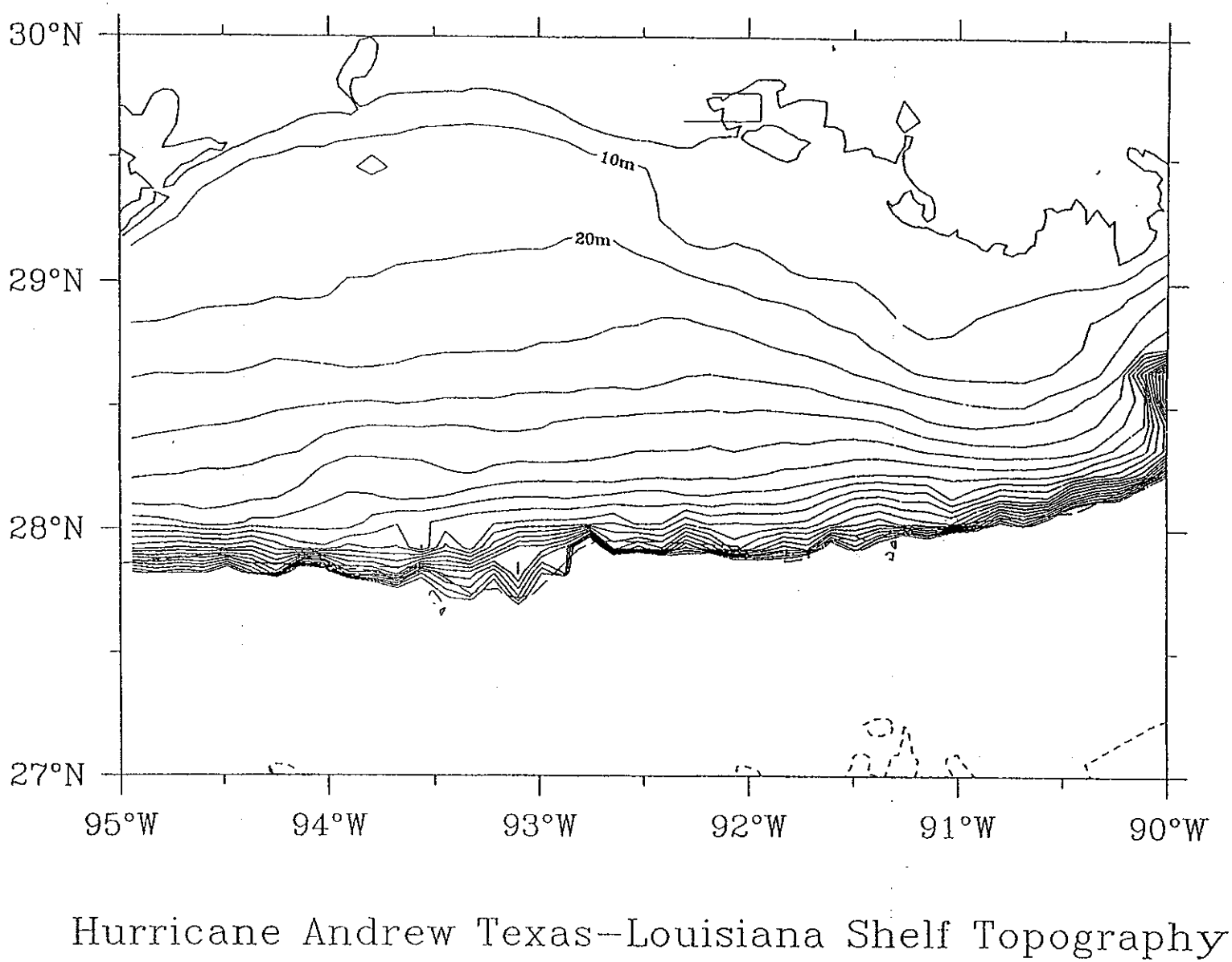

Figure 4.4 Louisiana shelf bottom topography.

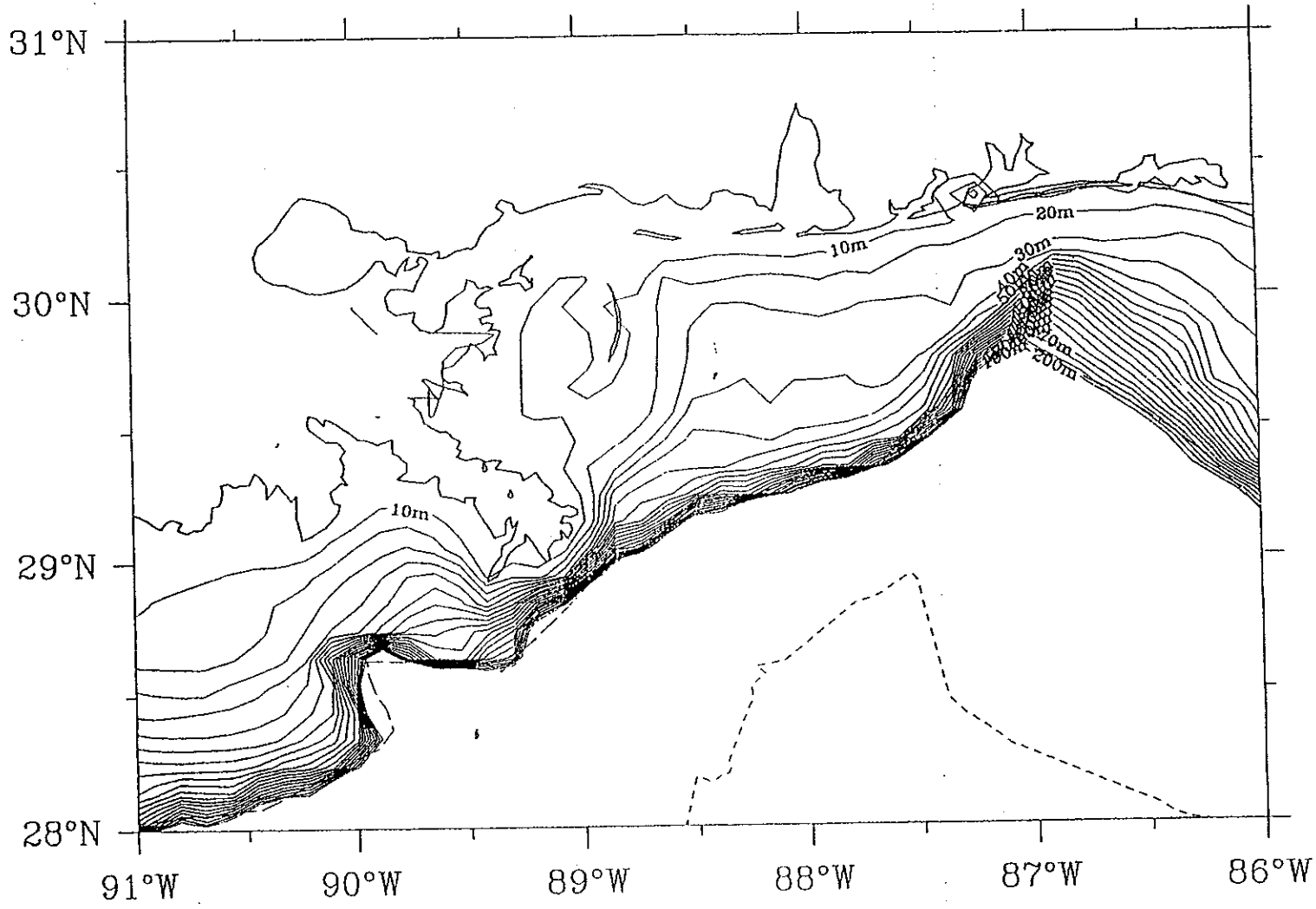

Figure 4.5 Mississippi shelf bottom topography.

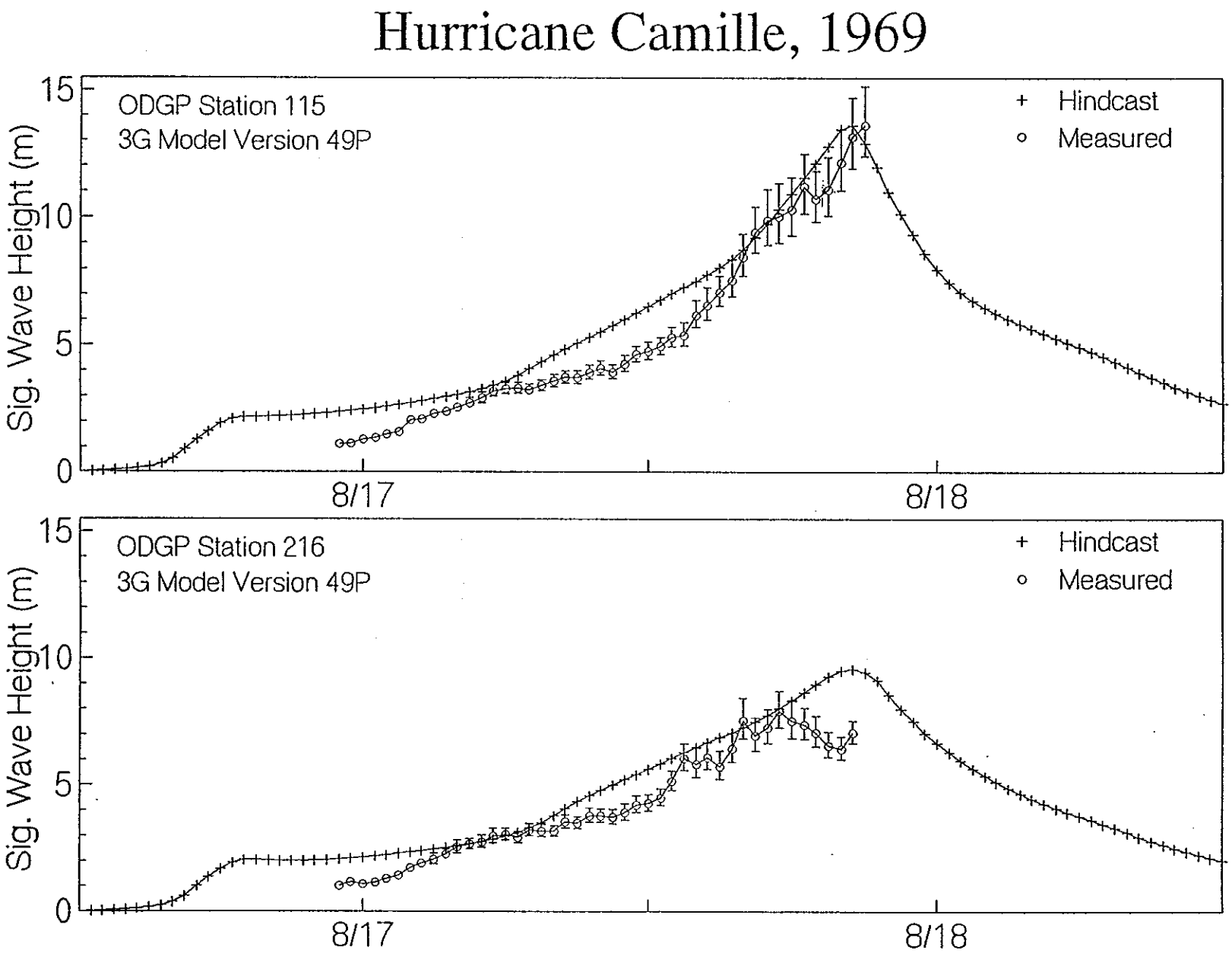

Figure 4.6 OWI3G wave model versus measured wave height in Camille (1969).

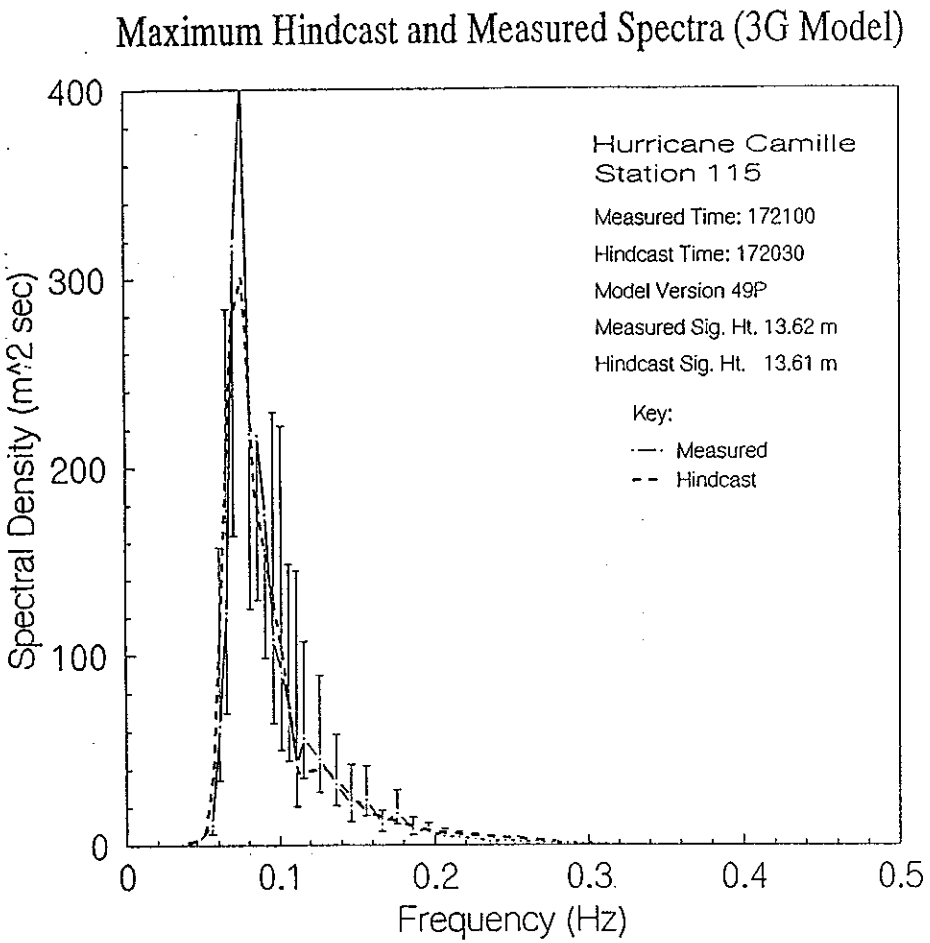

(a)

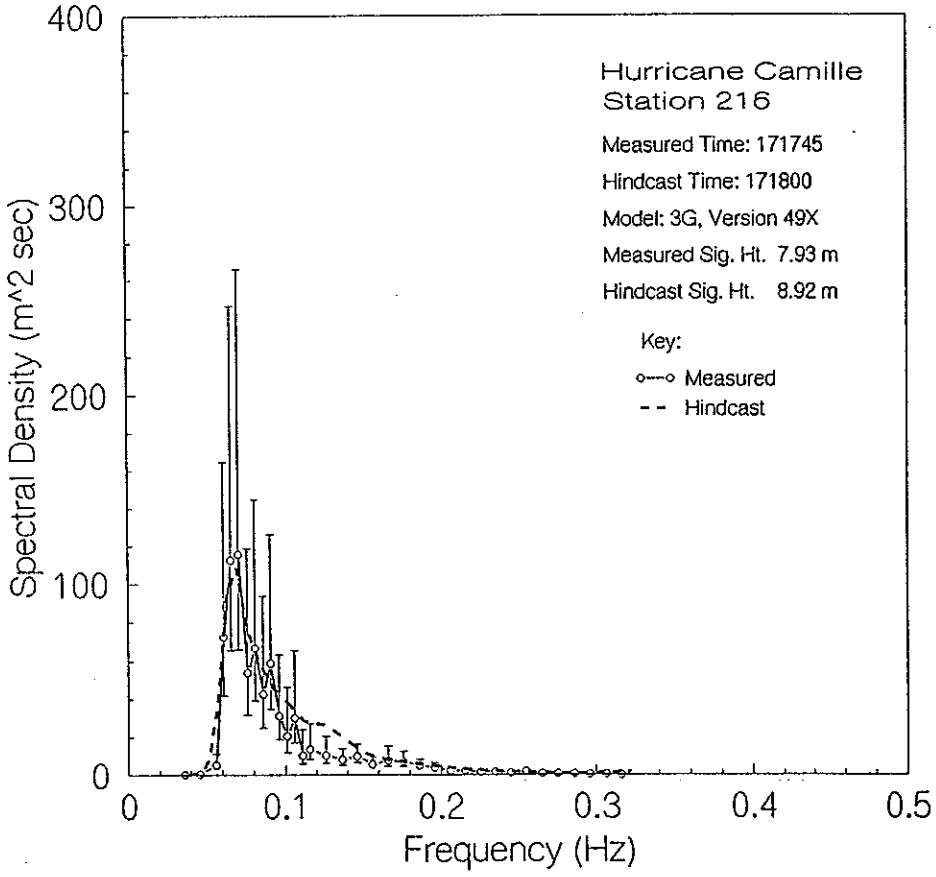

(b)

Figure 4.7 OWI3G wave model versus measured peak wave spectrum in Camille (1969) (a) ODGP Station 1; (b) ODGP Station 2.

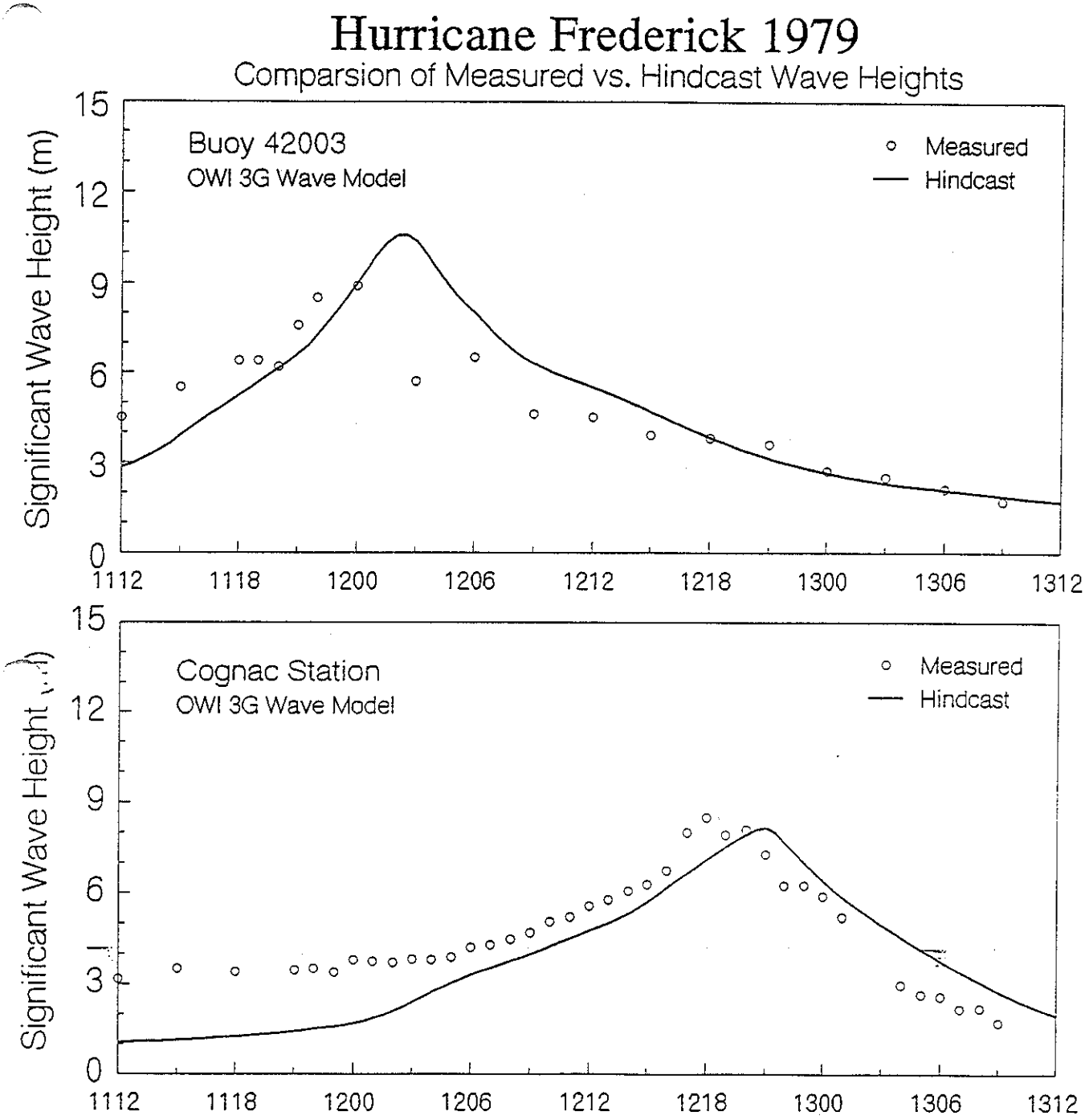

Figure 4.8 OWI3G wave model versus measured wave height in Frederick (1979).

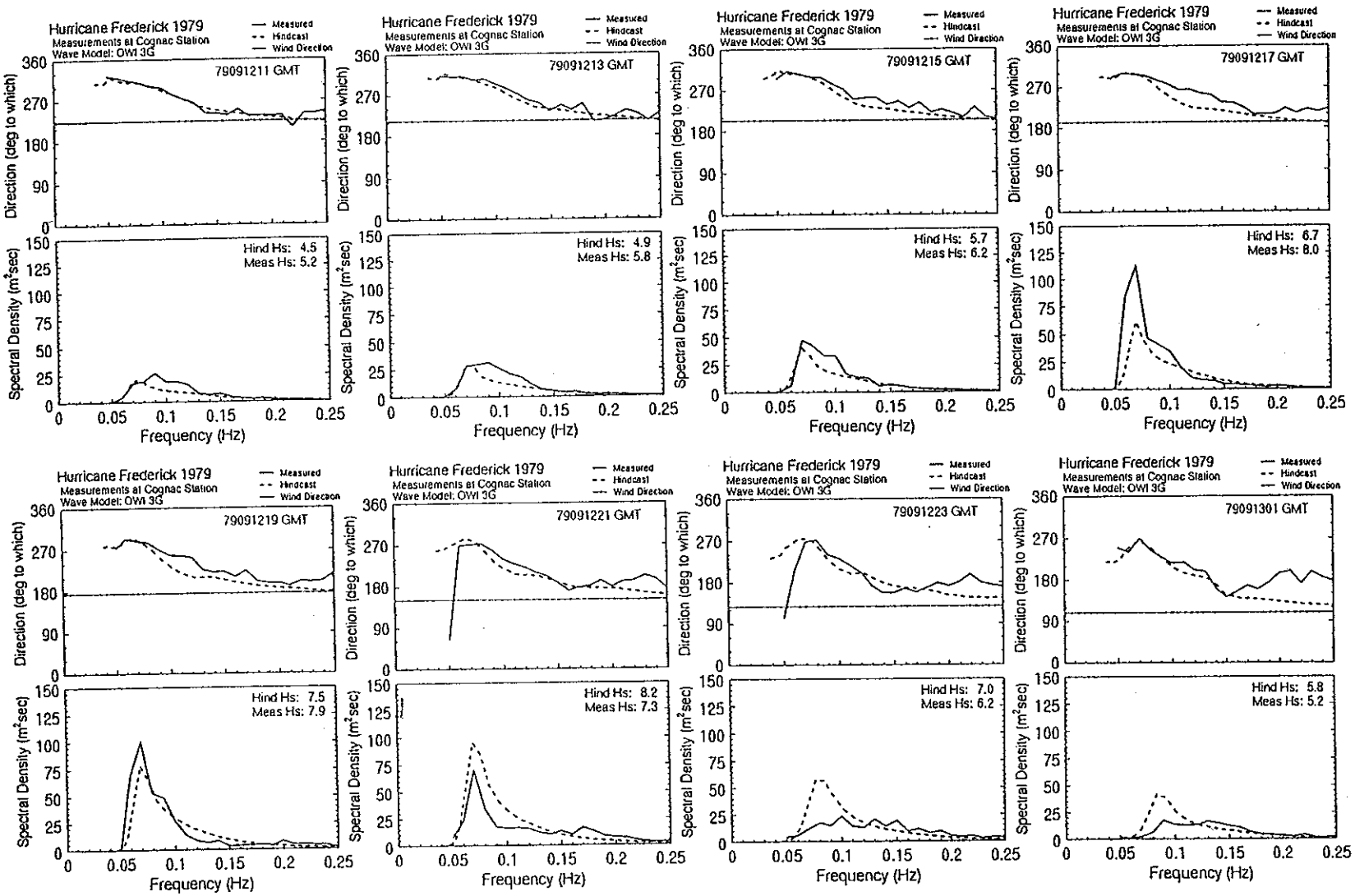

Figure 4.9 OWI3G wave model versus measured directional wave spectra in Frederick (1979) at Cognac platform.

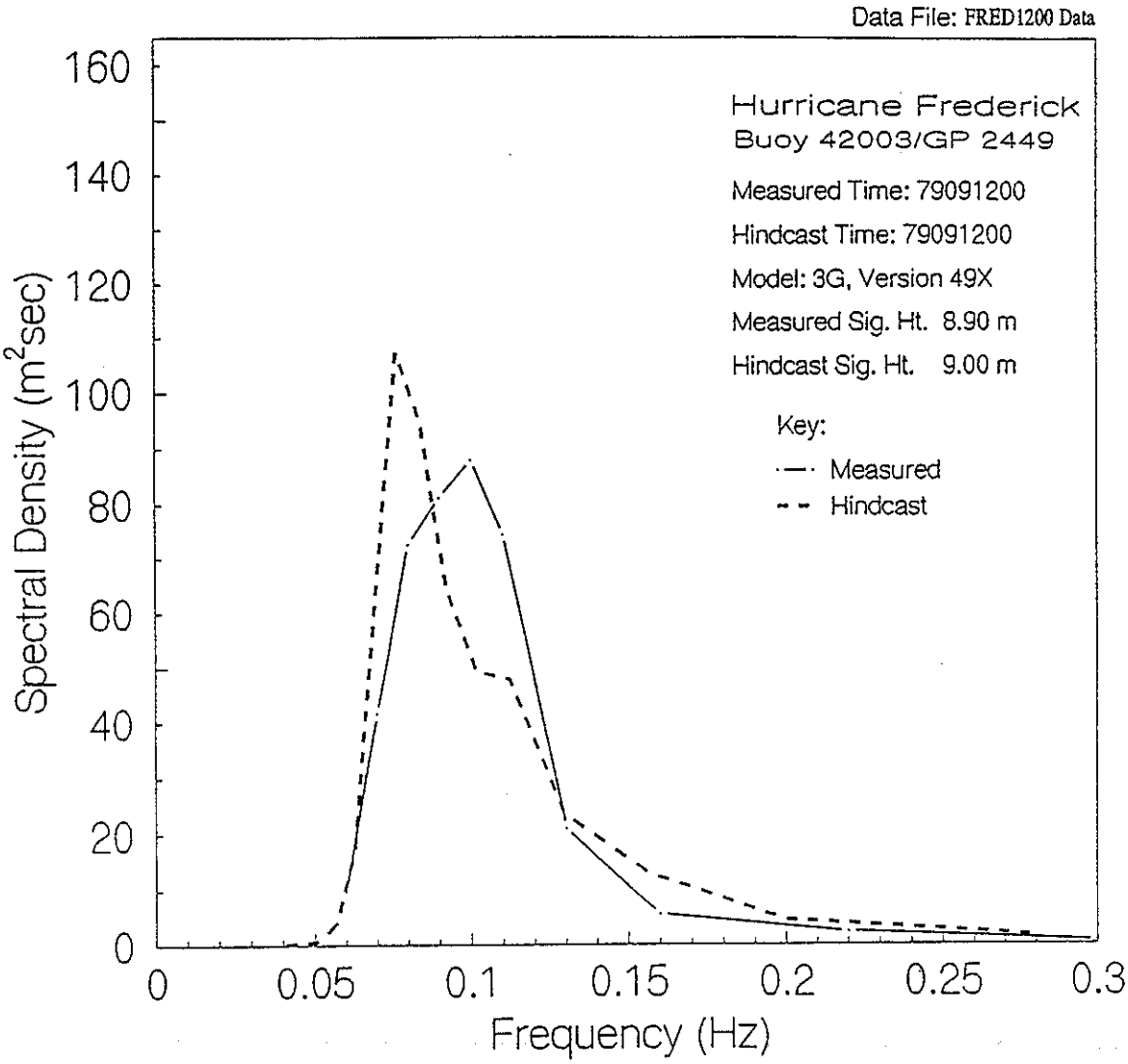

Figure 4.10 OWI3G wave model versus measured wave spectrum at NDBC buoy 42003 in Frederick (1979).

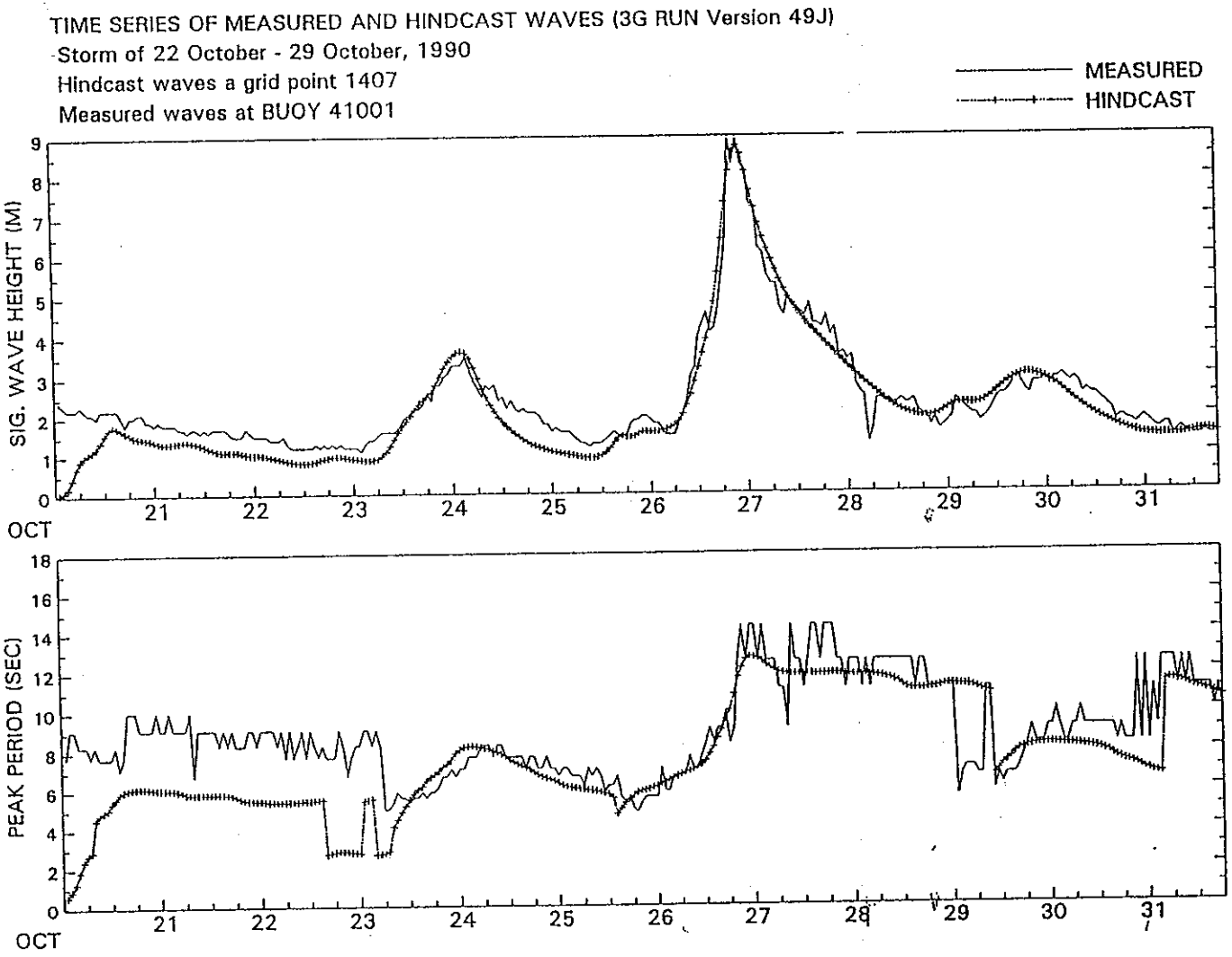

Figure 4.11 OWI3G wave model versus measured wave height and period at NDBC buoy 41001 in SWADE IOP-1.

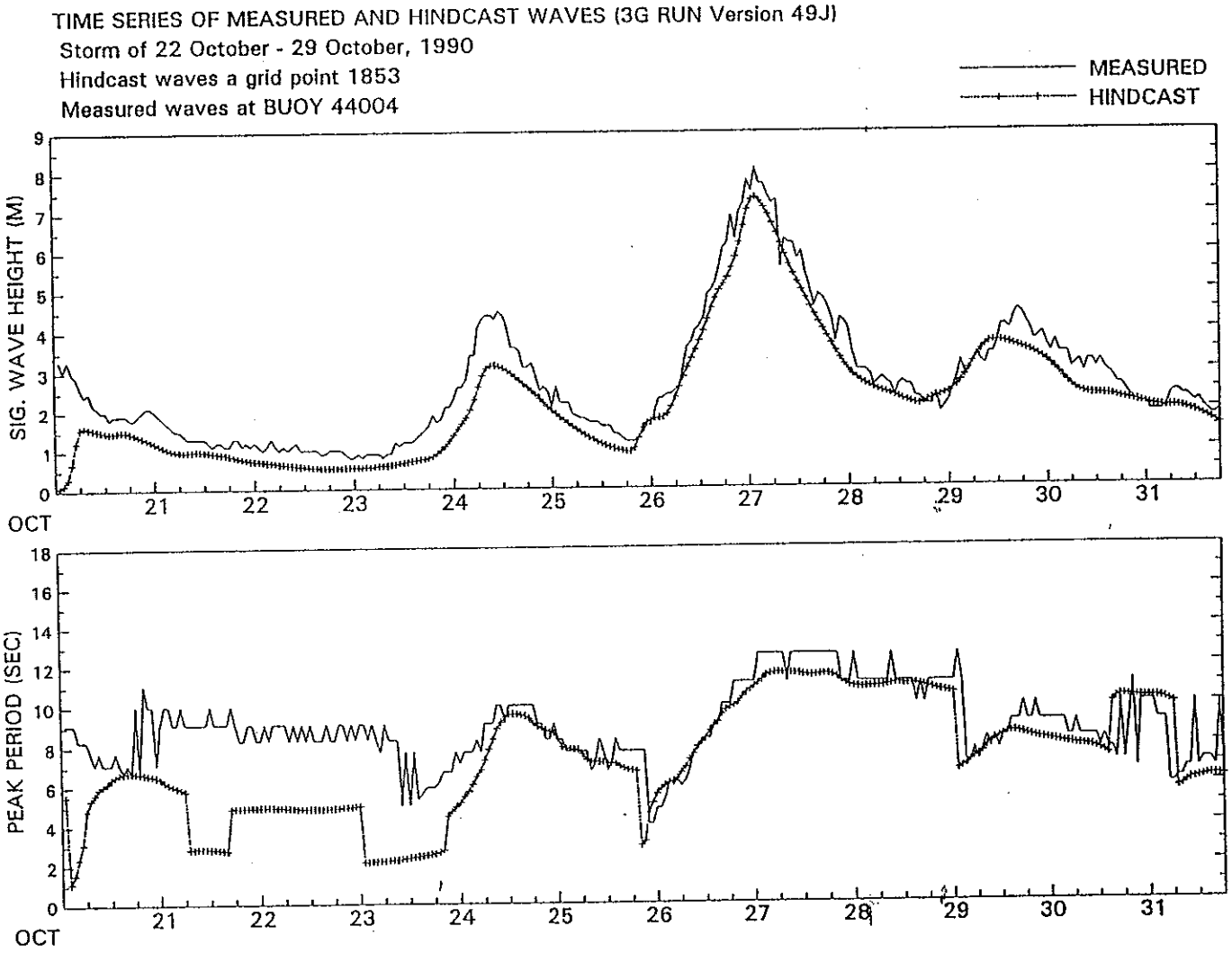

Figure 4.12 OWI3G wave model versus measured wave height and period at NDBC buoy 44004 in SWADE IOP-1.

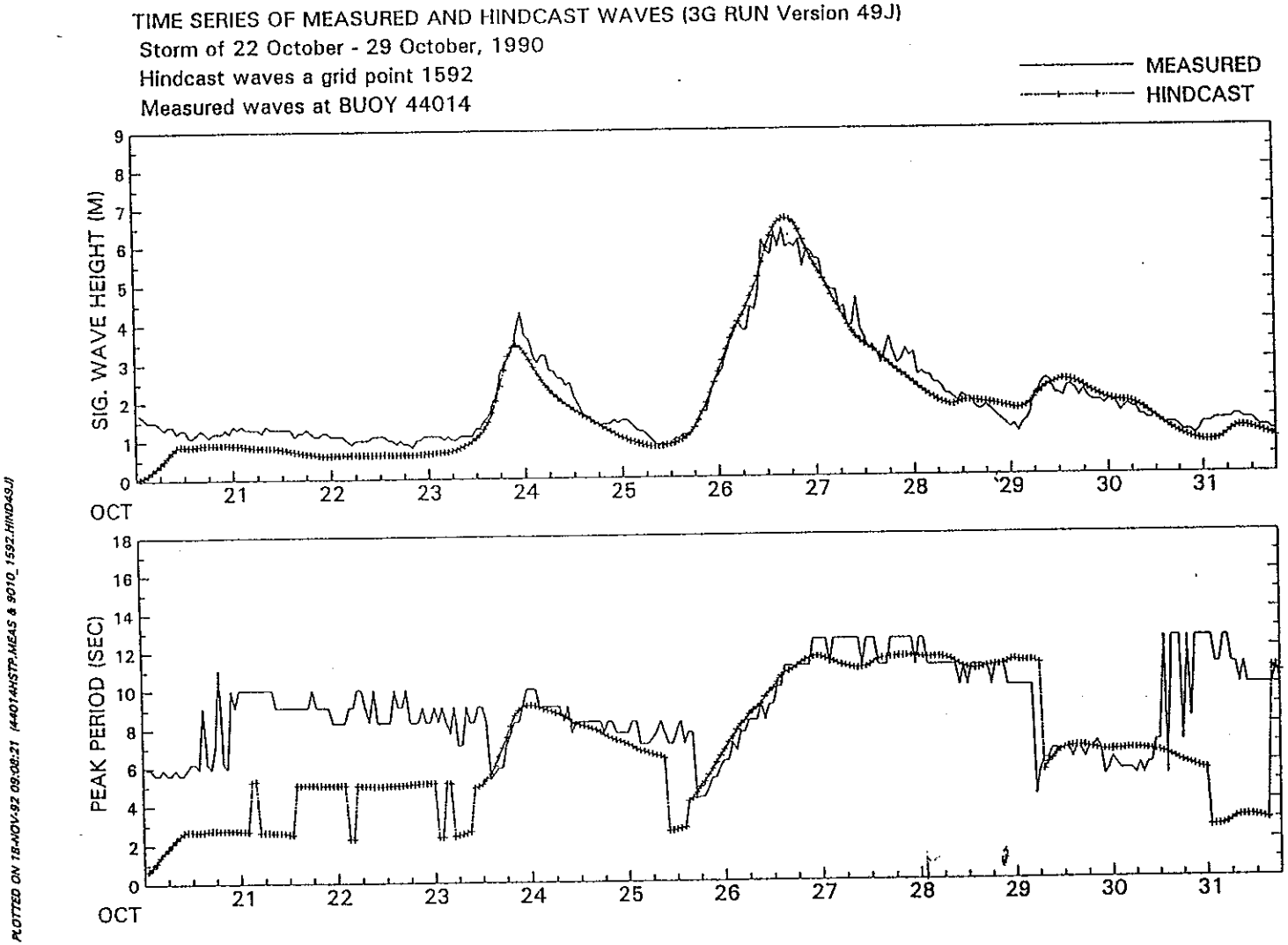

Figure 4.13 OWI3G wave model versus measured wave height and period at NDBC buoy 44014 in SWADE IOP-1.

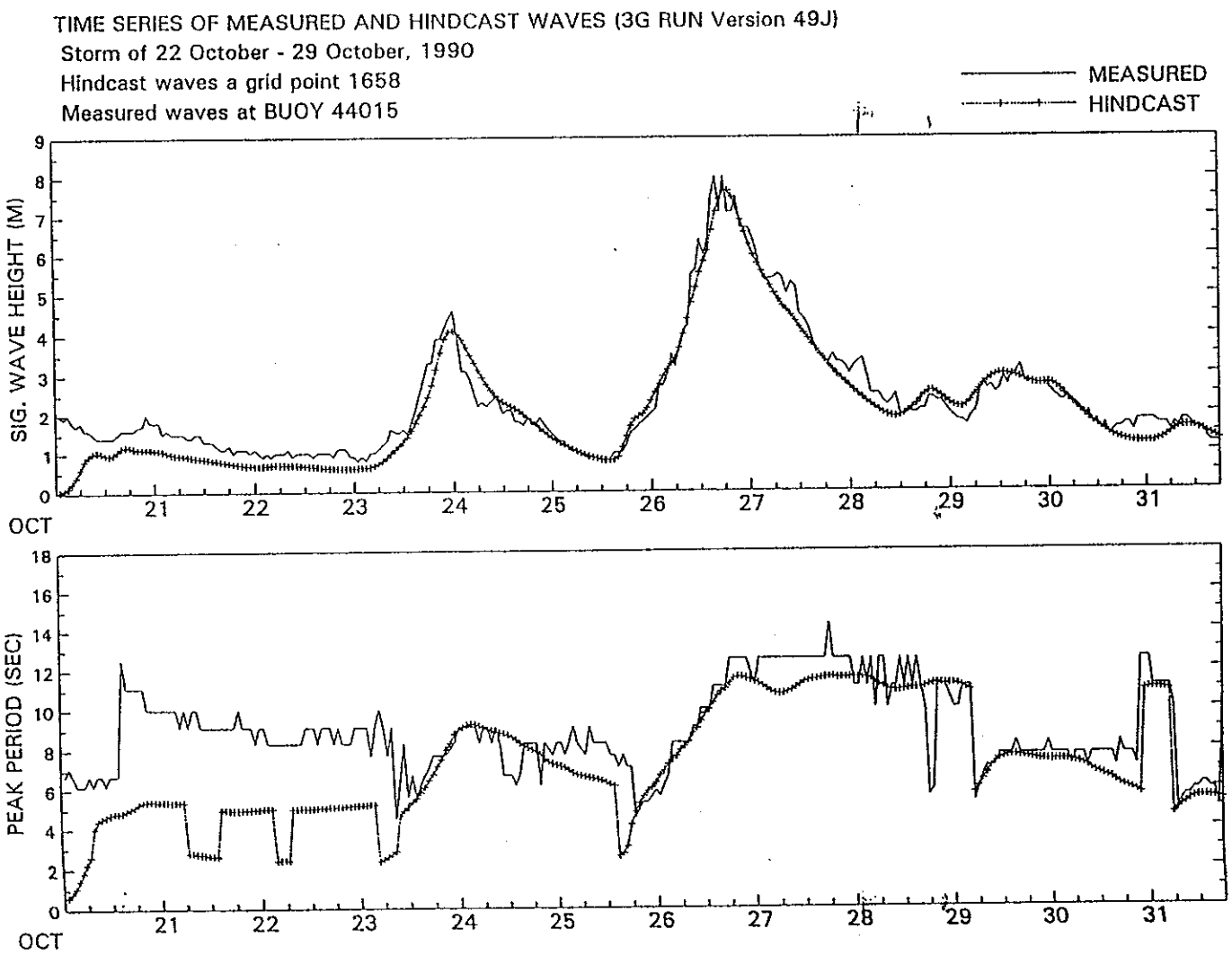

Figure 4.14 OWI3G wave model versus measured wave height and period at NDBC buoy 44015 in SWADE IOP-1.

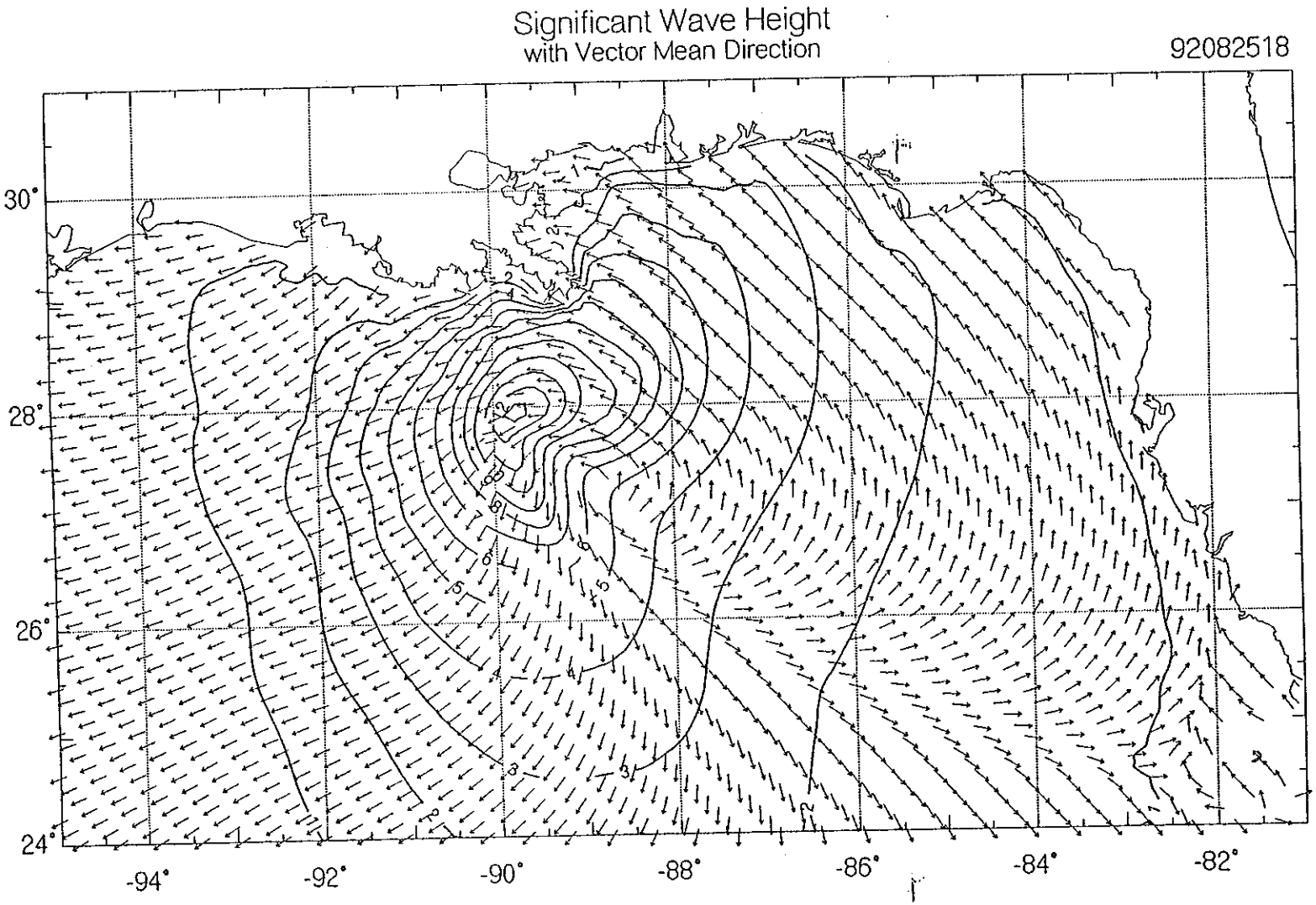

Figure 4.15 OWI3G hindcast of significant wave height (contours at 1 meter intervals) and mean wave direction (vectors) as the eye approached the shelf break.

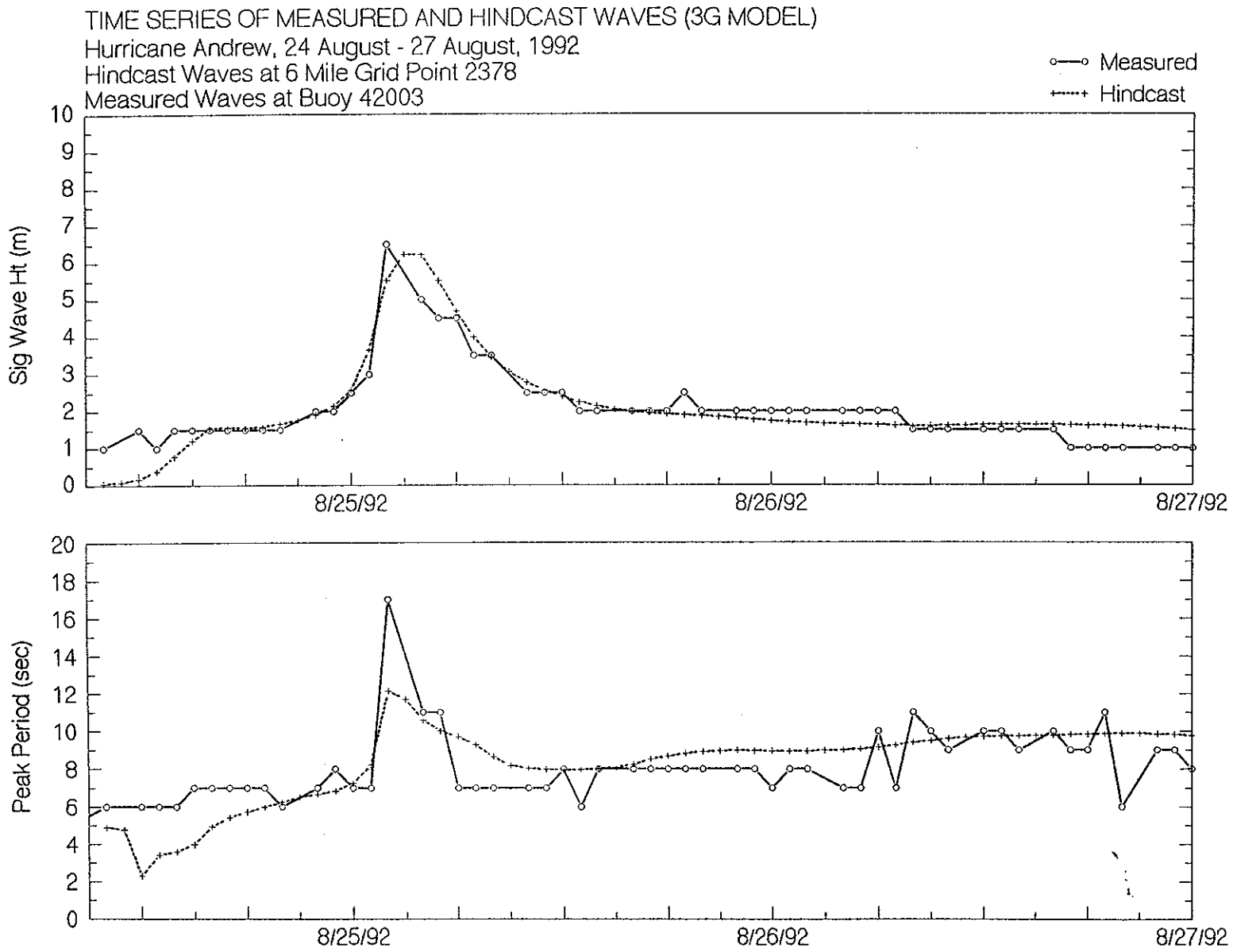

Figure 4.16 OWI3G wave model versus measured wave height and period at NDBC buoy 42003 in Hurricane Andrew.

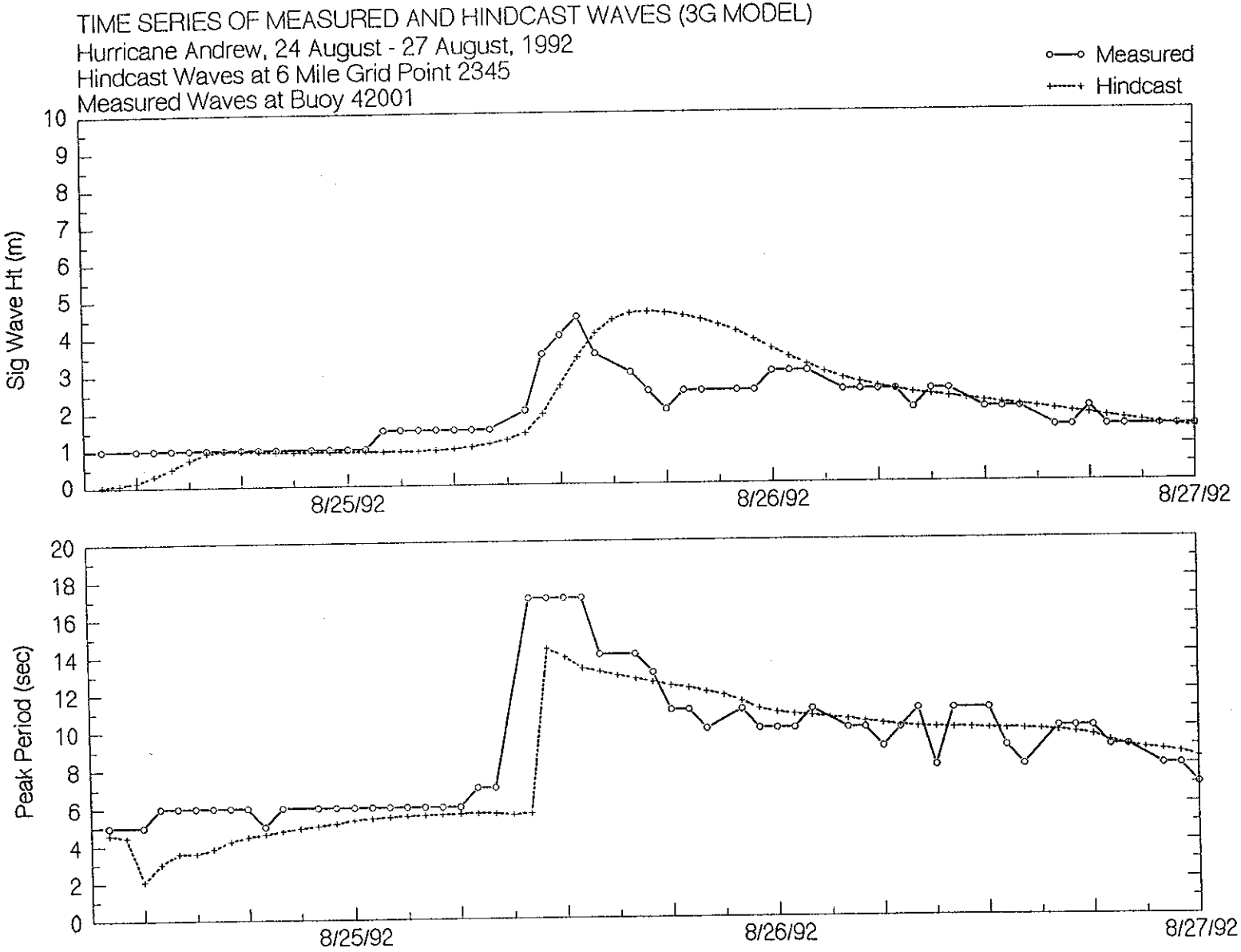

Figure 4.17 OWI3G wave model versus measured wave height and period at NDBC buoy 42001 in Hurricane Andrew.

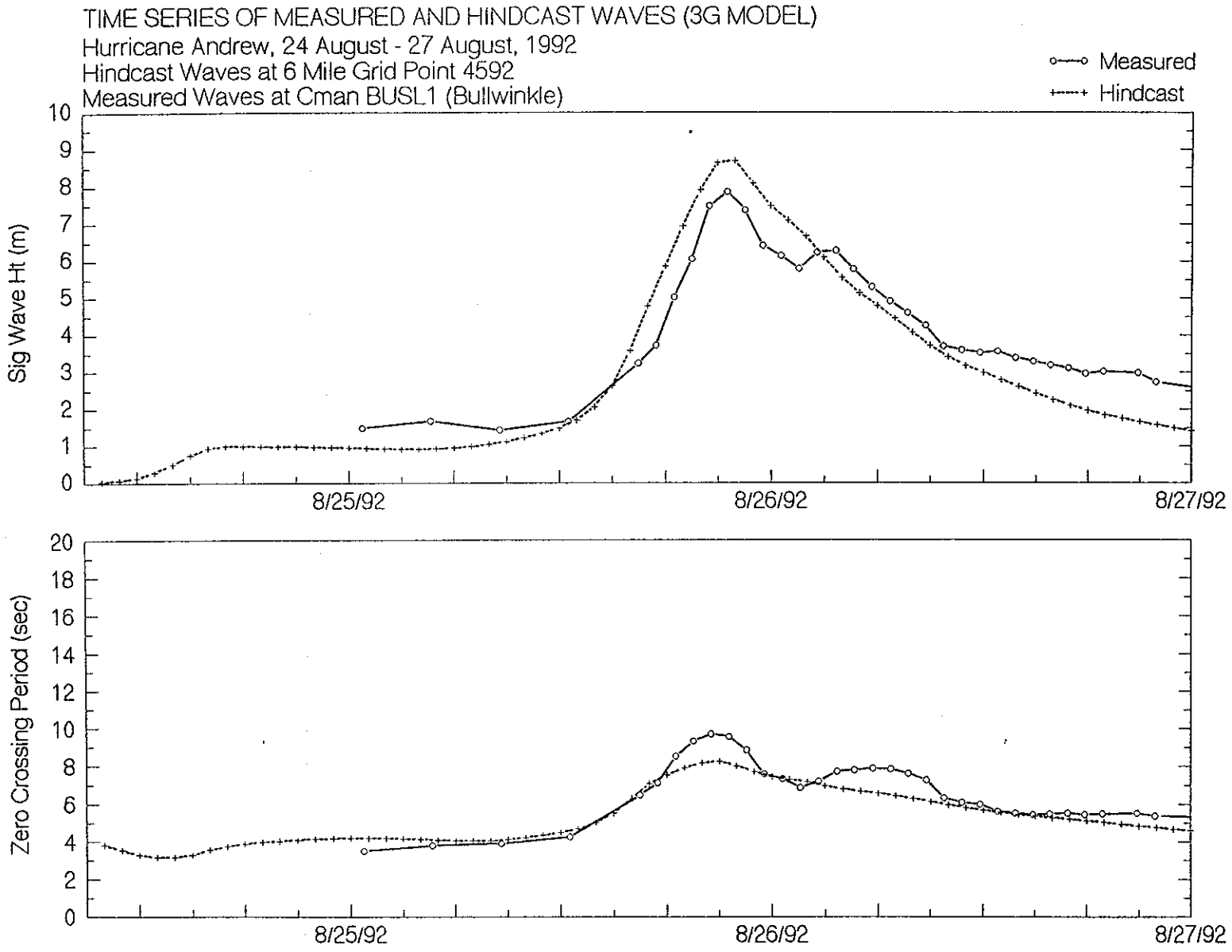

Figure 4.18 OWI3G wave model versus measured wave height and period at NDBC C-MAN station on Bullwinkle platform.

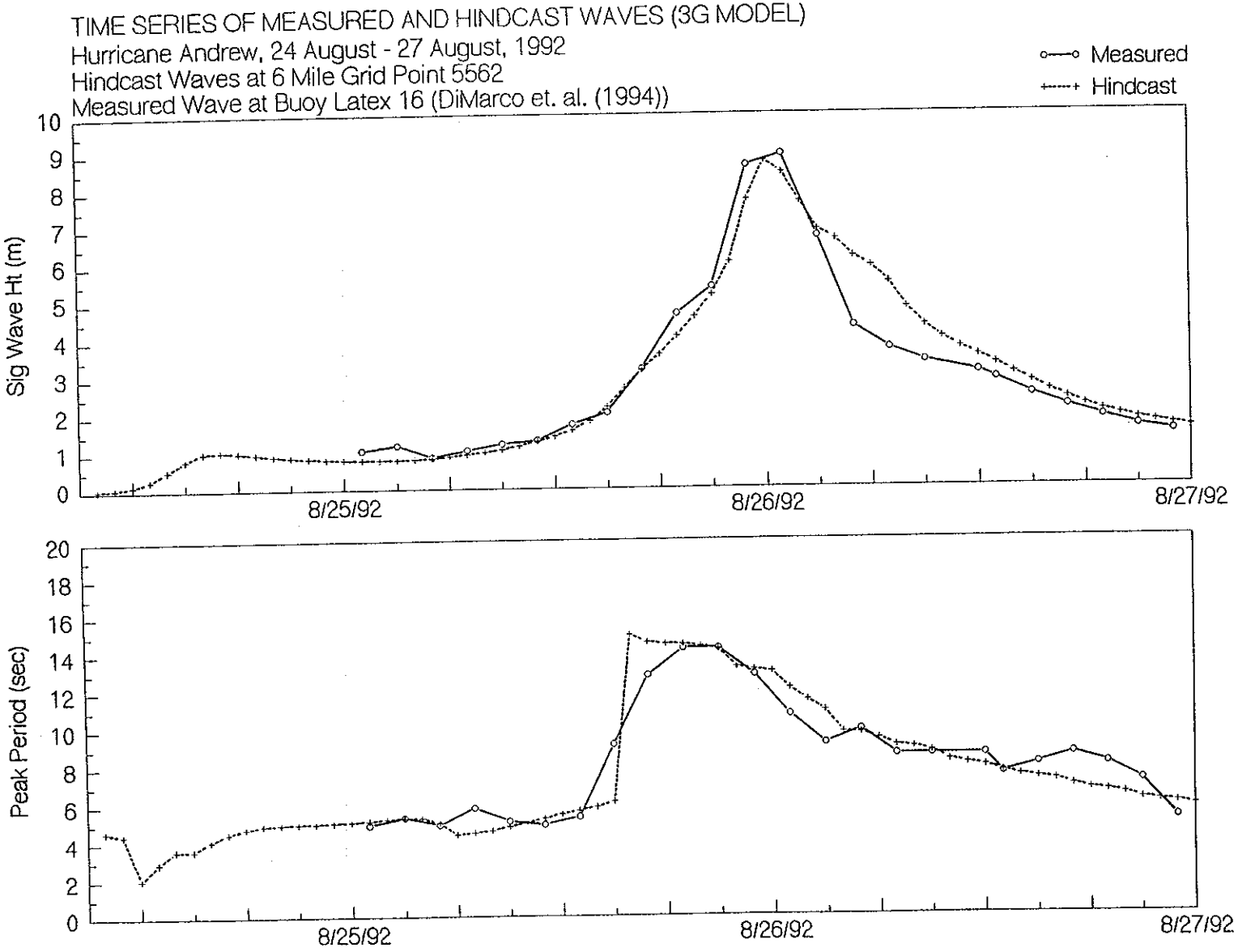

Figure 4.19 OWI3G wave model versus measured wave height and period at LATEX Station 16 .

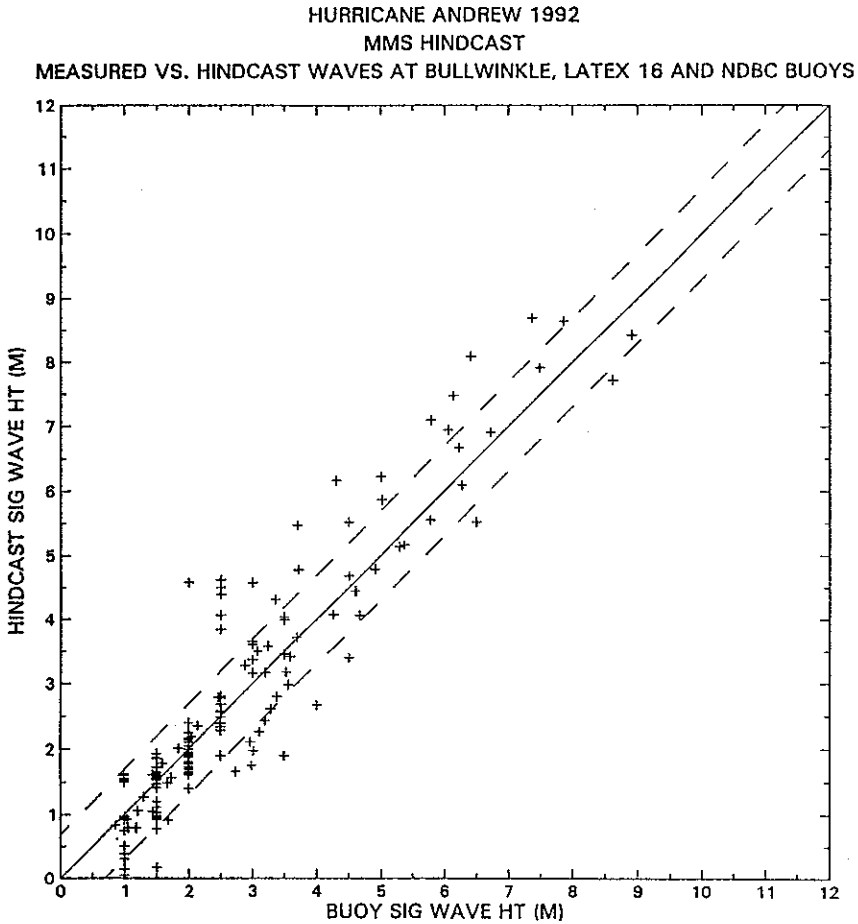

(a)

Number of points:	164
Mean Measurement:	2.62
Mean Hindcast:	2.67
Mean Difference:	.05
Root mean square:	.69
Standard deviation:	.69
Scatter index:	.26
Ratio:	.47
Correlation Coefficient:	.93

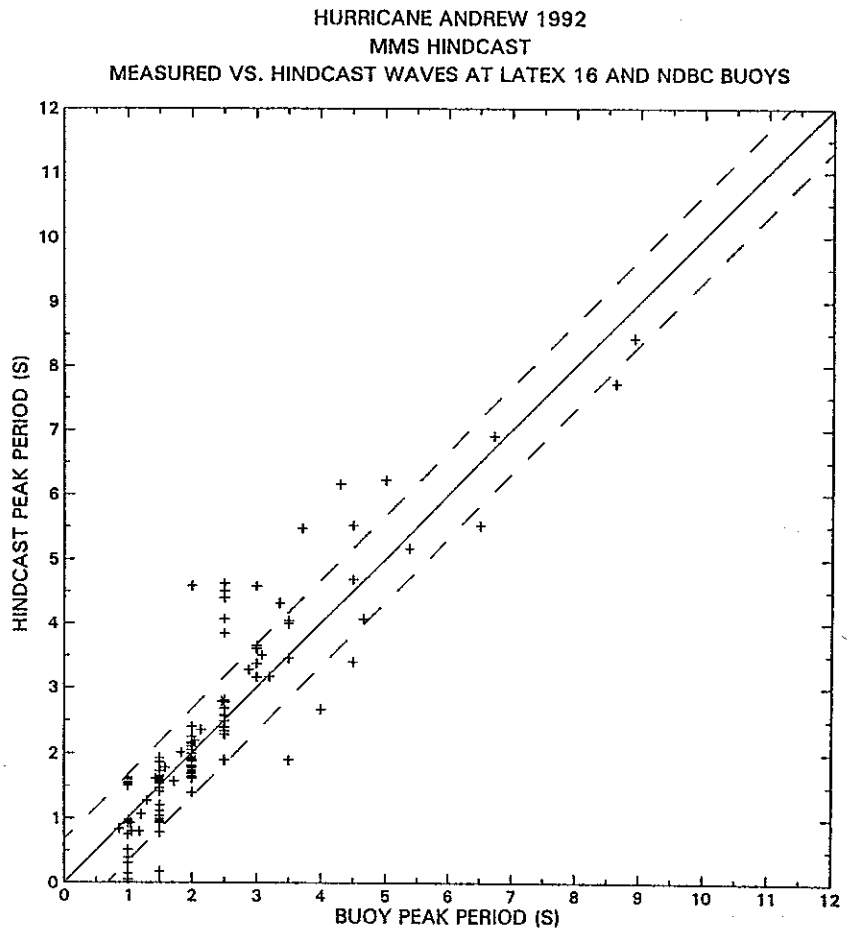

(b)

Number of points:	131
Mean Measurement:	2.19
Mean Hindcast:	2.26
Mean Difference:	.07
Root mean square:	.67
Standard deviation:	.67
Scatter index:	.30
Ratio:	.50
Correlation Coefficient:	.90

Figure 4.20 Scatter plot of OWI3G hindcast and measured time histories of (a) significant wave height and (b) spectral peak period in Hurricane Andrew

Figure 5.1 Regional map of Gulf of Mexico, showing the different grids used in the shallow water current simulations. The original wind and wave grid is the large outlined box. Grid A is the outline from 98 W to 85 W. Grid B is the small box. The path of Hurricane Andrew is indicated by the heavy dash line. The light dash line is the 200-m isobath and the long-short dash line is the 2000-m contour. The locations of the mooring arrays are indicated by the squares. Along the eastern array, the moorings are 12, 13, 14 and 15, starting offshore. Moorings 19 and 18 are located offshore and shoreward along the western array.

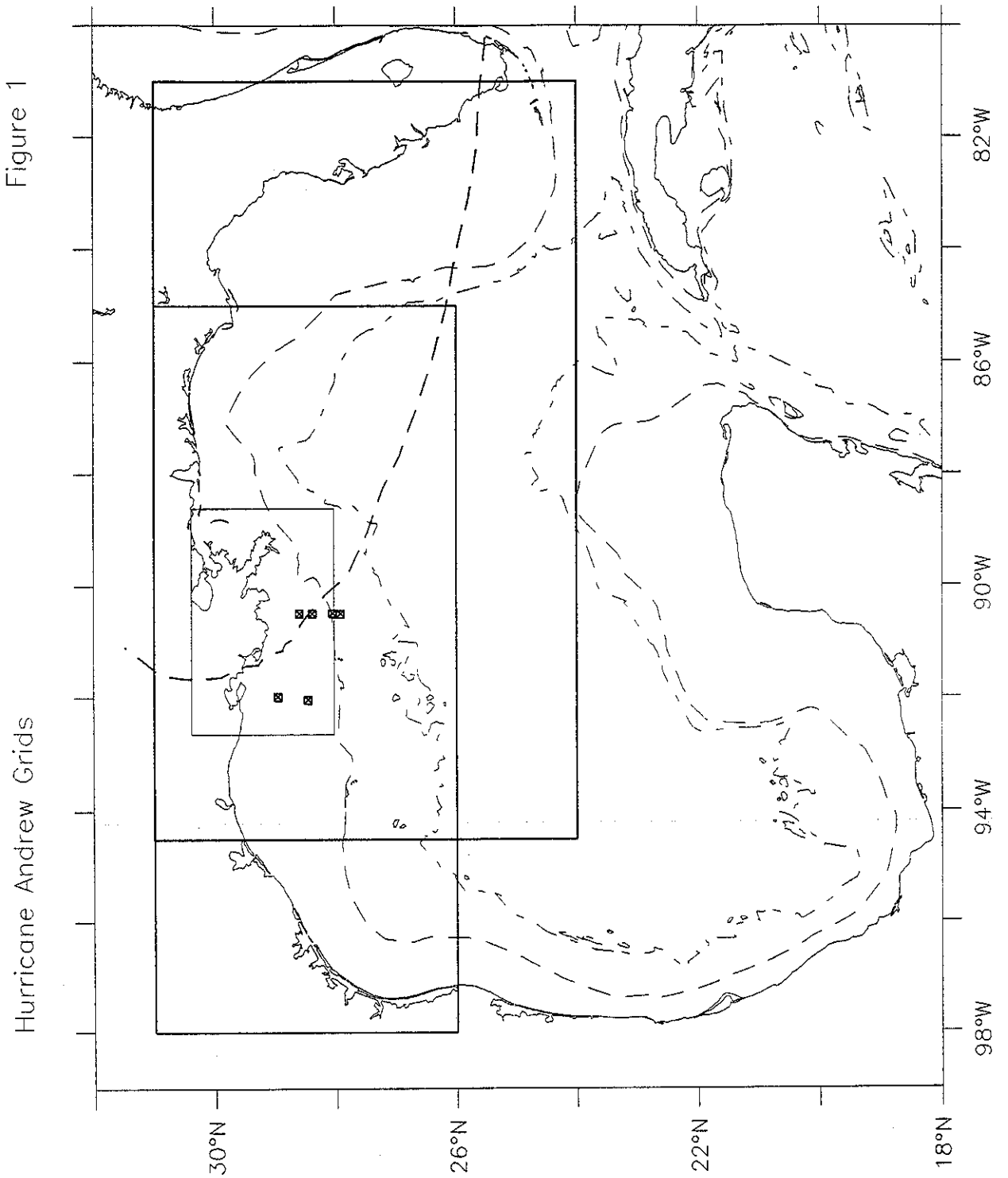

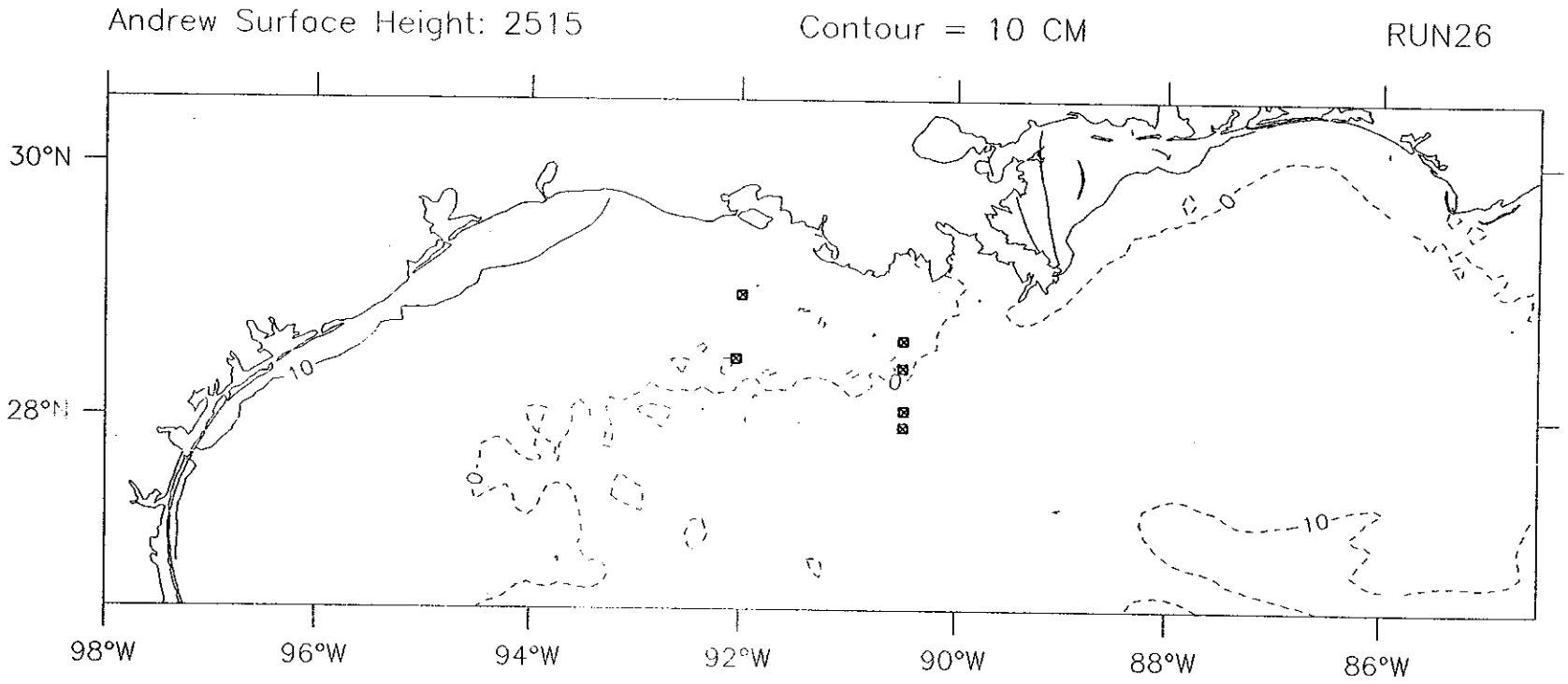

a.

Figure 5.2. Water surface height from the model simulations with Grid A. Contours are shown at (a) 1500 and (b) 2100 GMT Aug. 25, and (c) 0300, (d) 0900 (e) 1500 and (f) 2100 GMT Aug. 26. The locations of the mooring arrays are indicated by the squares. Solid contours indicate positive elevations.

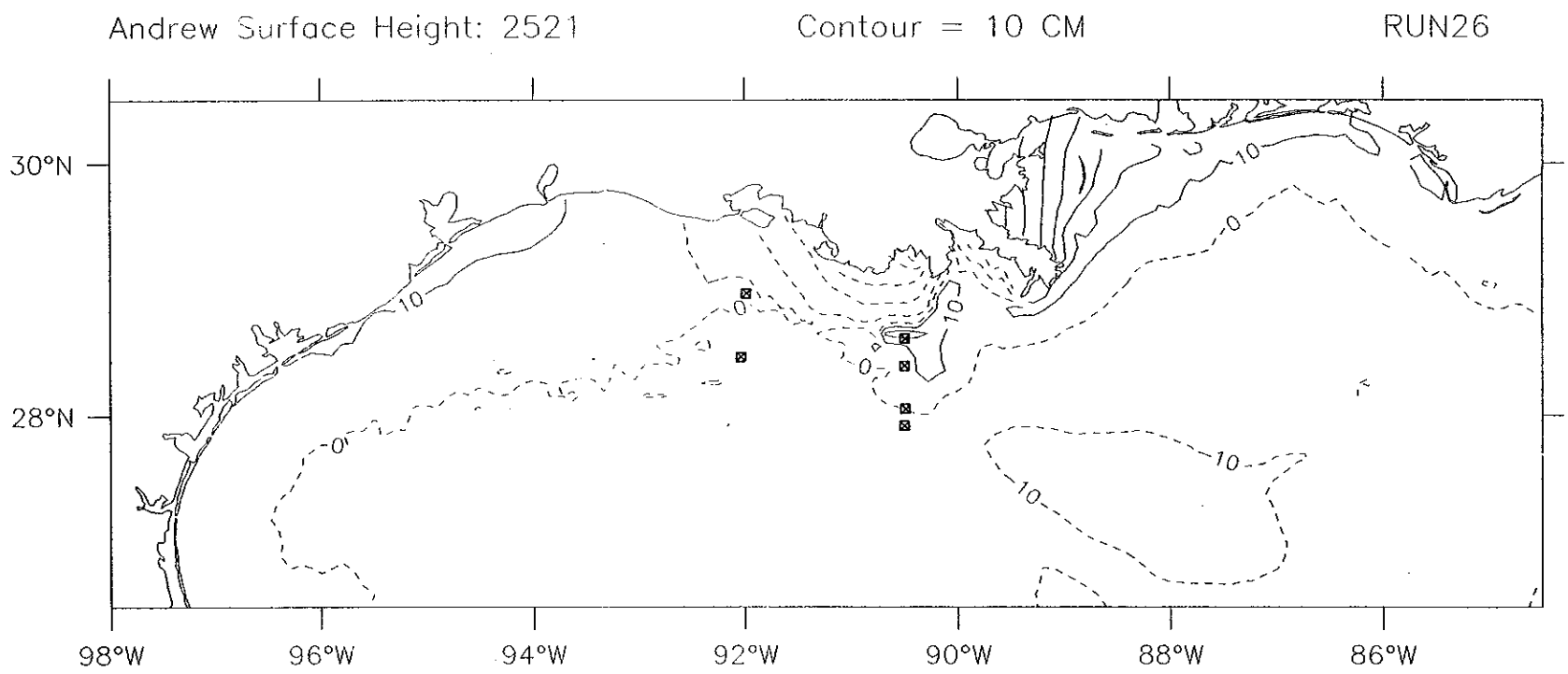
Andrew Surface Height: 2521
Contour = 10 CM
RUN26
30°N
28°N
98°W
96°W
94°W
92°W
90°W
88°W
86°W
10
0
10
0
10
0
10
10

Figure 5.2 b.

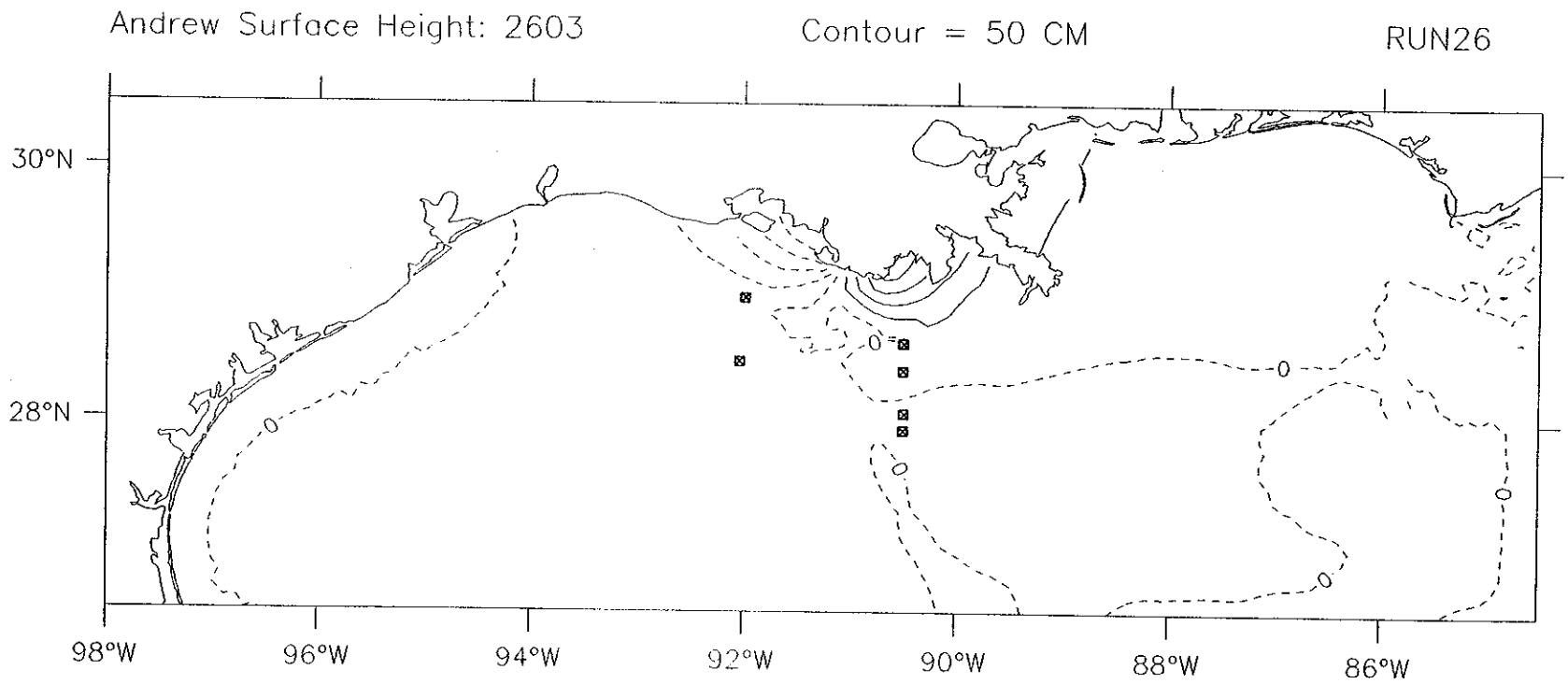
Andrew Surface Height: 2603
Contour = 50 CM
RUN26
30°N
28°N
98°W
96°W
94°W
92°W
90°W
88°W
86°W
0
0
0
0
0
0

Figure 5.2 c.

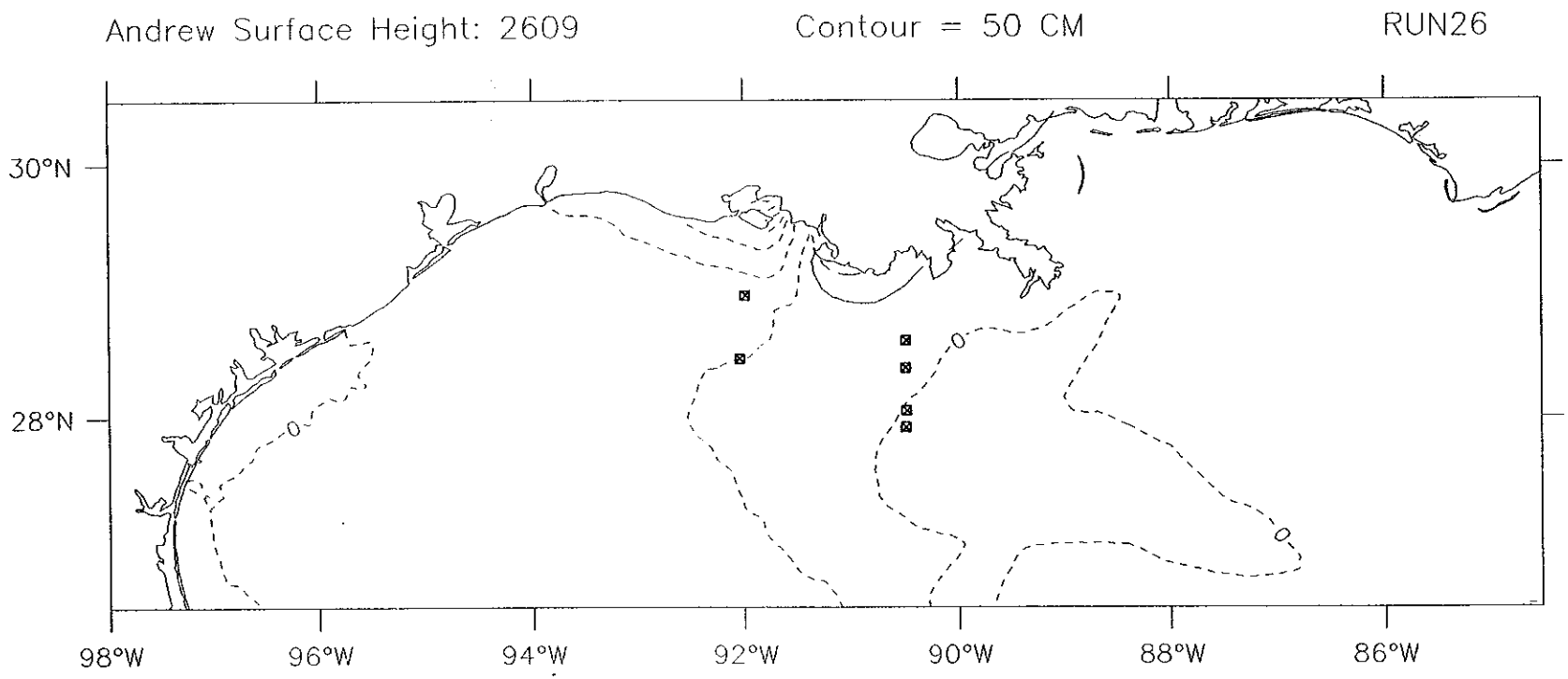
Andrew Surface Height: 2609
Contour = 50 CM
RUN26
30°N
28°N
98°W
96°W
94°W
92°W
90°W
88°W
86°W
0
0
0

Figure 5.2 d.

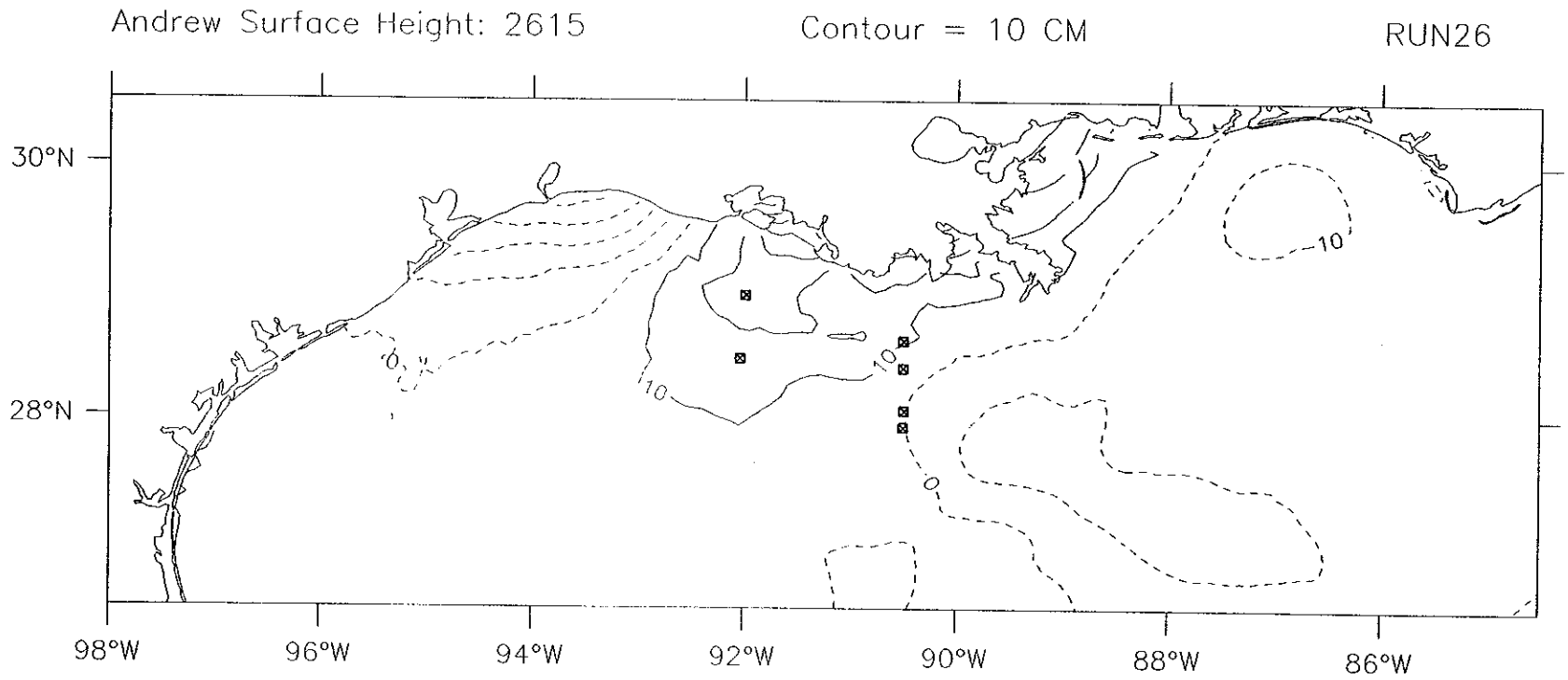
Andrew Surface Height: 2615
Contour = 10 CM
RUN26
30°N
28°N
98°W
96°W
94°W
92°W
90°W
88°W
86°W
0
10
10
10
0

Figure 5.2 e.

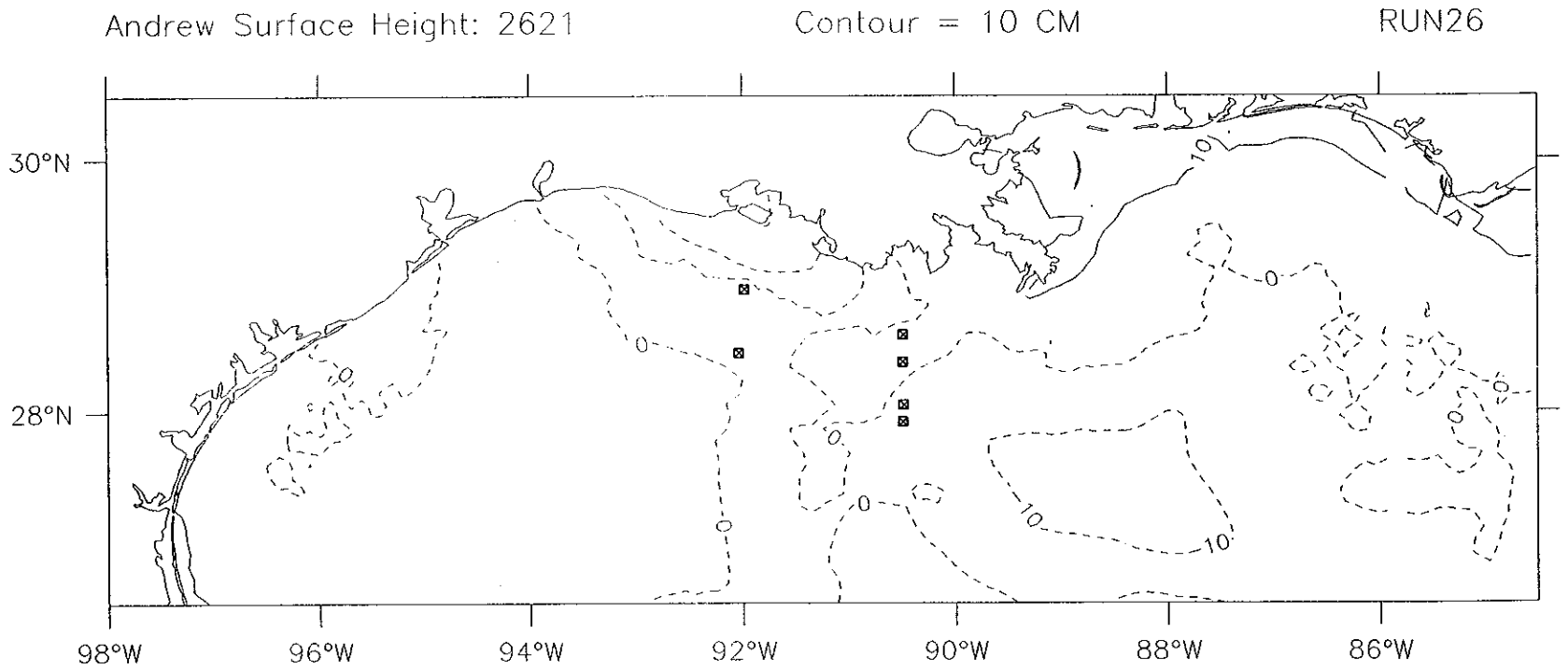
Andrew Surface Height: 2621
Contour = 10 CM
RUN26
30°N
28°N
98°W
96°W
94°W
92°W
90°W
88°W
86°W
0
10

Figure 5.2 f.

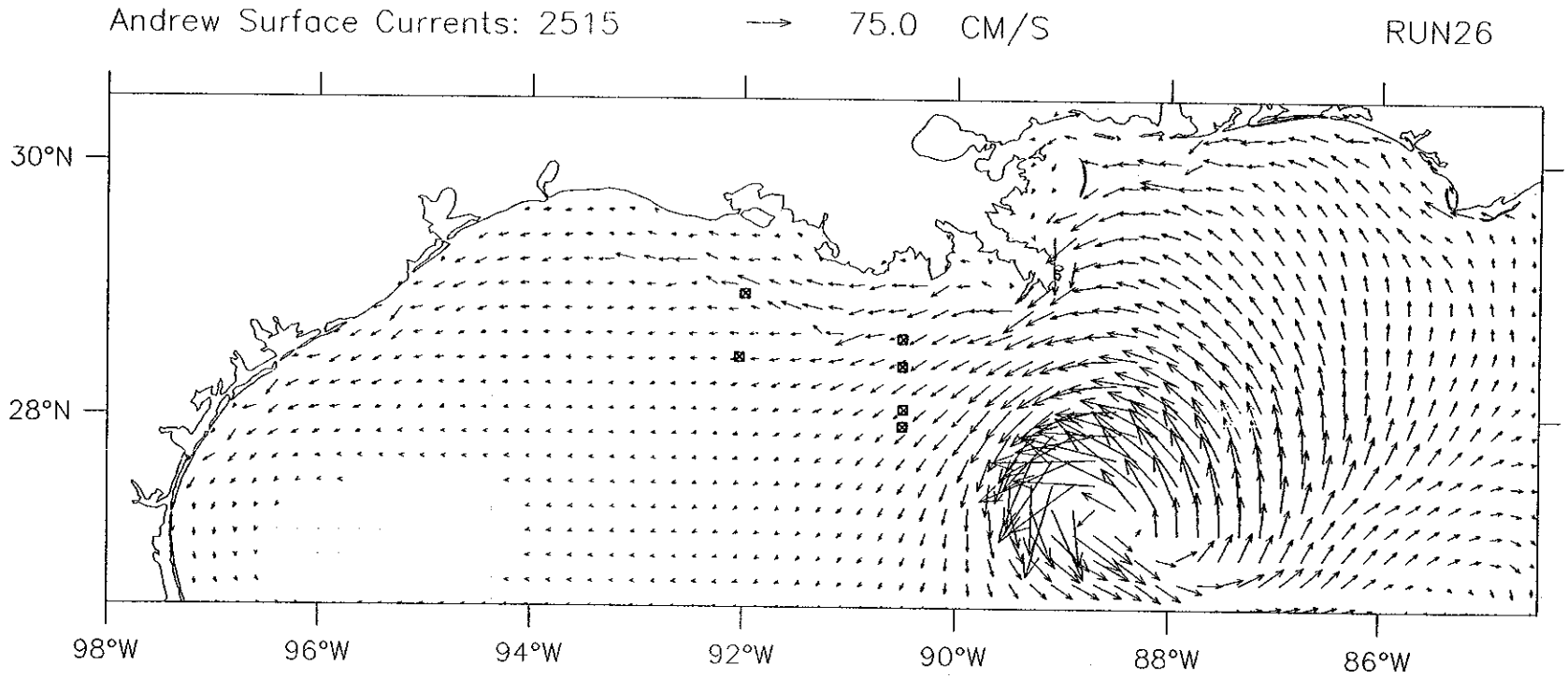

a.

Figure 5.3. Currents calculated in the upper model level (depth=5 m) from Grid A at (a) 1500 and (b) 2100 GMT Aug. 25, and (c) 0300, (d) 0900, (e) 1500 and (f) 2100 GMT Aug. 26. The locations of the mooring arrays are indicated by the squares.

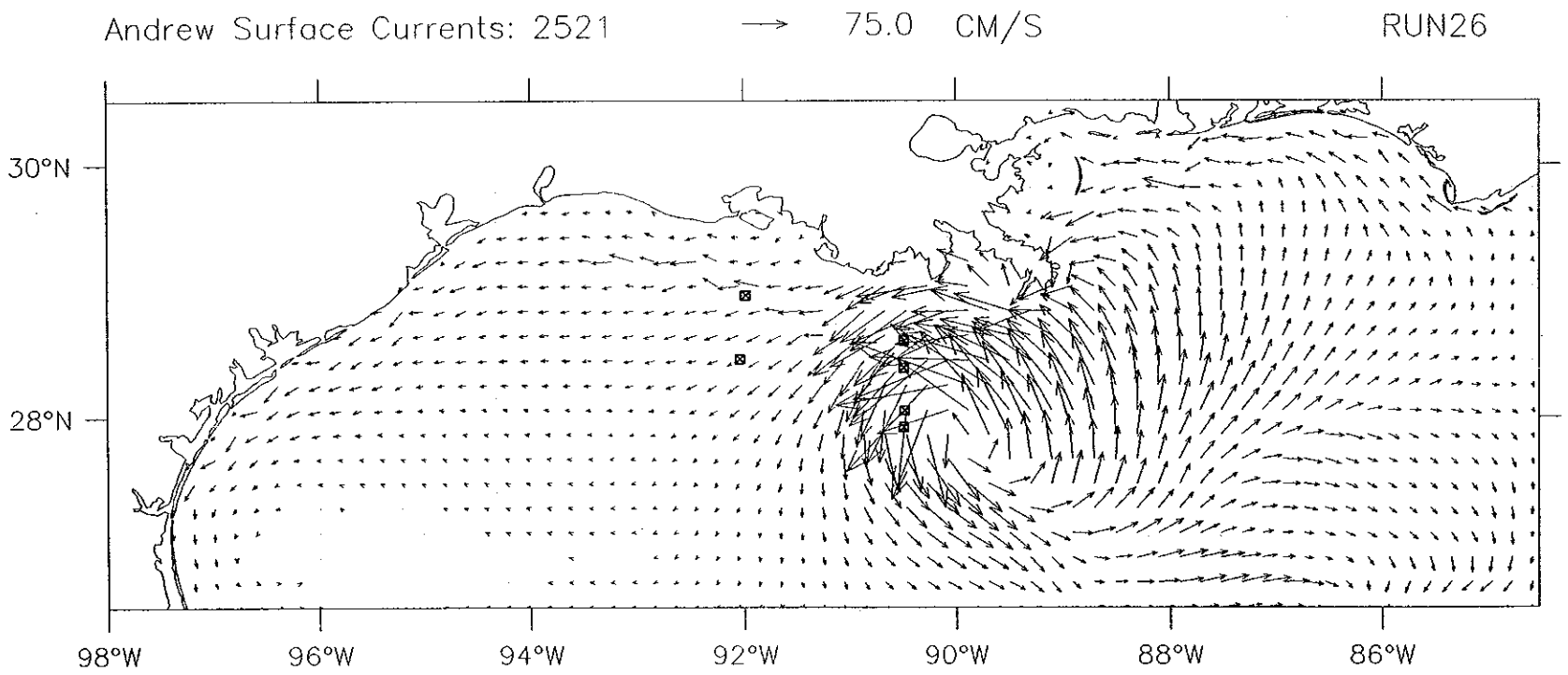
Andrew Surface Currents: 2521
75.0 CM/S
RUN26
30°N
28°N
98°W
96°W
94°W
92°W
90°W
88°W
86°W

Figure 5.3 b.

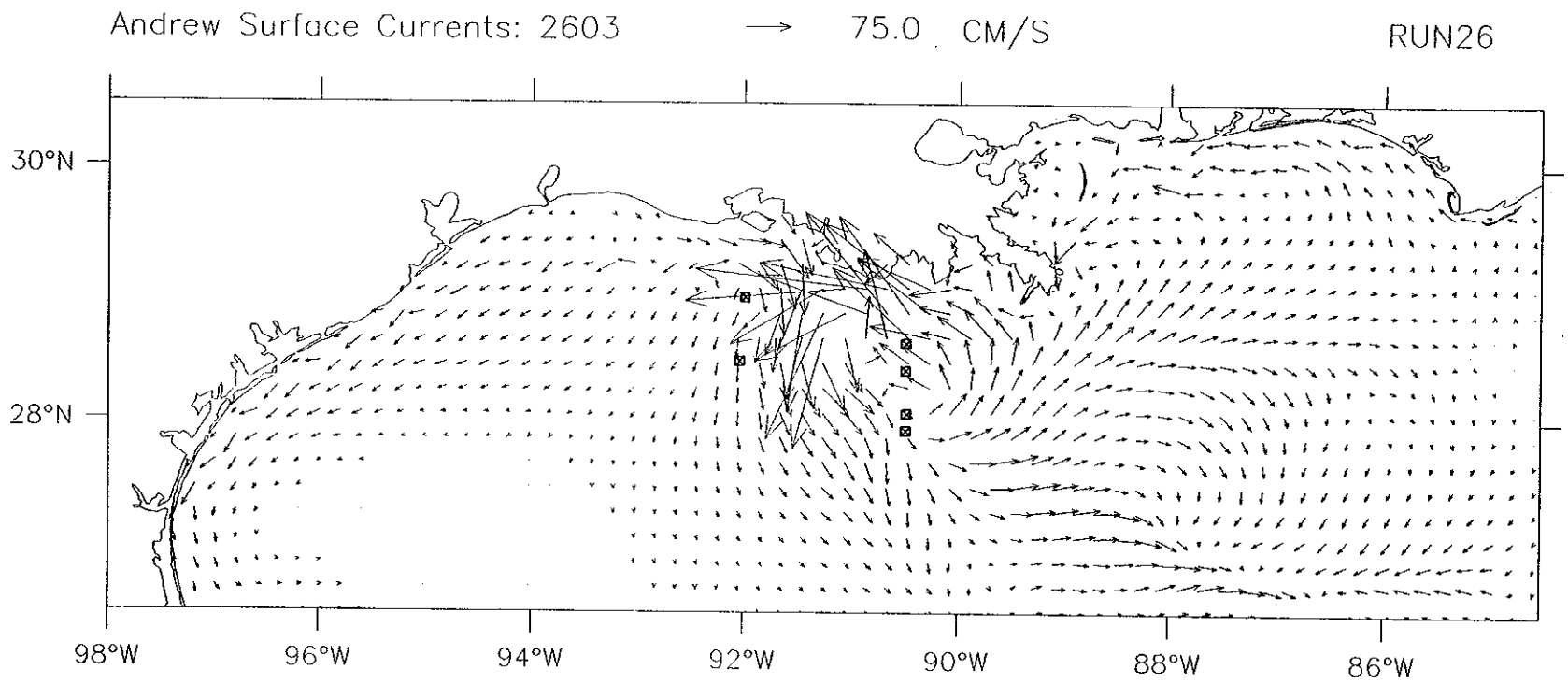
Andrew Surface Currents: 2603
75.0 CM/S
RUN26
30°N
28°N
98°W
96°W
94°W
92°W
90°W
88°W
86°W

Figure 5.3 c.

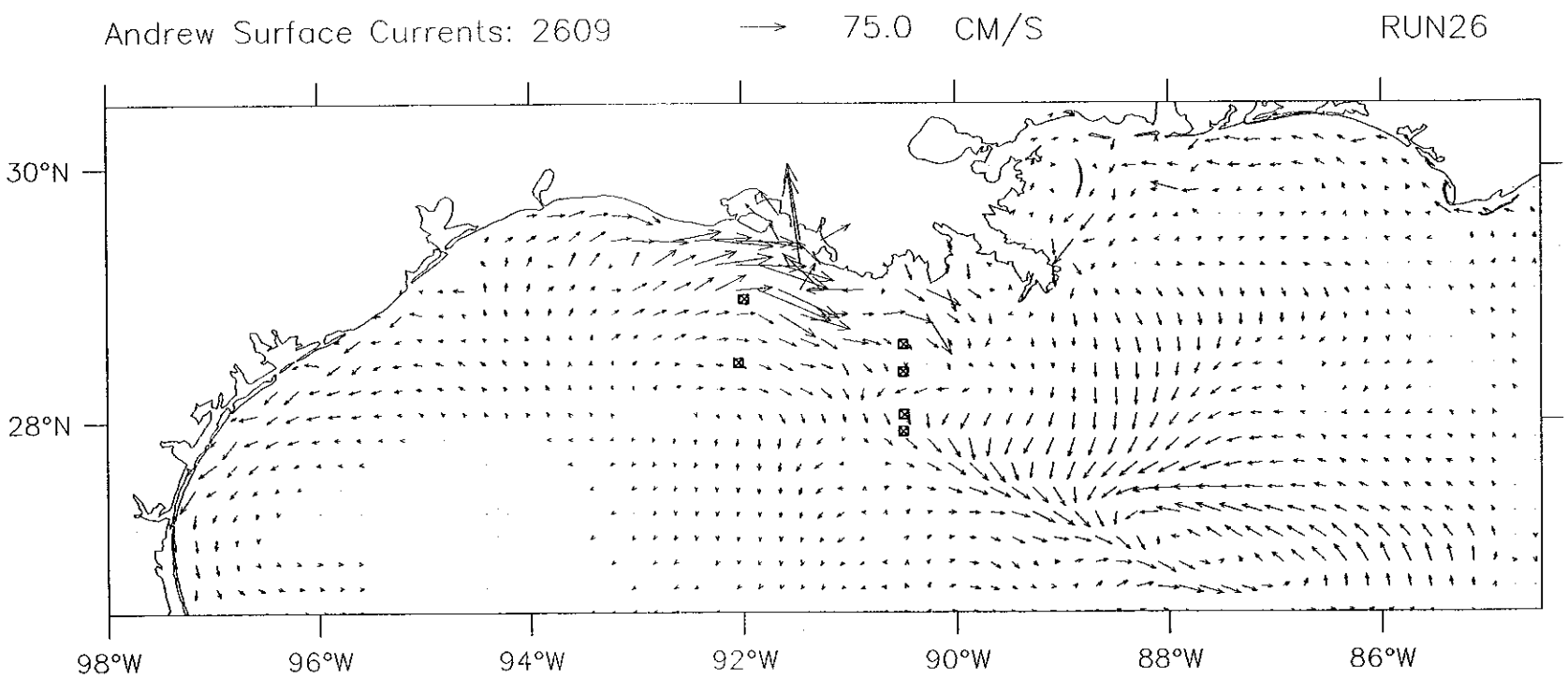
Andrew Surface Currents: 2609
75.0 CM/S
RUN26
30°N
28°N
98°W
96°W
94°W
92°W
90°W
88°W
86°W

Figure 5.3 d.

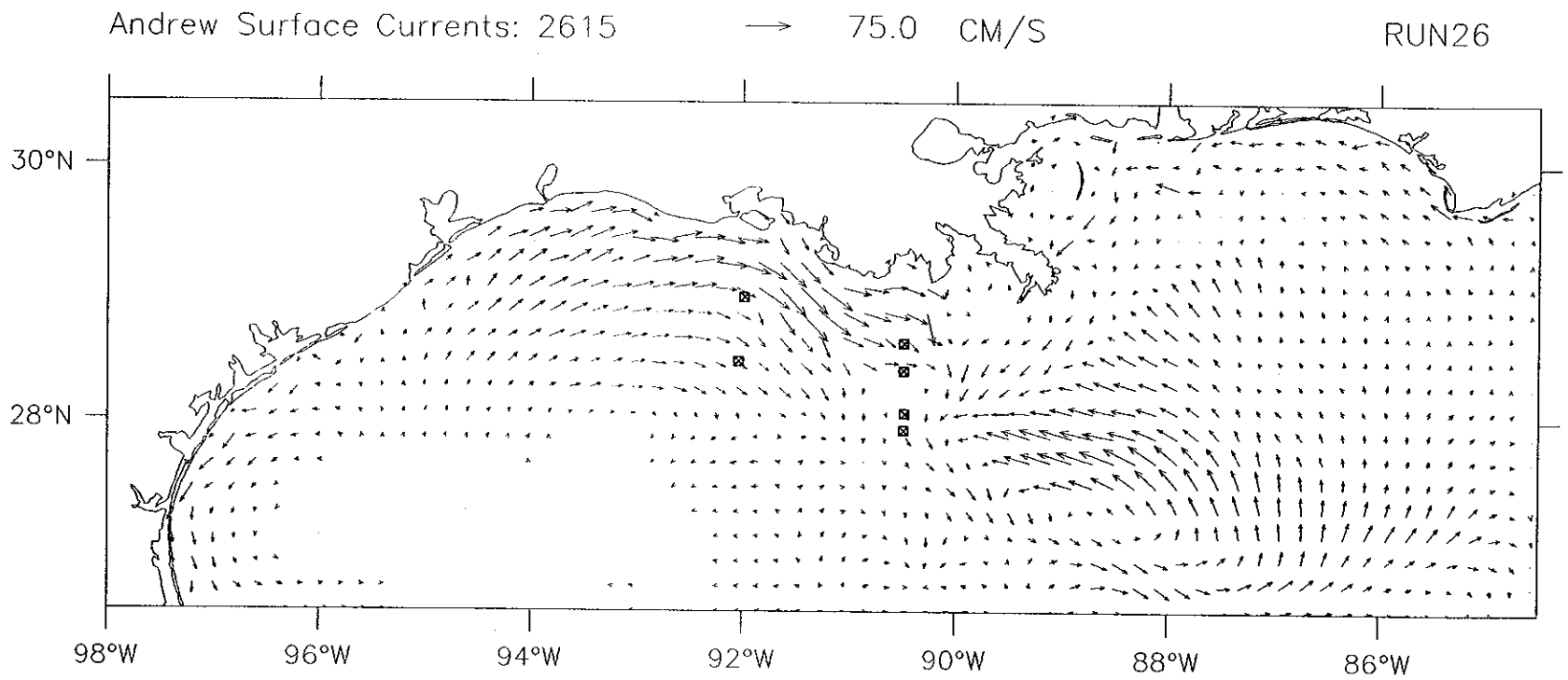
Andrew Surface Currents: 2615
75.0 CM/S
RUN26
30°N
28°N
98°W
96°W
94°W
92°W
90°W
88°W
86°W

Figure 5.3 e.

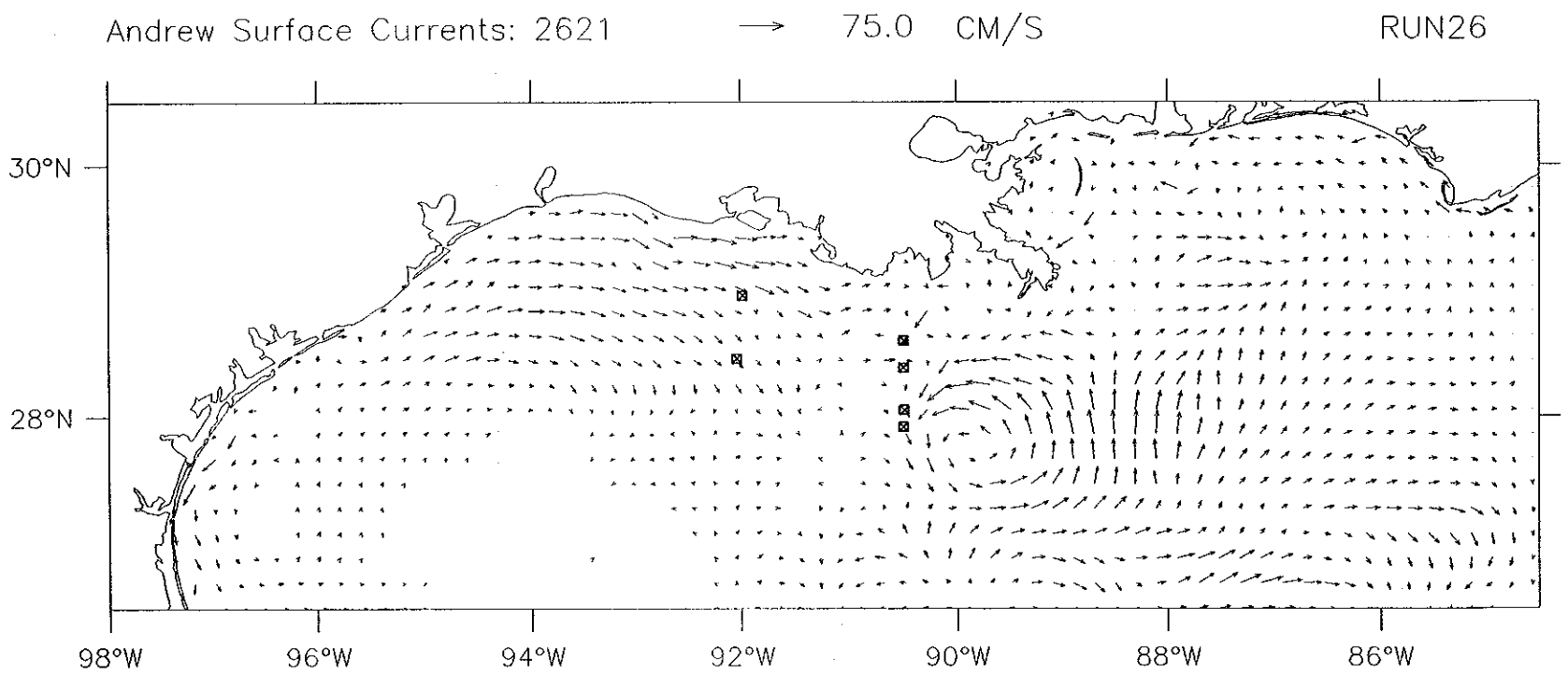
Andrew Surface Currents: 2621
75.0 CM/S
RUN26
30°N
28°N
98°W
96°W
94°W
92°W
90°W
88°W
86°W

Figure 5.3 f.

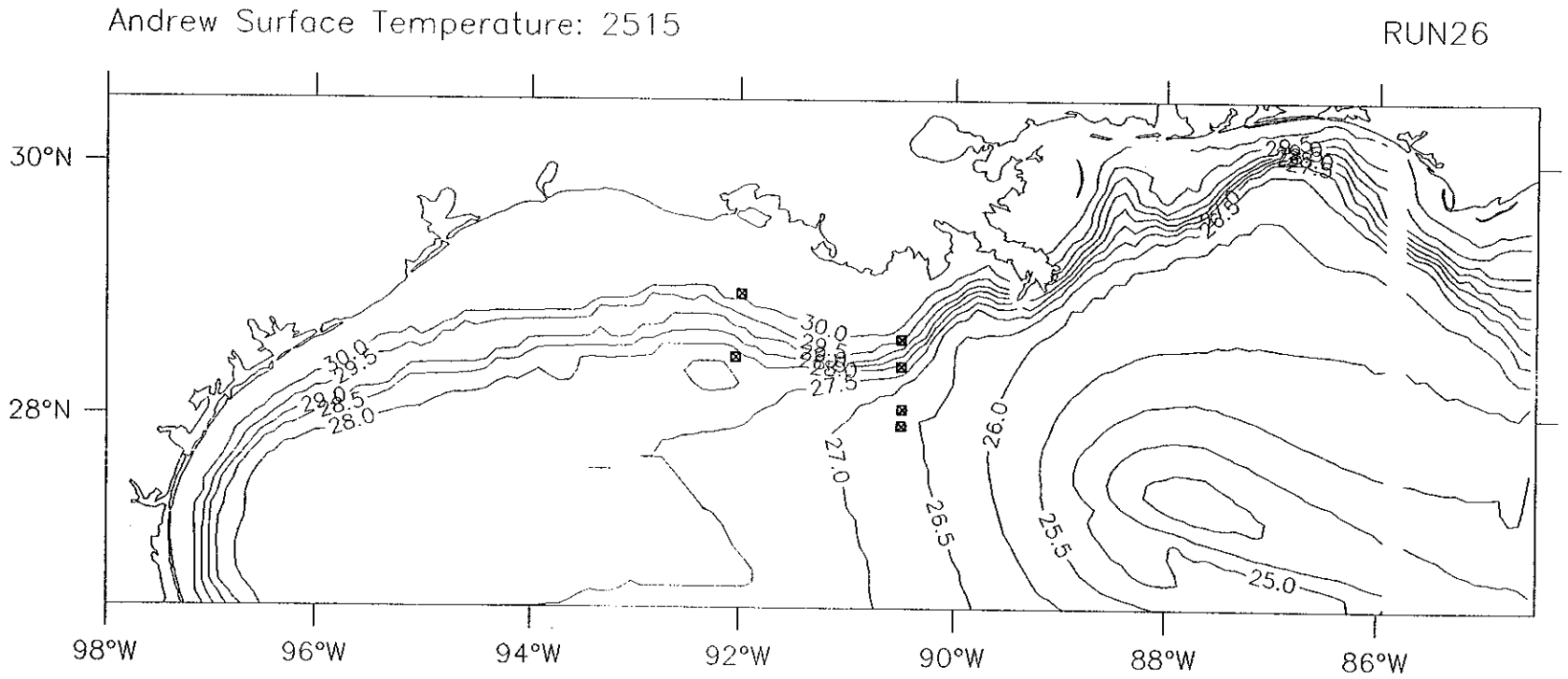

Figure 5.4. Temperature calculated in upper model level (depth=5 m) from Grid A at 1500 GMT Aug. 25 The first has a contour interval of 0.5 C and the second plot uses an interval of 1 C.The locations of the mooring arrays are indicated by the squares.

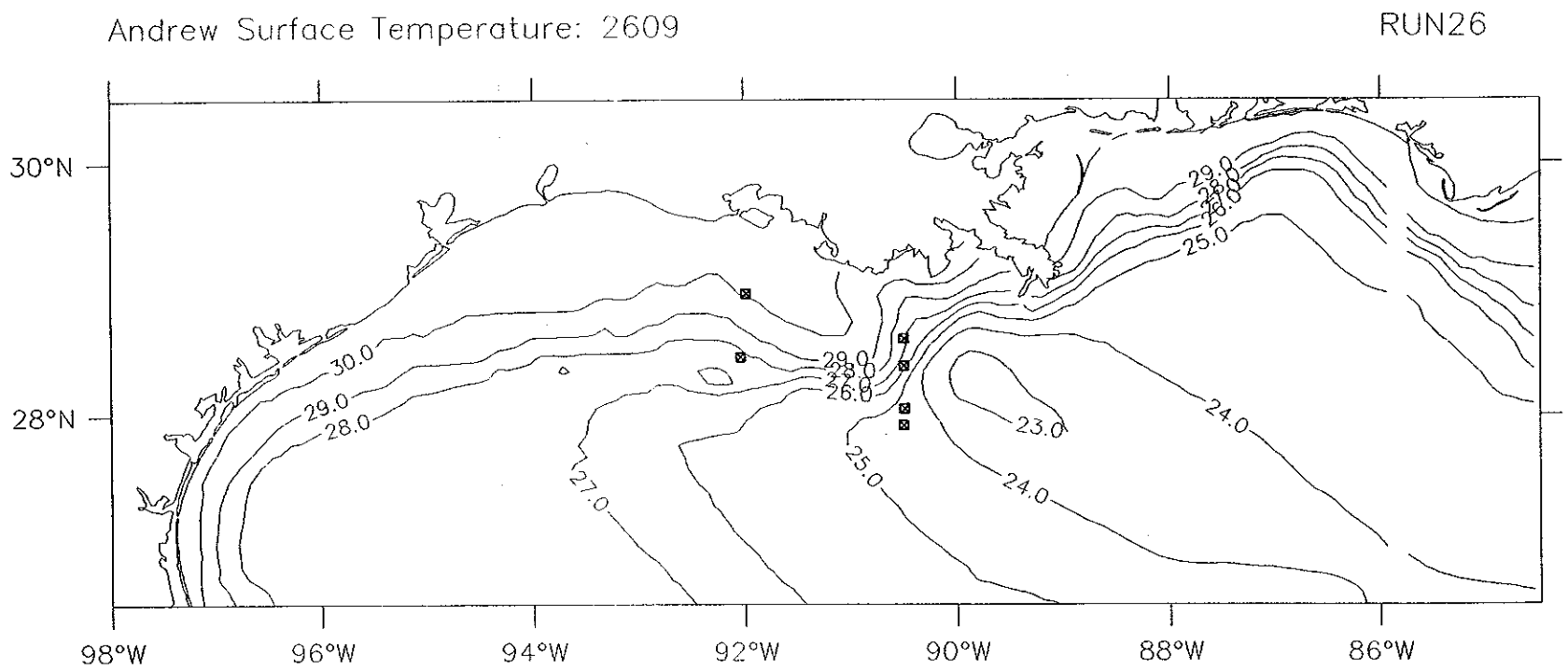

Figure 5.5 Same as Figure 5.4 except at 0900 GMT Aug. 26.

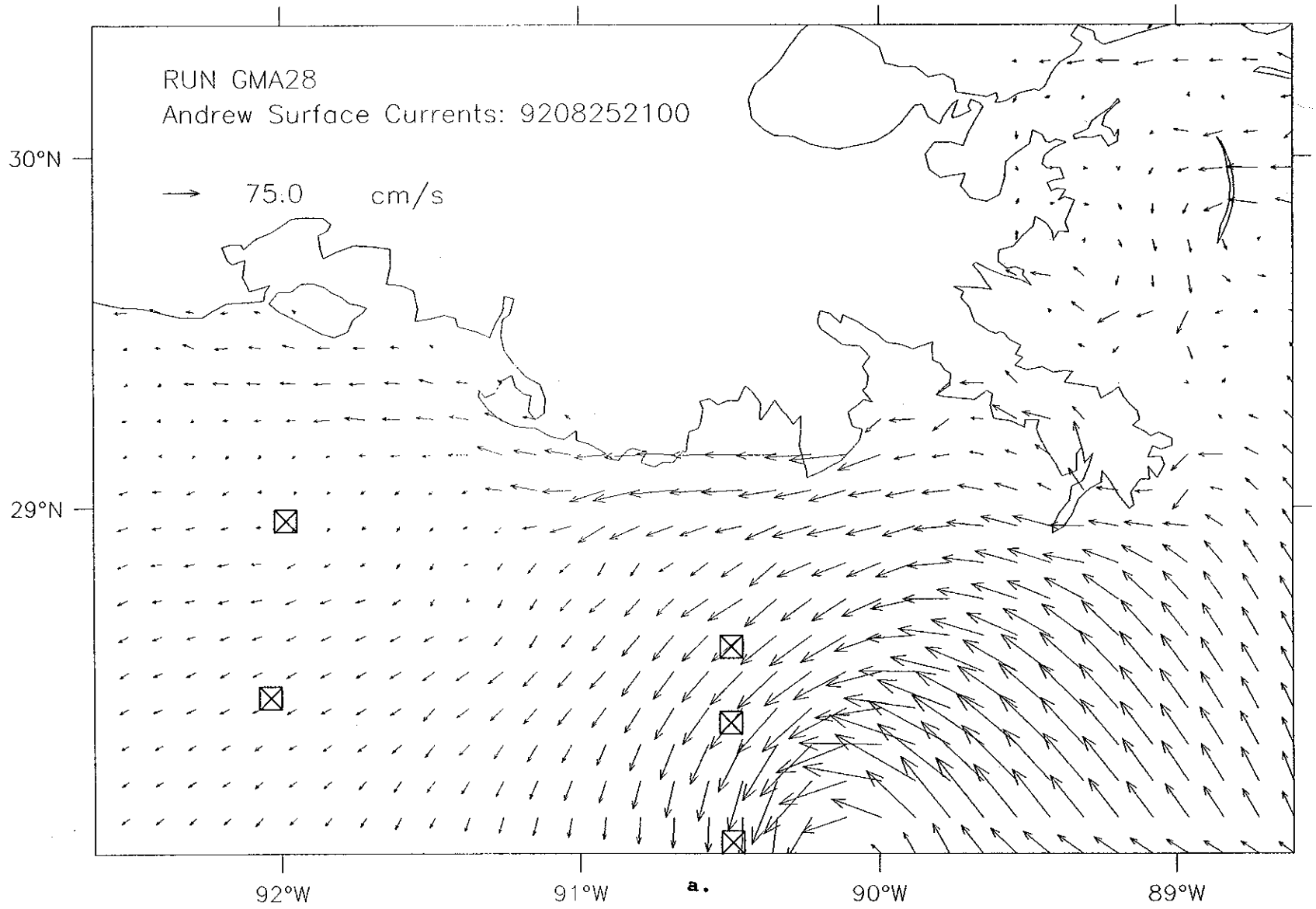

Figure 5.6 **Currents calculated in the upper model level (depth=2.5 m) for Grid B at (a) 2100 GMT Aug. 25, (b) 0300 and (c) 0900 GMT Aug. 26. Note that not all mooring locations are included in this grid. This simulation used the same parameters as for Grid A (Figure 5.3).**

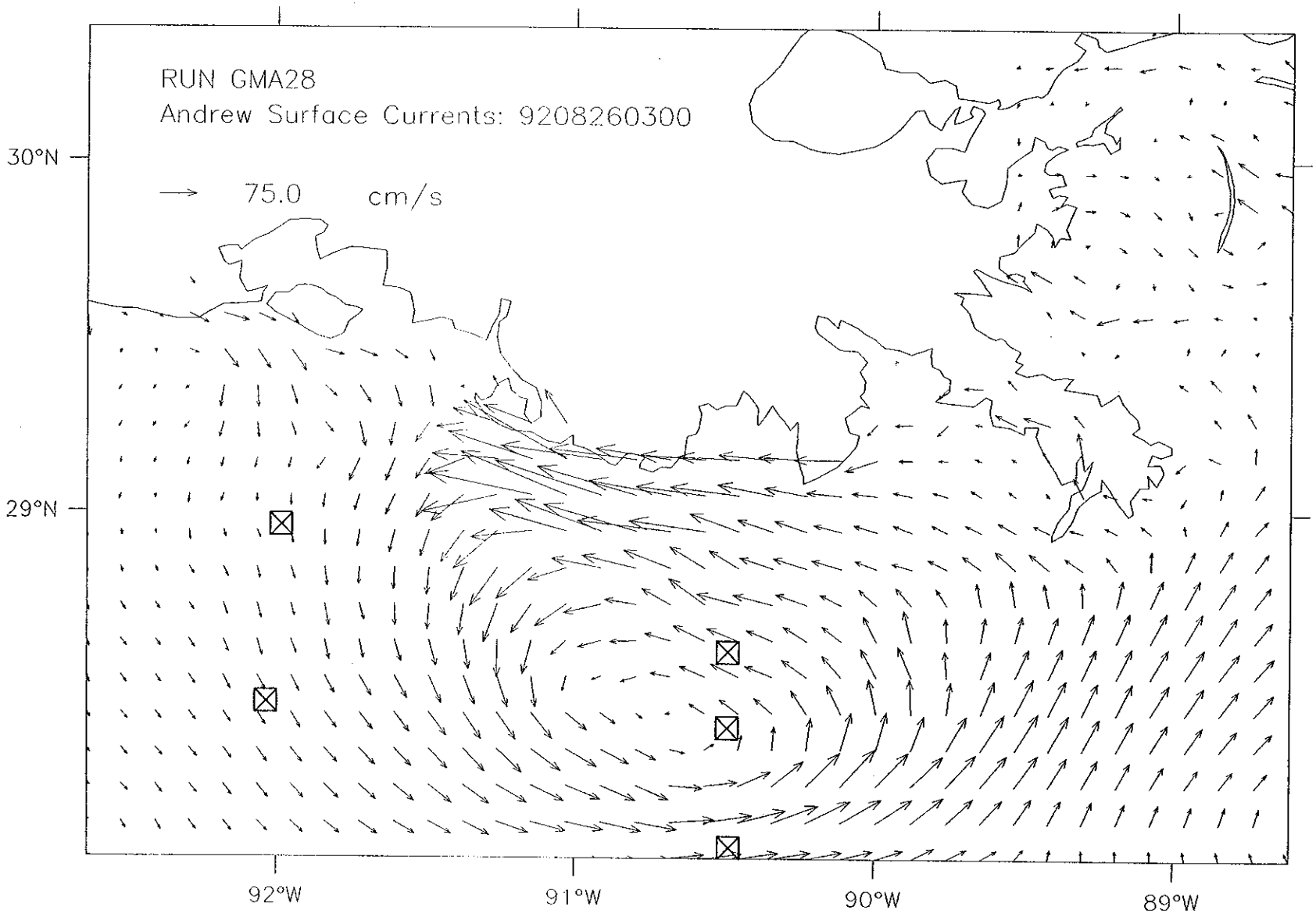
RUN GMA28
Andrew Surface Currents: 9208260300
75.0 cm/s
30°N
29°N
92°W
91°W
90°W
89°W

Figure 5.6 b.

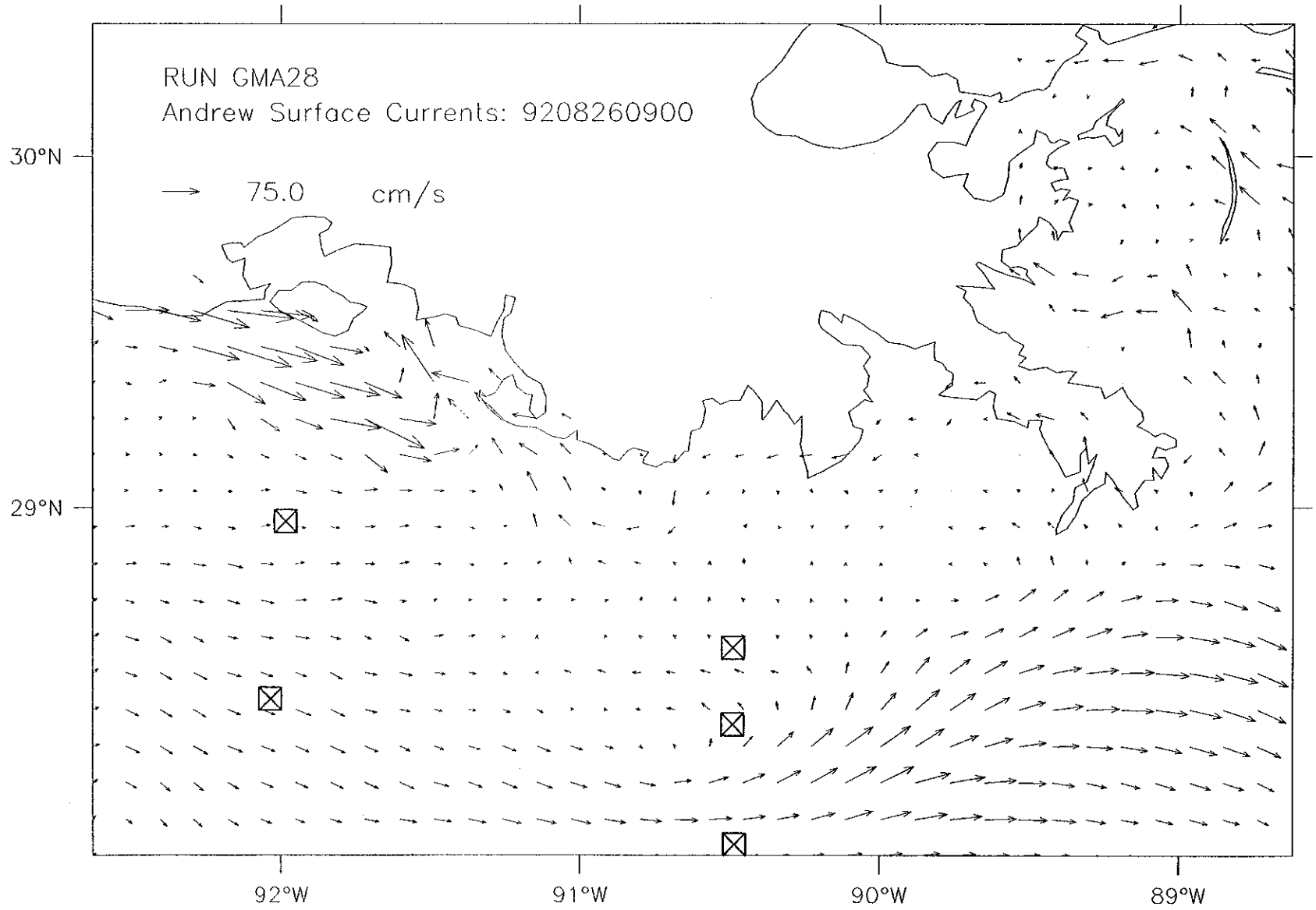
RUN GMA28
Andrew Surface Currents: 9208260900
75.0 cm/s
30°N
29°N
92°W
91°W
90°W
89°W

Figure 5.6 c.

Figure 5.7 Winds and observed surface currents near the LATEX moorings. Diamonds indicate mooring locations. The 100 m/sec wind scale vector is plotted above the chart. The hurricane track is plotted as the heavy solid line, the eye as the heavy cross, and the radius to maximum winds as the heavy circle. Plots at 6-hourly intervals are given in (a) through (h).

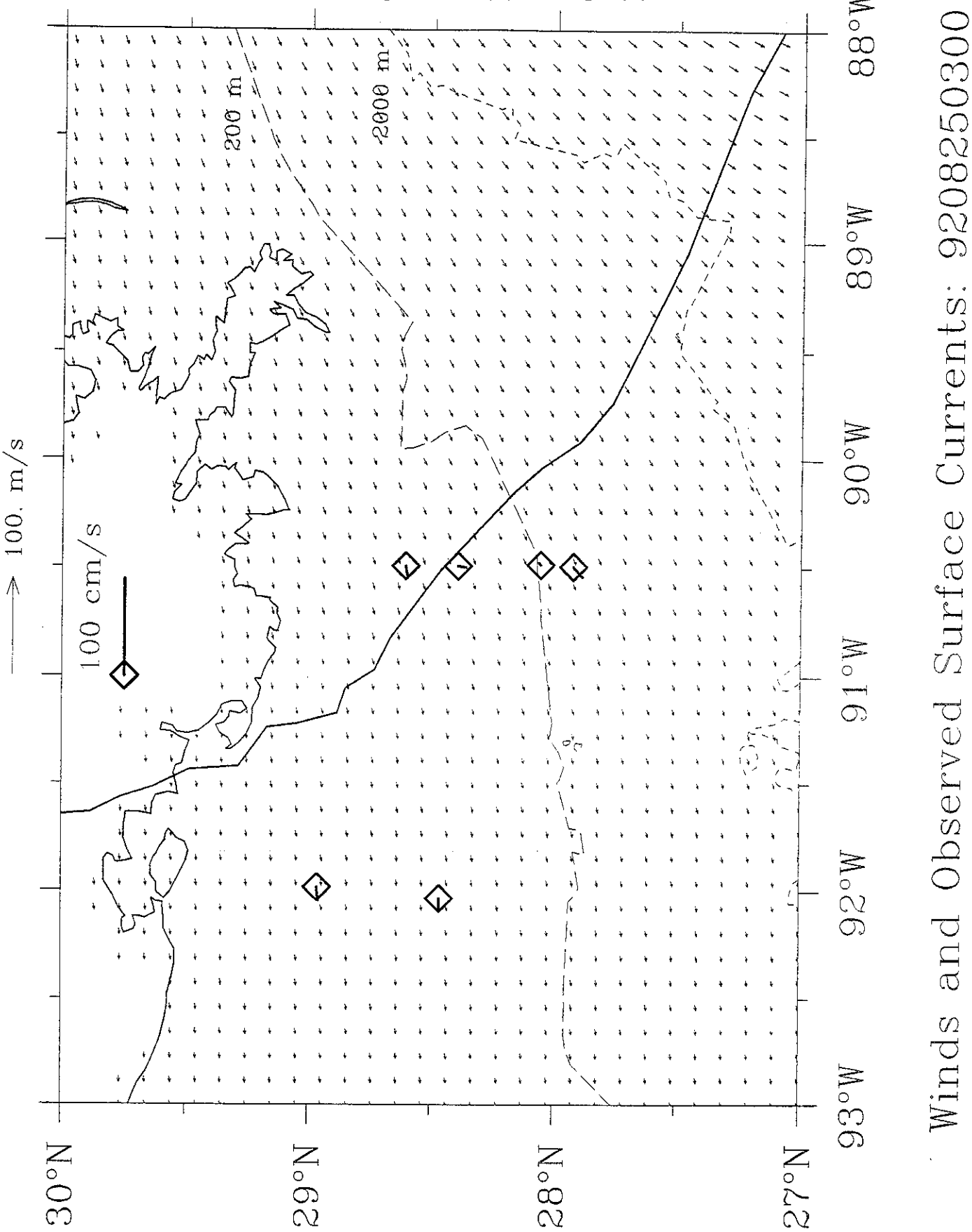

Figure 5.7 a.

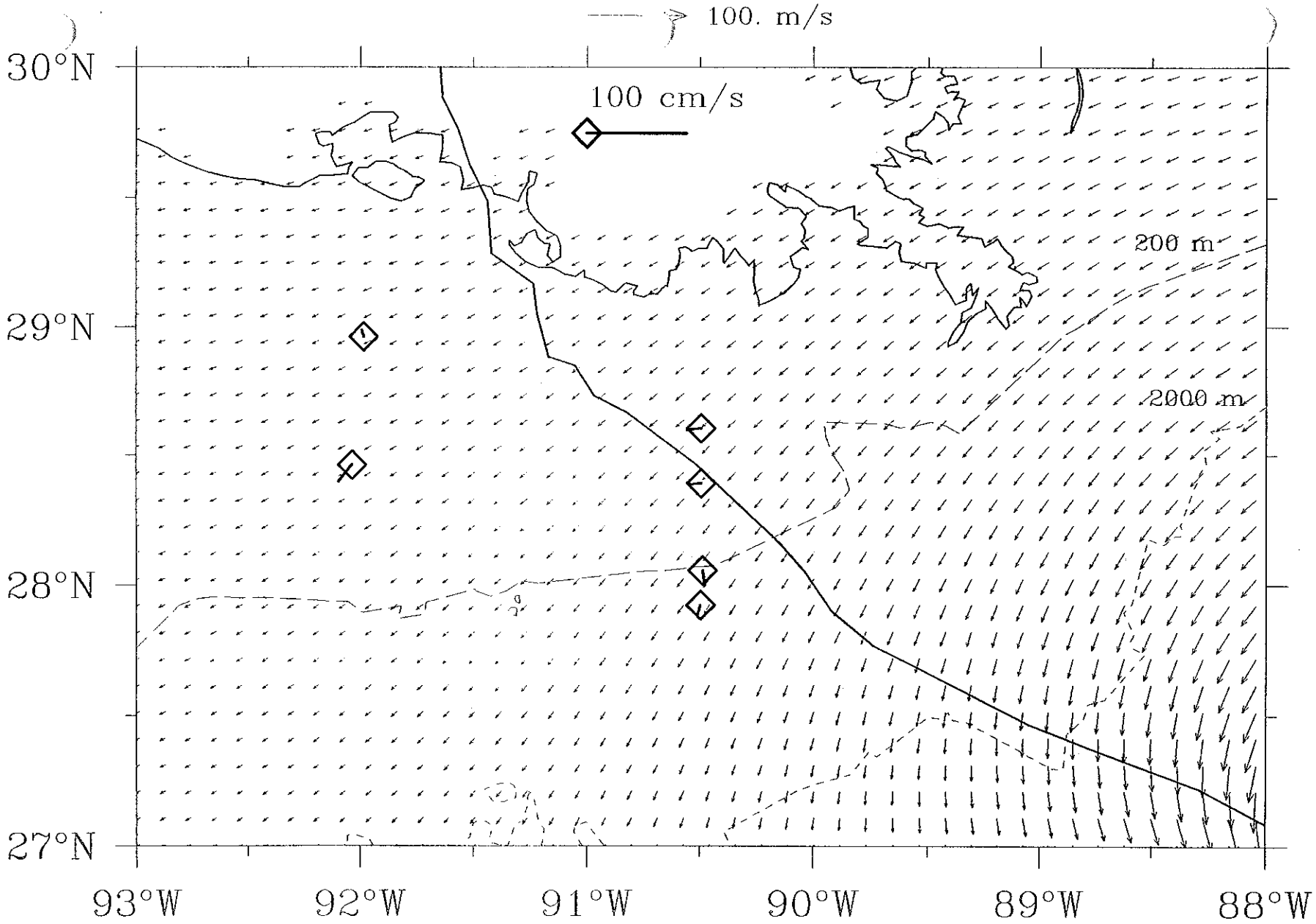

Winds and Observed Surface Currents: 9208250900

Figure 5.7 b.

Frame 018

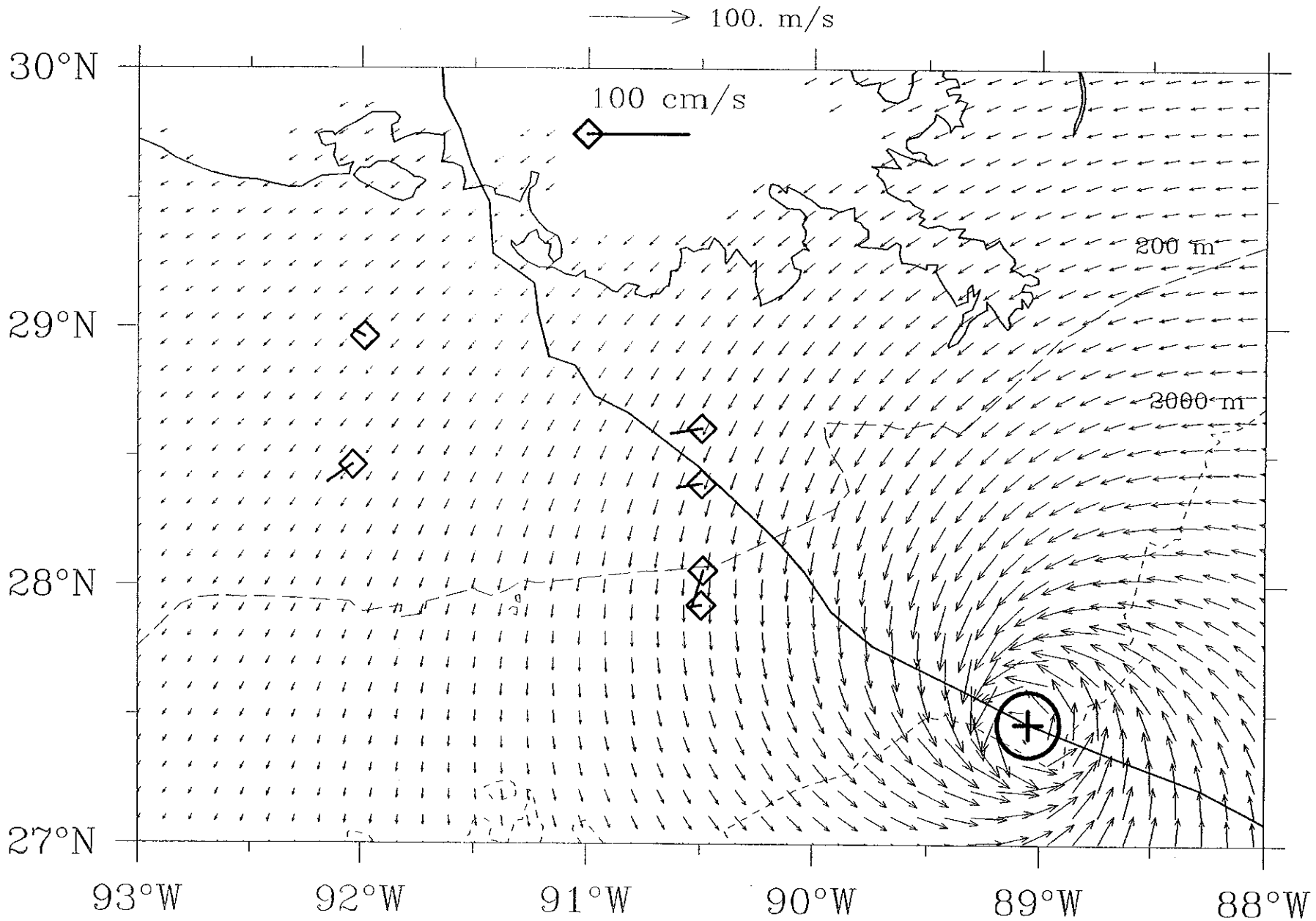

Winds and Observed Surface Currents: 9208251500

Figure 5.7 c.

Frame 030

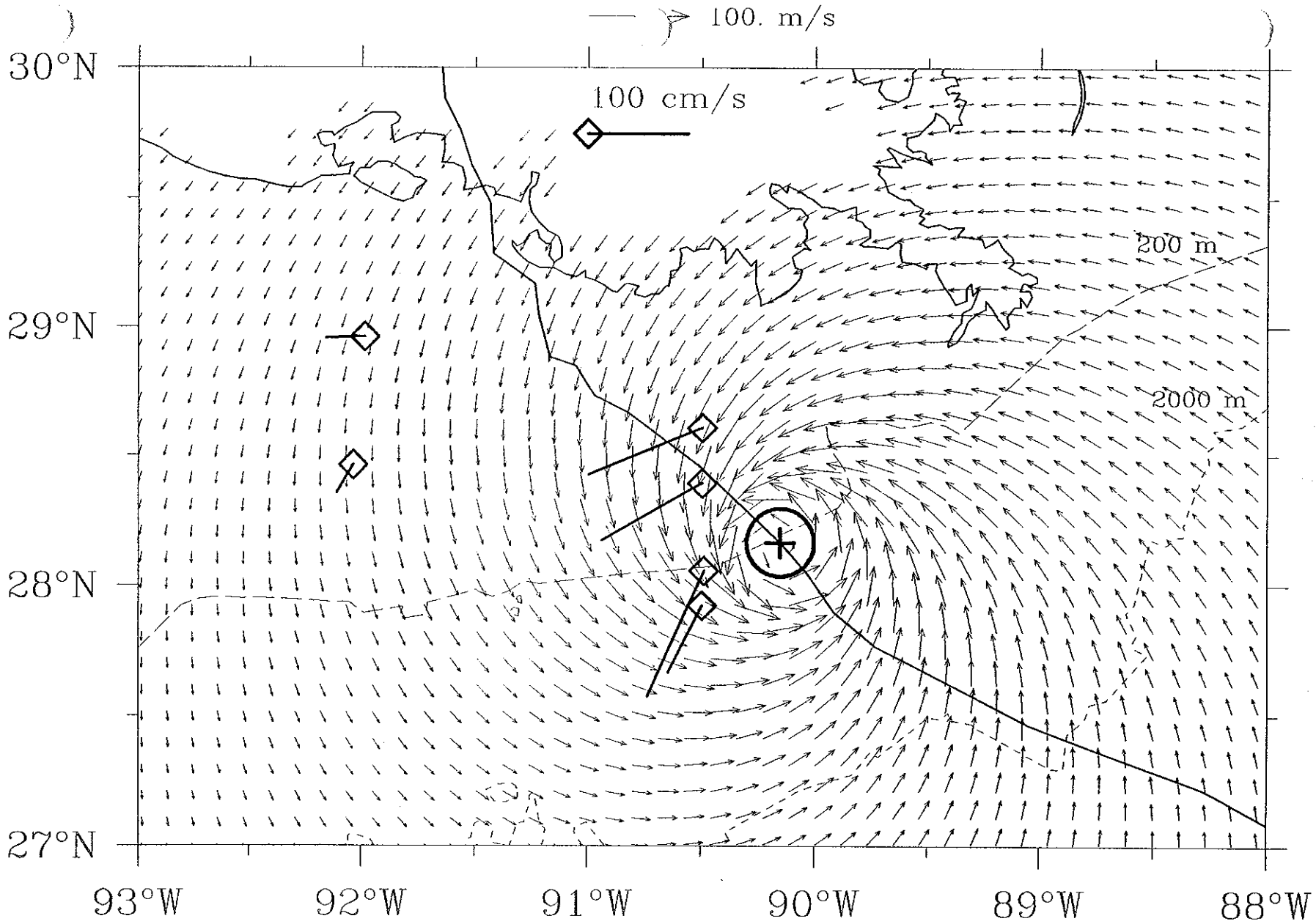

Winds and Observed Surface Currents: 9208252100

Figure 5.7 d.

Frame 042

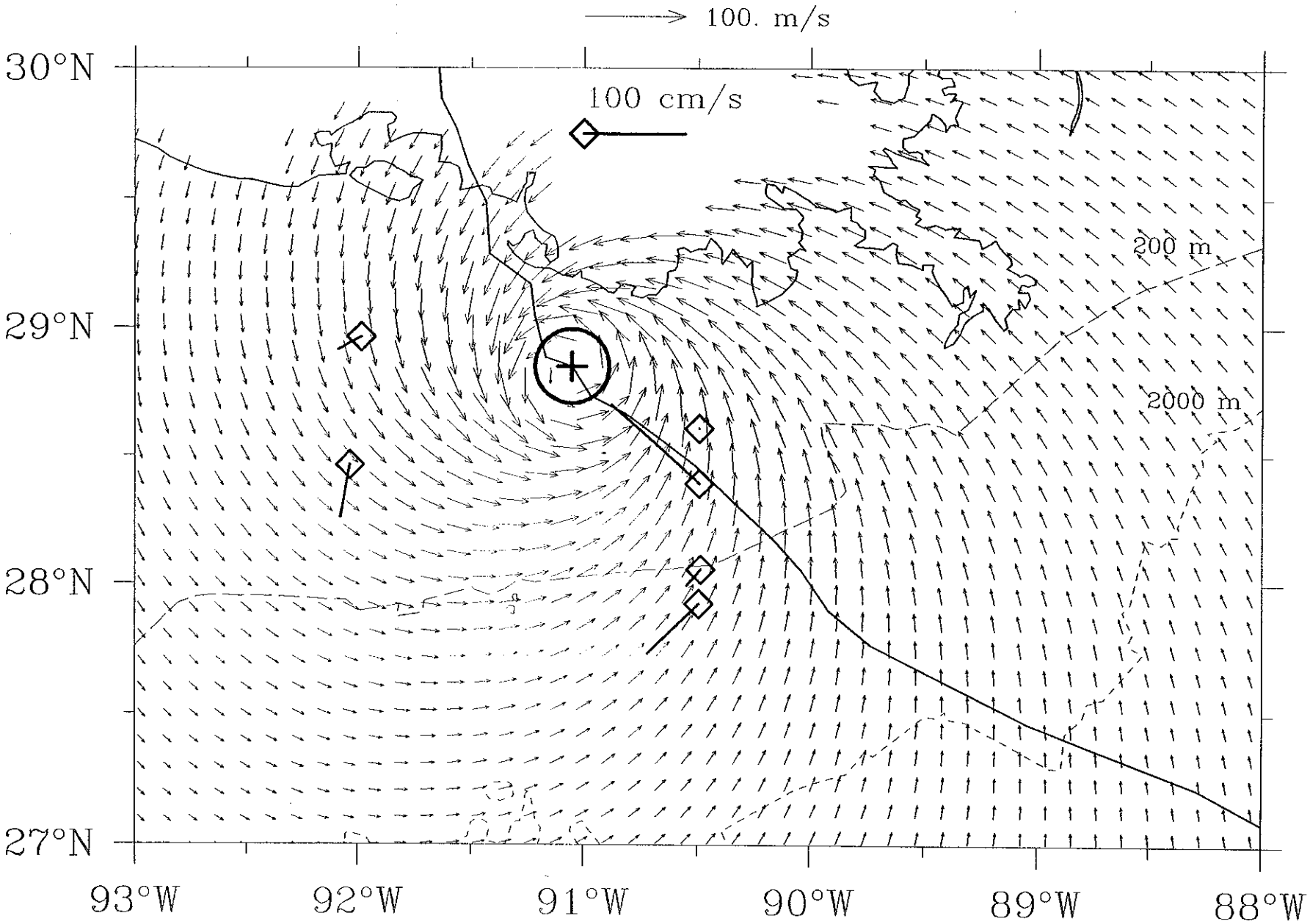

Winds and Observed Surface Currents: 9208260300

Figure 5 7 e.

Frame 05 1

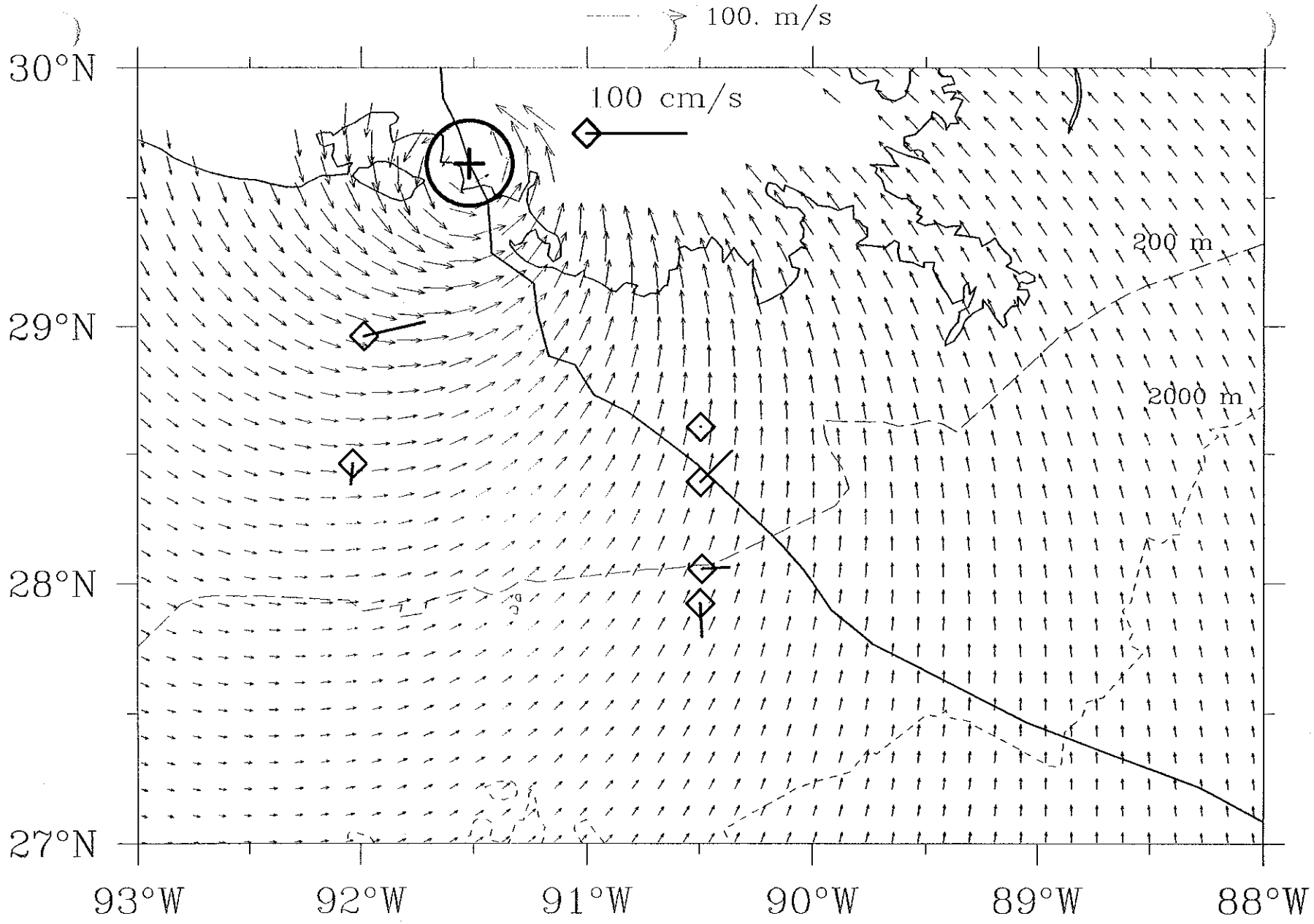

Winds and Observed Surface Currents: 9208260900

Figure 5.7 f.

Frame 066

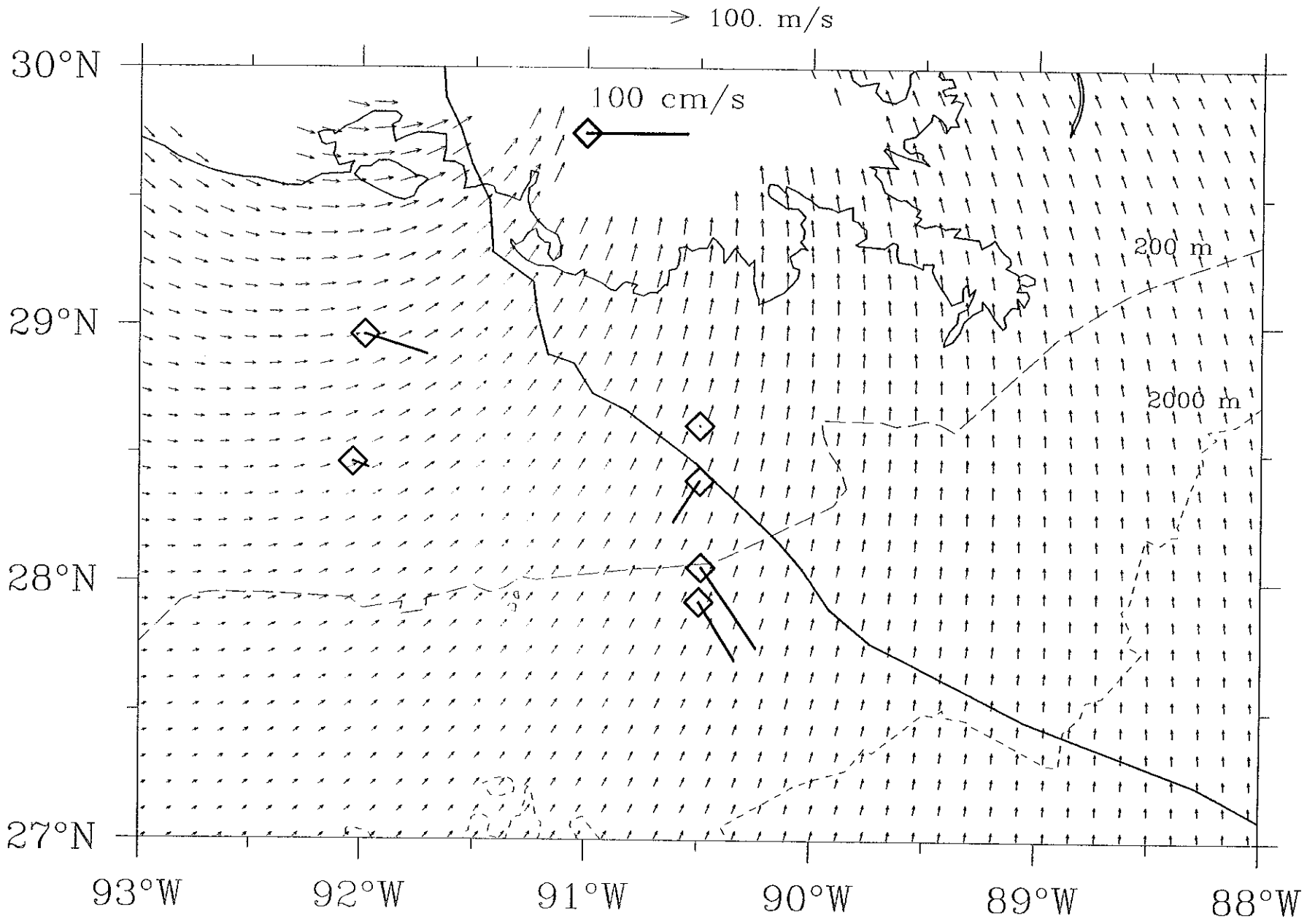

Winds and Observed Surface Currents: 9208261500

Figure 5.7 a.

Frame 078

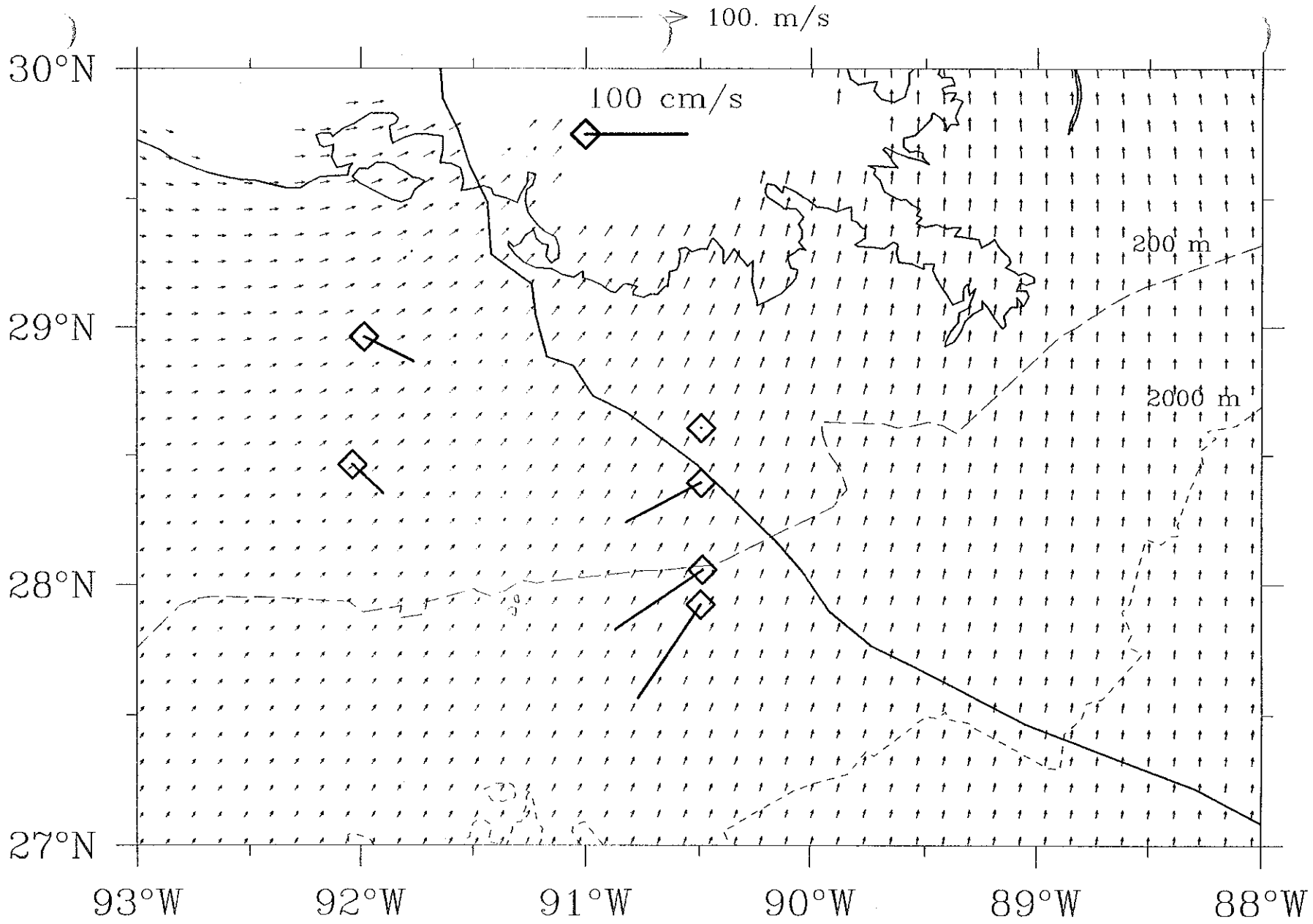

Winds and Observed Surface Currents: 9208262100

Figure 5.7 h.

Frame 090

Figure 5.8 Time series of observed and hindcast current speed at the LATEX moorings. The "t" signifies the top current meter, "m" the middle current meter, and "b" the bottom current meter. The vertical dashed lines indicate the hindcast interval. Plots at indicated meters are given in (a) through (m).

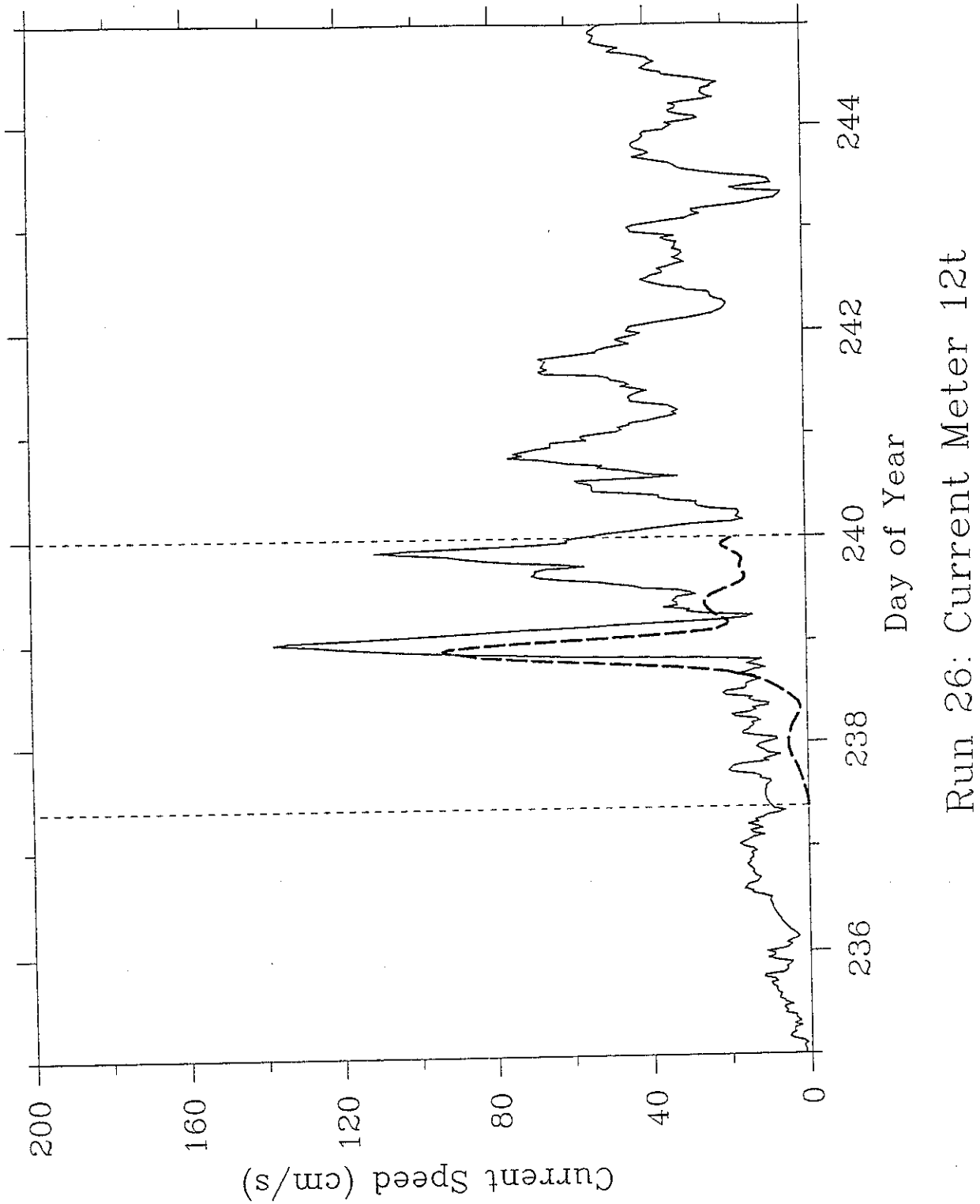

Figure 5.8 a.

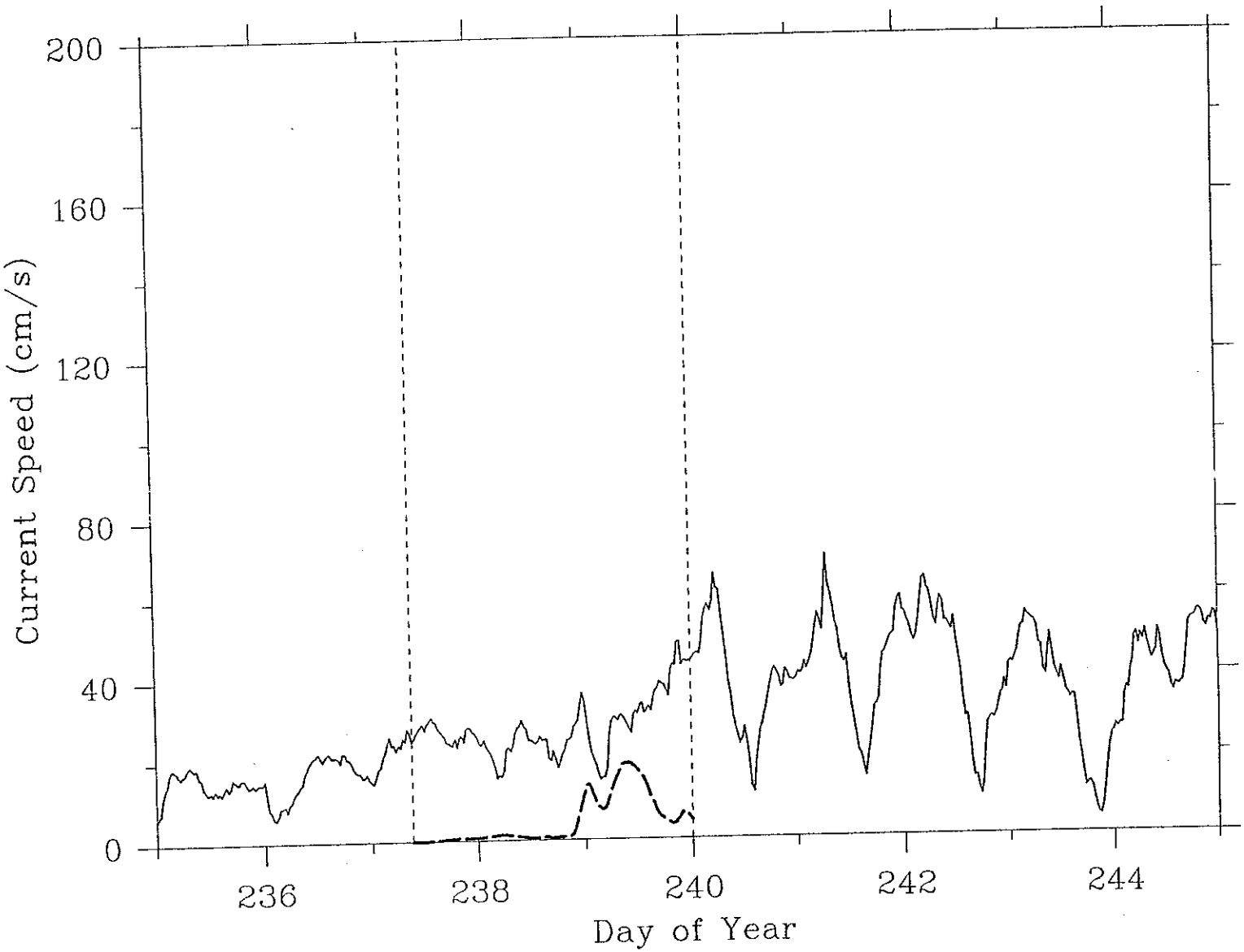

Run 26: Current Meter 12m

Figure 5.8 b.

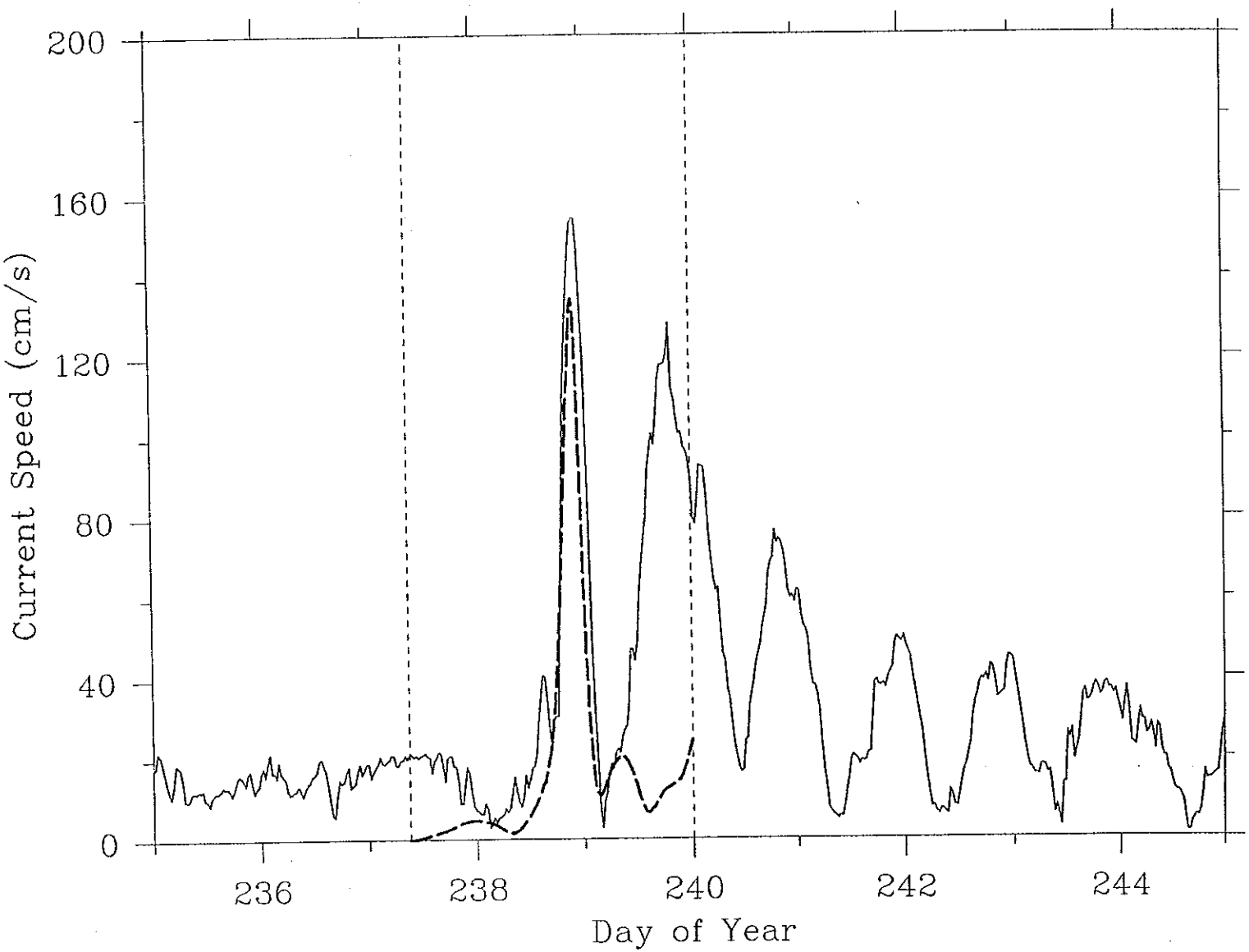
200
160
120
80
40
0
Current Speed (cm/s)
236
238
240
242
244
Day of Year
Run 26: Current Meter 13t

Figure 5.8 c.

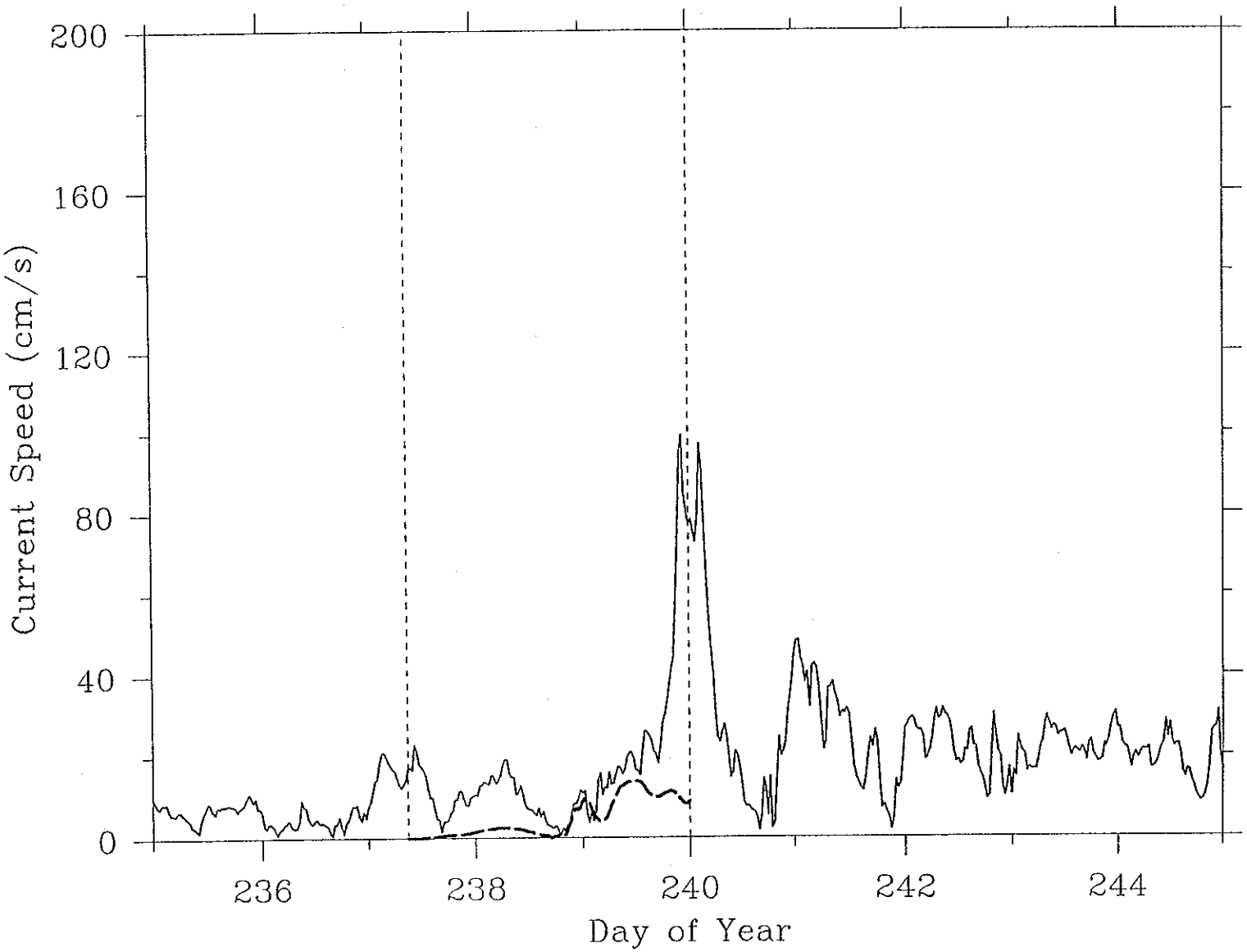
200
160
120
80
40
0
Current Speed (cm/s)
236
238
240
242
244
Day of Year
Run 26: Current Meter 13m

Figure 5.8 d.

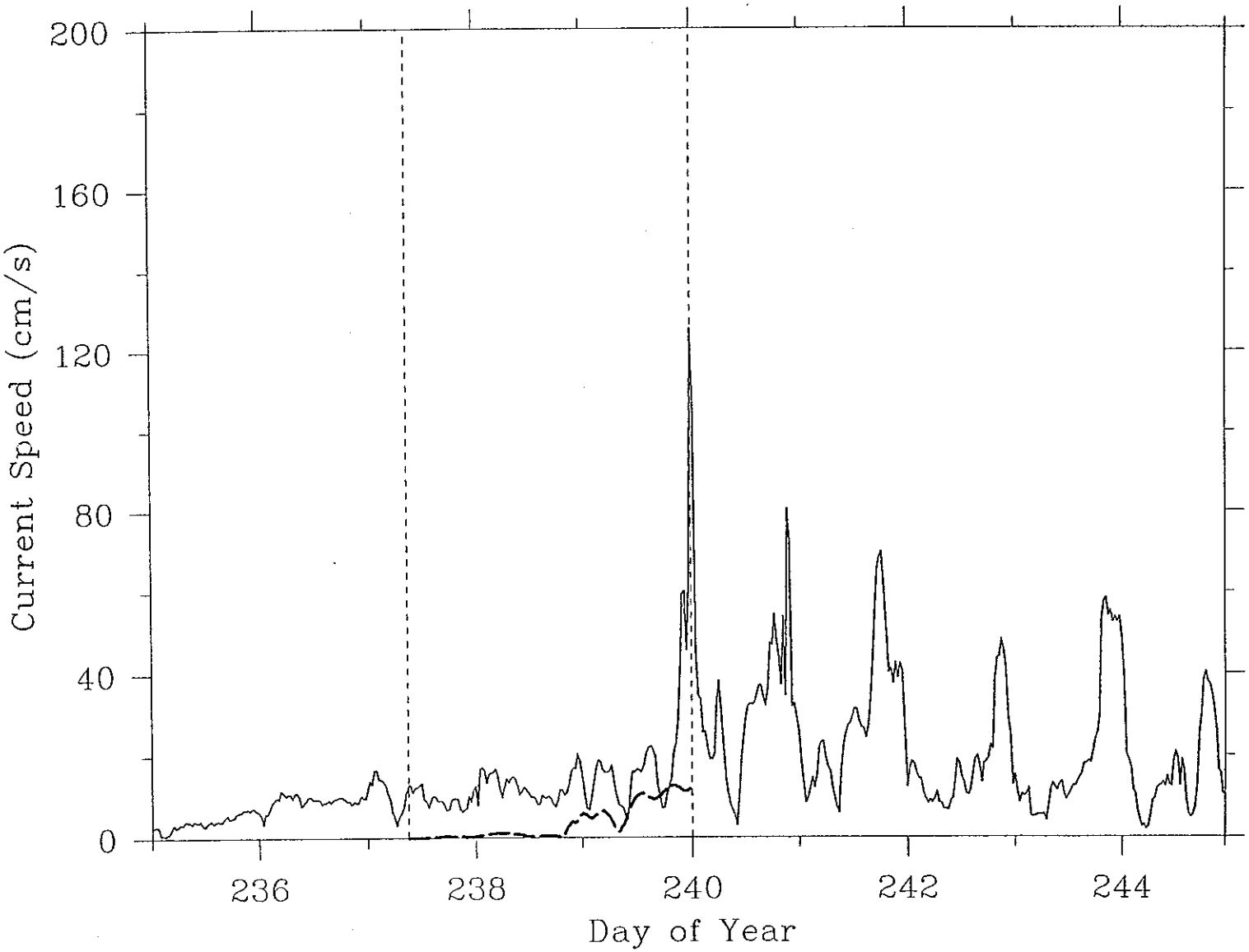
200
160
120
80
40
0
Current Speed (cm/s)
236
238
240
242
244
Day of Year
Run 26: Current Meter 13b

Figure 5.8 e.

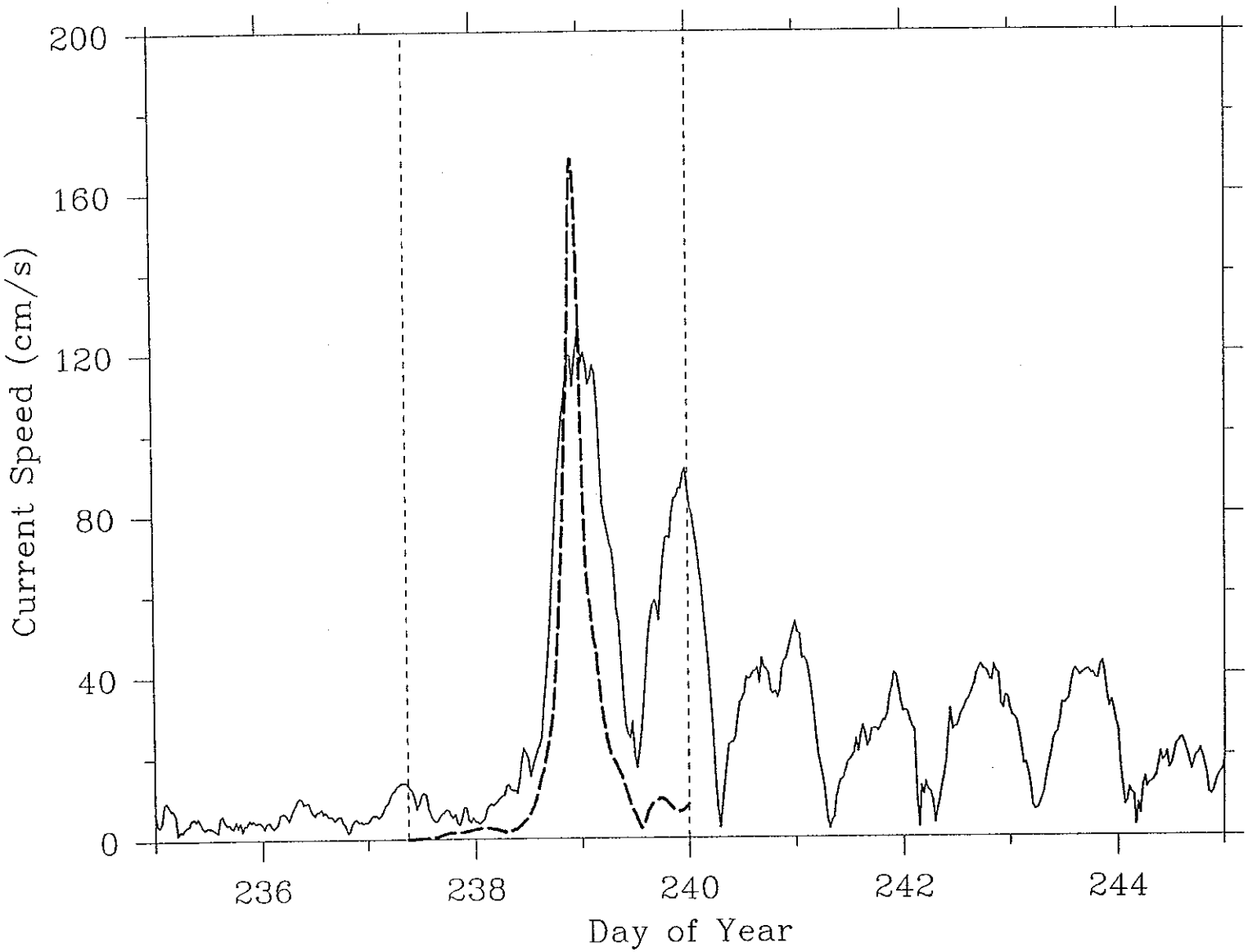
200
160
120
80
40
0
Current Speed (cm/s)
236
238
240
242
244
Day of Year
Run 26: Current Meter 14t

Figure 5.8 f.

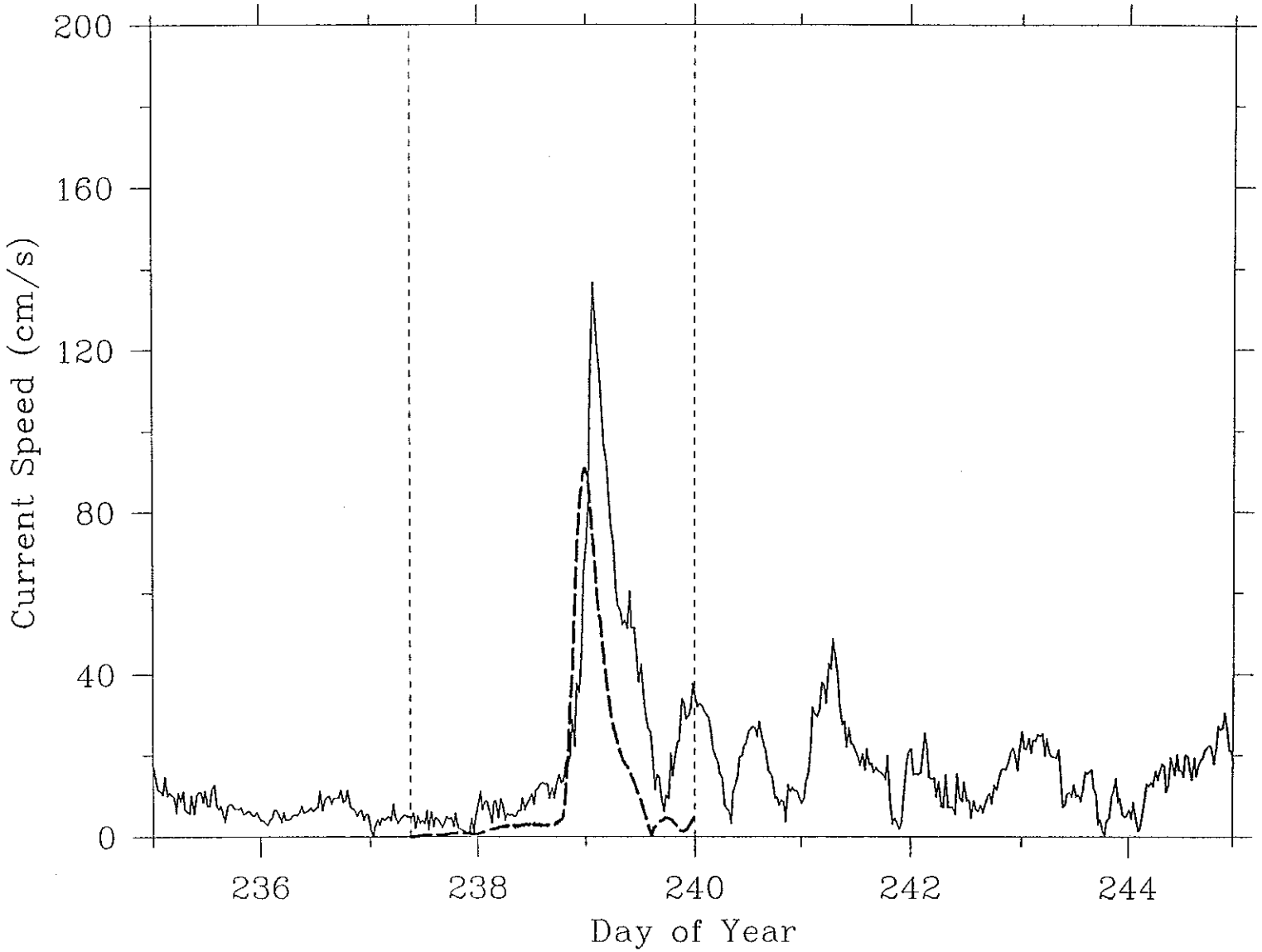
200
160
120
80
40
0
Current Speed (cm/s)
236
238
240
242
244
Day of Year
Run 26: Current Meter 14b

Figure 5.8 g.

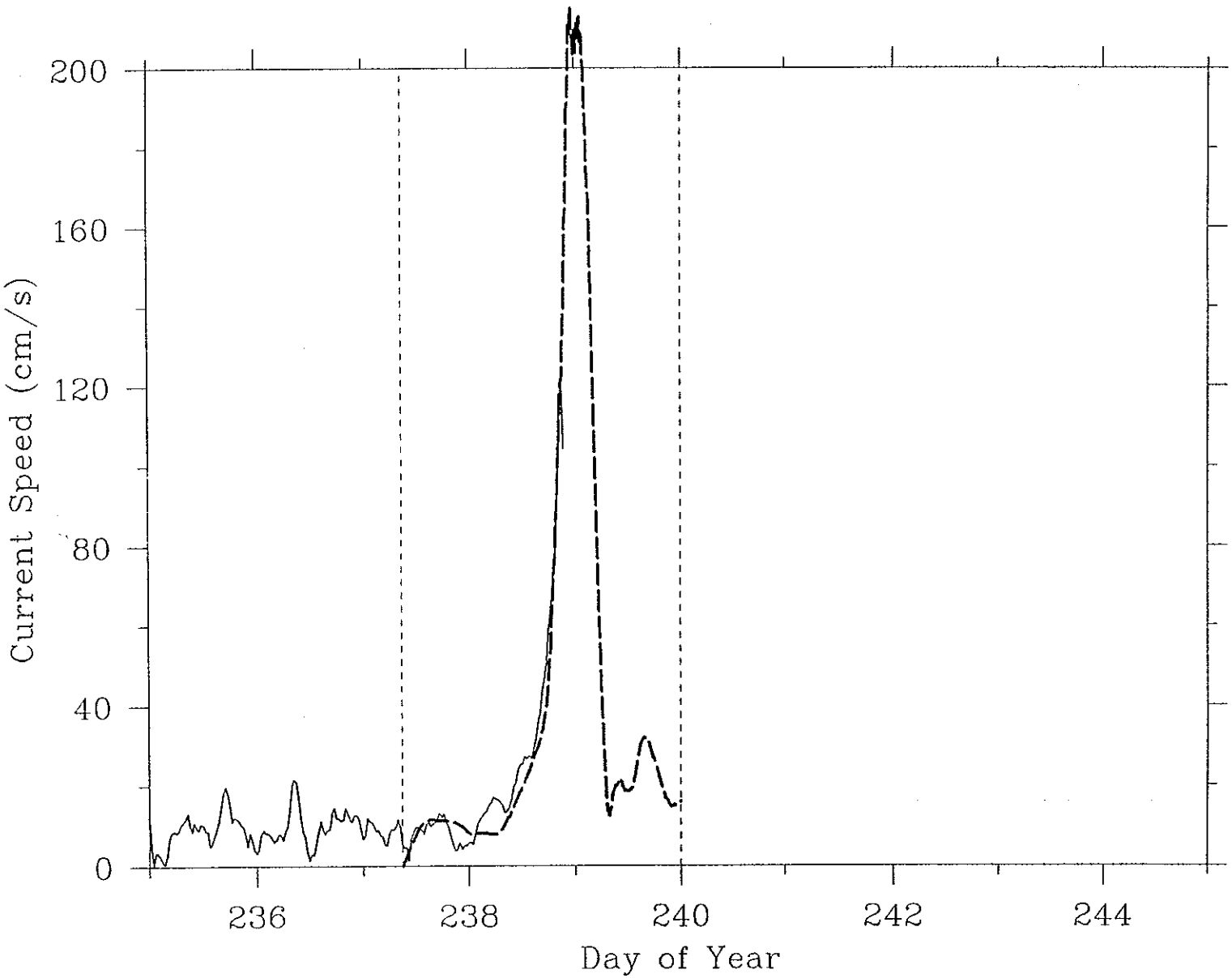
200
160
120
80
40
0
Current Speed (cm/s)
236
238
240
242
244
Day of Year
Run 26: Current Meter 15t

Figure 5.8 h.

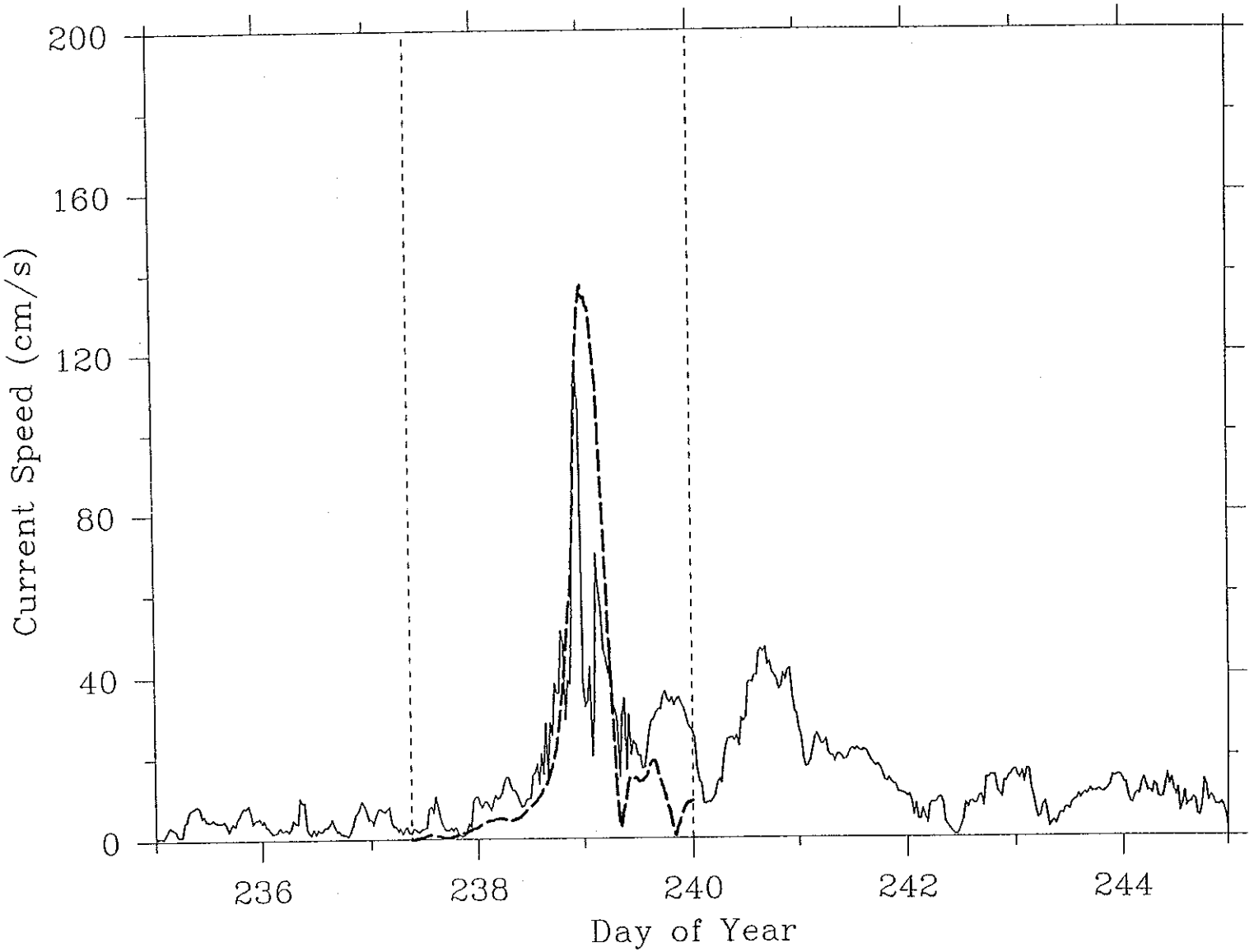
200
160
120
80
40
0
Current Speed (cm/s)
236
238
240
242
244
Day of Year
Run 26: Current Meter 15b

Figure 5.8 i.

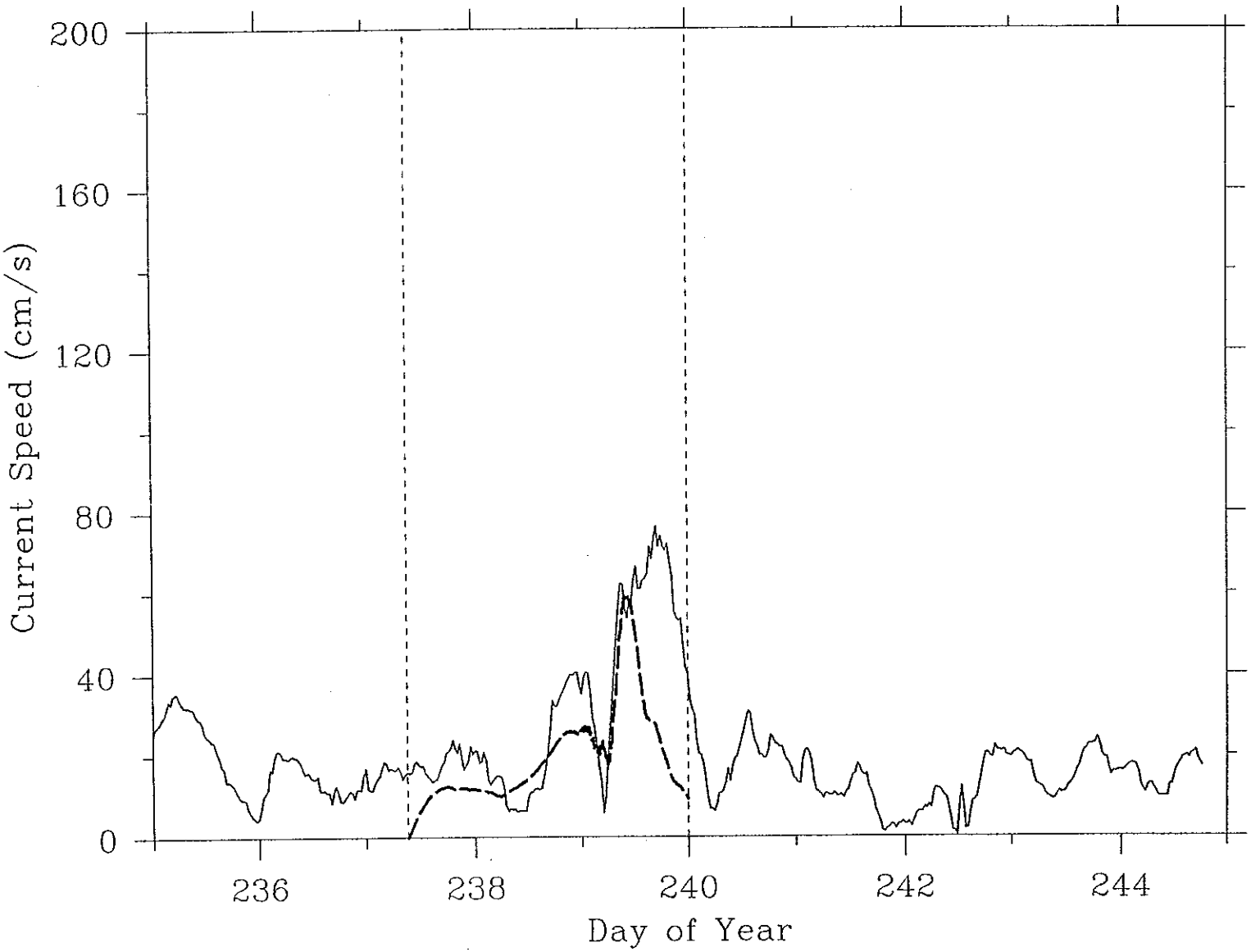
200
160
120
80
40
0
Current Speed (cm/s)
236
238
240
242
244
Day of Year
Run 26: Current Meter 18t

Figure 5.8 j.

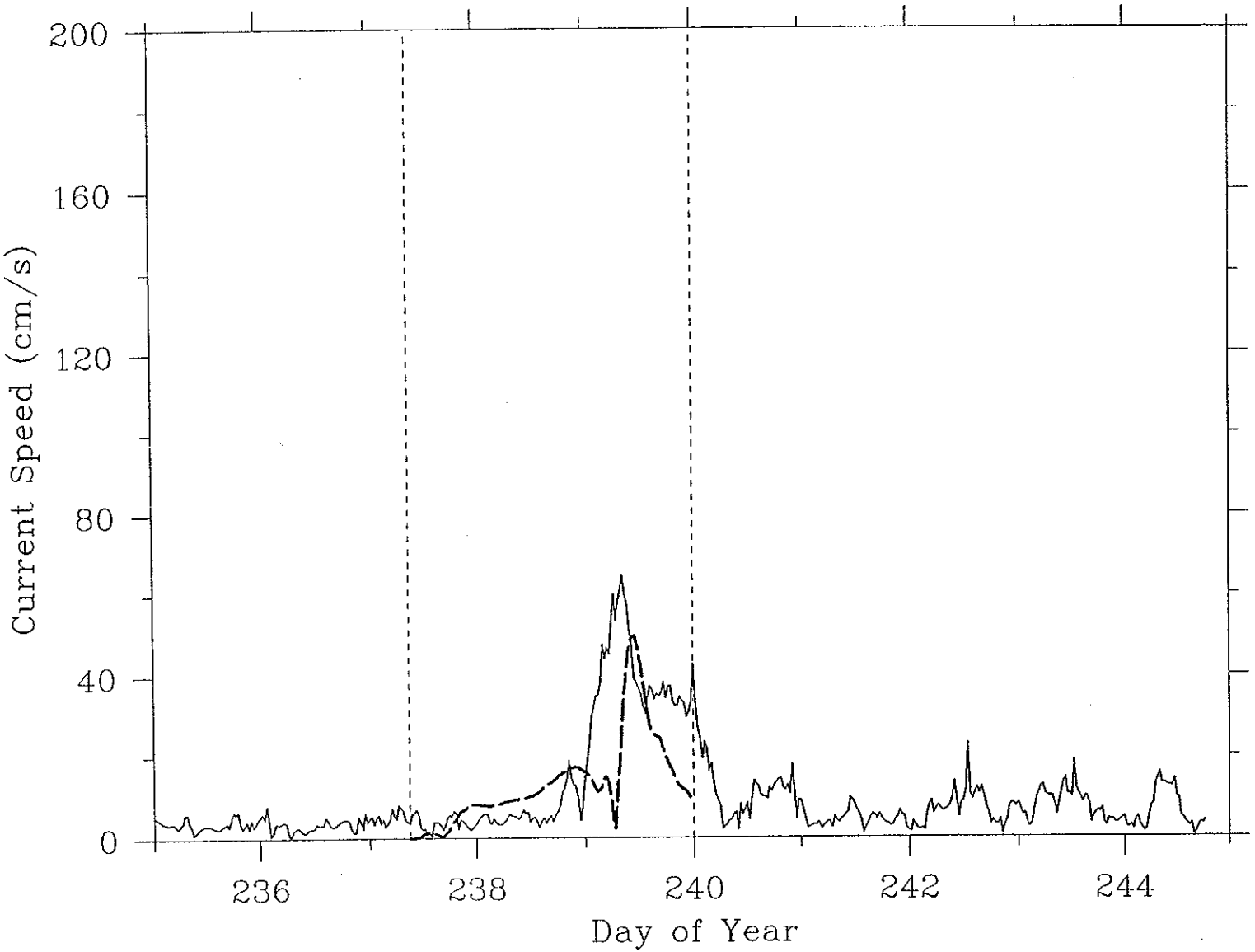
200
160
120
80
40
0
Current Speed (cm/s)
236
238
240
242
244
Day of Year
Run 26: Current Meter 18b

Figure 5.8 k.

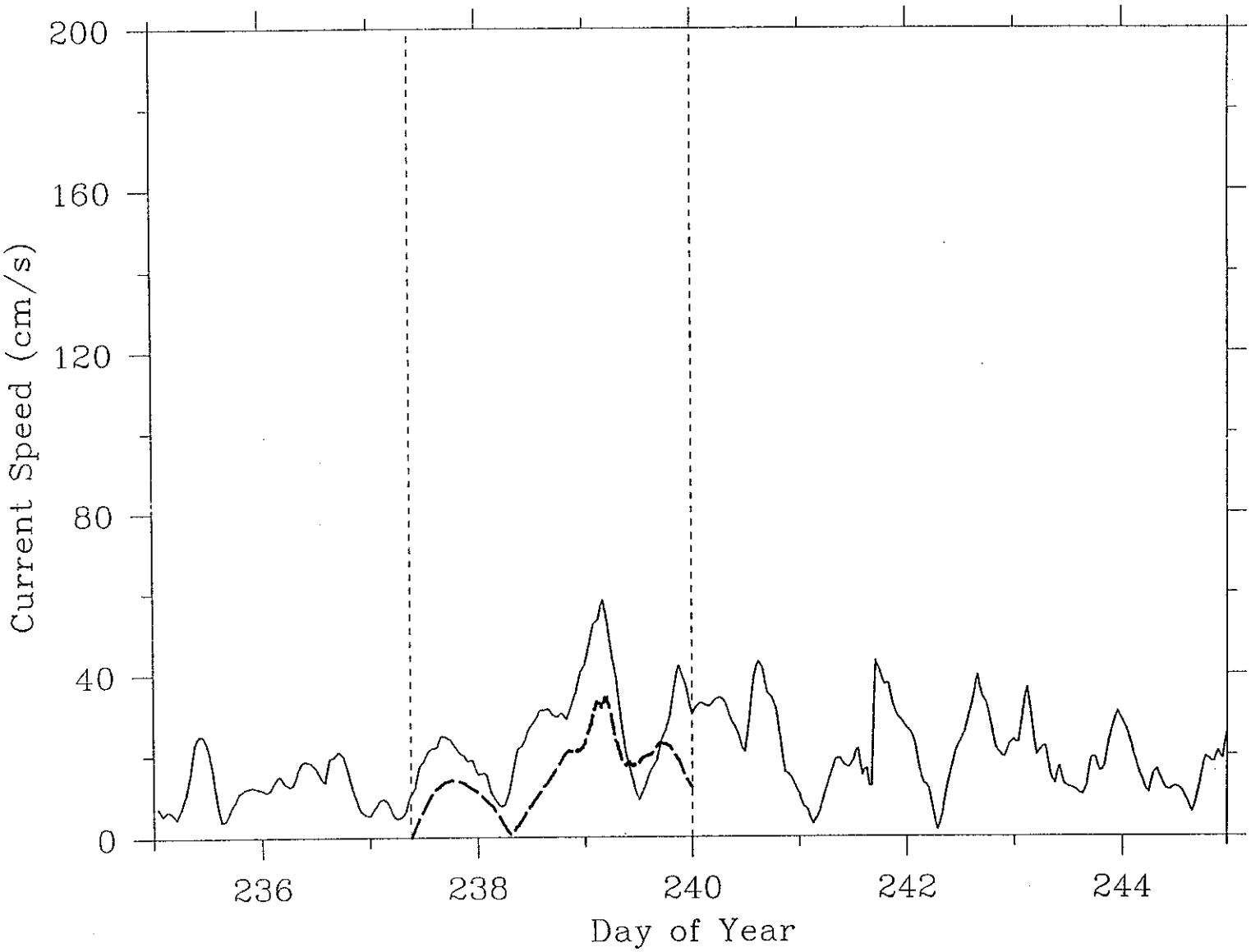
200
160
120
80
40
0
Current Speed (cm/s)
236
238
240
242
244
Day of Year
Run 26: Current Meter 19t

Figure 5.8 1.

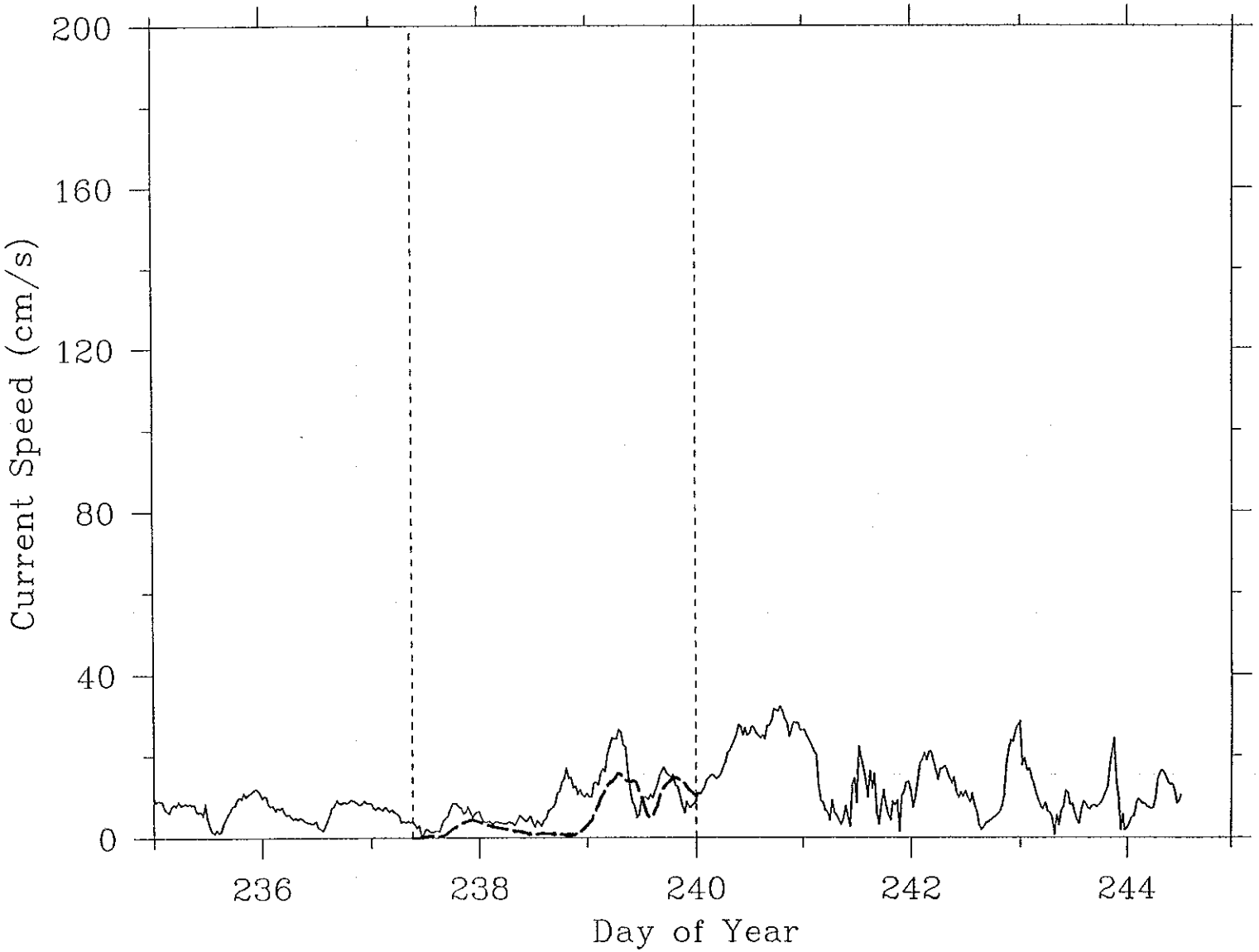

Run 26: Current Meter 19b

Figure 5.8 m.

Figure 5.9 Modeled and observed surface currents near the LATEX moorings. Diamonds indicate mooring locations. The 100 cm/sec hindcast current scale vector is plotted above the chart. The hurricane track is plotted as the heavy solid line, the eye as the heavy cross, and the radius to maximum winds as the heavy circle. Plots at 6-hourly intervals are given in (a) through (h).

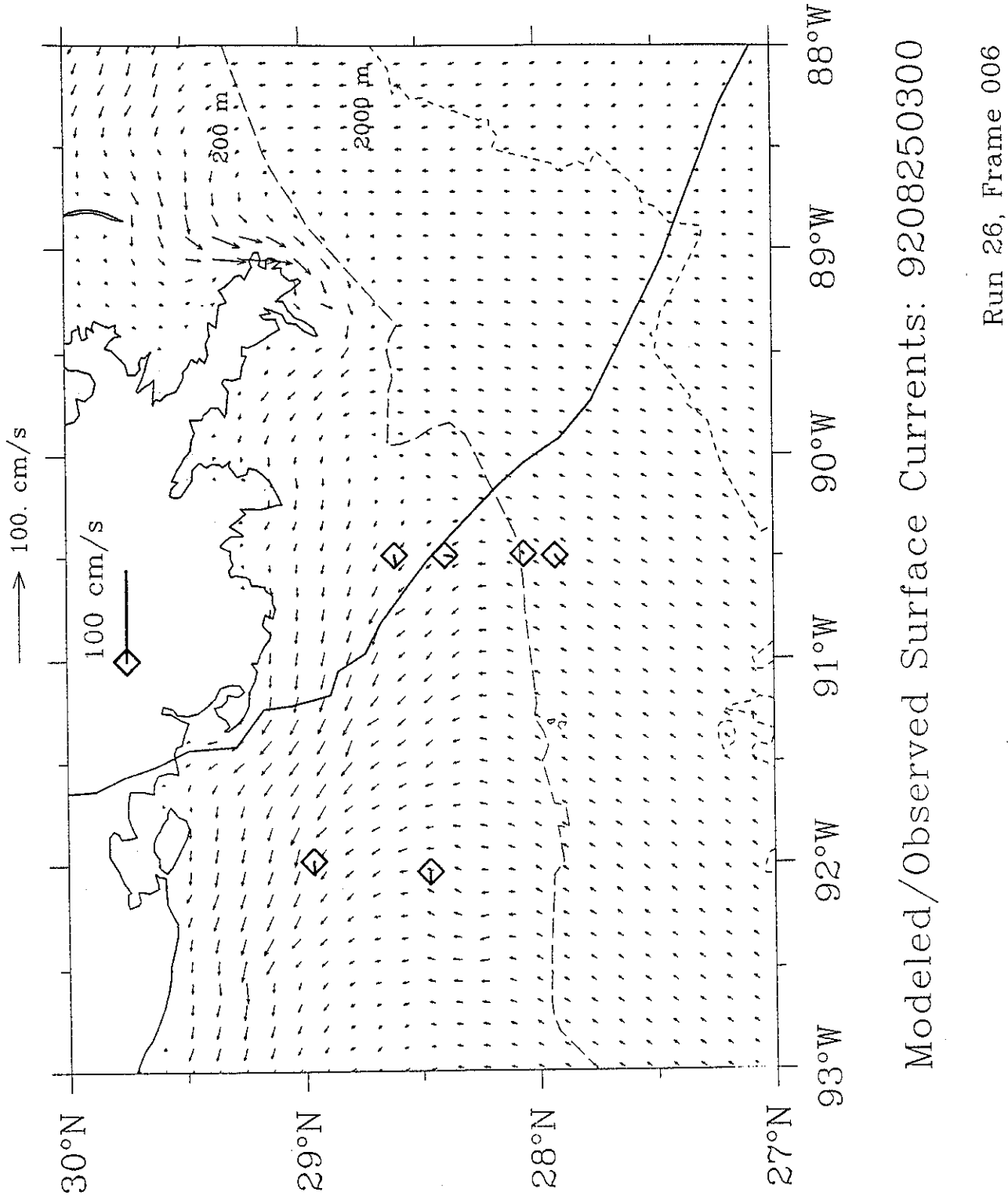

Figure 5.9 a.

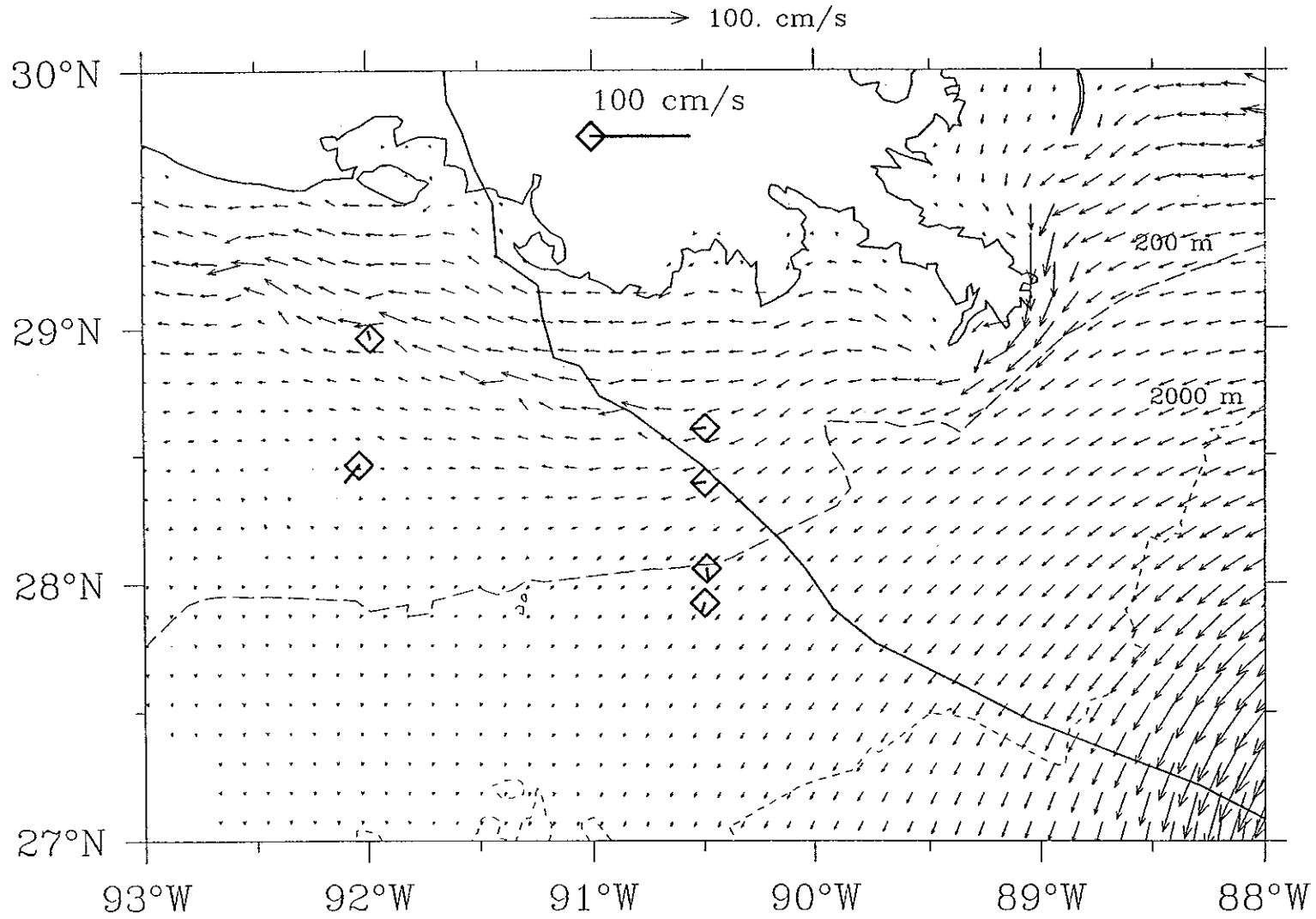

Modeled/Observed Surface Currents: 9208250900

Run 26, Frame 018

Figure 5.9 b.

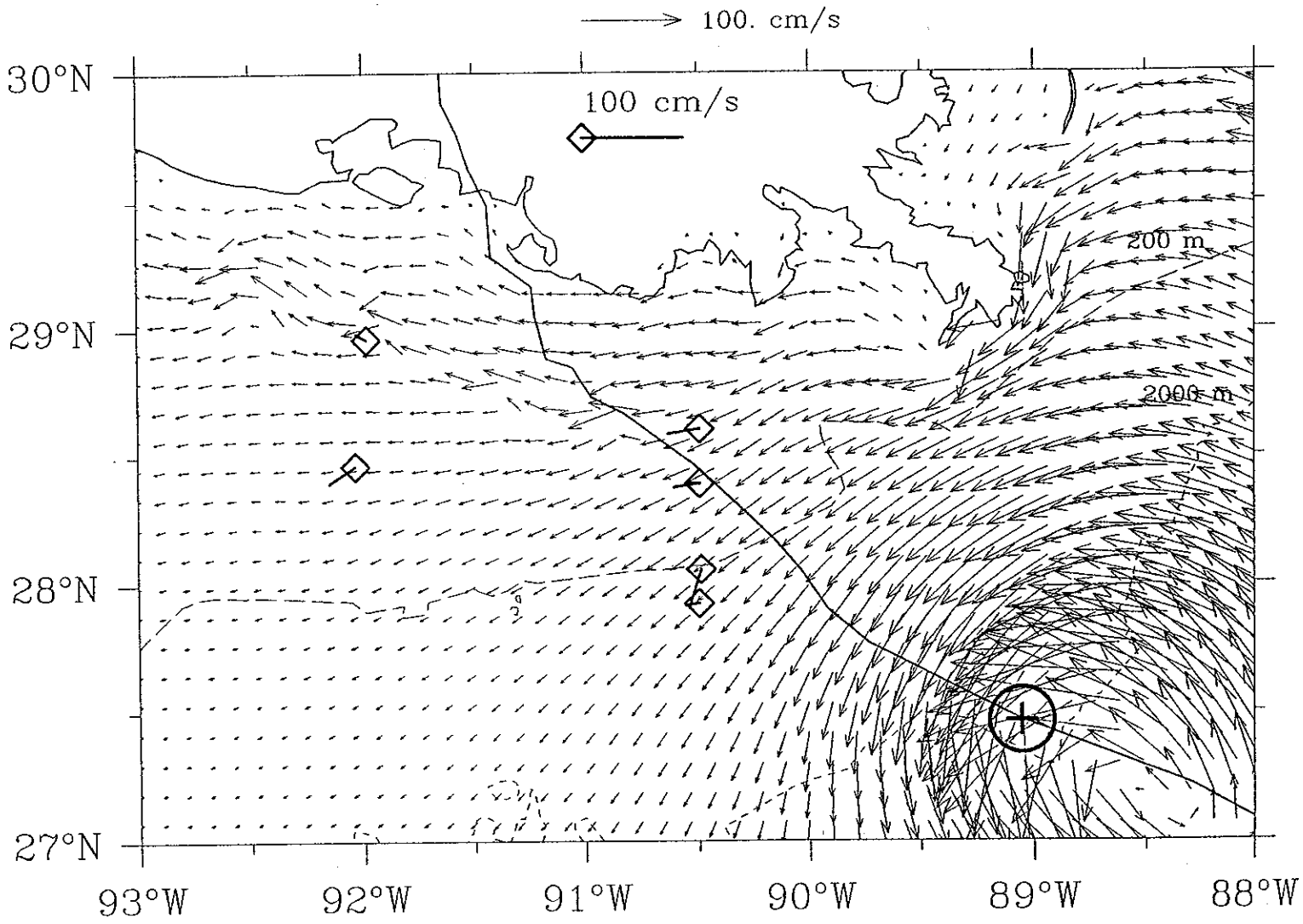

Modeled/Observed Surface Currents: 9208251500

Run 26, Frame 030

Figure 5.9 c.

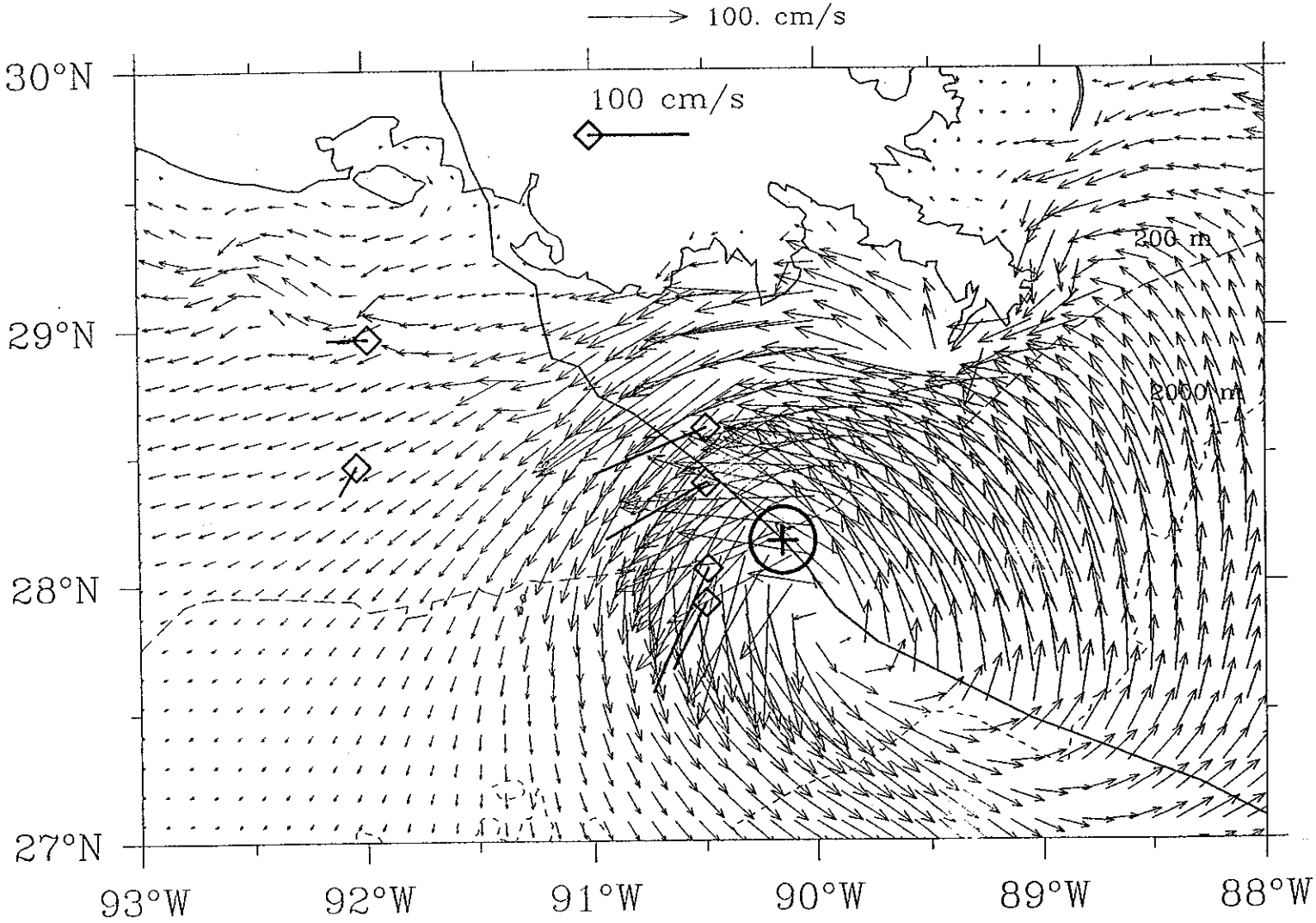

Modeled/Observed Surface Currents: 9208252100

Run 26, Frame 042

Figure 5.9 d.

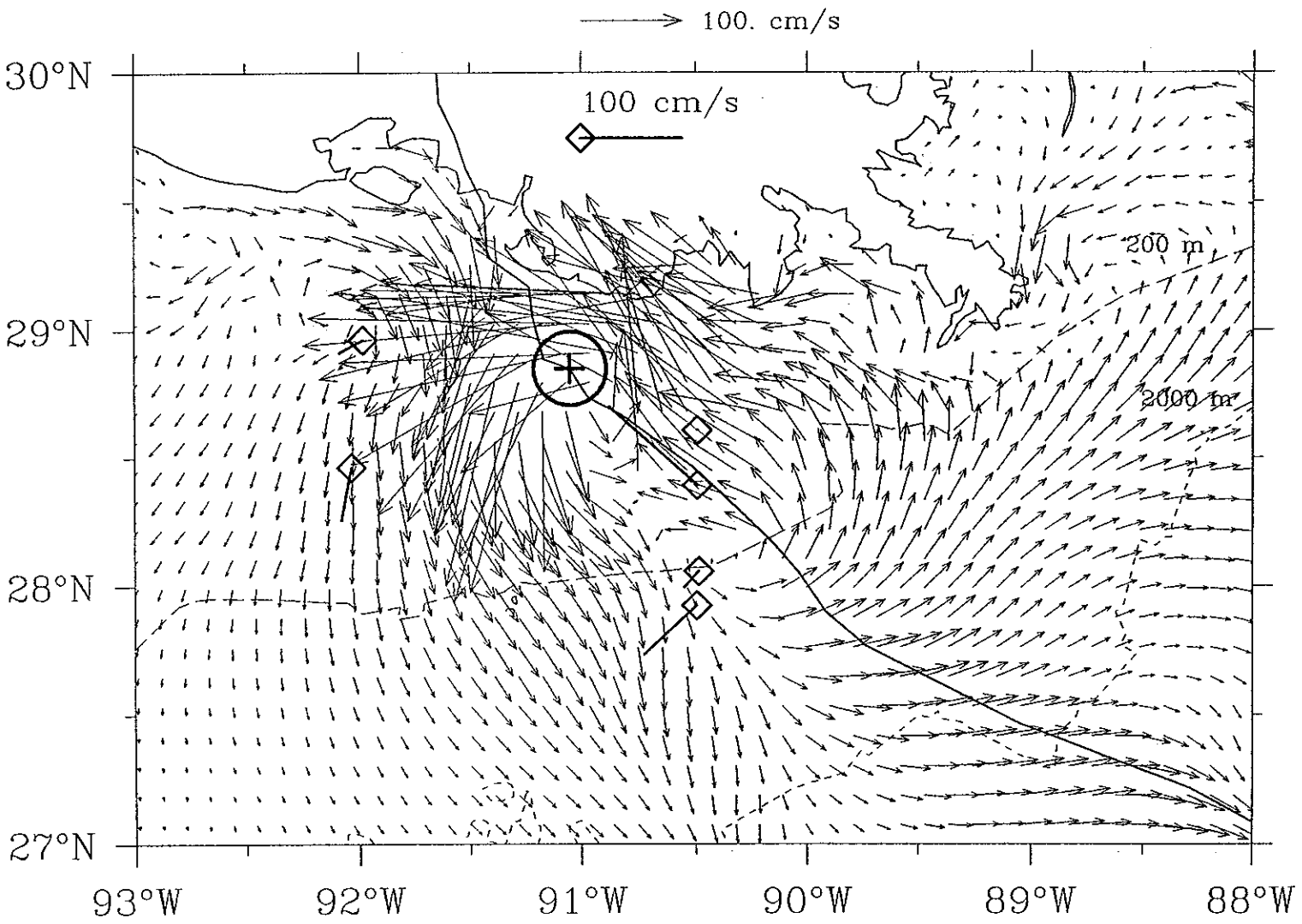

Modeled/Observed Surface Currents: 9208260300

Run 26, Frame 054

Figure 5.9 e.

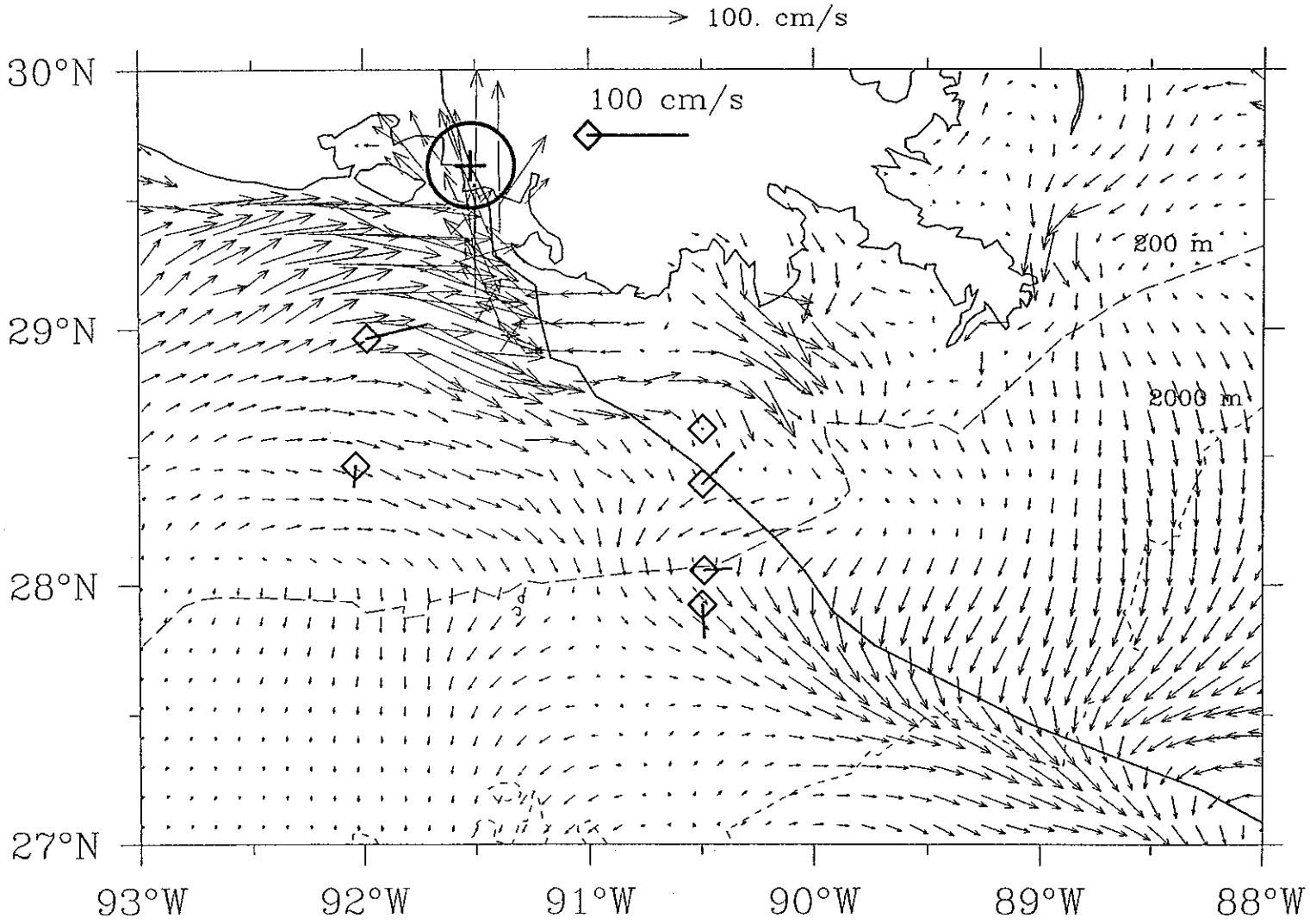

Modeled/Observed Surface Currents: 9208260900

Run 26, Frame 066

Figure 5.9 f.

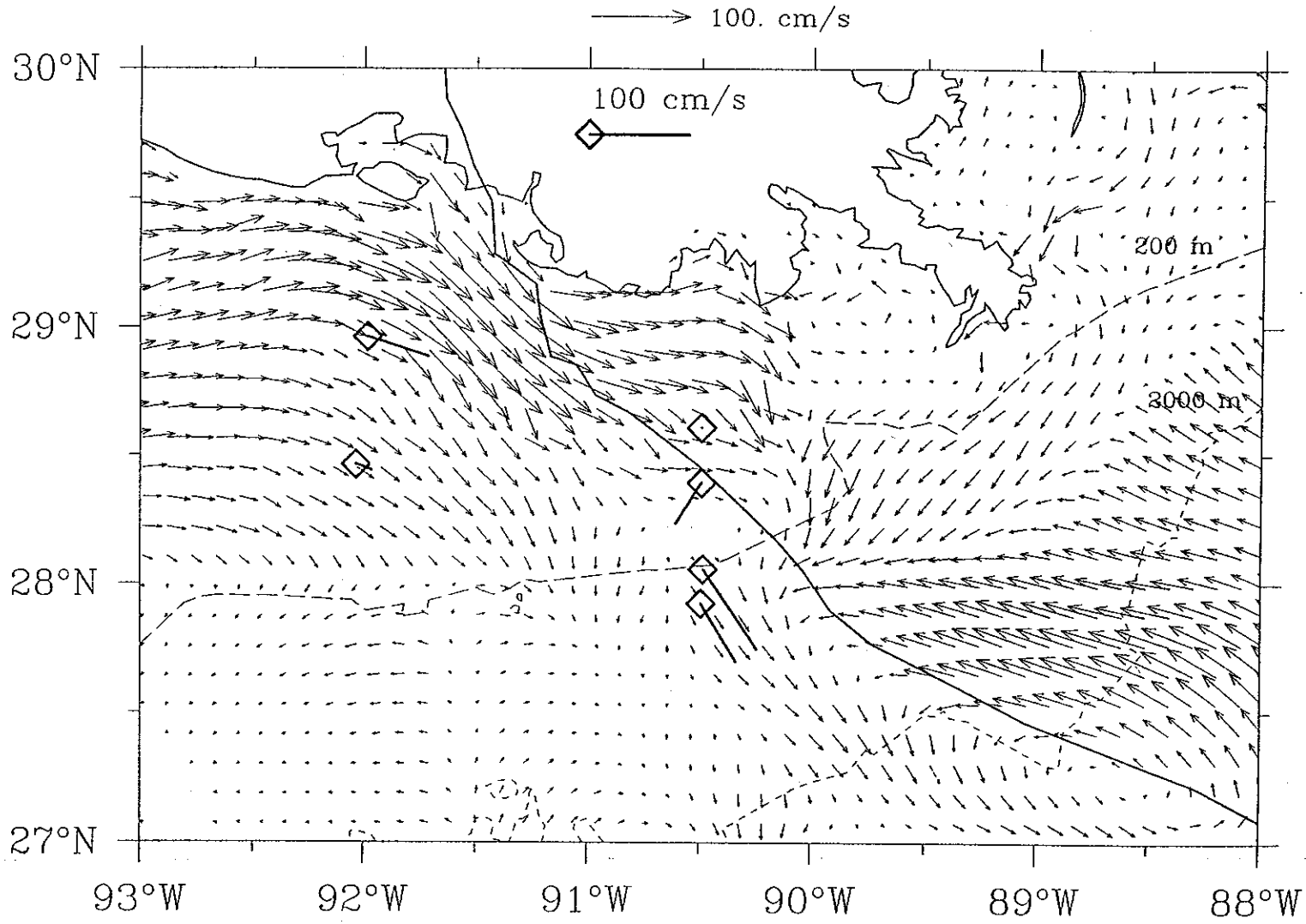

Modeled/Observed Surface Currents: 9208261500

Run 26, Frame 078

Figure 5.9 g.

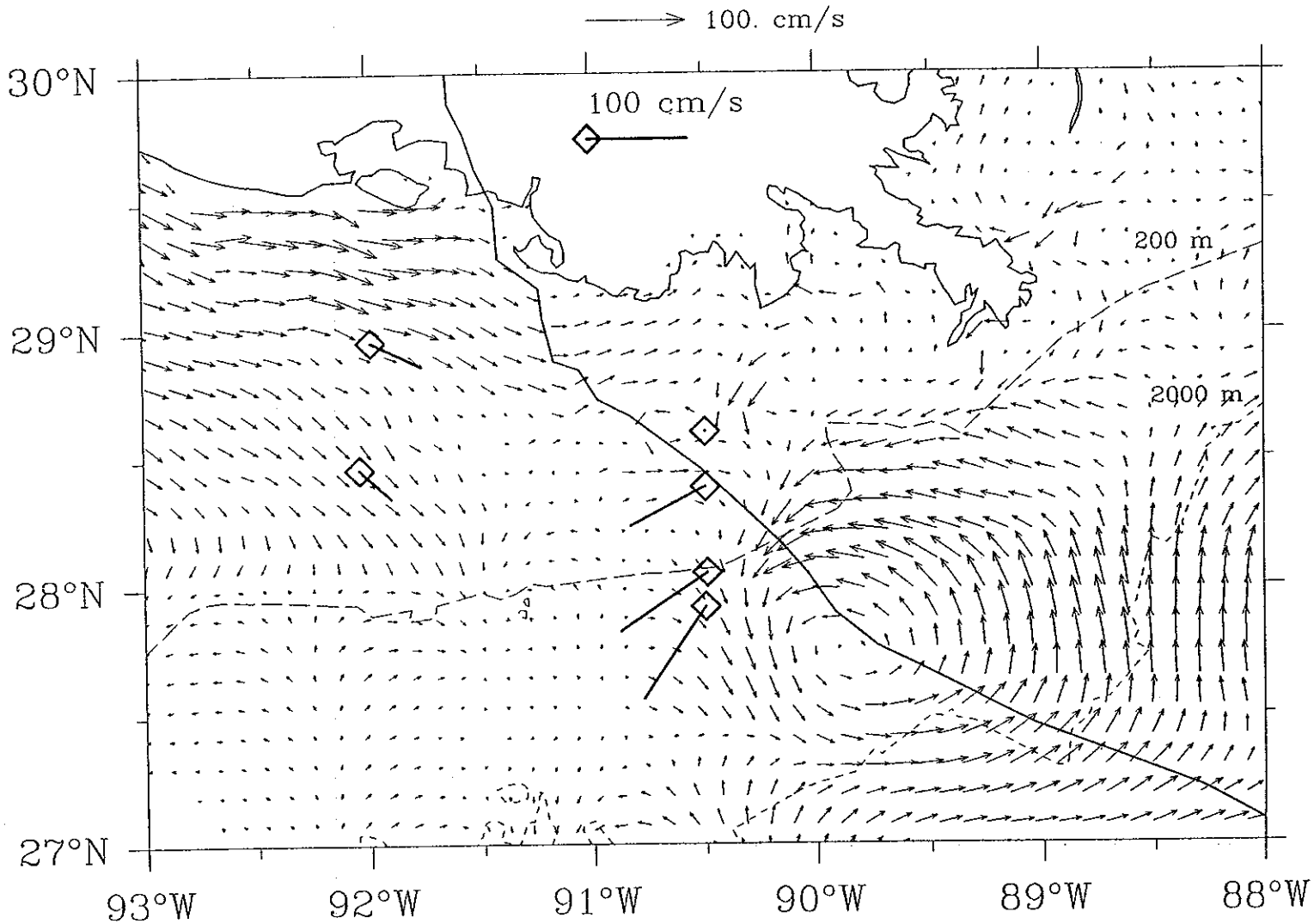

Modeled/Observed Surface Currents: 9208262100

Run 26, Frame 090

Figure 5.9 h.

Appendix A.

Final Report

SHALLOW WATER STUDY OF WAVE AND CURRENT FIELDS ASSOCIATED WITH HURRICANES

- Data Collection and Analysis Phase -

Submitted to:

Oceanweather, Inc.

Submitted by:

Evans-Hamilton, Inc.

August 16, 1994

Douglas J. Evans
Harriet Feldman

9211

Eastern Region
932 Hungerford Drive
Suite 35A
Rockville, Maryland 20850
(301) 762-8070

Douglas J. Evans
Project Manager

Subcontract to:
Minerals Management Service
Department of Interior
Contract No. 14-35-0001-30746

Table of Contents

TABLES

FIGURES

1.0 Introduction

1.1 Objective of the Data Collection Program

The hindcast analysis of Hurricane Andrew is dependent on the acquisition and subsequent analysis of measured meteorological and oceanographic data. For each of the wind, wave, tide or current velocity models used in this project, selected boundary and/or initial conditions must be specified from measurements and updated periodically. Other measured data are used to either validate the results of the model or to fine tune selected parameters usually involved with the frictional stresses at the sea surface and along the bottom or in the turbulent structure of the air/water. Note that most of the measured data must be analyzed to isolate the parameters from Hurricane Andrew since they are often superimposed on the preexisting conditions. Since the hurricane generated oceanographic and meteorological parameters dominate the relatively weak ambient conditions, this may not be a major concern. However, those conditions should be evaluated to insure that is the case.

Andrew was a major hurricane which caused considerable damage to 241 oil platforms (62 toppled or leaning) at an estimated cost in excess of $200 million (Ocean Industry, 1992). Several reports documenting Andrew's meteorological and oceanographic conditions have been published using data readily available from coastal measurement sites and/or transmitting buoys or oil platforms. These include studies by Breaker et al. (1994), Stone et al. (1994) and DiMarco et al. (in progress) which have concentrated on the surface observations. The present study concentrates primarily on the analysis of both the surface and subsurface parameters. These parameters are used in the development of the extreme wind, wave, storm tide and current velocity over the entire region affected by Andrew through the use of the hindcast models. Selected data sets from the earlier studies have been incorporated herein when they have provided useful results for the above objective.

1.1 Background

Due to the considerable marine activity in the Gulf of Mexico, various government and industry data collection programs were in progress during Andrew's transit. The Minerals Management Service's LATEX Physical Oceanographic program was by far the most extensive of these measurement programs and has provided considerable data which can be used in the hindcast analysis of the wind, wave, storm tide and current velocity as well as for the initial hydrographic conditions. Other data acquisition programs include the National Data Buoy Center's C-MAN measurements both on the coast and on oil platforms, the National Ocean Service's coastal tide gauge installations, the Army Corps of Engineers' (WES/COE) coastal wave measurement program on oil platforms, the National Hurricane Center's and the Reserve Air Force's reconnaissance aircraft flights, the oil industry's measurements on selected platforms, especially Shell's Bullwinkle structure. These measurement sites are shown in Figure 1.1.1 which also shows Andrew's track.

The available data from each of these programs is briefly described in the following sections as well as their potential use in either model initialization, and verification or calibration.

Figure 1.1.1

Location of Hurricane Track and Meteorological Measurement Sites

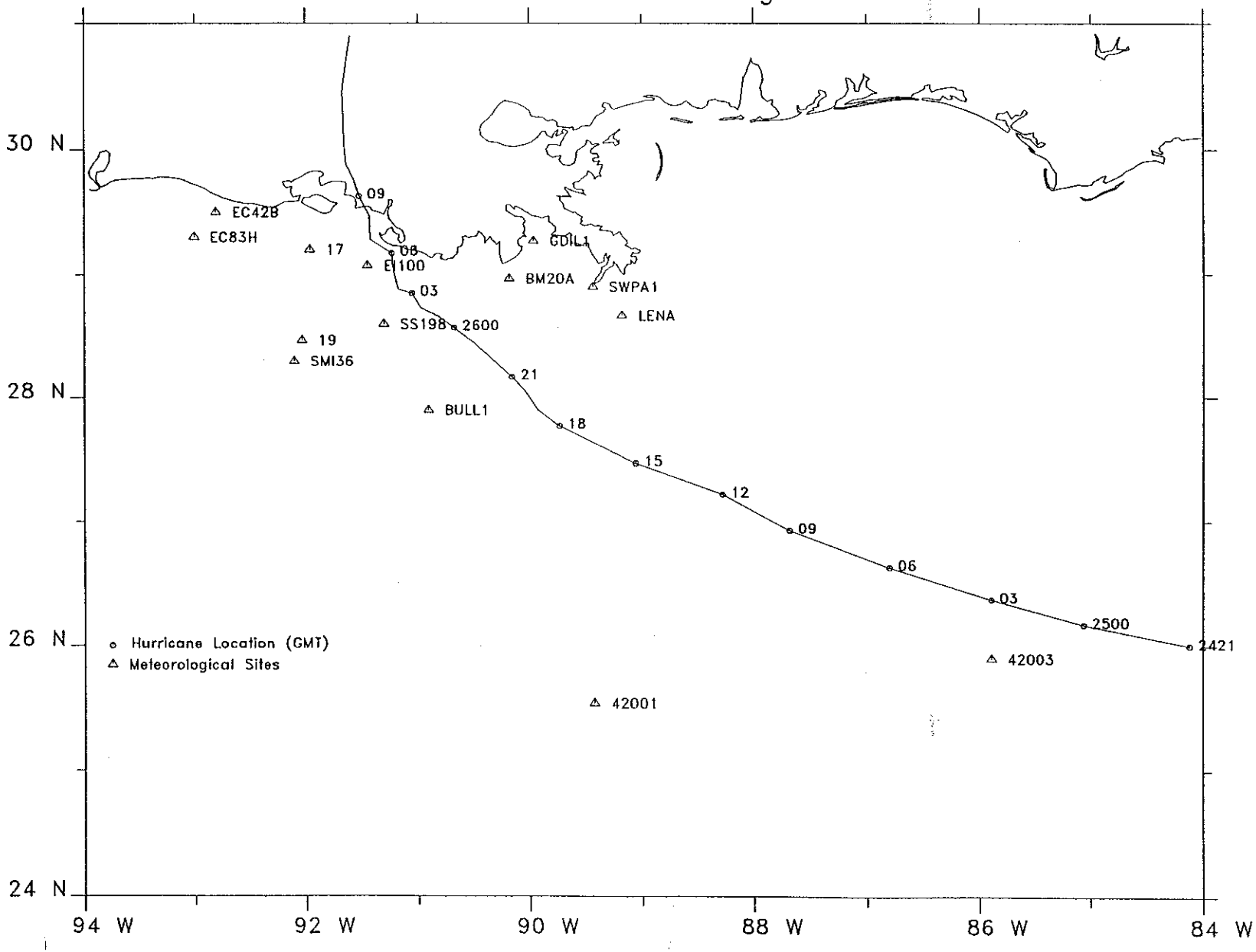

2.0 Hurricane Andrew Data Acquisition

2.1 Meteorological Parameters

The meteorological parameters of greatest importance are the hurricane's track, forward speed, barometric pressure distribution from the hurricane center to the periphery and the ambient pressure system through which the hurricane is moving. The measured wind speed is used to verify the accuracy of the wind model and is thus a tuning parameter as opposed to a boundary condition. The following sections provide a variety of measurement platforms which range from deep water buoys to near coastal oil platforms and light towers. Table 2.1.1 summarizes the locations, sensor elevations and averaging intervals at the measurement sites described in the following sections.

2.1.1 Hurricane Reconnaissance Aircraft

Daily reconnaissance flights were made into and around Hurricane Andrew as it crossed the Gulf of Mexico collecting pressure, temperature and upper level wind data as well as eye shape and diameter observations by Air Force and NOAA personnel. These data have been collated at the National Hurricane Center in Coral Gables and at the National Hurricane Research Division of the Atlantic Meteorological and Oceanographic Laboratory of NOAA. NOAA satellite data also provided daily observations of hurricane location, movement and size which were supplemented by coastal radar stations. Since these measured parameters are extremely important in the development of the wind field for the hindcast of both the wave and current parameters and require considerable analysis and interpretation, these data were processed in the wave hindcast analysis part of this combined study and are presented in that part of the study. These data are used primarily for forcing the models as opposed to verification, although the interim product, the wind field, can be compared to measured time series wind fields presented in this section once they have been adjusted to common elevations and durations.

2.1.2 NDBC Buoy, Oil Platforms and C-MAN

Wind velocity and barometric pressure data were observed at NDBC buoys, oil production platforms, and C-MAN stations along the coast. Air/sea temperature was also recorded at the buoys and C-MAN locations. The maximum values of wind speed and pressure was reported for several oil platforms. The location of these measurement sites are given in Figure 1.1.1 and Table 2.1.1. Some parameters are missing due to sensor failure and some records are truncated due to system failure. A description of the NDBC buoys used in this study is given in Gilhousen et. al. (1990). The data for Hurricane Andrew were obtained from National Oceanographic Data Center in Washington, D.C.

The C-MAN data are also acquired by NDBC and the instrumentation systems are described in detail in Coastal-Marine Automated Network (C-MAN) Users Guide (NDBC, 1992). C-MAN stations are generally located in relatively shallow water near the coast located on aids-to-navigation structures or other existing platforms. Instrumented oil platforms are usually privately installed and maintained on existing platforms in deeper water than the C-MAN stations, but much shallower water than the NDBC buoys.

Met-ocean data was also acquired during Hurricane Andrew from two oil platforms which were part of a joint oil industry and NDBC project called the Meteorological and

Table 2.1.1

Platform Location and Meteorological Sensor Characteristics

Station	Latitude (deg N)	Longitude (deg W)	Barometer Elevation (m)	Anemometer Elevation (m)	Anemometer Duration (min)
42001	25.54	89.42	0.0	10.0	8
42003	25.90	85.90	0.0	10.0	8
Shell Bullwinkle	27.90	90.90	20.1	93.6	2/10
Exxon Lena	28.67	89.17	34.8	60.1	2/10
Grand Isle	29.27	89.96	9.1	15.8	2/10
Southwest Pass	28.90	89.43	33.2	33.8	2/10
LATEX Mooring 17	29.20	91.96	0.0	3.6	??
LATEX Mooring 19	28.47	92.03	0.0	3.6	??
Ship Shoal 198G	28.6	91.3	NA	NA	1
East Cameron 83H	29.3	93.0	NA	NA	1
East Cameron 42B	29.5	92.8	NA	NA	1
South Marsh Is. 136	28.3	92.1	NA	NA	1

Oceanographic Measurement System (MOMS). Shell's Bullwinkle platform (40 nm southwest) and Exxon's Lena platform (60 nm northeast) were the two closest MOMS structures to Andrew (see Figure 1.1.1). Only barometric pressure was reported at the Lena platform. Meteorological data was also reported for Chevron's Garden Bank 236A platform, considerably west (125 nm) of the hurricane track. The measurements are useful for peripheral values of wind barometric pressure and wind speed which are used in the formulation of the model hurricane wind field. These data were reported as part of the C-MAN program in near real time during the hurricane. All platforms were just beyond the edge of the continental shelf. Meteorological data were also at the Grand Isle C-MAN station as reported by Breaker et. al. (1994, in progress). Locations are given in Table 2.1.1.

2.1.3 MMS/LATEX

There were three LATEX meteorological buoy mooring sites (17, 19 and 53) located in the path of Hurricane Andrew as shown in Figure 1.1.1 and locations are reported in Table 2.1.1. However, the met buoy at mooring 53 and three others in the western Gulf were removed to decrease the possibility of considerable mooring losses during the hurricane season. The hurricane eye passed over mooring 53's normal location. The hurricane passed very close to the met buoy at LATEX mooring 17 where both wind velocity, barometric pressure and temperature data were recorded. The anemometer on mooring 17, located 30 nm to the west of the track, was lost prior to Andrew's arrival; however wind speed and pressure was recorded. At mooring 19, located 55 nm to the west of the track, both wind velocity and pressure were recorded.

2.1.4 Other Measurements

Maximum 1-minute average and peak surface wind speeds were recorded at Ship Shoal 198G, East Cameron 83H and 42B and South Marsh Island 136B (Rappaport, 1992) and pressure and wind speed at Grand Isle Coast Guard Station (Breaker, in progress). Time histories of these data were not obtained. Locations are given in Table 2.1.1.

2.2 Hydrographic Data

2.2.1 MMS/LATEX

The water mass distribution is an important part of the initialization of the turbulent energy closure mechanism for the proposed current velocity modelling effort, especially since the shelf waters are well-stratified during the summer months. For that part of the Gulf where Andrew crossed the continental, there had been a LATEX hydrographic cruise several weeks earlier. Both ADCP and CTD data had been acquired. Additional data will be searched for at NODC for the area east of the crossing where the survey ended or else averaged summer conditions will be used. The location of the hydrographic stations are shown in Figure 2.2.1.

2.3 Water Elevation

Storm water elevations over the continental shelf and along the coast are used to assist in the verification/calibration of the numerical-hydrodynamic current and storm tide model as well as in the computation of the hindcast wave parameters in shallow water. The NOS gauges along the coast acquired these data; however, offshore measurements are more suitable to the verification of the model as applied to the continental shelf.

Figure 2.2.1
Location of Hurricane Track and Oceanographic Measurement Sites

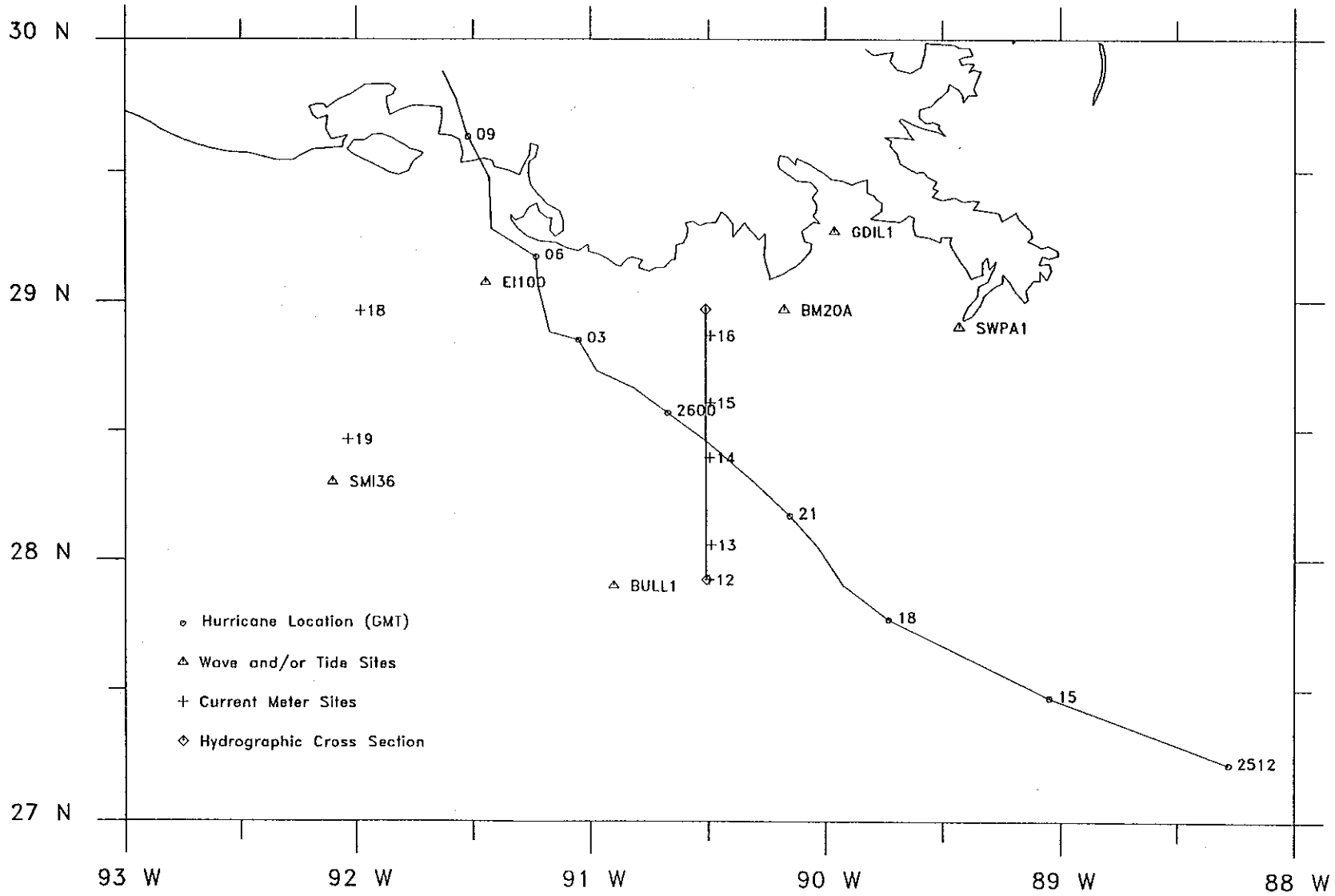

2.3.1 Corps of Engineers

Three U. S. Army Corps of Engineers' wave pressure gauges were installed in water depths from 11.3 to 12.2 meters. These gauges sites and data status are shown in Table 2.3.1.1.

Table 2.3.1.1

Corps of Engineers Pressure Gauges

MMS Block	Latitude (deg min N)	Longitude (deg min W)	Depth (m)	Data Status
Bay Marchand 20A	28 58.80	90 10.50	11.5	Large data gaps, not used
Eugene Island 100	29 04.03	91 26.70	11.3	Few data gaps, OK
West Cameron 178	29 34.00	93 16.00	12.2	Too far west of hurricane

Only the Eugene Island 100 data were processed in this project as the other gauges were either too far away or too much data was missing.

2.3.2 NDBC Buoy and C-MAN

The NDBC C-MAN station Grand Isle also had water level data information which has been reported in Breaker et. al. (1994, in progress). A complete list of the maximum measured water elevations for Hurricane Andrew from the Florida coast to Grand Isle was also reported in Table 5 of Beaker et. al. (1994, in progress) with maximum elevations reported for Florida, Mississippi and Louisiana at coastal locations where NOAA tide gauges were installed. Many negative storm water elevations were initially reported on the west coast of Florida as the hurricane moved offshore.

2.3.3 MMS/LATEX

Water elevation data was available from the LATEX pressure gauge at mooring 16 which was located near the hurricane track. Although the pressure gauge tipped over during the hurricane, it was possible to account for this depth change and to use the entire record. The location of mooring 16 is shown in Figure 2.2.1 and also given in Table 3.2.1.1. Note that other water level data was measured at LATEX sites (20, 23 and 1) further west; however, these were too far away to provide useful information for the hurricane model calibration.

2.4 Wave Parameters

2.4.1 NDBC Buoy and C-MAN

The NDBC buoys in deep water provided the earliest measurement of Andrew's wave generating capabilities. These buoys (42001 and 42003) were earlier described in the meteorological section. Regarding their potential for observing large waves, the buoys were located on the weaker side of the hurricane (south of the hurricane track) and were not close to the hurricane track, 25 nm and 100 nm for buoys 42003 and 42001, respectively.

Of the two C-MAN stations located on oil platforms, the Bullwinkle location was

Table 3.2.1.1

LATEX Measured Current Velocity Moorings
during Hurricane Andrew (1992)

Mooring No.	Water Depth (m)	Meter Depth (m)	Start Date	Stop Date	Latitude (deg min N)	Longitude (deg min W)
12	505	12	6/2	9/10	27 55.432	90 29.676
		100	6/8	9/11		
13	200	12	7/23	10/22	28 03.452	90 29.153
		100	7/23	10/22		
		190	7/23	10/22		
14	47	11	6/2	9/1	28 23.674	90 29.572
		26	6/2	9/2		
		37	-	-		
15	20	10	6/2	8/26	28 36.498	90 29.459
		17	6/2	9/2		
16	19	11[1]	-	-	28 52.024	90 29.451
		17	6/1	8/25		
17	7	3[2]	-	-	29 11.762	91 57.893
		5[3]	-	-		
18	22	10	6/1	9/2	28 57.764	91 58.963
		19	6/1	8/31		
19	51	3	7/24	10/20	28 27.910	92 02.088
		20	-	-		
		47	6/2	8/30		

1. Mooring and meter lost during Andrew
2. Meter impeller lost during Andrew
3. Minispec not installed during Andrew

relatively close to the hurricane track (45 nm) and thus provided good wave measurements. It was located on the weaker (southwest) side of the hurricane, so that the waves would be much lower than those located the same distance to the northeast of the track. Wave data was not located for the Lena platform about 55 nm to the northwest of the track at the closest point.

2.4.2 Corps of Engineers

Wave data were also recorded at the three instrumented platforms in where water level data were reported in Table 2.3.1.1. However, the only nearly complete data set at Eugene Island 100 was located a few miles in the lee of a relatively shallow shoal (3 to 4 m deep) to the east through southeast, thereby limiting the wave heights by the breaking wave criteria (about 3/4 the storm water depth).

2.4.3 MMS/LATEX

Measured wave height data were obtained from LATEX mooring 16 which was about 20 nm northeast of the track at the closest point. A Coastal Leasing Inc. MimiSpec PUV type gauge was installed at this location. The mean water depth of the pressure gauge was 17.63 m before the pressure gauge housing turned over and 18.81 m thereafter. The pressure and current velocity data was used to obtain the directional wave spectra until it was overturned by Andrew. However, the pressure gauge continued to operate correctly thereafter and the non-directional wave spectra could be obtain from these data. Mooring 17, about 25 miles west of the hurricane track was not installed at this time.

2.5 Current Velocity Data

2.5.1 MMS/LATEX

The measured current velocity data represent the greatest source of information due to the extensive installation of the LATEX program. Only one current meter was lost during Andrew (at mooring 16) as the largest waves passed through this location and several other nearby meters were damaged or tangled with debris at some point in the hurricane. A total of 7 moorings (16 meters) were selected from the available data set of 31 moorings as having potentially useful current velocities for model calibration. These moorings are shown in Figure 2.2.1 and are also listed in Table 3.2.1.1. The dates were selected in order to obtain 90-day records for tidal analysis. These LATEX moorings contained two meters in shallow water and three meters in water depths greater than 45 m. Vector averaging meters were used at the surface and in shallow water where wave contamination would be a problem.

The LATEX current velocity data is the only data that could be found for the period and location of Hurricane Andrew.

3.0 Data Analysis and Presentation

The measured data has been analyzed and presented using a 10-day window encompassing Hurricane Andrew. This 10-day window is used throughout the data presentation to provide the normal conditions before and after the hurricane passage. The degree of data processing varied according to the type of data and the final use of the data in the numerical models.

3.1 Meteorological Parameters

Barometric pressure data does not require any analysis and was presented as recorded after any corrections for instrument calibration.

In order to make meaningful comparisons to the boundary layer wind model, the measured wind data must be processed to determine the sustained velocity for a given interval and at a given elevation. Peak velocities are also important, but they must be similarly quantified to be of use. Duration and elevations of all time series wind data are given in Table 2.1.1. Winds are normally adjusted to either the 10 m or 19.5 m elevations using the one-seventh power law and are adjusted to a sustained value of either 10 minute or one hour using one of several distributions in the literature. The duration depends on how the model has been formulated and/or calibrated. For the various data sources, we have combined the barometric pressure, the wind speed and the wind direction on each figure using the same 10-day window. All wind speeds are the sustained wind speed for the period of measurement.

3.1.1 Hurricane Reconnaissance Aircraft

As previously noted, these data are presented in the wave hindcast report since they are used to drive the wind and hence wave and current velocity models and are not used for verification purposes. The wind model uses specific hurricane eye and radially distributed parameters which are developed from an analysis of the reconnaissance data.

3.1.2 NDBC Buoy and C-MAN

As Hurricane Andrew traversed the Gulf of Mexico from Florida to Louisiana, the NDBC buoys first recorded its meteorological characteristics. Figures 3.1.2.1 and 3.1.2.2 give the barometric pressure and wind speed and direction for NDBC buoys 42001 and 42003, respectively, for a ten-day period encompassing the hurricane. Their geographical positions are both south of Andrew's track (Figure 1.1.1), about 25 nm and 105 nm from 42003 and 42001, respectively, on the weaker side of the hurricane. The barometric pressure and wind velocity exhibit the same patterns except the greater distance to 42001 resulted in much more weaker magnitudes of pressure and wind speed.

Wind speed measurements from the Shell Bullwinkle platform (Figure 3.1.2.3) are among the highest recorded offshore although the platform was some 40 nm away from the hurricane track and on the weak side of the hurricane. The peak winds of 26.7 m/s at 93.6 m would reduce to 19.4 m/s at 10 m, the standard reference level, using the one-seventh power law. At the Chevron Garden Banks platform, both pressure and wind speed (Figure 3.1.2.4) were considerably more benign since the platform was over 125 nm further away. As noted earlier, these values represent peripheral conditions in which the hurricane was embedded. The maximum reported values of pressure reduction and wind speed and direction are given in Table 3.1.1.

The coastal C-MAN station at Southwest Pass was about the same distance (60 nm) and proximity as the Lena platform from the hurricane track and had peak winds of 29 m/s (Figure 3.1.2.5) and approximately the same pressure (1006 mbs). The corrected 10-meter wind speed would be 24.4 m/s. At the Grand Isle Coast Guard Station the pressure was about 1 mb lower and the wind speed was also 24.7 m/s (Figure 3.1.2.6). The corrected wind speed would be 25.0 m/s.

Table 3.1.1

Minimum Observed Barometric Pressure and Maximum Wind Velocity

Station	Latitude (deg N)	Longitude (deg W)	Barometer Pressure (mbs)	Wind Velocity Speed (kt)	Wind Velocity Direction (deg)
42001	25.54	89.42	-	12.3	235.0
42003	25.90	85.90	997.4	23.4	310.0
Shell Bullwinkle	27.90	90.90	998.5	26.6	277.0
Exxon Lena	28.67	89.17	1007.7	-	-
Grand Isle	29.27	89.96	1005.2	24.7	80.0
Southwest Pass	28.90	89.43	1006.1	25.1	67.0
LATEX Mooring 17	29.20	91.96	993.3	-	-
LATEX Mooring 19	28.47	92.03	1004.2	15.4	328.2
Ship Shoal 198G	28.6	91.3	-	78.0	-
East Cameron 83H	29.3	93.0	-	46.0	-
East Cameron 42B	29.5	92.8	-	38.0	-
South Marsh Is. 136	28.3	92.1	-	38.0	-

Figure 3.1.2.1

Buoy 42001: Barometric Pressure, Wind Speed and Direction

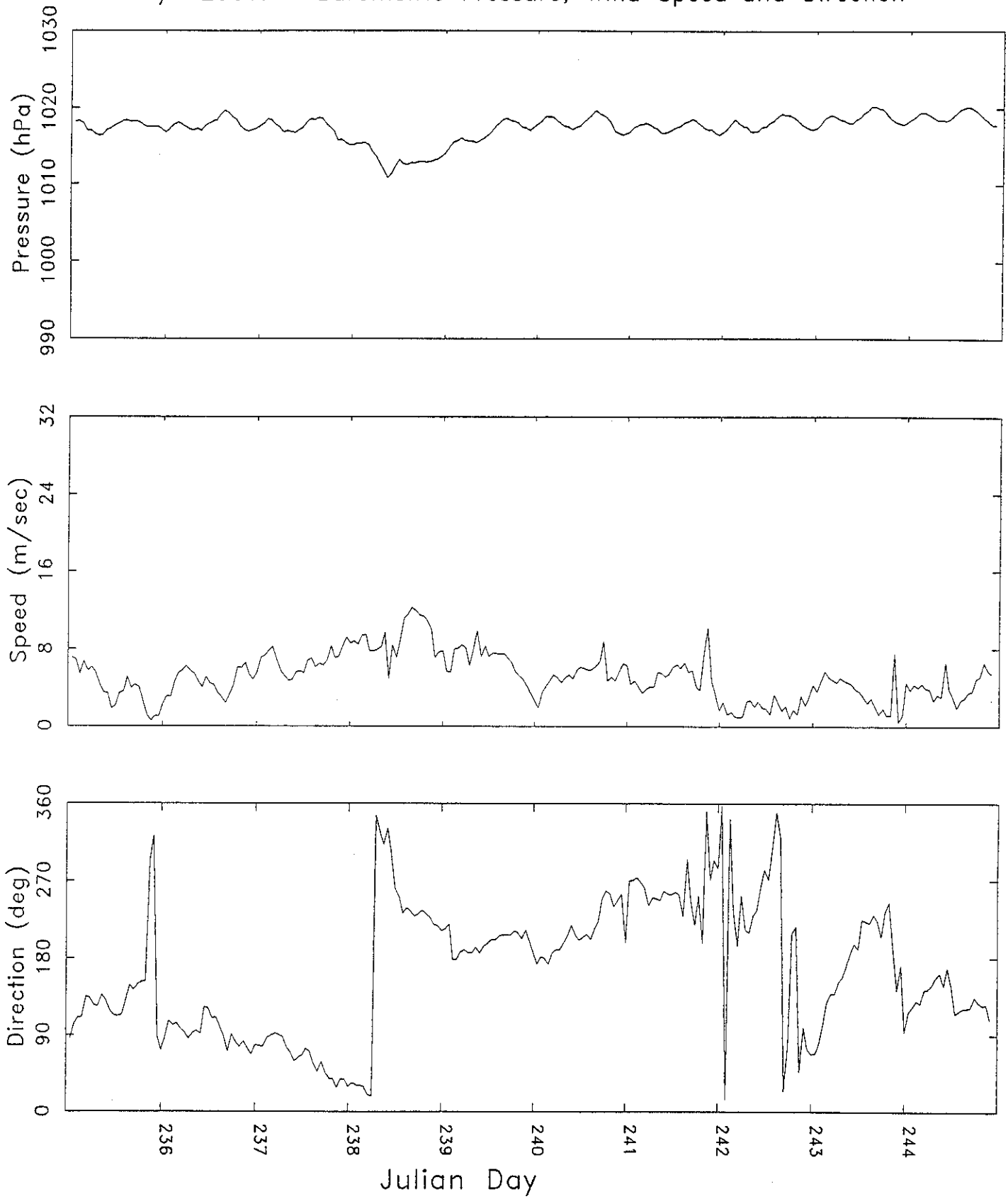

Figure 3.1.2.2

Buoy 42003: Barometric Pressure, Wind Speed and Direction

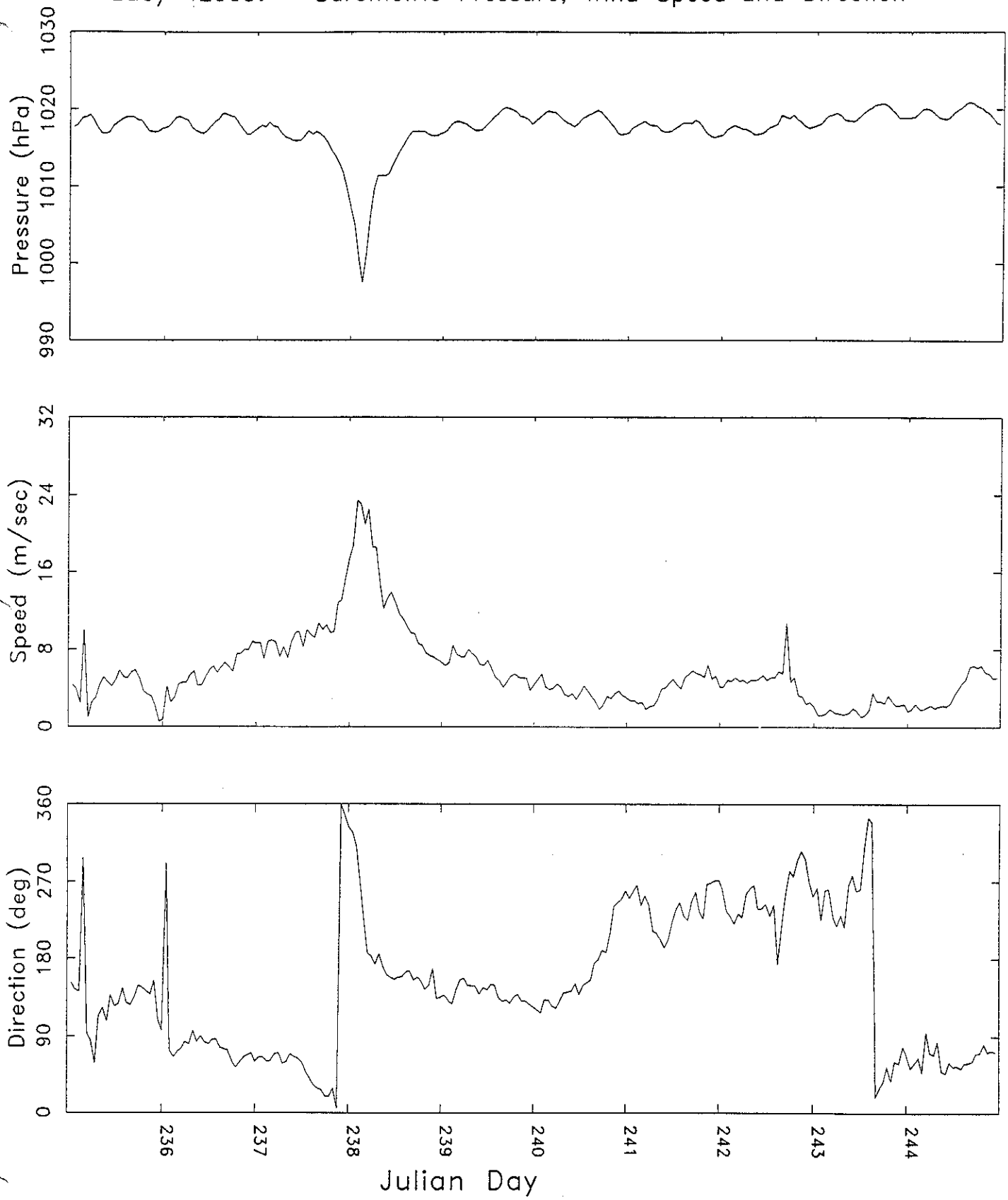

Figure 3.1.2.3
Shell Bullwinkle: Barometric Pressure, Wind Speed and Direction

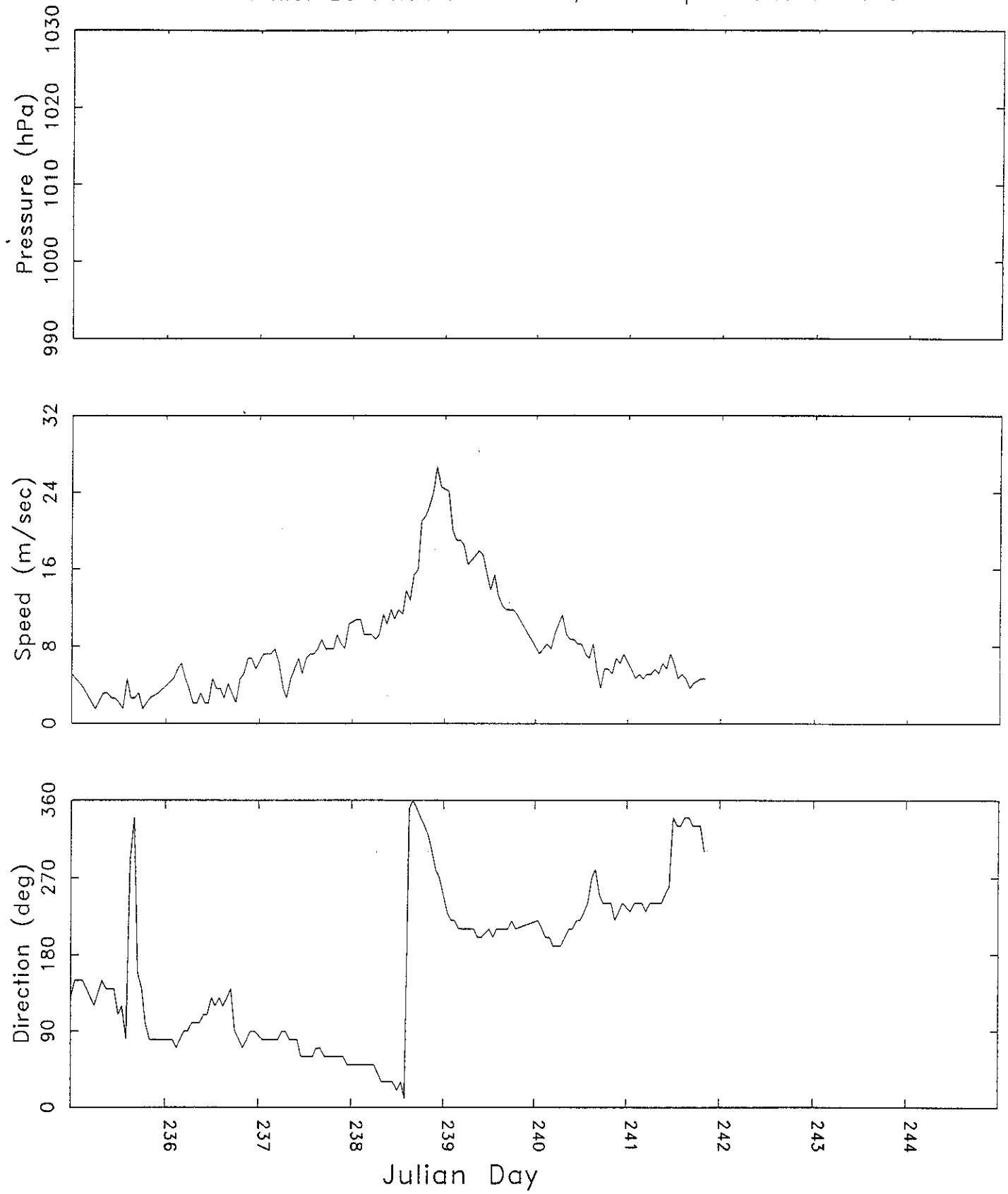

Figure 3.1.2.4
Garden Banks: Barometric Pressure, Wind Speed and Direction

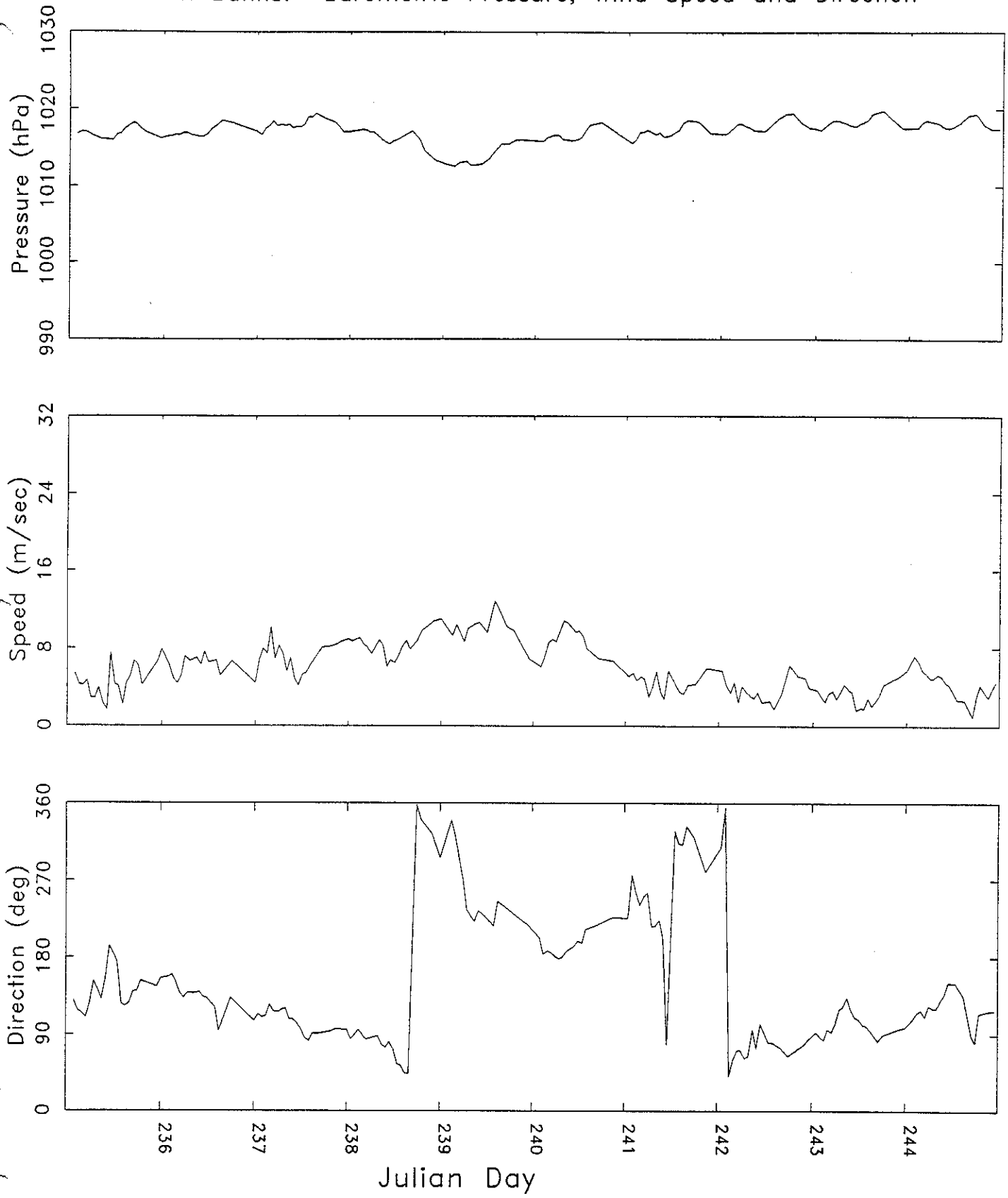

Figure 3.1.2.5
Southwest Pass: Barometric Pressure, Wind Speed and Direction

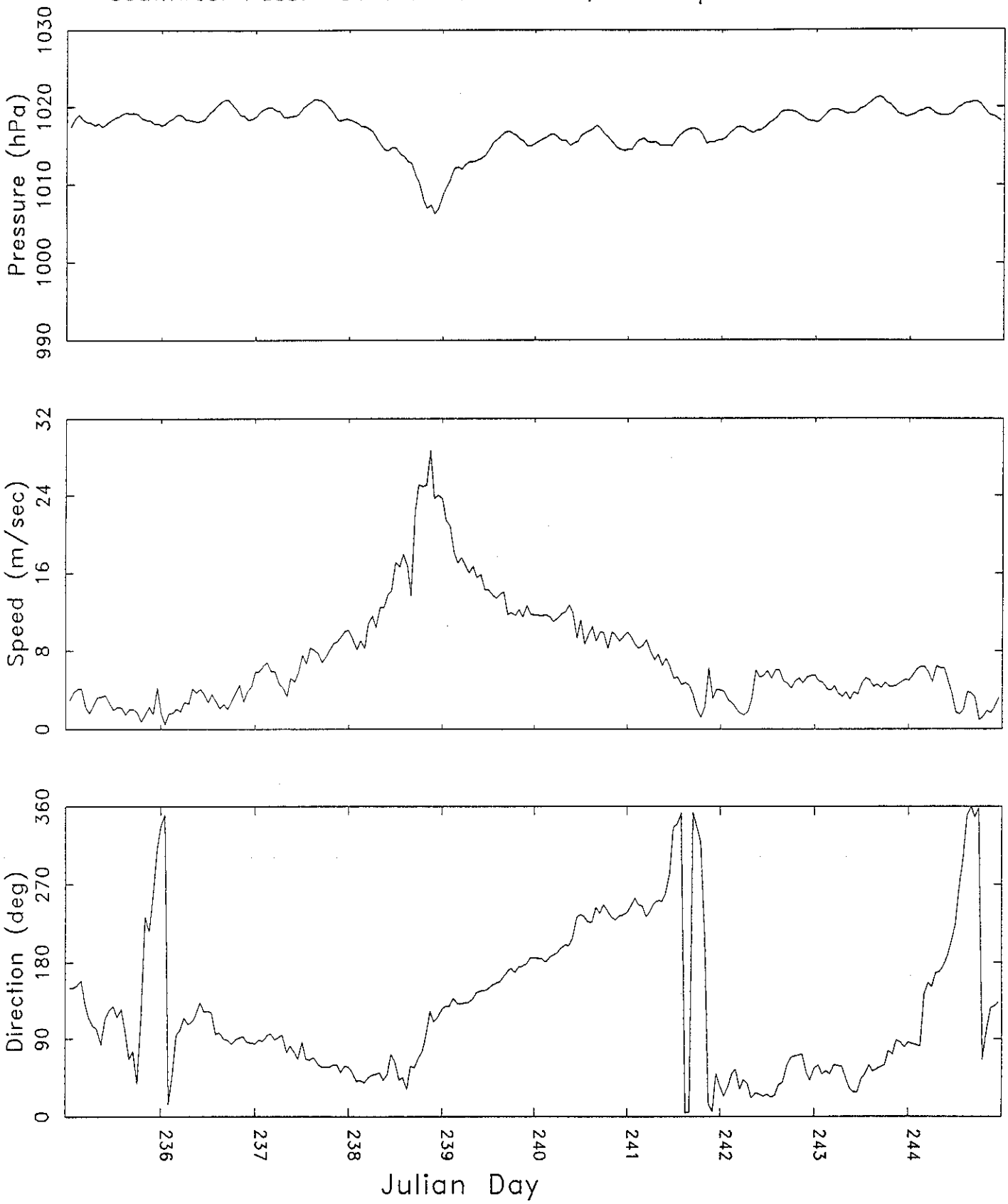

Figure 3.1.2.6

Grand Isle USCG: Barometric Pressure, Wind Speed and Direction

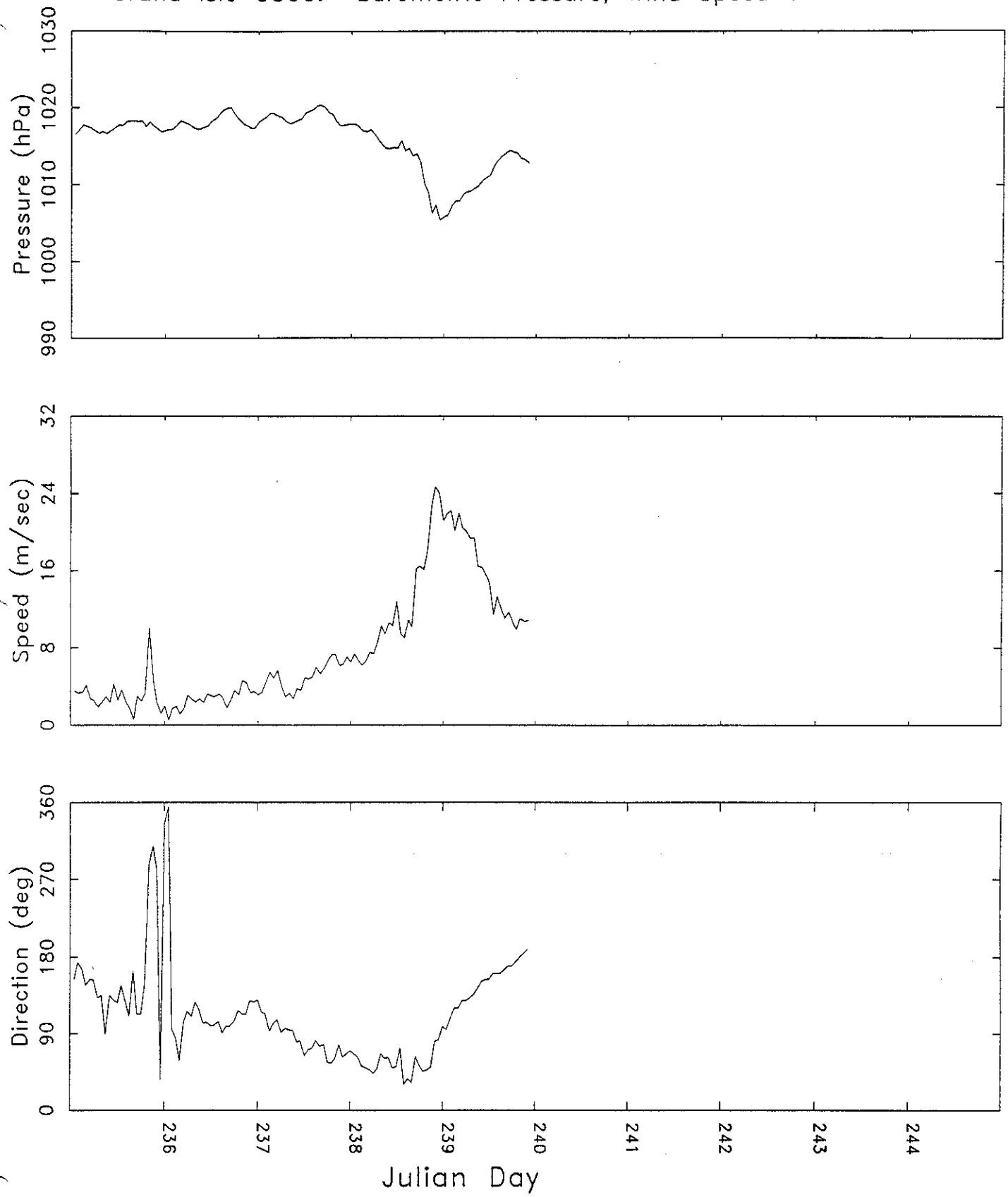

3.1.3 MMS/LATEX

The LATEX mooring 17 meteorological was located about 32 nm west of the hurricane track and recorded a minimum sea level pressure of 993 mbs (Figure 3.1.3.1), one of the lowest time series measurements away from the coast. The met buoy lost its anemometer and no speed records were obtained although direction was still being recorded. LATEX mooring 19 was approximately 55 nm west of the hurricane track. Since the anemometer elevation is so low (3.6 m), the measured wind speed of 15.6 m/s (Figure 3.1.3.2) would increase to 18.0 m/s at the standard reference level. This compares to 19.4 m/s measured at the Bullwinkle site which was slightly closer to the hurricane track.

3.2 Hydrographic Data

3.2.1 MMS/LATEX

The potential temperature and salinity data were acquired in both synoptic and time series measurements. The time series data are presented in Figures 3.2.1.1 to 3.2.1.6 for LATEX moorings 12, 13, 14, 15, 18 and 19, respectively, for the top, middle and bottom current meters (where data was available). The depths and locations of these meters is given Table 3.2.1.1. The effects of the hurricane was to mix the water column, thereby reducing the surface potential temperature and increasing the salinity. At the bottom over the shelf, the mixing process was reversed, although the change in these two parameters was considerably less. At mooring 13, which was very close to the hurricane track, inertial oscillations were set-up at both the middle (100 m) and bottom (190 m) meter depths. These oscillations started on JD 239, a day after the hurricane passed through the site and lasted for 5 to 6 days. These oscillations were not as developed in shallower water (47 m) at mooring 14 and lasted only 1 to 2 days.

The synoptic hydrographic data, acquired about a week before Andrew's transit, are given as vertical, cross-shelf profiles of potential temperature, salinity and sigma-t in Figures 3.2.1.7 to 3.2.1.9, respectively. These cross-shelf data show a warm surface layer of 30°C water from 5 m to 15 m and salinity less than 33 ppt in the depths. There is a cross-shelf salinity gradient due to the fresh water river outflow along the coast. The density gradient is the strongest between 10 m and 20 m of depth. There was no post-Andrew hydrographic survey for two months. These data were used to initiate the boundary conditions in the current velocity model. The time series measurements were used to verify the temperature and salinity changes at discrete locations and depths.

3.3 Water Elevation Data

Measured storm water elevations contain both astronomical and hurricane generated components to the total elevation. These must be separated in order to be used in the evaluation of the proposed three-dimensional storm tide/current velocity model.

3.3.1 Corps of Engineers

The pressure gauge records from Eugene Island 100 were analyzed to determine the mean water elevation every three hours. As Hurricane Andrew approached the measurement site, the gauge began to malfunction intermittently, missing the more intense part of the hurricane which passed through the area at about 0600 GMT on August 26th. There is a 12-hour data gap from 0220 GMT to 1420 GMT, thus the observations missed the peak water

Figure 3.1.3.1

Latex 17: Barometric Pressure, Wind Speed and Direction

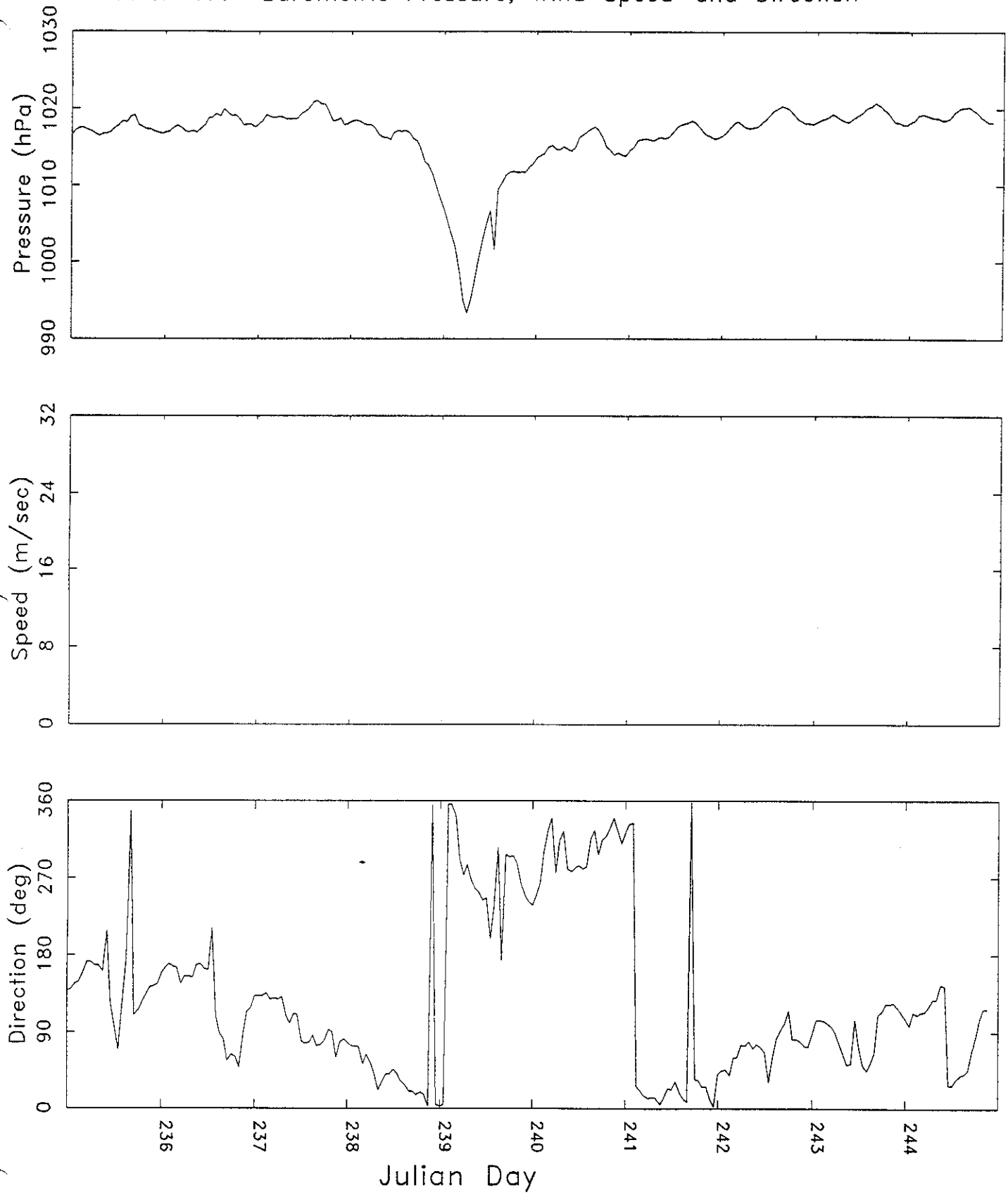

Figure 3.1.3.2

Latex 19: Barometric Pressure, Wind Speed and Direction

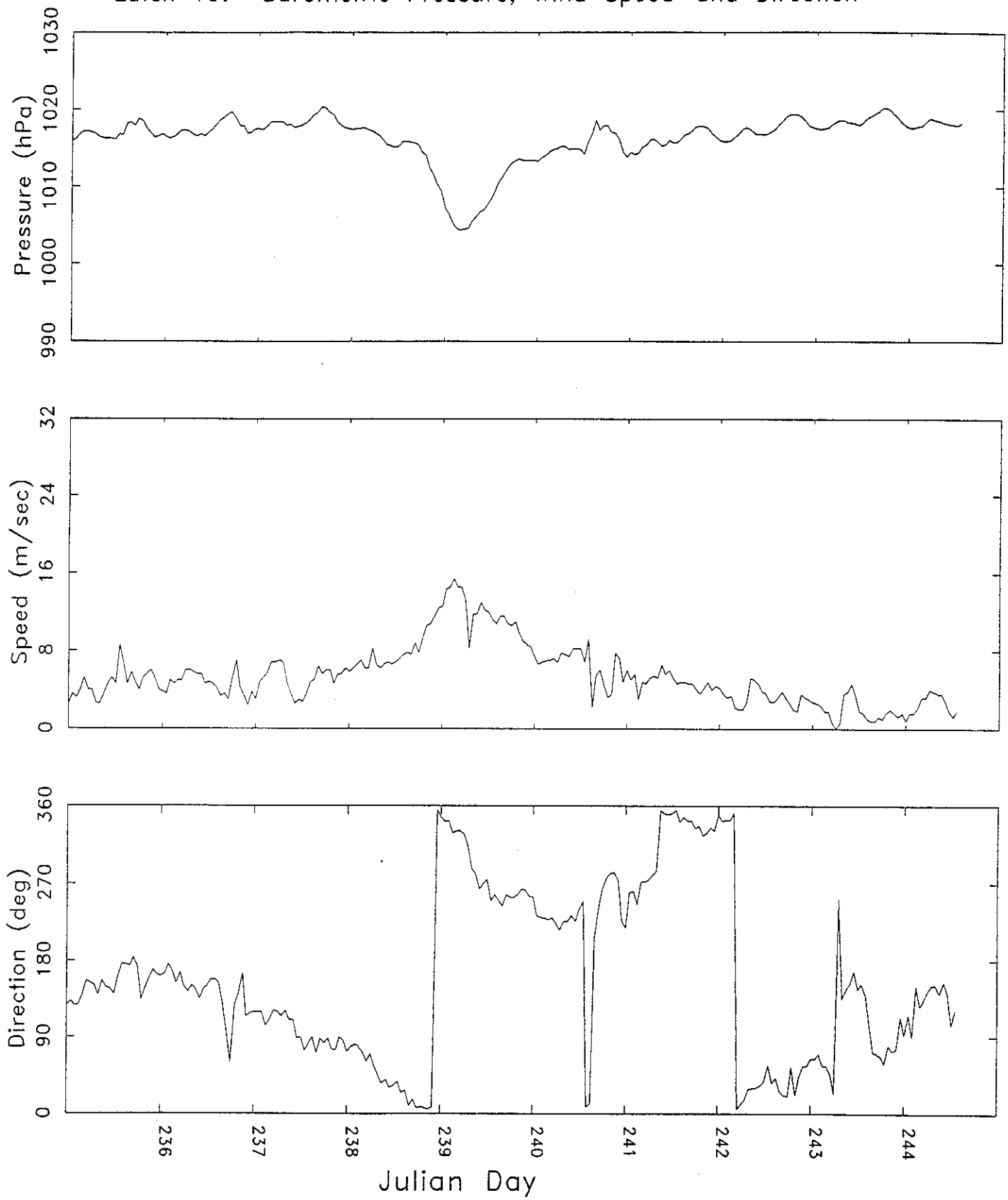

Figure 3.2.1.1
Mooring 12: Temperature & Salinity

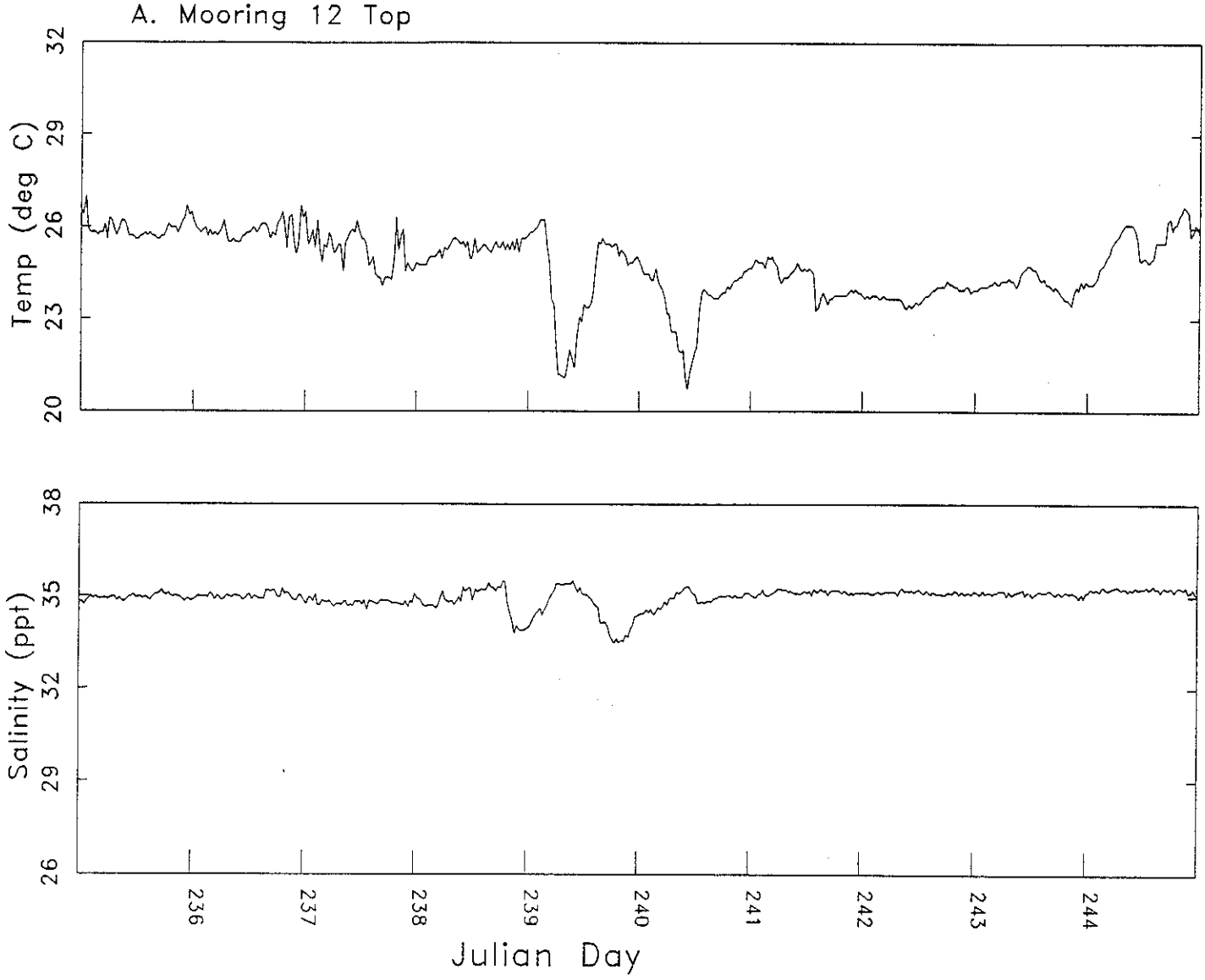

Figure 3.2.1.2
Mooring 13: Temperature & Salinity

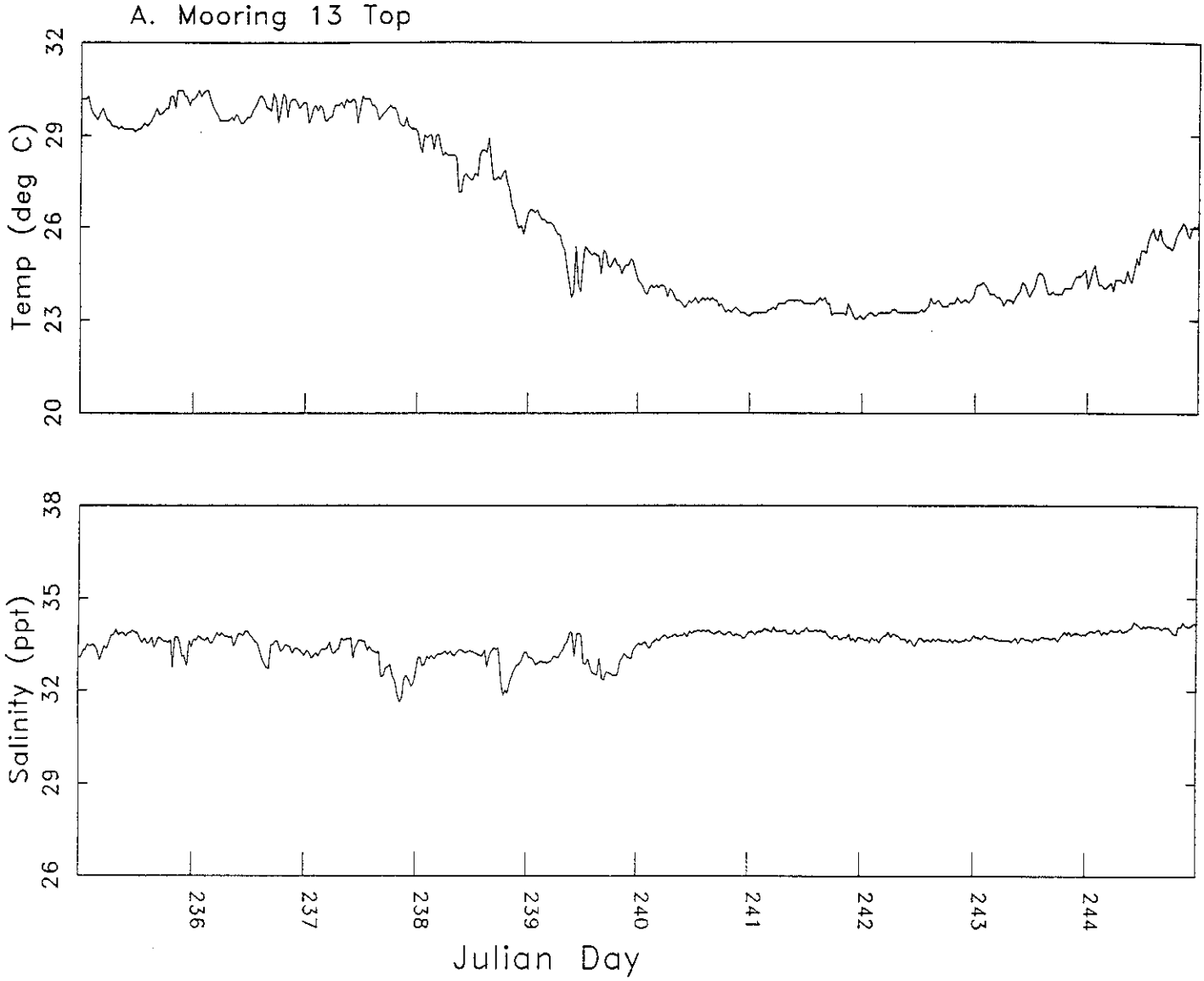

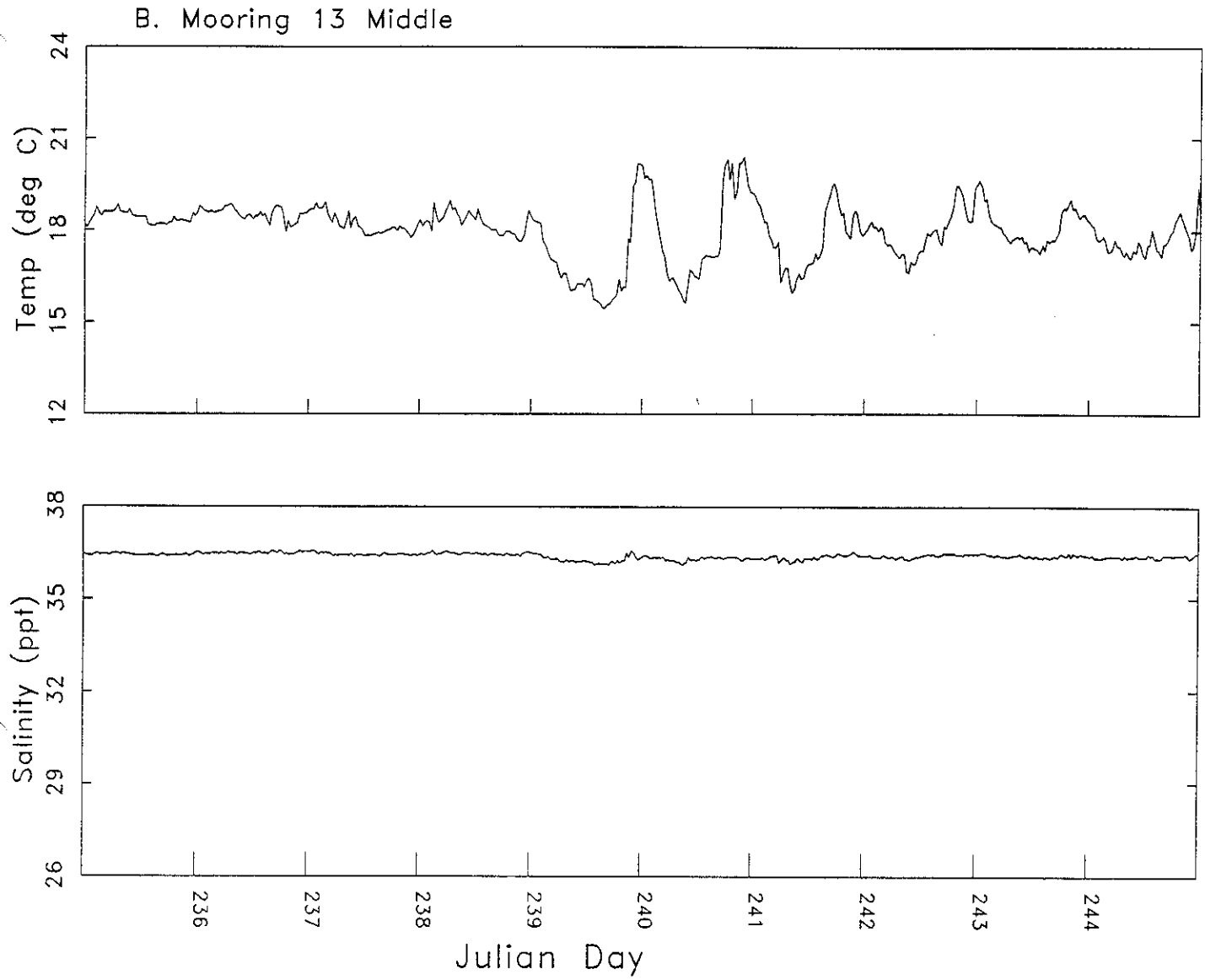
B. Mooring 13 Middle
Temp (deg C)
12
15
18
21
24
Salinity (ppt)
26
29
32
35
38
236
237
238
239
240
241
242
243
244
Julian Day

Figure 3.2.1.2 (cont)

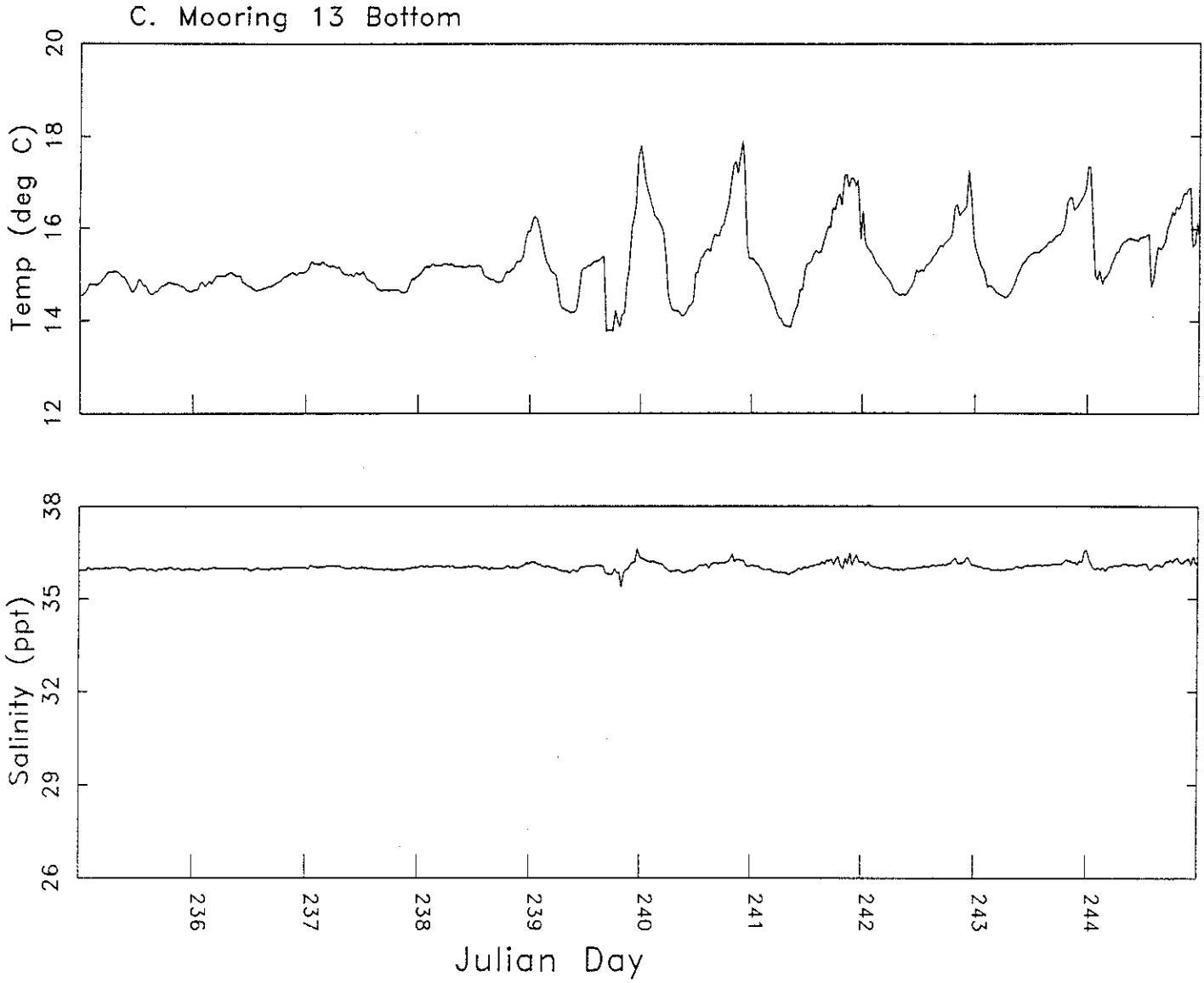

Figure 3.2.1.3
Mooring 14: Temperature & Salinity

A. Mooring 14 Top

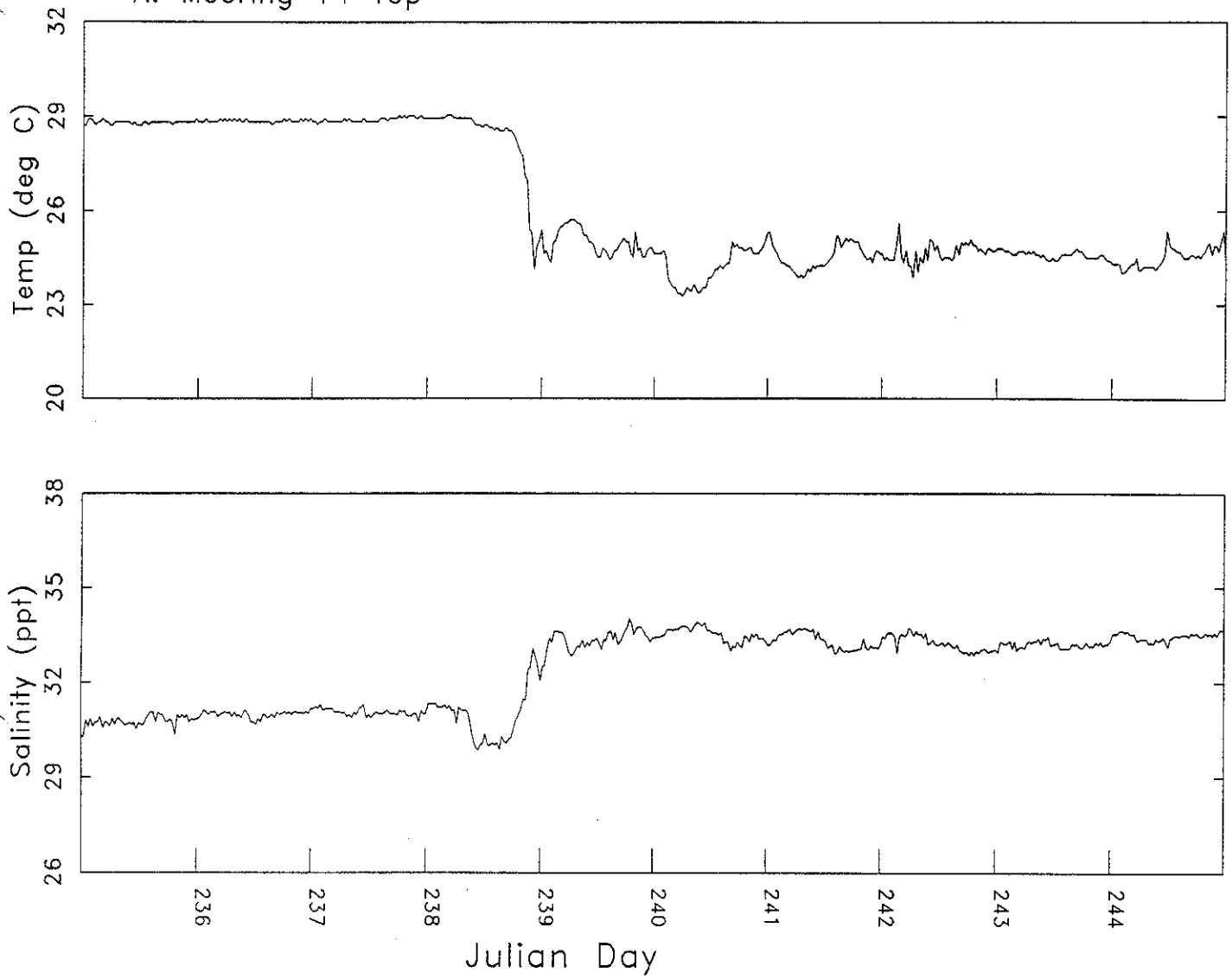

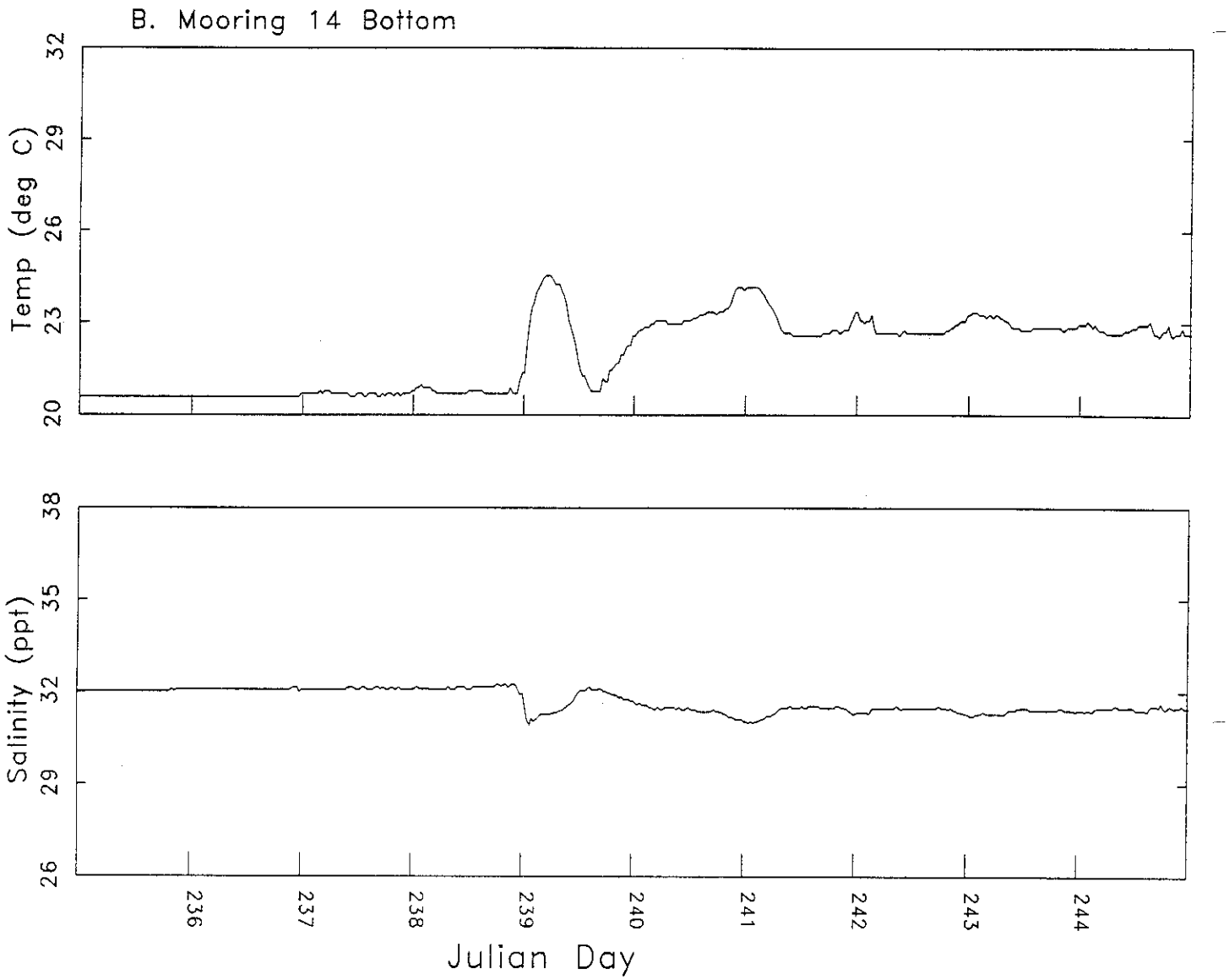
B. Mooring 14 Bottom
Temp (deg C)
20
23
26
29
32
Salinity (ppt)
26
29
32
35
38
236
237
238
239
240
241
242
243
244
Julian Day

Figure 3.2.1.4
Mooring 15: Temperature & Salinity

A. Mooring 15 Top

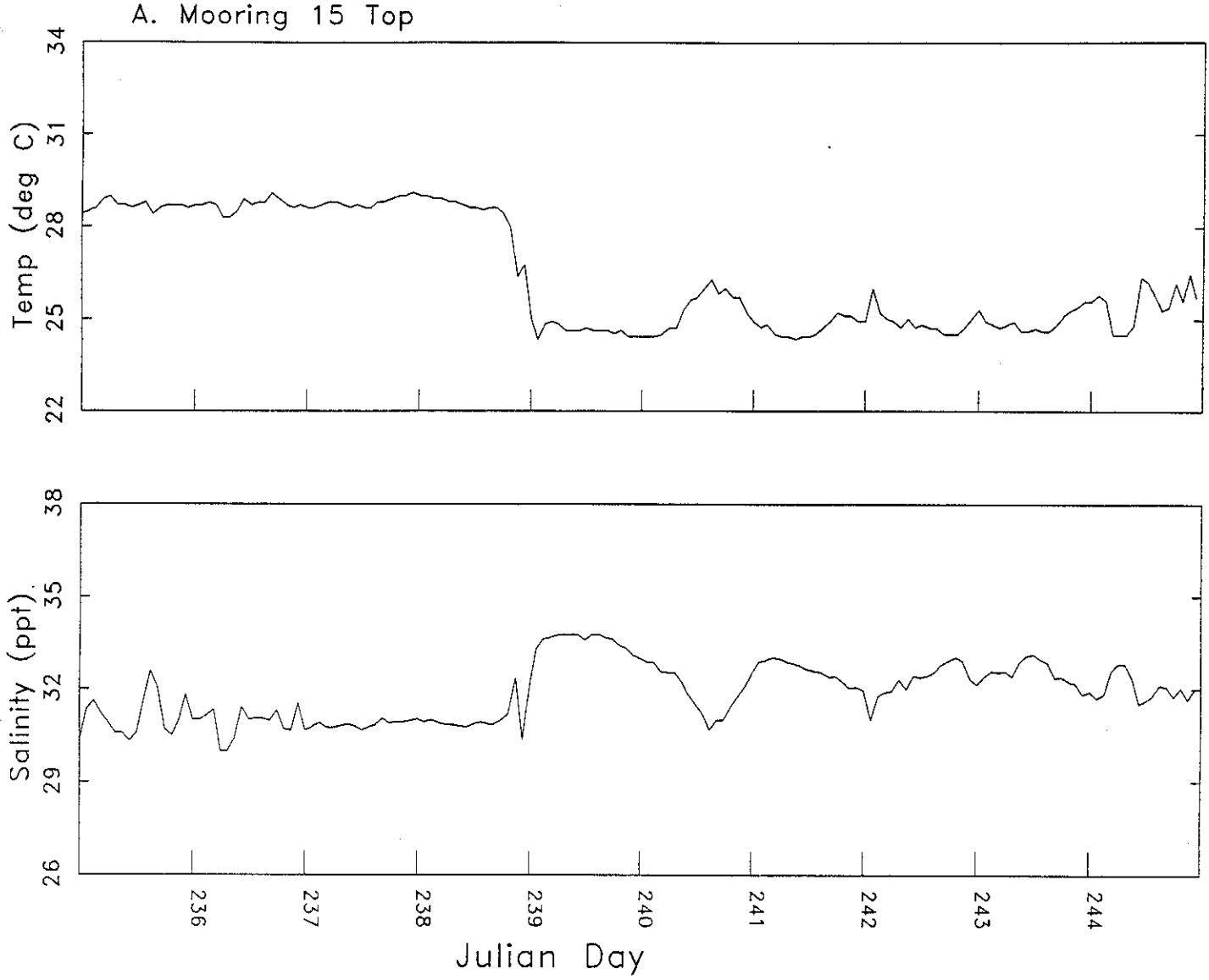

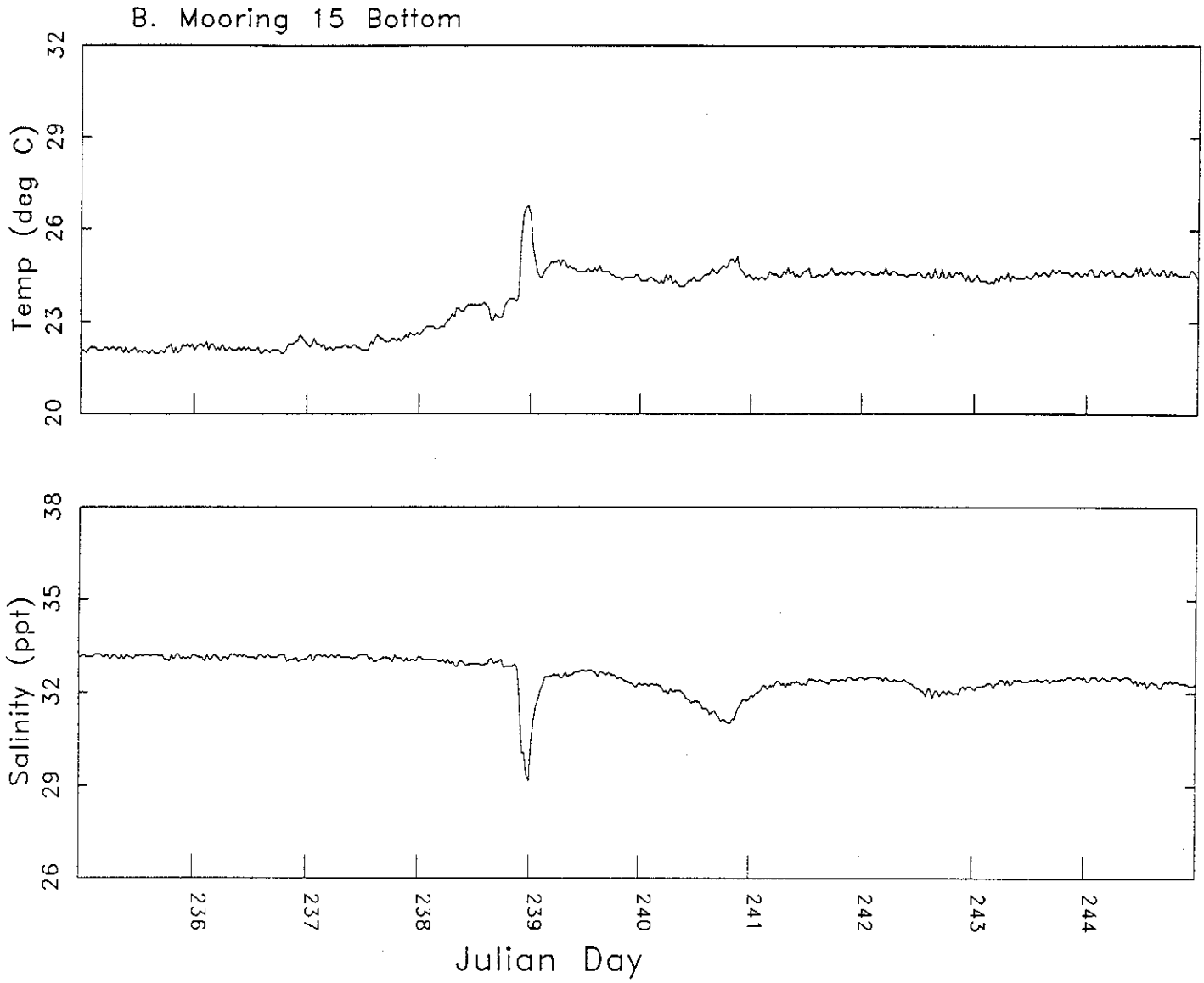
B. Mooring 15 Bottom
Temp (deg C)
20
23
26
29
32
Salinity (ppt)
26
29
32
35
38
236
237
238
239
240
241
242
243
244
Julian Day

Figure 3.2.1.5
Mooring 18: Temperature & Salinity

A. Mooring 18 Top

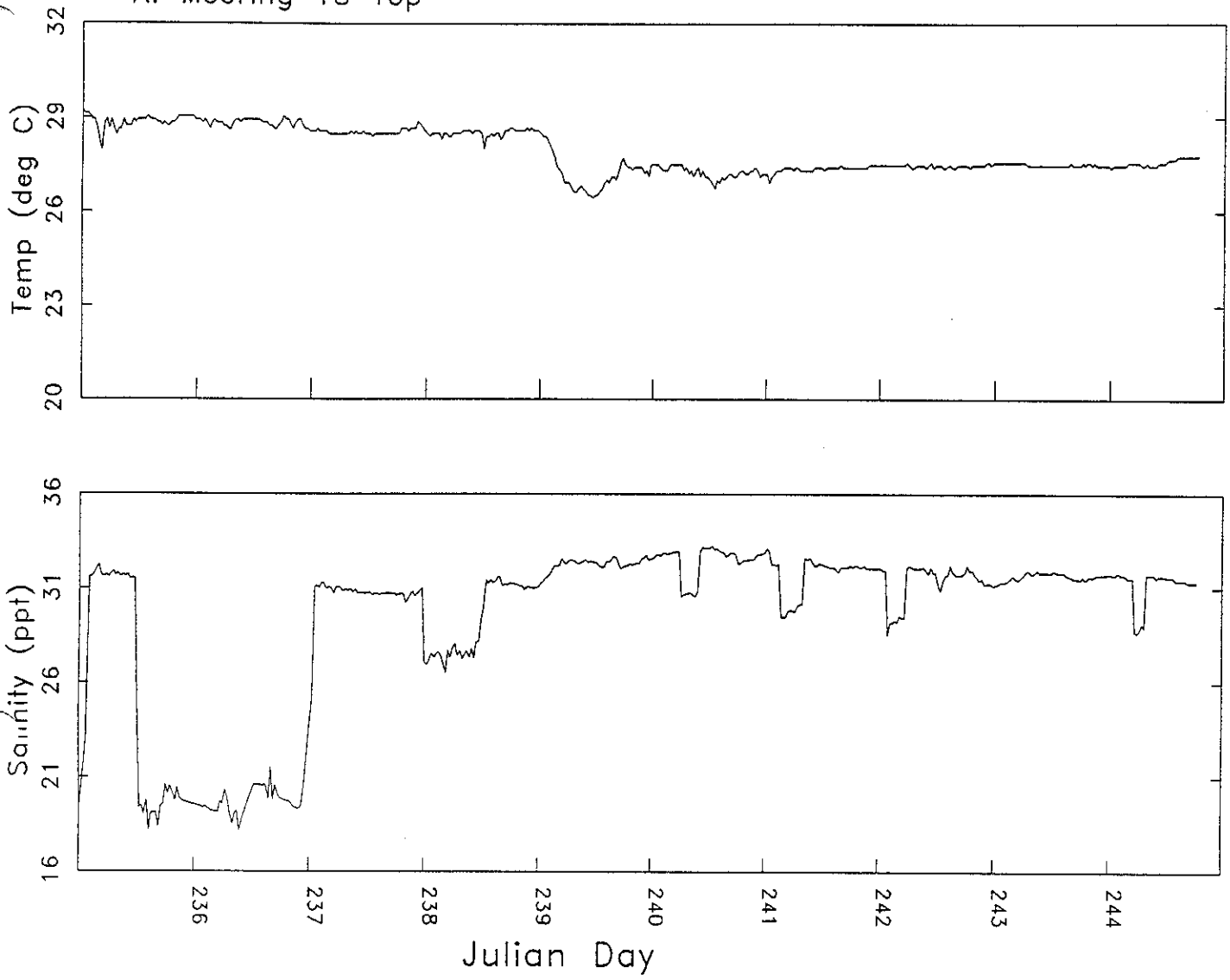

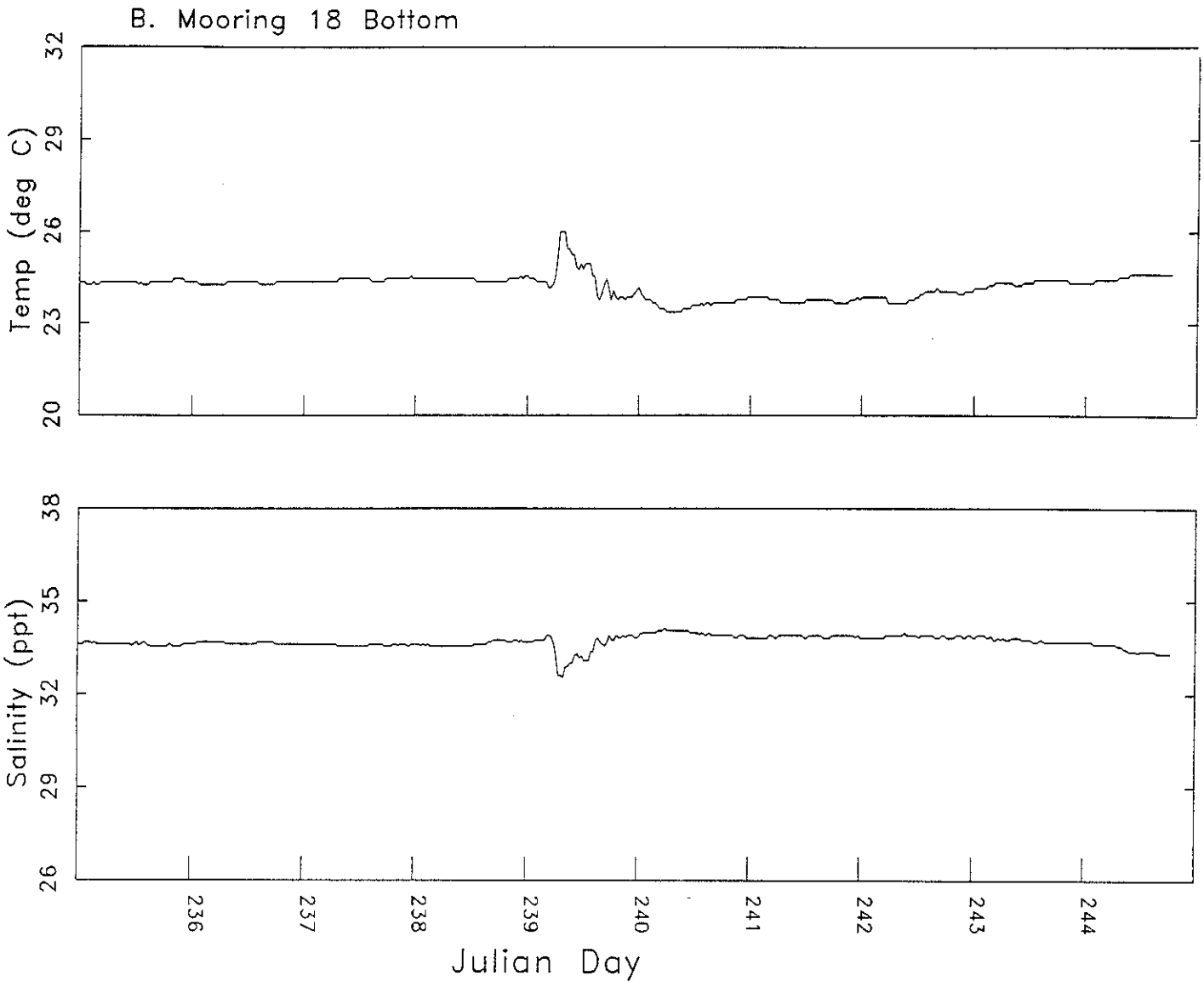
B. Mooring 18 Bottom
Temp (deg C)
32
29
26
23
20
Salinity (ppt)
38
35
32
29
26
236
237
238
239
240
241
242
243
244
Julian Day

Figure 3.2.1.6
Mooring 19: Temperature & Salinity

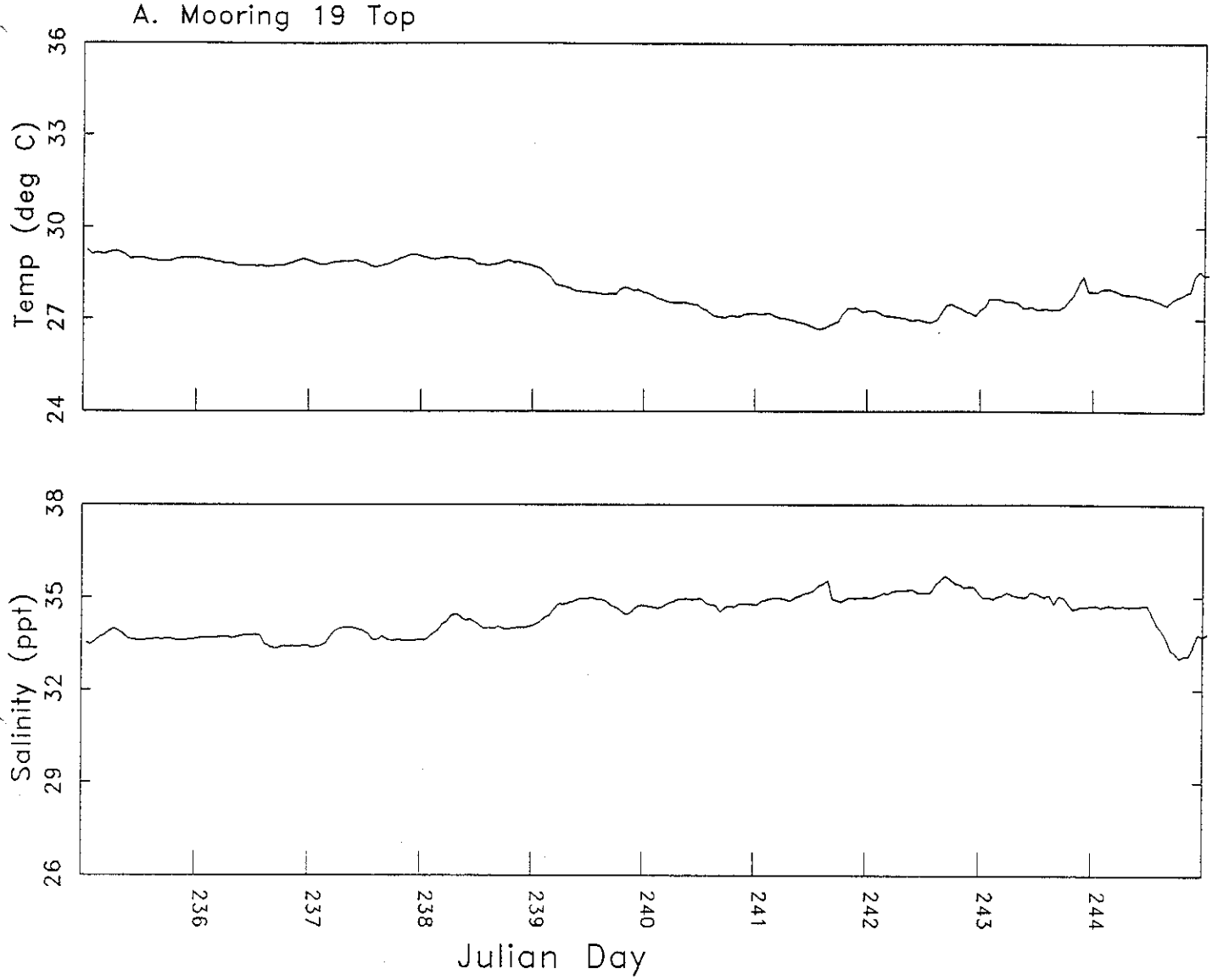

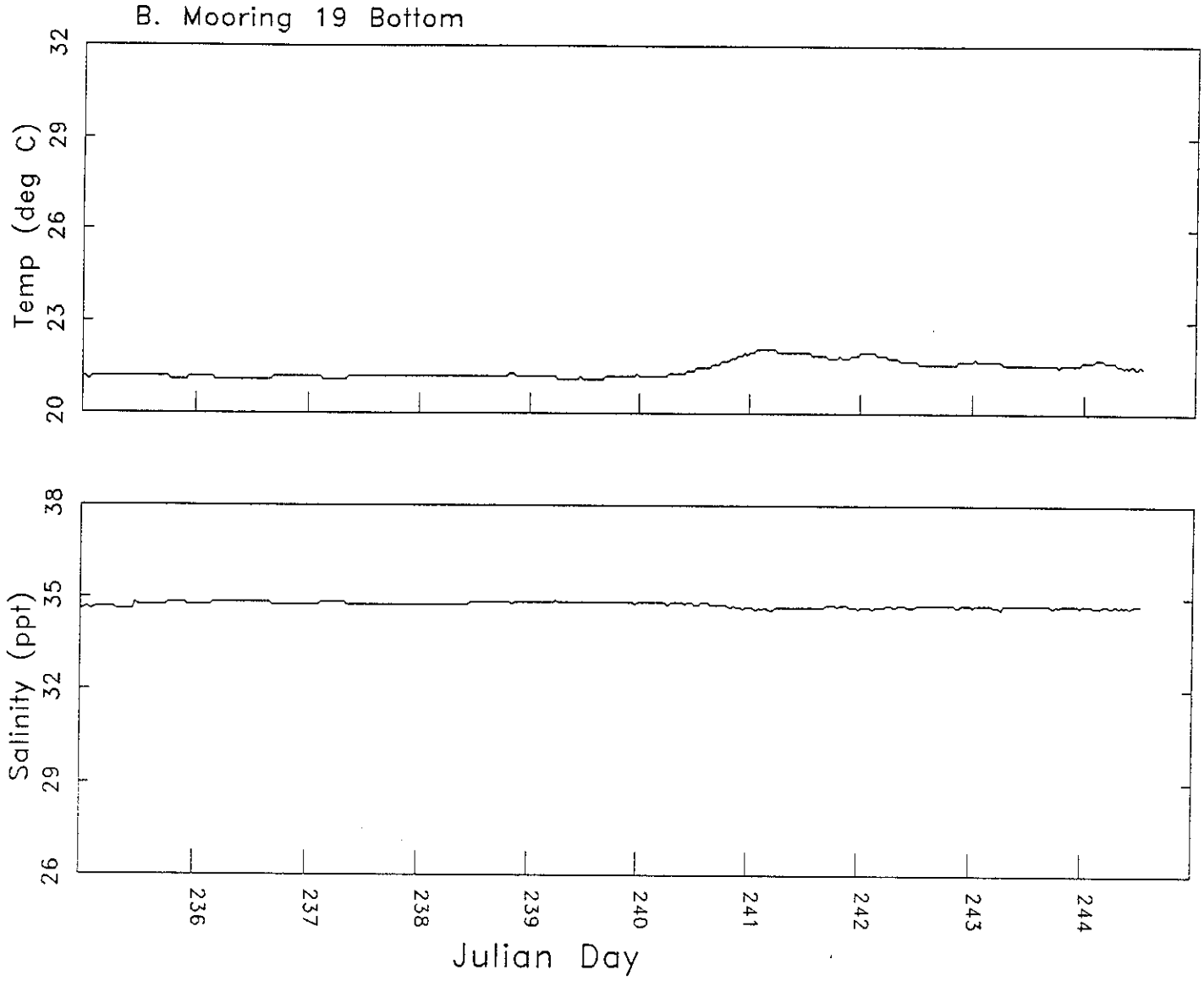
B. Mooring 19 Bottom
Temp (deg C)
20
23
26
29
32
Salinity (ppt)
26
29
32
35
38
236
237
238
239
240
241
242
243
244
Julian Day

Figure 3.2.1.7

Cross Shelf Potential Temperature August 15–20, 1992

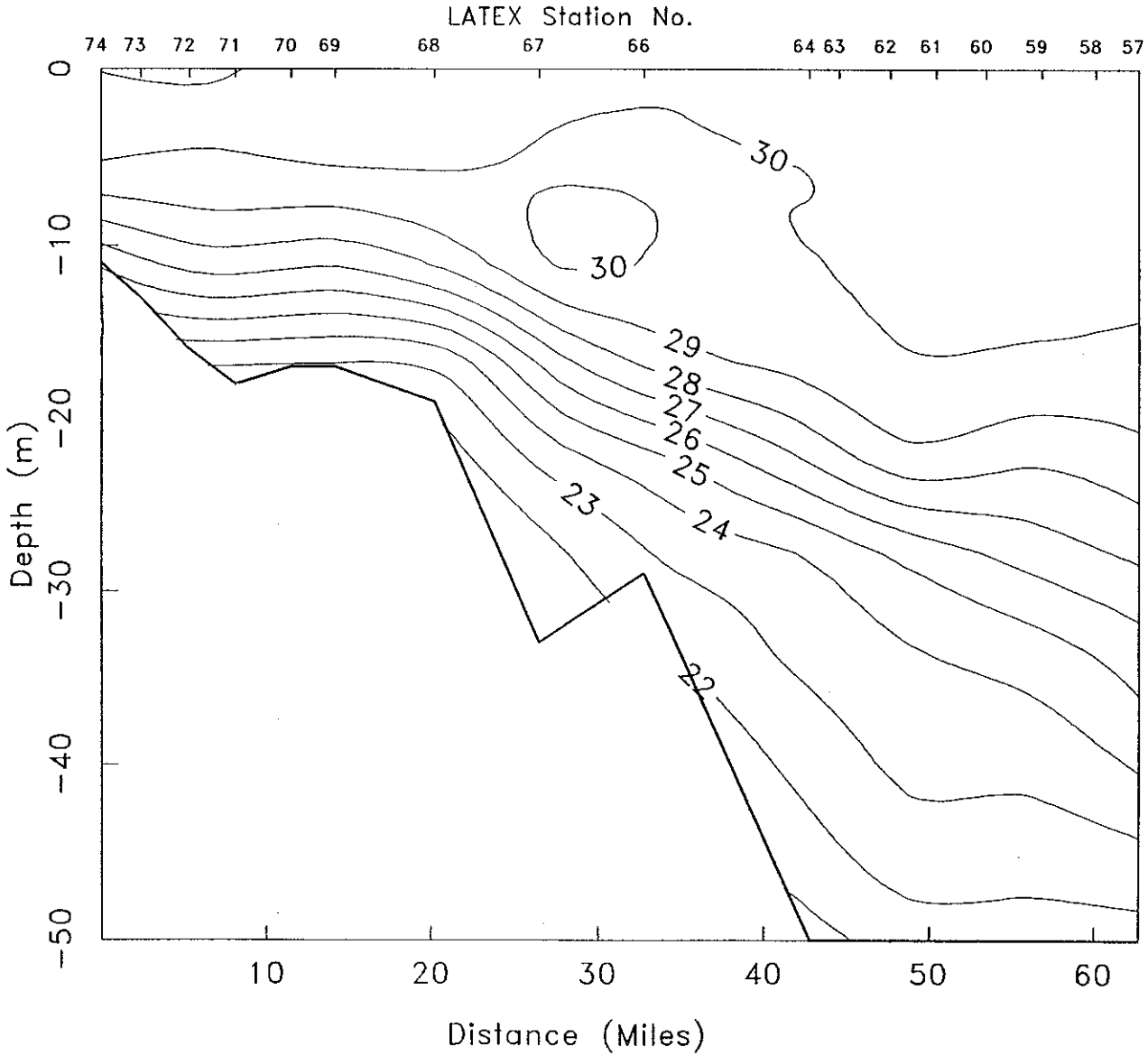

Figure 3.2.1.8

Cross Shelf Salinity Distribution August 15–20, 1992

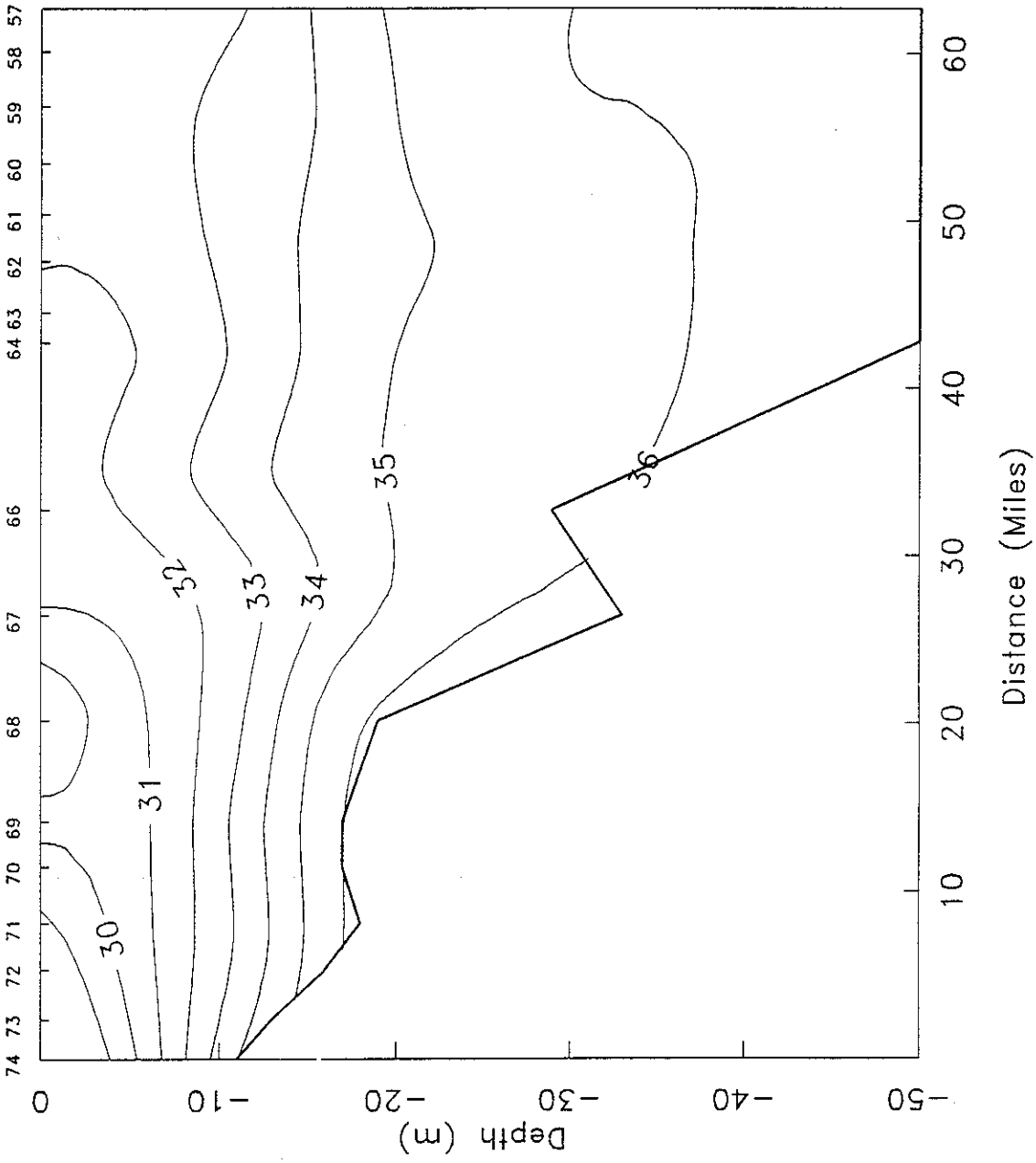

Figure 3.2.1.9

Cross Shelf Sigma-T Distribution August 15-20, 1992

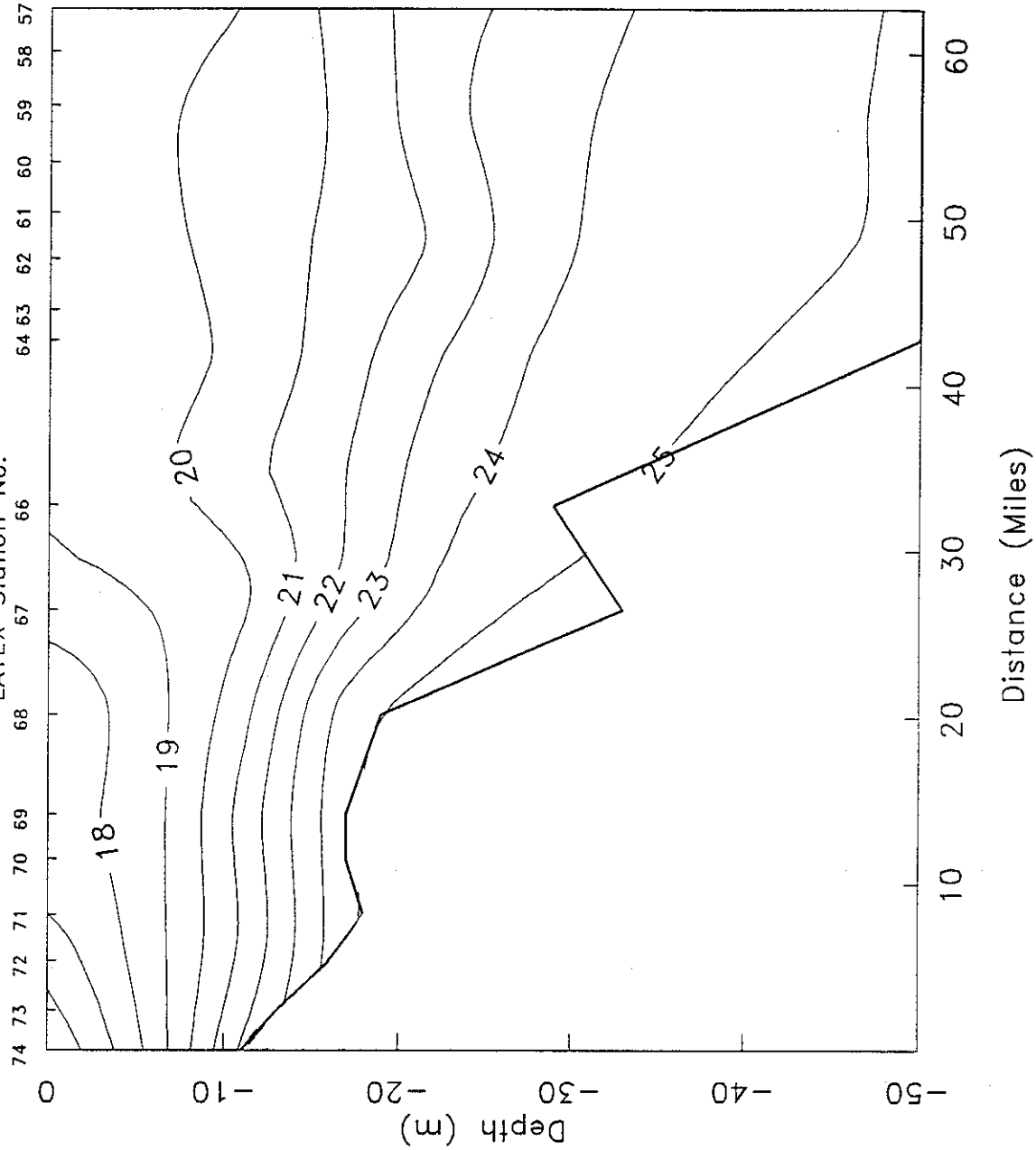

elevation. The observed water elevation is shown in Figure 3.3.1.1. Due the gaps in the record, the water elevations were not detided. Note that the initial drop in storm water elevation below mean sea level is most likely due to the offshore winds before the hurricane approached the site plus the relatively shallow water depths.

3.3.2 NDBC Buoy and C-MAN

There are obviously, no water elevations from the buoys. For the coastal C-MAN and NOS stations, the water elevation records were analyzed by Breaker et. al., (1994, in progress) and shown here as Figure 3.3.2.1. At Grand Isle the maximum storm surge was 1.11 m above MLLW and the maximum water elevation was 1.16 m. These were their largest measured values reported west of the Mississippi Delta.

3.3.3 MMS/LATEX

LATEX mooring 16 pressure gauge operated throughout the hurricane including the period when the Minispec frame turned on its side. The change in the water depth was easily determined by comparing the mean depth of the gauge before the hurricane with the mean depth after the hurricane. The 10-day period of the corrected water elevation data is given in Part A. of Figure 3.3.3.1. Using a much longer period of record (60 days), a harmonic analysis was performed on the measured data to determine the tidal constituents. These constituents were then used to determine the tidal heights relative to mean sea level for the 10-day period as shown in Part B. of Figure 3.3.3.1. The tidal heights were then subtracted from the measured water elevations to give the storm water elevation or storm tide which was 68.5 cm (Part C.).

3.4 Wave Parameters

Both significant and spectral (and directional spectral) wave parameters were computed from these buoys, staffs and pressure gauges, depending on their configuration and condition. Time series data were developed at intervals consistent with the recording intervals which ranged from one-half to three hours. These data were used to verify both the deep and shallow water parts of the hindcast wave model. As a result of the difficulty in measuring extreme waves in shallow water from pressure gauges and reconstructing the water elevation, the records tend to be gappy at times and/or require considerable work to reconstruct the true wave elevations. Some of these problems occurred in the following sections.

3.4.1 NDBC Buoy and C-MAN

The measured wave heights and periods for the NDBC buoys are given in Figures 3.4.1.1 and 3.4.1.2 for buoys 42001 and 42003, respectively. Buoy 42001 was considerably south of the hurricane track (125 nm) and the wave heights were dominated by the long period swell which arrived before the hurricanes had generated the maximum local sea conditions, accounting for the spike in Figure 3.4.1.1. The largest significant height was 4.4 m with a 10.9 sec spectral period. The significant wave heights were computed from the wave spectra. Buoy 42003 was considerably closer to the hurricane track (25 nm) and the maximum significant wave height was 6.2 m with a spectral period of 9.0 sec. The wave direction was from the east-northeast and rapidly shifted to the northwest as the hurricane passed by.

At the Shell Bullwinkle platform the wave heights increased to 7.8(?) m and wave period was 9.8 sec (Figure 3.4.1.3). Note that the double peaked wave height and period profiles are

Figure 3.3.1.1
Measured Water Elevation at Eugene Island Blk 100

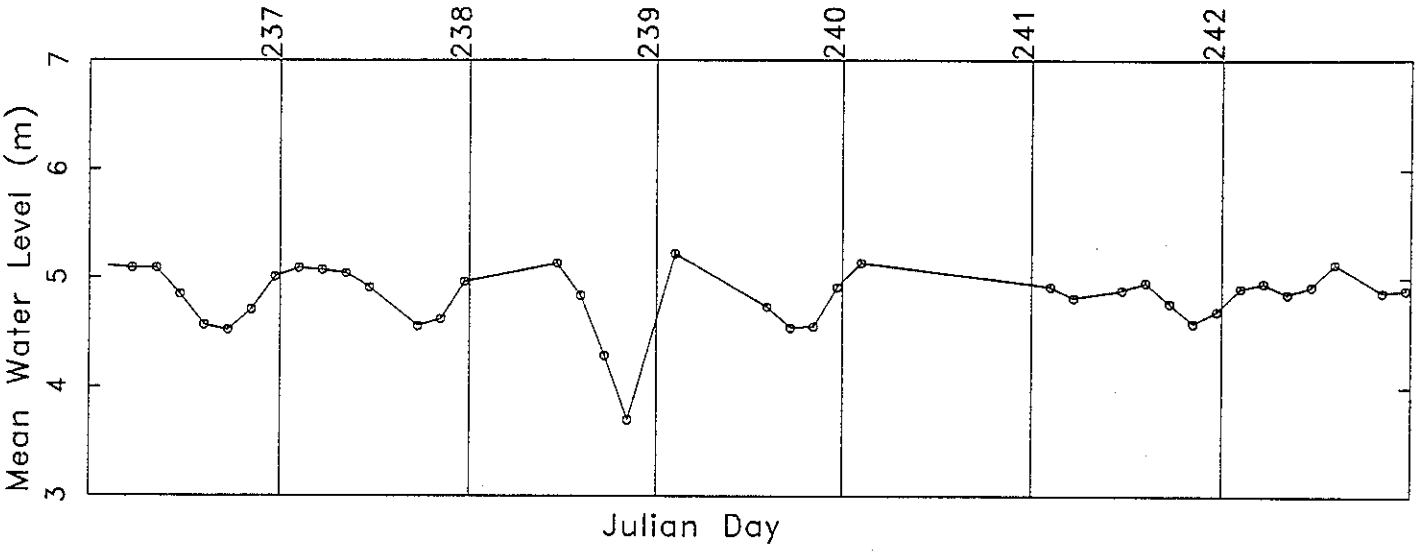

Figure 3.3.2.1

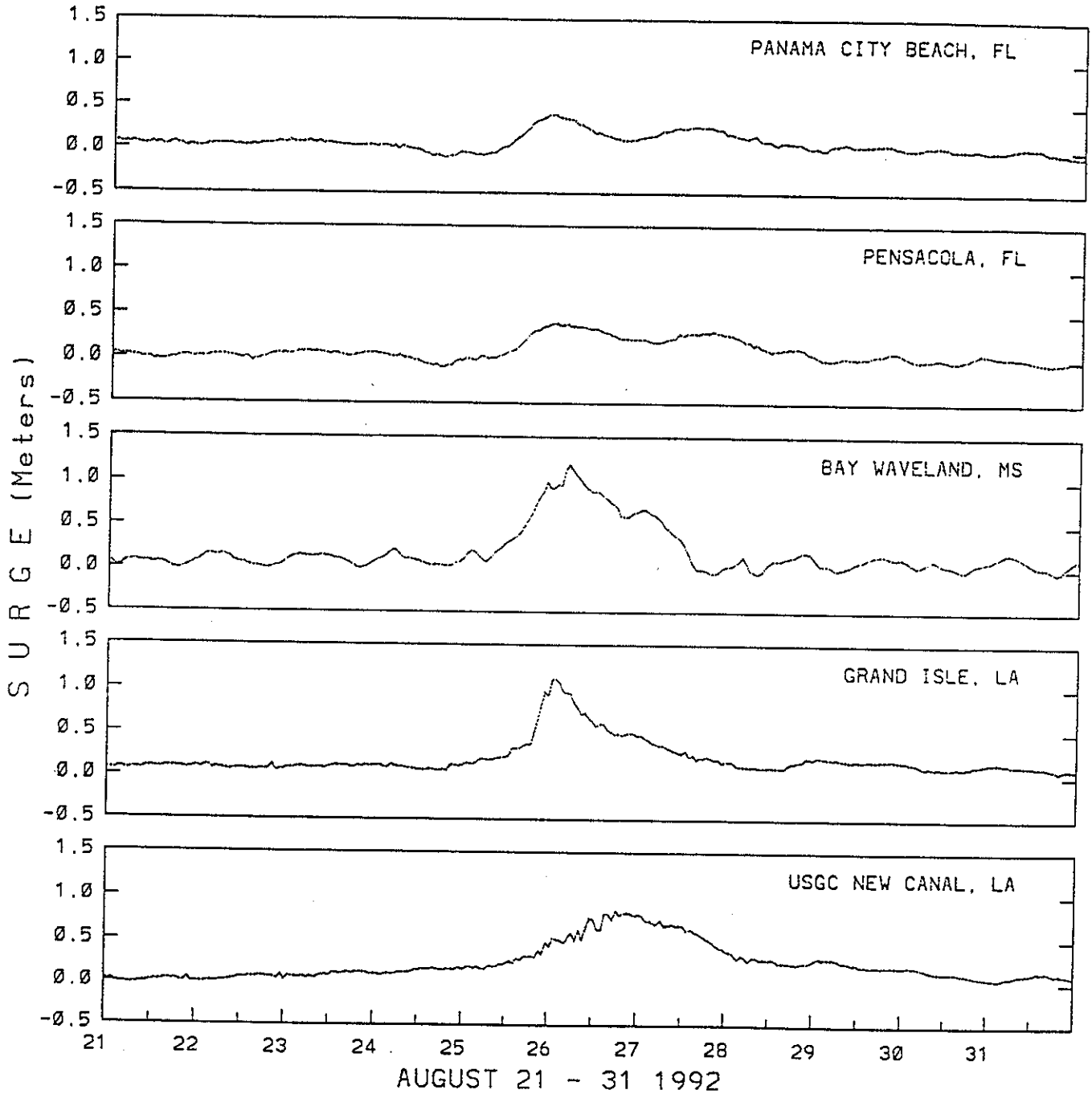

Figure 3.3.2.1 Measured Water Elevations for Coastal C-MAN and NOS Stations

(from Breaker, et. al.,1994)

Figure 3.3.3.1
Water Elevation at LATEX Mooring 16

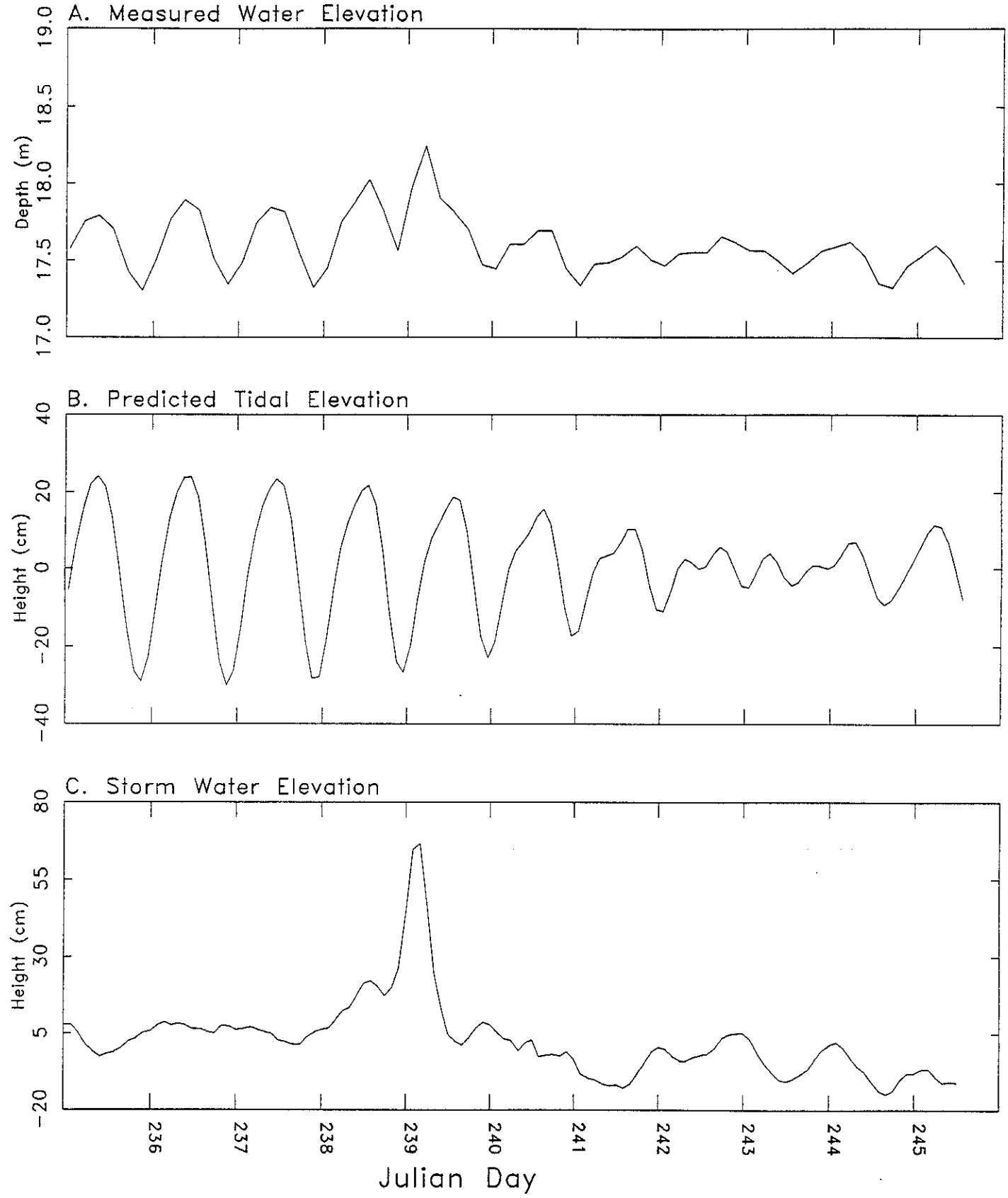

Figure 3.4.1.1
Buoy 42001 Wave Parameters

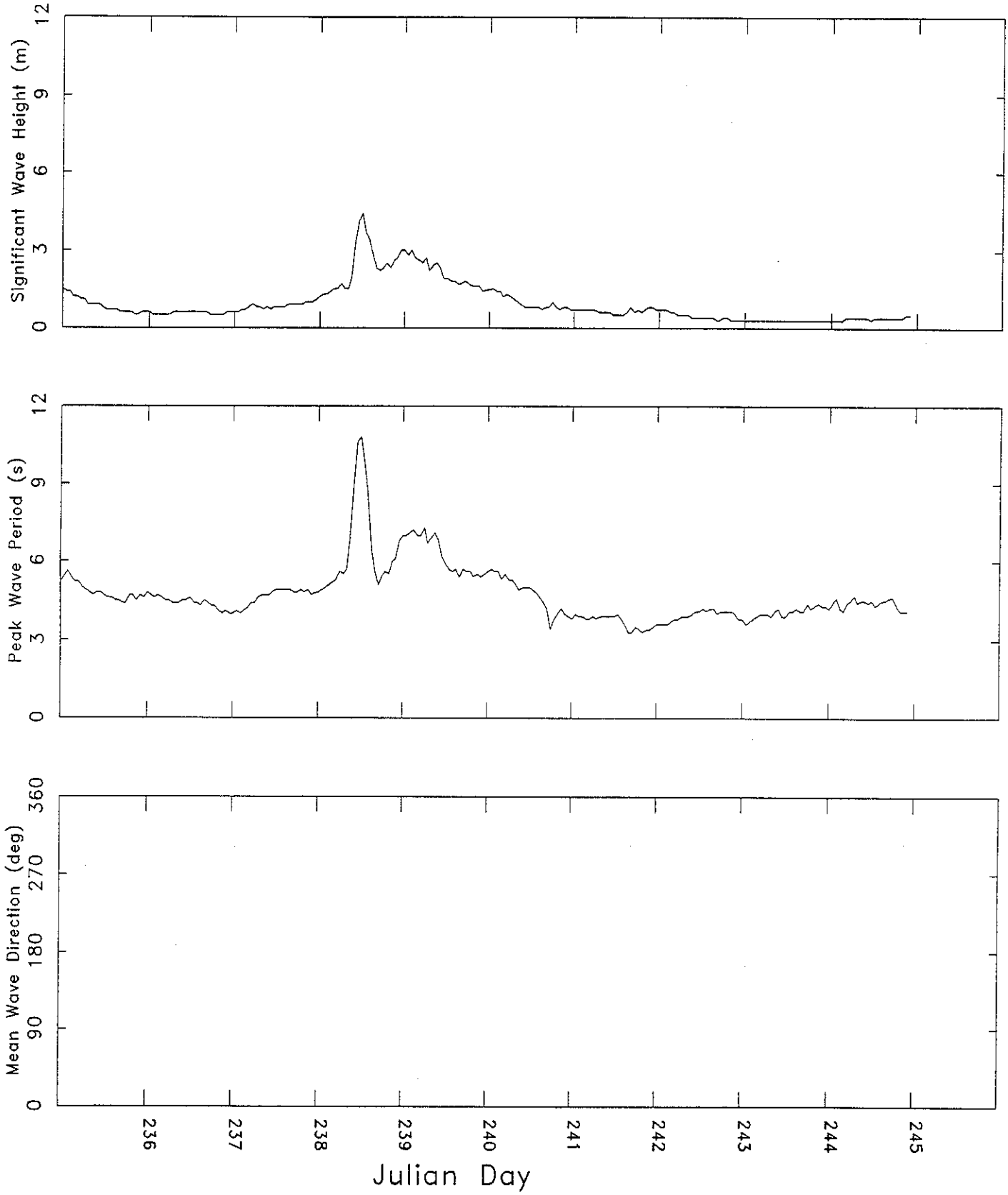

Figure 3.4.1.2
Buoy 42003 Wave Parameters

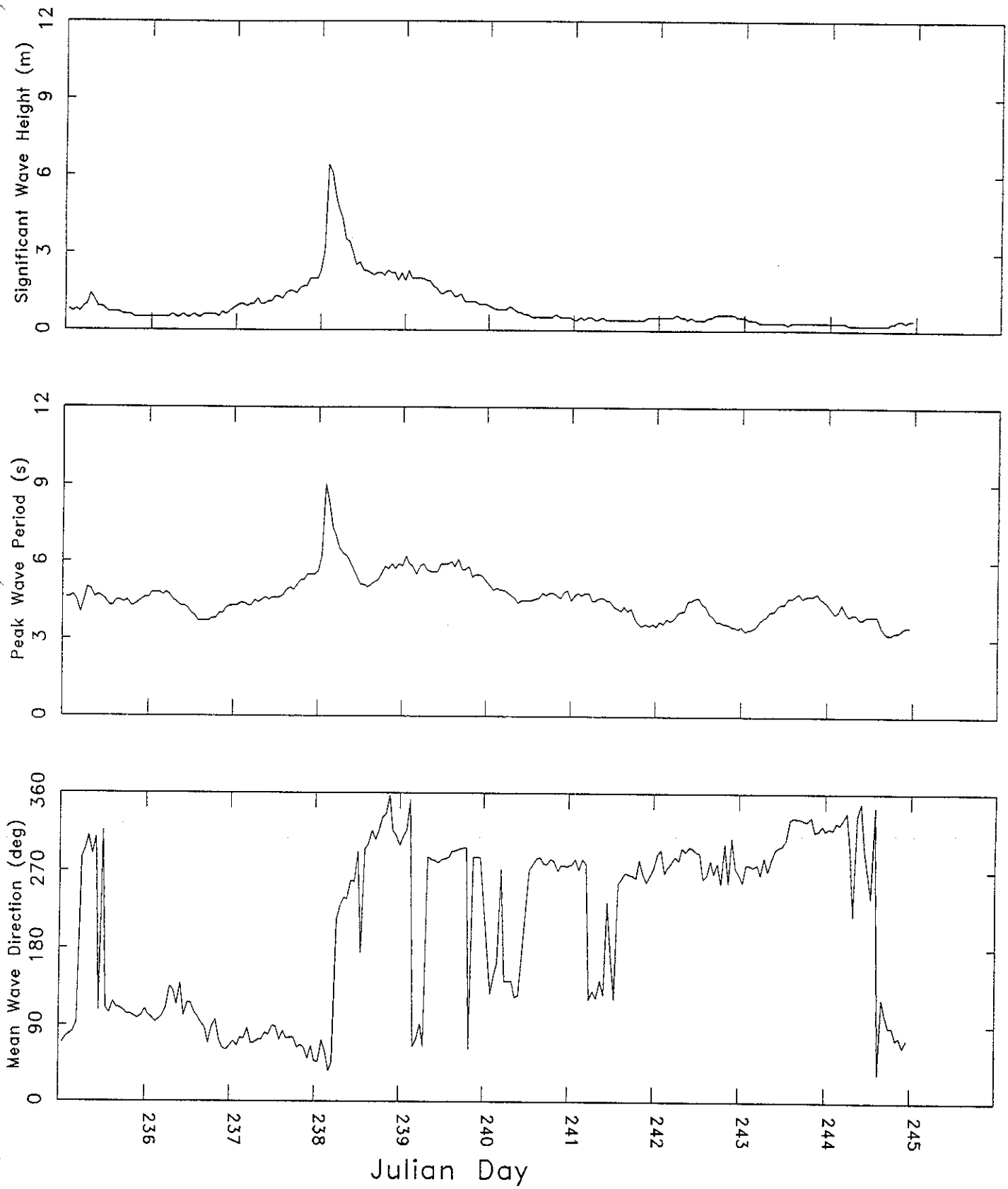

Figure 3.4.1.3
Shell Bullwinkle Wave Parameters

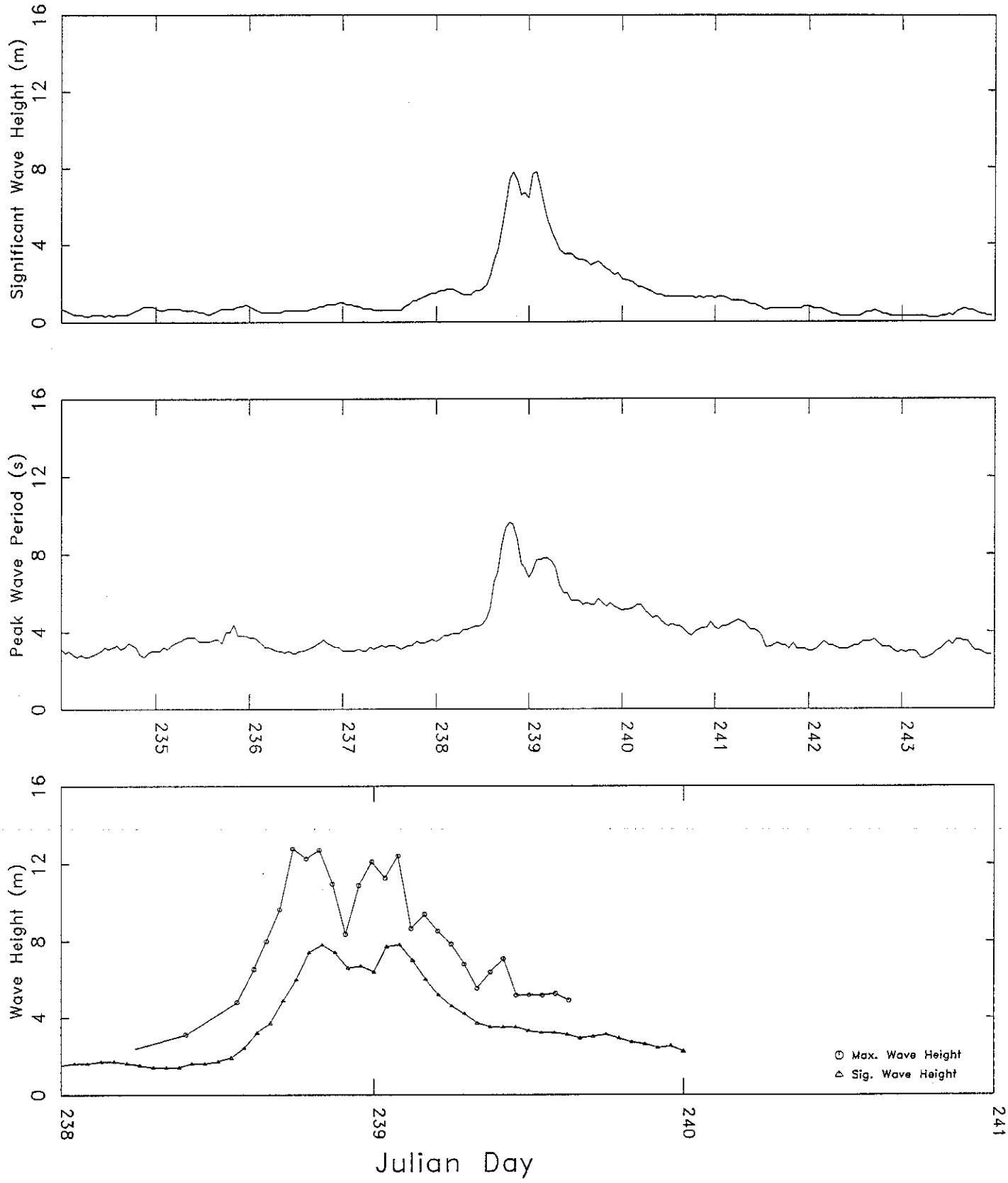

due to the initial arrival of the swell followed by the local sea.

3.4.2 Corps of Engineers

Wave height and wave period observations at Eugene Island 100 presented in Figure 3.4.2.1. As noted earlier in Section 3.3.1, the pressure gauge provided intermittent data during the peak of Hurricane Andrew's transit through the area which occurred around 0600 GMT on JD 240. The peak wave heights may have passed through during the period from 0220 to 1420 when the data were not useable. Therefore, the maximum significant wave height of 3.0 m at 0220 may not be the highest that occurred. However, as noted earlier, the maximum wave heights would be limited by the depth of the shoal water to the east and the short fetch length to the northeast. A three to four meter wave would be the maximum height under these conditions. The wind direction prior to the hurricane eye arriving at this location was from the east-northeast, resulting in offshore winds and waves.

3.4.3 MMS/LATEX

LATEX mooring 16, located about 20 nm northeast of the hurricane track at the closest point of approach and in 19 m of water was in the direct path of the largest waves in Hurricane Andrew, located just beyond the radius of maximum wind speed (Rmax). Bretschneider computed the radius to maximum waves at 1.2 Rmax. Subsequent to the measurement of the waves in Hurricane Andrew, the MiniSpec was determined to have a number of unrelated problems including electronic noise, signal clipping, warm-up transients, and the lack of calibration for temperature effects. These problems were addressed by LATEX personnel (Kelly et. al., 1993) to reconstruct the wave measurements during Andrew as best possible. The tide mode (averaged) data remains questionable. The pressure data during Andrew has been corrected for these problems and verified by computing the wave heights using independent means, using both the pressure spectrum and the velocity spectrum. The overturning problem was discussed in Section 3.3.3 and did not present a problem to the wave analysis, except that the wave heights could no longer be constructed using the velocity spectrum after that event, just from the pressure spectrum.

The results of the wave data analysis are provided in Figure 3.4.3.1 for the 48-period encompassing the maximum wave height at mooring 16. These results were produced by the LATEX Data Management Office (DiMarco et. al., 1994, in progress) after the measured data had been corrected for the above problems. The details of the analysis are contained in that study. The surface directional wave spectra were developed using linear wave theory to convert the pressure measurements to a surface wave spectrum. DiMarco (1994, personal communication) qualified the results in Figure 3.4.3.1 accordingly, noting that the "energy seen in the 5-7 second period band can be attributed to nonlinear wave-wave interaction of the longer wave periods of 10-14 seconds" and that the "measurements should be regarded only as a first approximation". Additional work is required to determine the correct wave energy in the high frequency end of the spectrum which is a non-trivial task.

The maximum significant wave occurred at 0100 GMT on August 26th and had a height of 8.9 m and a peak period of 10.7 seconds. Several hours earlier, a peak period of 14.2 sec was observed with lower wave heights. Due to the location of mooring 16 relative to the hurricane track, these were the largest measured wave heights in Hurricane Andrew.

Figure 3.4.2.1

Wave Parameters Eugene Island Blk 100

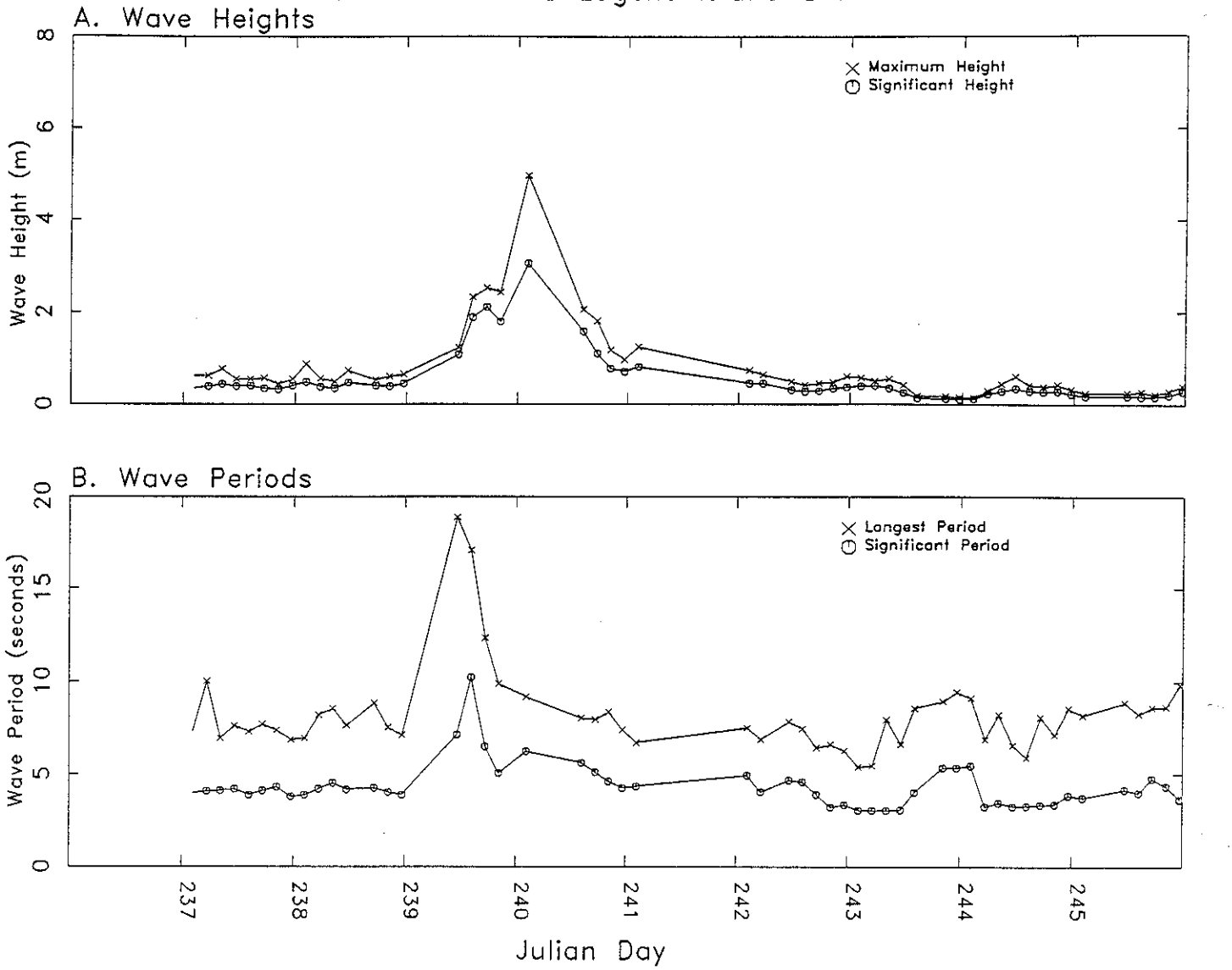

Figure 3.4.3.1

LATEX Mooring 16 Wave Parameters

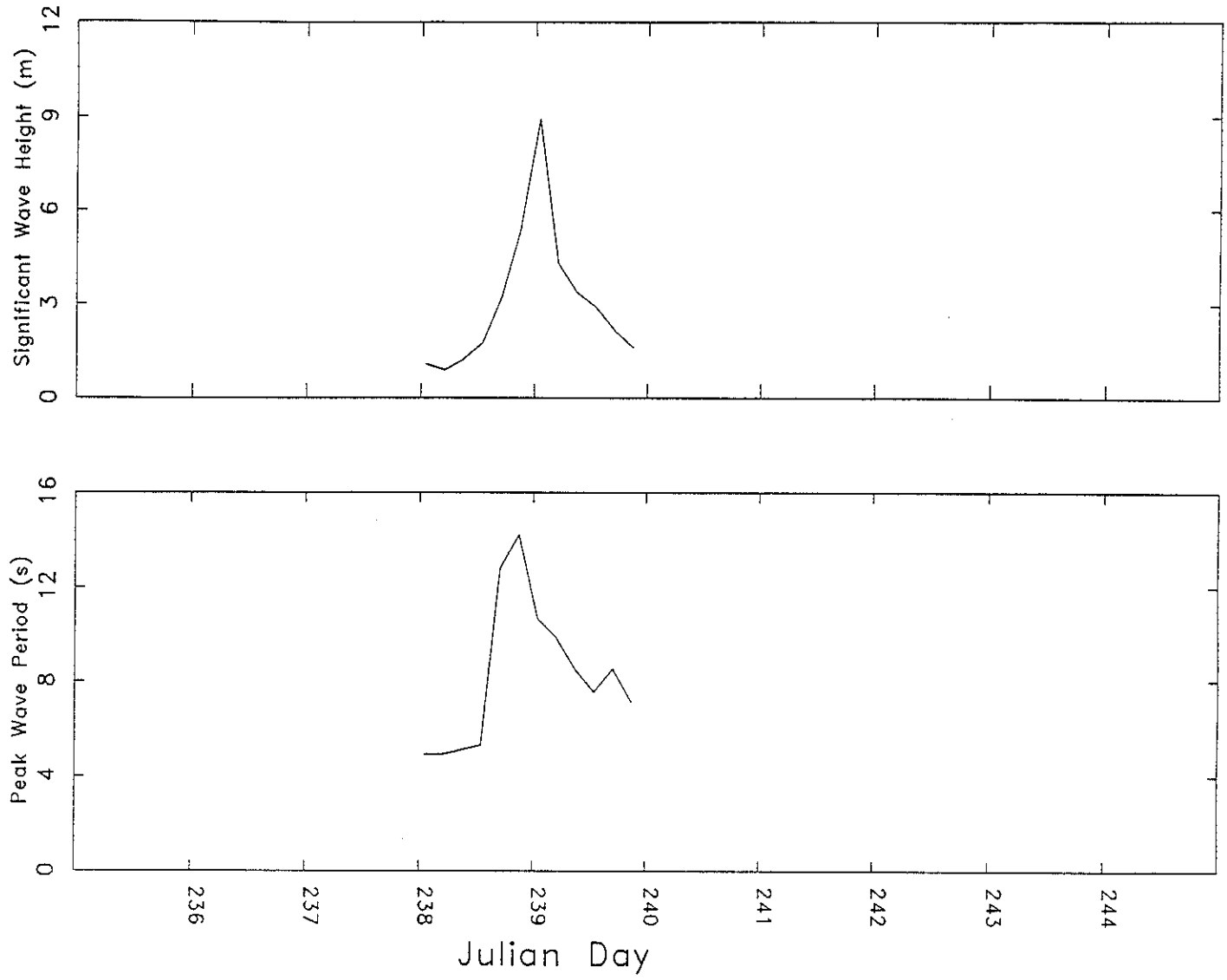

3.5 Current Velocity Data

The current meter measurements contain both wind-driven and tidal components in the records. These components must be separated into tidal and non-tidal components so that the non-tidal (wind plus inertial) can be quantitatively compared to the wind-driven current velocity model results.

3.5.1 MMS/LATEX

Of the 31 current meter moorings installed during Hurricane Andrew, only one mooring (#16) with one meter was lost even though Andrew passed directly over the eastern part of the LATEX mooring arrays (see Figure 2.2.1). One mooring was dragged a few hundred feet and two current meters either lost their impellers or were tangle with broken tag lines to the platforms or other lines. The MiniSpec frame (mooring 16) turned on its side at the peak of the hurricane, invalidating the current direction.

The 7 moorings with the 16 current meters analyzed in this study are shown in Figure 2.2.1 and listed in Table 3.2.1.1. The reasons for the varied start and stop dates are the result of the requirements for a long, continuous record ($\geq$90 days) for the harmonic analysis of the tidal currents which is discussed next. Figure 3.5.1.1 shows the periods of available current meter measurements for the period April 1992 to April 1993.

There are two indigenous problems in analyzing the tidal signal in the northern Gulf of Mexico. First, the tidal currents are relatively weak compared to the mean, inertial and wind-driven currents. Second, the O_1 component of the tidal current has a period (25.8194 hrs) which is very close to the inertial period at the latitudes of the northern Gulf of Mexico. Table 3.5.1.1 shows how the period of the O_1 constituent compares to the inertial periods at selected latitudes and also the synodic time require to be able to separate these constituents.

Table 3.5.1.1

Comparison of O_1 and Inertial Periods in Northern Gulf of Mexico

Latitude (deg-N)	O1 Period (deg/hr)	Inertial Period (deg/hr)	Difference (deg/hr)	Synodic Period (days)
30	25.8194	25.9173	.0979	153.2
29	"	26.1754	.3560	42.1
28	"	26.4237	.6043	24.8

Theoretically, with nearly all moorings being located south of 29 deg-N for record lengths greater than 42 days, the inertial currents should not be a problem. However, it appears that the wind currents rotate at periods near the inertial period which overlap the $O_{1\text{ and }K1}$ constituent's period. Therefore a sufficiently long record is needed to minimize the influence of the inertial current.

In order to evaluate the interference of the inertial currents on the tidal current analysis, an 180-day record was analyzed using mooring 12 day in deep water at 28 deg-N. The record

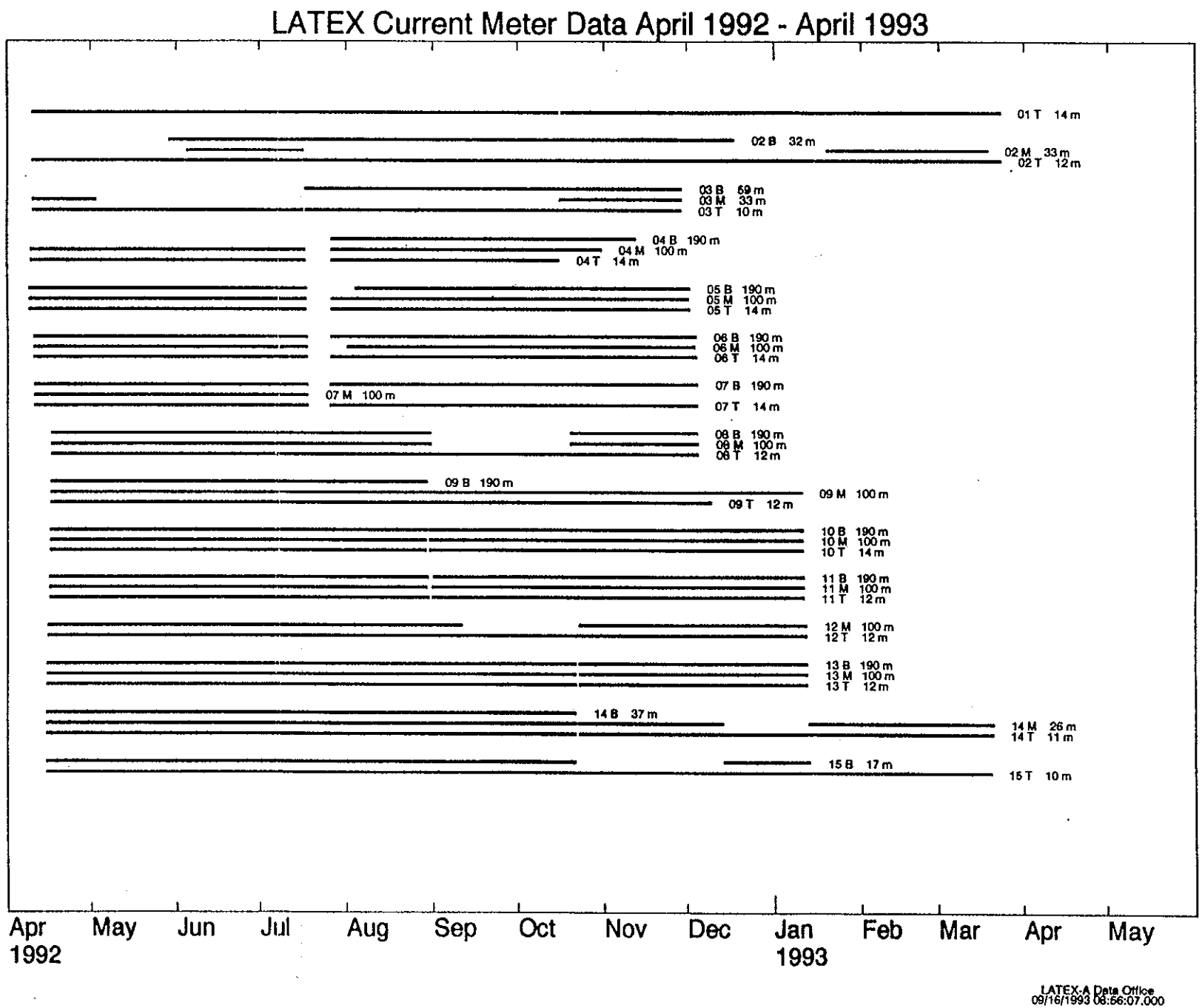
LATEX Current Meter Data April 1992 - April 1993
01 T 14 m
02 B 32 m
02 M 33 m
02 T 12 m
03 B 69 m
03 M 33 m
03 T 10 m
04 B 190 m
04 M 100 m
04 T 14 m
05 B 190 m
05 M 100 m
05 T 14 m
06 B 190 m
06 M 100 m
06 T 14 m
07 B 190 m
07 M 100 m
07 T 14 m
08 B 190 m
09 M 100 m
08 T 12 m
09 B 190 m
09 M 100 m
09 T 12 m
10 B 190 m
10 M 100 m
10 T 14 m
11 B 190 m
11 M 100 m
11 T 12 m
12 M 100 m
12 T 12 m
13 B 190 m
13 M 100 m
13 T 12 m
14 B 37 m
14 M 26 m
14 T 11 m
15 B 17 m
15 T 10 m
Apr 1992
May
Jun
Jul
Aug
Sep
Oct
Nov
Dec
Jan 1993
Feb
Mar
Apr
May
LATEX-A Data Office
09/16/1993 08:56:07.000

FIGURE 3.5.1.1 (Cont.)

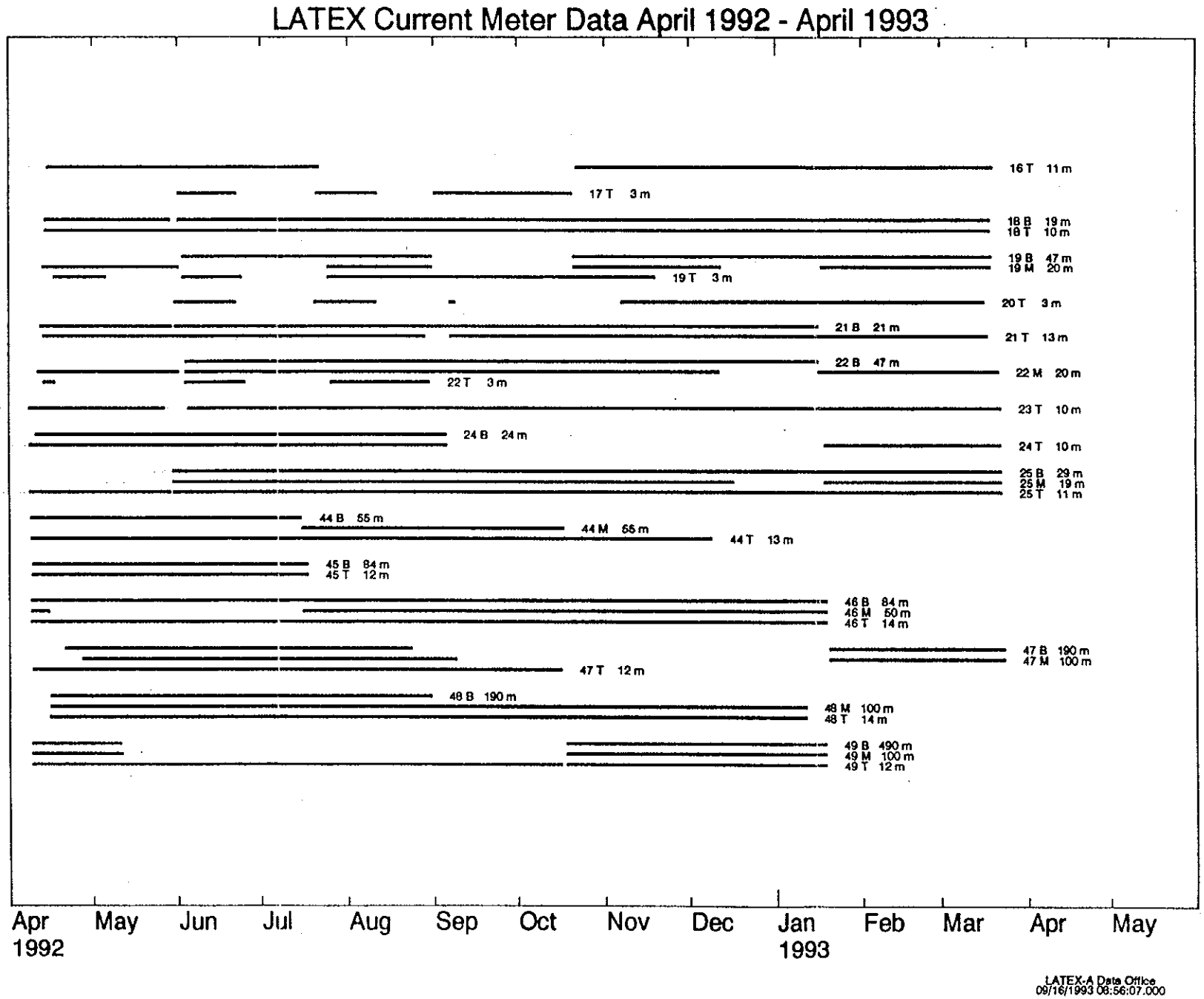

was broken into two subsets of 90-day intervals and the latter subset broken into two subsets of 45-day intervals. Hurricane Andrew measurements were in the second 90-day subset and then in the first of the 45-day subsets. The results are given in Table 3.5.1.2 for both the current velocity amplitude (speed) and phase (degrees) for the east-west and north-south components for the 5 largest constituents. The mean current over the record length and the fractional residual variance are also given, the latter being a measure of the current velocity attributed to non-tidal sources. A least-square, best-fit type of tidal analysis program was used to determine the tidal amplitudes and phase angles from the measurements.

The results in Table 3.5.1.2 show that the tidal current velocity is relatively very weak. Assuming that the 180-day record starting on 4-15-92 was sufficiently long that any inertial current would not be significant, then the fractional residual variance attributed to the non-tidal component is .99 and .98 for the E-W and N-S components, respectively (or .01 and .02 for the tidal components, respectively). For the two 90-day records starting 4-15 and 7-22, the same tidal current fractional residual variances have increased very slightly to .02 and .03 -.04, respectively. The increase in amplitude of the O_1 component occurred mainly in the record which included Hurricane Andrew. When this latter 90-day record starting on 7-22 was divided into two 45-day records, the presence of the inertial currents in Andrew was observed in the record containing Andrew, as it strongly increased the amplitudes of both the K_1 and O_1 components and thereby increased the fractional residual variance to .10 for both the E-W and N-S tidal current components. The 45-day record which did not contain Andrew was relatively unchanged.

The conclusion from the above analysis was that a 180-record (or longer) would probably be the best for the tidal analysis to minimize the influence of the inertial currents on the diurnal tidal components. However, in practice, this is very hard to obtain due to mooring/instrument malfunctions. A continuous 90-day record for the period encompassing Hurricane Andrew was found to be available for all but two meters (14 middle and 19 middle) and this period was used in the subsequent current velocity analysis to detide the measured current velocity record.

The results of the current velocity analysis at mooring 12 (surface meter) also show that the mean current varied considerable depending on the period of observation. For example, the 180-day record shows a very weak mean current. When broken into the two 90-day components, the mean current is shown to consist of a moderate current to the northeast for the first 90-days followed by an equally strong current to the west-southwest for 90-days. Finally, when this latter 90-day current was divided into two-45 day periods, the mean current in both records was still west-southwest, but with considerably different velocities. Therefore, the mean current is quite variable with time in response to external forcing. No seasonal patterns were investigated.

The results of the measured current velocity analysis are given in Figures 3.5.1.1 to 3.5.1.8 for moorings 12-16 and 18-19, respectively for A. Current Speed and B. Current Direction or the measured, the tidal and the non-tidal currents at the various depths of measurement. These results are also summarized in Table 3.5.1.3 by mooring with the order given by north to south orientation and in Table 3.5.1.4 by meter position on the mooring (top, middle and bottom). The surface tidal currents in shallow water have increased speeds relative to the deep water surface current meters as expected. Also, the moorings further to the west (18 and 19) have stronger semi-diurnal components, especially in the north-south direction. Finally, the maximum values of the total, the tidal and the non-tidal currents have been summarized in Table 3.5.1.5.

Table 3.5.1.2

Current Velocity Analysis at Site 12T
for Varying Durations (days)

Start Date	Duration in Days	Mean E-W cm/s	Mean N-S cm/s	C.V. E-W cm/s	C.V. N-S cm/s	East - West Amplitude M2 (cm/sec)	S2	N2	K1	O1	North - South Amplitude M2 (cm/s)	S2	N2	K1	O1
4-15[2]	180	-0.4	1.4	.99	.98	0.6	0.2	0.3	2.4	1.0	0.0	0.4	0.3	2.1	1.4
4-15	90	7.4	6.2	.98	.96	1.0	0.4	0.3	2.3	0.9	0.7	0.5	0.5	1.6	1.7
7-22[2]	90	-8.1	-3.3	.98	.97	0.4	0.4	0.6	2.6	1.6	0.6	0.4	0.2	2.7	1.7
7-22[2]	45	-4.2	-3.0	.90	.90	0.3	0.6	1.4	6.6	3.0	0.6	0.4	0.6	6.2	3.0
9-4	45	-12.0	-3.6	.97	.98	0.6	0.8	0.2	2.1	1.9	0.5	0.8	0.6	1.4	1.7

Start Date	Duration in Days	Mean E-W cm/s	Mean N-S cm/s	C.V. E-W cm/s	C.V. N-S cm/s	East - West Phases M2 (degrees)	S2	N2	K1	O1	North - South Phases M2 (degrees)	S2	N2	K1	O1
4-15[2]	180	-0.4	1.4	.99	.98	278	103	163	120	317	179	353	013	043	205
4-15	90	7.4	6.2	.98	.96	260	180	036	114	264	133	017	359	050	167
7-19[2]	90	-8.1	-3.3	.98	.97	326	051	178	124	343	313	334	020	039	247
7-19[2]	45	-4.2	-3.0	.90	.90	340	116	172	106	307	320	047	074	025	221
9-4	45	-12.0	-3.6	.97	.98	309	007	315	243	024	295	307	291	151	279

1. F.R.V. (Fractional Residual Variance - variance due to the non-tidal currents)
2. Period includes Hurricane Andrew

Table 3.5.1.3

Summary of Current Velocity Analysis by Mooring Location

Moor/ Meter	Depth: Meter/ Water	Mean C.V. E-W cm/s	N-S cm/s	F.R.V.[1] E-W cm/s	N-S cm/s	East - West Amplitude (cm/sec) M2	S2	N2	K1	O1	North - South Amplitude (cm/s) M2	S2	N2	K1	O1
16B	17/19	-2.1	0.0	.87	.93	2.1	0.7	0.8	0.7	0.3	0.4	0.5	0.4	0.9	1.3
15T	10/20	10.8	4.8	.78	.71	0.3	0.1	0.3	6.5	6.2	1.2	0.9	0.3	5.5	4.8
15B	17/20	0.1	-0.1	.94	.94	1.6	0.3	0.5	1.4	1.5	1.0	0.3	0.5	0.8	1.7
14T	11/47	6.2	2.2	.88	.89	1.3	0.7	0.9	5.3	6.6	0.4	0.9	0.7	4.0	5.3
14M	26/47														
14B	37/47	0.4	-0.2	.97	.98	1.1	0.6	0.2	1.6	0.4	0.4	0.4	0.3	1.0	0.3
13T	12/200	-3.4	-2.5	.98	.98	0.7	0.2	0.2	2.4	1.7	0.6	0.3	0.4	3.1	1.5
13M	100/200	-10.7	-1.5	.98	.95	0.7	0.5	0.8	0.6	2.1	0.3	0.4	0.5	1.2	2.2
13B	190/200	-6.5	-3.2	.98	.97	0.7	0.4	0.3	0.7	1.5	0.7	0.7	0.4	1.3	1.9
12T	12/505	-8.1	-3.3	.98	.97	0.4	0.4	0.6	2.6	1.6	0.5	0.4	0.2	2.7	1.7
12M	100/505	-1.1	3.4	.99	.99	0.6	0.5	0.4	0.3	0.7	0.1	0.3	0.4	0.5	0.5
18T	10/22	10.4	-2.5	.89	.64	1.9	0.8	1.2	3.0	4.7	3.7	1.8	0.8	4.8	5.3
18B	19/22	1.6	0.4	.94	.75	1.2	0.1	0.5	1.1	0.5	3.6	0.9	1.0	1.0	0.3
19T	4/51	-4.1	2.3	.96	.94	1.5	1.0	1.1	5.6	1.3	2.4	0.6	1.0	4.1	2.2
19M	20/51	(record too short for tidal analysis)													
19B	47/51	0.7	-0.4	.95	.77	0.7	0.3	0.4	1.2	0.4	2.6	1.2	1.0	1.6	1.2

1. F.R.V. (Fractional Residual Variance - variance due to the non-tidal currents)

Table 3.5.1.4

Summary of Current Velocity Analysis By Meter Depth

Moor/ Meter	Depth: Meter/ Water	Mean E-W cm/s	Mean N-S cm/s	C.V. F.R.V.[1] E-W cm/s	C.V. F.R.V.[1] N-S cm/s	East - West Amplitude M2 (cm/sec)	S2	N2	K1	O1	North - South Amplitude M2 (cm/s)	S2	N2	K1	O1
Top Meter															
15T	10/20	10.8	4.8	.78	.71	0.3	0.1	0.3	6.5	6.2	1.2	0.9	0.3	5.5	4.8
14T	11/47	6.2	2.2	.88	.89	1.3	0.7	0.9	5.3	6.6	0.4	0.9	0.7	4.0	5.3
13T	12/200	-3.4	-2.5	.98	.98	0.7	0.2	0.2	2.4	1.7	0.6	0.3	0.4	3.1	1.5
12T	12/505	-8.1	-3.3	.98	.97	0.4	0.4	0.6	2.6	1.6	0.5	0.4	0.2	2.7	1.7
18T	10/22	10.4	-2.5	.89	.64	1.9	0.8	1.2	3.0	4.7	3.7	1.8	0.8	4.8	5.3
19T	4/51	-4.1	2.3	.96	.94	1.5	1.0	1.1	5.6	1.3	2.4	0.6	1.0	4.1	2.2
Middle Meter															
14M	26/47	7.6	-1.1	(record too short for tidal analysis)											
13M	100/200	-10.7	-1.5	.98	.95	0.7	0.5	0.8	0.6	2.1	0.3	0.4	0.5	1.2	2.2
12M	100/505	-1.1	3.4	.99	.99	0.6	0.5	0.4	0.3	0.7	0.1	0.3	0.4	0.5	0.5
19M	20/51	4.1	-0.6	(record too short for tidal analysis)											
Bottom Meter															
16B	17/19	-2.1	0.0	.87	.93	2.1	0.7	0.8	0.7	0.3	0.4	0.5	0.4	0.9	1.3
15B	17/20	0.1	-0.1	.94	.94	1.6	0.3	0.5	1.4	1.5	1.0	0.3	0.5	0.8	1.7
14B	37/47	0.4	-0.2	.97	.98	1.1	0.6	0.2	1.6	0.4	0.4	0.4	0.3	1.0	0.3
13B	190/200	-6.5	-3.2	.98	.97	0.7	0.4	0.3	0.7	1.5	0.7	0.7	0.4	1.3	1.9
18B	19/22	1.6	0.4	.94	.75	1.2	0.1	0.5	1.1	0.5	3.6	0.9	1.0	1.0	0.3
19B	47/51	0.7	-0.4	.95	.77	0.7	0.3	0.4	1.2	0.4	2.6	1.2	1.0	1.6	1.2

1. F.R.V. (Fractional Residual Variance - variance due to the non-tidal currents)

Table 3.5.1.5

Maximum Values of Total, Tidal and Non-Tidal Current Velocity

Location	Day & Time	Maximum Vel.	Maximum Dir.
12T Total:	239.0000	138.6	204.0
12T Tidal:	240.5208	7.9	30.9
12T Non-Tidal:	239.0000	137.4	204.5
12M Total:	241.2917	69.7	276.9
12M Tidal:	238.6250	1.5	207.6
12M Non-Tidal:	241.2917	69.9	274.1
13T Total:	238.9375	163.5	198.0
13T Tidal:	239.9792	5.9	216.4
13T Non-Tidal:	238.9375	154.6	196.5
13M Total:	240.1042	111.2	274.9
13M Tidal:	242.2292	4.4	268.6
13M Non-Tidal:	239.9375	99.3	213.7
13B Total:	240.0000	126.9	182.0
13B Tidal:	243.8542	4.4	199.8
13B Non-Tidal:	240.0000	125.7	180.1
14T Total:	239.0000	133.9	241.0
14T Tidal:	238.0625	14.6	267.6
14T Non-Tidal:	239.0000	128.0	242.3
14B Total:	239.0694	139.2	266.9
14B Tidal:	242.1736	3.6	275.1
14B Non-Tidal:	239.0694	136.7	267.0
15T Total:	238.8750	116.0	243.0
15T Tidal:	237.0625	12.8	278.8
15T Non-Tidal:	238.8750	122.2	247.6
15B Total:	238.9583	114.4	253.0
15B Tidal:	242.4167	6.0	129.8
15B Non-Tidal:	238.9583	114.1	252.7
16B Total:	238.8958	96.0	254.0
16B Tidal:	236.6875	1.8	15.8
16B Non-Tidal:	238.8958	93.9	252.6
18T Total:	239.7083	87.7	111.0
18T Tidal:	238.1458	14.7	338.6
18T Non-Tidal:	239.7083	76.5	111.6
18B Total:	239.3542	61.4	36.0
18B Tidal:	241.7083	6.5	342.0
18B Non-Tidal:	239.3542	64.6	31.8
19T Total:	239.1625	54.0	202.0
19T Tidal:	237.8708	9.2	192.3
19T Non-Tidal:	239.1625	58.7	188.8
19B Total:	240.3958	32.8	199.0
19B Tidal:	239.3750	5.4	182.7
19B Non-Tidal:	240.7917	32.3	209.6

Figure 3.5.1.2.A
LATEX Mooring 12 Top Meter

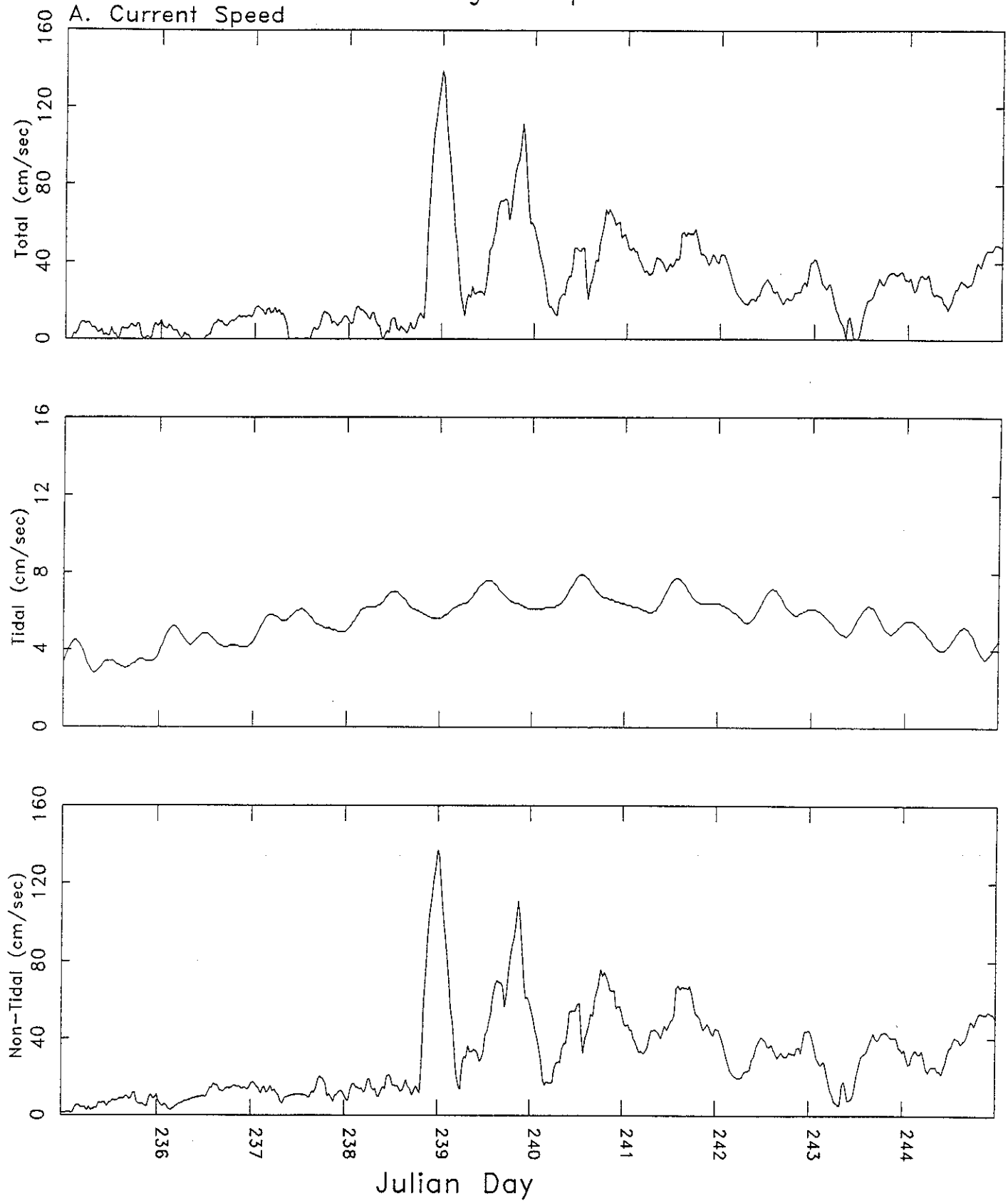

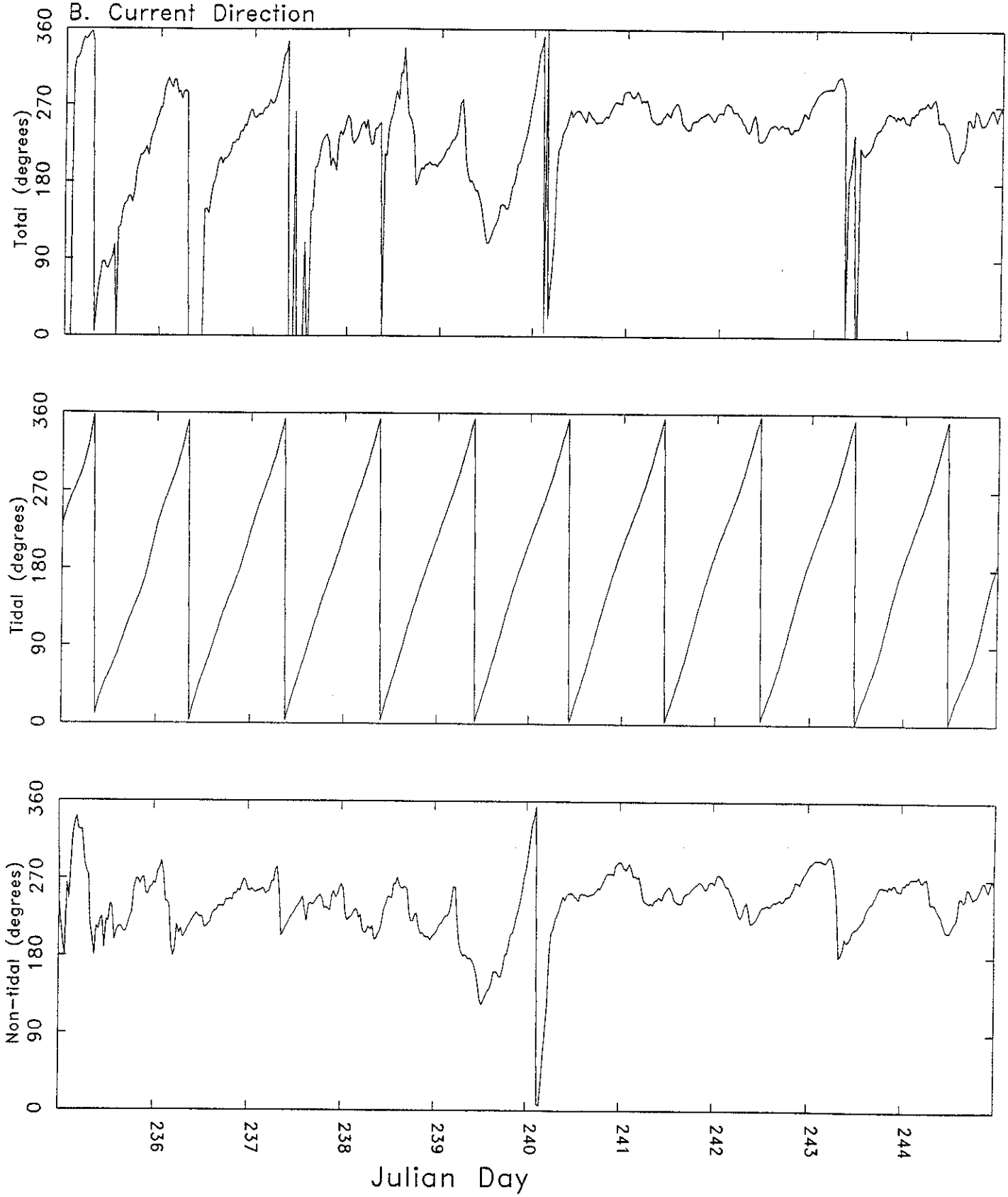
B. Current Direction
Total (degrees)
Tidal (degrees)
Non-tidal (degrees)
0
90
180
270
360
236
237
238
239
240
241
242
243
244
Julian Day

Figure 3.5.1.2.B

LATEX Mooring 12 Middle Meter

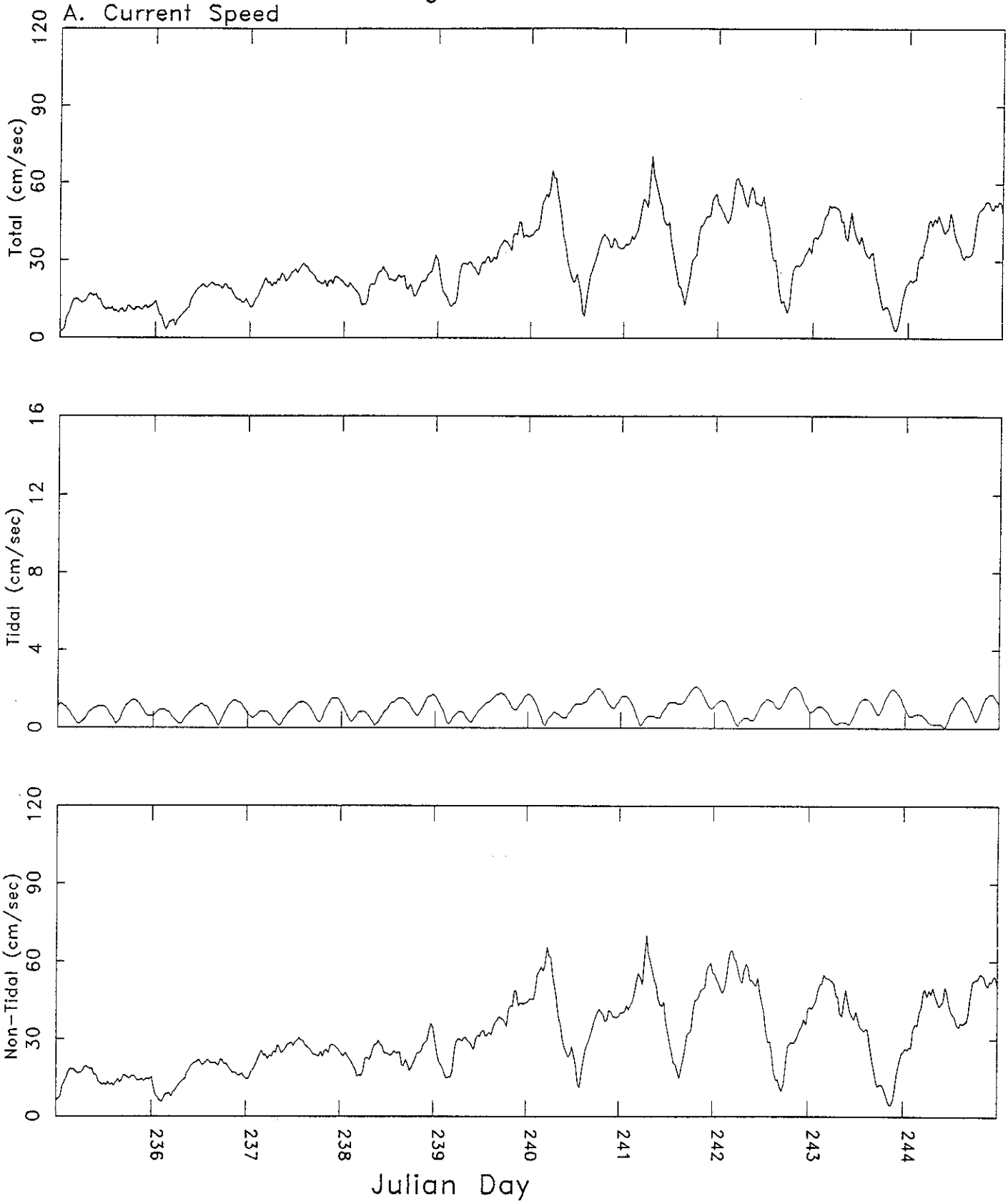

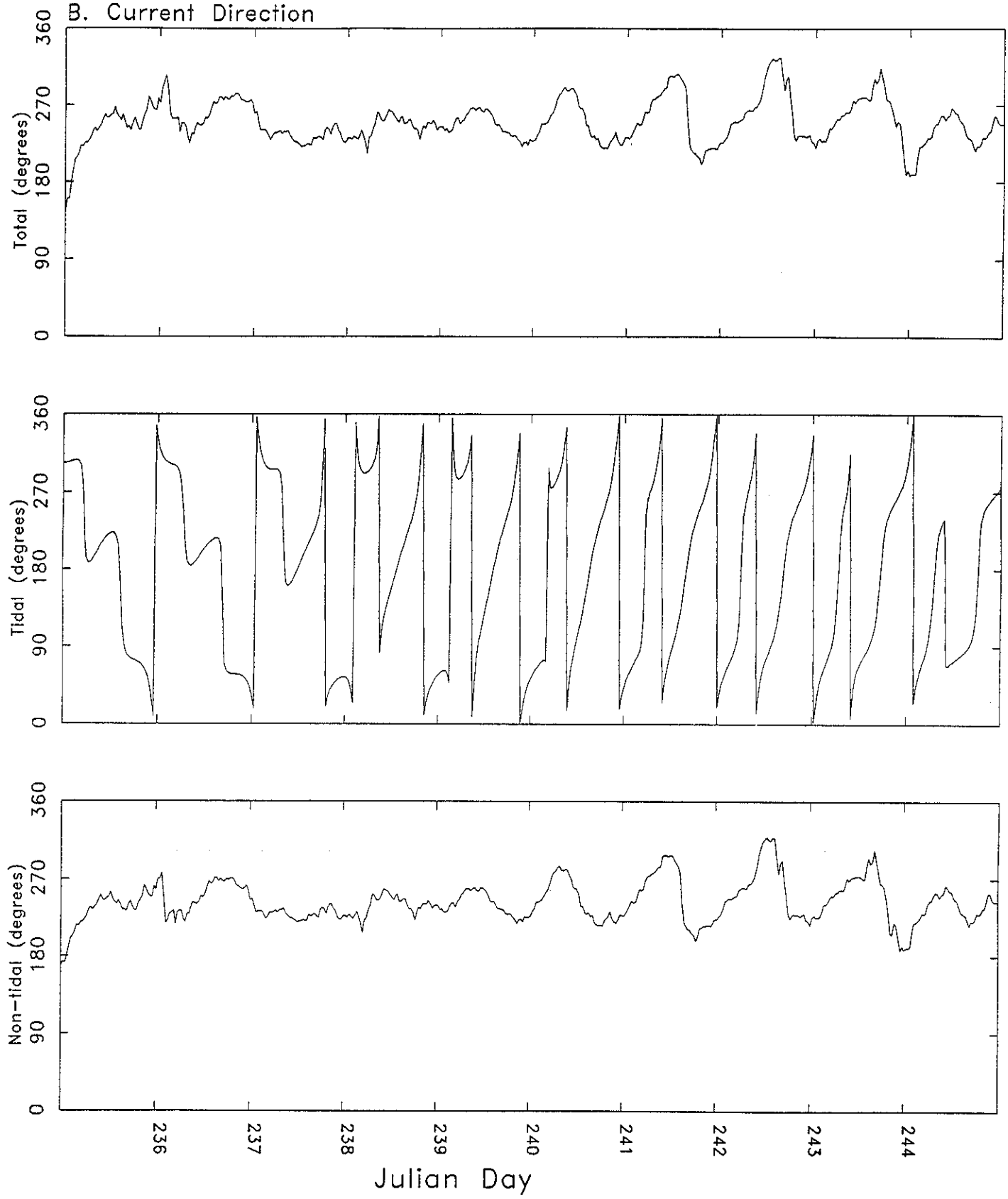
B. Current Direction
Total (degrees)
Tidal (degrees)
Non-tidal (degrees)
0
90
180
270
360
236
237
238
239
240
241
242
243
244
Julian Day

Figure 3.5.1.3.A
LATEX Mooring 13 Top Meter

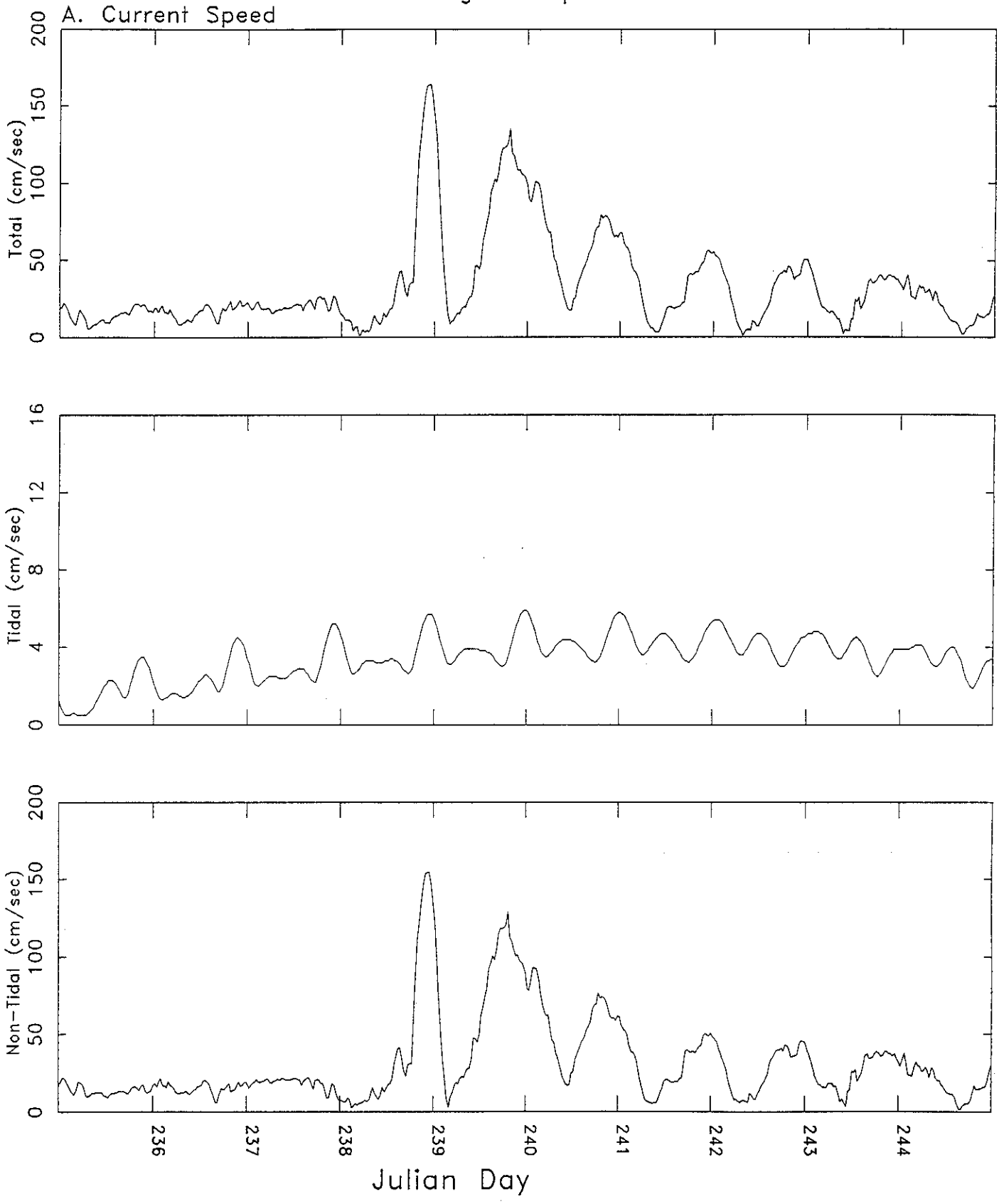

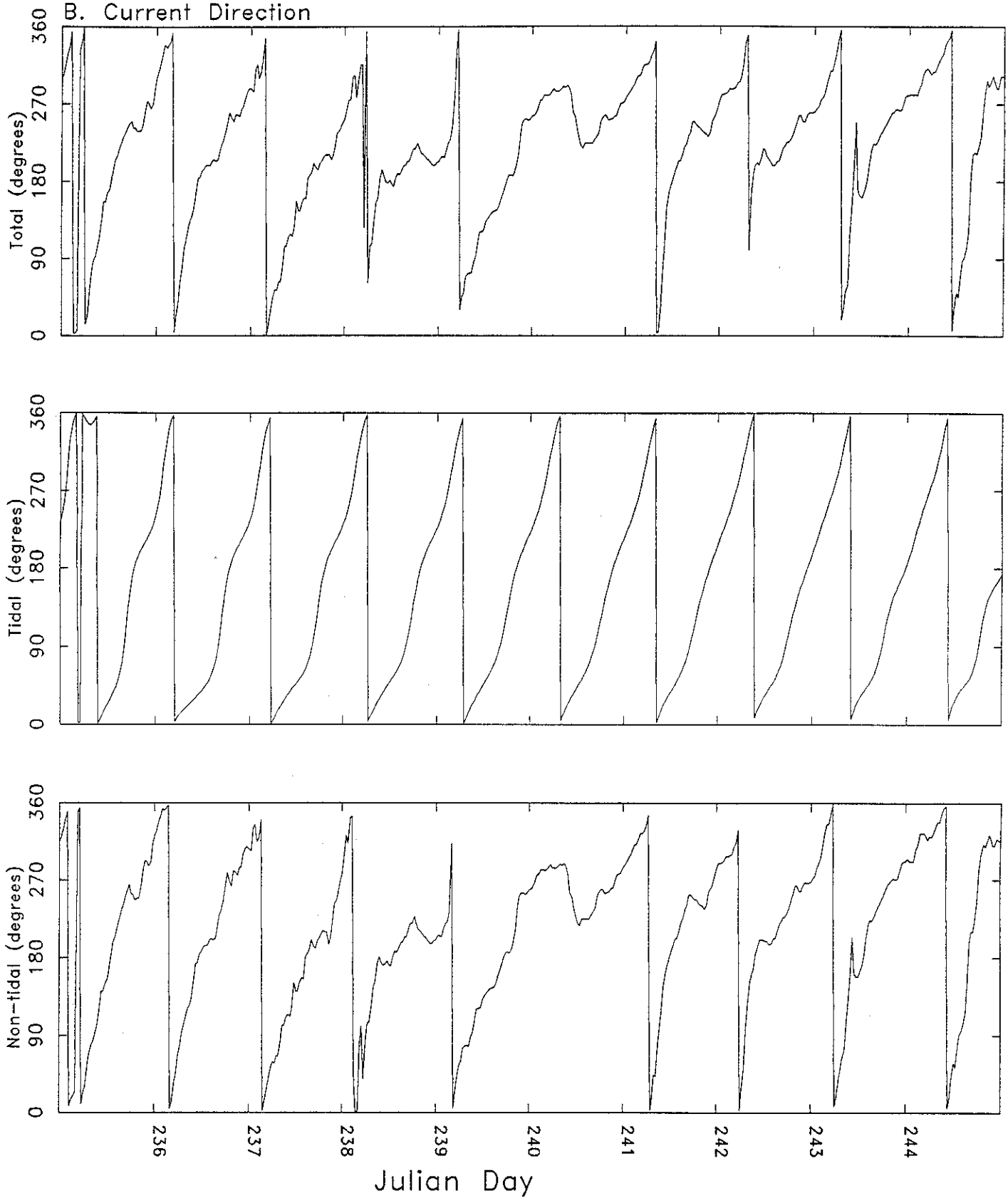
B. Current Direction
Total (degrees)
Tidal (degrees)
Non-tidal (degrees)
0
90
180
270
360
236
237
238
239
240
241
242
243
244
Julian Day

Figure 3.5.1.3.B

LATEX Mooring 13 Middle Meter

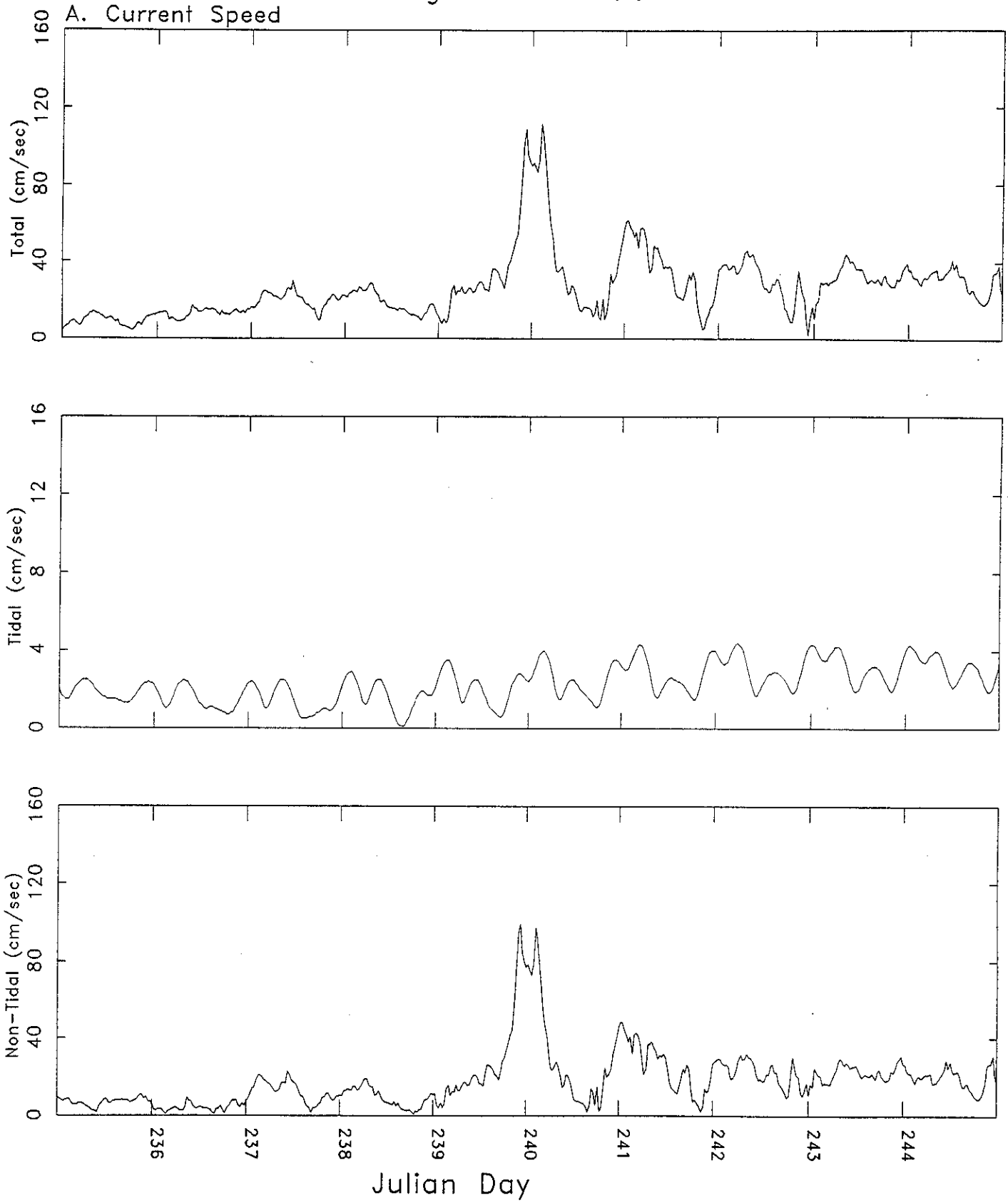

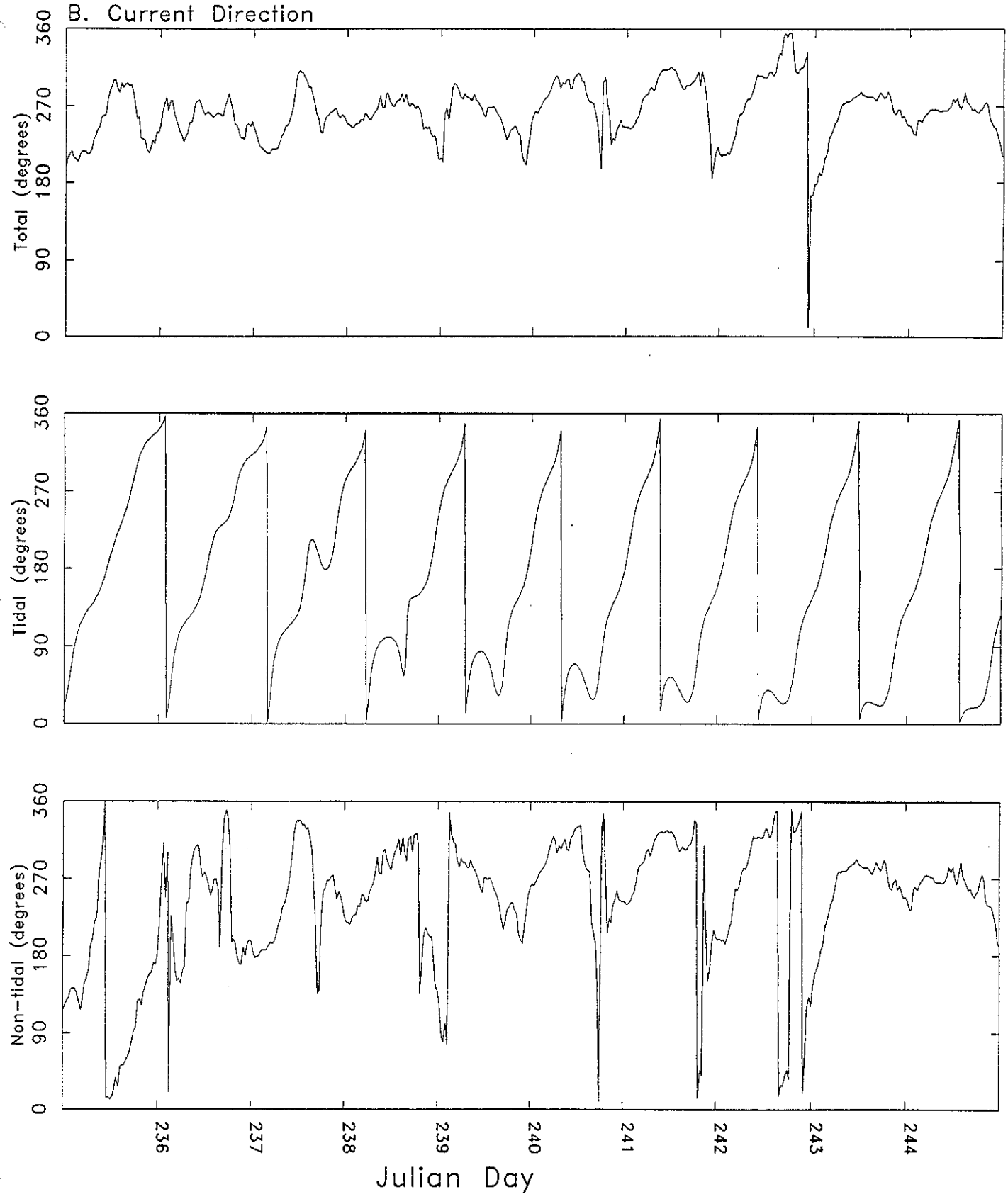
B. Current Direction
Total (degrees)
Tidal (degrees)
Non-tidal (degrees)
0
90
180
270
360
236
237
238
239
240
241
242
243
244
Julian Day

Figure 3.5.1.3.C

LATEX Mooring 13 Bottom Meter

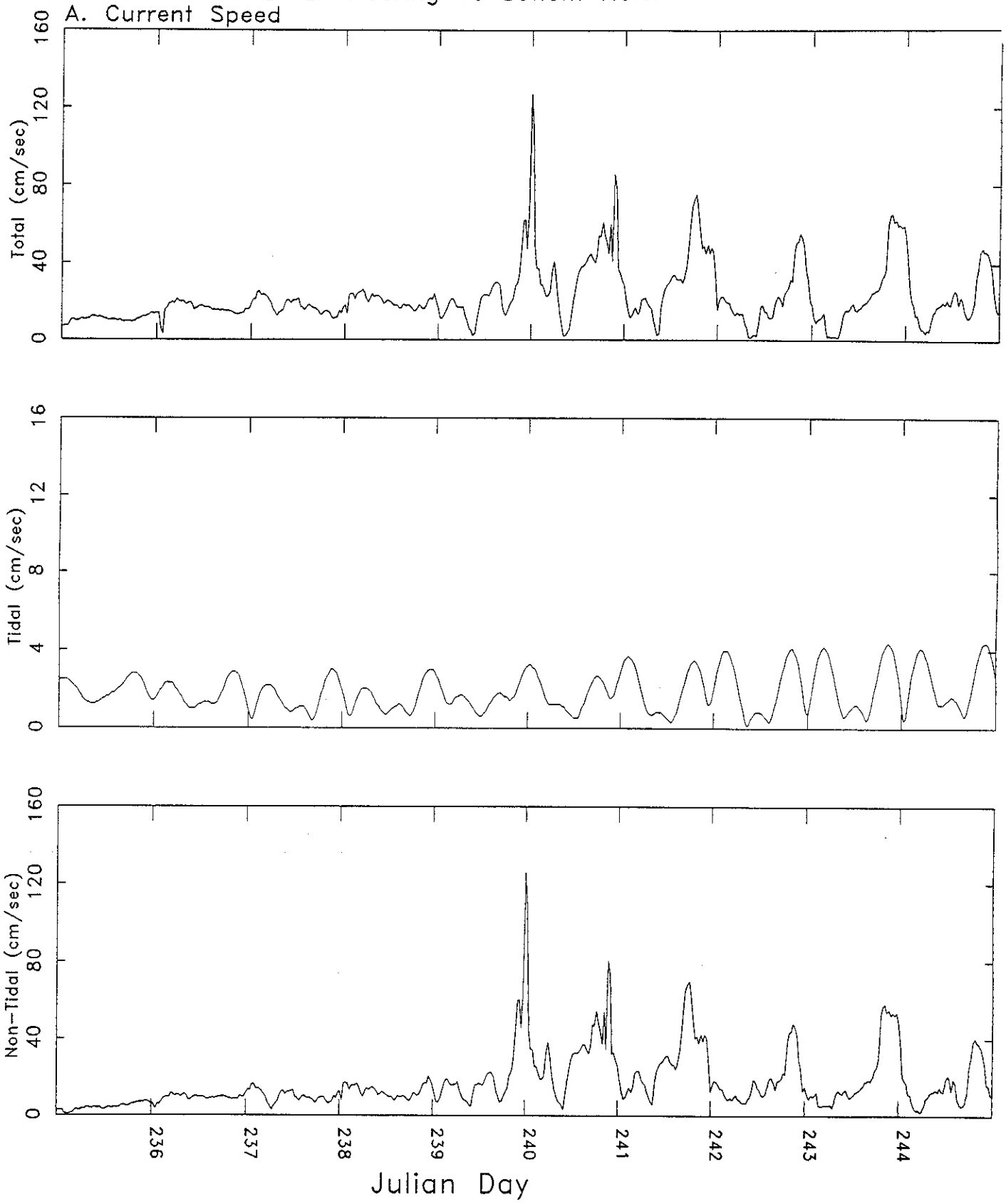

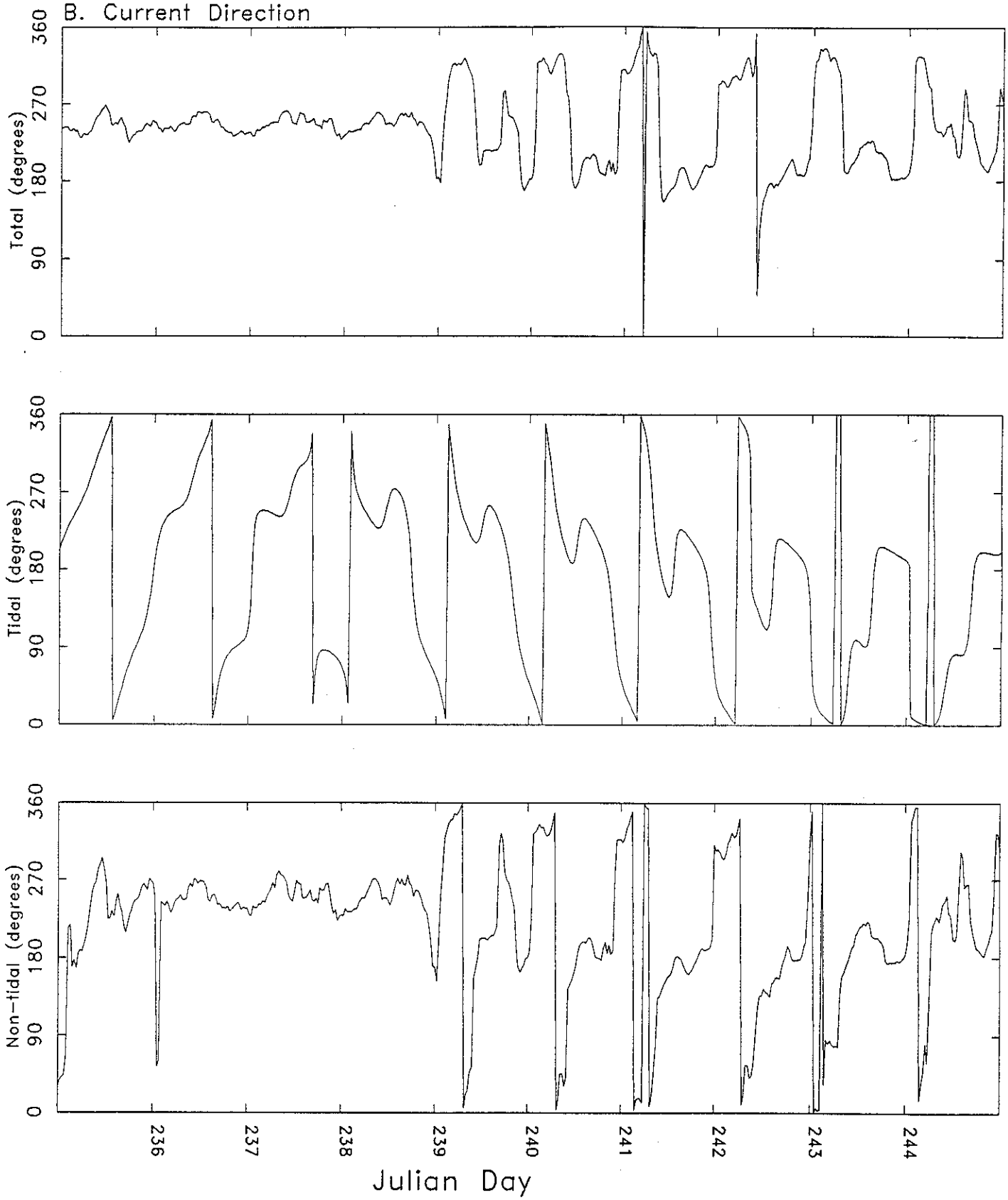
B. Current Direction
Total (degrees)
Tidal (degrees)
Non-tidal (degrees)
0
90
180
270
360
236
237
238
239
240
241
242
243
244
Julian Day

Figure 3.5.1.4.A
LATEX Mooring 14 Top Meter

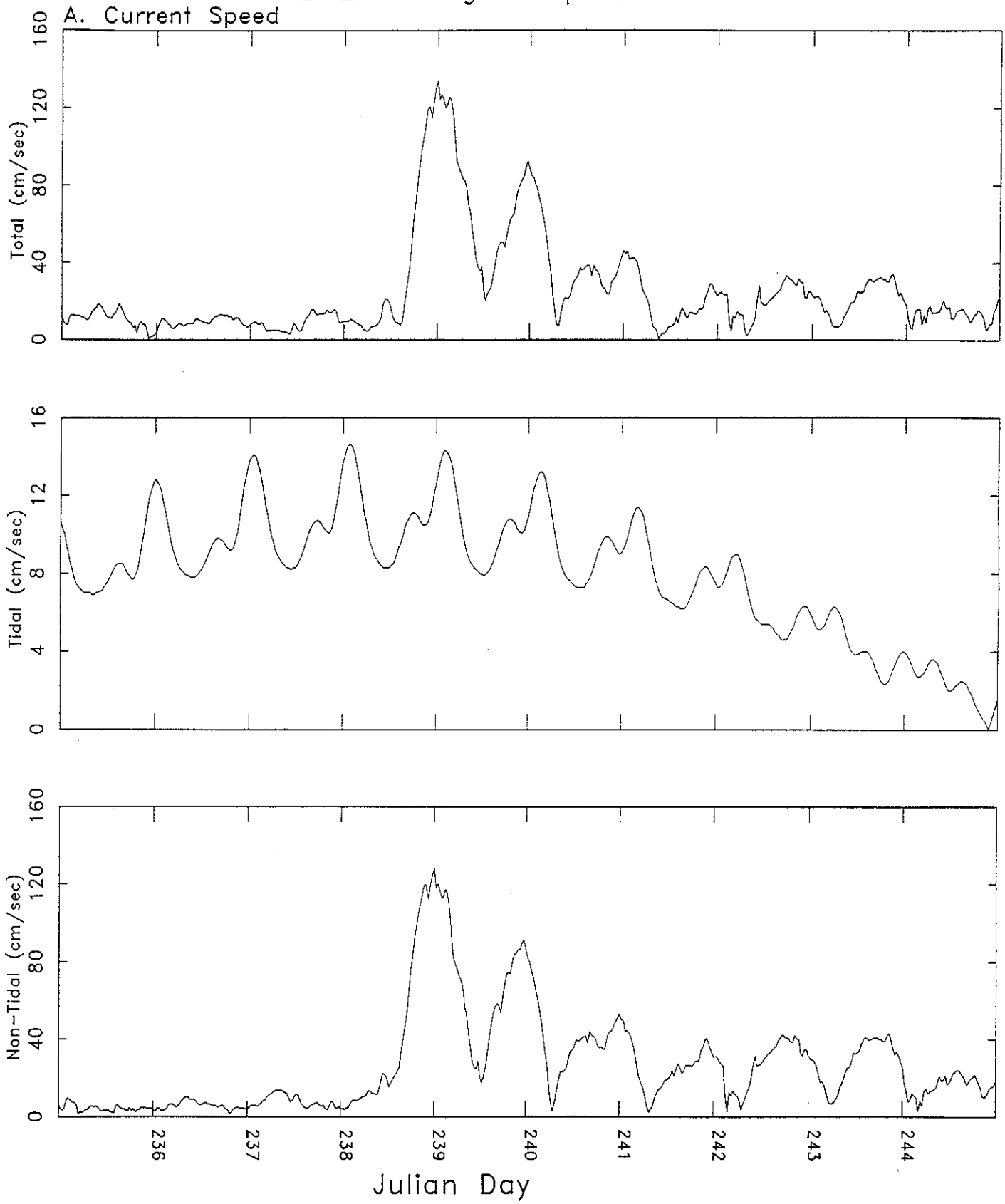

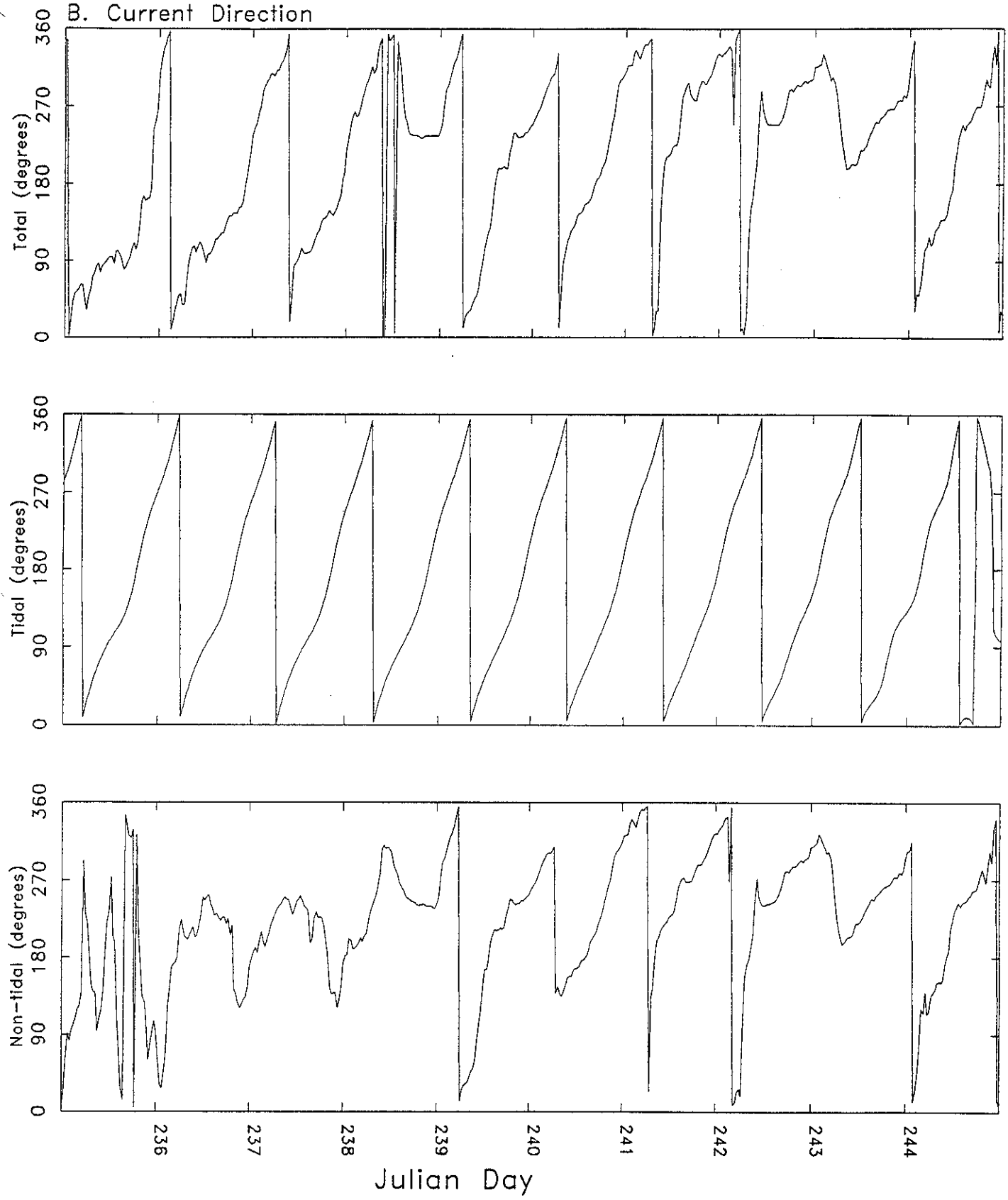
B. Current Direction
Total (degrees)
Tidal (degrees)
Non-tidal (degrees)
0
90
180
270
360
236
237
238
239
240
241
242
243
244
Julian Day

Figure 3.5.1.4.B

LATEX Mooring 14 Bottom Meter

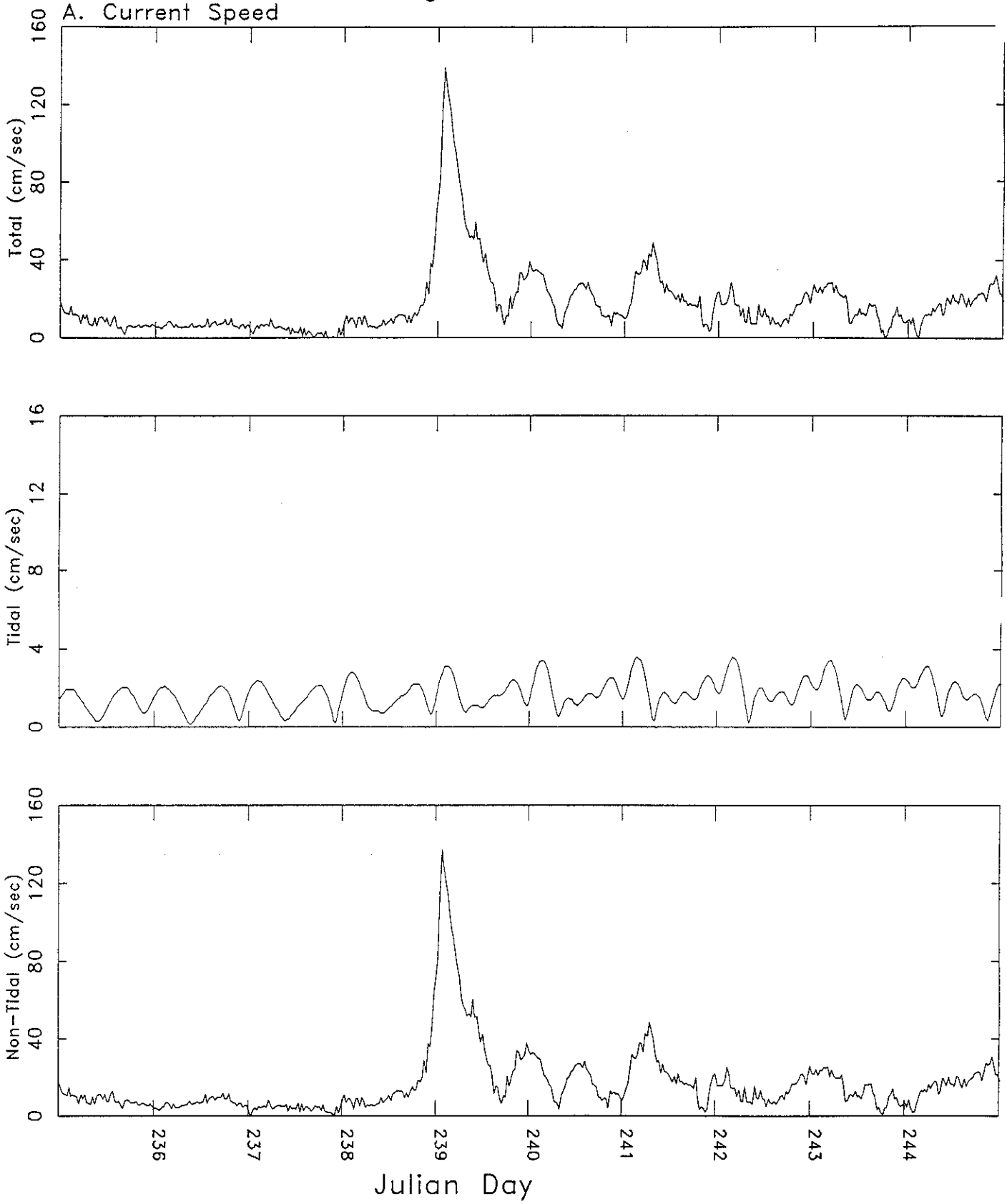

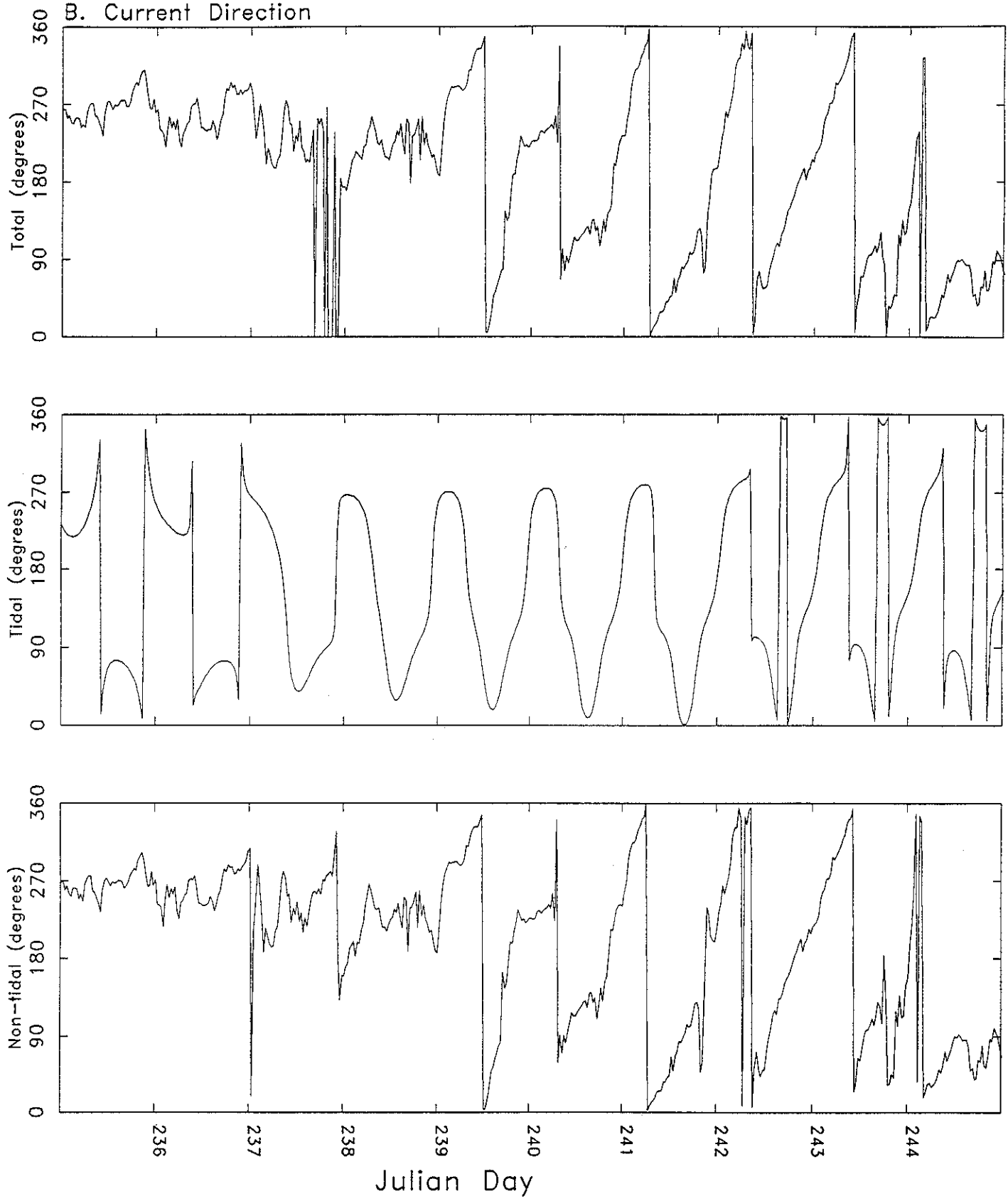
B. Current Direction
Total (degrees)
Tidal (degrees)
Non-tidal (degrees)
0
90
180
270
360
236
237
238
239
240
241
242
243
244
Julian Day

Figure 3.5.1.5.A
LATEX Mooring 15 Top Meter

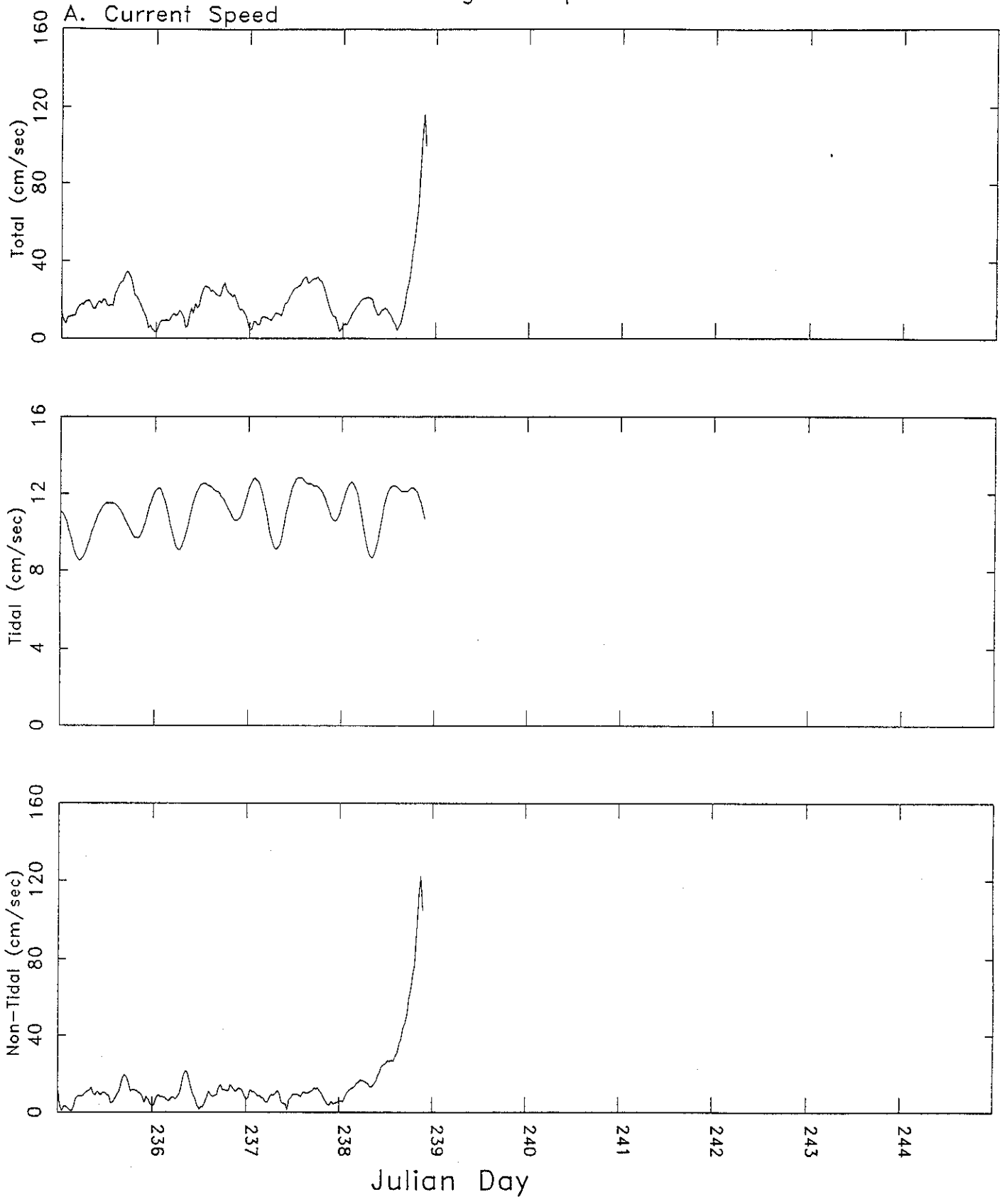

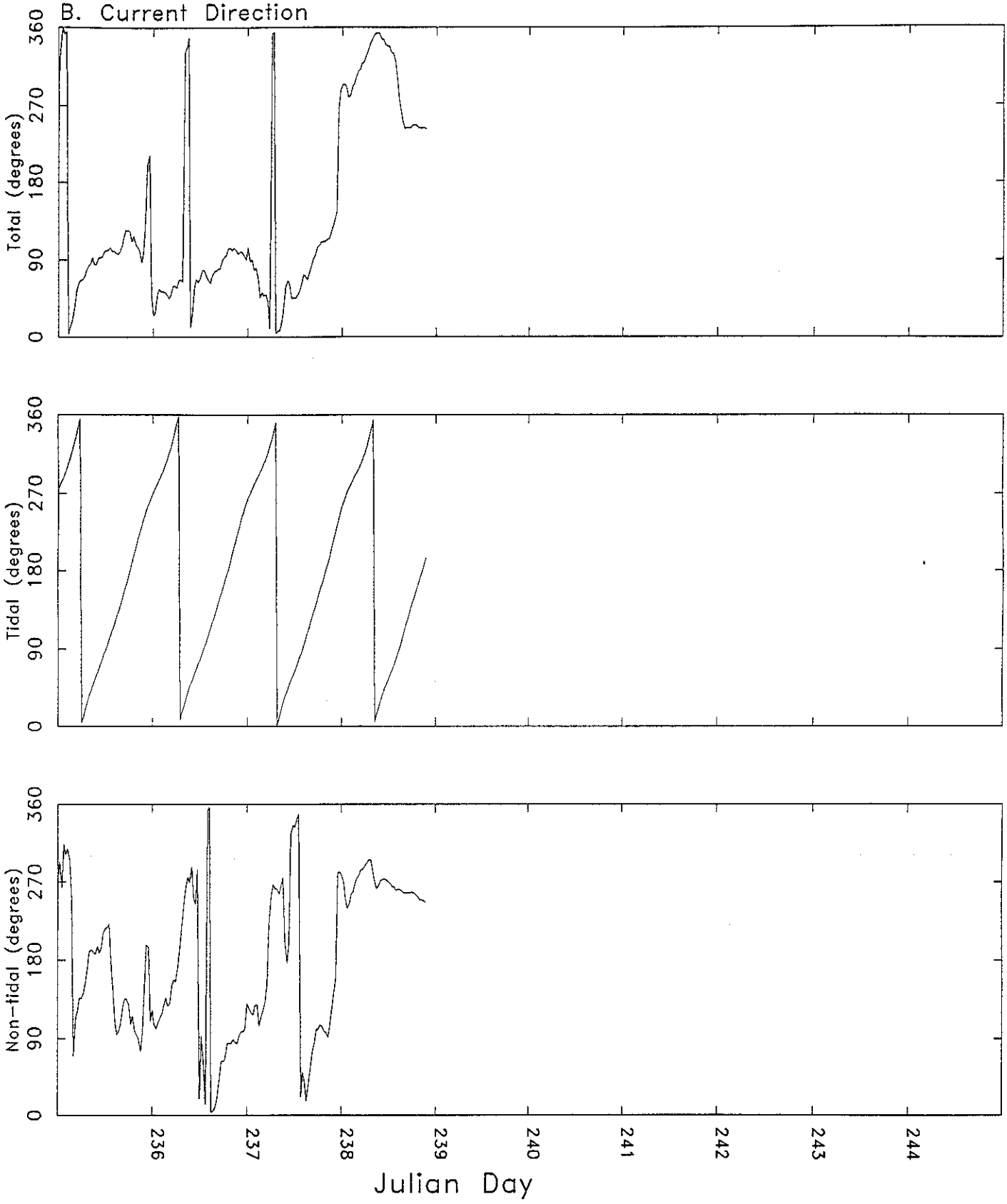
B. Current Direction
Total (degrees)
Tidal (degrees)
Non-tidal (degrees)
0
90
180
270
360
236
237
238
239
240
241
242
243
244
Julian Day

Figure 3.5.1.5.B

LATEX Mooring 15 Bottom Meter

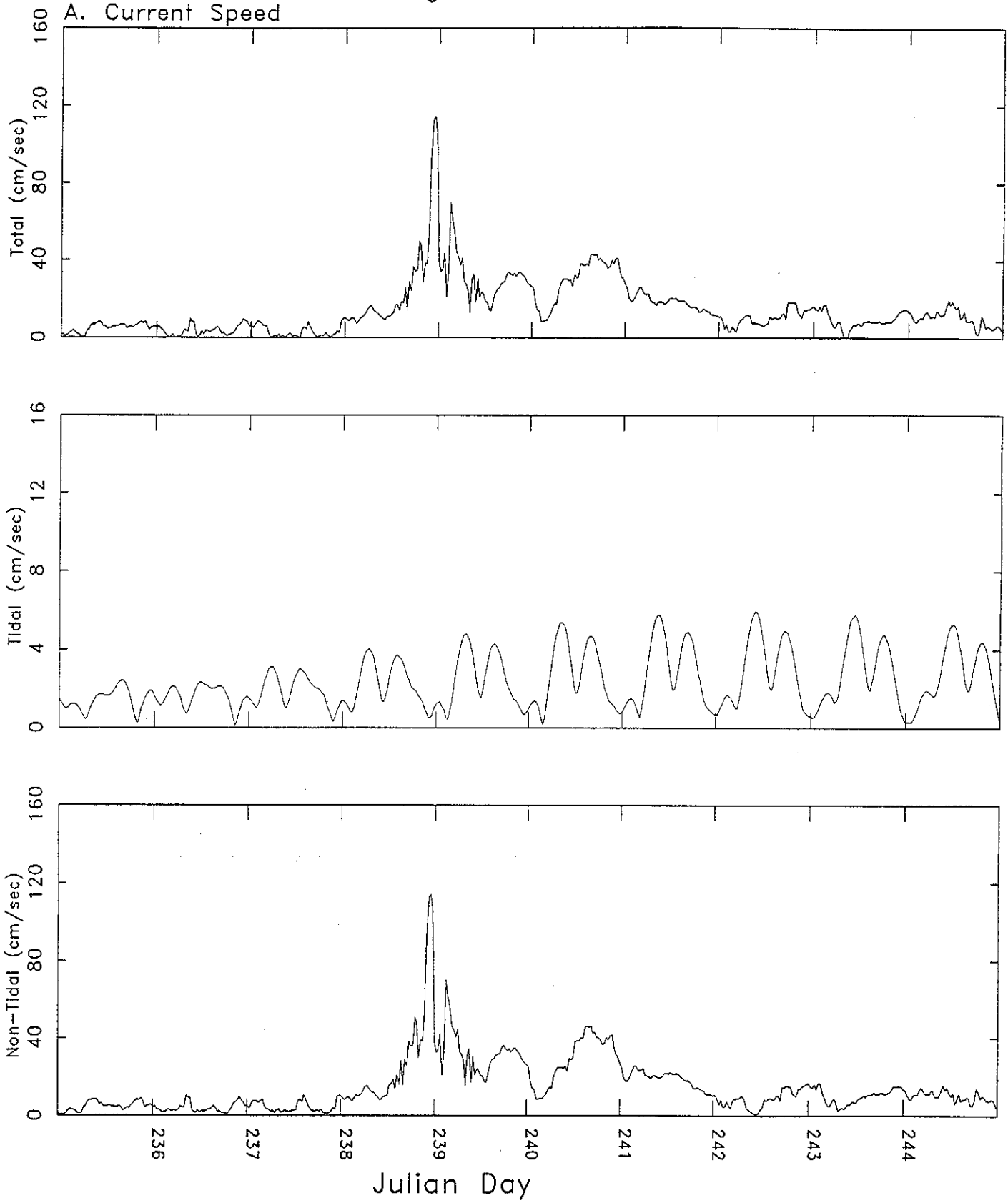

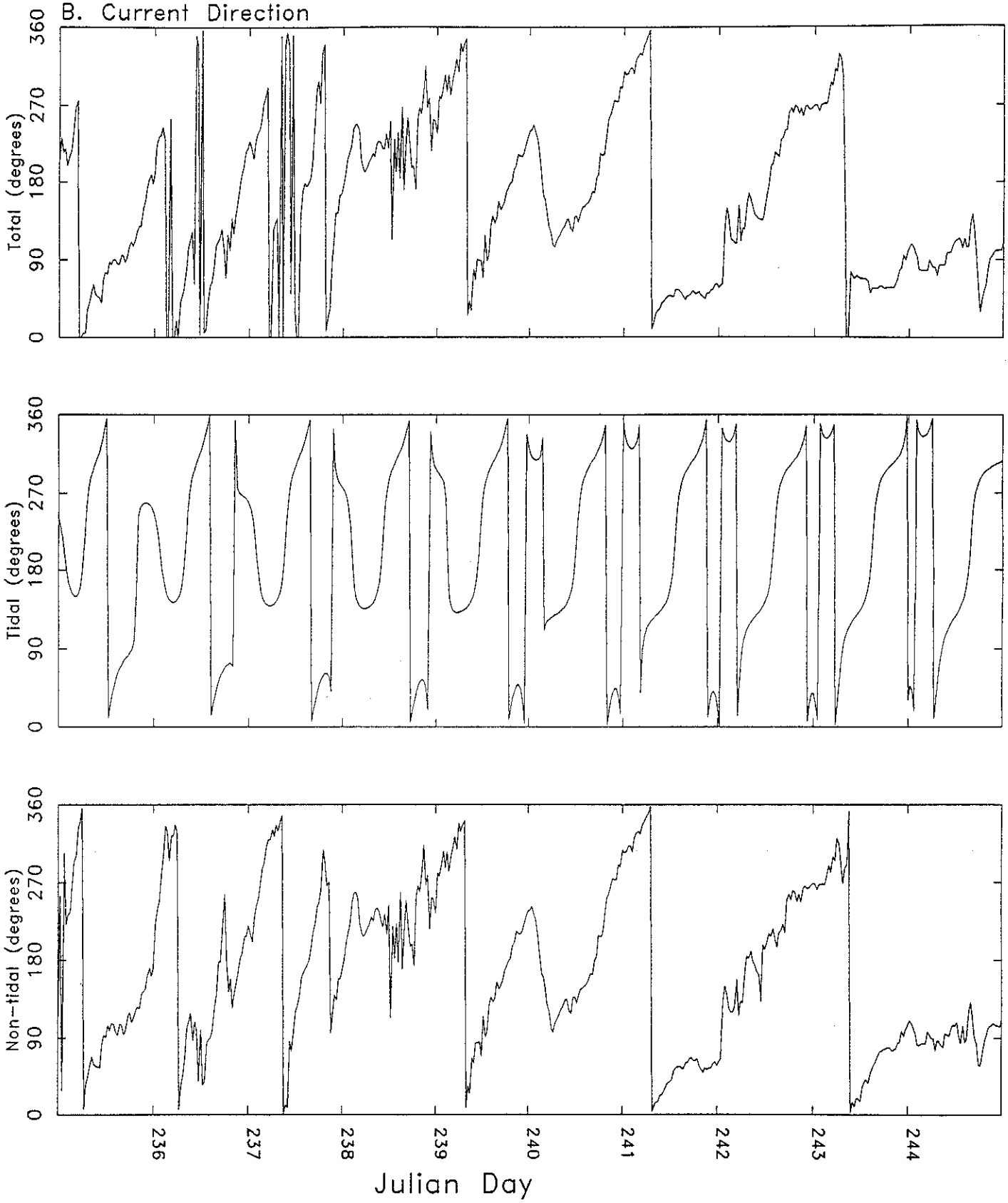
B. Current Direction
Total (degrees)
Tidal (degrees)
Non-tidal (degrees)
0
90
180
270
360
236
237
238
239
240
241
242
243
244
Julian Day

Figure 3.5.1.6.A

LATEX Mooring 16 Bottom Meter

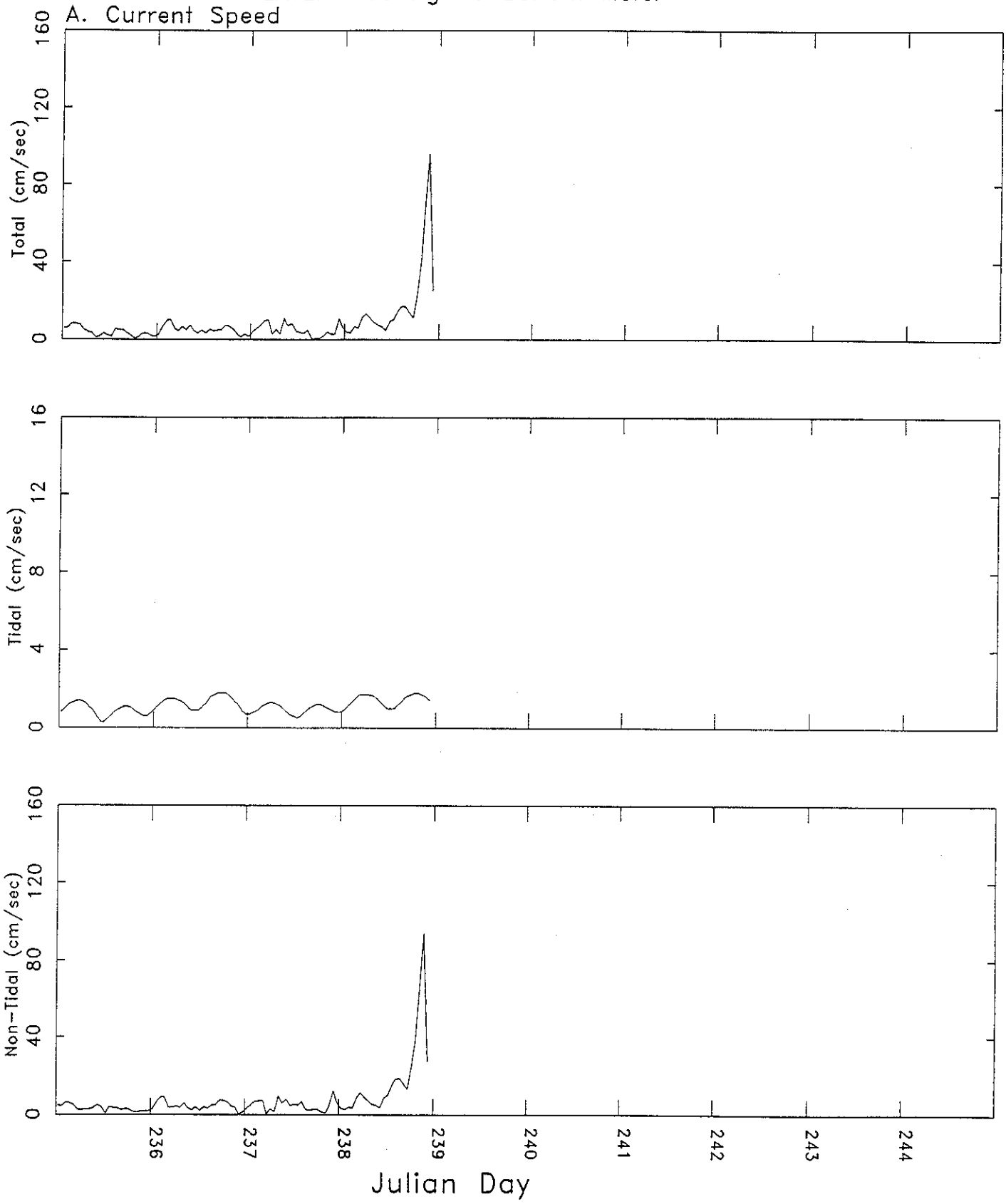

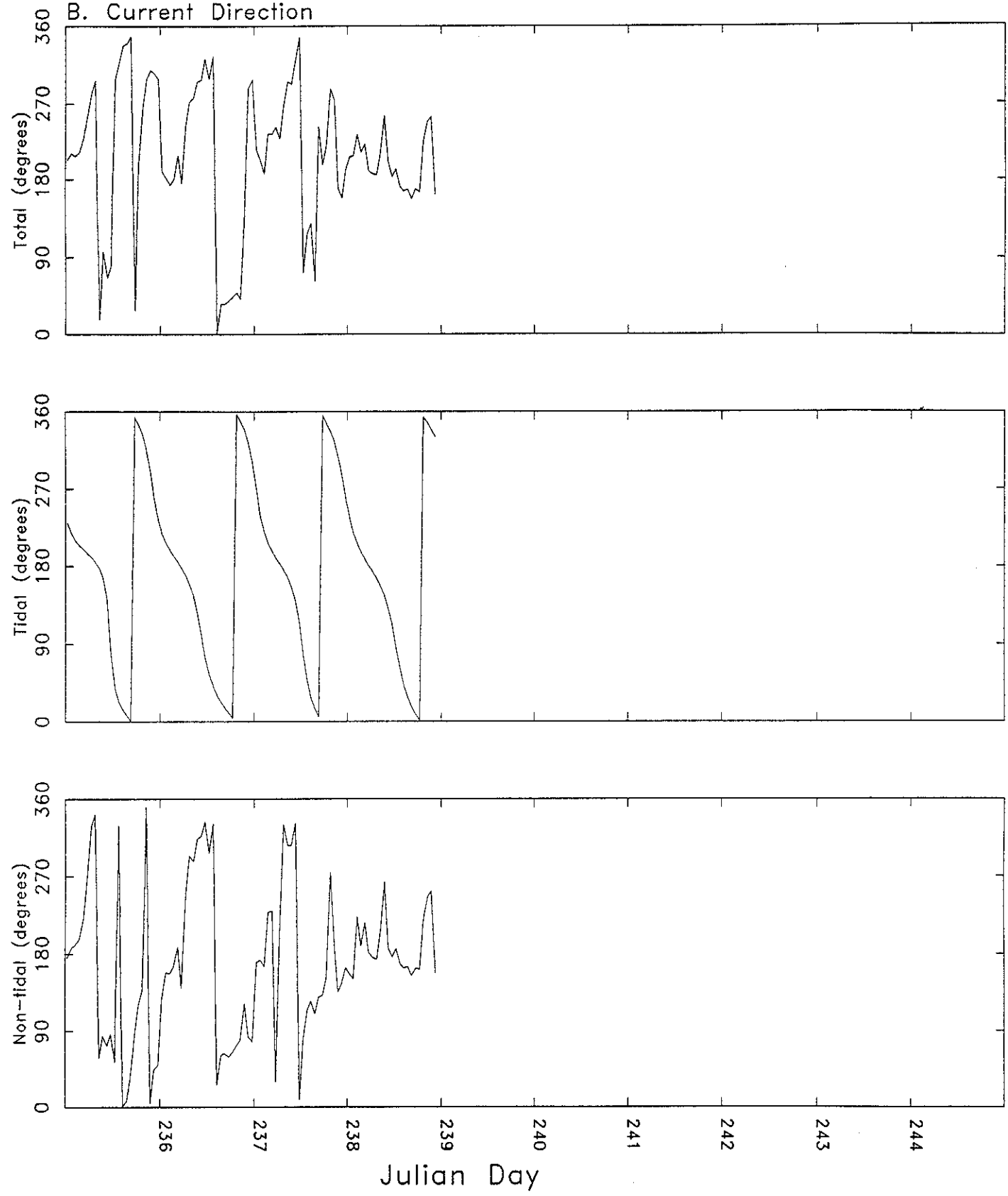
B. Current Direction
Total (degrees)
Tidal (degrees)
Non-tidal (degrees)
0
90
180
270
360
236
237
238
239
240
241
242
243
244
Julian Day

Figure 3.5.1.7.A
LATEX Mooring 18 Top Meter

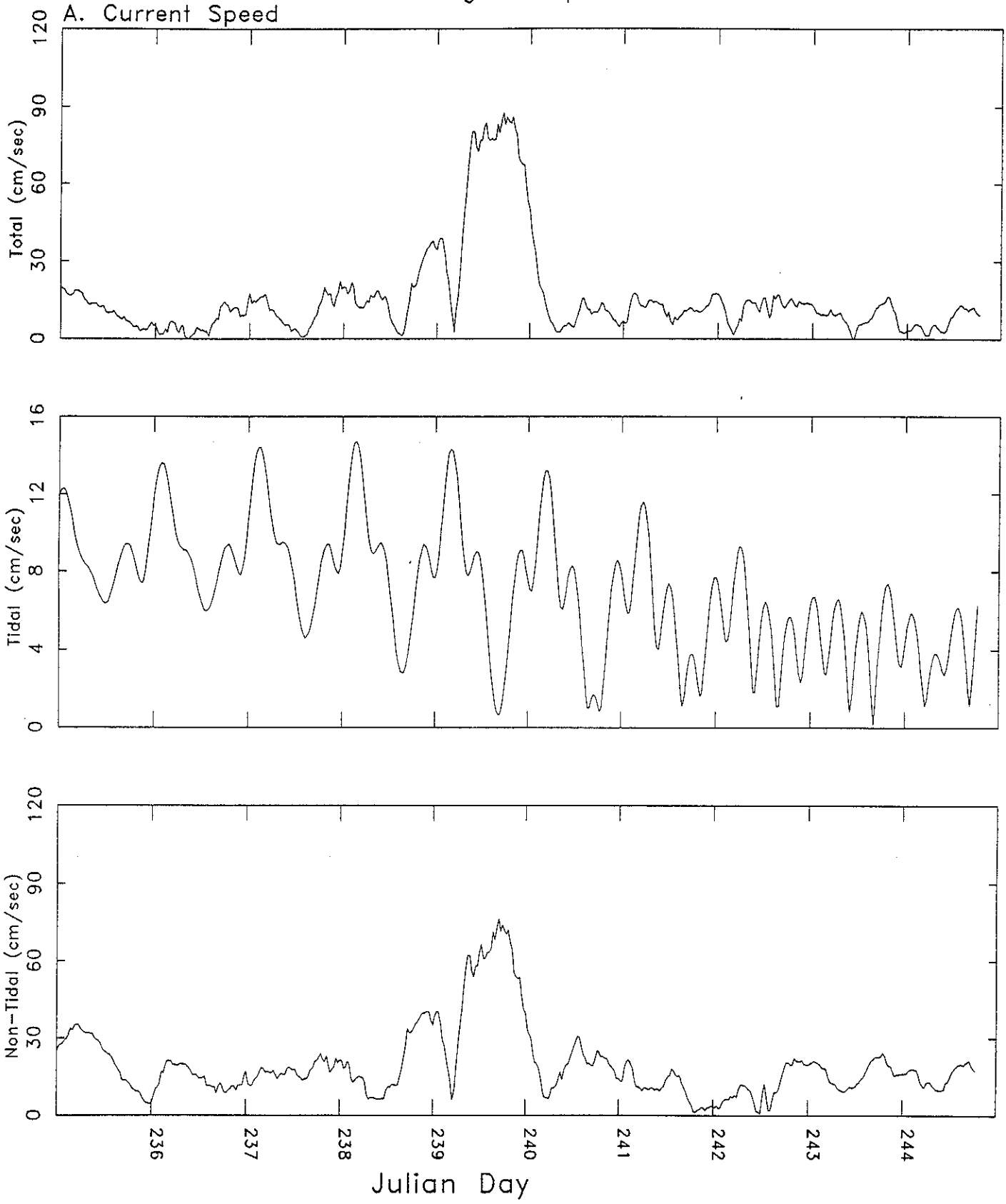

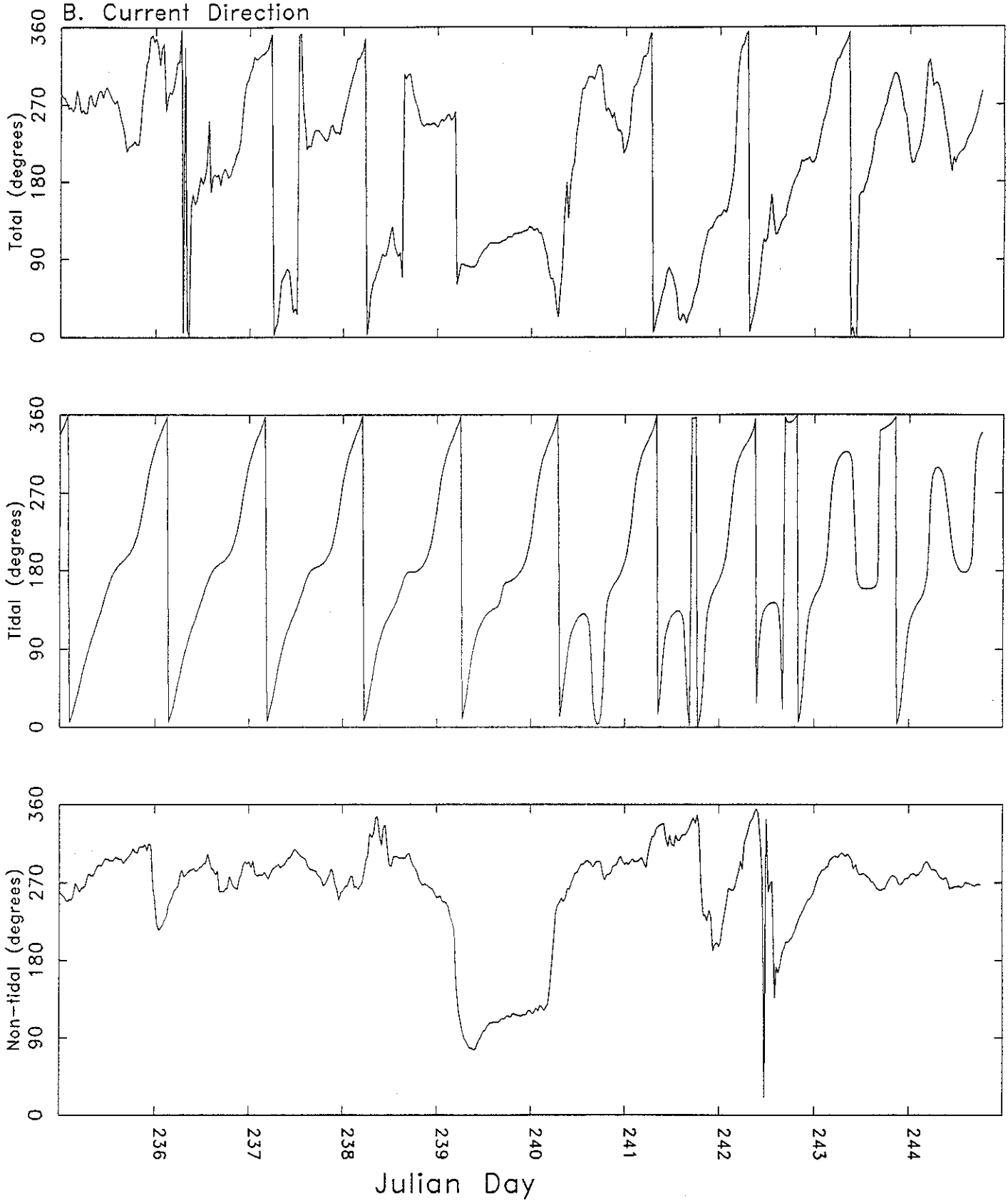
B. Current Direction
Total (degrees)
Tidal (degrees)
Non-tidal (degrees)
0
90
180
270
360
236
237
238
239
240
241
242
243
244
Julian Day

Figure 3.5.1.7.B

LATEX Mooring 18 Bottom Meter

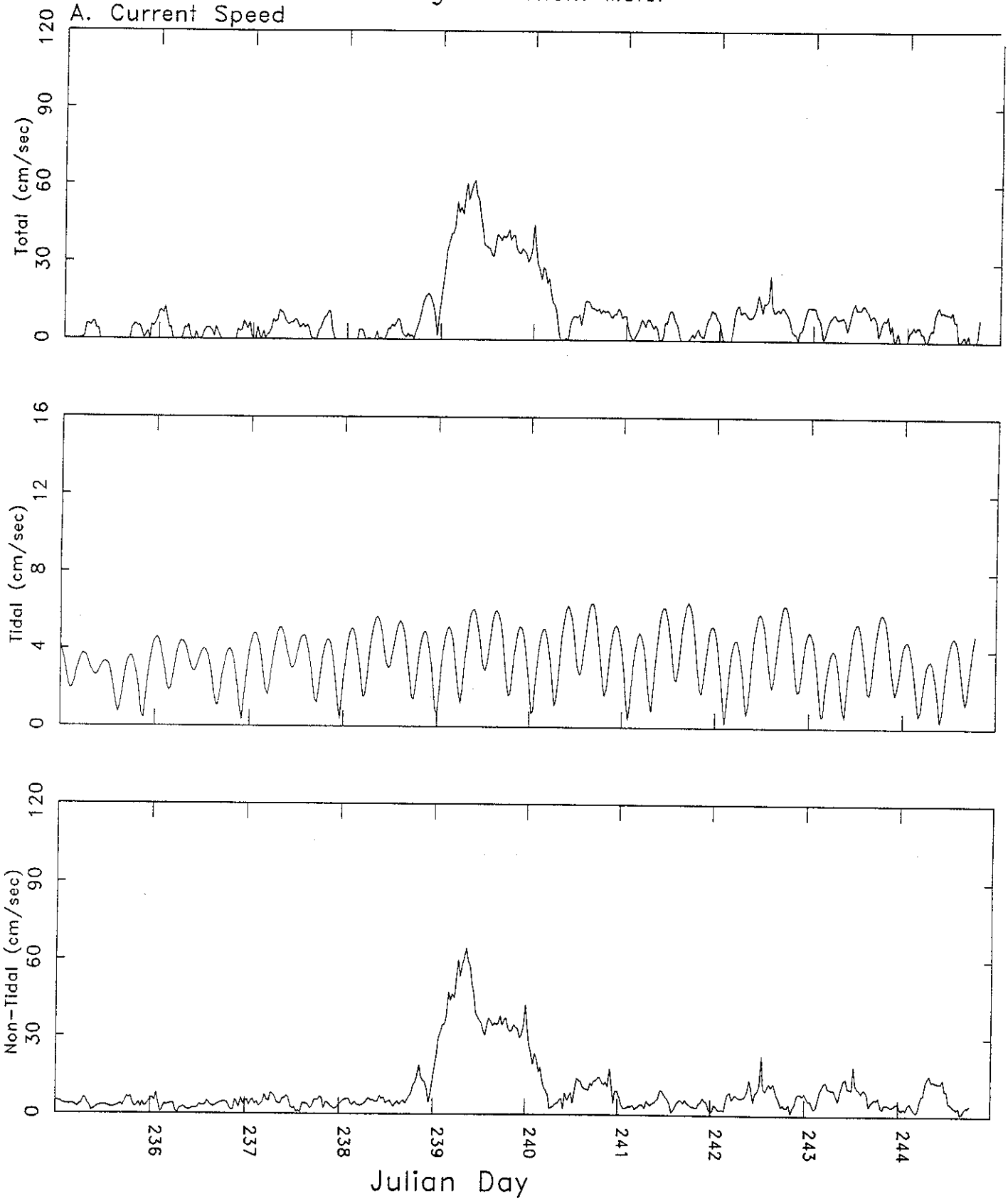

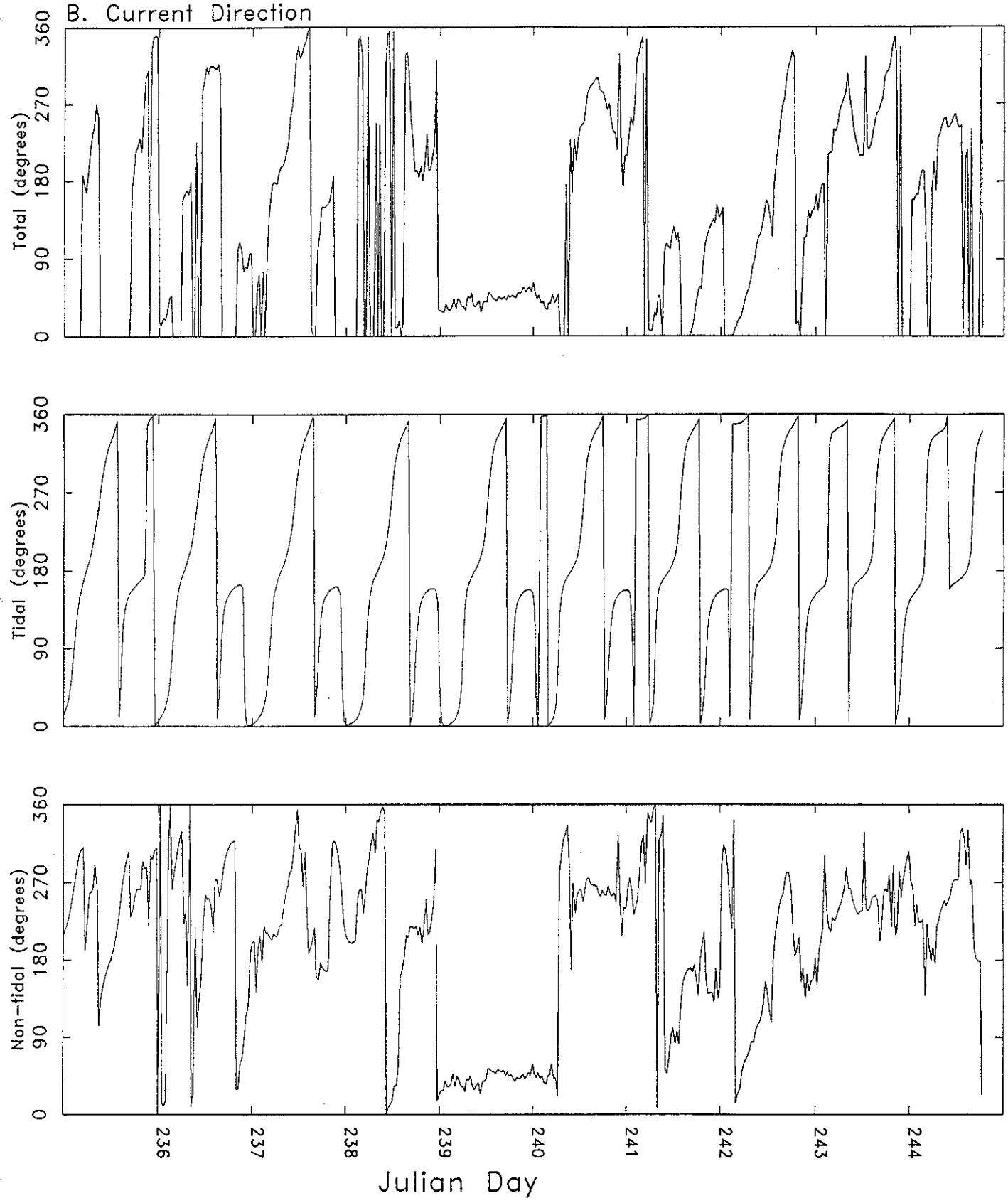
B. Current Direction
Total (degrees)
Tidal (degrees)
Non-tidal (degrees)
0
90
180
270
360
236
237
238
239
240
241
242
243
244
Julian Day

Figure 3.5.1.8.A
LATEX Mooring 19 Top Meter

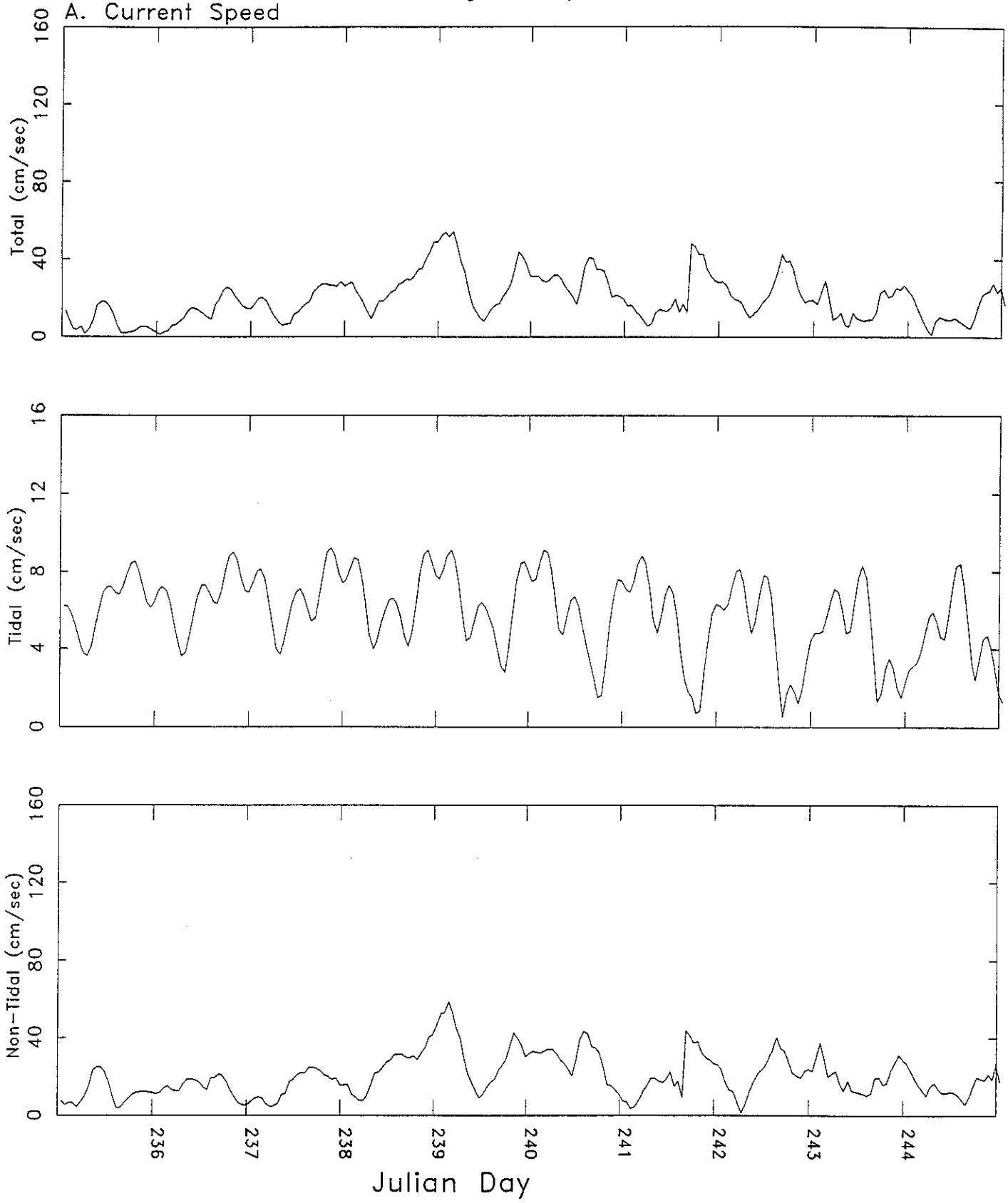

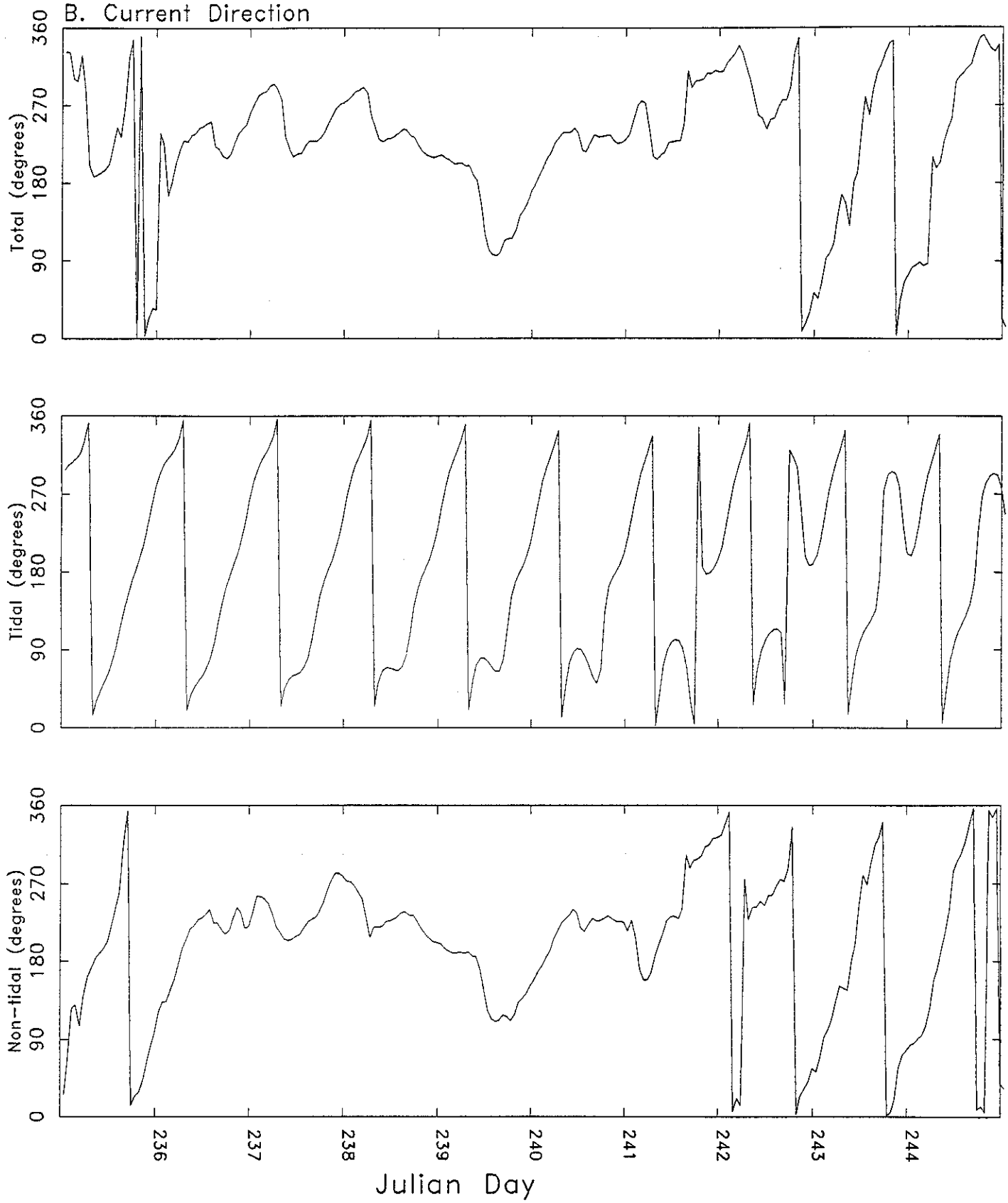
B. Current Direction
Total (degrees)
Tidal (degrees)
Non-tidal (degrees)
0
90
180
270
360
236
237
238
239
240
241
242
243
244
Julian Day

Figure 3.5.1.8.B

LATEX Mooring 19 Middle Meter

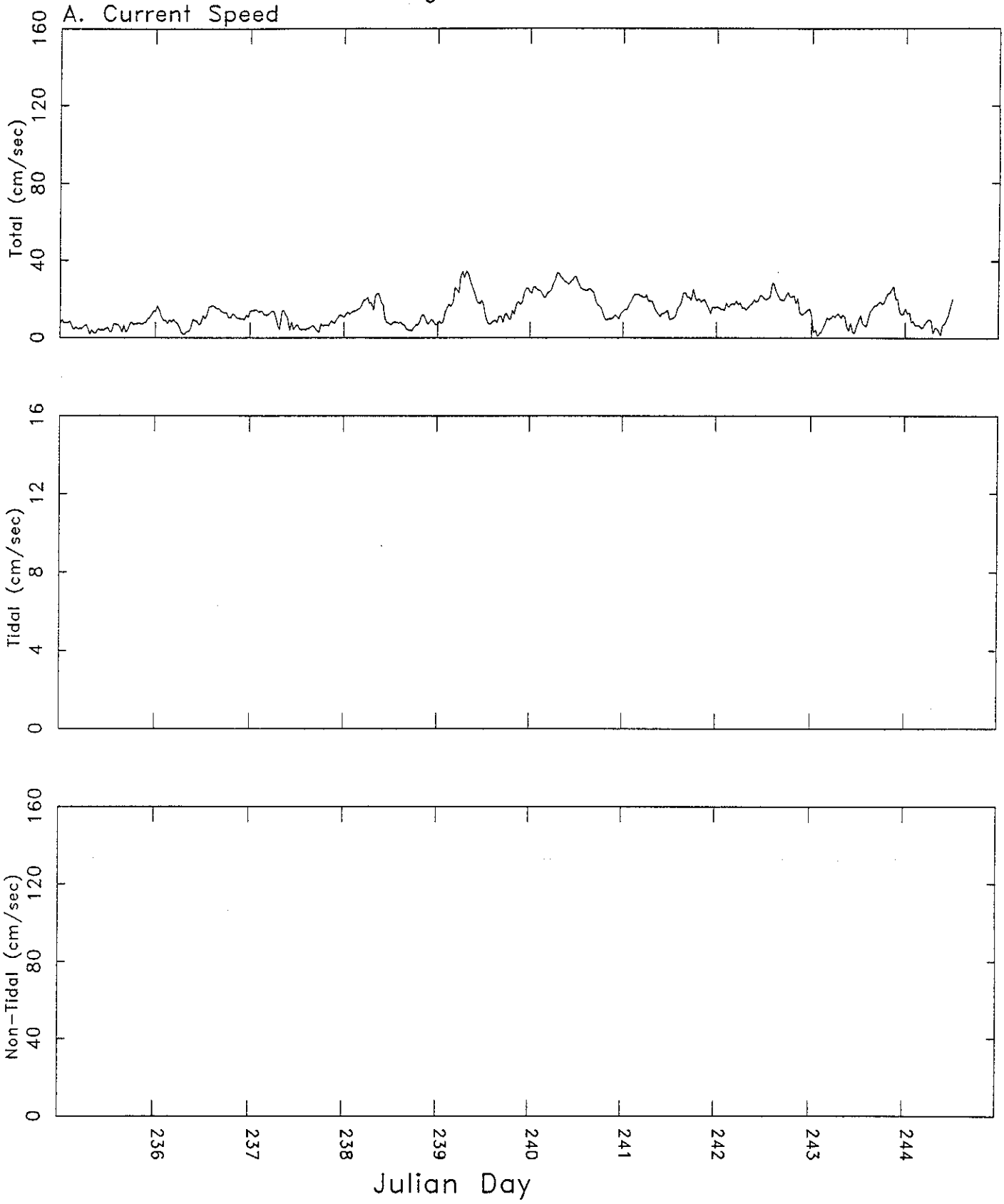

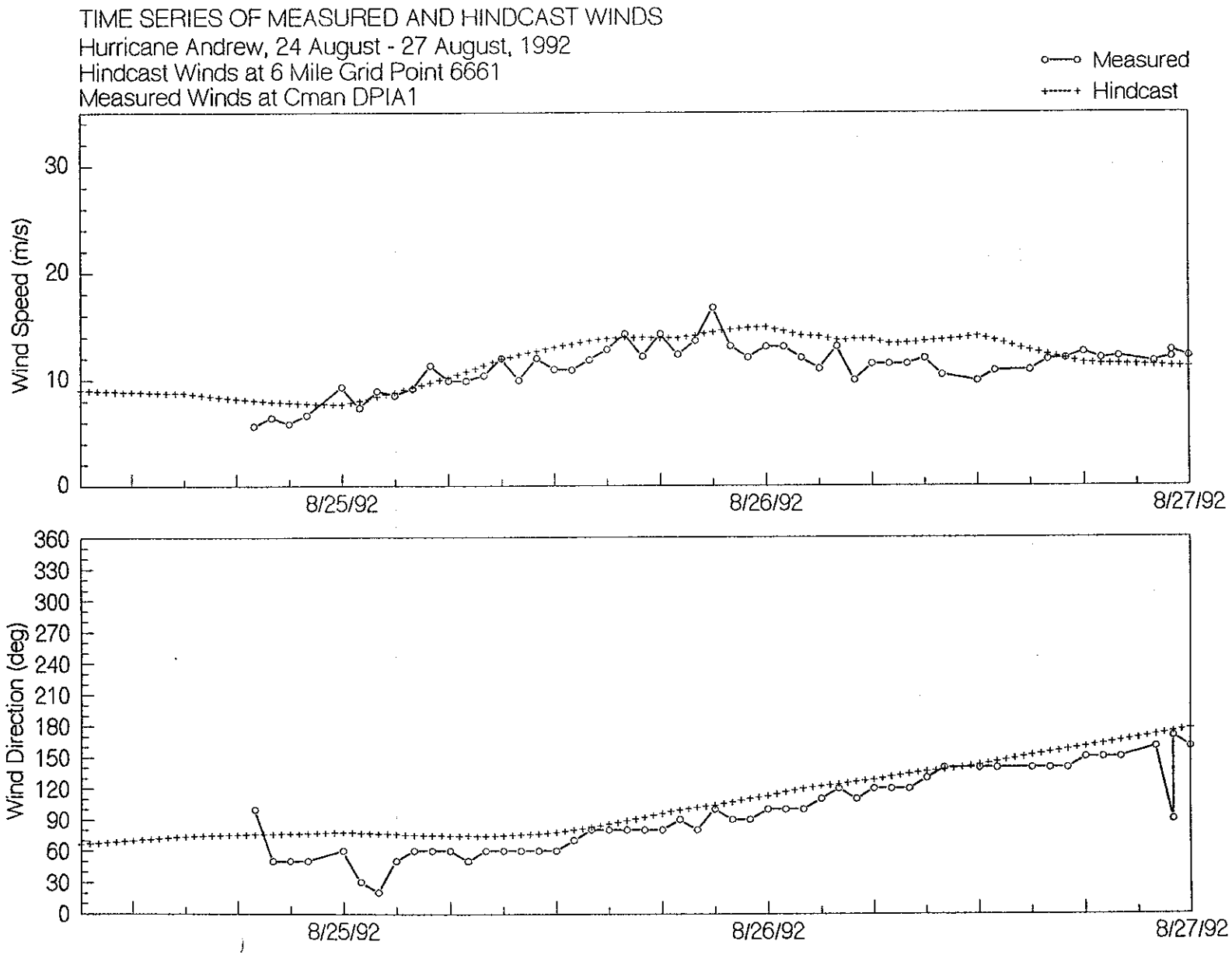

Figure 3.18 Modeled and measured wind speed and direction (at 20 meters) at DPIA C-MAN.

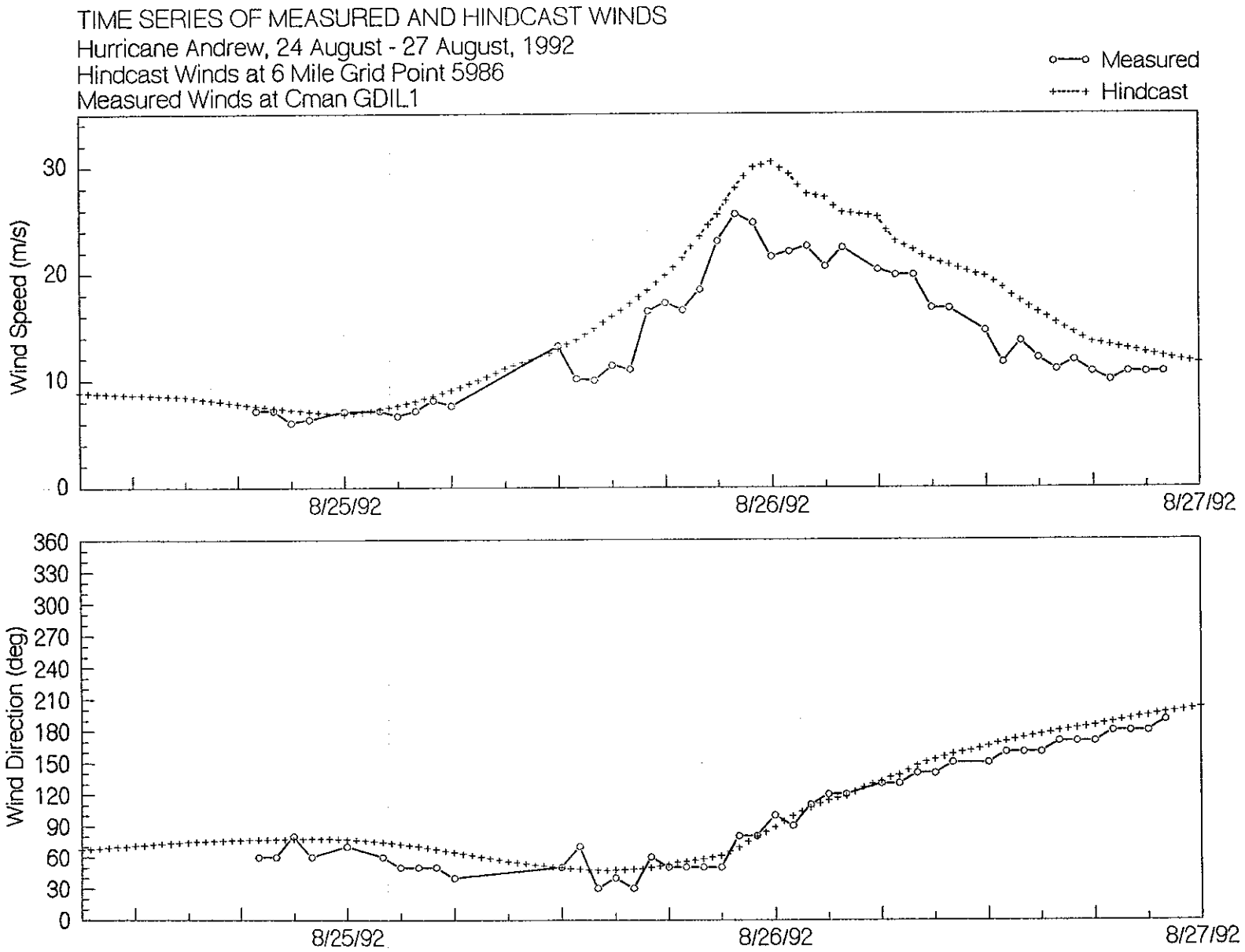

Figure 3.19 Modeled and measured wir speed and direction (at 20 meters) at GDIL C-MAN.

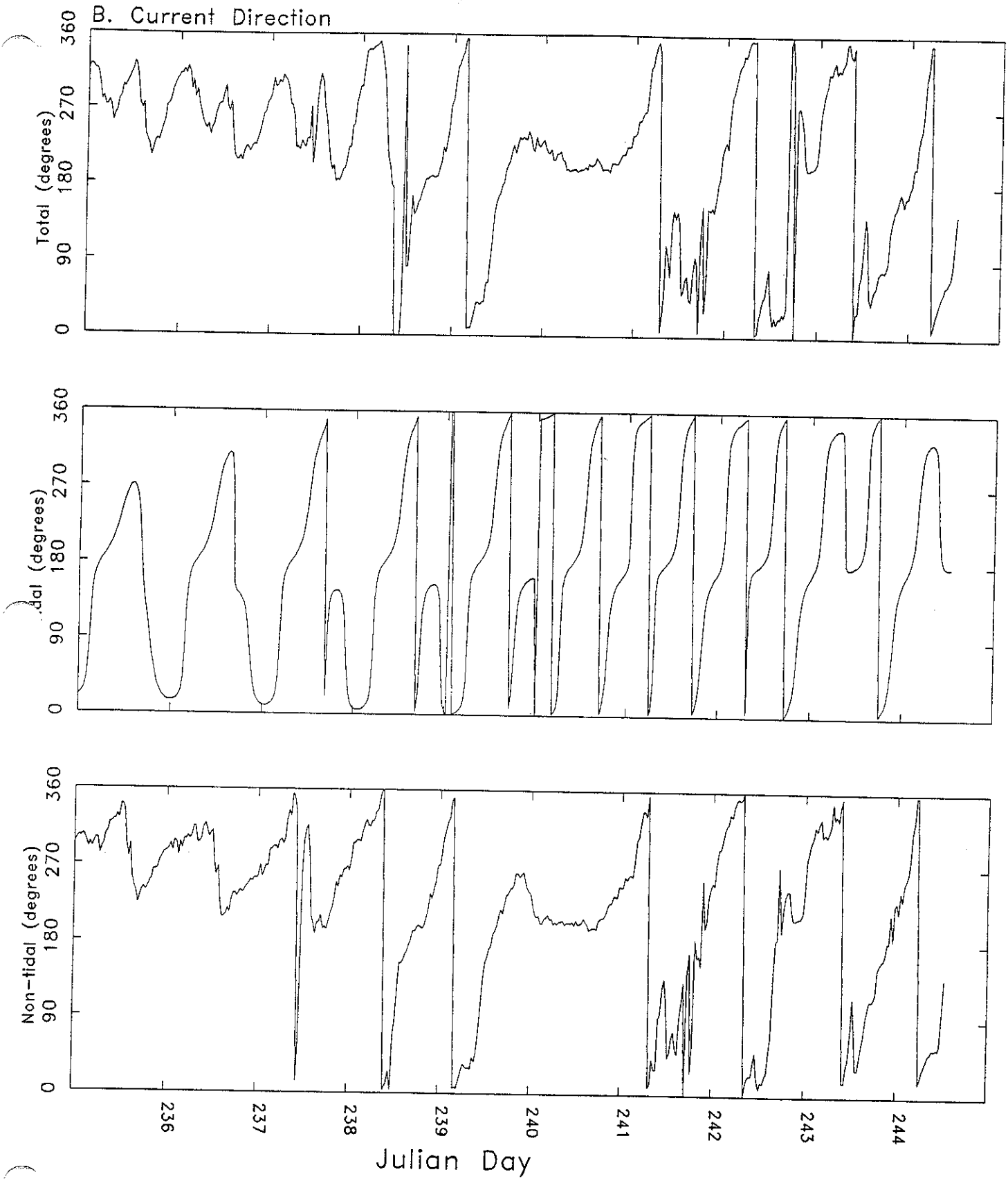
B. Current Direction
Total (degrees)
Tidal (degrees)
Non-tidal (degrees)
0
90
180
270
360
236
237
238
239
240
241
242
243
244
Julian Day

REFERENCES

Breaker, L.C., L.D. Burroughs, Y.Y. Chao, J.F Culp, N.L Guinasso, Jr., R.L Teboulle and C.R. Wong, 1994: The Impact of Hurricane Andrew on the Near-Surface Marine Environment in the Bahamas and the Gulf of Mexico. OPC Technical Note/NMC Office, Wahington, D.C.,1994 (in progress).

Coastal-Marine Automated Network (C-MAN) Users Guide. Techincal Report 1203-01.03-2B. NOAA, NDBC, September 1992.

DiMarco, S.F., F.J. Kelly and N.L. Guinasso, Jr., 1994: Directional Wave Spectra on the Louisiana-Texas Shelf During Hurricane Andrew. Geochemical and Environmental Research Group, Texas A&M University (in progress).

Gilhousen, D.B., E.M. Meindl, M.J. Changery, P.L. Franks, M.G. Burgin and D.A. McKittrick, 1990: Climatic Summaries for NDBC Buoys and Stations Update 1. NOAA, NDBC.

Kelly, J.F., S.F. DiMarco, N.L. Guinasso, Jr., R.C. Hamilton and K.A. Kurrus, 1993: Calibration and Performance of the Pressure and Temperature Sensors in the Coastal Leasing, Inc., MiniSpec Directional Wave Gage. Texas A&M University, Dept. of Oceanography, Reference No. 93-07-T.

Rappaport, E.: Hurricane Andrew - A Preliminary Look. Mariners Weather Log, Fall 1992.

Stone, G.W., J.M. Grymes, III, K.D. Robbins, S.G. Underwood, G.D. Steyer, R.A. Muller, 1994, Shore and Beach 61(2), 2-12.

Tubb. M.: Industry Efforts Minimize Andrew's Destruction. Ocean Industry, October, 1992.

Appendix B.

Distribution of conventional synoptic surface observations at 3-hourly intervals in the Gulf of Mexico during the passage of hurricane Andrew. Reports of surface pressure and surface wind speed and direction are plotted for NDBC buoys (e.g. 42001), C-MAN stations (e.g. BUSL1) and transient ships (e.g. KGKV). Wind speeds are referred to equivalent neutral 20 m elevation. The two digits near the wind barb denote, respectively, the "tens" place of wind direction (e.g. 9 for 90 degrees) and the units place of wind speed in knots (e.g. 7 for 17 knots).

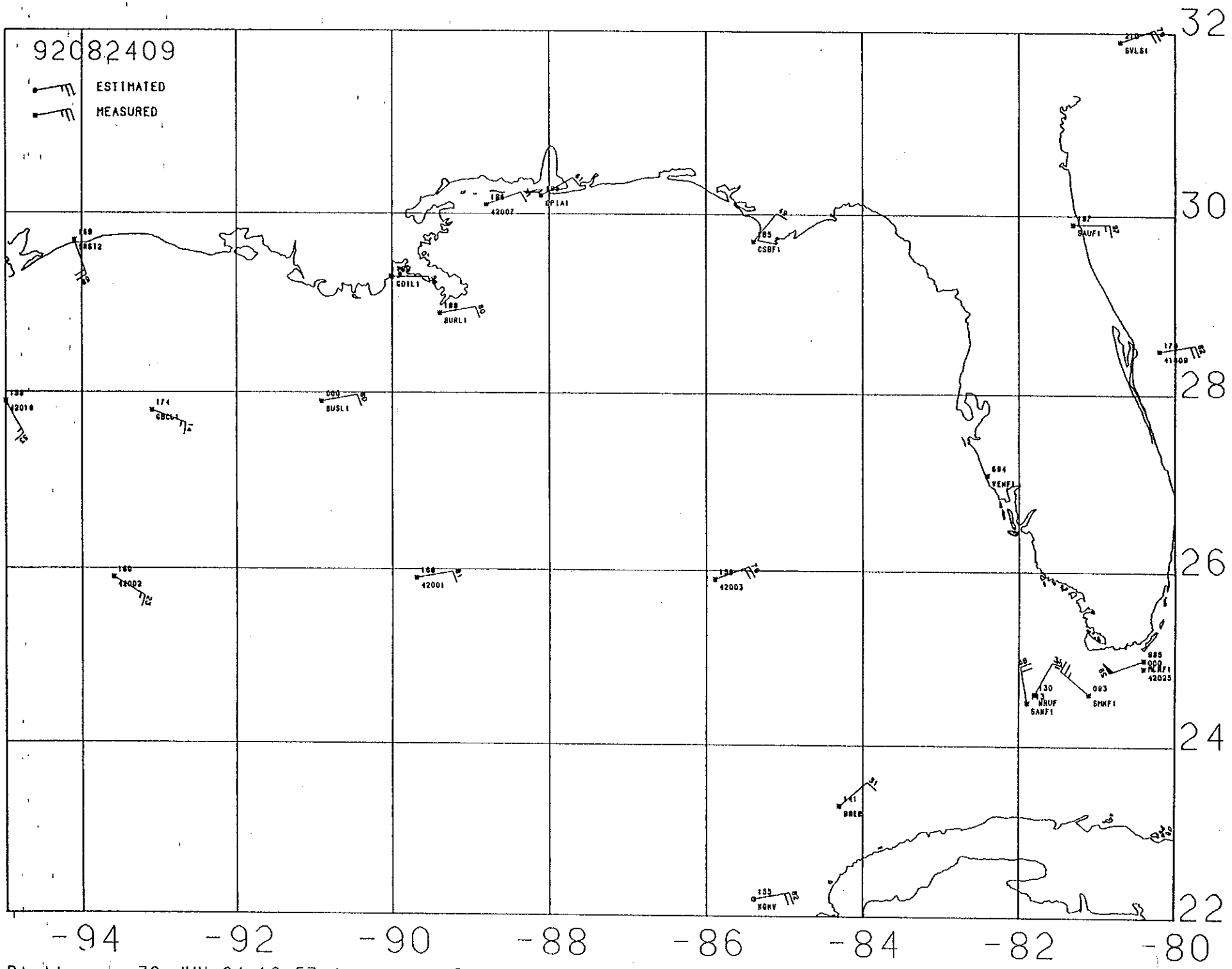

Plotted On 30-JUN-94 12:53 from file [MMANDREW.PLO]JANDREW92-SHIP.SORT;1 30-JUN-1994 11:32

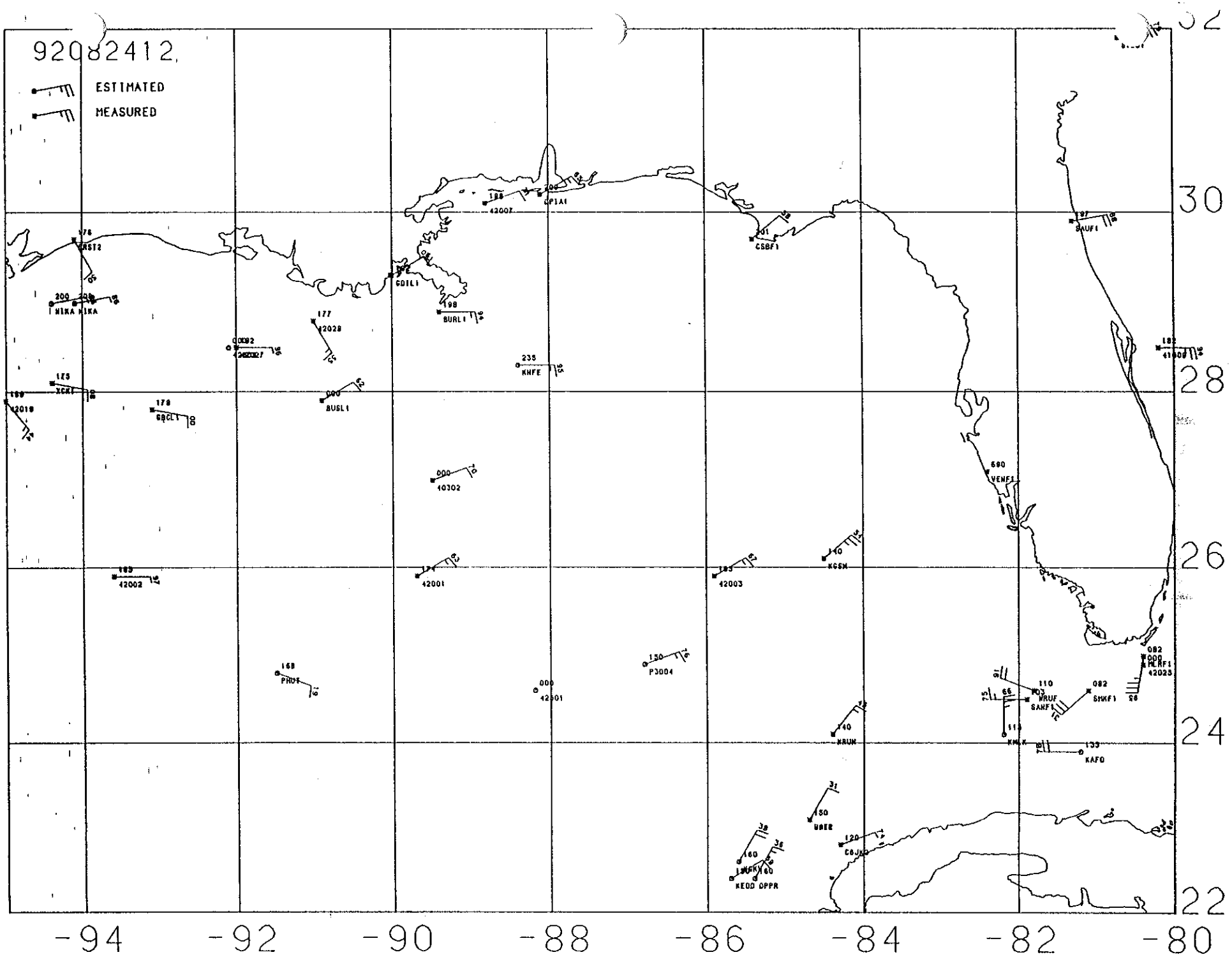
92082412
ESTIMATED
MEASURED
32
30
28
26
24
22
-94
-92
-90
-88
-86
-84
-82
-80
Plotted on 30-JUN-94 12:56 from file [MMANDREW.PLOT]ANDREW92-SHIP.SORT;1 30-JUN-1994 11:32

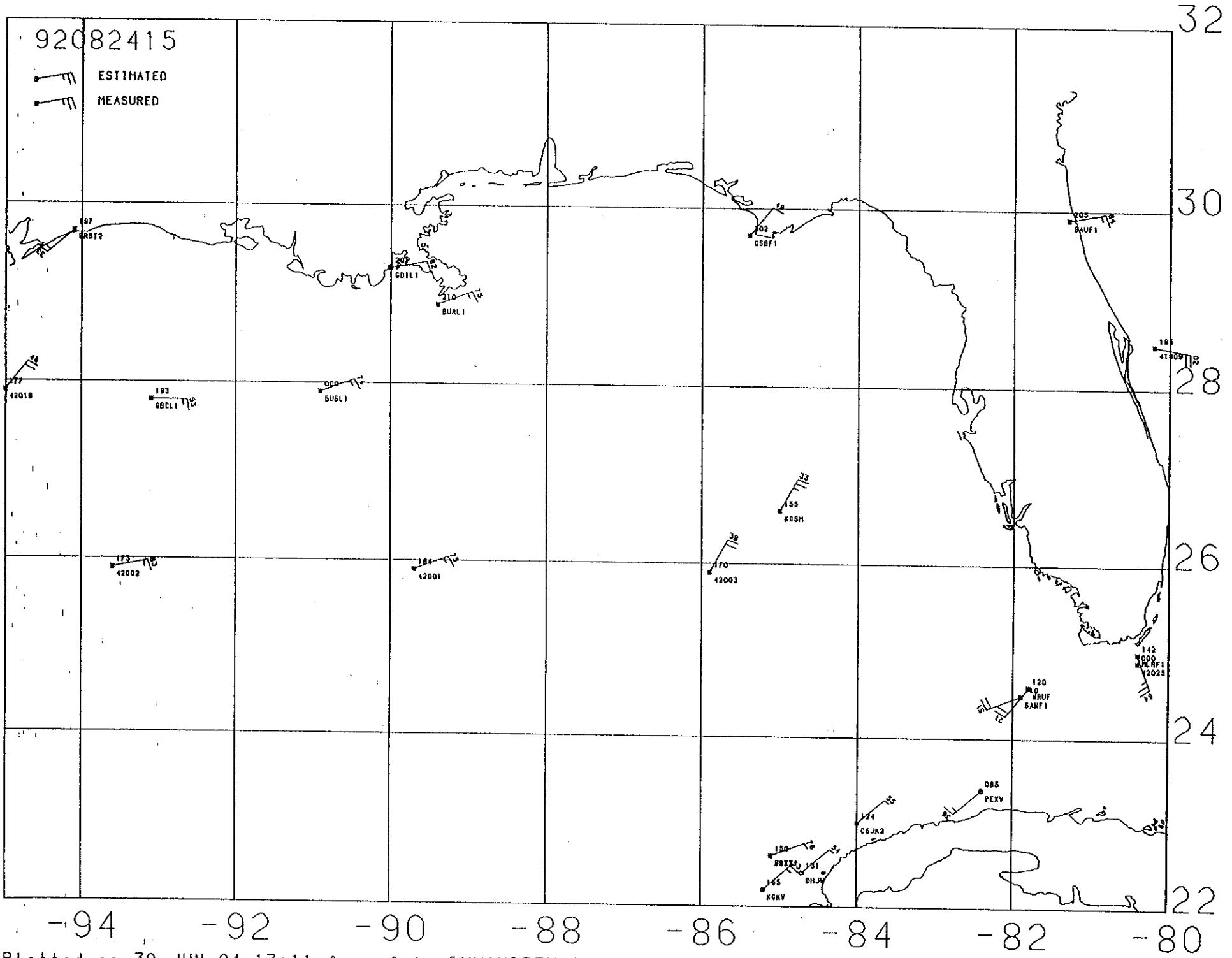

Plotted on 30-JUN-94 13:11 from file [MMANDREW.PL[illegible]]ANDREW92-SHIP.SORT;1 30-JUN-1994 11:32

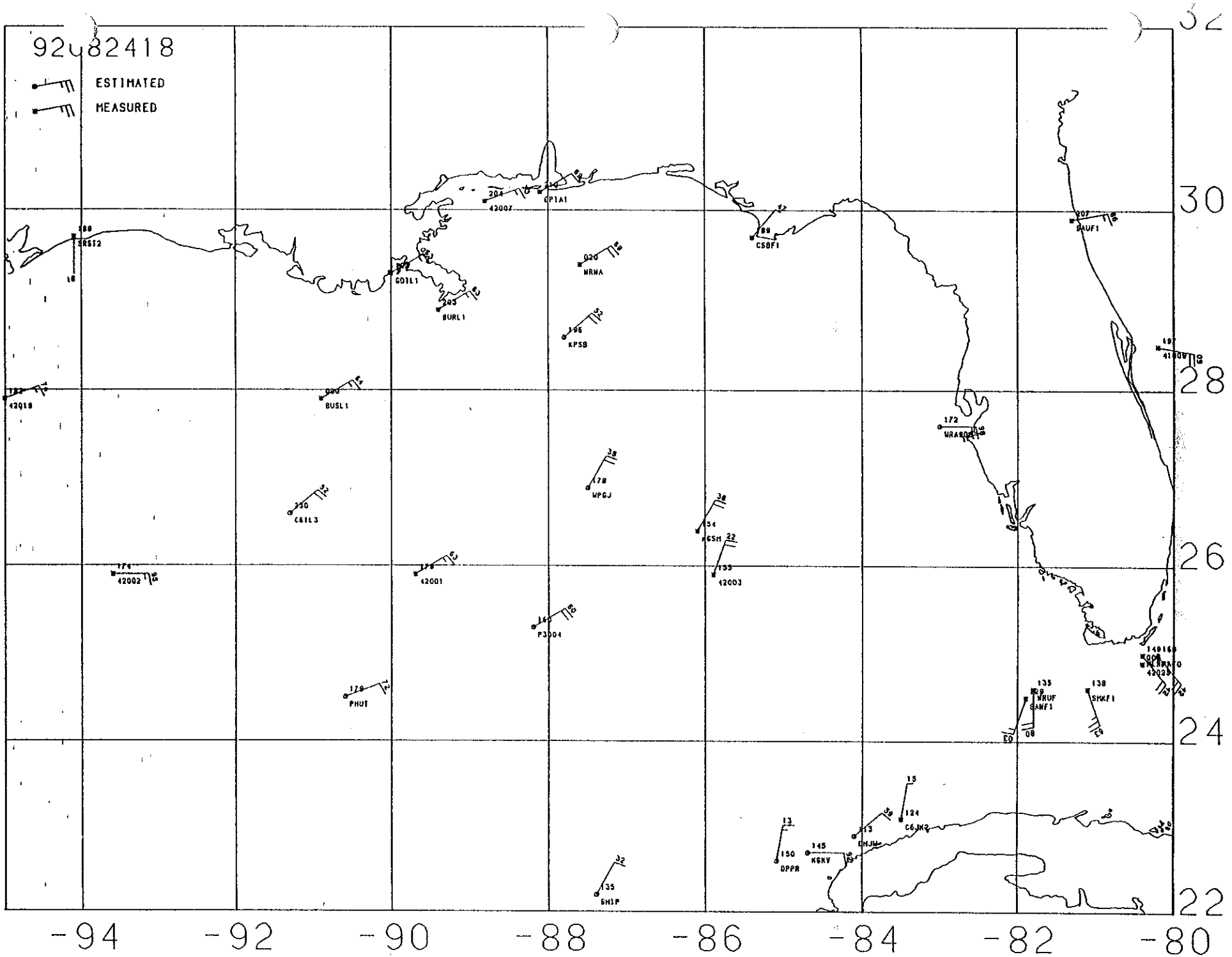

Plotted on 30-JUN-94 13:22 from file [MMANDREW.PLOT]ANDREW92-SHIP.SORT;1 30-JUN-1994 11:32

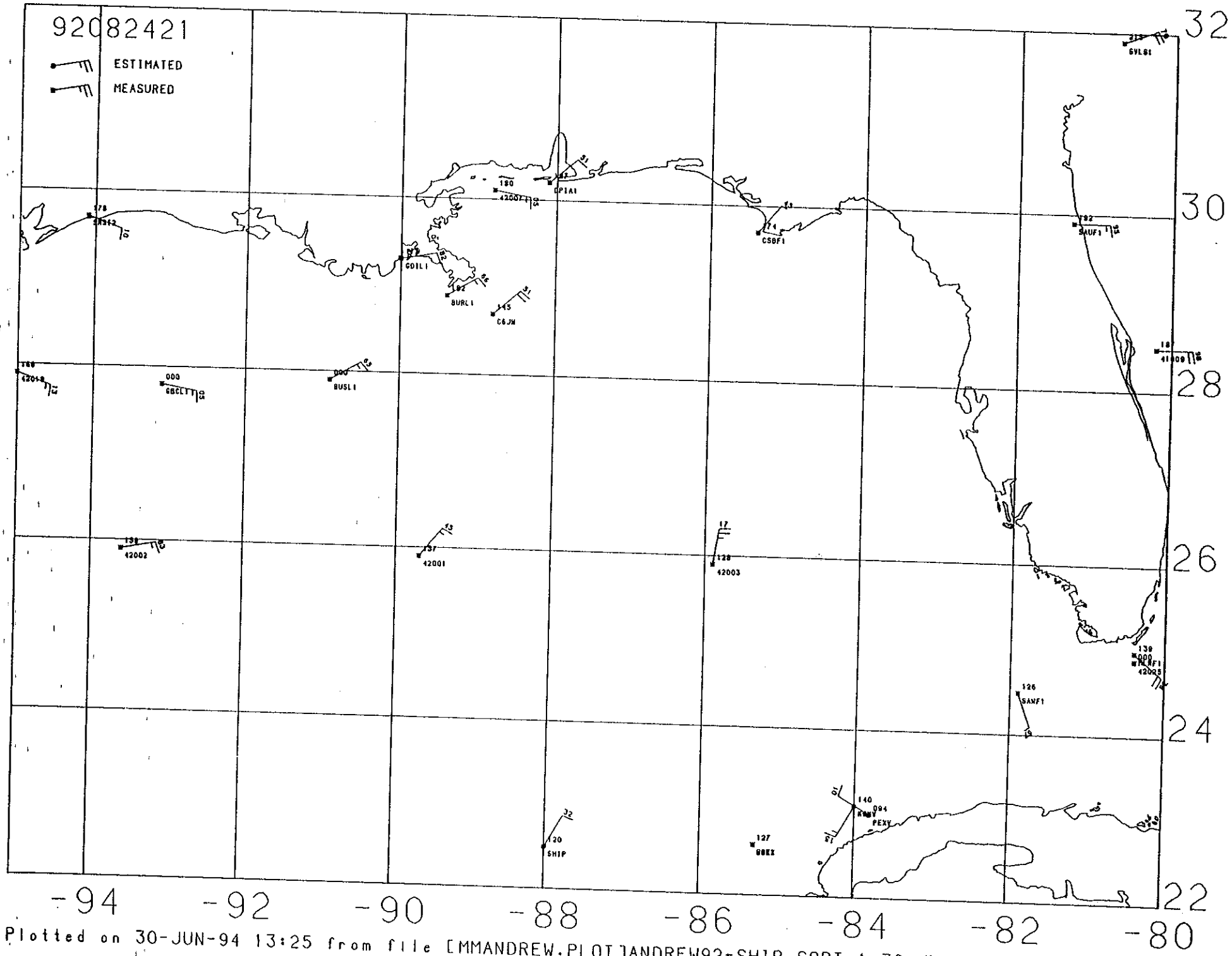

Plotted on 30-JUN-94 13:25 from file [MMANDREW.PLOT]ANDREW92-SHIP.SORT;1 30-JUN-1994 11:32

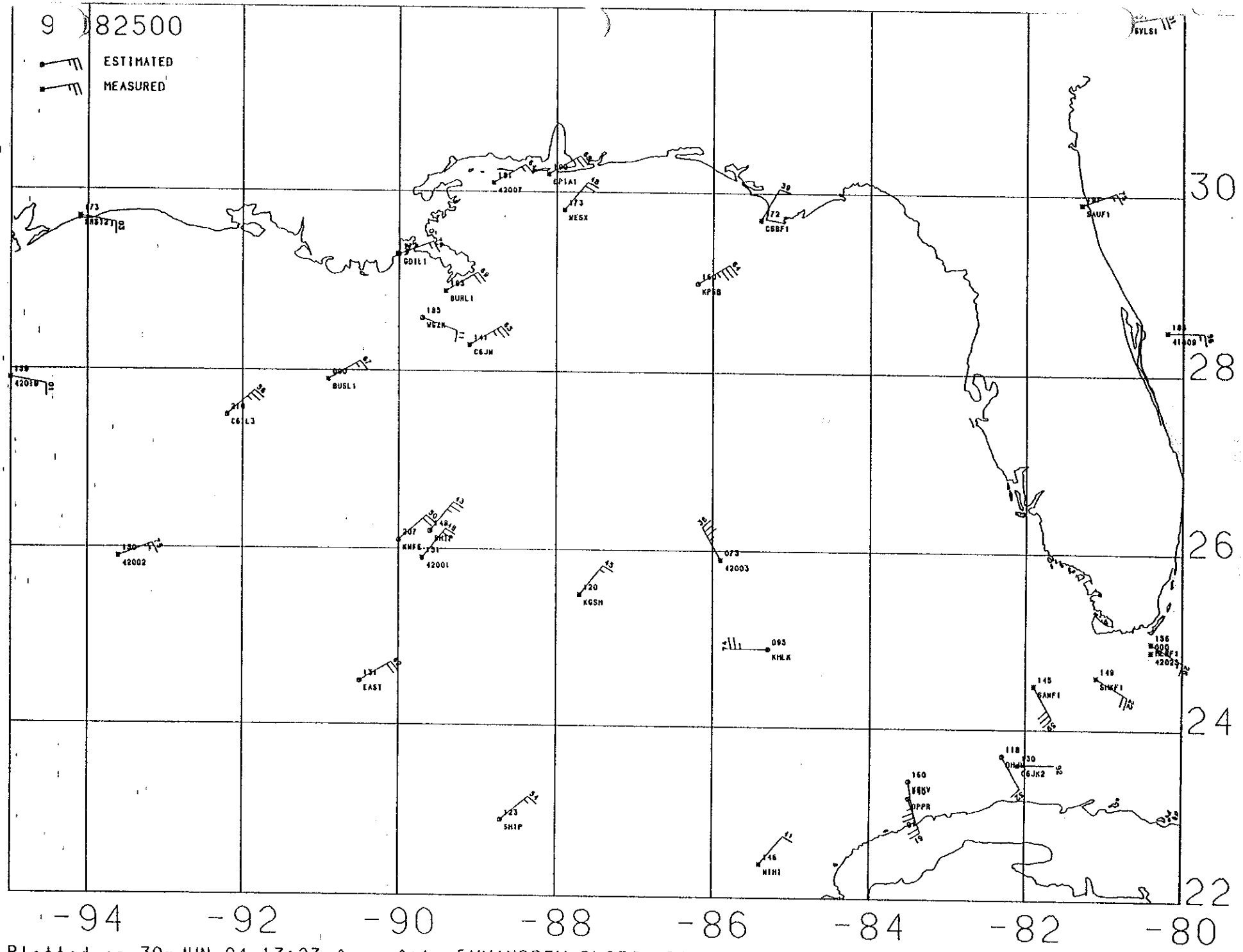
9 82500
ESTIMATED
MEASURED
30
28
26
24
22
-94
-92
-90
-88
-86
-84
-82
-80
Plotted on 30-JUN-94 13:27 from file EMMANDREW.PLOTJANDREW92-SHIP.SORT;1 30-JUN-1994 11:32

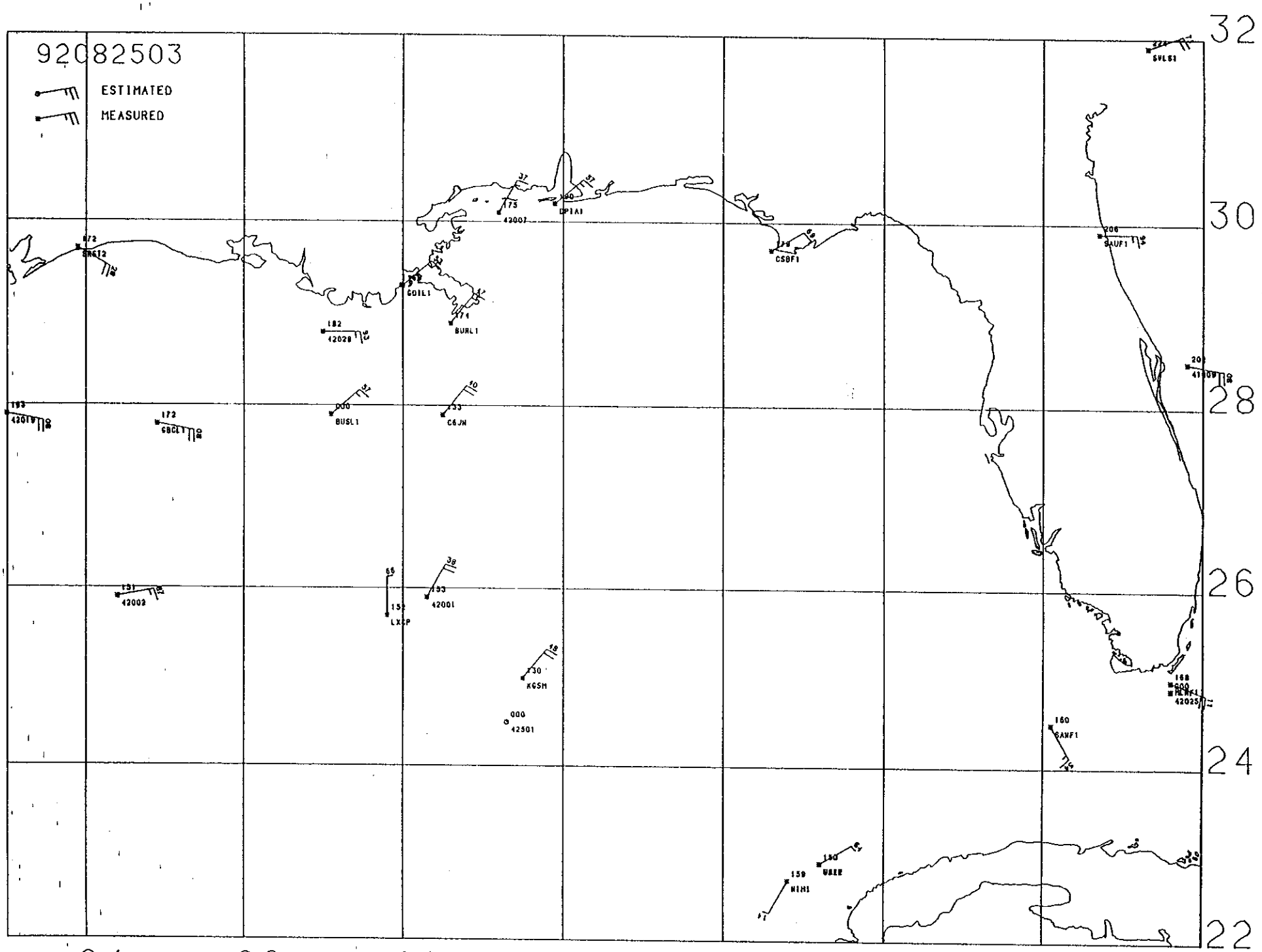

Plott on 30-JUN-94 13:31 from file EMMANDREW.P TJANDREW92-SHIP.SORT;1 30-JUN-1994 11:32

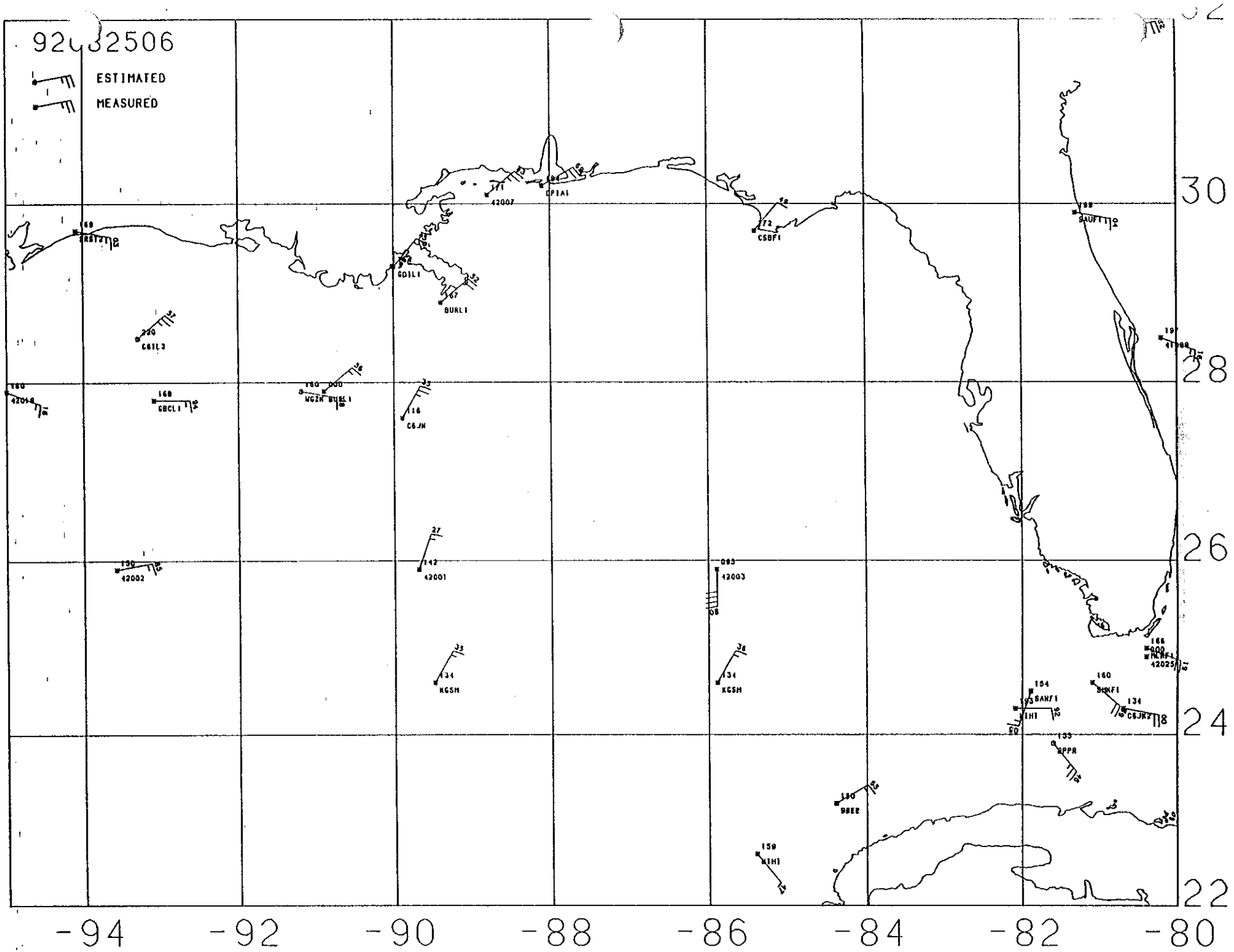

Plotted on 30-JUN-94 13:33 from file [MMANDREW.PLOT]ANDREW92-SHIP.SORT;1 30-JUN-1994 11:32

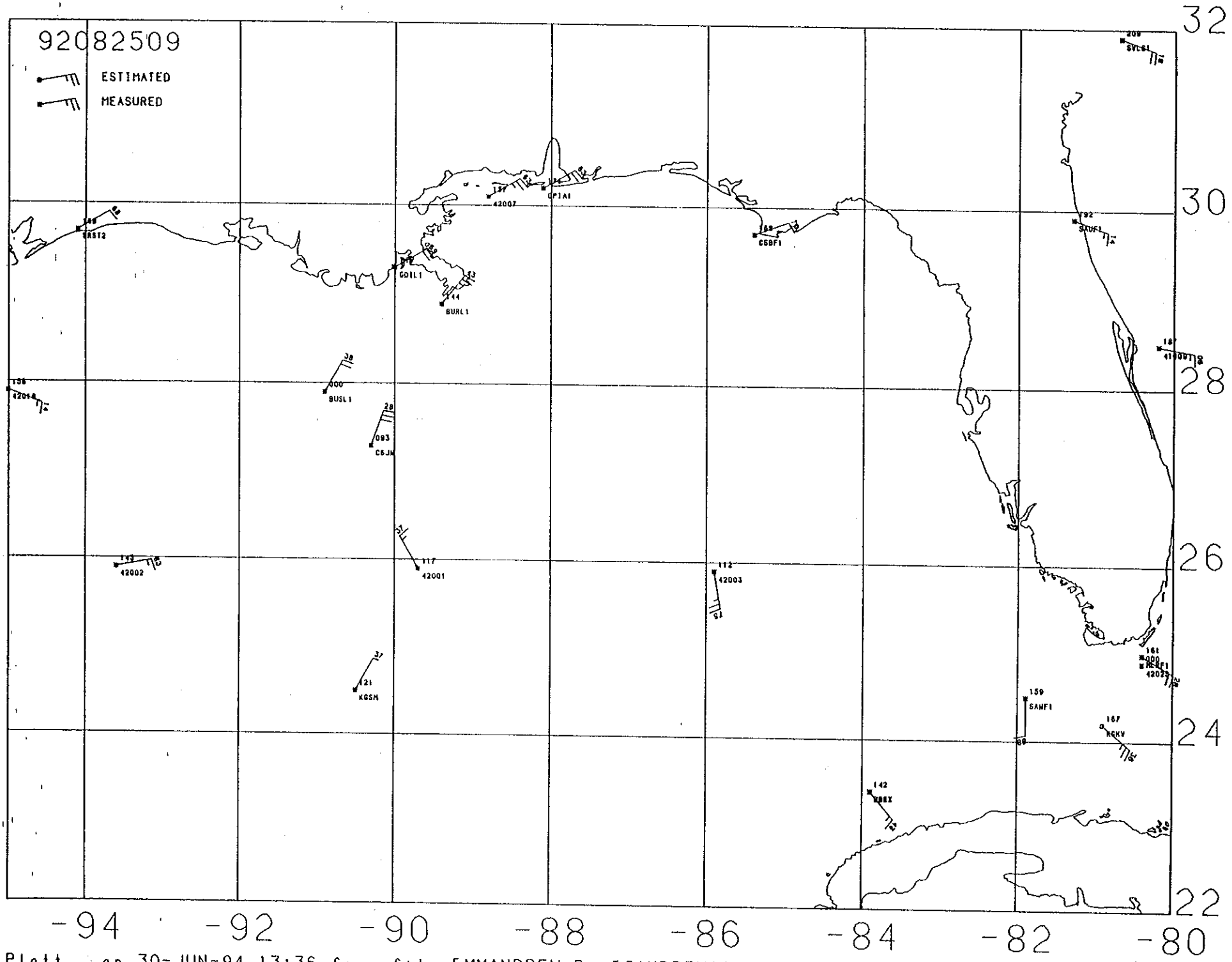

Plott on 30-JUN-94 13:36 from file [MMANDREW.F]JANDREW92-SHIP.SORT;1 30-JUN-1994 11:32

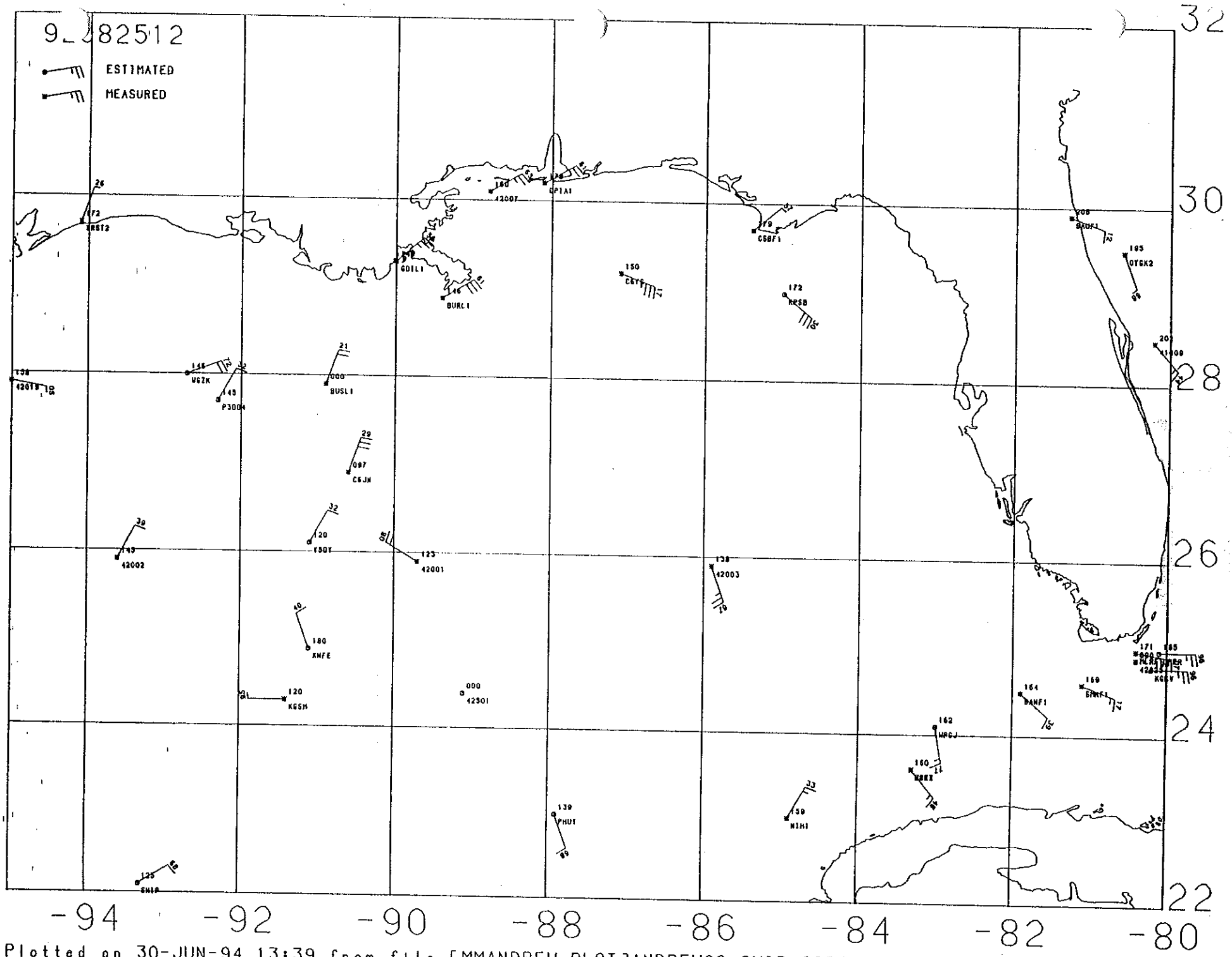
9_082512
ESTIMATED
MEASURED
32
30
28
26
24
22
-94
-92
-90
-88
-86
-84
-82
-80
Plotted on 30-JUN-94 13:39 from file [MMANDREW.PLOT]ANDREW92-SHIP.SORT;1 30-JUN-1994 11:32

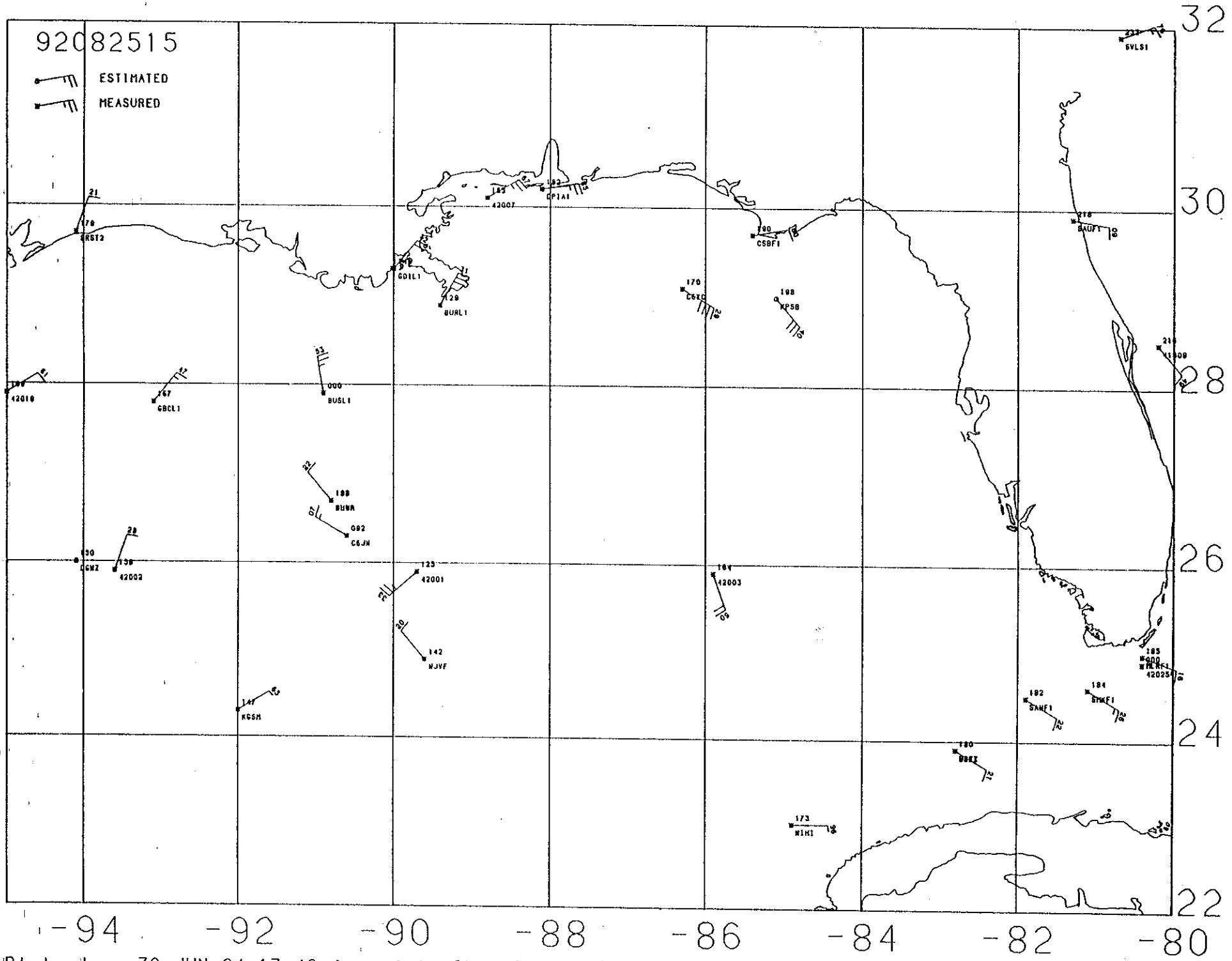
92082515
ESTIMATED
MEASURED
32
30
28
26
24
22
-94
-92
-90
-88
-86
-84
-82
-80
Plot) on 30-JUN-94 13:42 from file CMMANDREW. DTJANDREW92-SHIP.SORT;1 30-JUN-1994 11:32

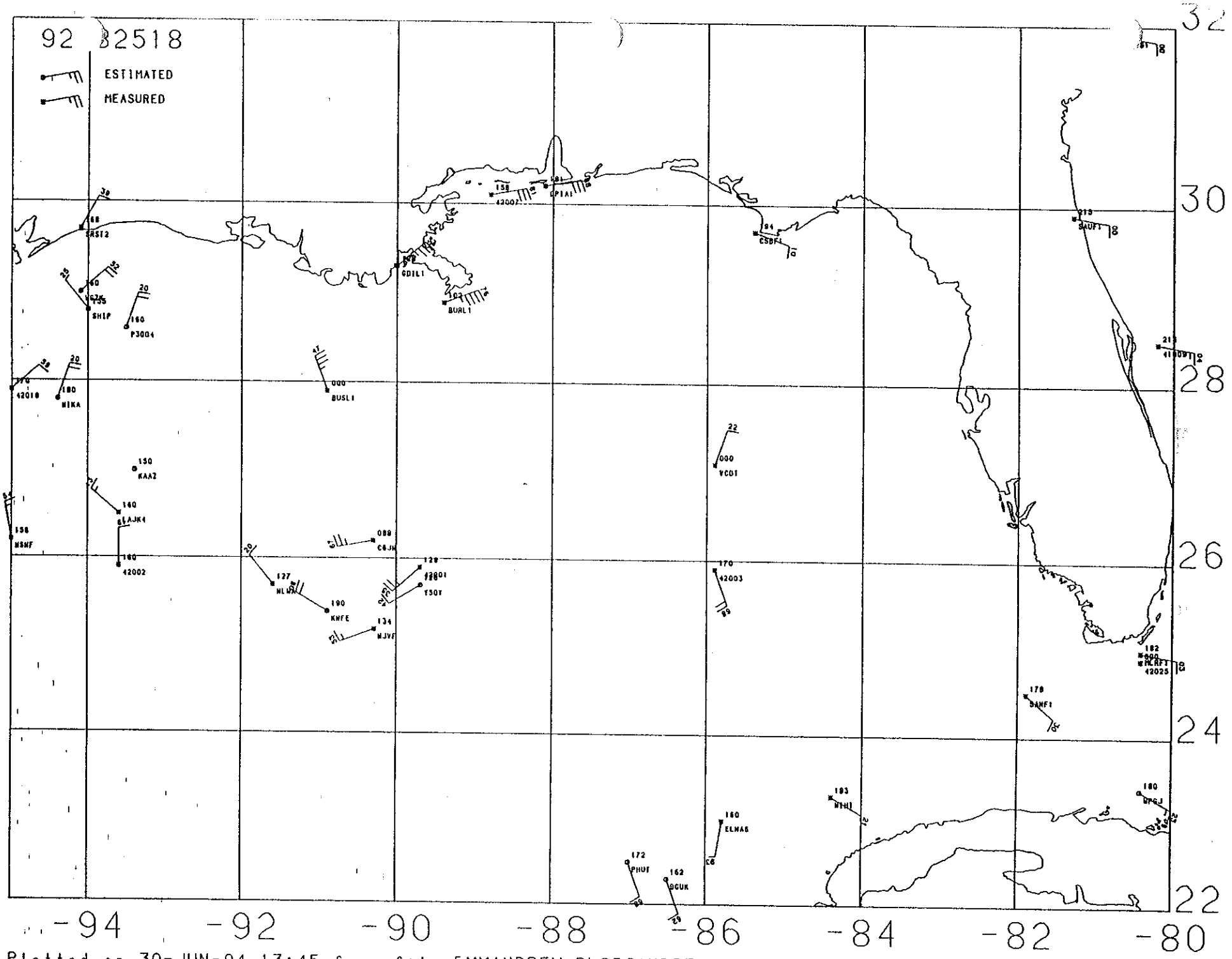

Plotted on 30-JUN-94 13:45 from file EMMANDREW.PLOTJANDREW92-SHIP.SORT;1 30-JUN-1994 11:32

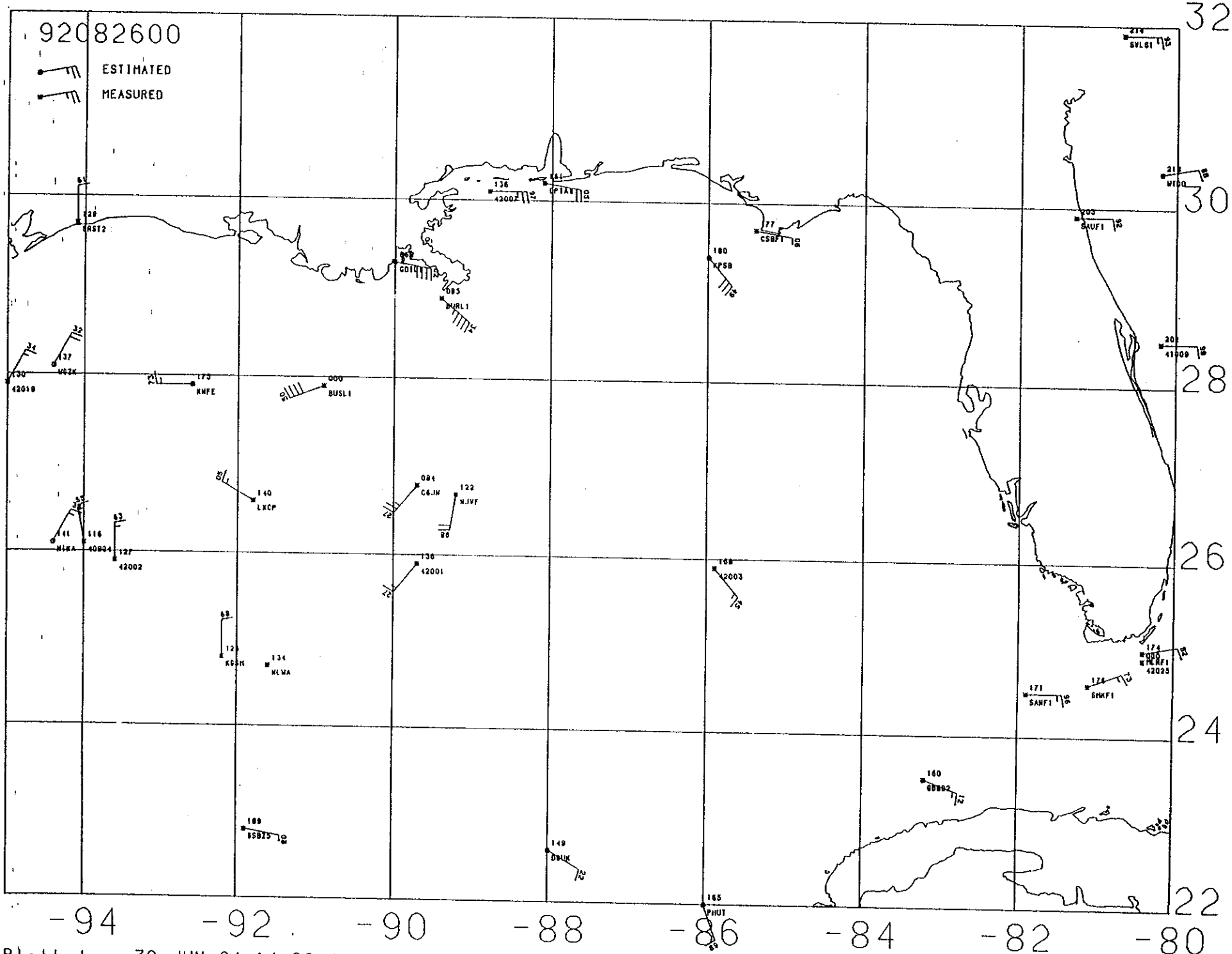

Plotted on 30-JUN-94 14:29 from file EMMANDREW.P JANDREW92-SHIP.SORT;1 30-JUN-1994 11:32

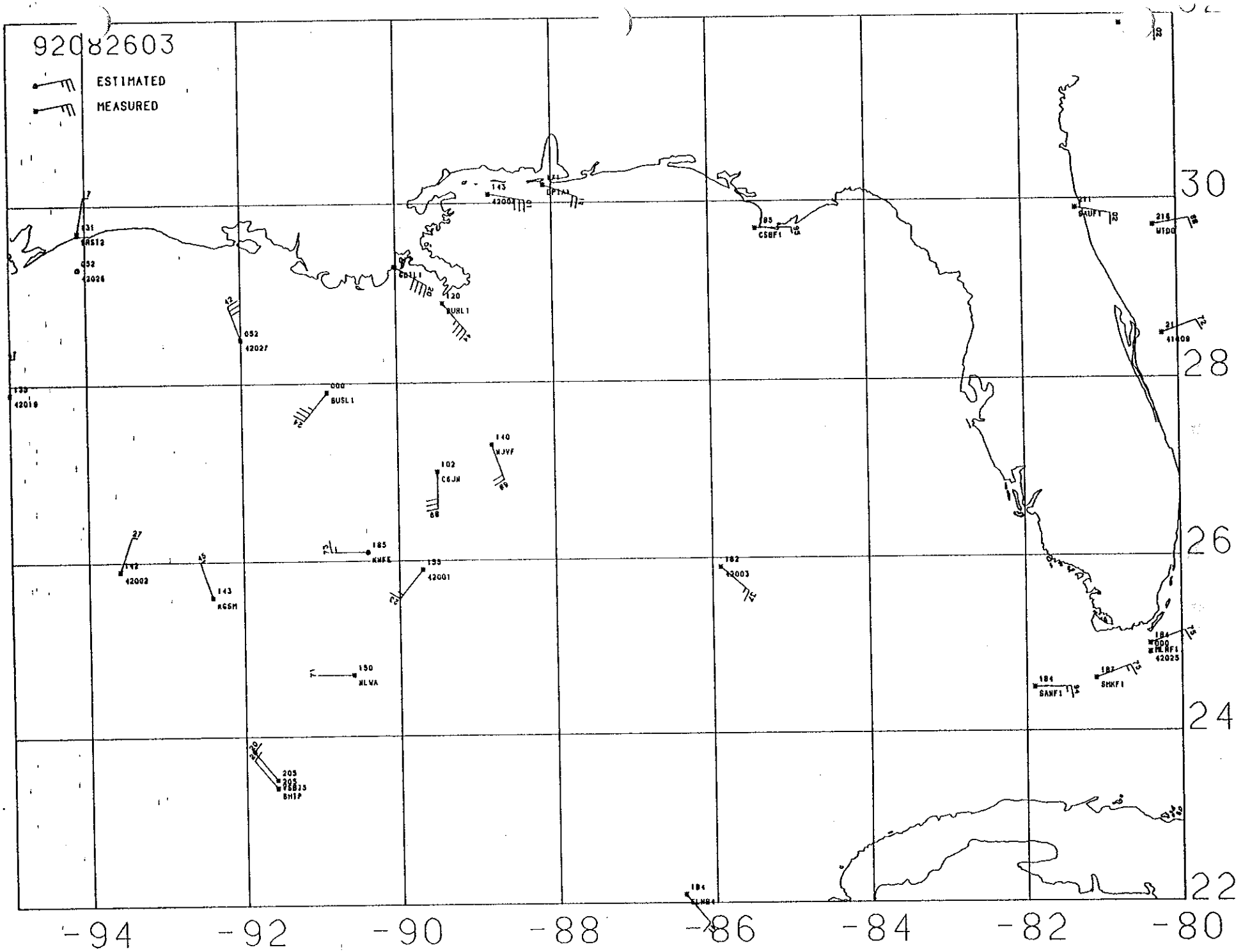
92082603
ESTIMATED
MEASURED
30
28
26
24
22
-94
-92
-90
-88
-86
-84
-82
-80
Plotted on 30-JUN-94 14:32 from file [MMANDREW.PLOT]ANDREW92-SHIP.SORT;1 30-JUN-1994 11:32

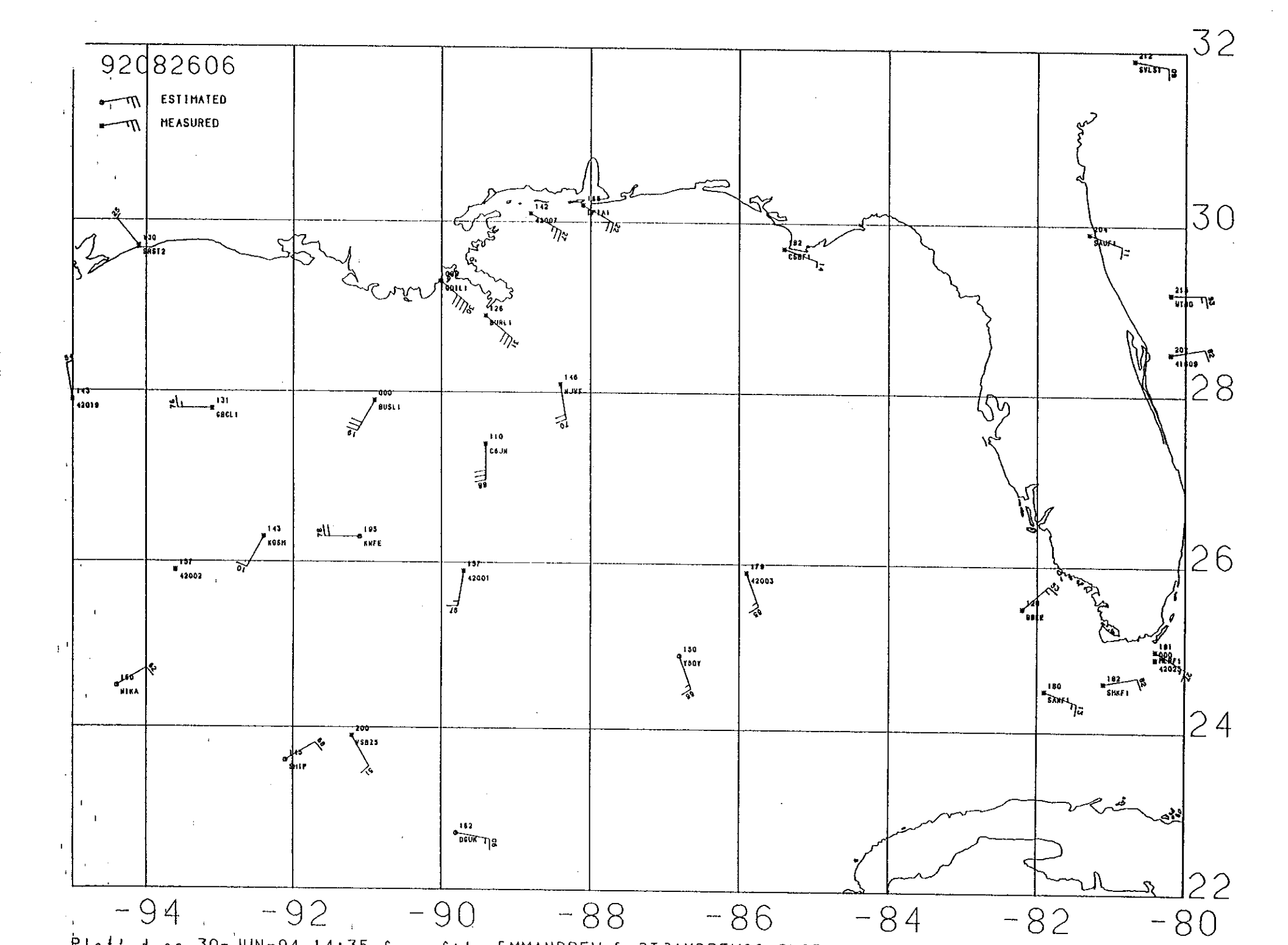
92082606
ESTIMATED
MEASURED
32
30
28
26
24
22
-94
-92
-90
-88
-86
-84
-82
-80
Plot 1 on 30-JUN-94 14:35 from file [MMANDREW.']TJANDREW92-SHIP.SORT;1 30-JUN-1994 11:32

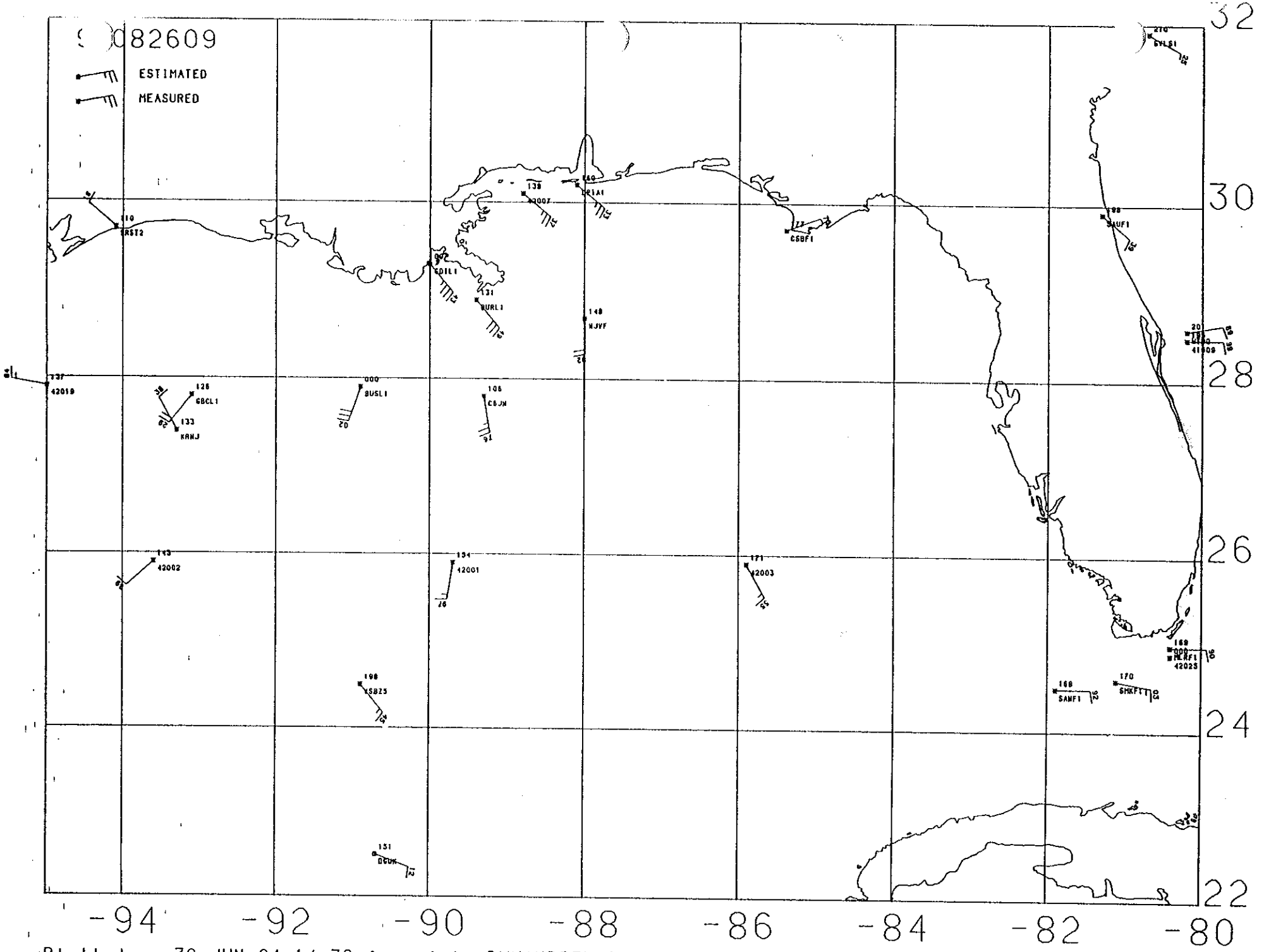
082609
ESTIMATED
MEASURED
32
30
28
26
24
22
-94
-92
-90
-88
-86
-84
-82
-80
Plotted on 30-JUN-94 14:38 from file EMMANDREW.PLOT]ANDREW92-SHIP.SORT;1 30-JUN-1994 11:32

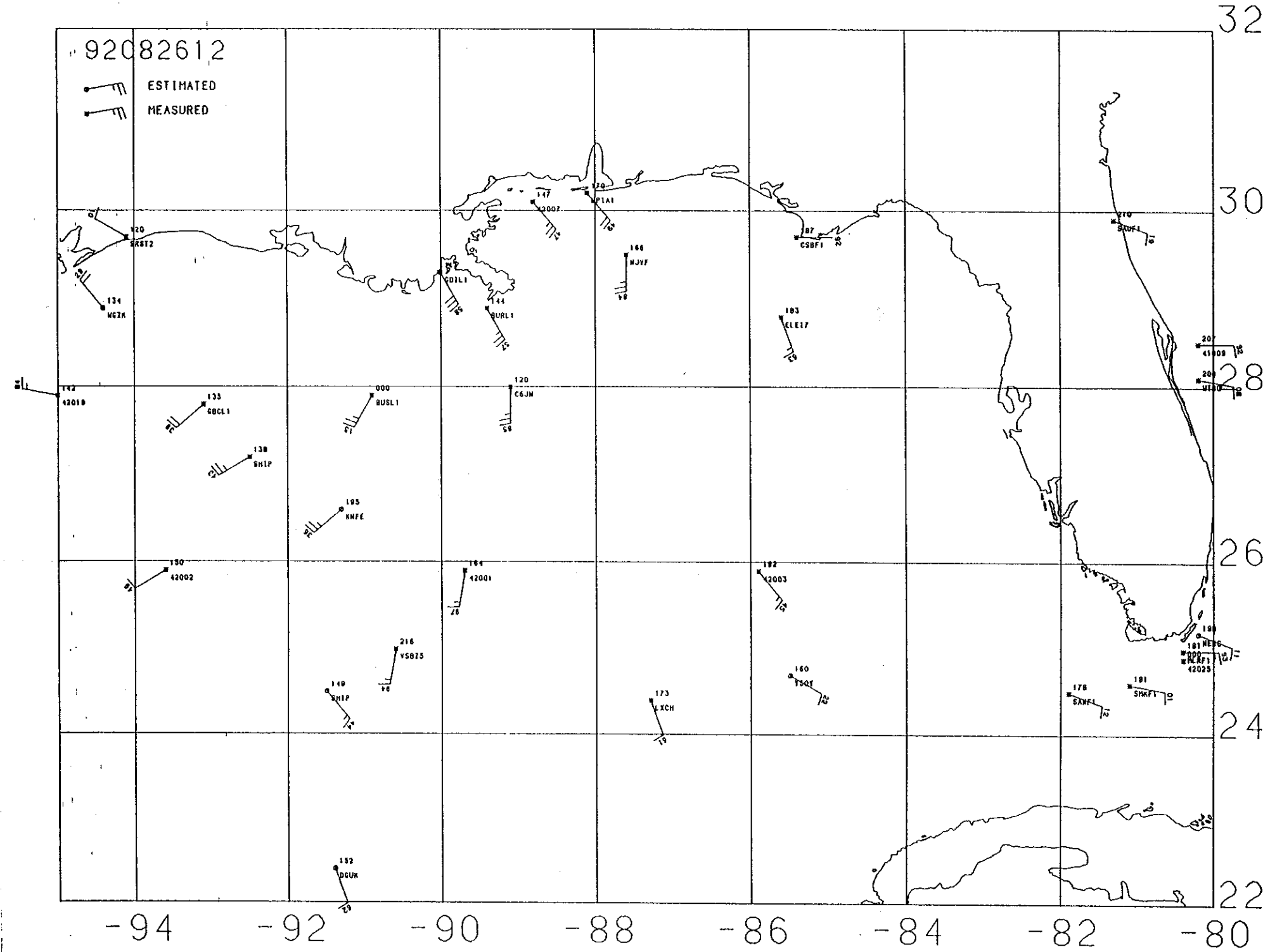

Plotted on 30-JUN-94 14:41 from file [MMANDREW.PI]ANDREW92-SHIP.SORT;1 30-JUN-1994 11:32

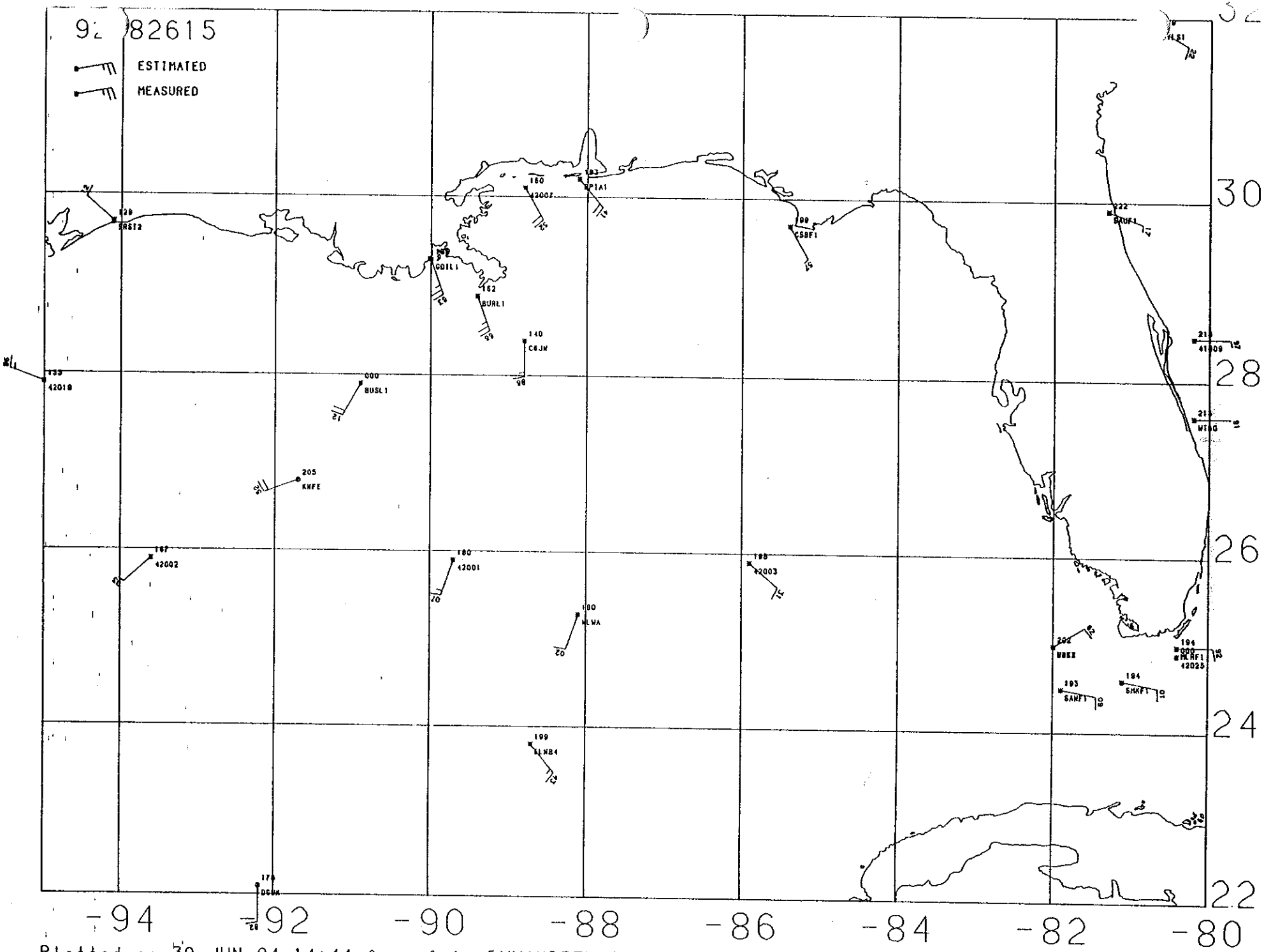
92082615
ESTIMATED
MEASURED
32
30
28
26
24
22
-94
-92
-90
-88
-86
-84
-82
-80
Plotted on 30-JUN-94 14:44 from file [MMANDREW.PLOT]ANDREW92-SHIP.SORT;1 30-JUN-1994 11:32

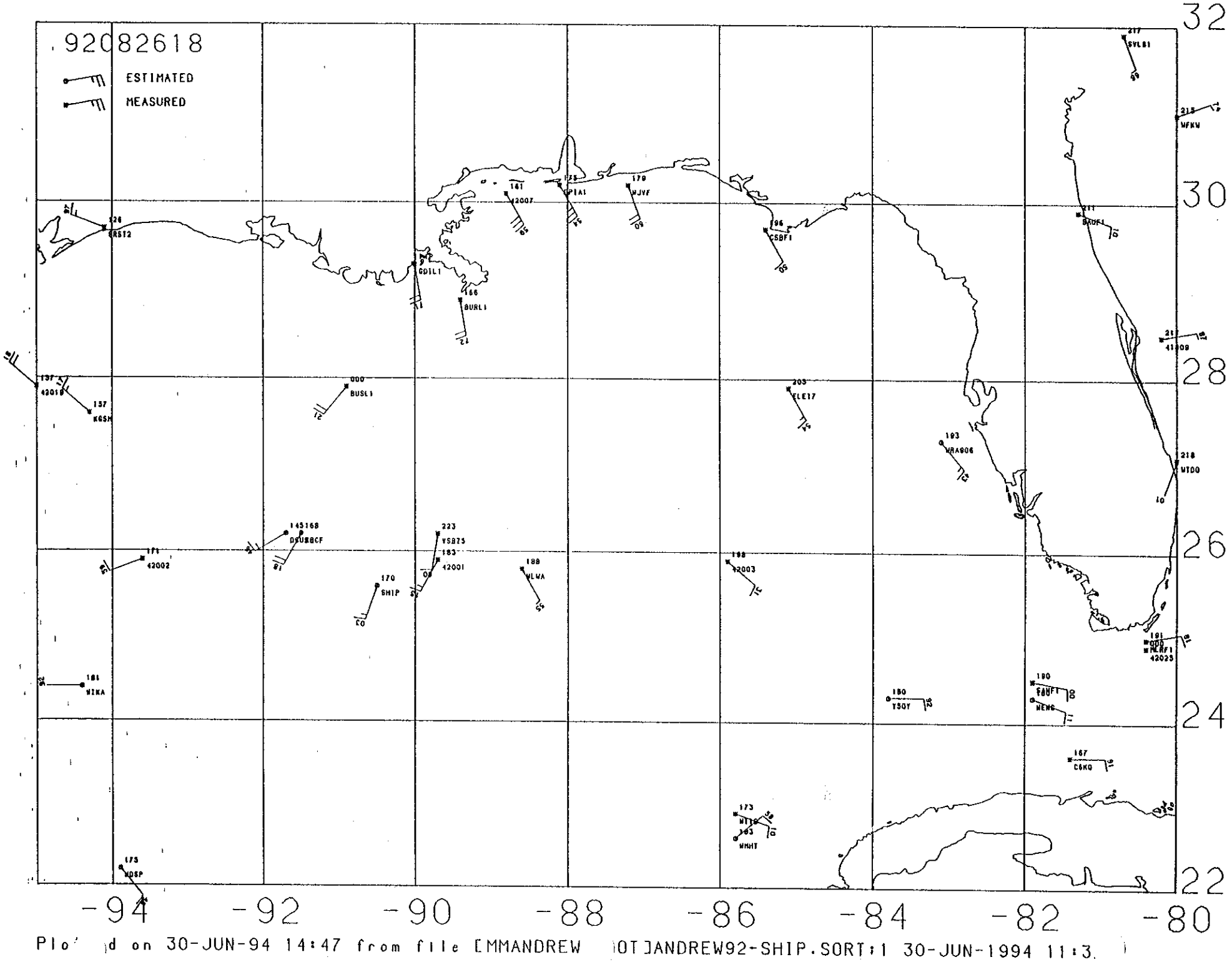
92082618
ESTIMATED
MEASURED
32
30
28
26
24
22
-94
-92
-90
-88
-86
-84
-82
-80
Plotted on 30-JUN-94 14:47 from file EMMANDREW [OTJANDREW92-SHIP.SORT;1 30-JUN-1994 11:3

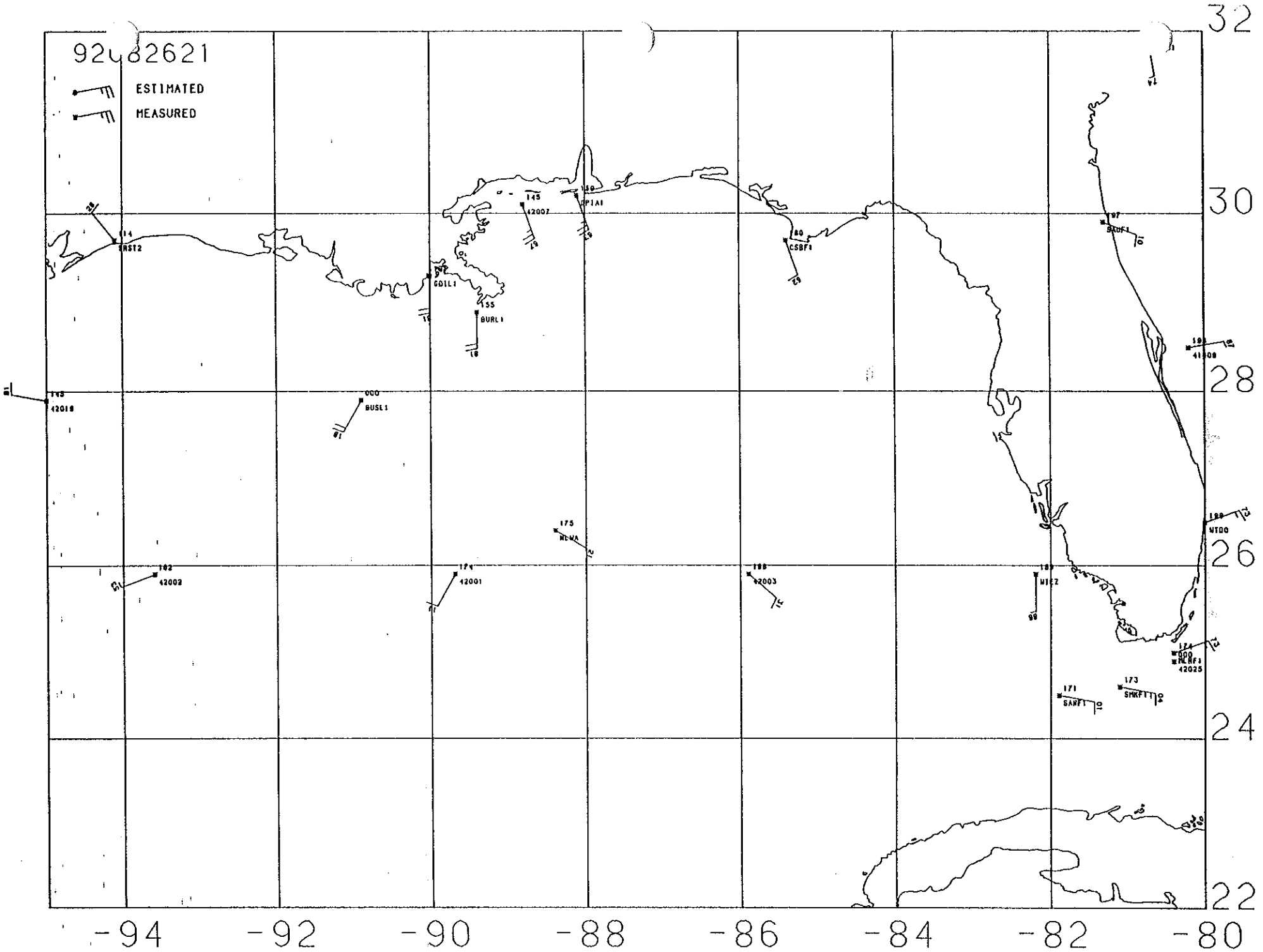

Plotted on 30-JUN-94 14:50 from file CMMANDREW.PLOTJANDREW92-SHIP.SORT;1 30-JUN-1994 11:32

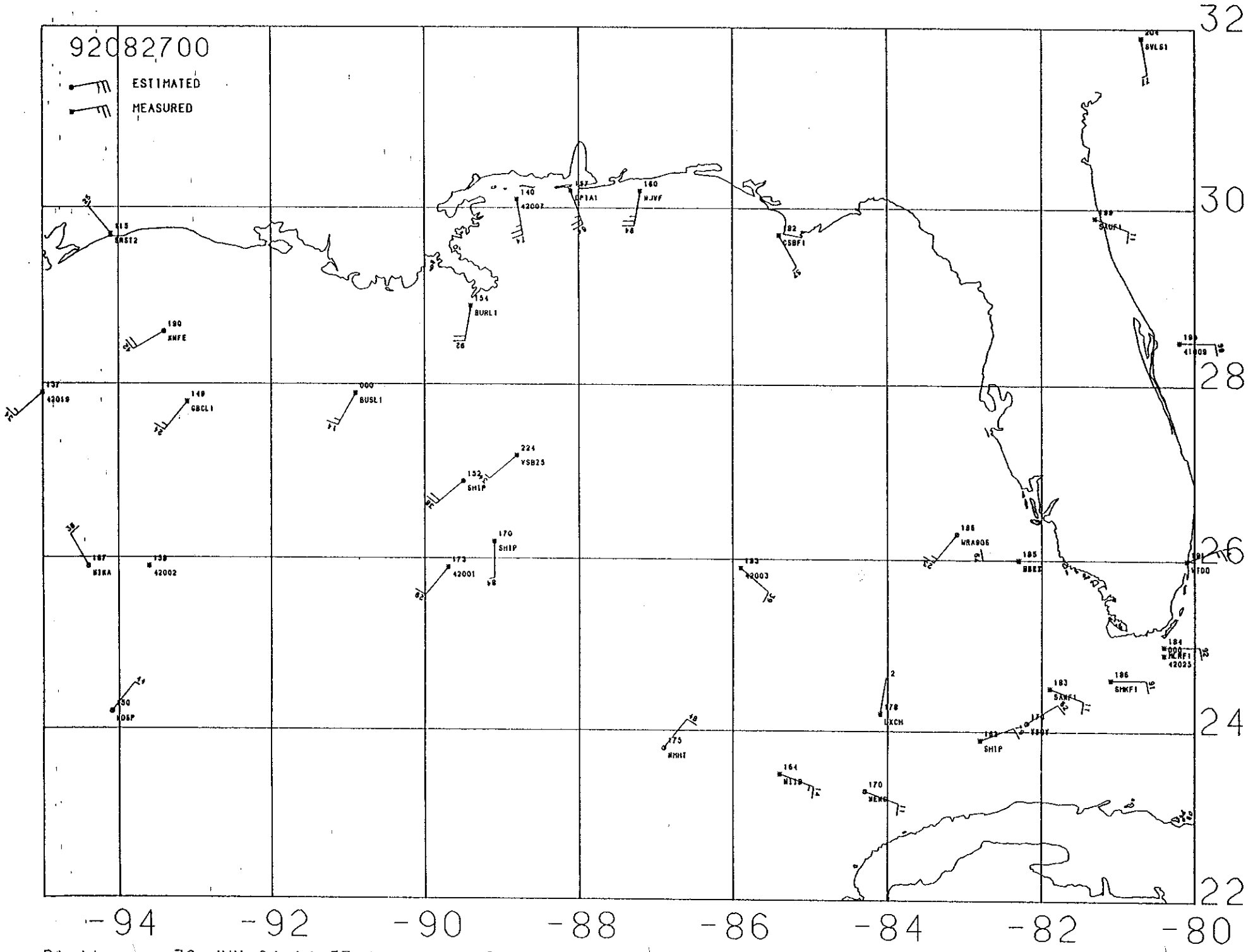

Plott on 30-JUN-94 14:53 from file [MMANDREW.P.]ANDREW92-SHIP.SORT;1 30-JUN-1994 11:32

Appendix C.

Screen display of workstation display of program used to fit parameters of radial pressure profile at 2-hourly intervals from reconnaissance measurements.

Oceanweather Tropical System Analysis

Surface Winds and Pressures Estimated from
Vortex and Minob Data Messages

Hurricane Andrew 1992
92082409 +/- 3hrs

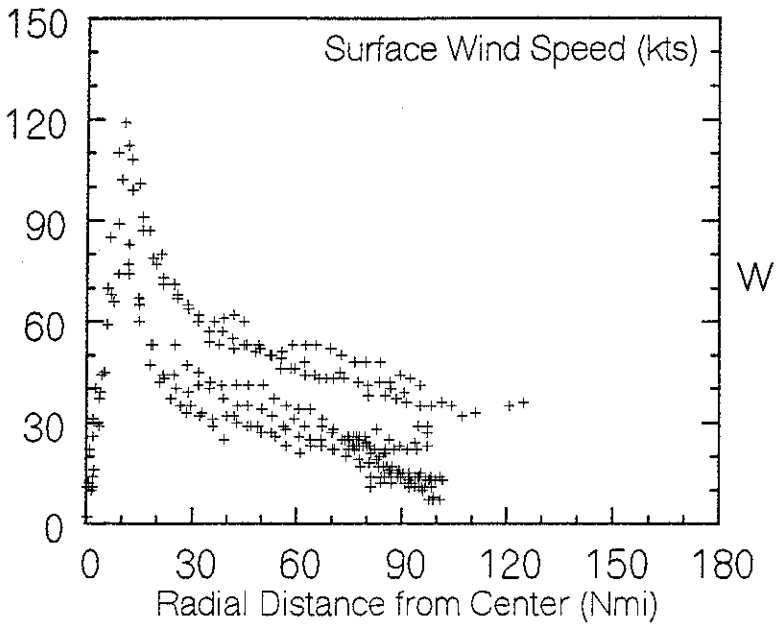

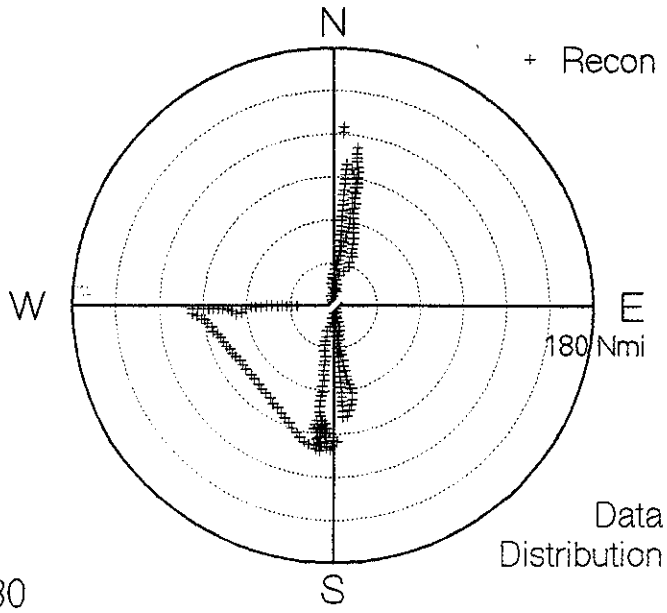

Created on 7/8 13:30

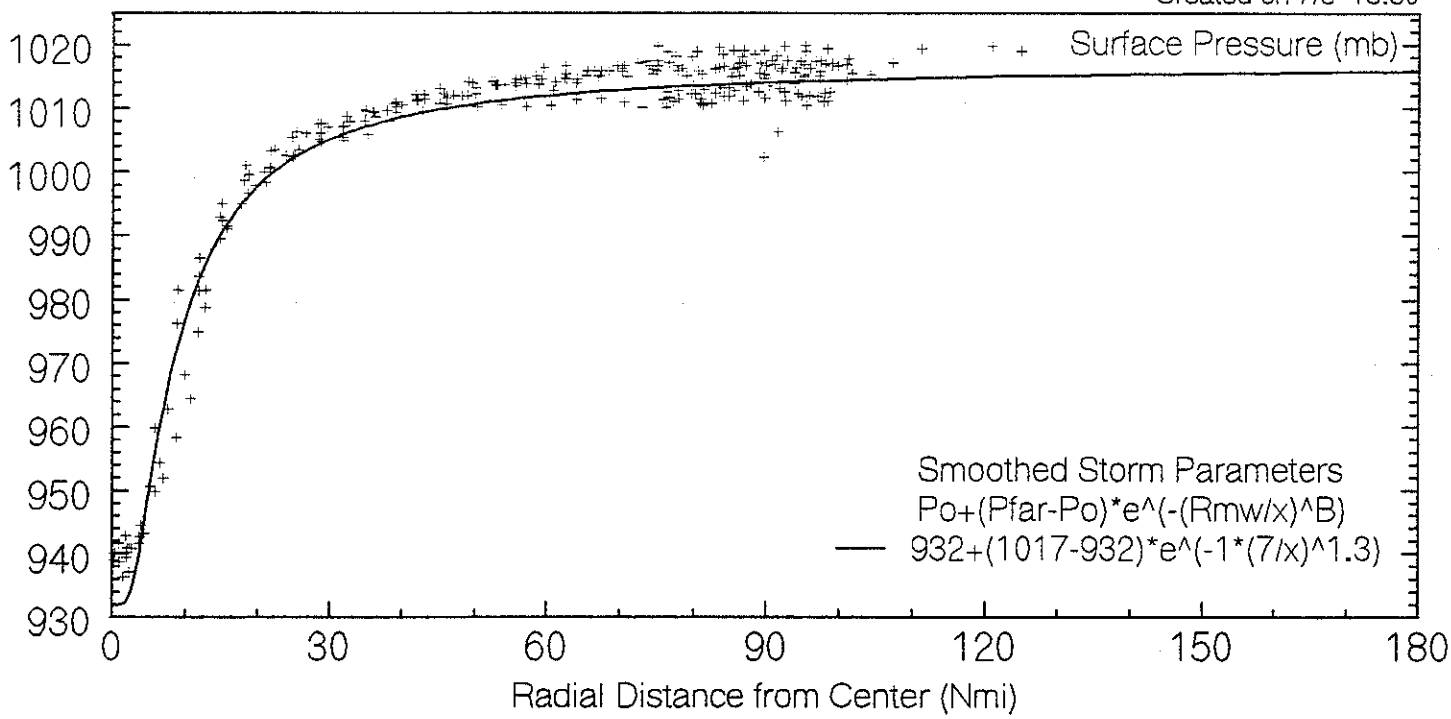

Oceanweather Tropical System Analysis

Surface Winds and Pressures Estimated from
Vortex and Minob Data Messages

Hurricane Andrew 1992
92082415 +/- 3hrs

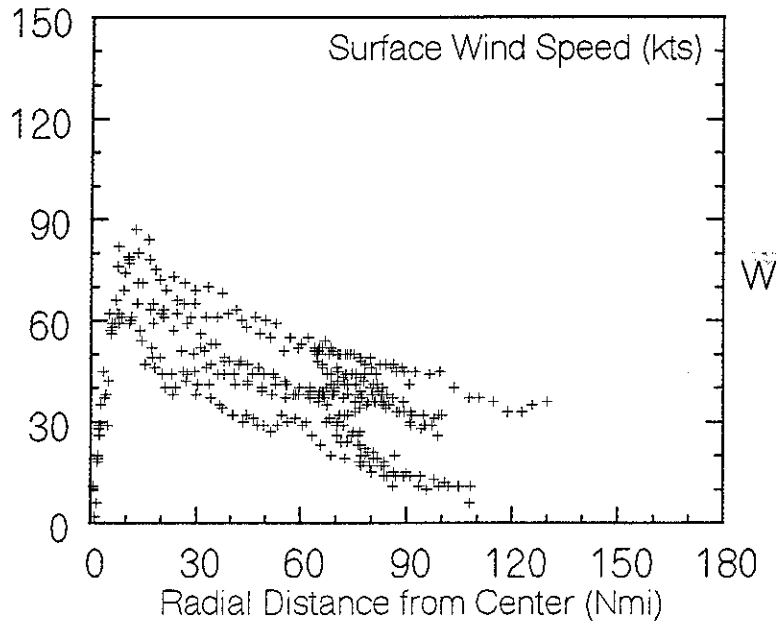

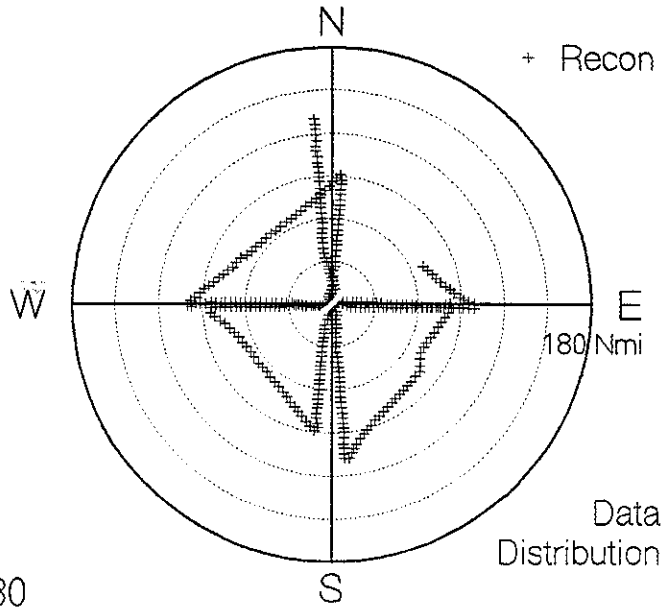

Created on 7/8 13:34

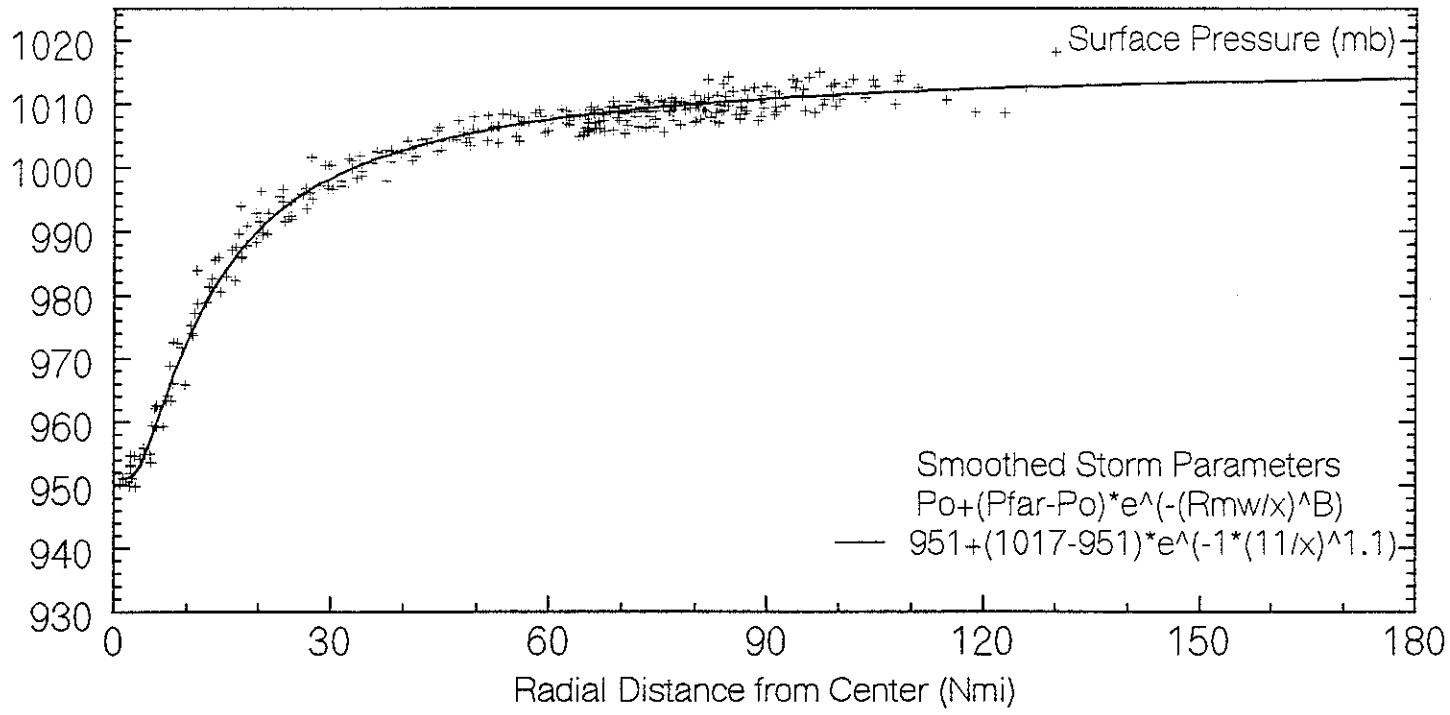

Oceanweather Tropical System Analysis

Surface Winds and Pressures Estimated from
Vortex and Minob Data Messages

Hurricane Andrew 1992

92082418 +/- 3hrs

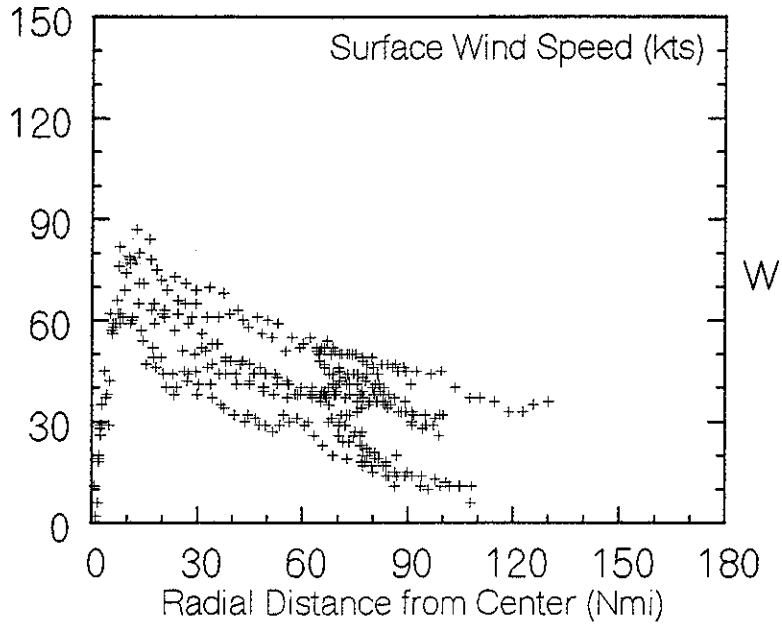

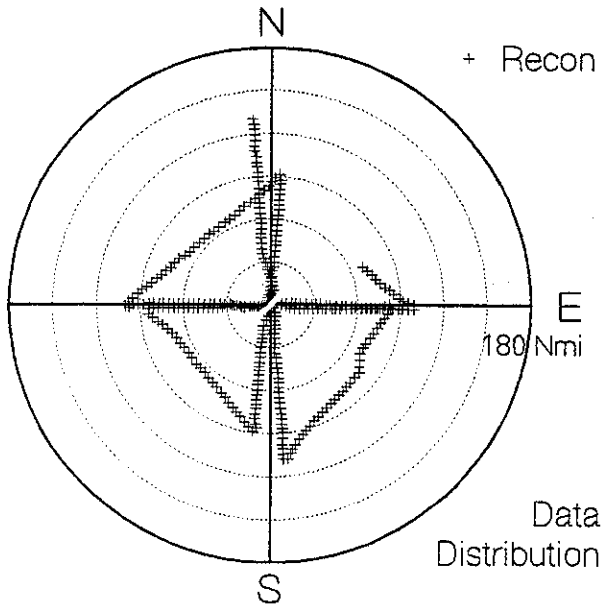

Created on 7/8 13:36

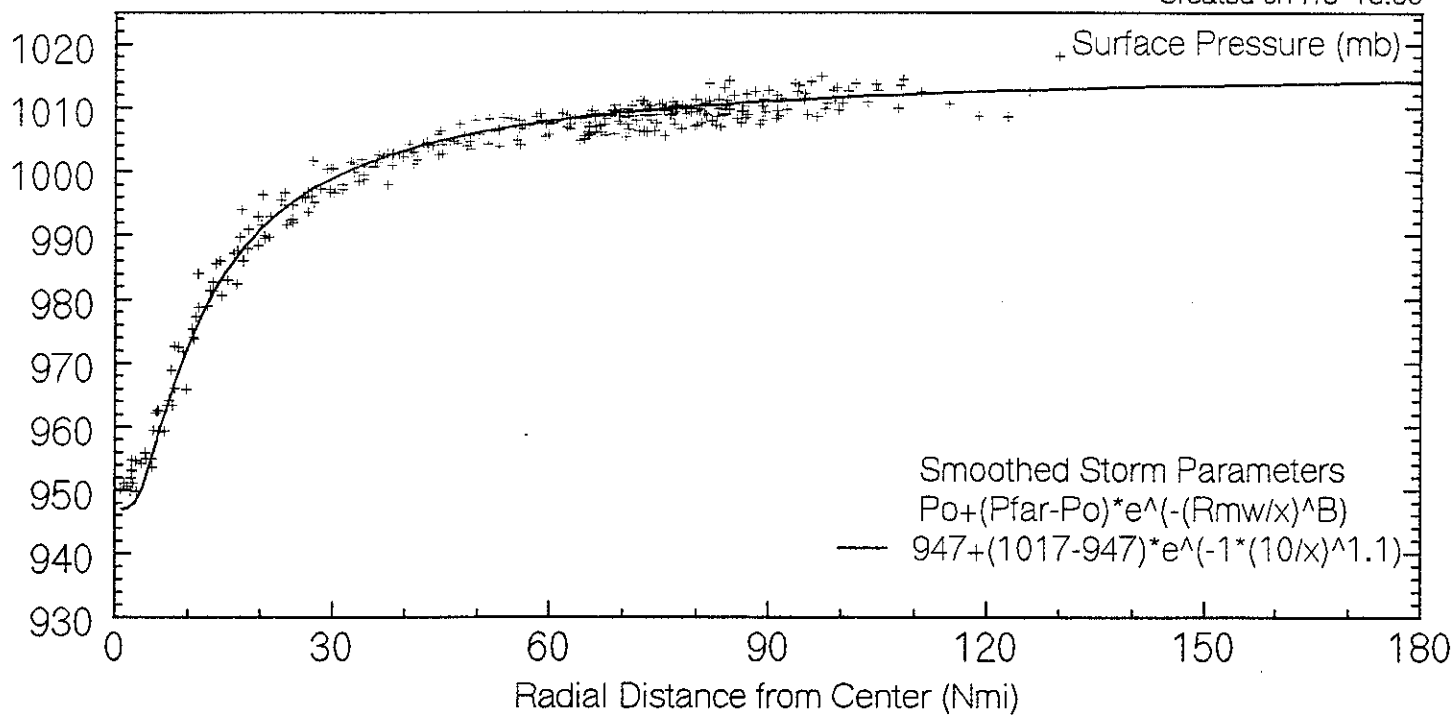

Oceanweather Tropical System Analysis

Surface Winds and Pressures Estimated from
Vortex and Minob Data Messages

Hurricane Andrew 1992

92082421 +/- 3hrs

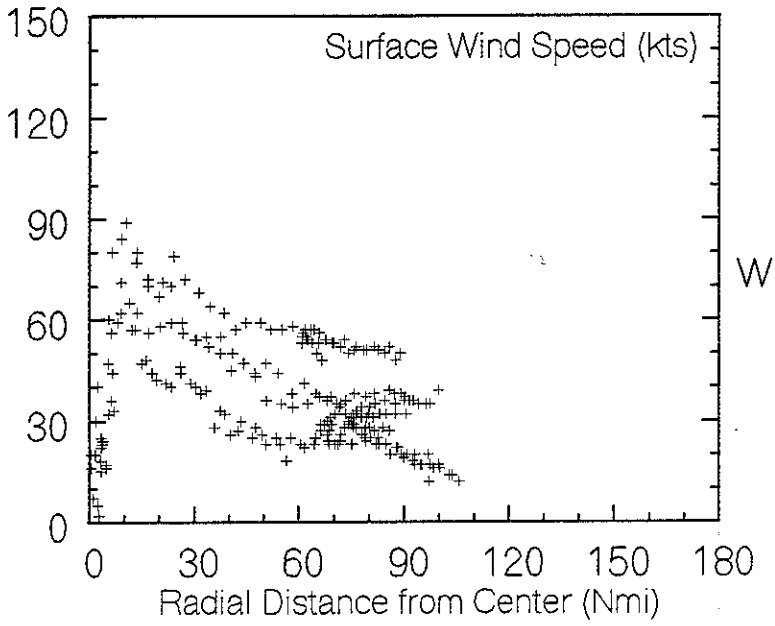

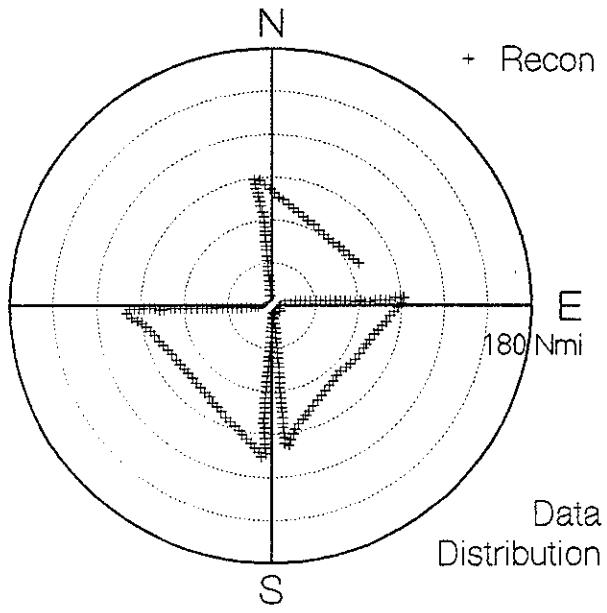

Created on 7/8 13:39

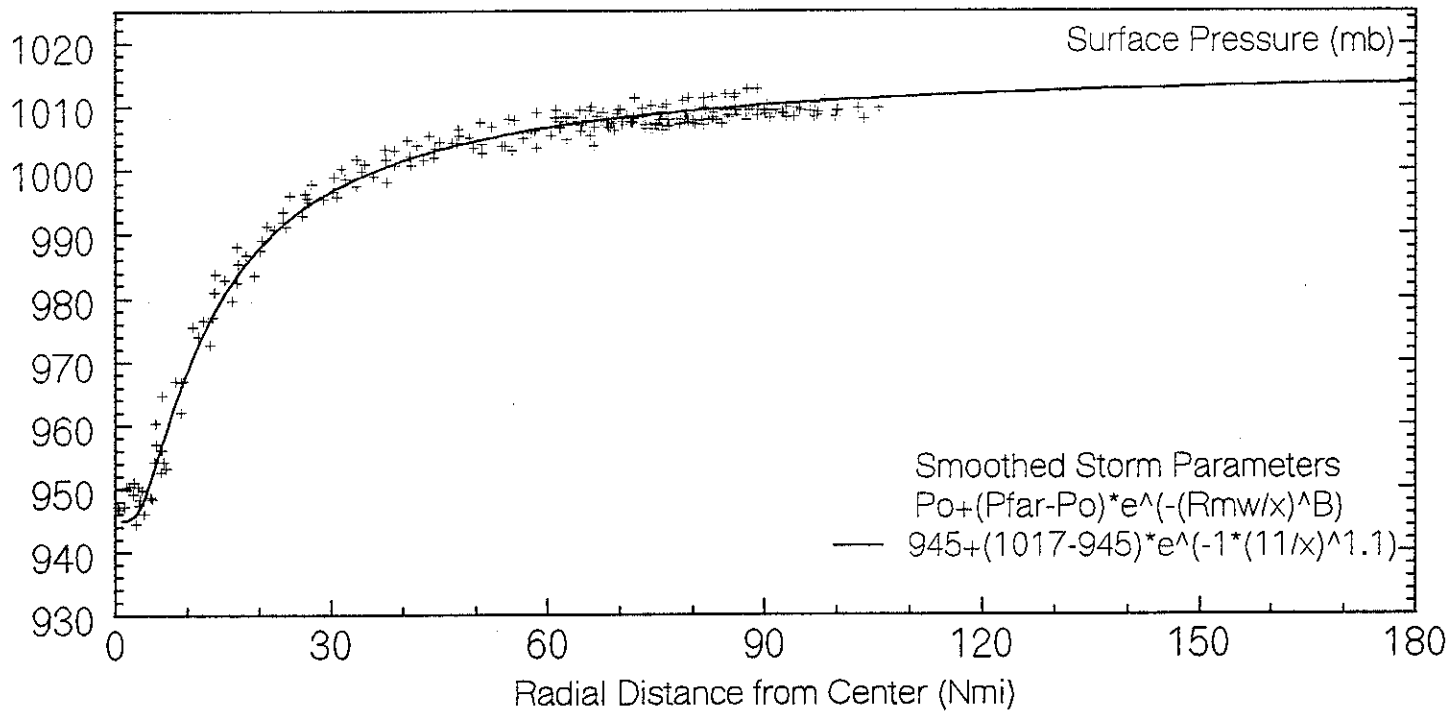

Oceanweather Tropical System Analysis

Surface Winds and Pressures Estimated from
Vortex and Minob Data Messages

Hurricane Andrew 1992
92082500 +/- 3hrs

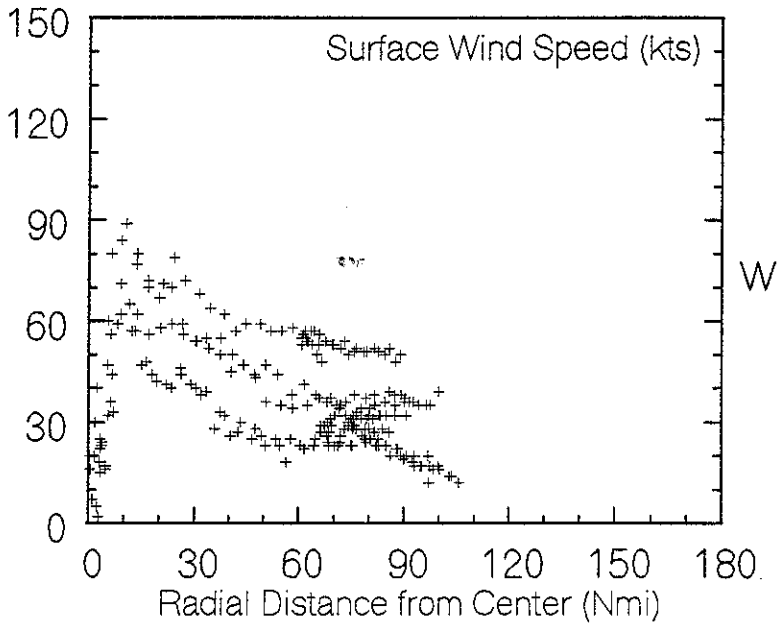

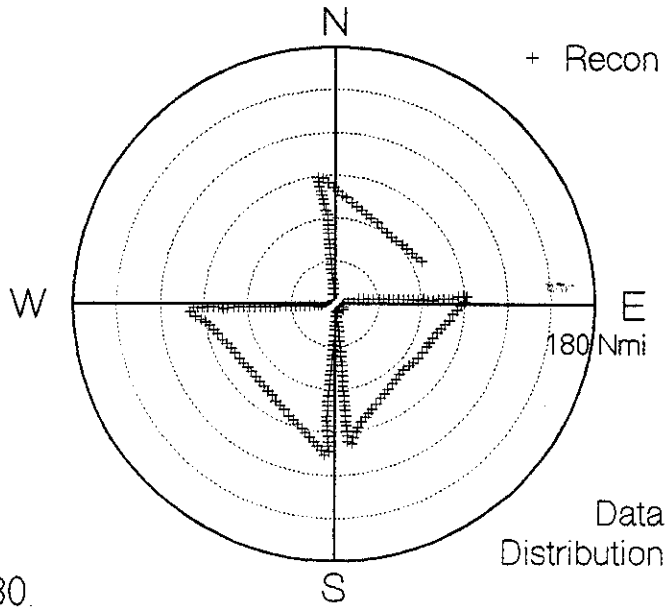

Created on 7/8 19:31

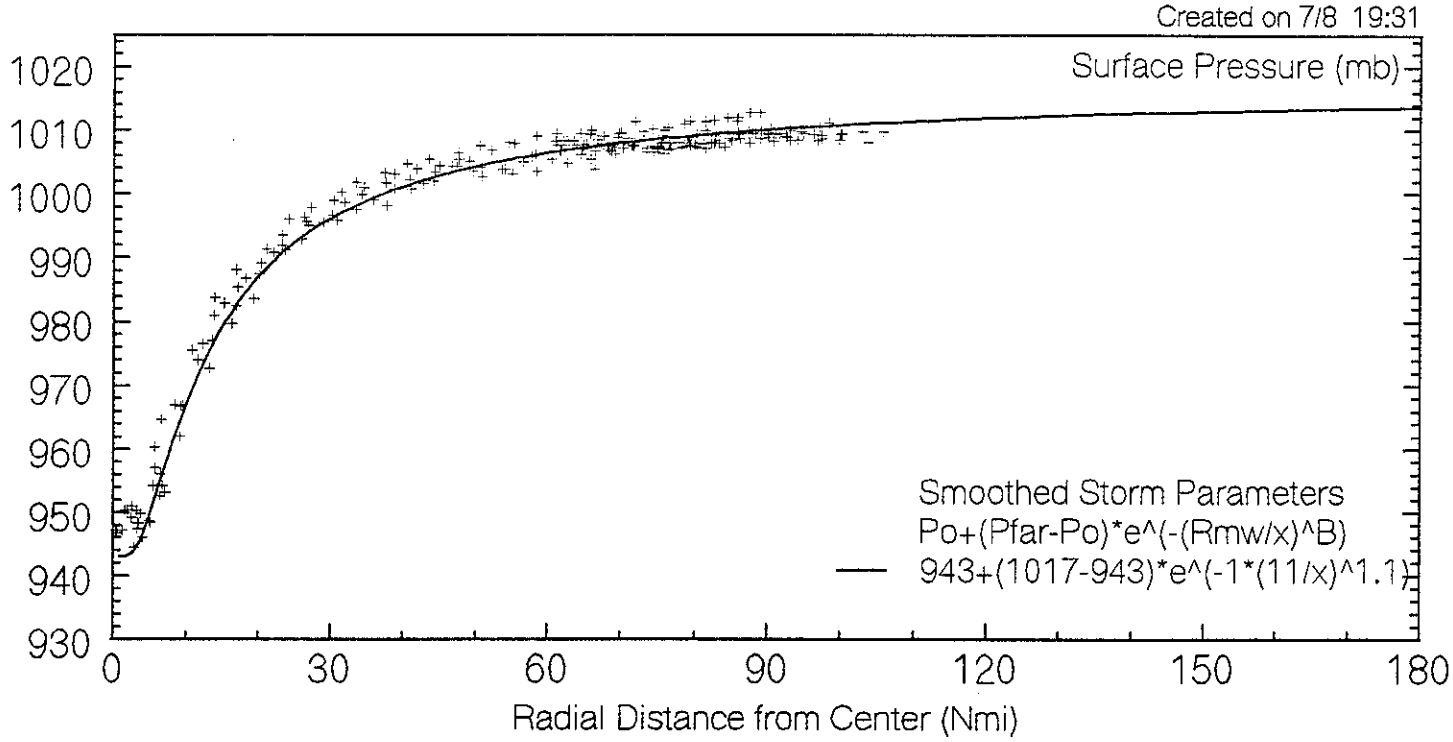

Oceanweather Tropical System Analysis

Surface Winds and Pressures Estimated from
Vortex and Minob Data Messages

Hurricane Andrew 1992

92082503 +/- 3hrs

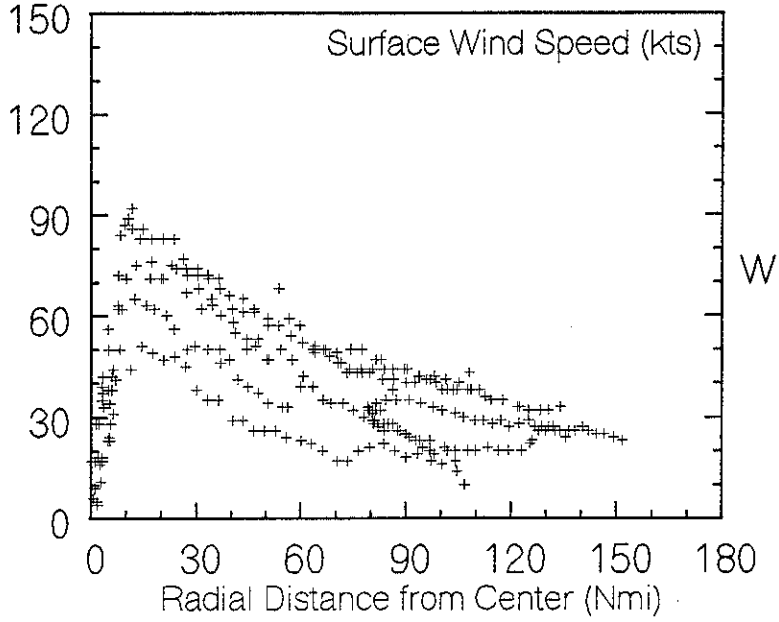

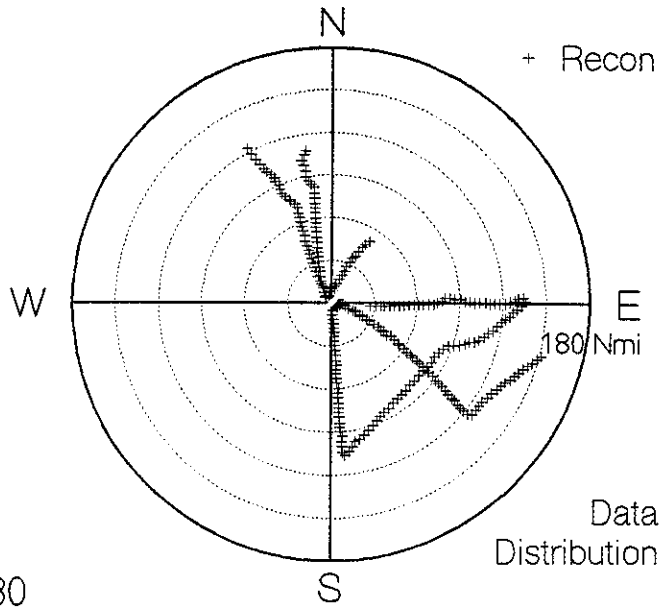

Created on 7/8 19:33

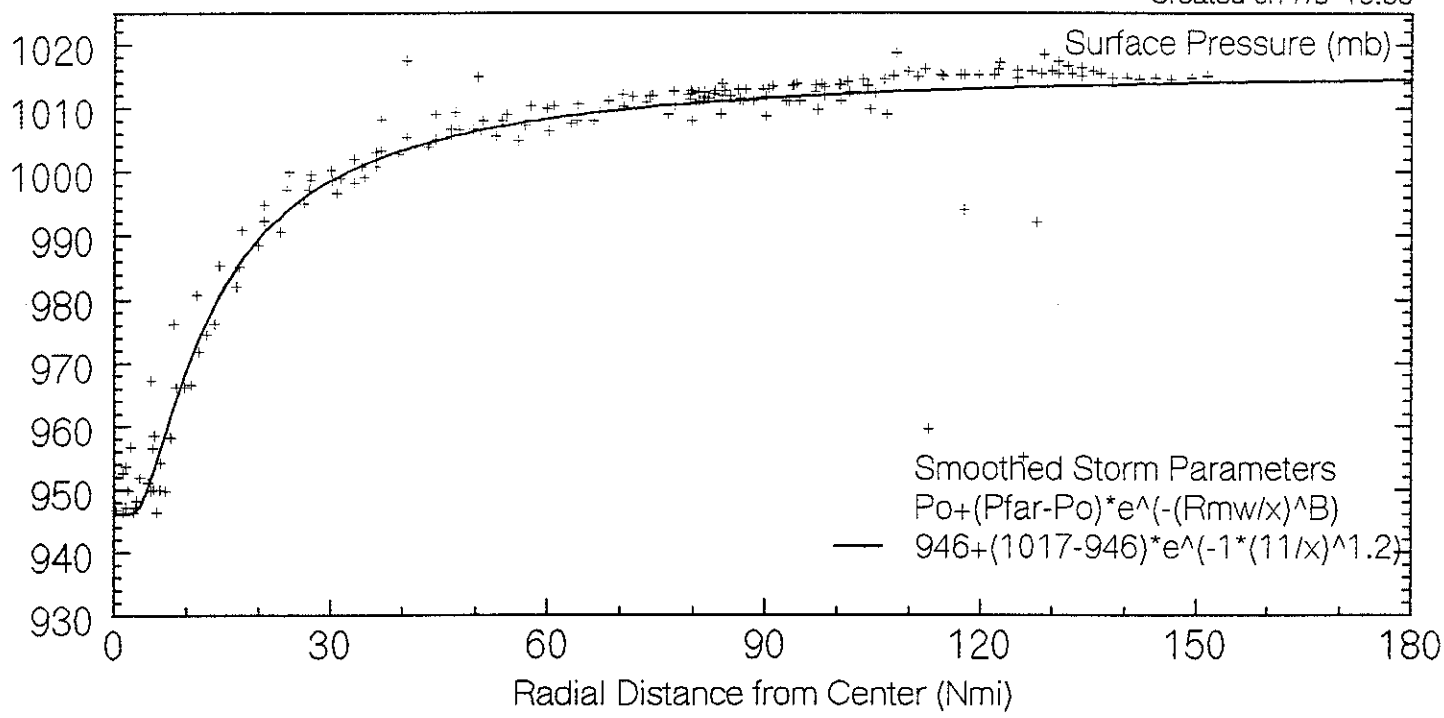

Oceanweather Tropical System Analysis

Surface Winds and Pressures Estimated from
Vortex and Minob Data Messages

Hurricane Andrew 1992
92082506 +/- 3hrs

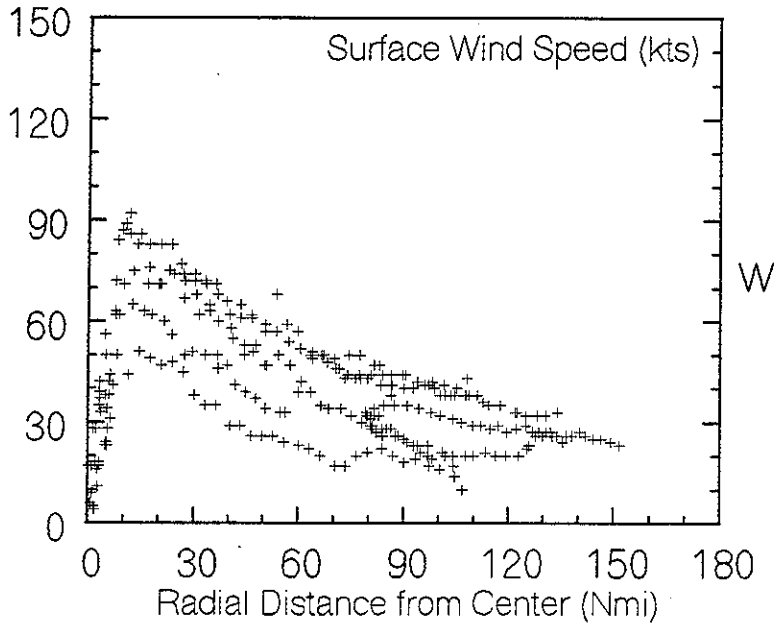

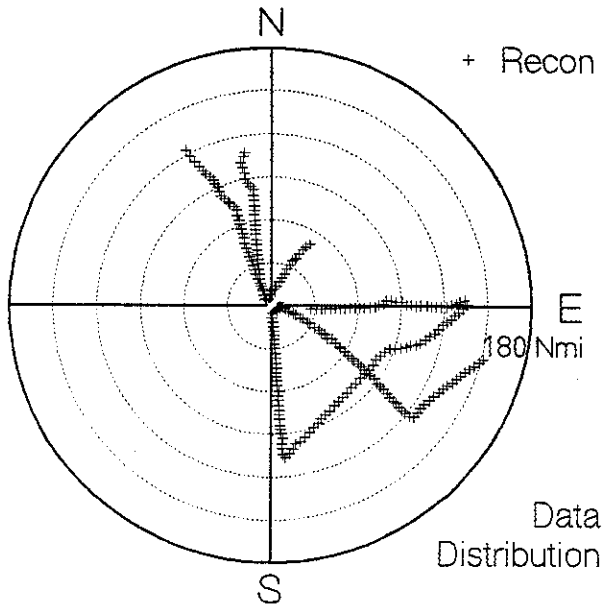

Created on 7/8 19:44

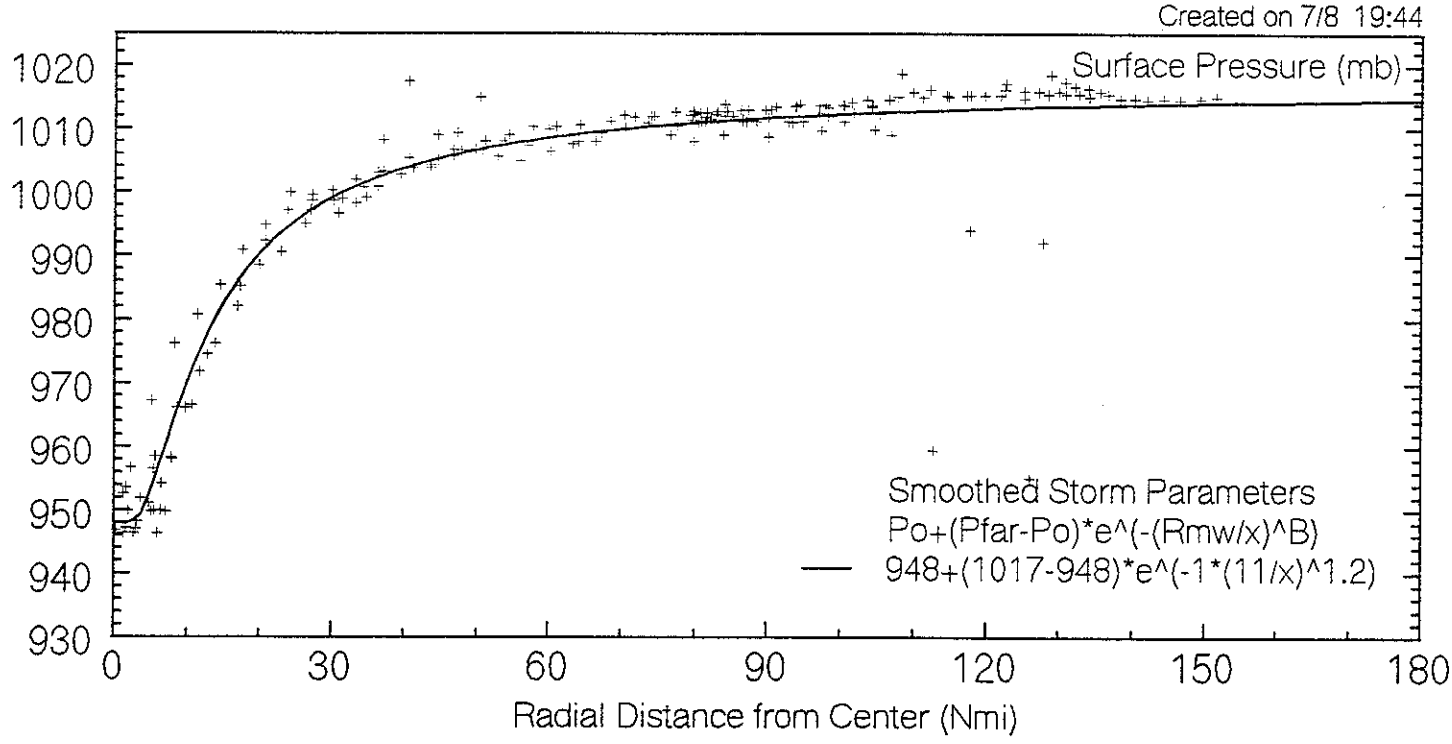

Oceanweather Tropical System Analysis

Surface Winds and Pressures Estimated from
Vortex and Minob Data Messages

Hurricane Andrew 1992

92082512 +/- 3hrs

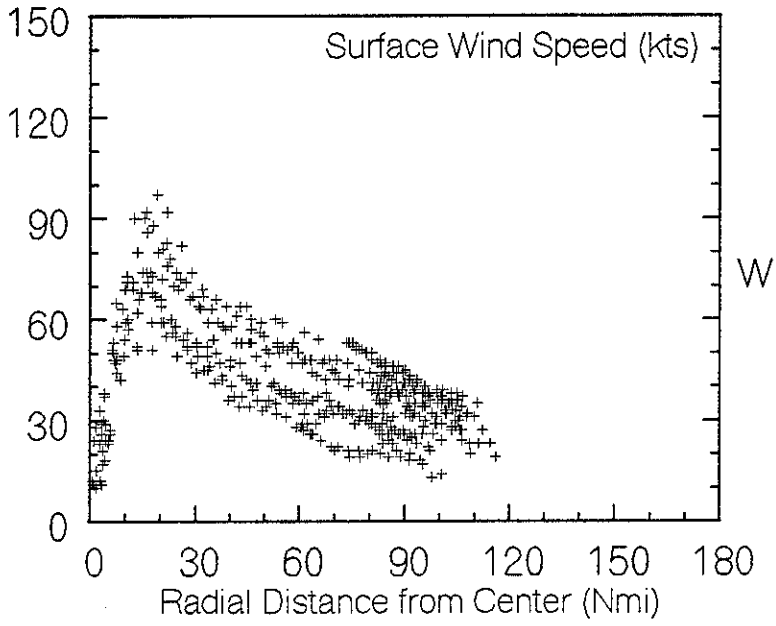

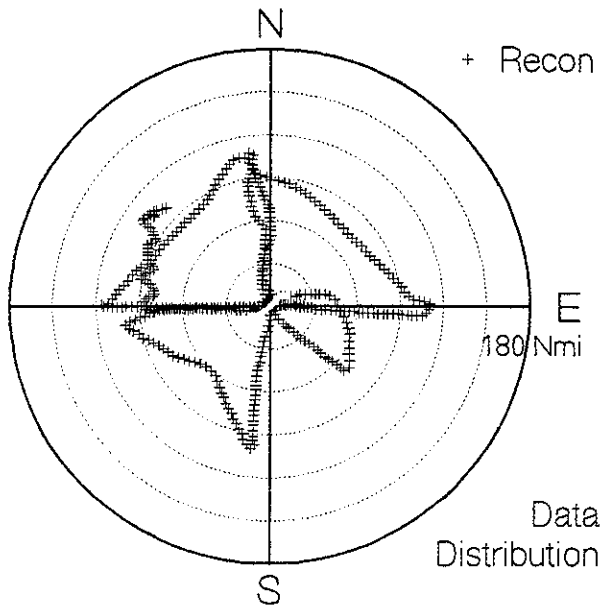

Created on 7/8 19:46

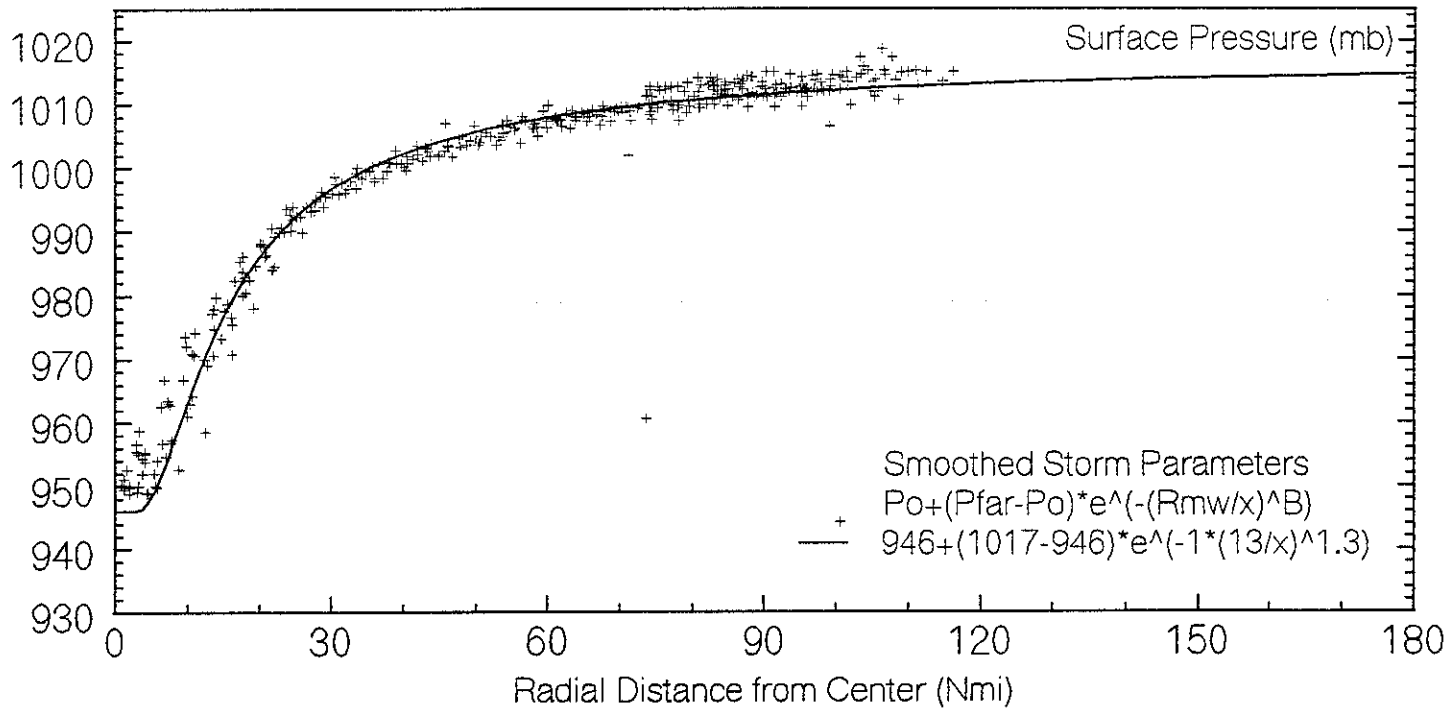

Oceanweather Tropical System Analysis

Surface Winds and Pressures Estimated from
Vortex and Minob Data Messages

Hurricane Andrew 1992
92082518 +/- 3hrs

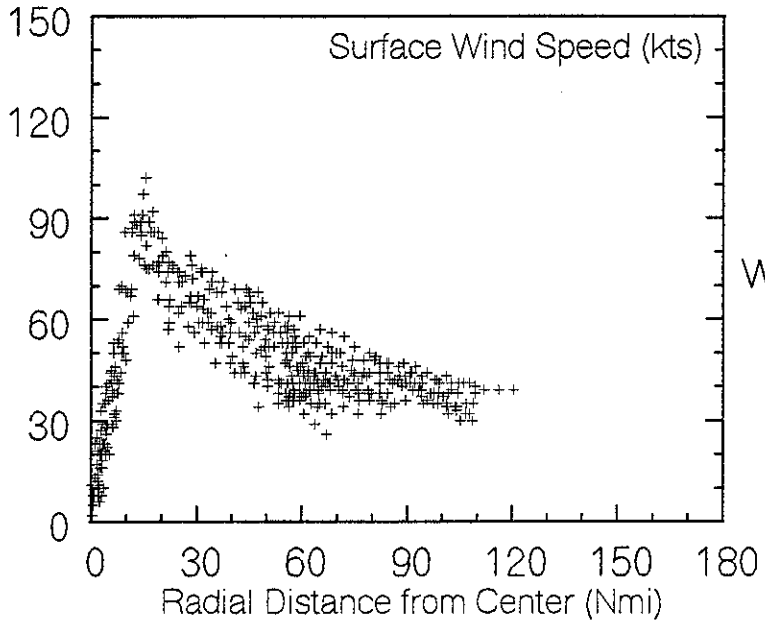

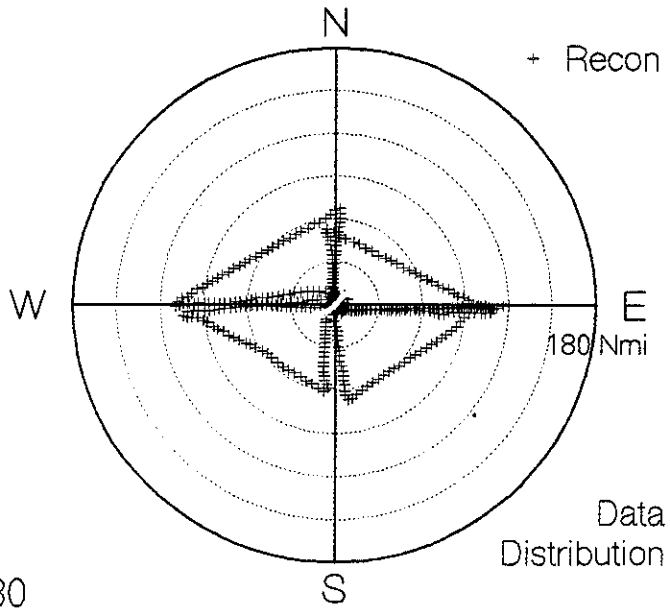

Created on 7/8 19:48

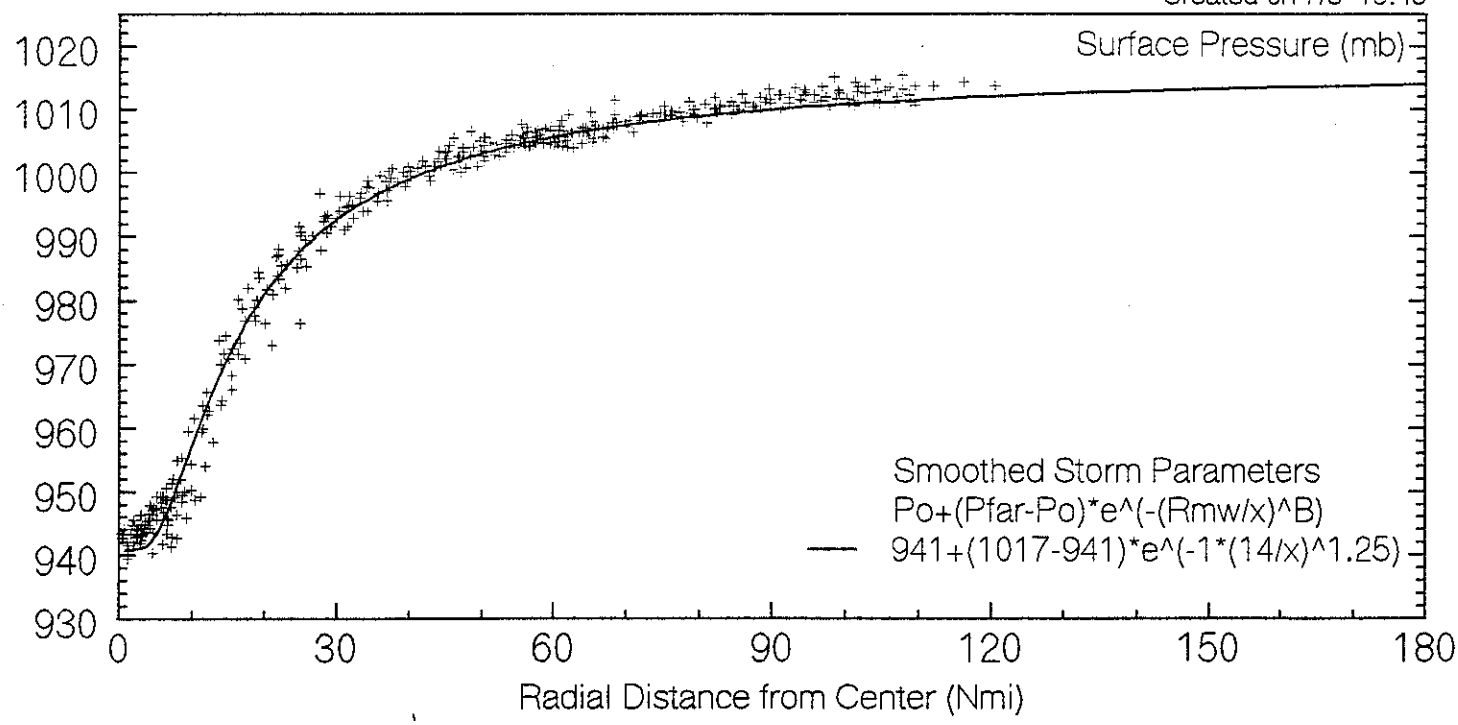

Oceanweather Tropical System Analysis

Surface Winds and Pressures Estimated from
Vortex and Minob Data Messages

Hurricane Andrew 1992

92082521 +/- 3hrs

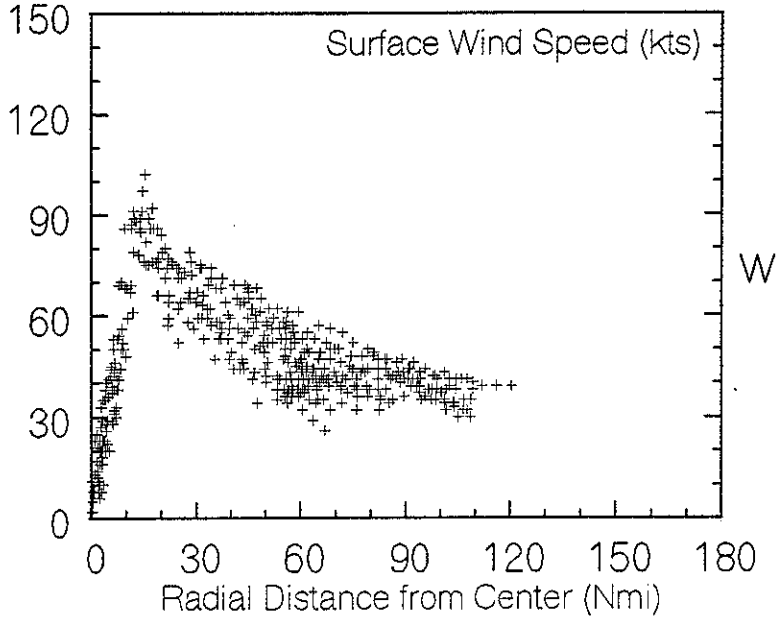

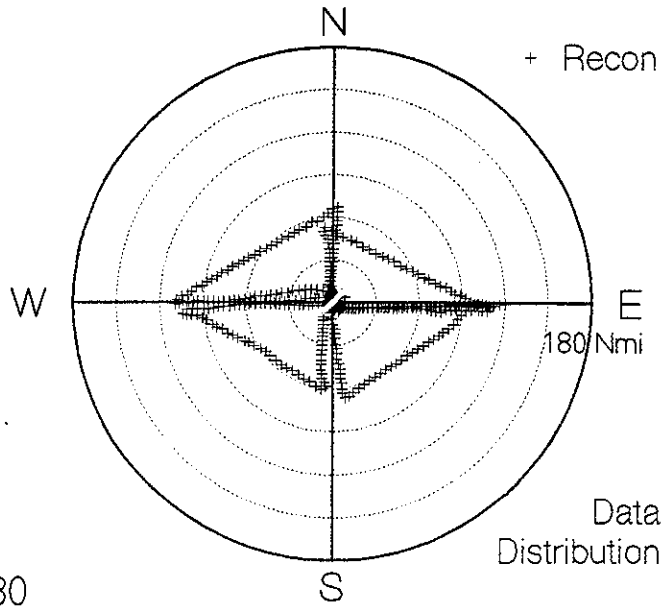

Created on 7/8 19:50

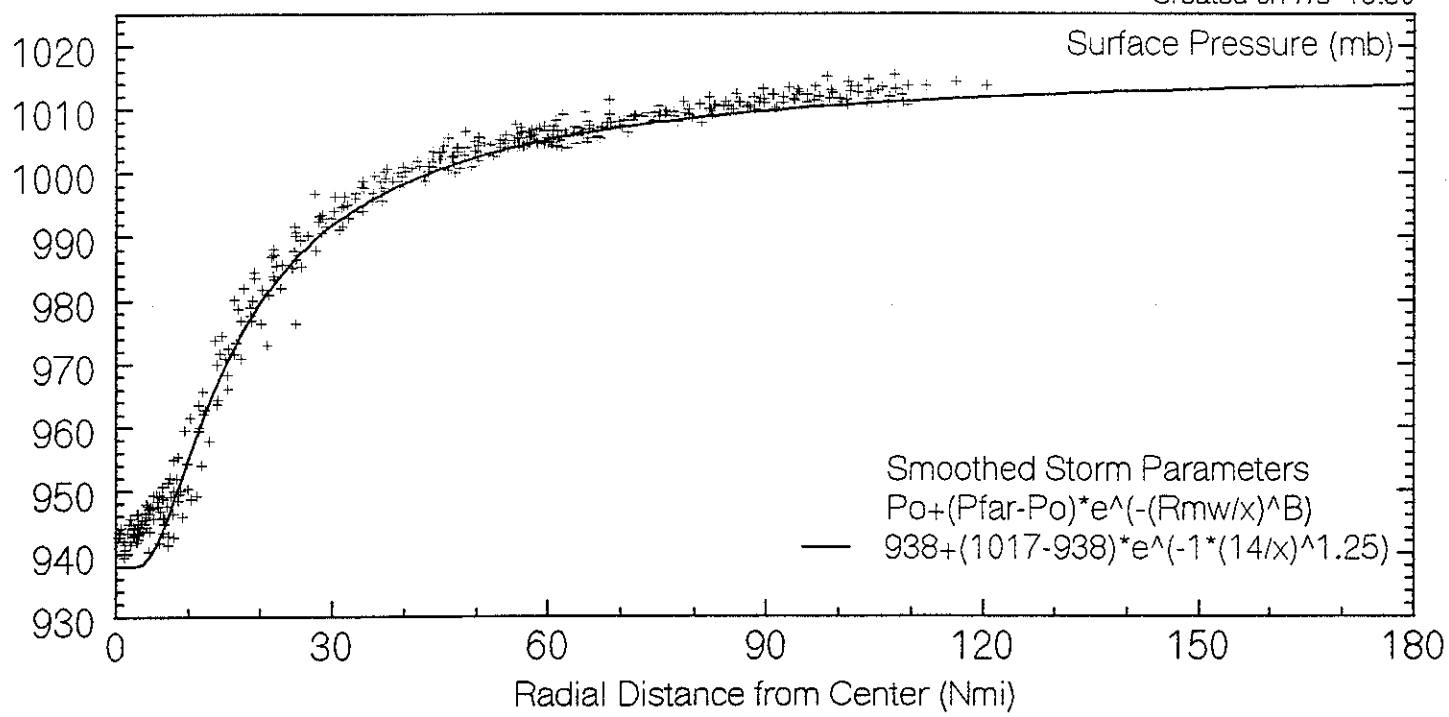

Oceanweather Tropical System Analysis

Surface Winds and Pressures Estimated from
Vortex and Minob Data Messages

Hurricane Andrew 1992
92082606 +/- 3hrs

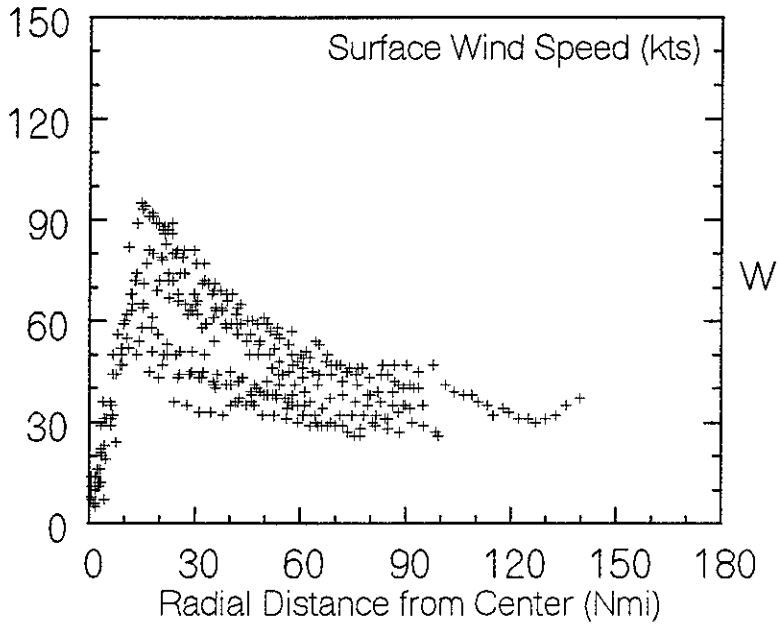

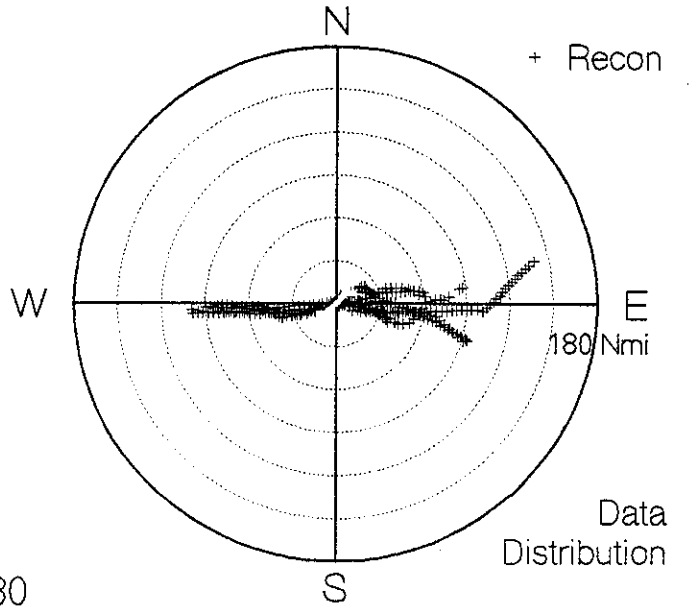

Created on 7/8 19:59

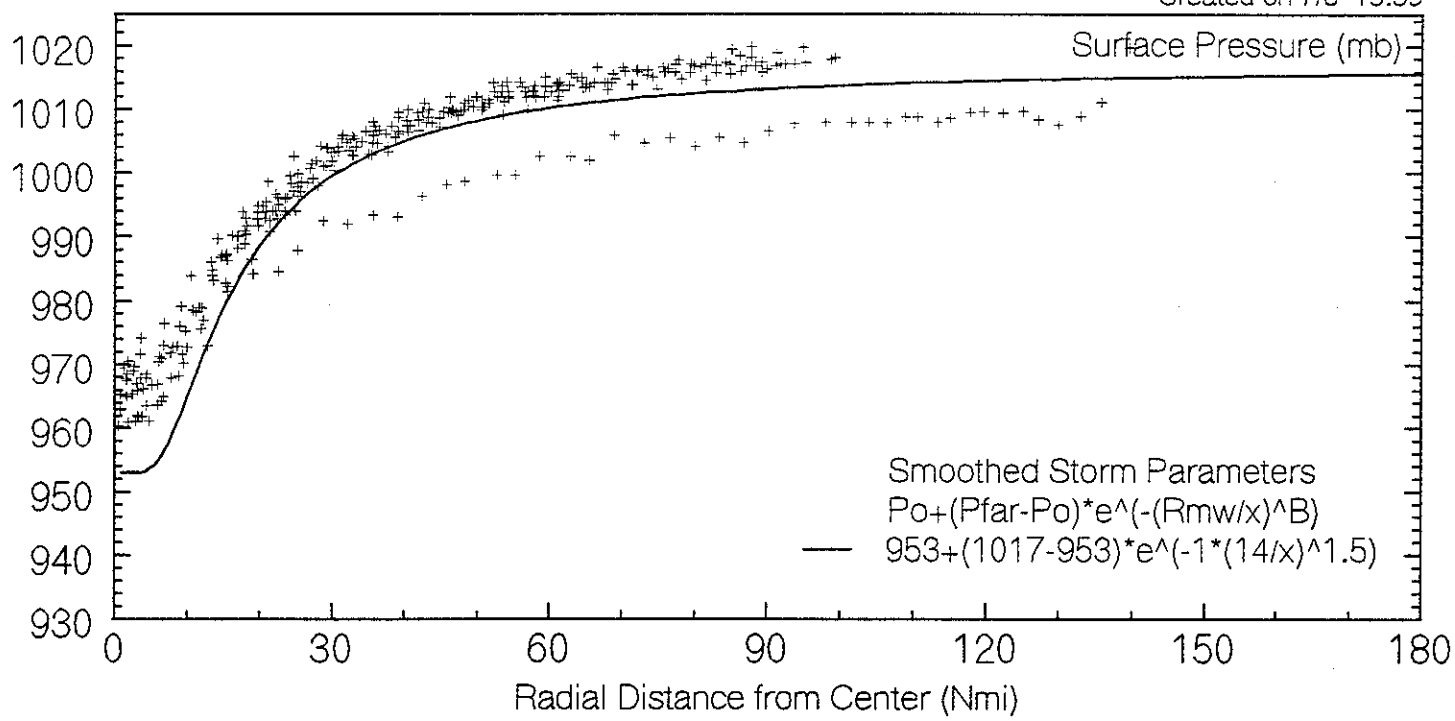

Oceanweather Tropical System Analysis

Surface Winds and Pressures Estimated from
Vortex and Minob Data Messages

Hurricane Andrew 1992

92082609 +/- 3hrs

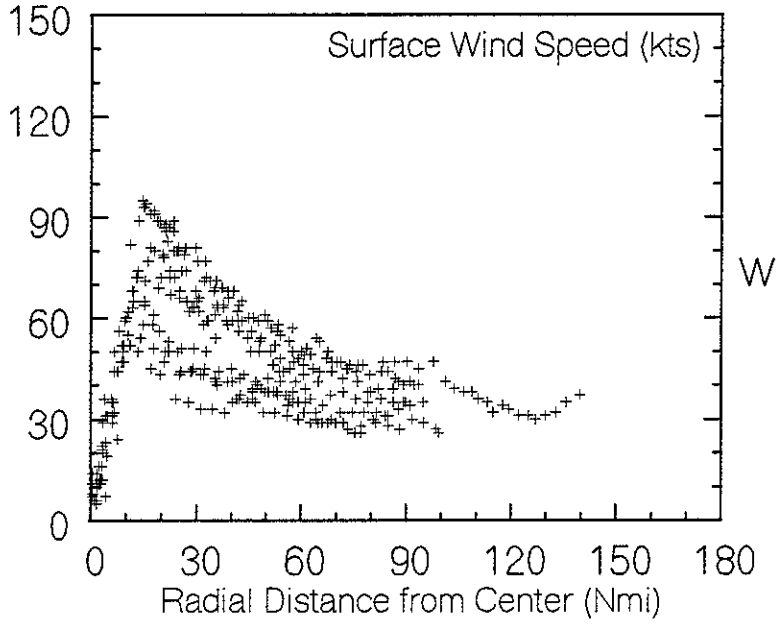

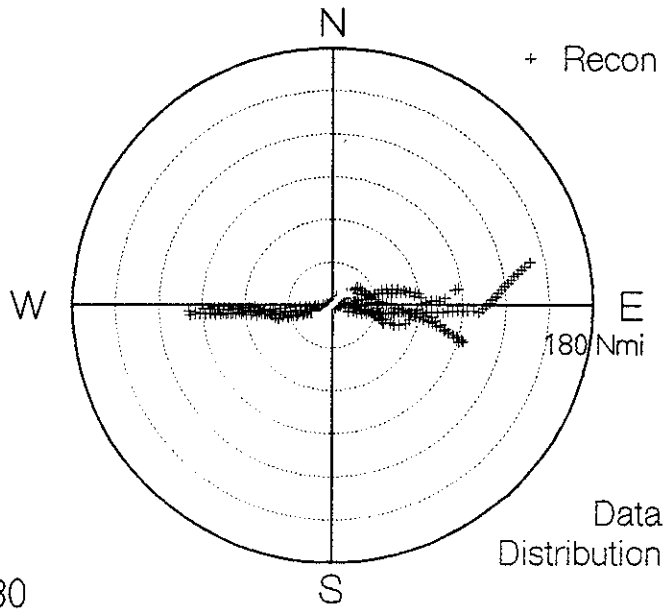

Created on 7/8 20:01

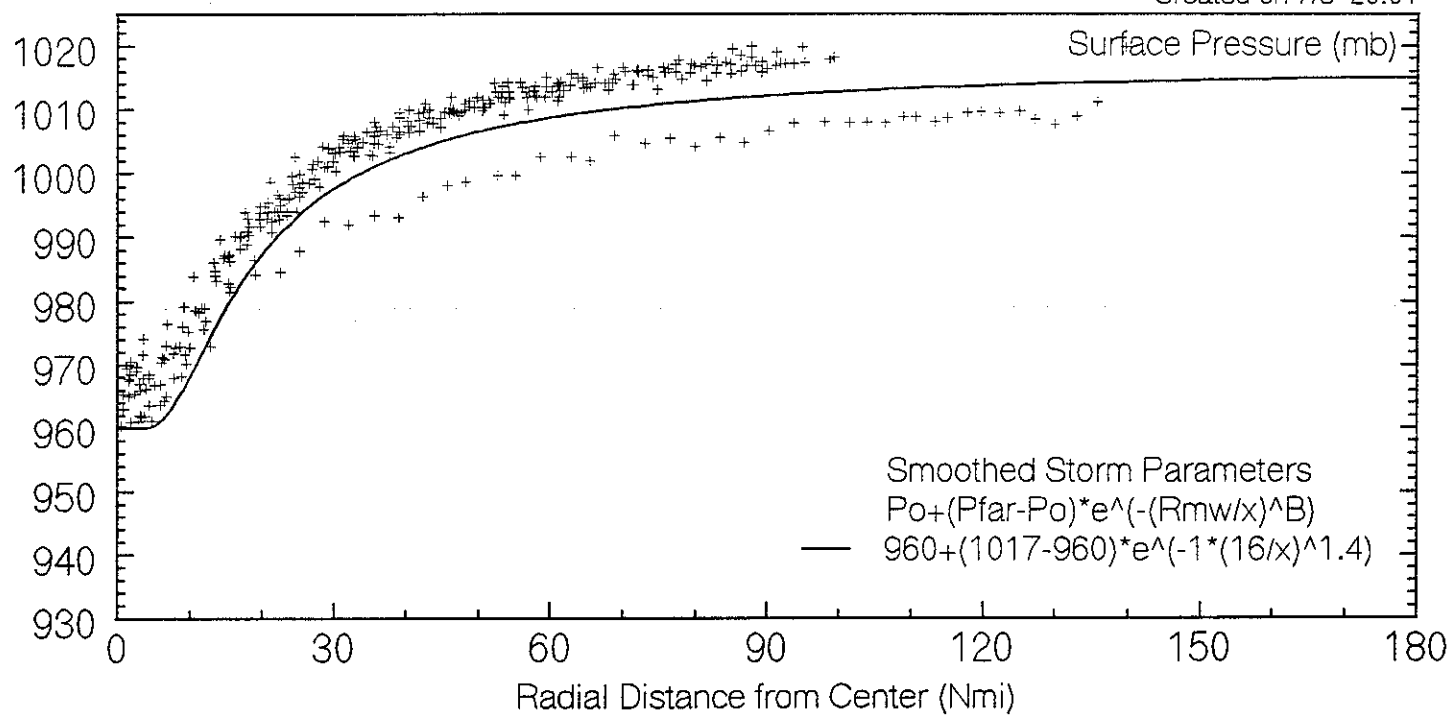

Appendix D.

Wind distribution in Hurricane Andrew at 3-hourly intervals over the full hindcast period and spatial domain modelled. Each half (full) barb represents 5 (10) knots, each flag 50 knots, of the effective neutral 20-m 1-hour average wind speed. Winds are plotted at every other row and column of grid points of the grid used for the wave and current hindcasts.

MMS Andrew 1992

92082409

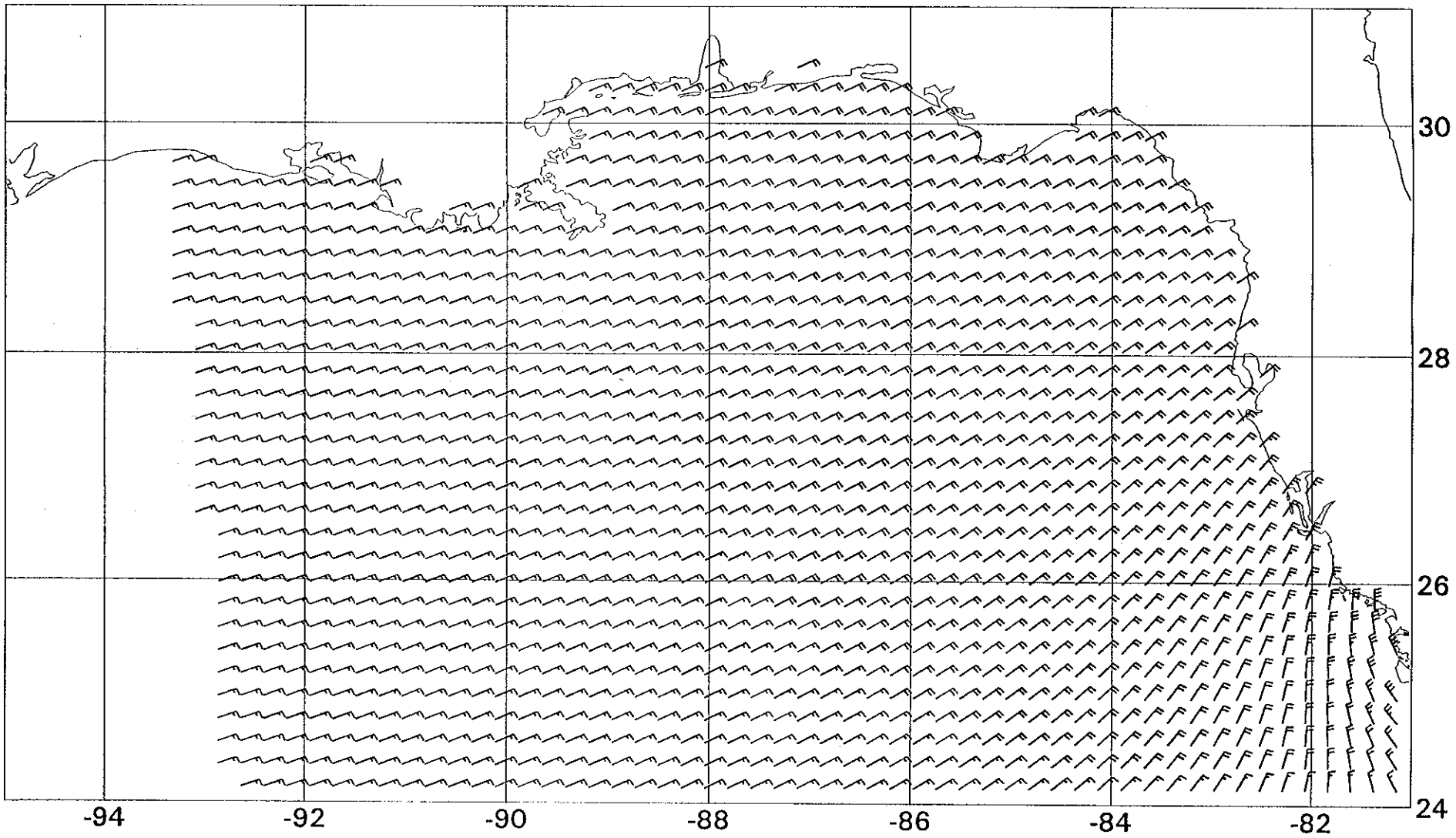

PLOTTED ON 8-JUL-94 08:34:19

MMS Andrew 1992

92082412

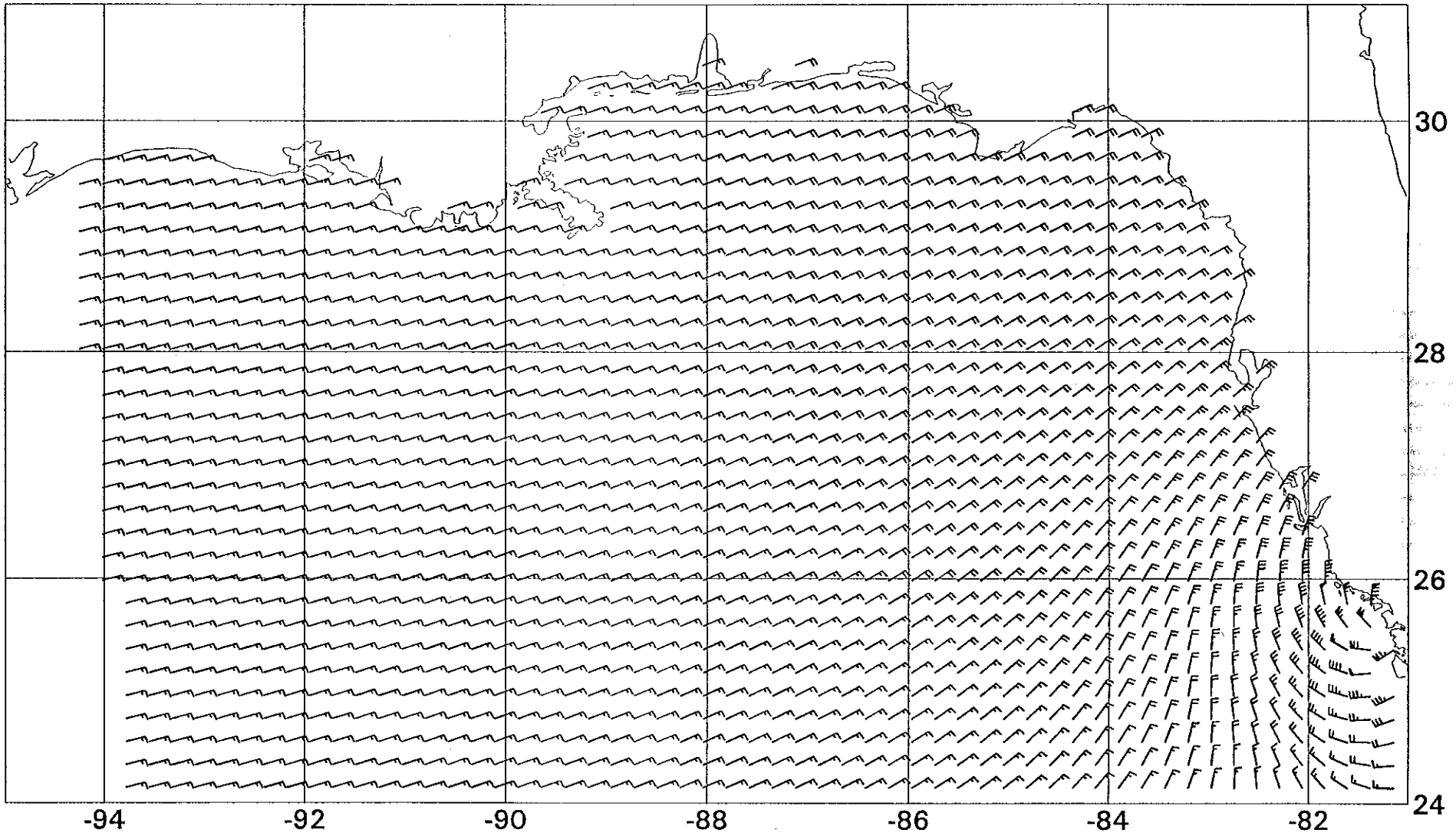

PLOTTED ON 8-JUL-94 08:34:38

MMS Andrew 1992

92082415

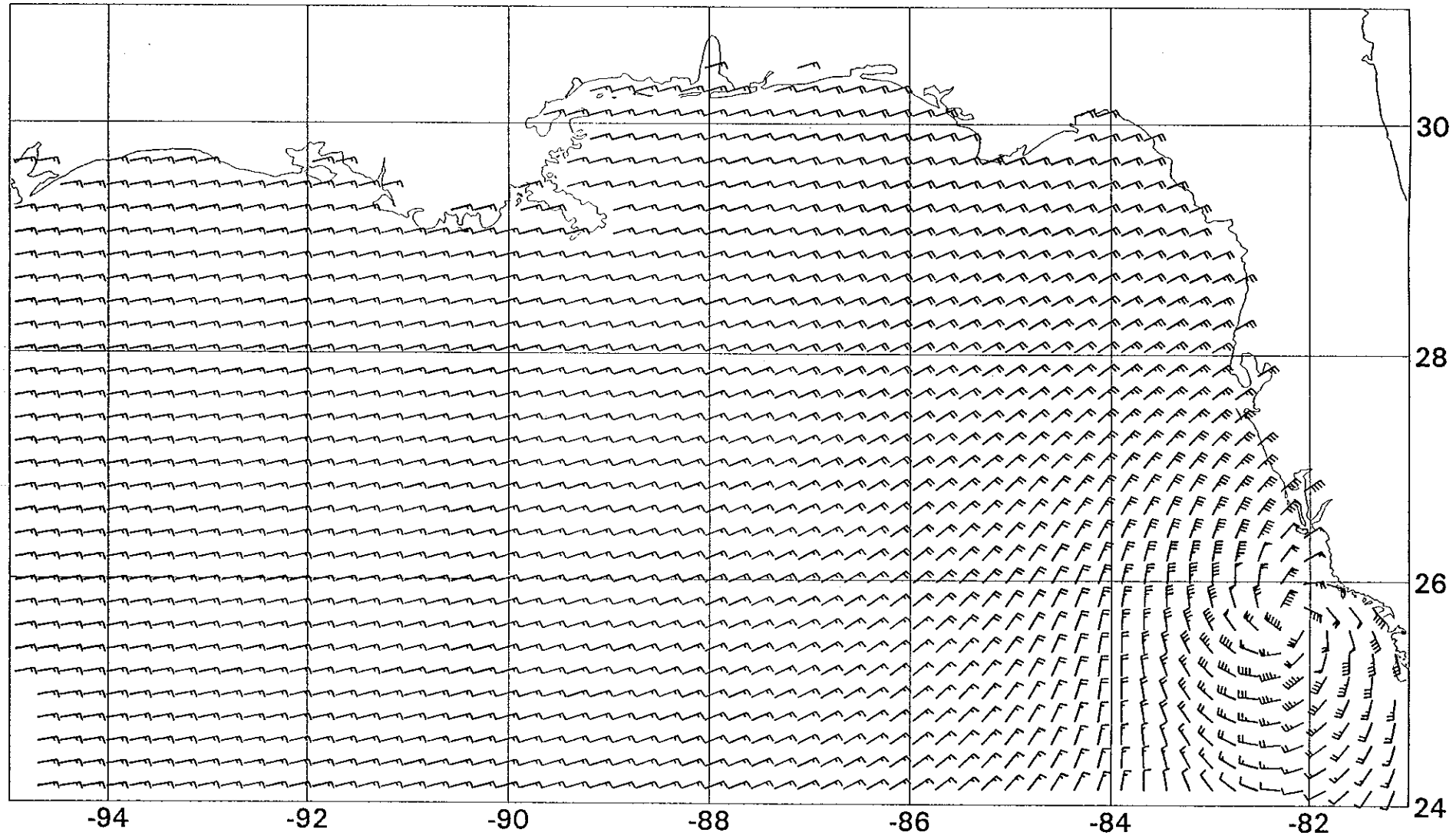

PLOTTED ON 8-JUL-94 08:35:12

MMS Andrew 1992

92082418

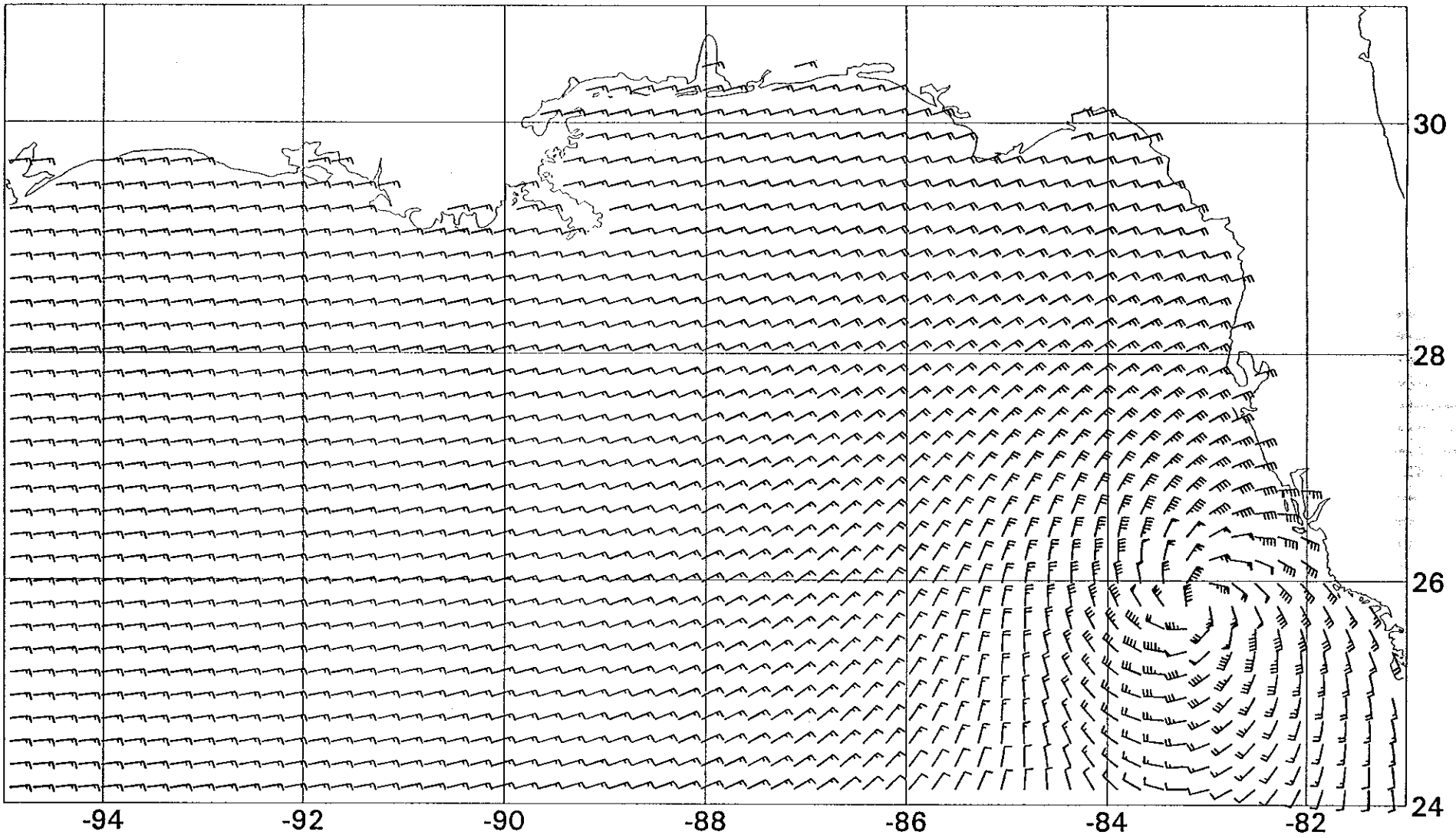

PLOTTED ON 8-JUL-94 08:35:56

MMS Andrew 1992

92082421

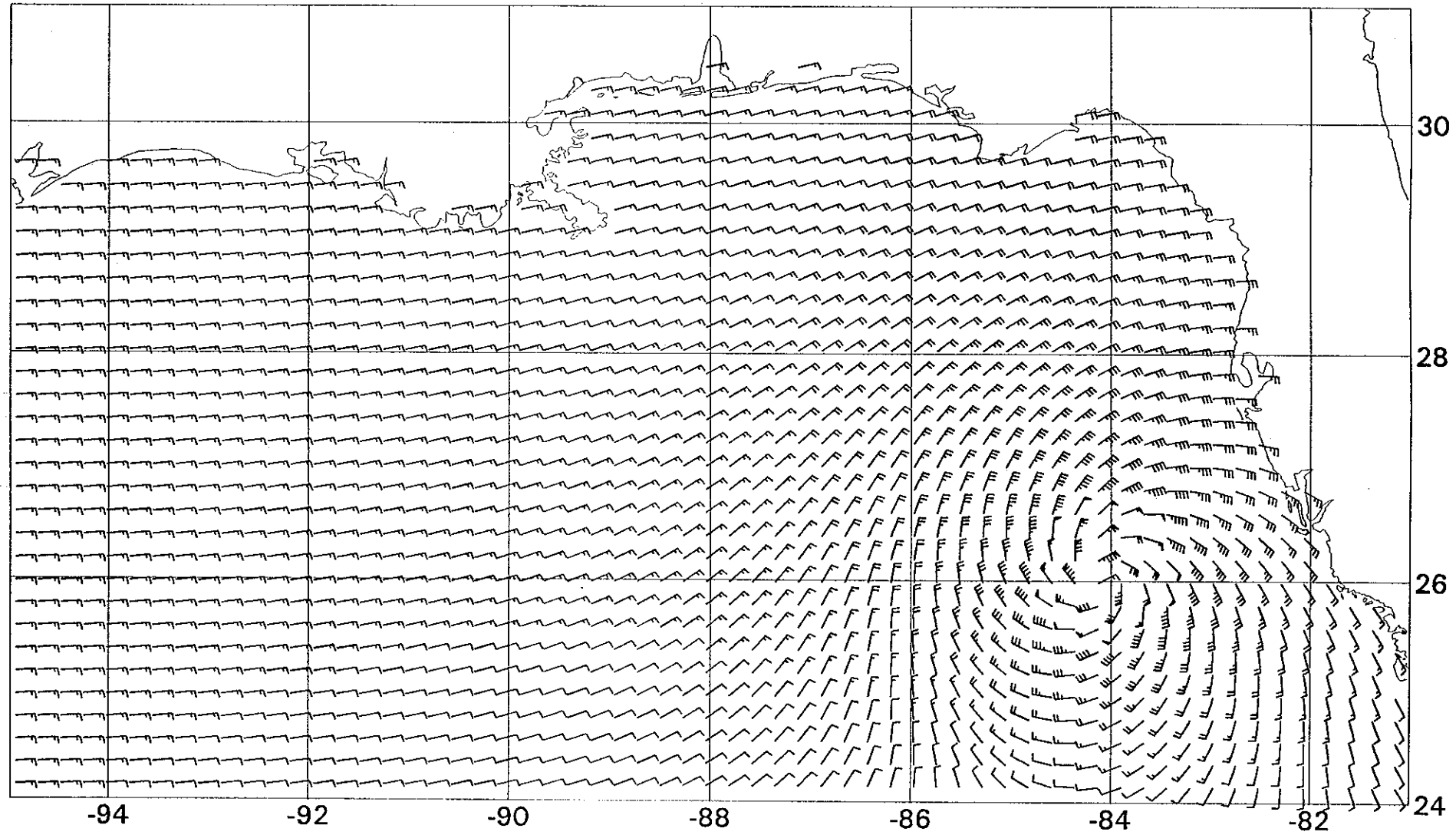

PLOTTED ON 8-JUL-94 08:36:46

MMS Andrew 1992

92082500

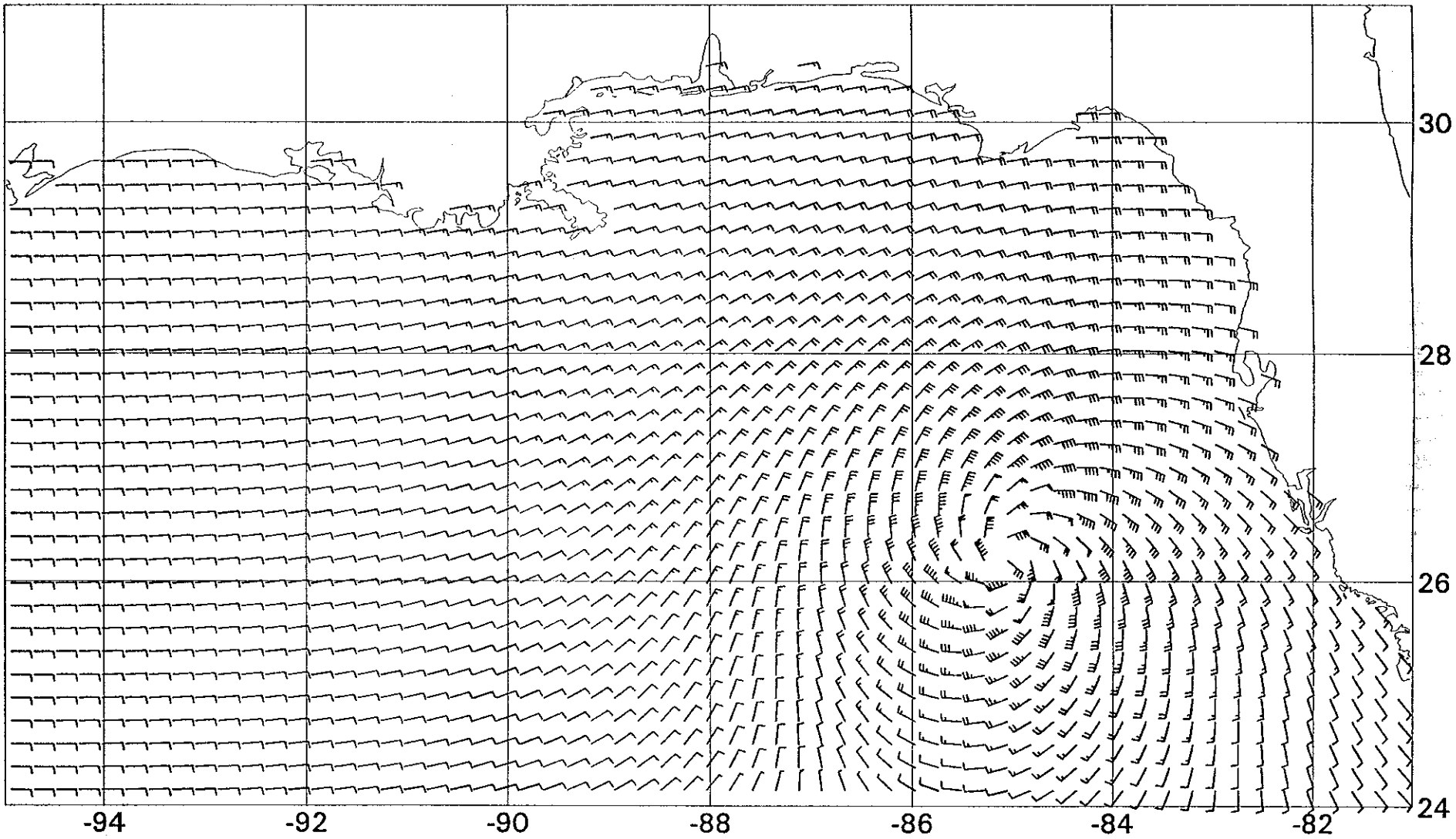

PLOTTED ON 8-JUL-94 08:37:20

MMS Andrew 1992

92082503

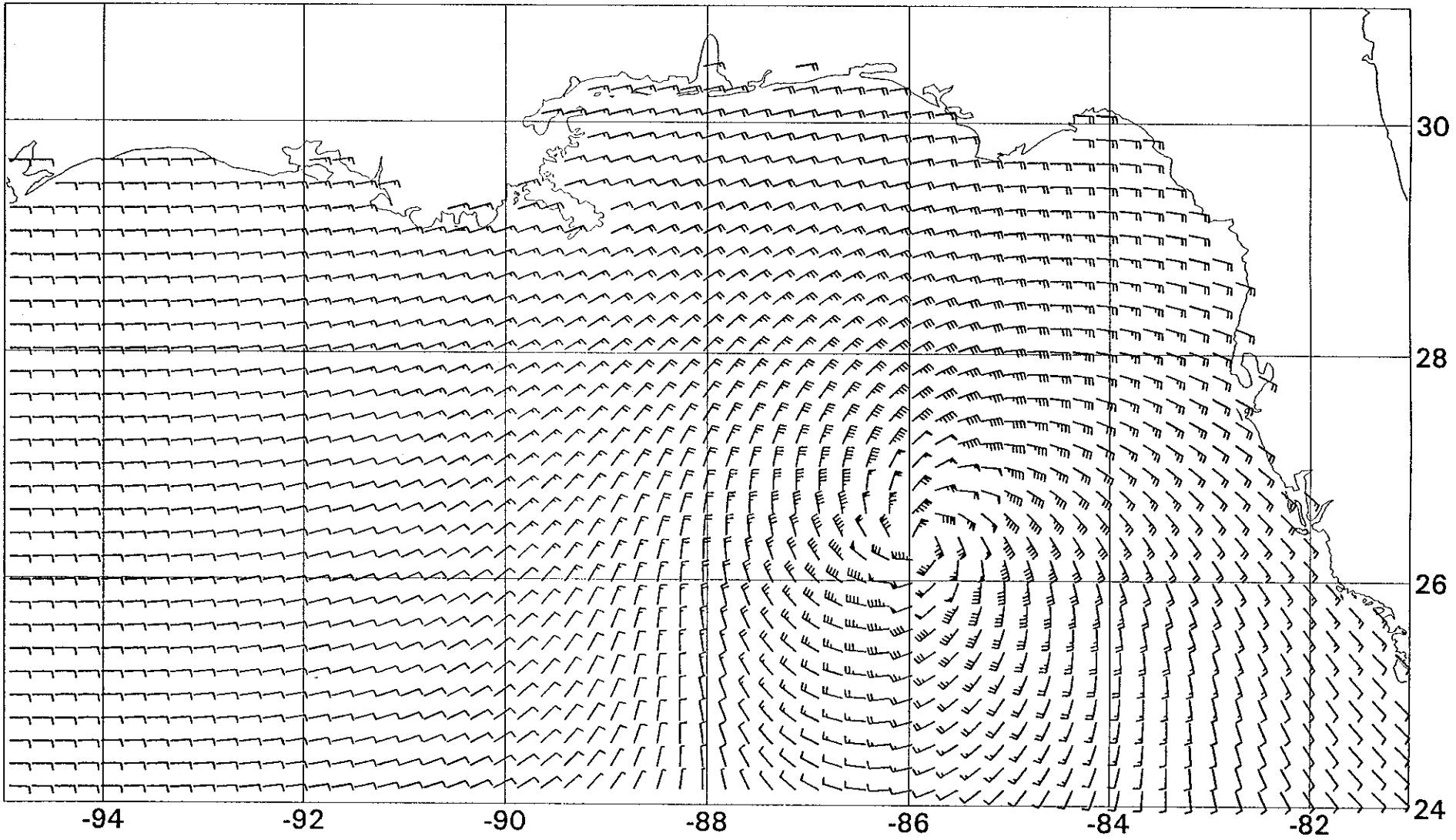

PLOTTED ON 8-JUL-94 08:37:47

MMS Andrew 1992

92082506

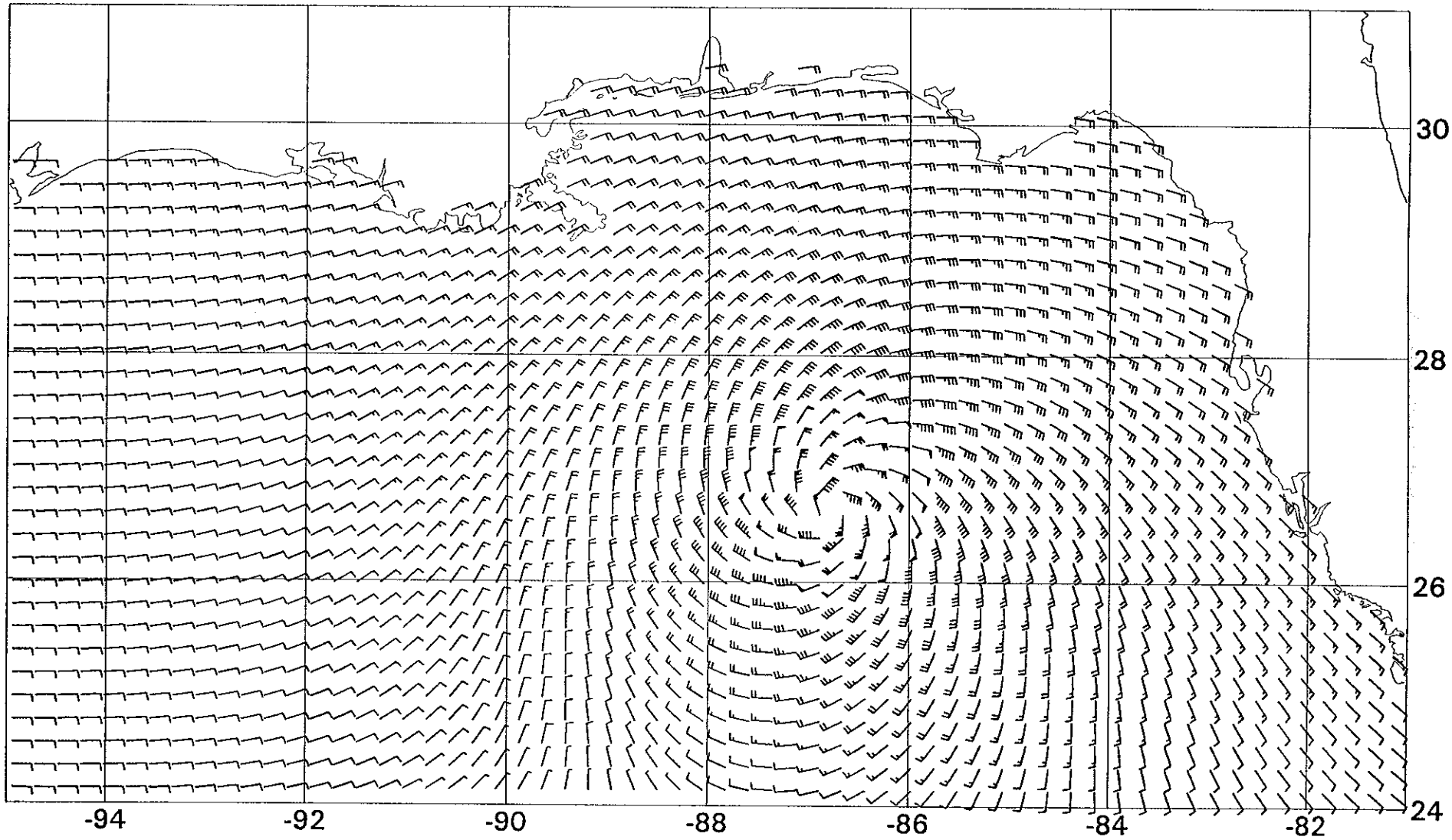

PLOTTED ON 8-JUL-94 08:38:17

MMS Andrew 1992

92082509

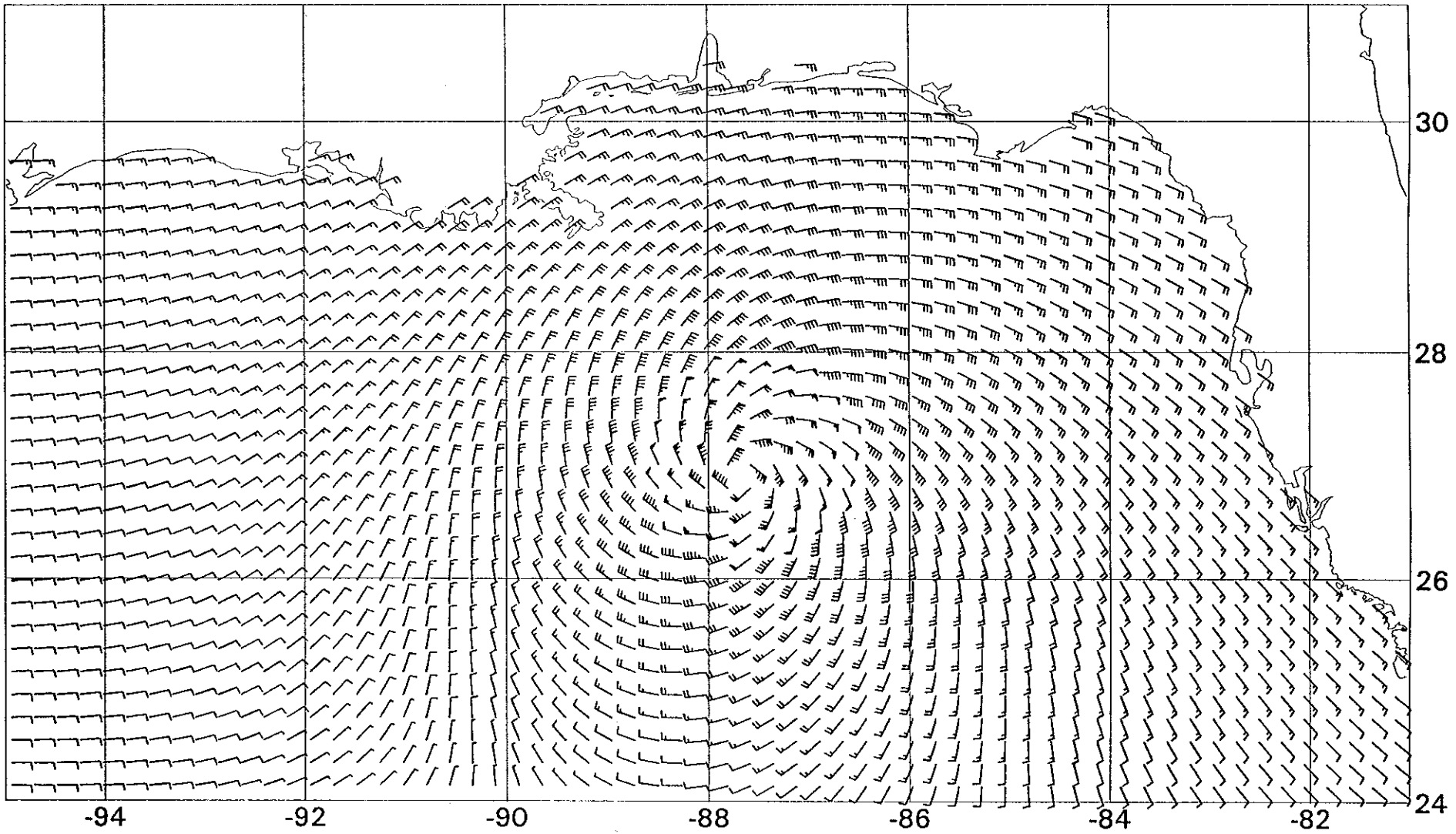

PLOTTED ON 8-JUL-94 08:38:44

MMS Andrew 1992

92082512

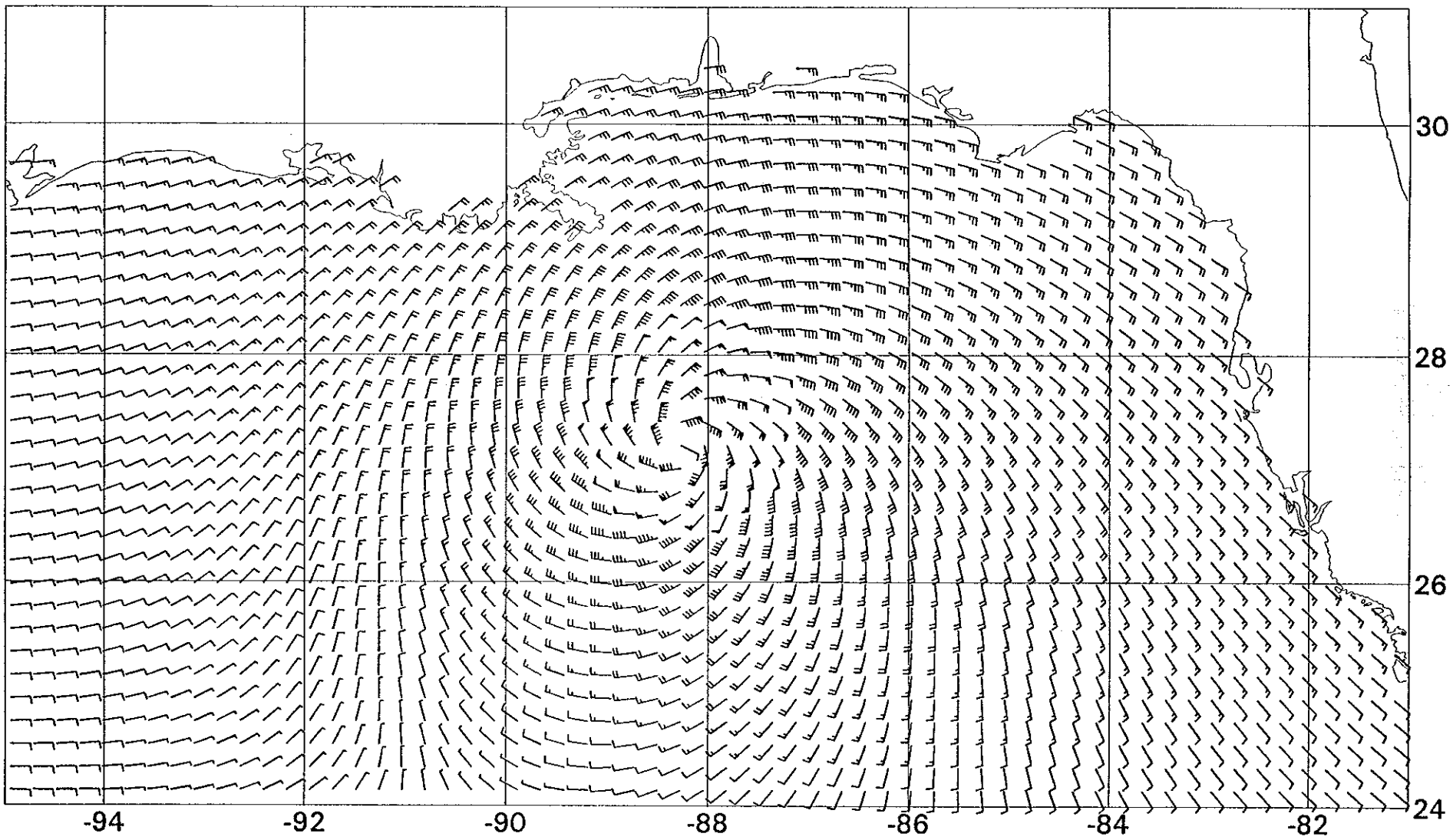

PLOTTED ON 8-JUL-94 08:39:24

MMS Andrew 1992

92082518

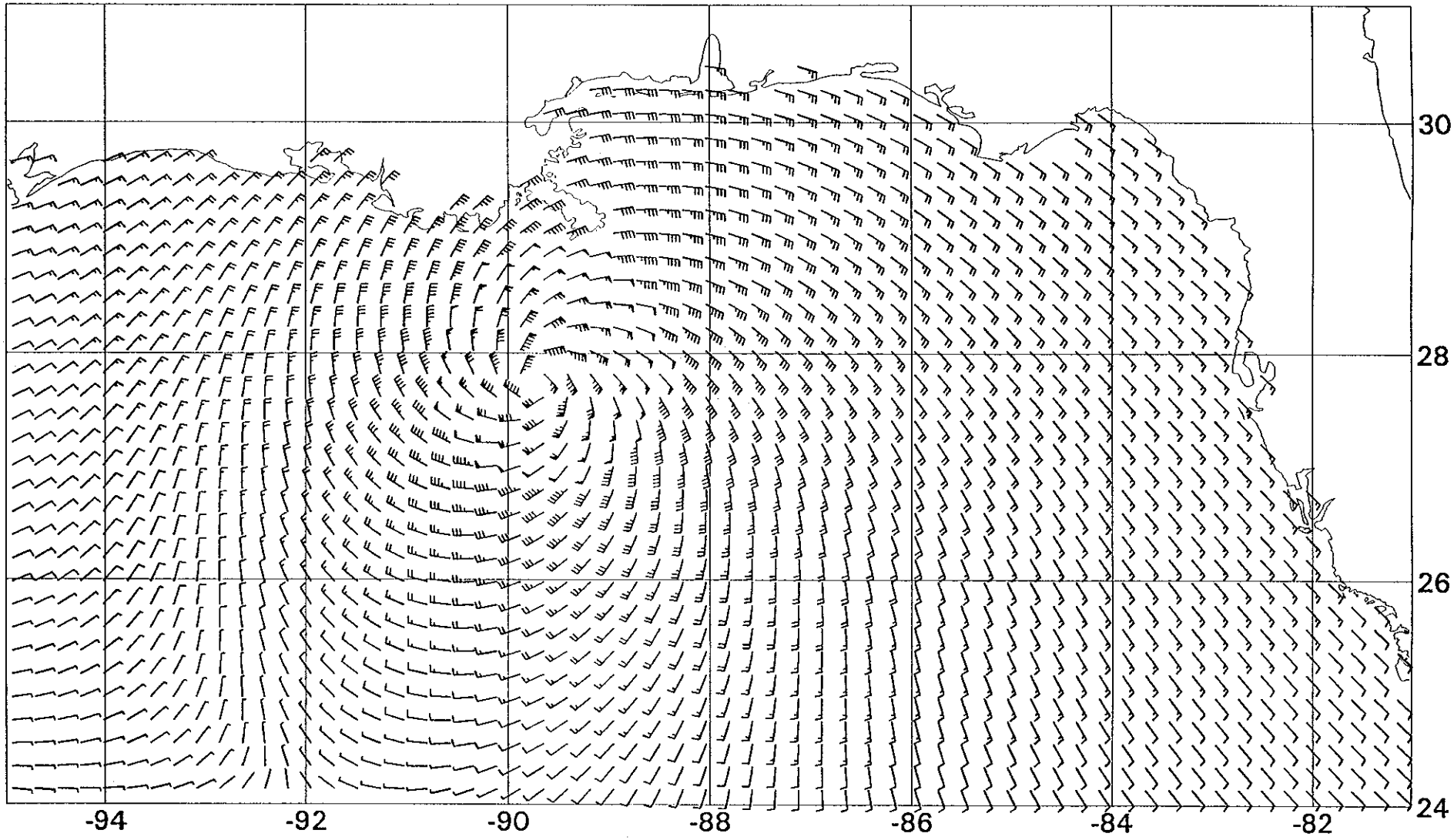

PLOTTED ON 8-JUL-94 08:41:03

MMS Andrew 1992

92082521

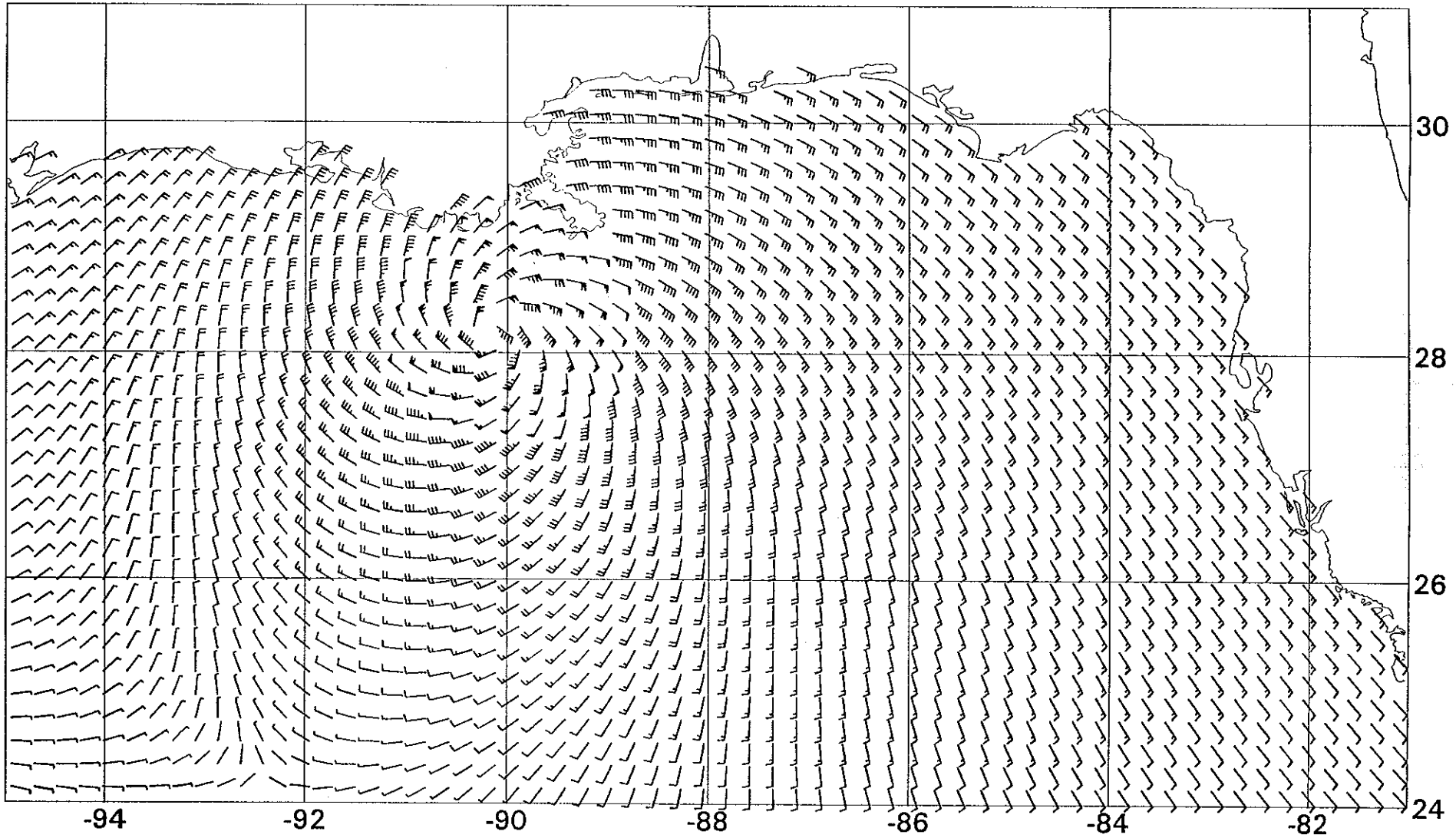

PLOTTED ON 8-JUL-94 08:42:04

MMS Andrew 1992

92082600

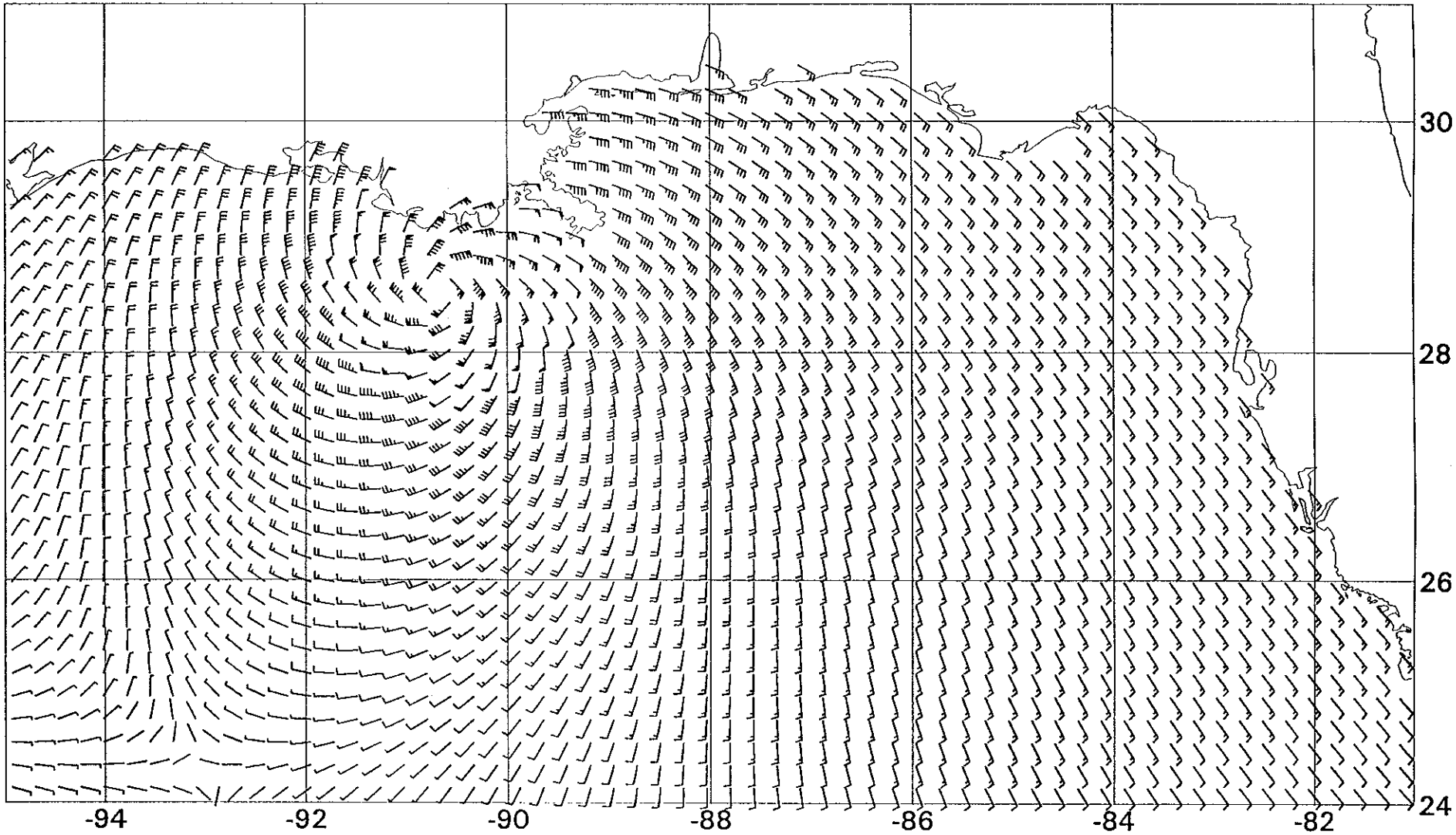

PLOTTED ON 8-JUL-94 08:42:35

MMS Andrew 1992

92082603

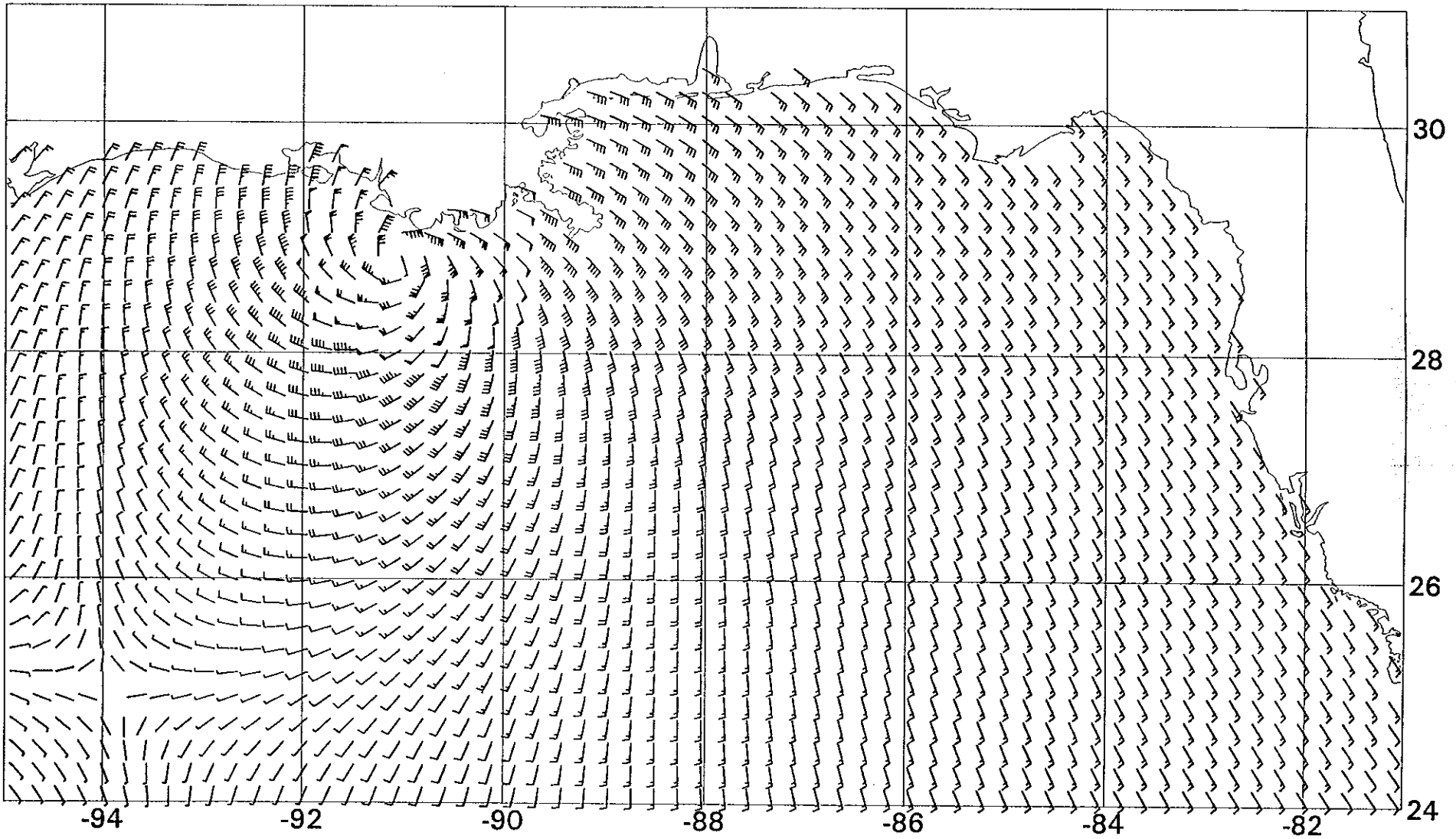

PLOTTED ON 8-JUL-94 08:43:45

MMS Andrew 1992

92082606

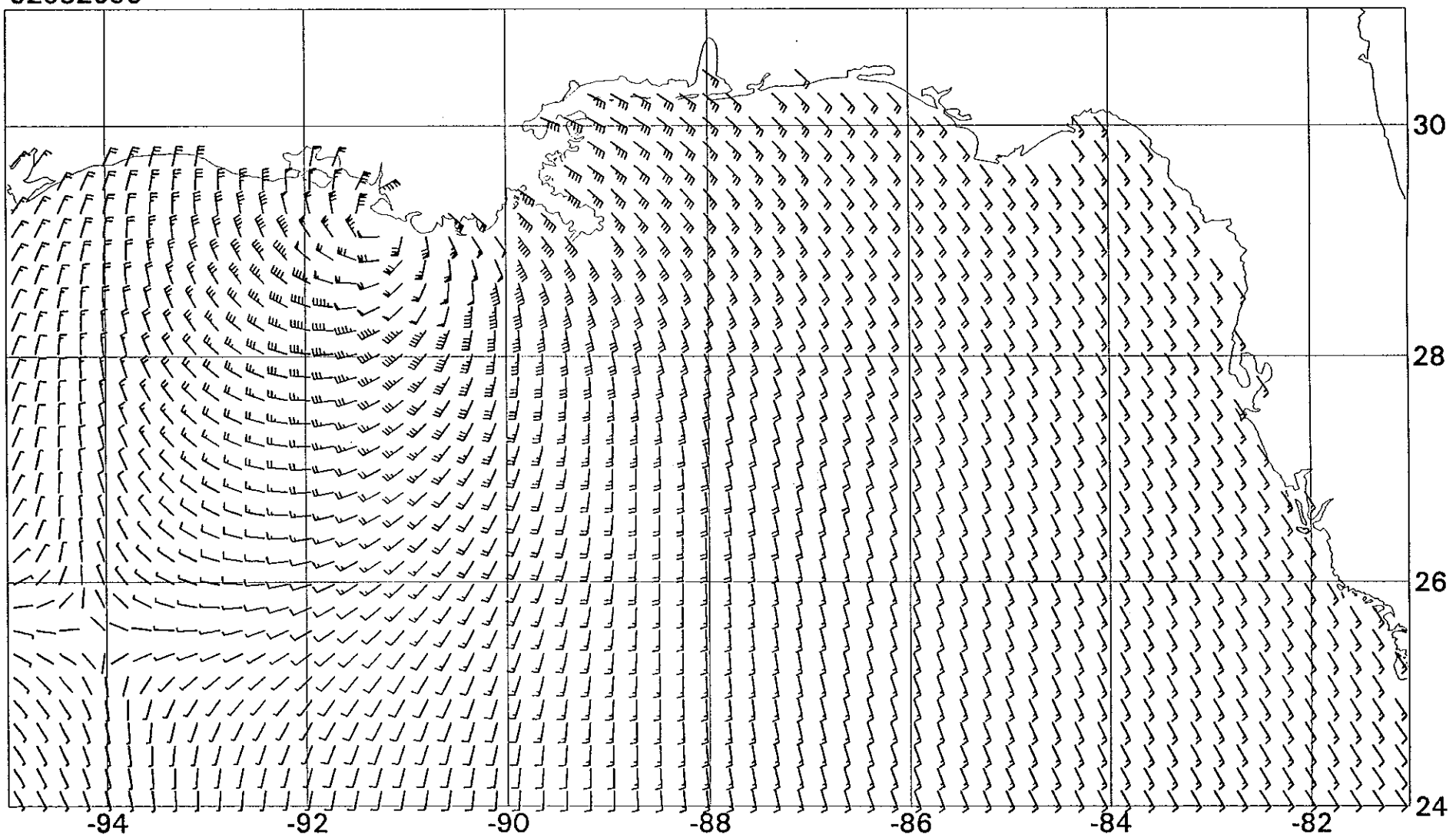

PLOTTED ON 8-JUL-94 08:45:12

MMS Andrew 1992

92082609

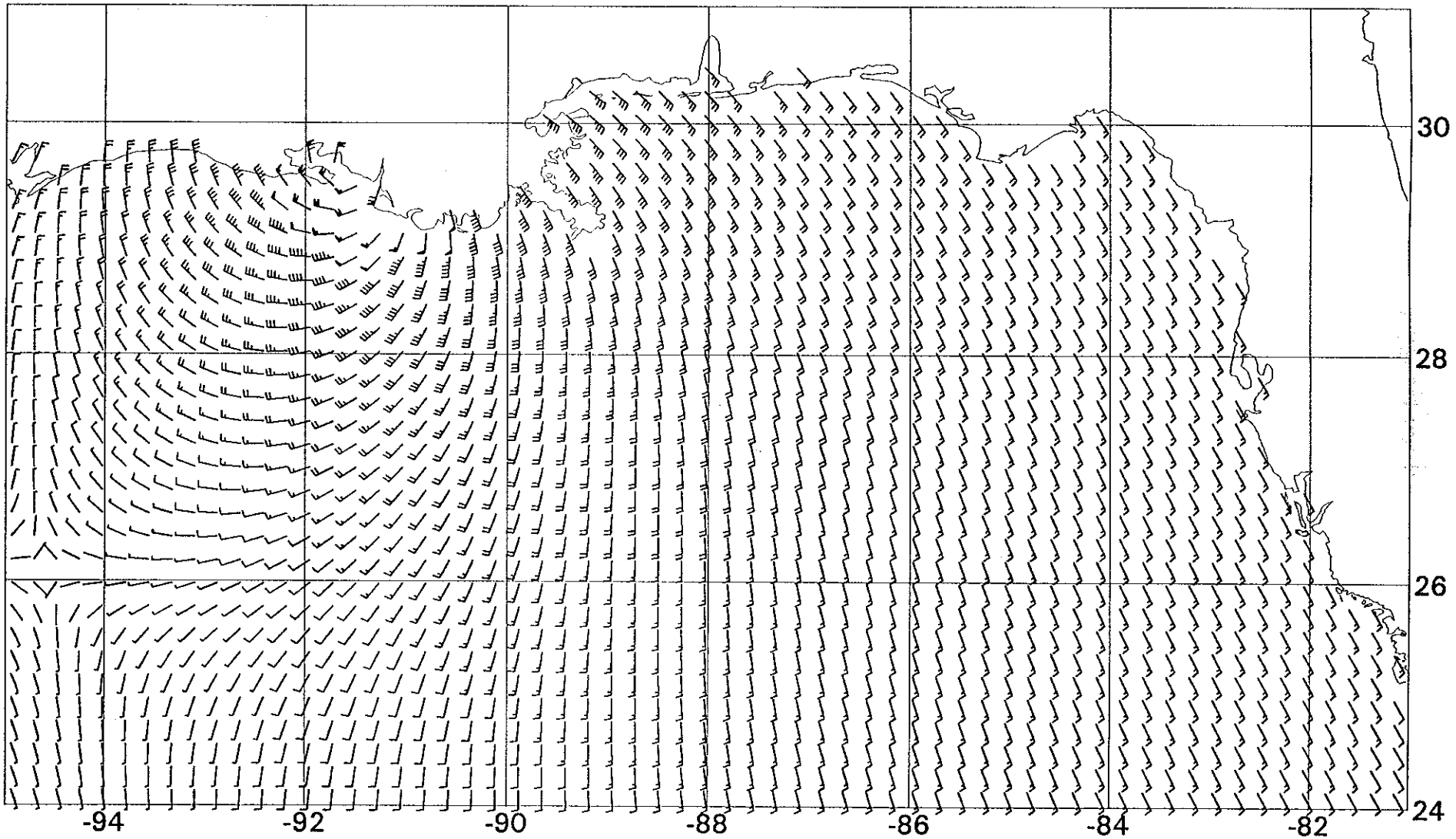

PLOTTED ON 8-JUL-94 08:46:24

MMS Andrew 1992

92082612

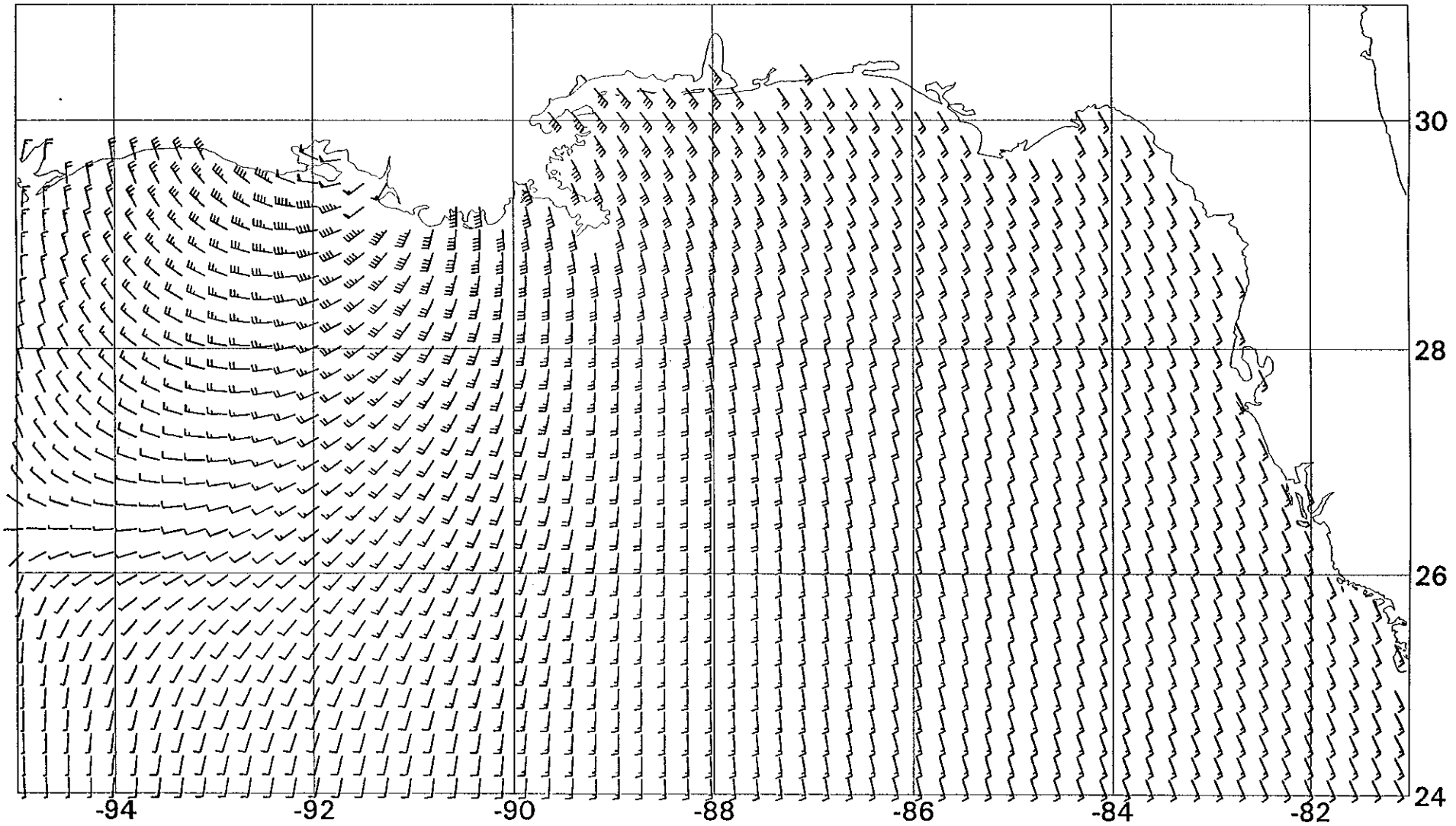

PLOTTED ON 8-JUL-94 08:47:28

MMS Andrew 1992

92082615

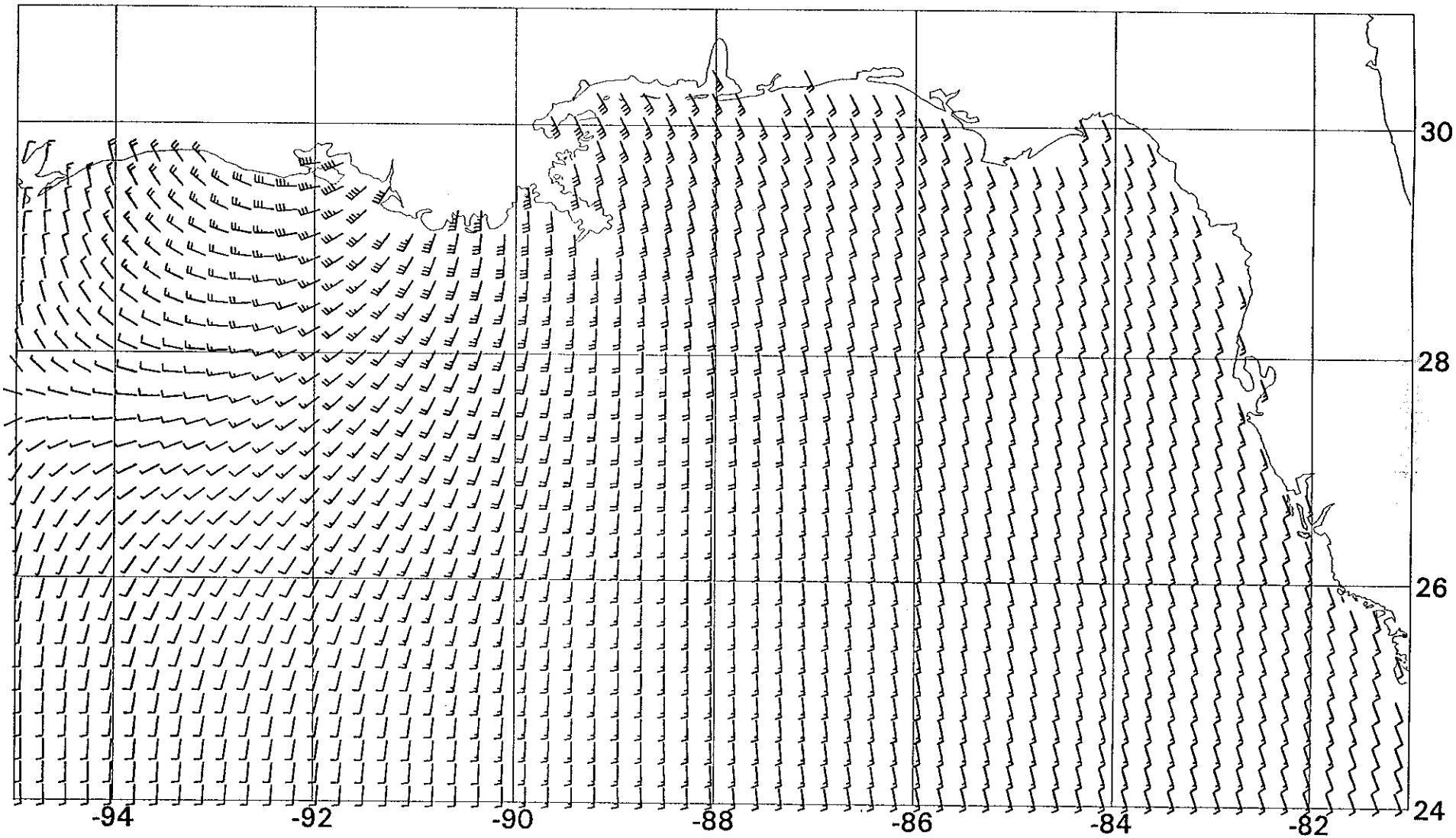

PLOTTED ON 8-JUL-94 08:48:33

MMS Andrew 1992

92082618

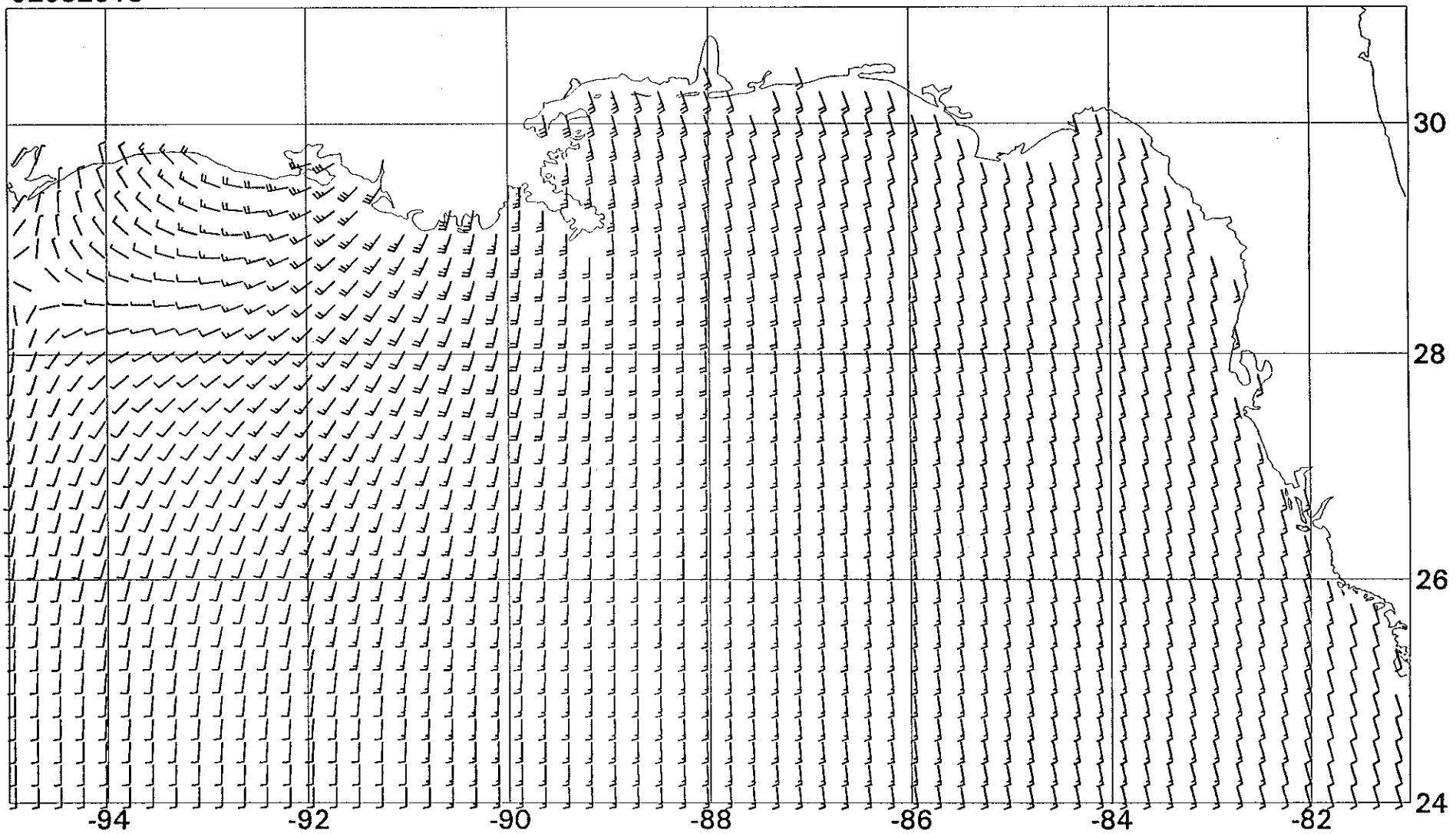

PLOTTED ON 8-JUL-94 08:49:36

MMS Andrew 1992

92082621

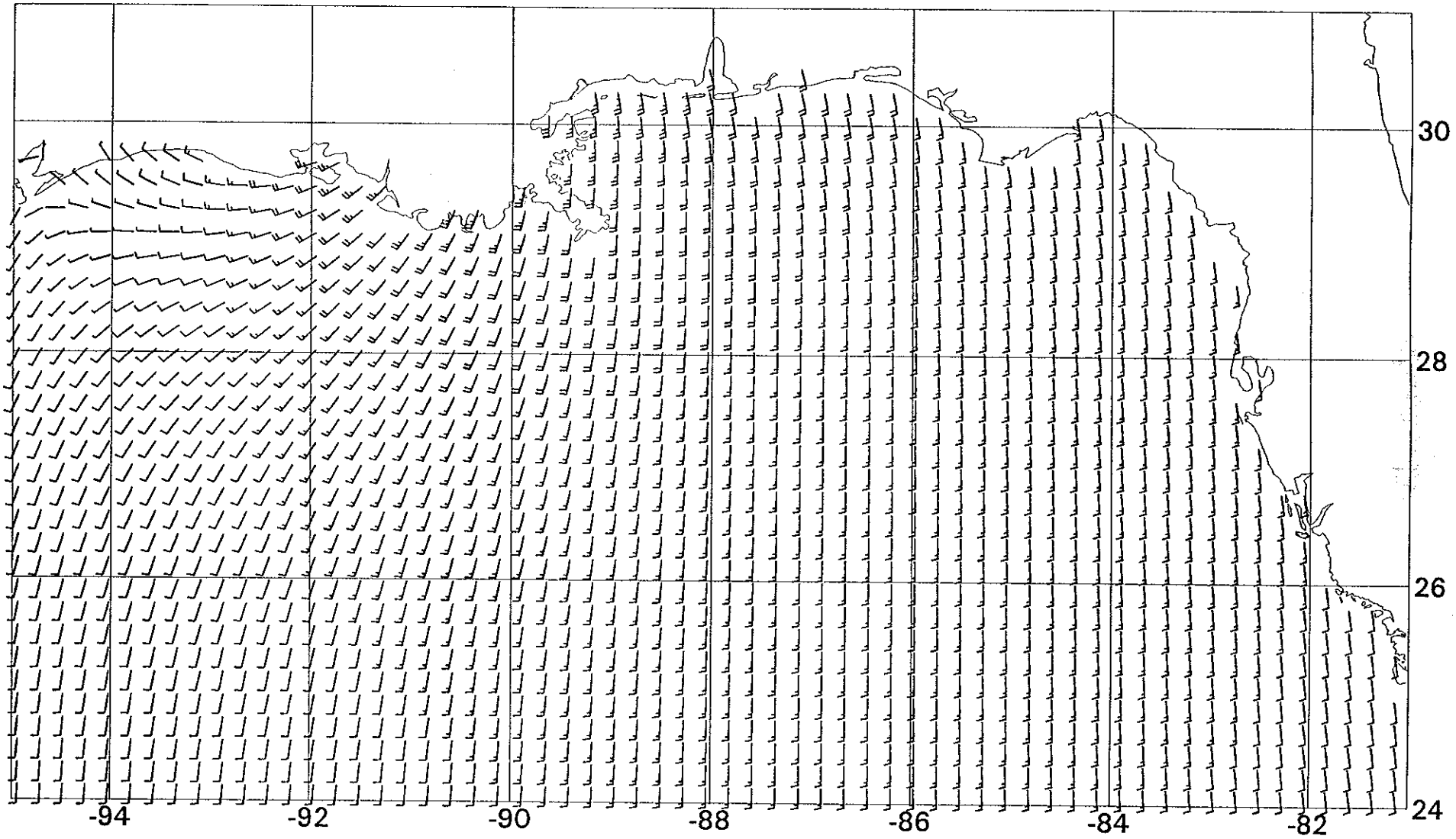

PLOTTED ON 8-JUL-94 08:50:54

MMS Andrew 1992

92082700

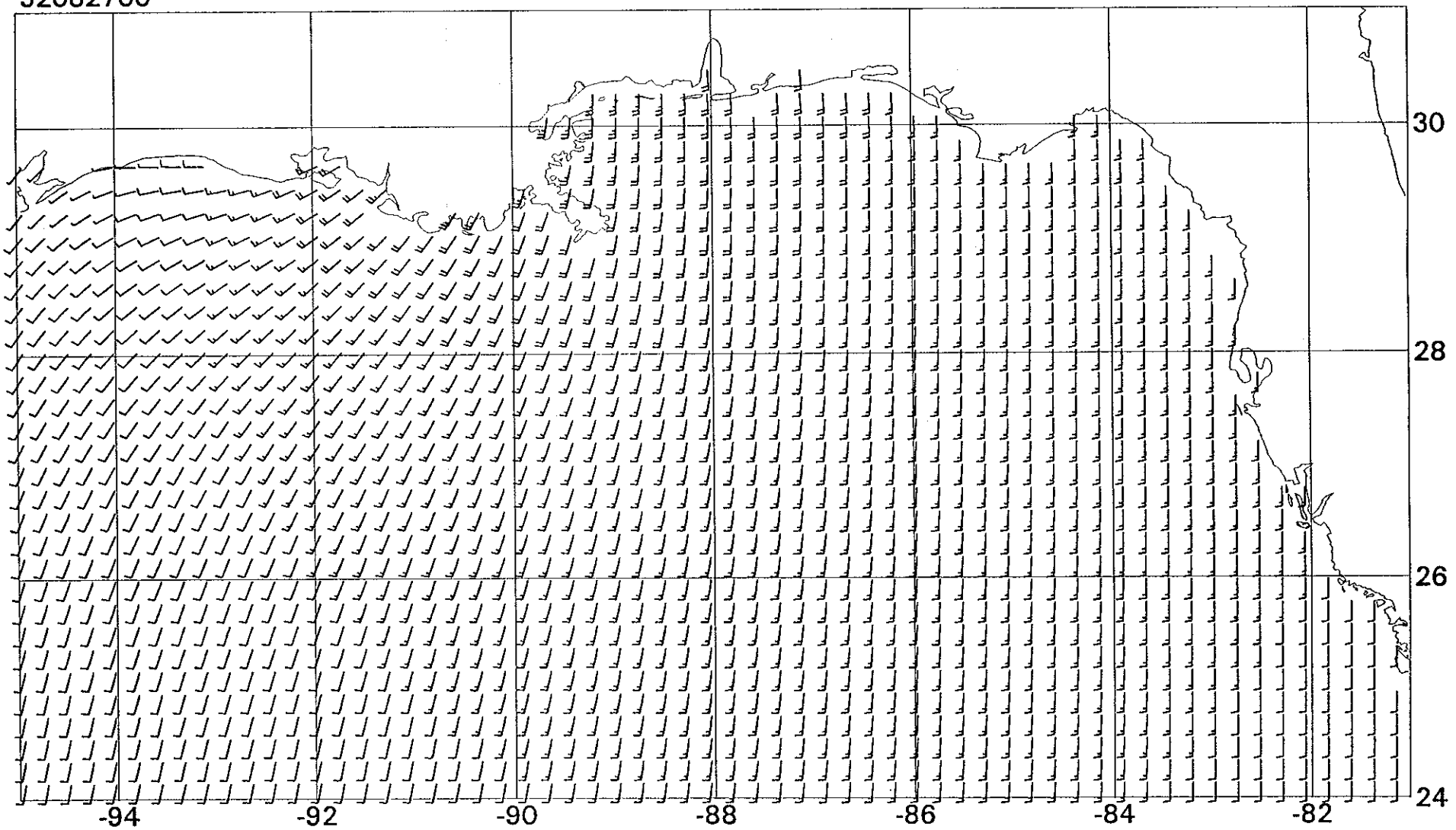

PLOTTED ON 8-JUL-94 08:52:08

Appendix E.

Wind distribution in Hurricane Andrew at 3-hourly intervals over a part of the grid. Each half (full) barb represents 5 (10) knots, each flag 50 knots, of the effective neutral 20-m 1-hour average wind speed. Winds are plotted at every other row and column of grid points of the grid used for the wave and current hindcasts. The two digits near the wind barb denote, respectively, the "tens" place of wind direction (e.g. 9 for 90 degrees) and the units place of wind speed in knots (e.g. 7 for 17 knots).

92082506

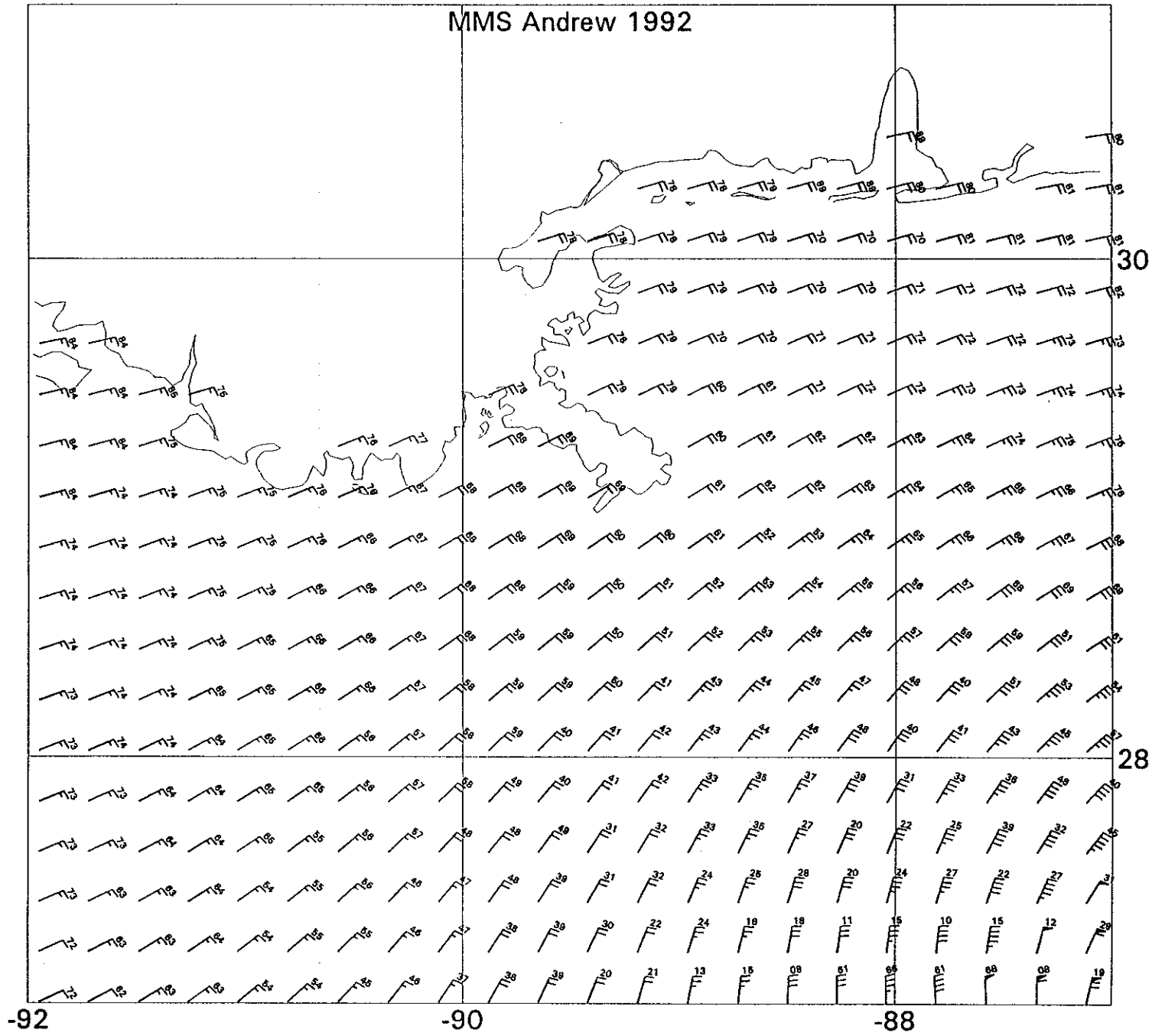

92082509

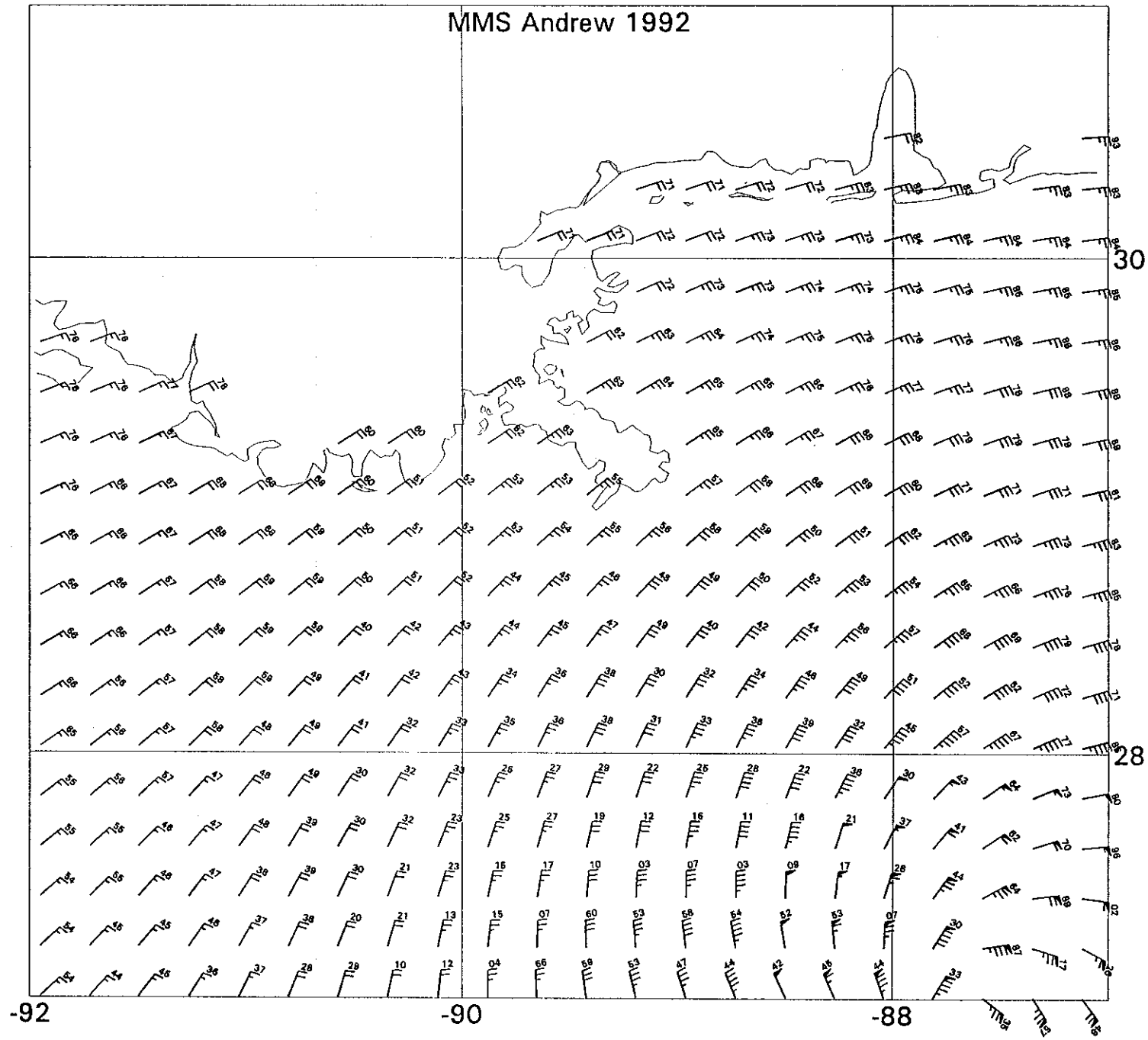

PLOTTED ON 9-JUL-94 12:23:56

92082512

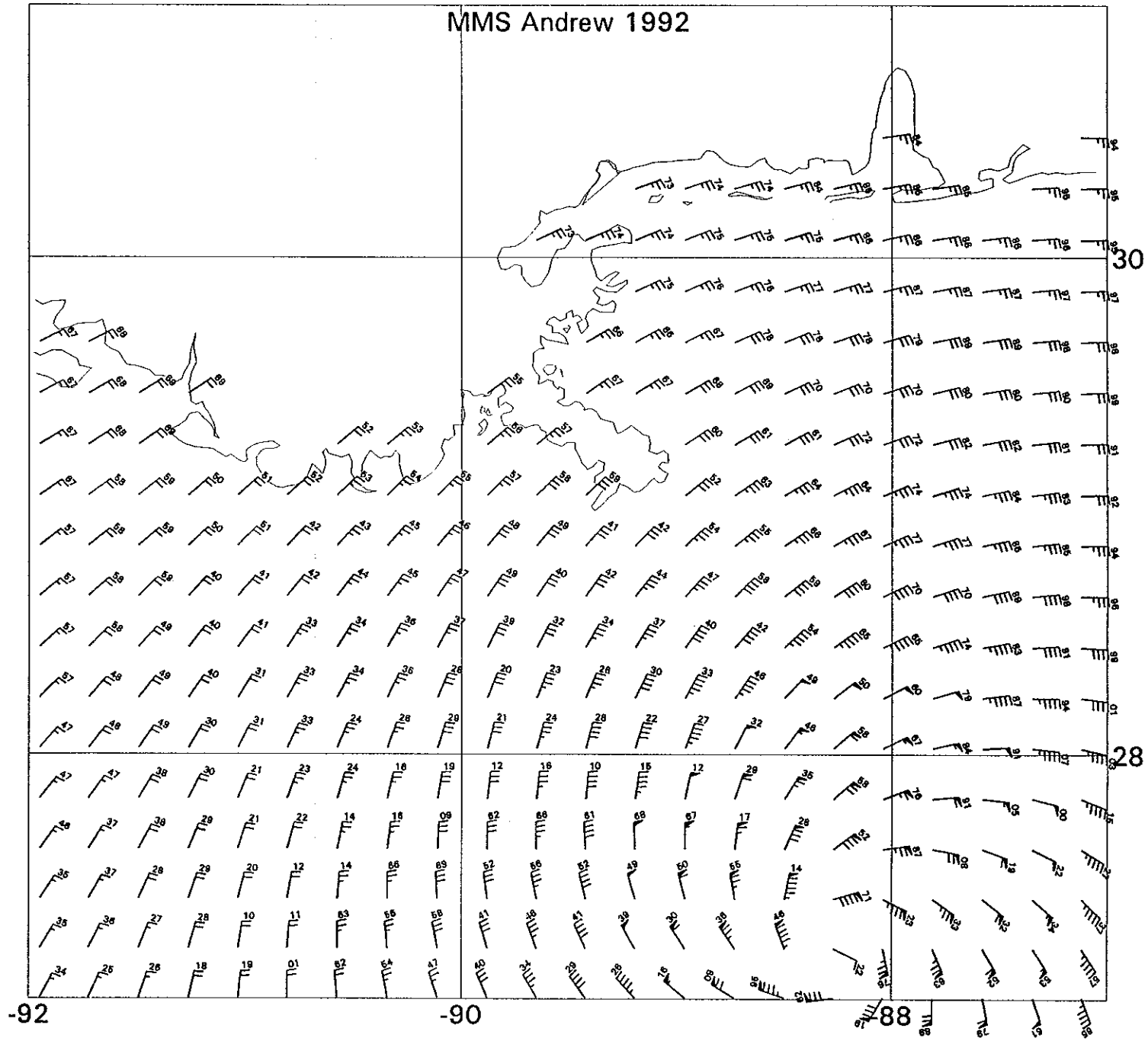

PLOTTED ON 9-JUL-94 12:24:00

92082518

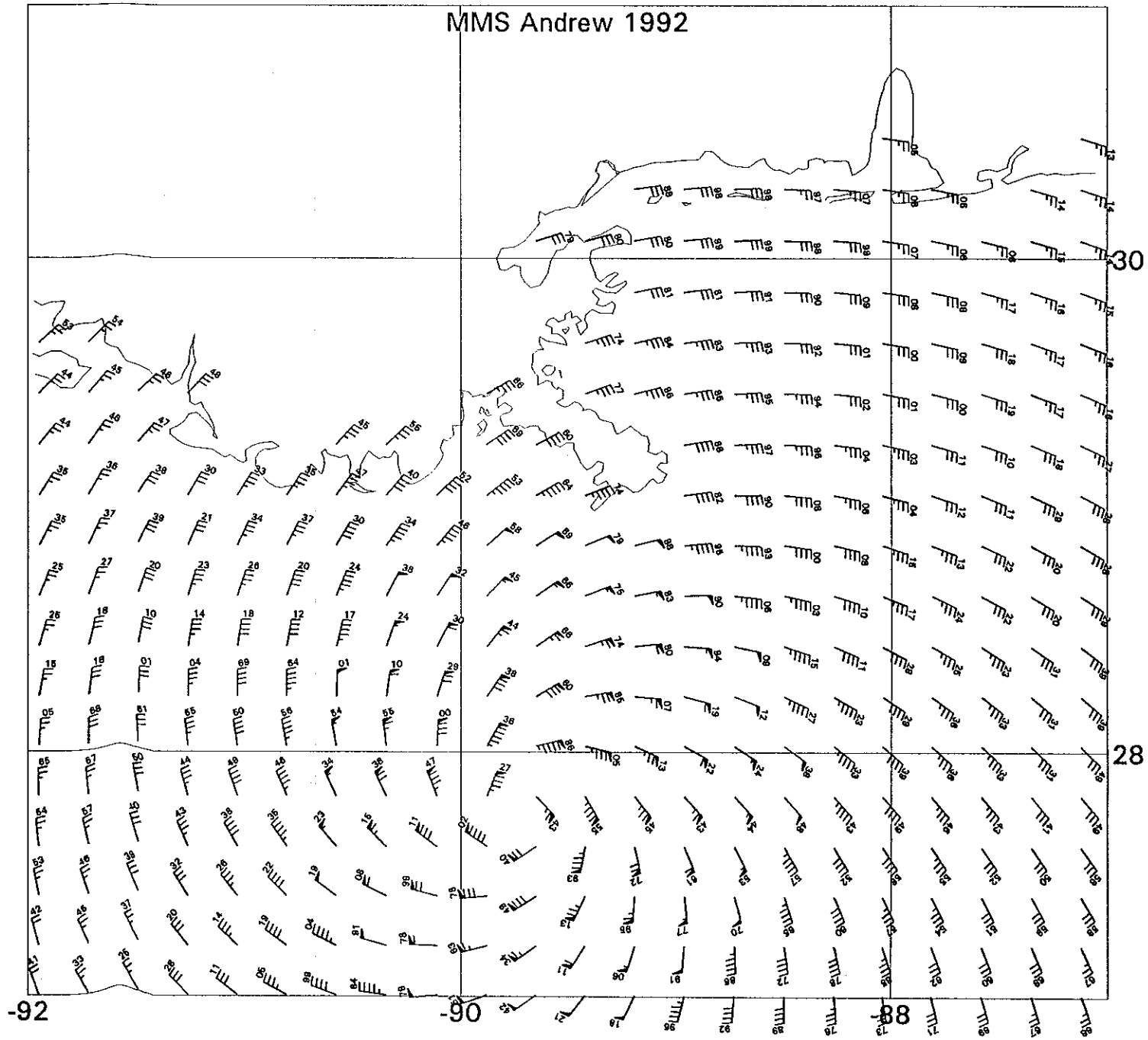

PLOTTED ON 9-JUL-94 12:24:05

92082521

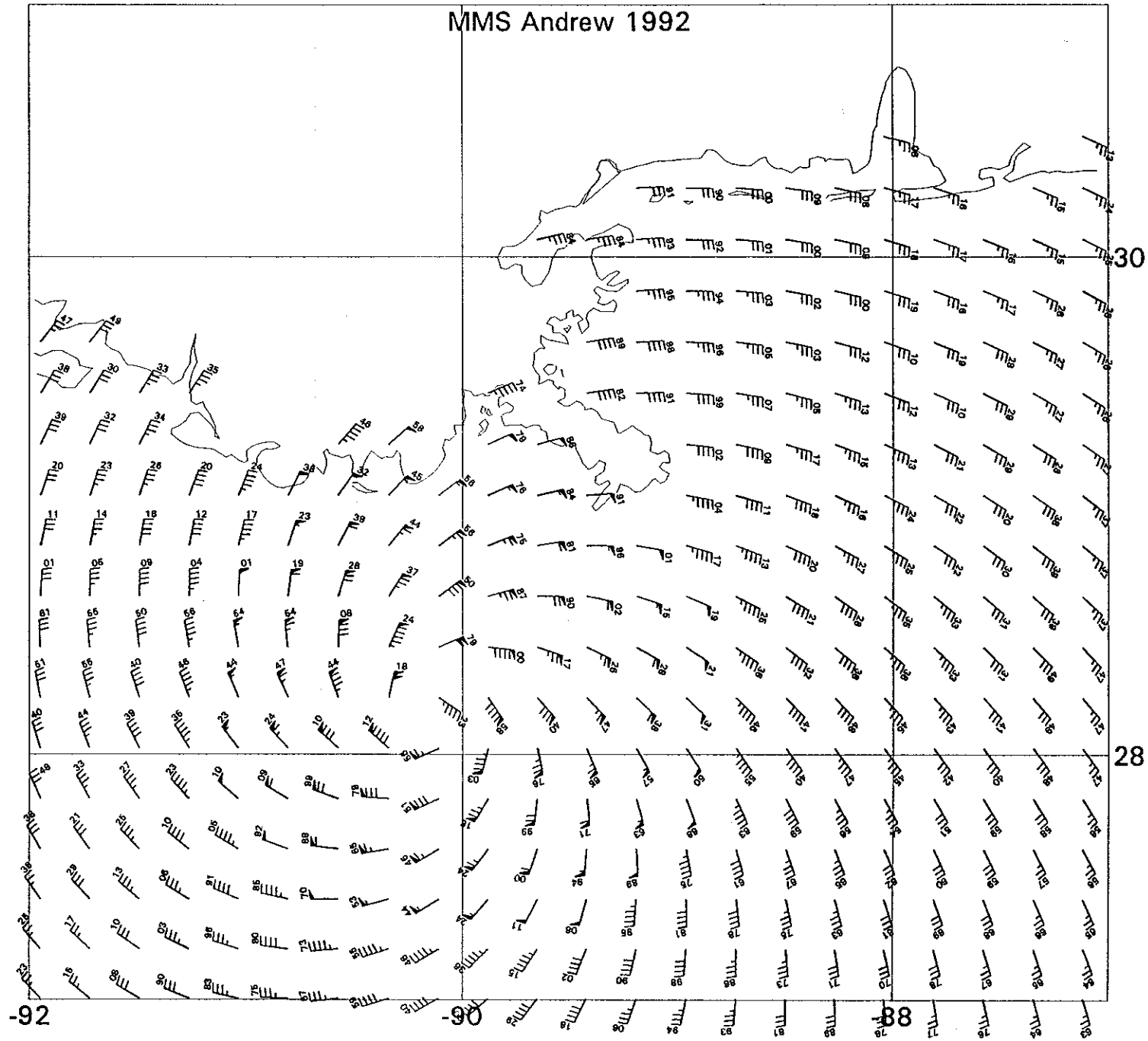

92082600

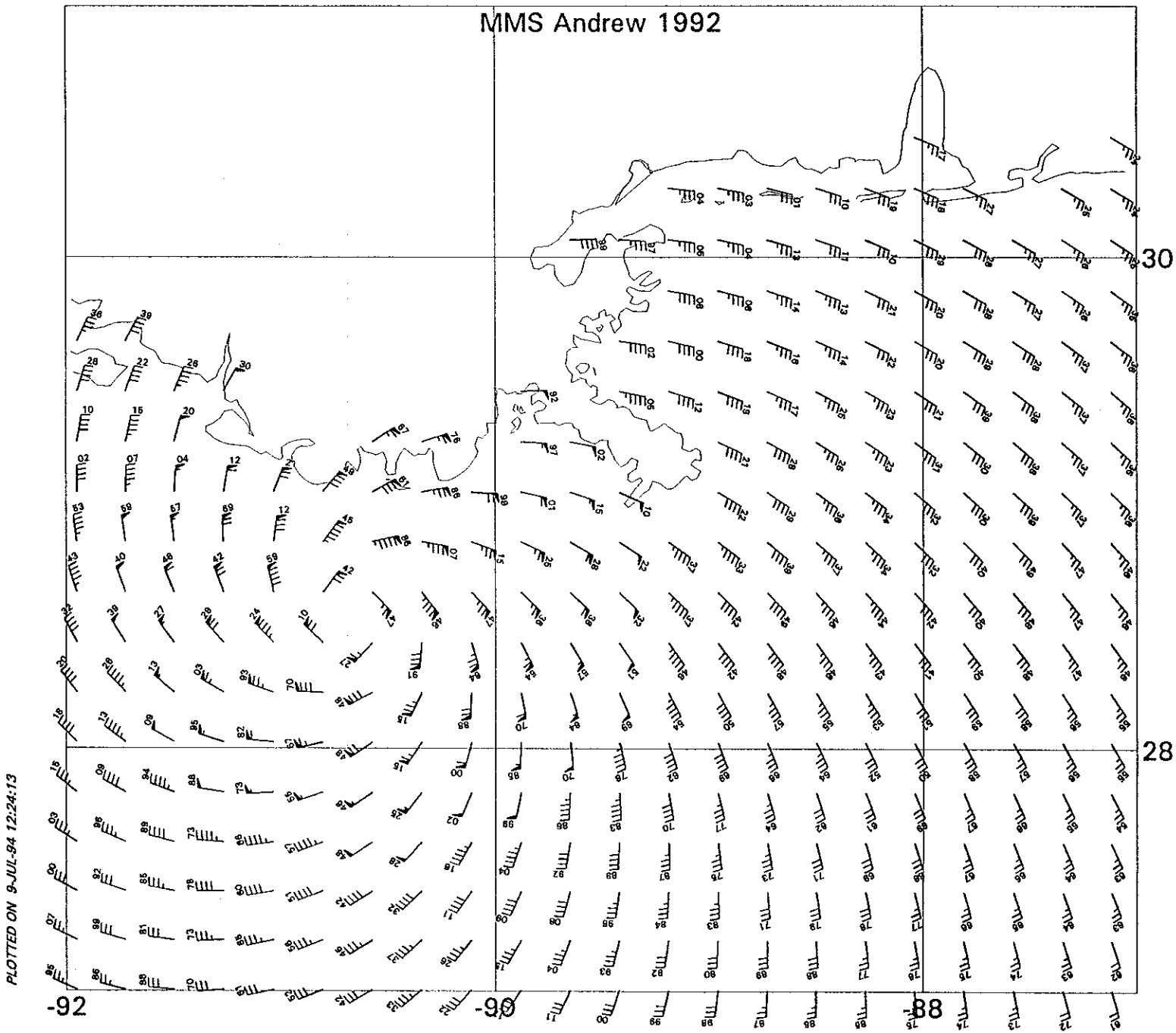

92082603

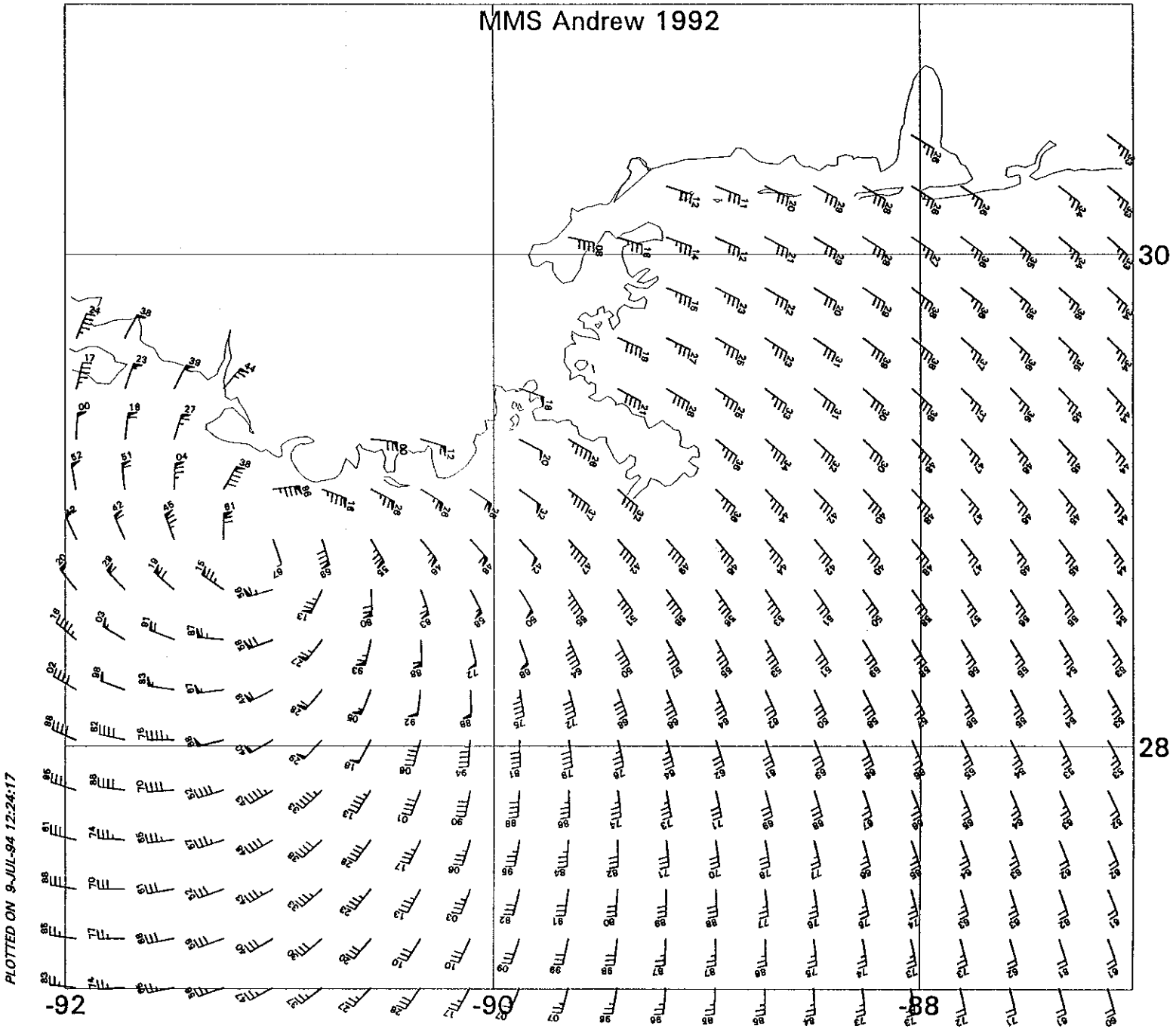

92082606

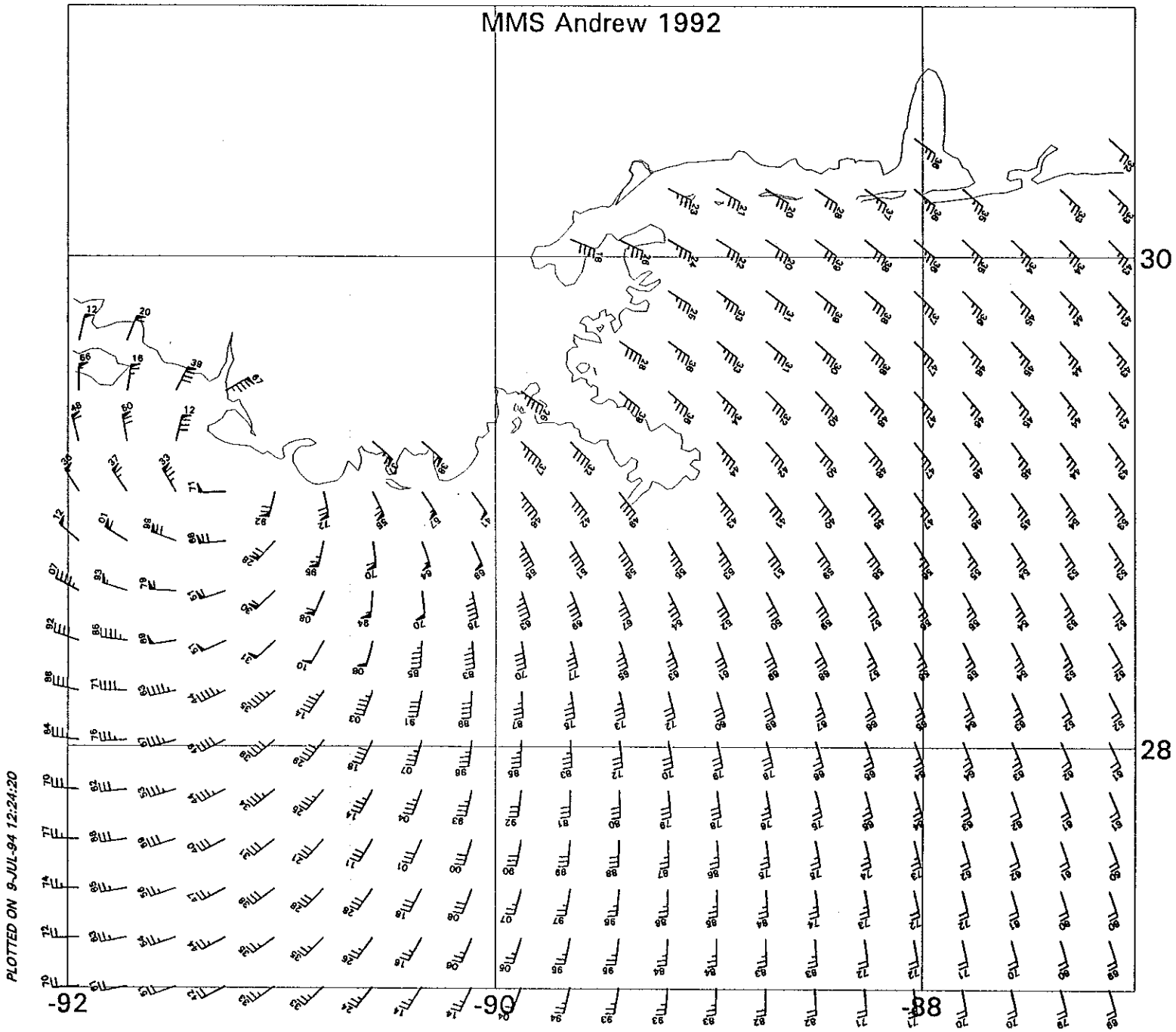

92082609

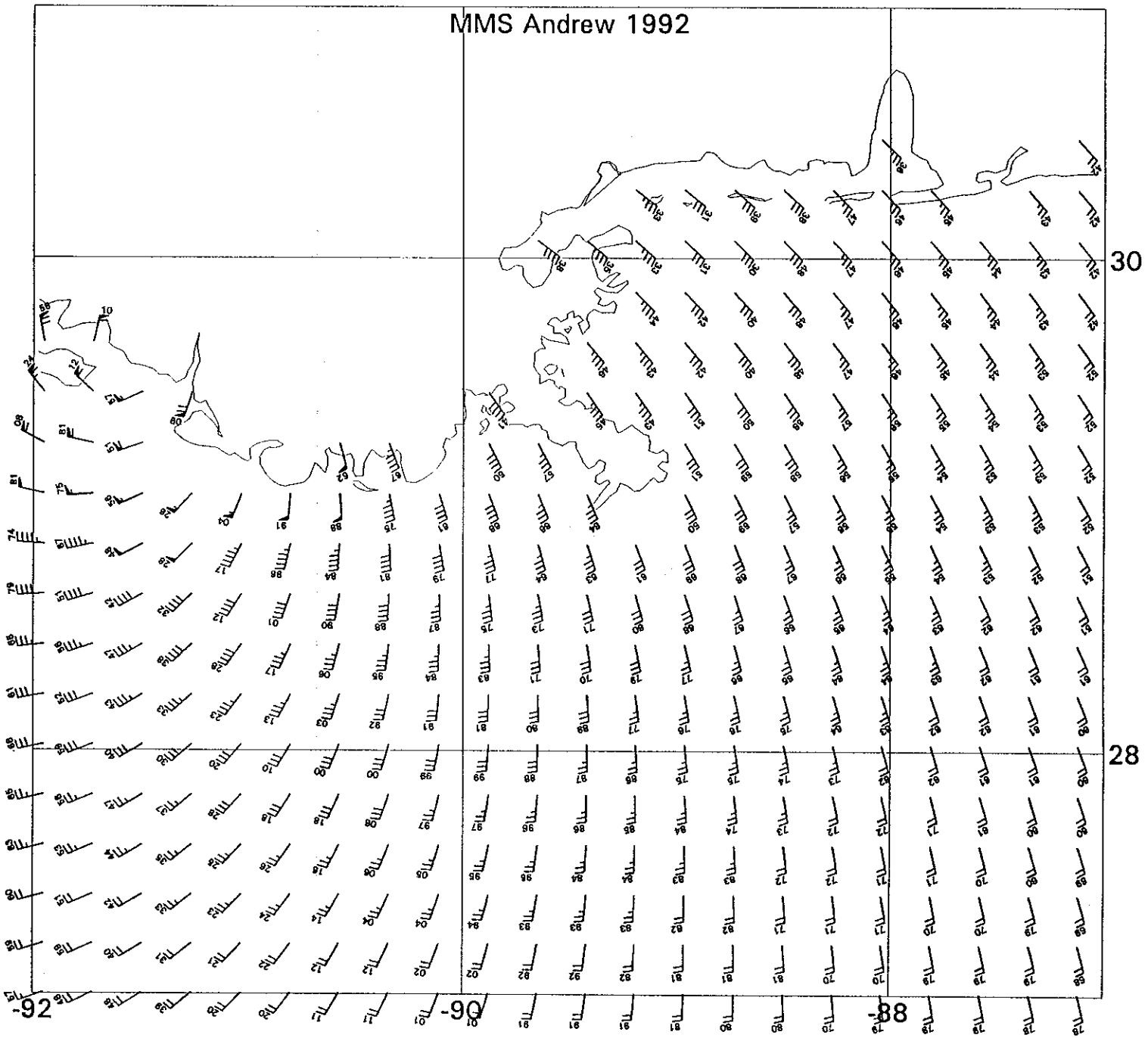

92082612

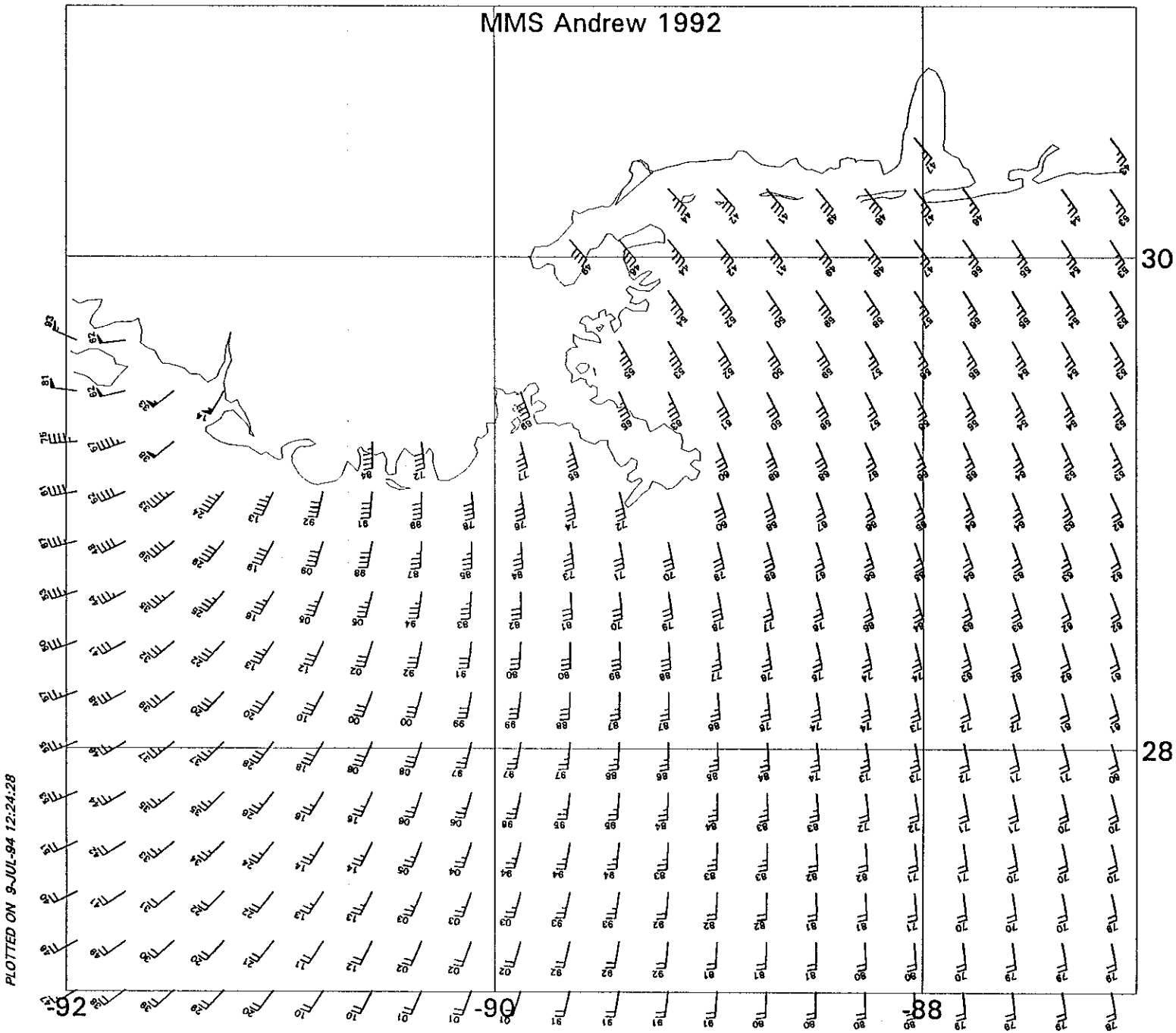

92082615

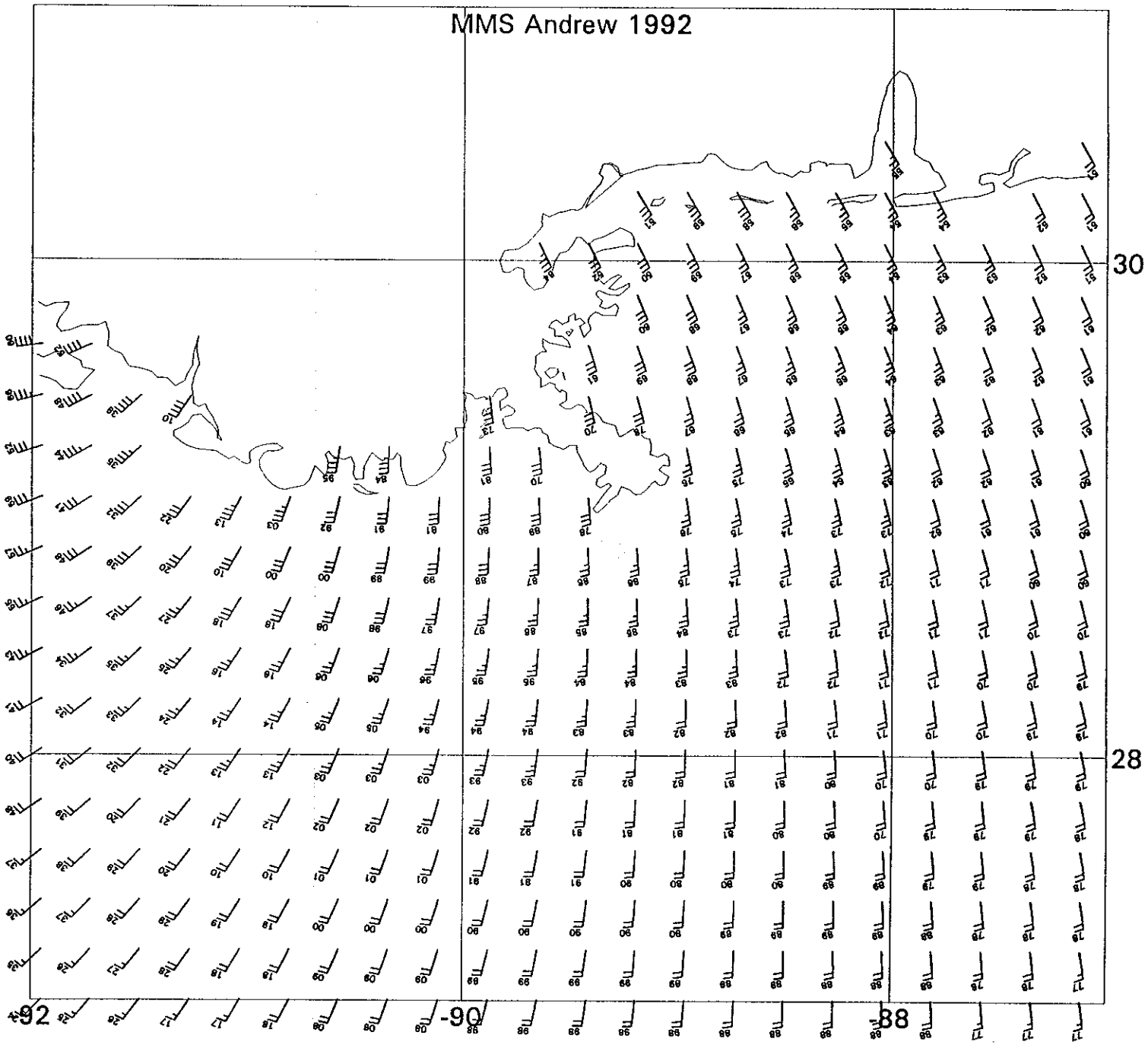

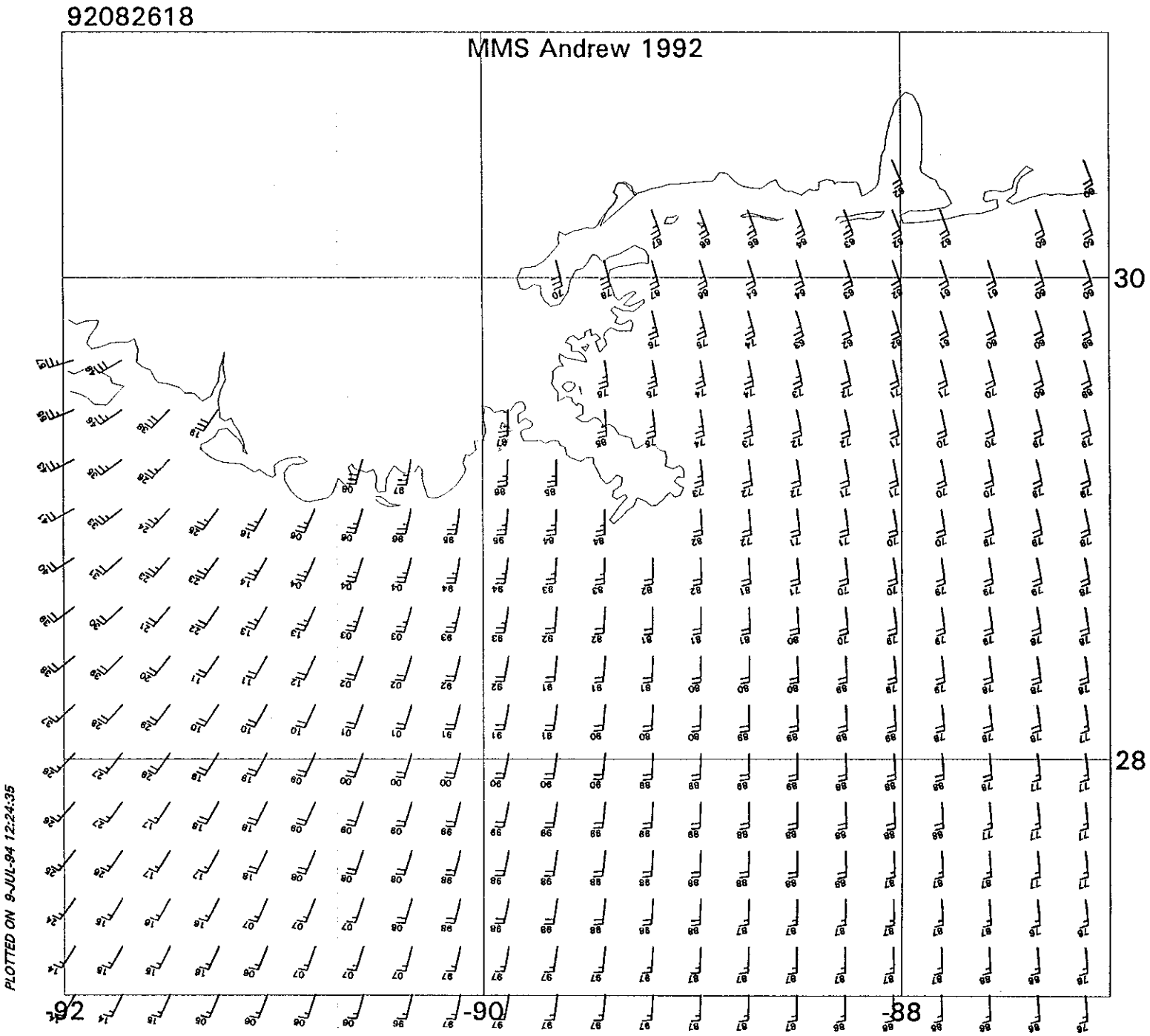
92082618
MMS Andrew 1992
30
28
-92
-90
-88
PLOTTED ON 9-JUL-94 12:24:35

Appendix F.

Plots of hindcast significant wave height and vector mean wave direction at 3-hourly intervals in Hurricane Andrew. Contours of significant wave height are labelled in meters. The last plot shows the envelope of maximum hindcast significant wave height throughout the storm history.

Significant Wave Height
with Vector Mean Direction

92082412

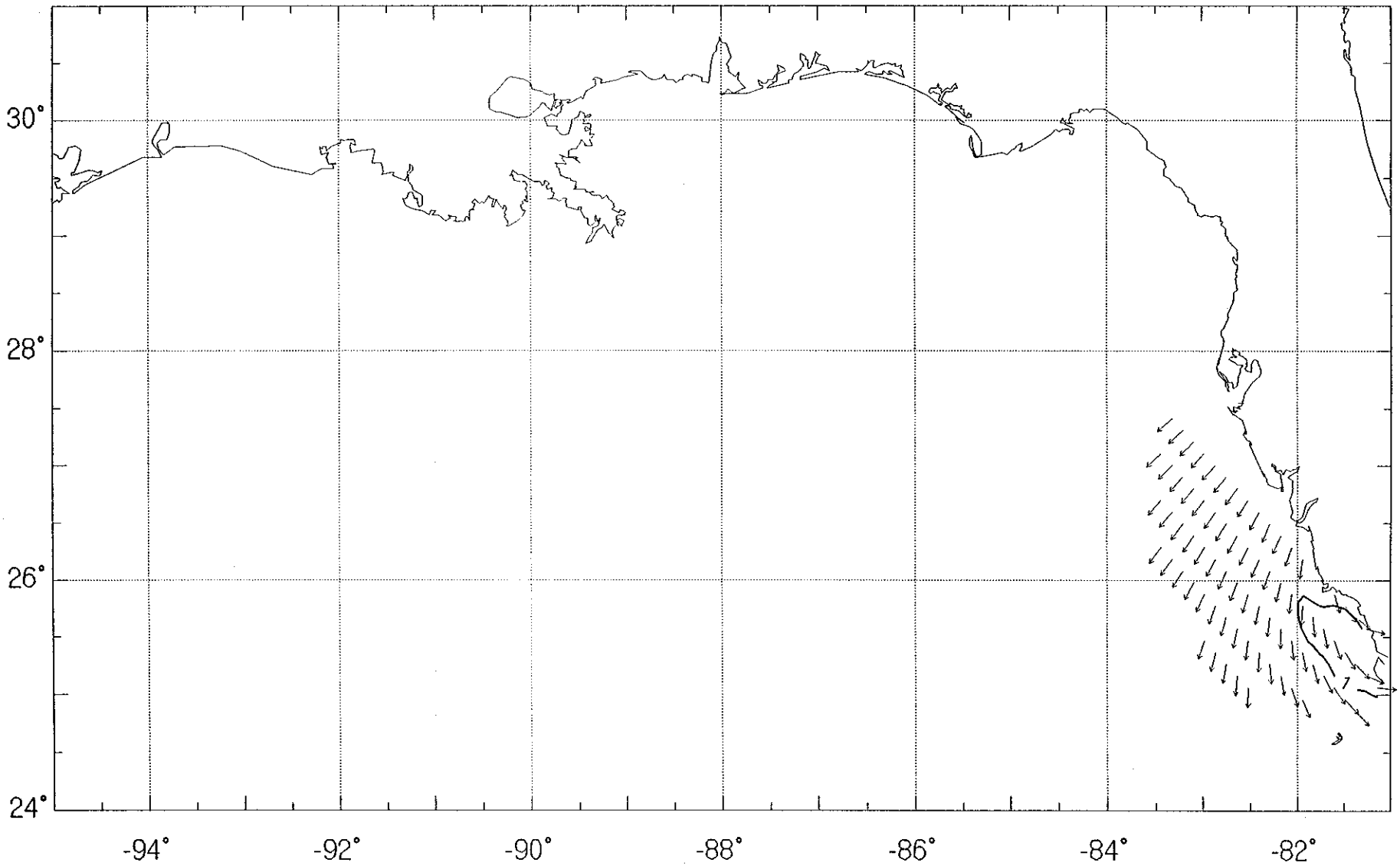

Significant Wave Height
with Vector Mean Direction

92082415

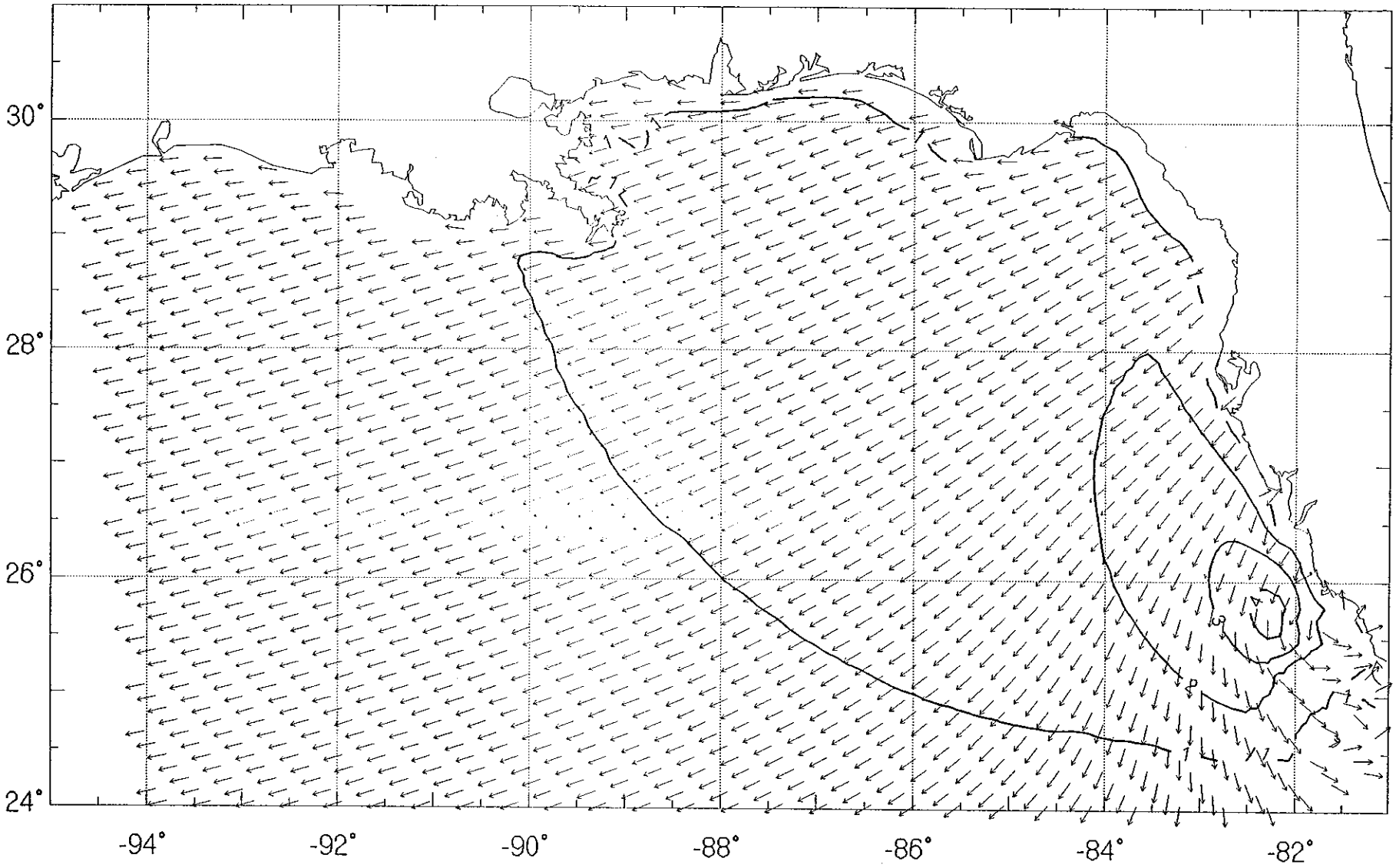

Significant Wave Height
with Vector Mean Direction

92082418

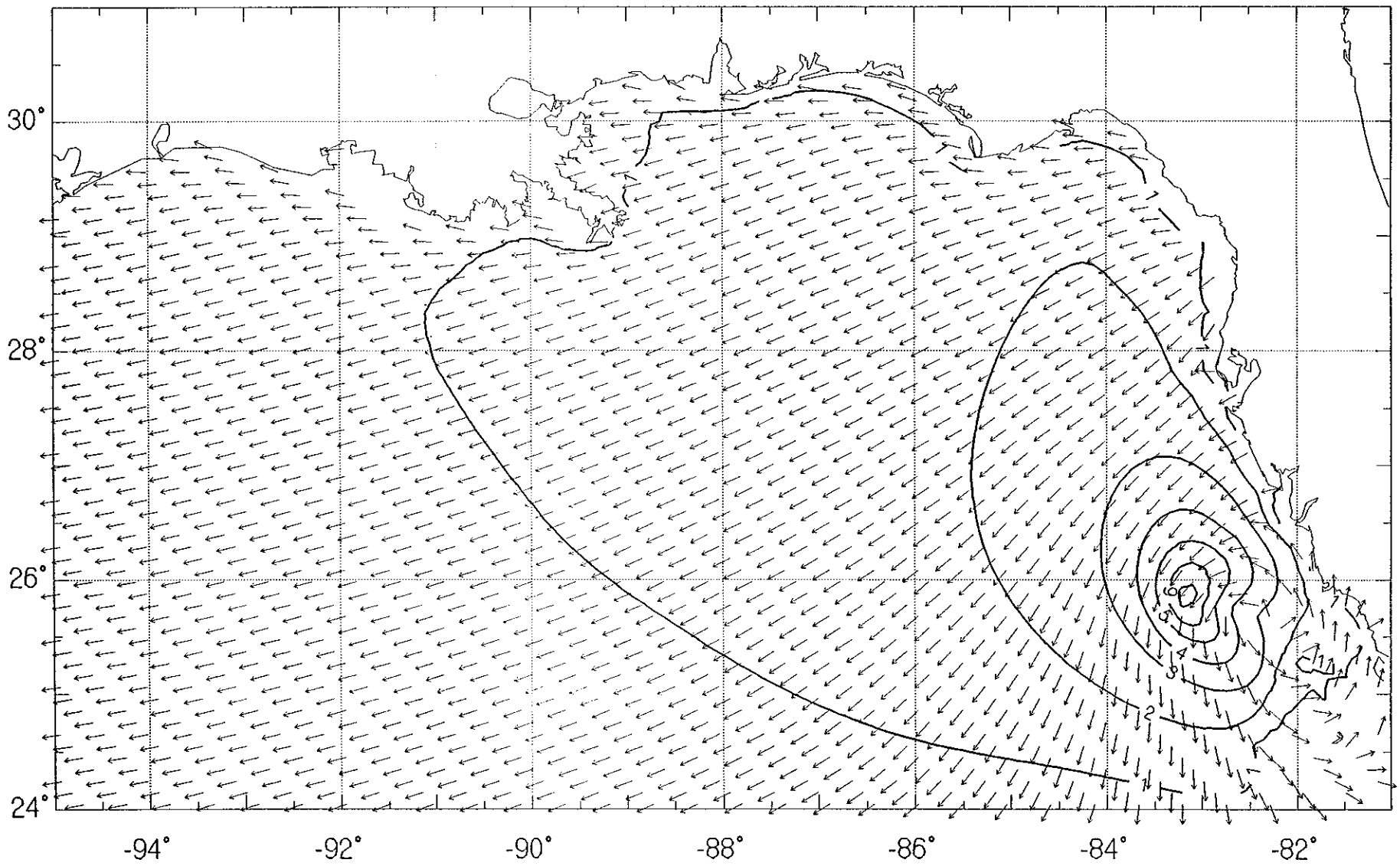

Significant Wave Height
with Vector Mean Direction

92082421

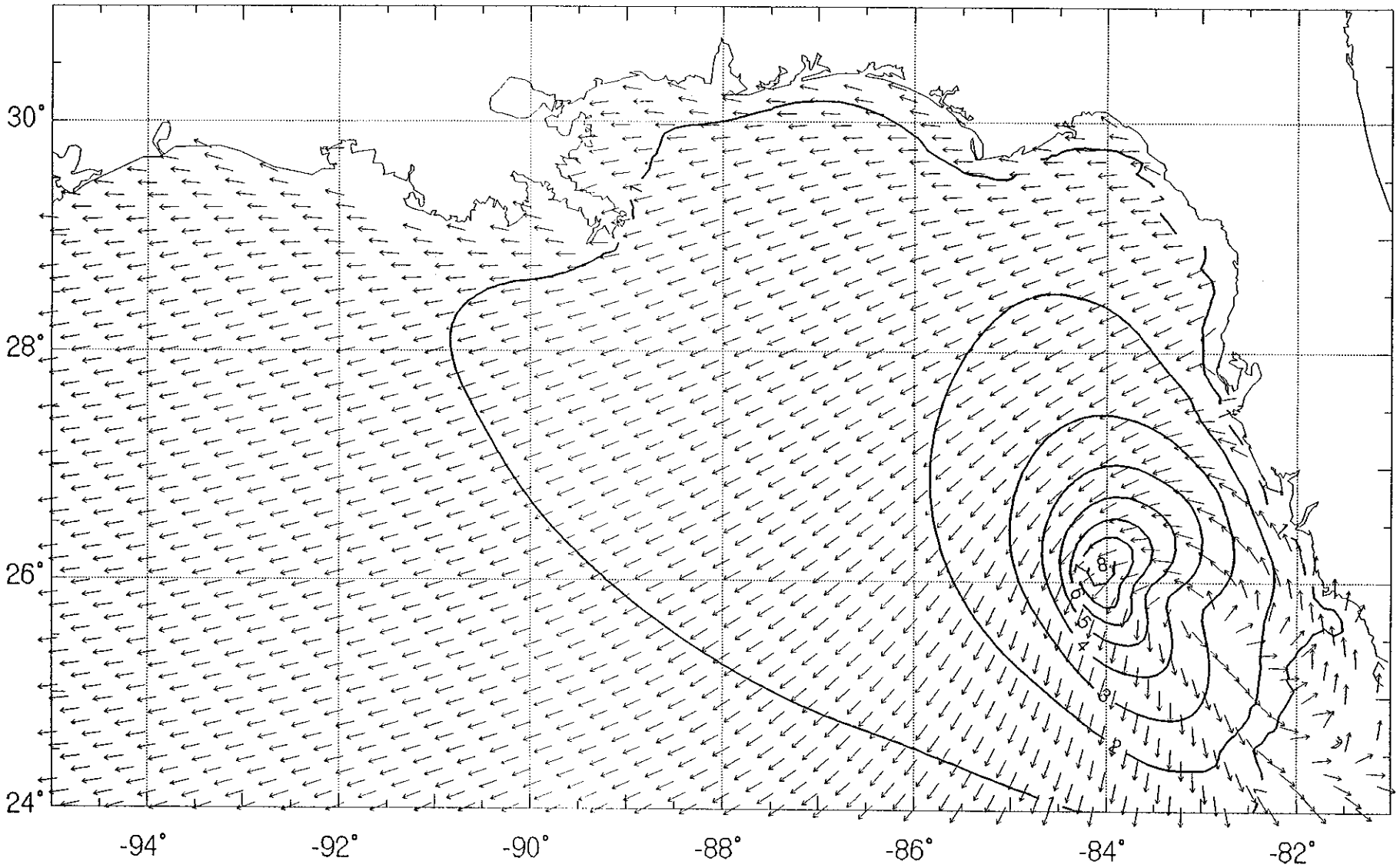

Significant Wave Height
with Vector Mean Direction

92082500

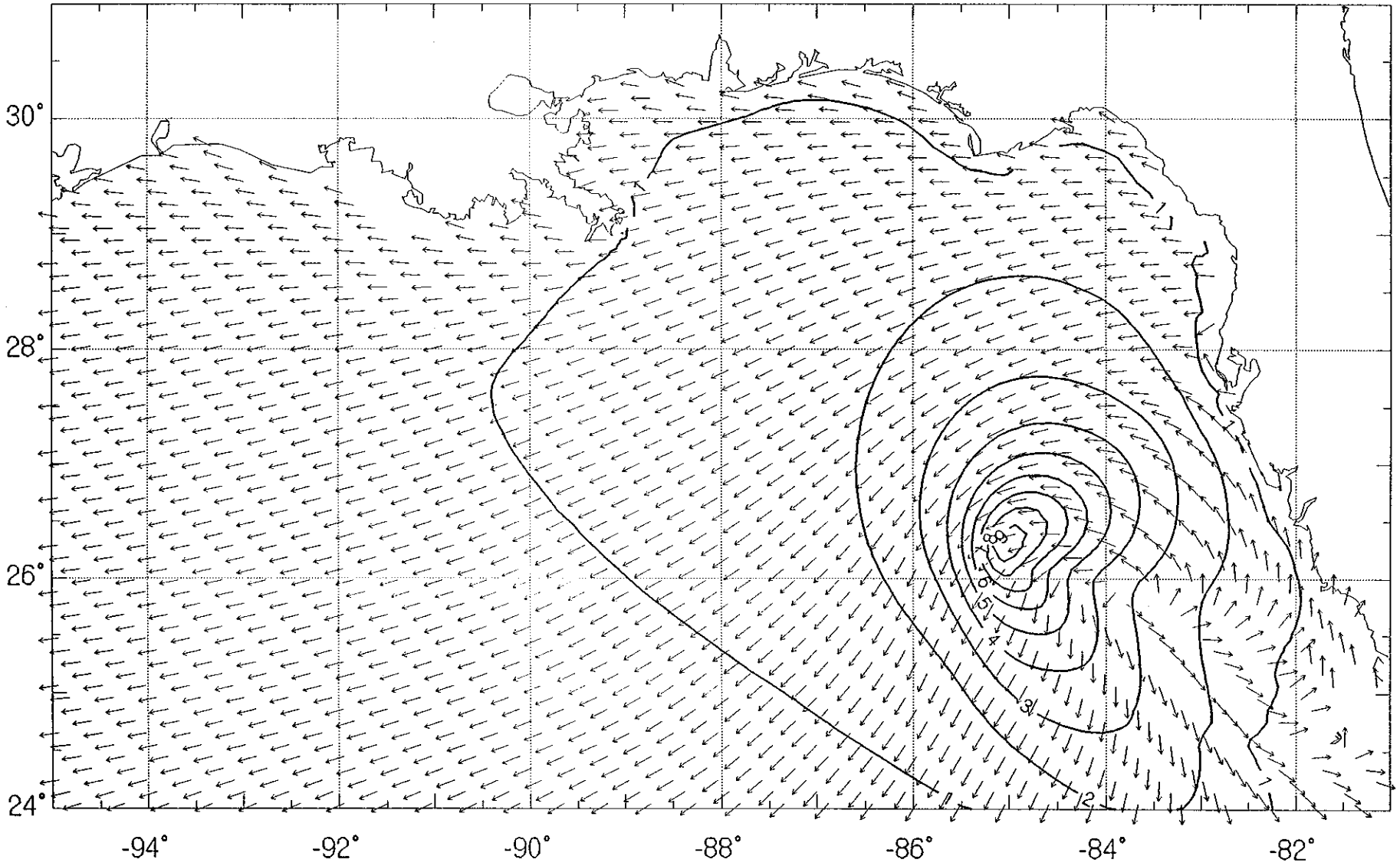

Significant Wave Height
with Vector Mean Direction

92082503

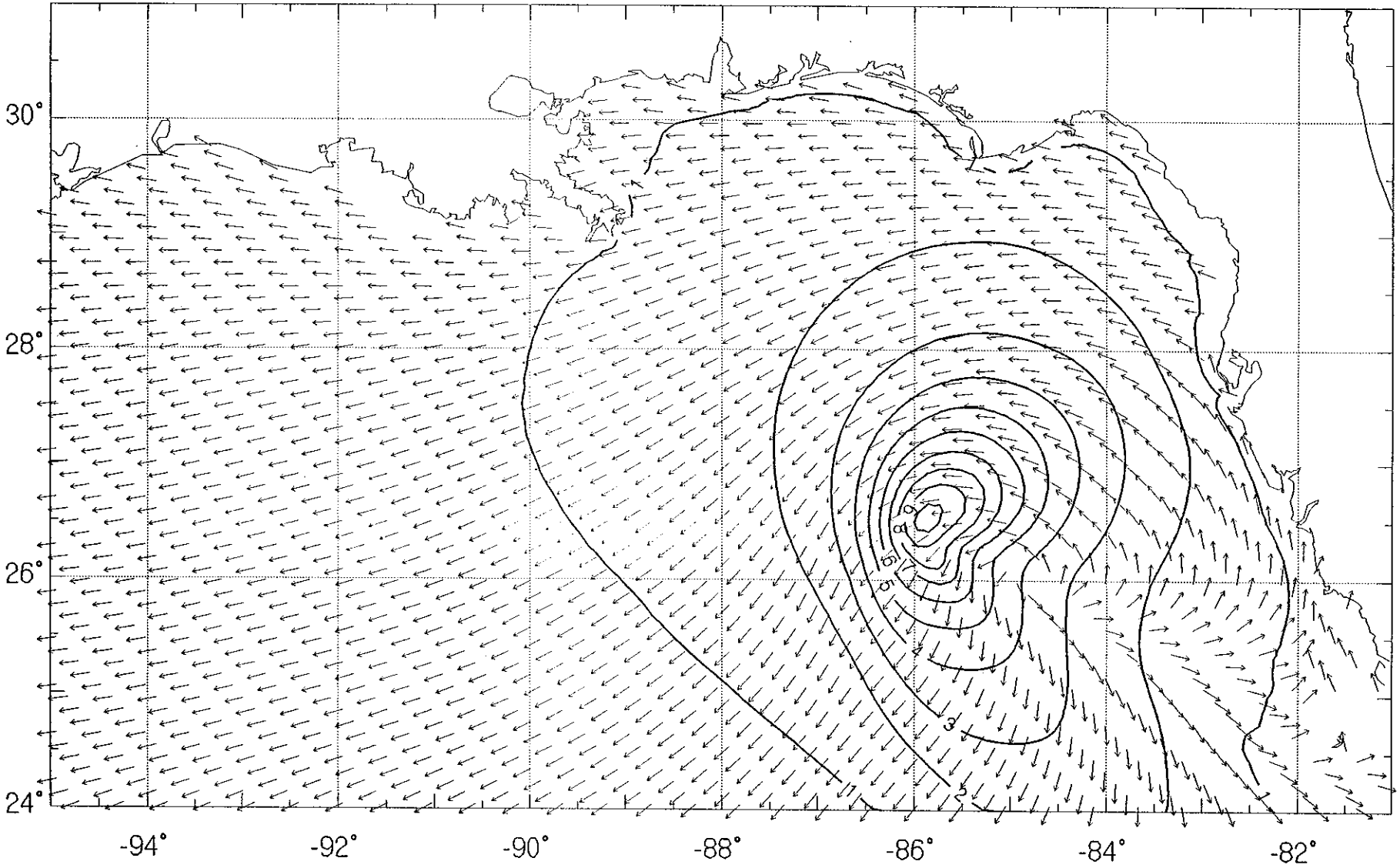

Significant Wave Height
with Vector Mean Direction

92082506

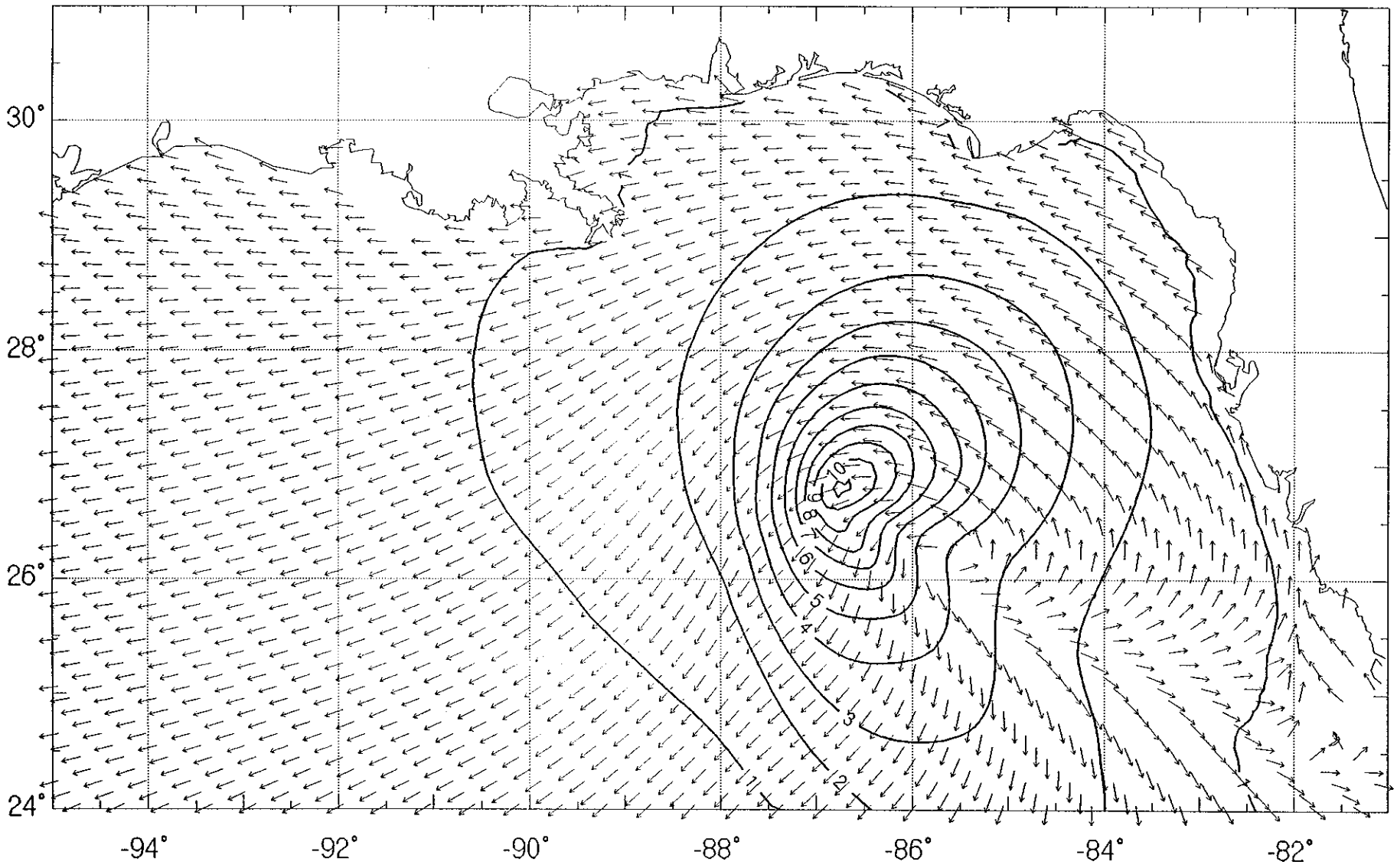

Significant Wave Height
with Vector Mean Direction

92082509

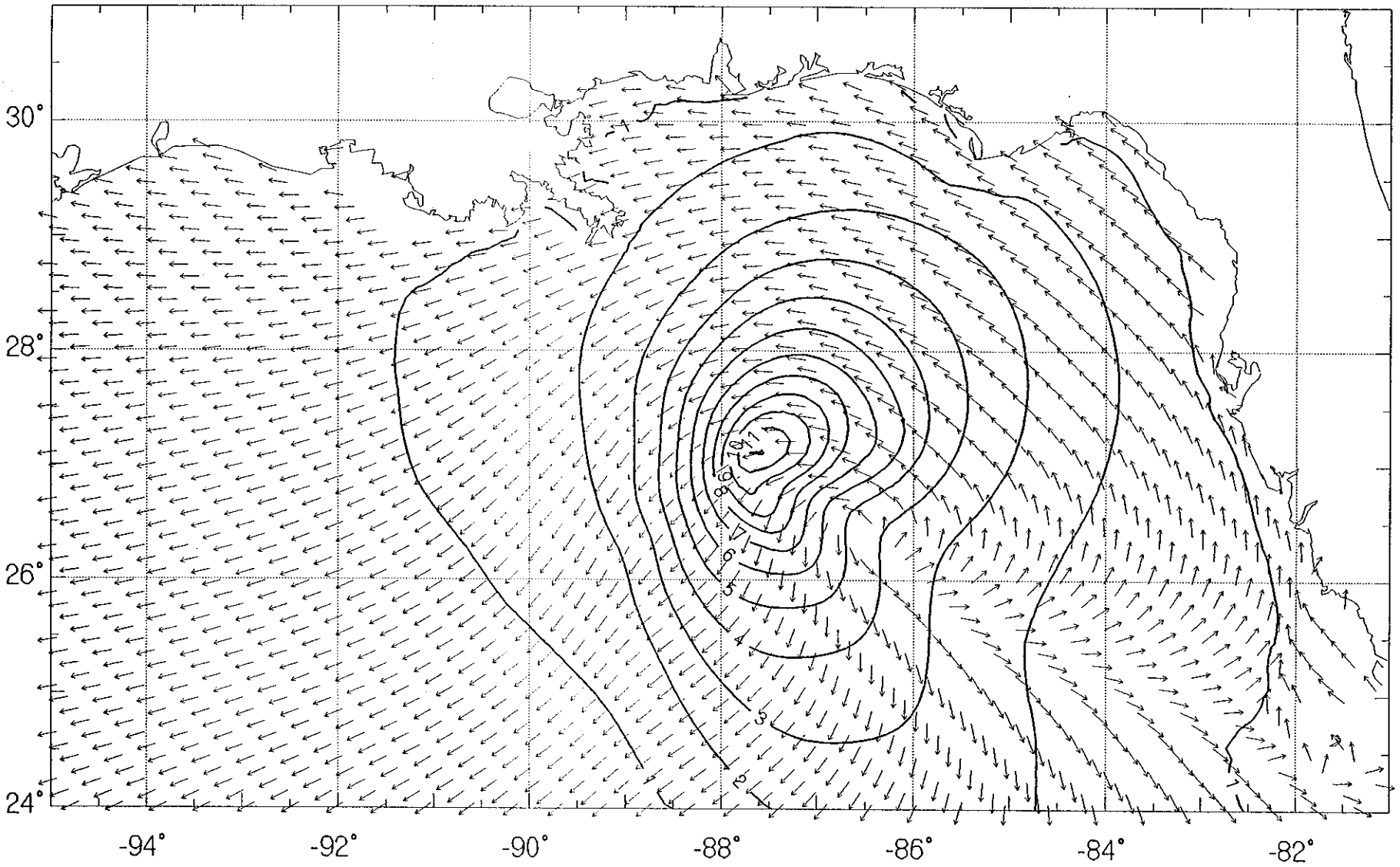

Significant Wave Height
with Vector Mean Direction

92082512

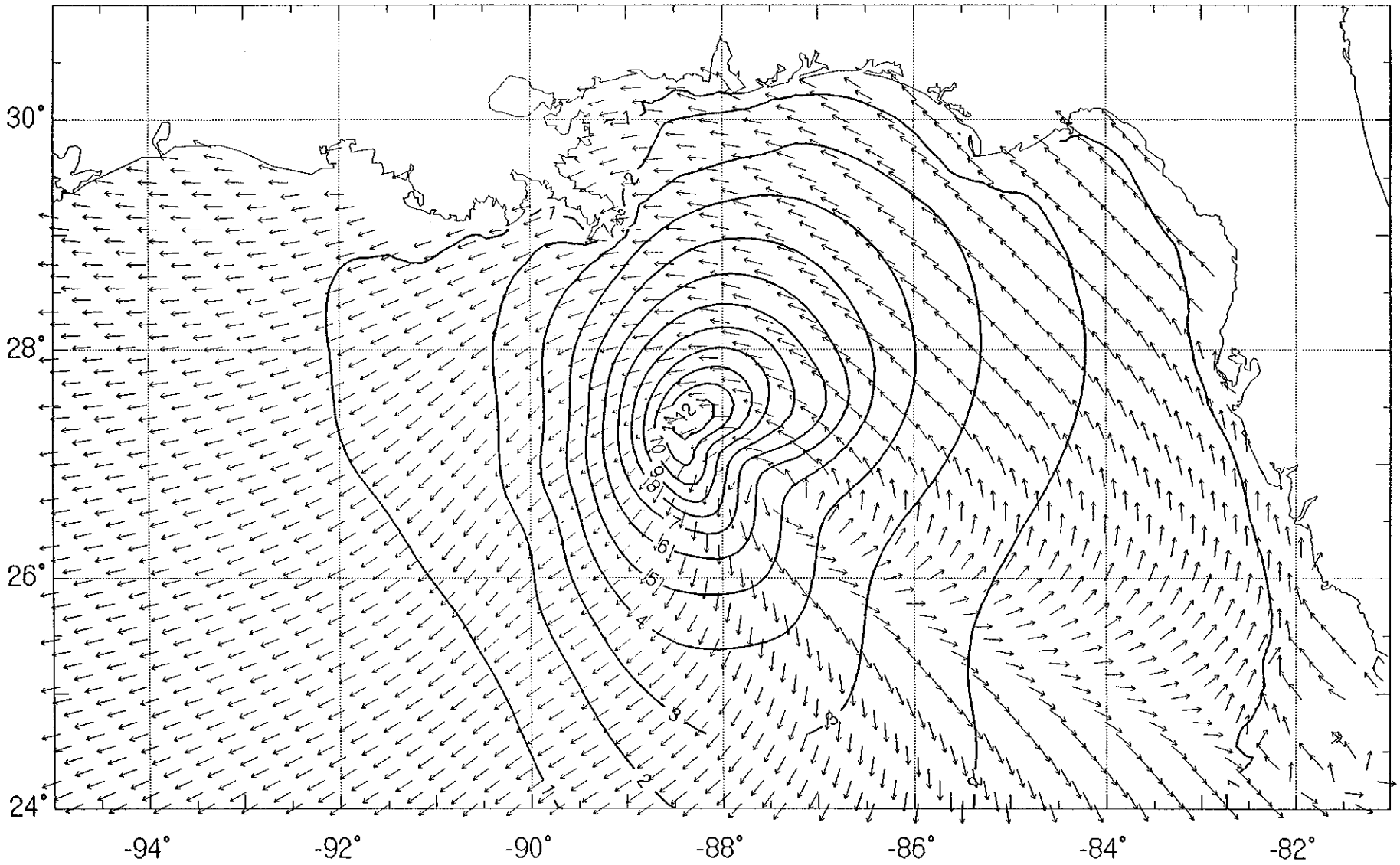

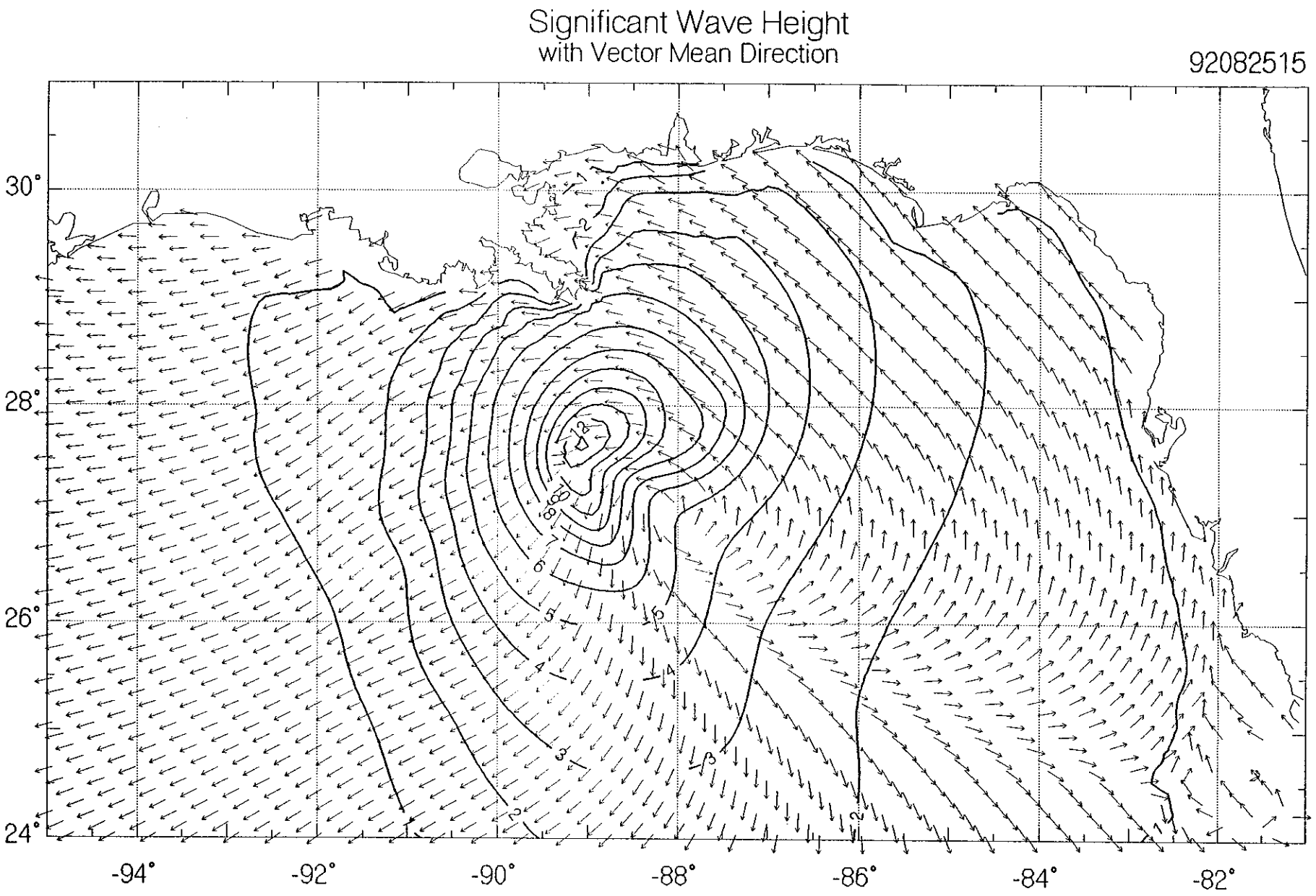
Significant Wave Height
with Vector Mean Direction
92082515
30°
28°
26°
24°
-94°
-92°
-90°
-88°
-86°
-84°
-82°

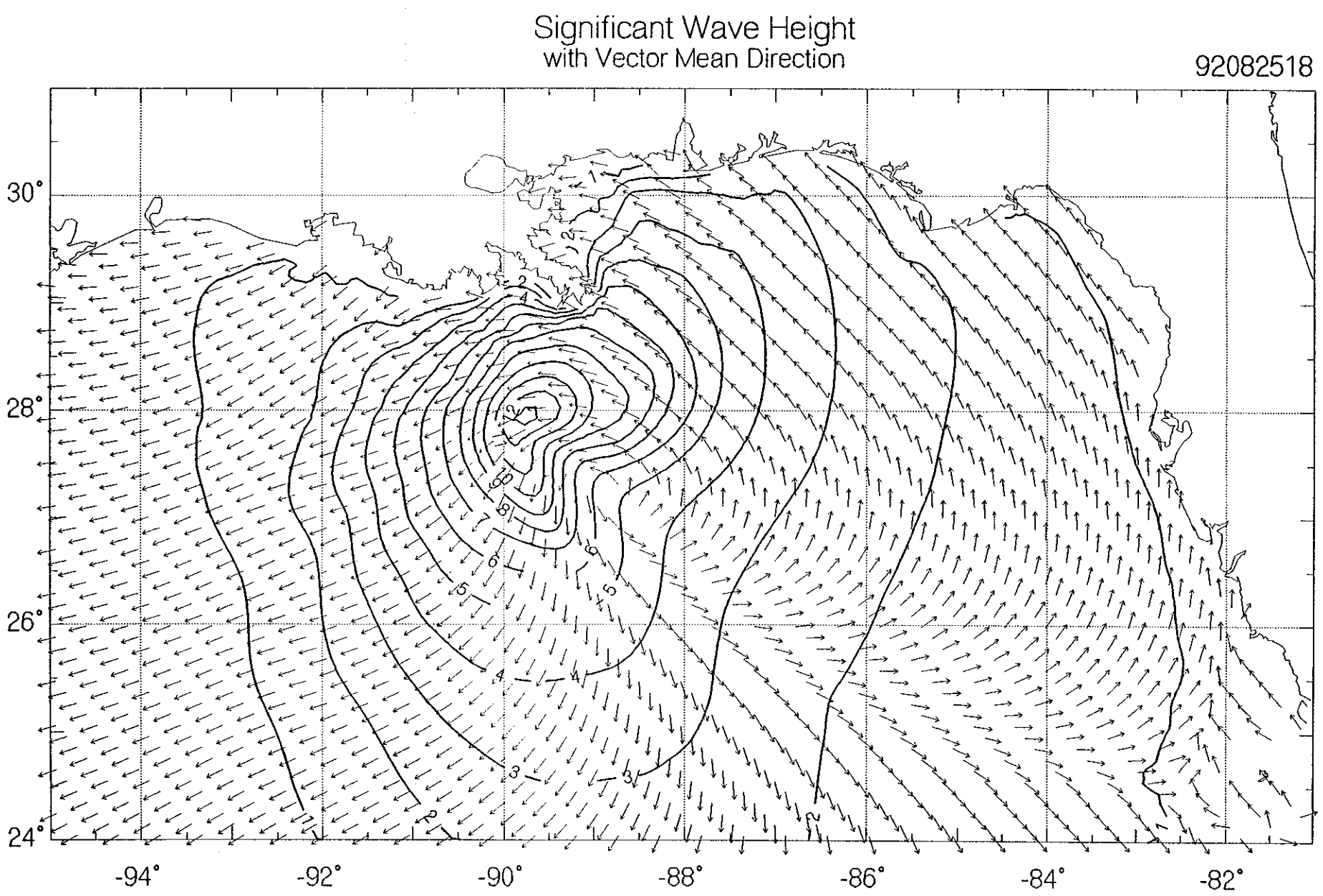
Significant Wave Height
with Vector Mean Direction
92082518
30°
28°
26°
24°
-94°
-92°
-90°
-88°
-86°
-84°
-82°

Significant Wave Height
with Vector Mean Direction

92082521

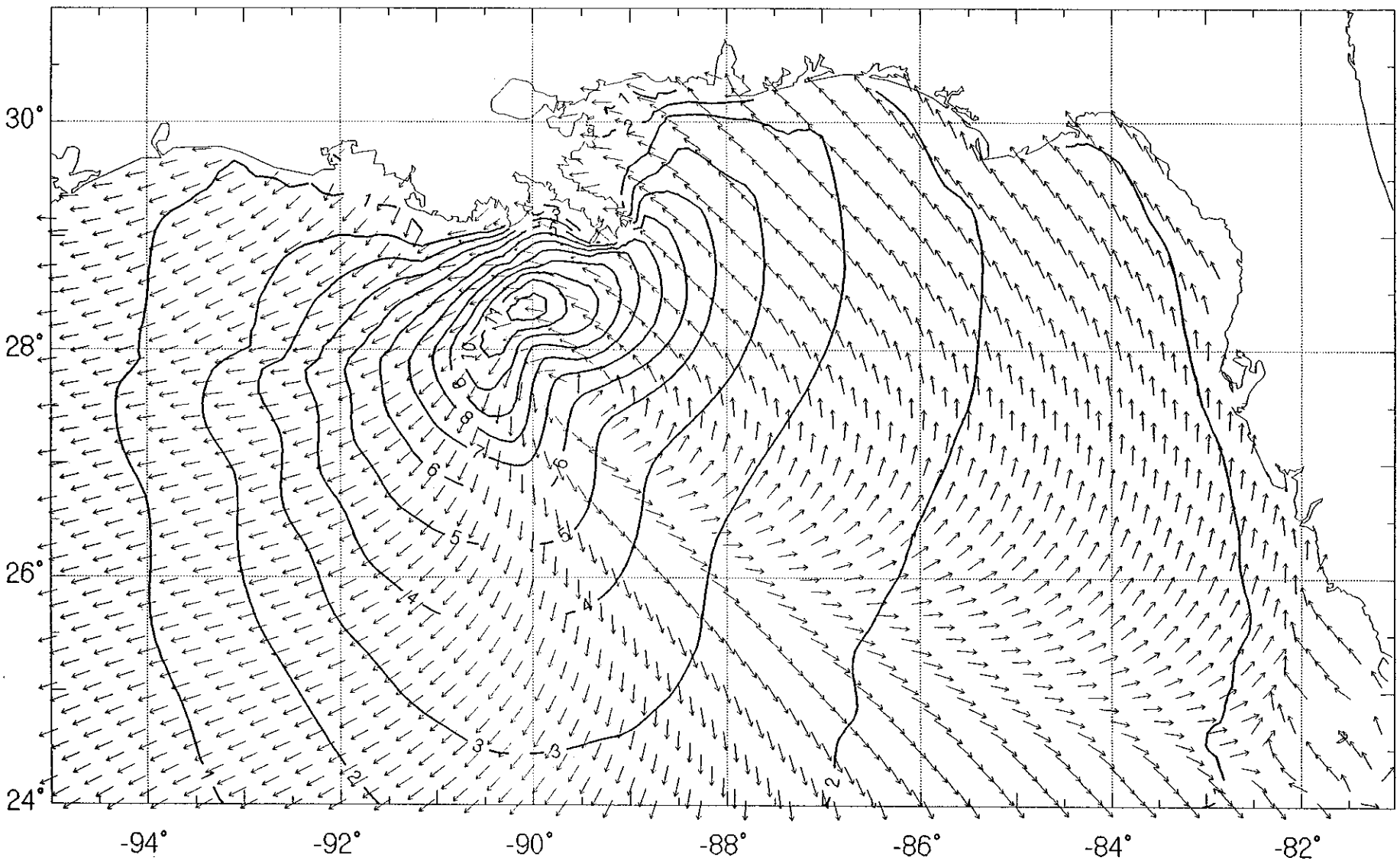

Significant Wave Height
with Vector Mean Direction

92082600

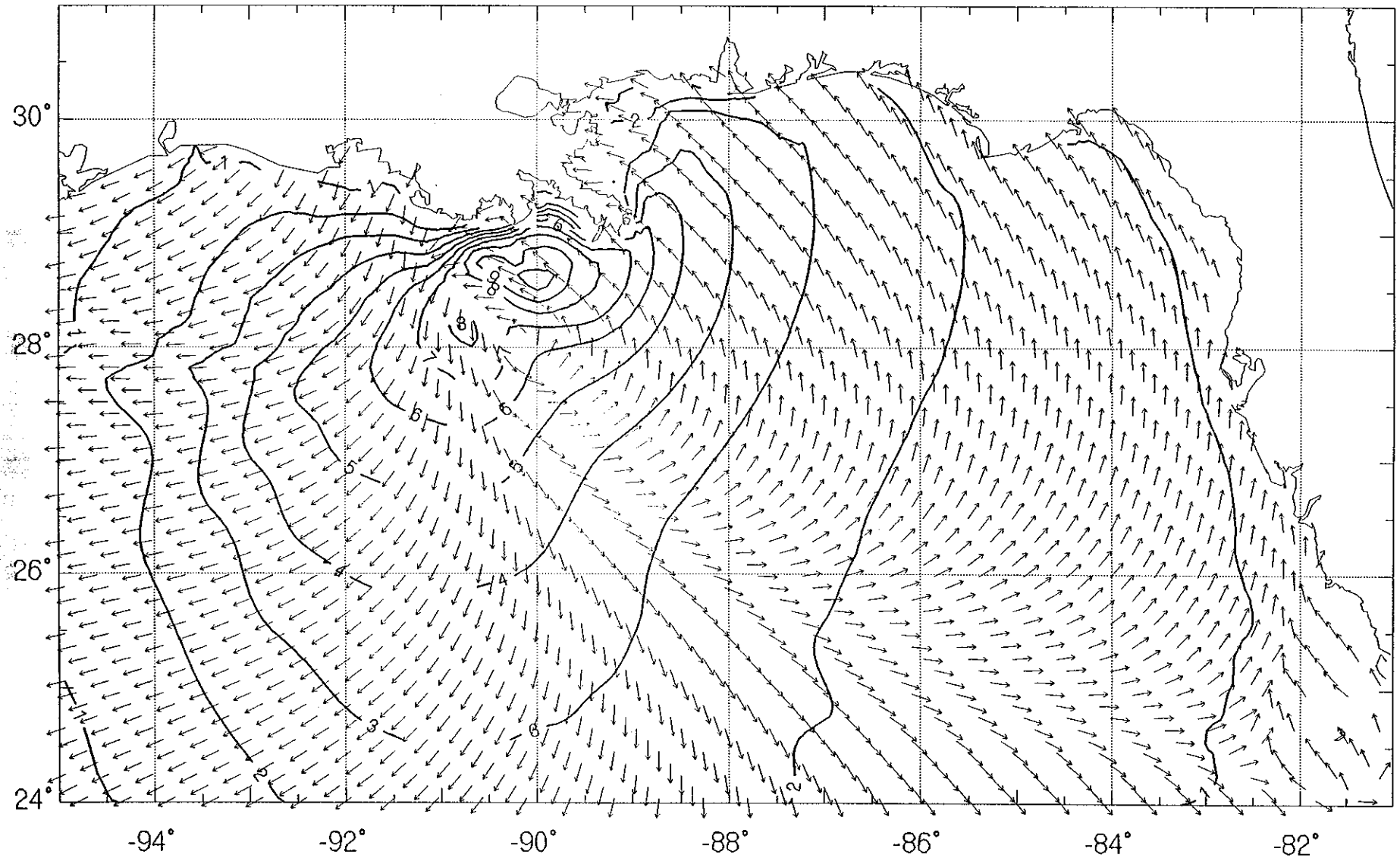

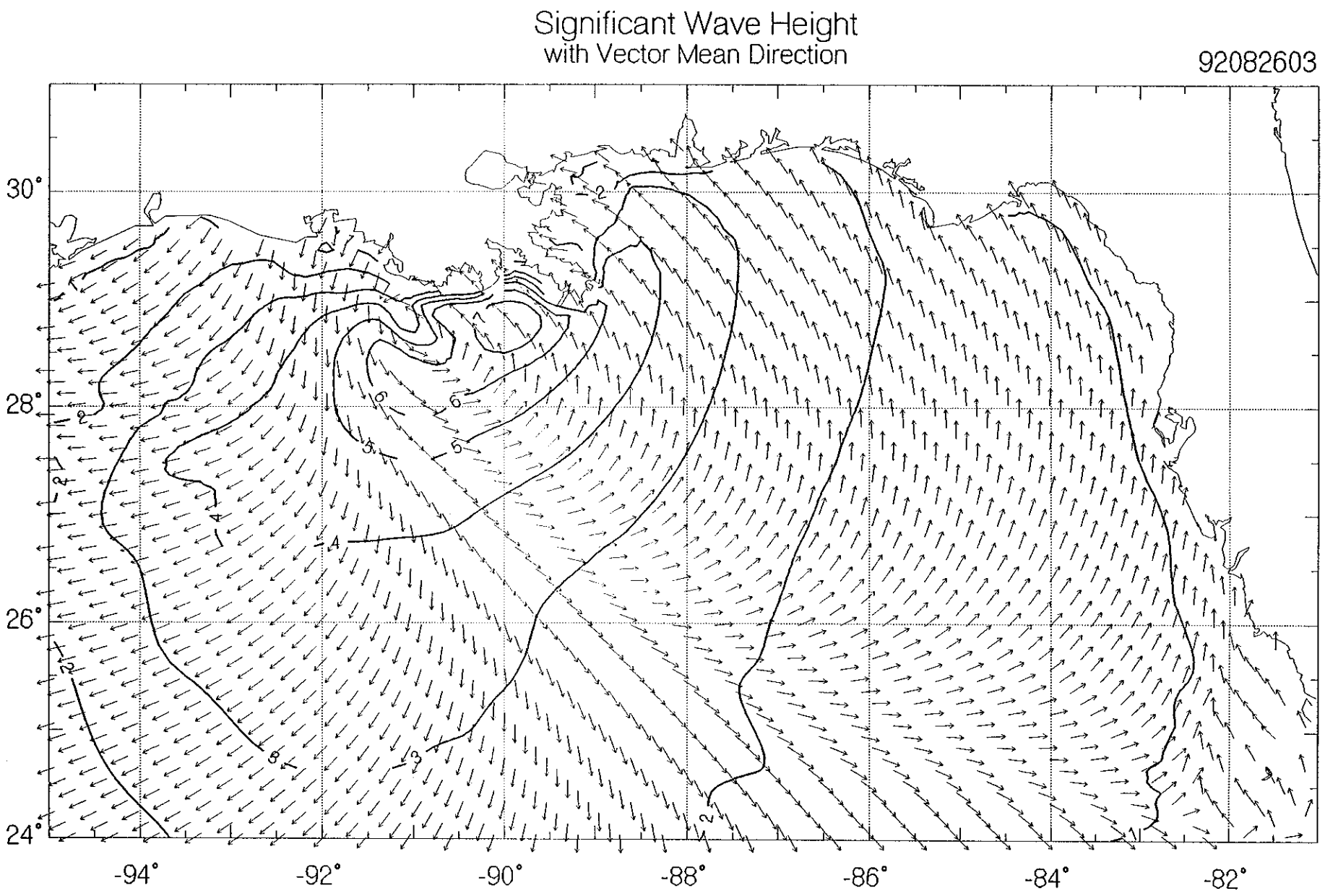
Significant Wave Height
with Vector Mean Direction
92082603
30°
28°
26°
24°
-94°
-92°
-90°
-88°
-86°
-84°
-82°

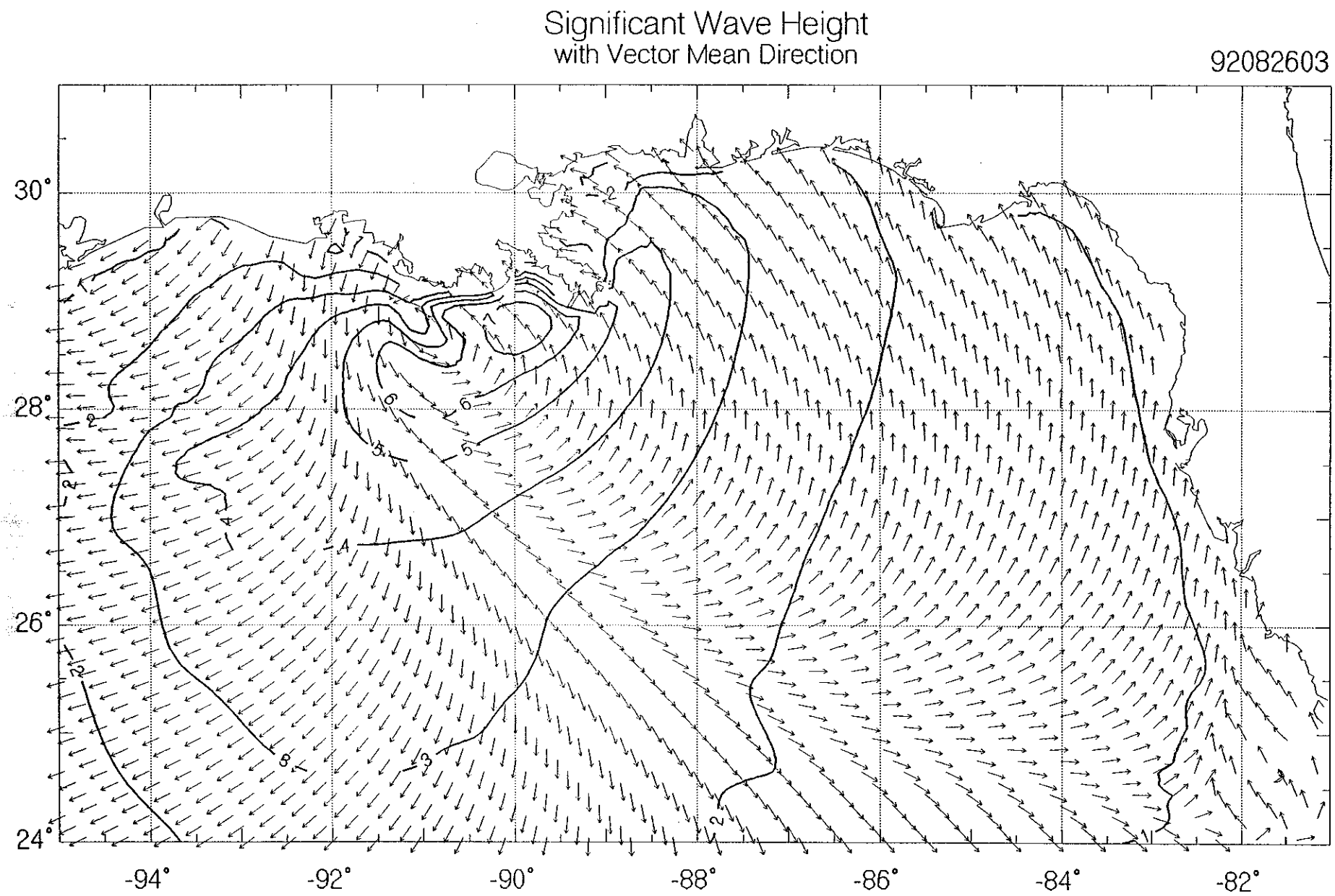
Significant Wave Height
with Vector Mean Direction
92082603
30°
28°
26°
24°
-94°
-92°
-90°
-88°
-86°
-84°
-82°

Significant Wave Height
with Vector Mean Direction

92082606

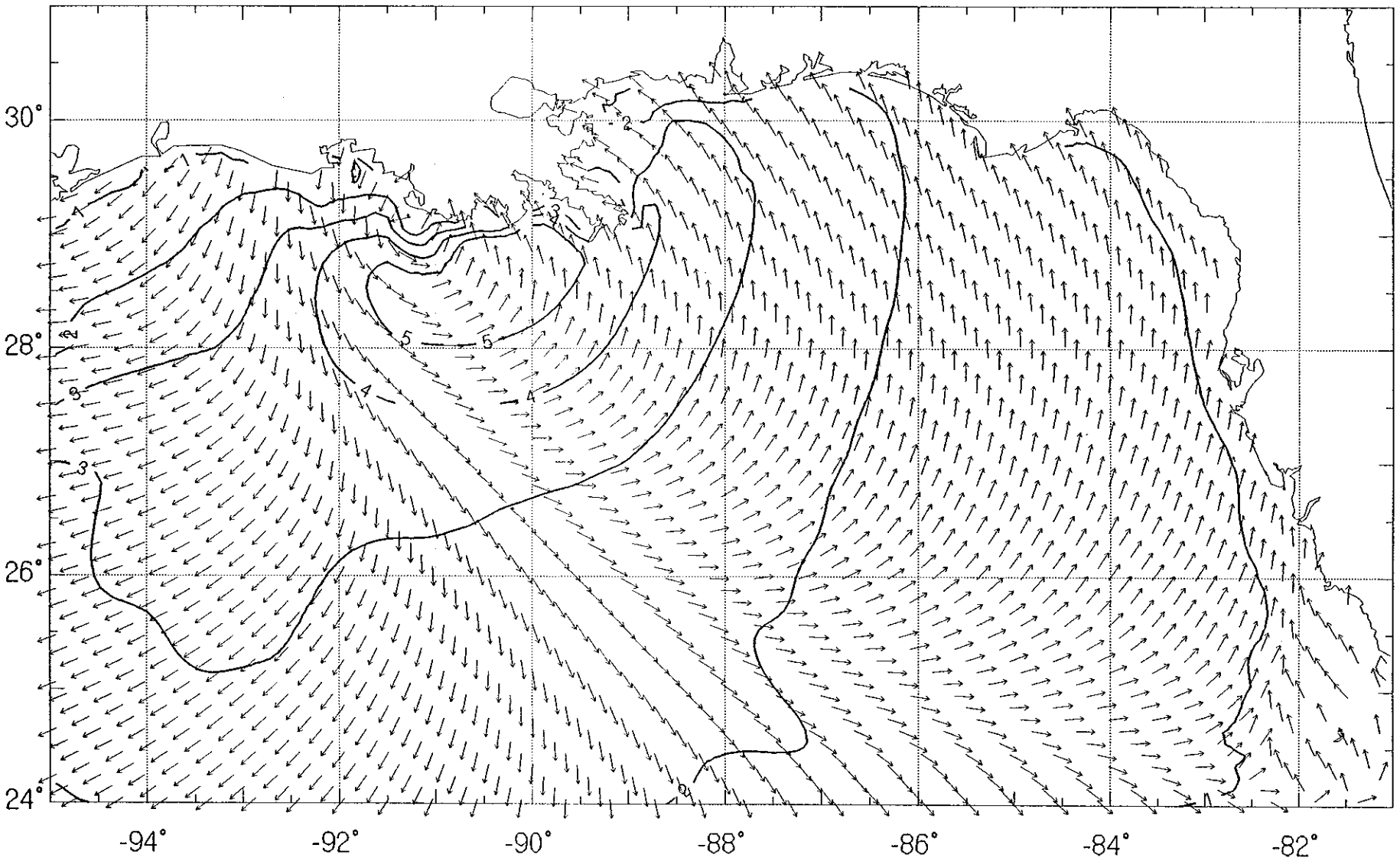

Significant Wave Height
with Vector Mean Direction

92082609

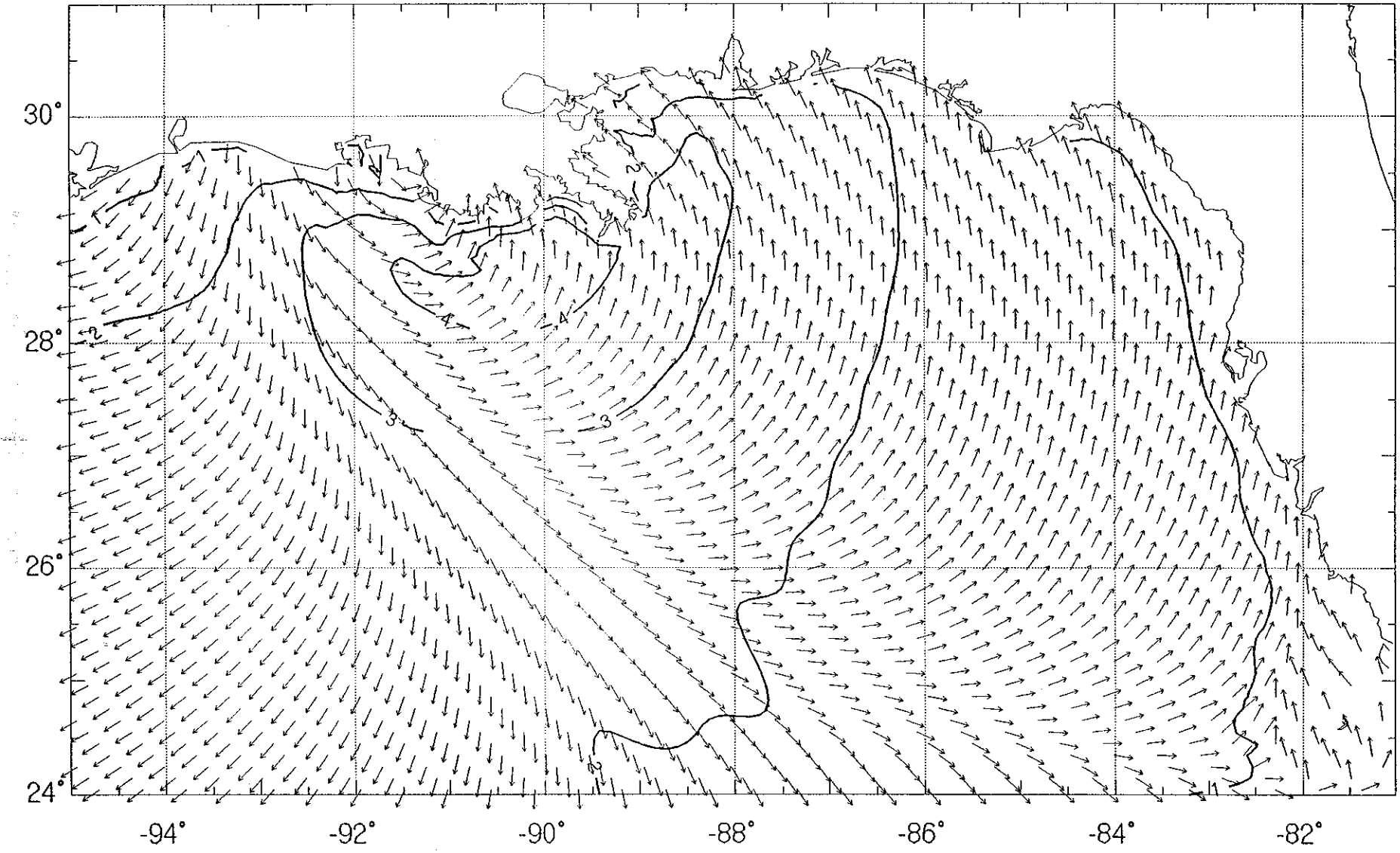

Significant Wave Height
with Vector Mean Direction

92082612

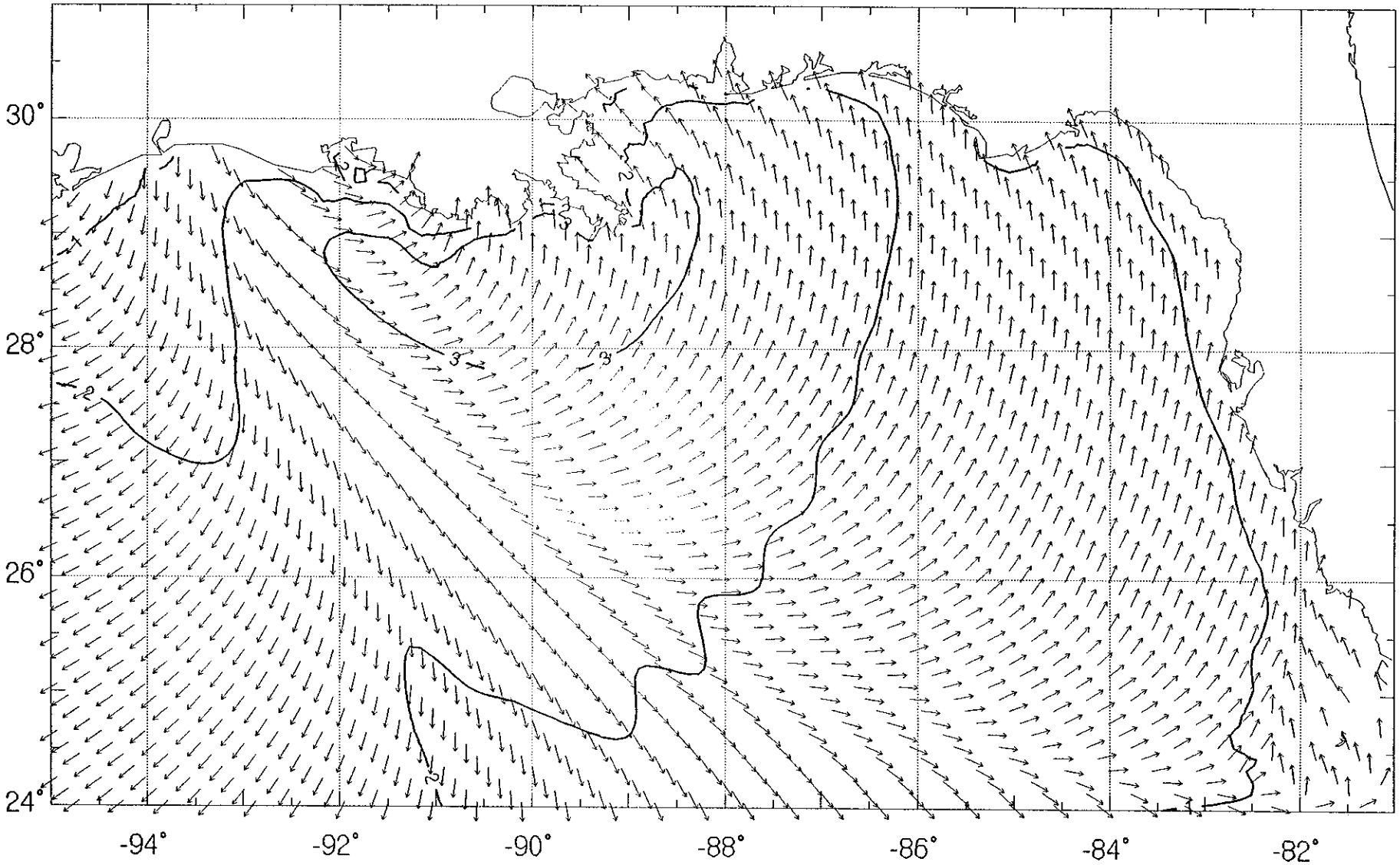

Significant Wave Height
with Vector Mean Direction

92082615

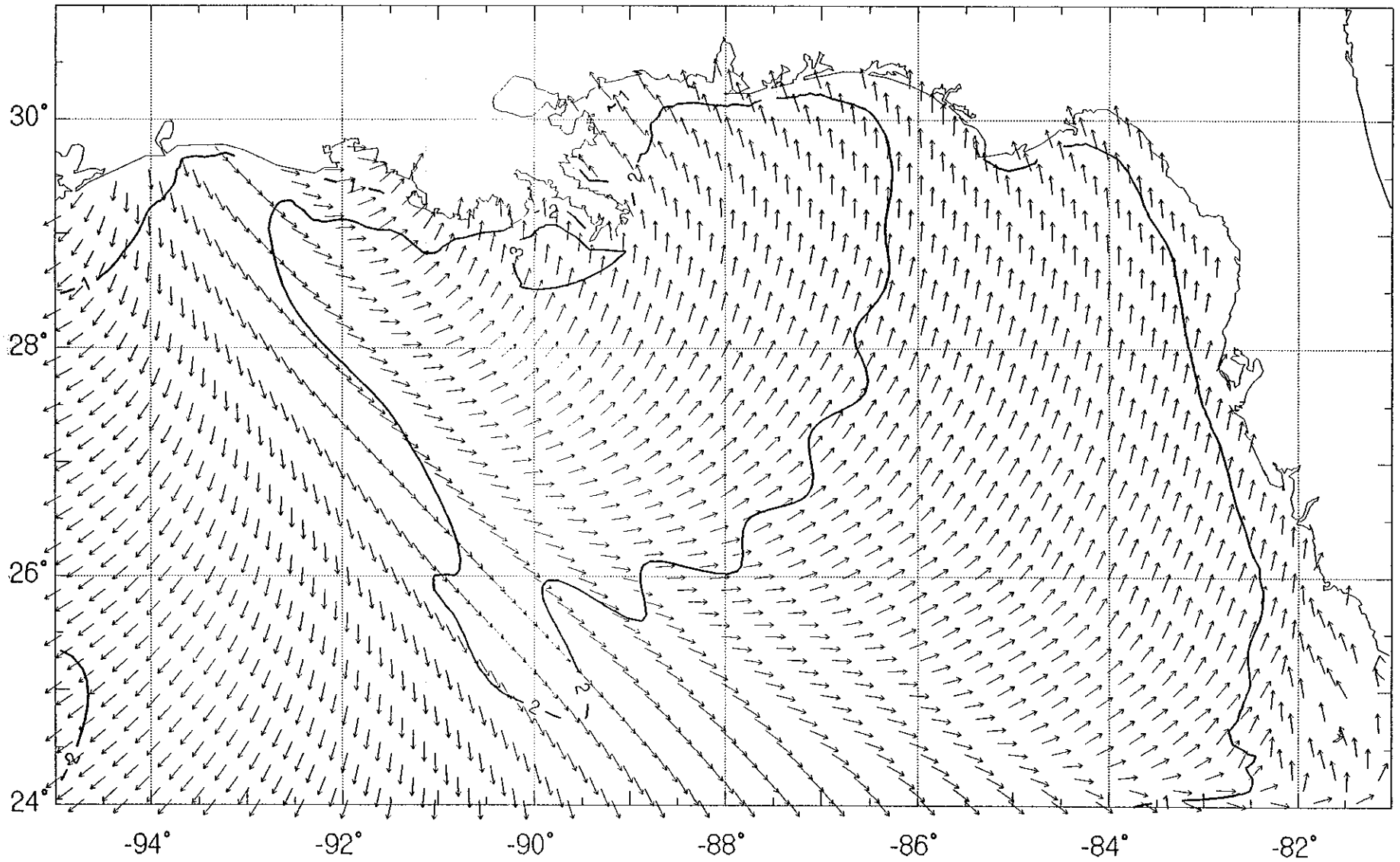

Significant Wave Height
with Vector Mean Direction

92082618

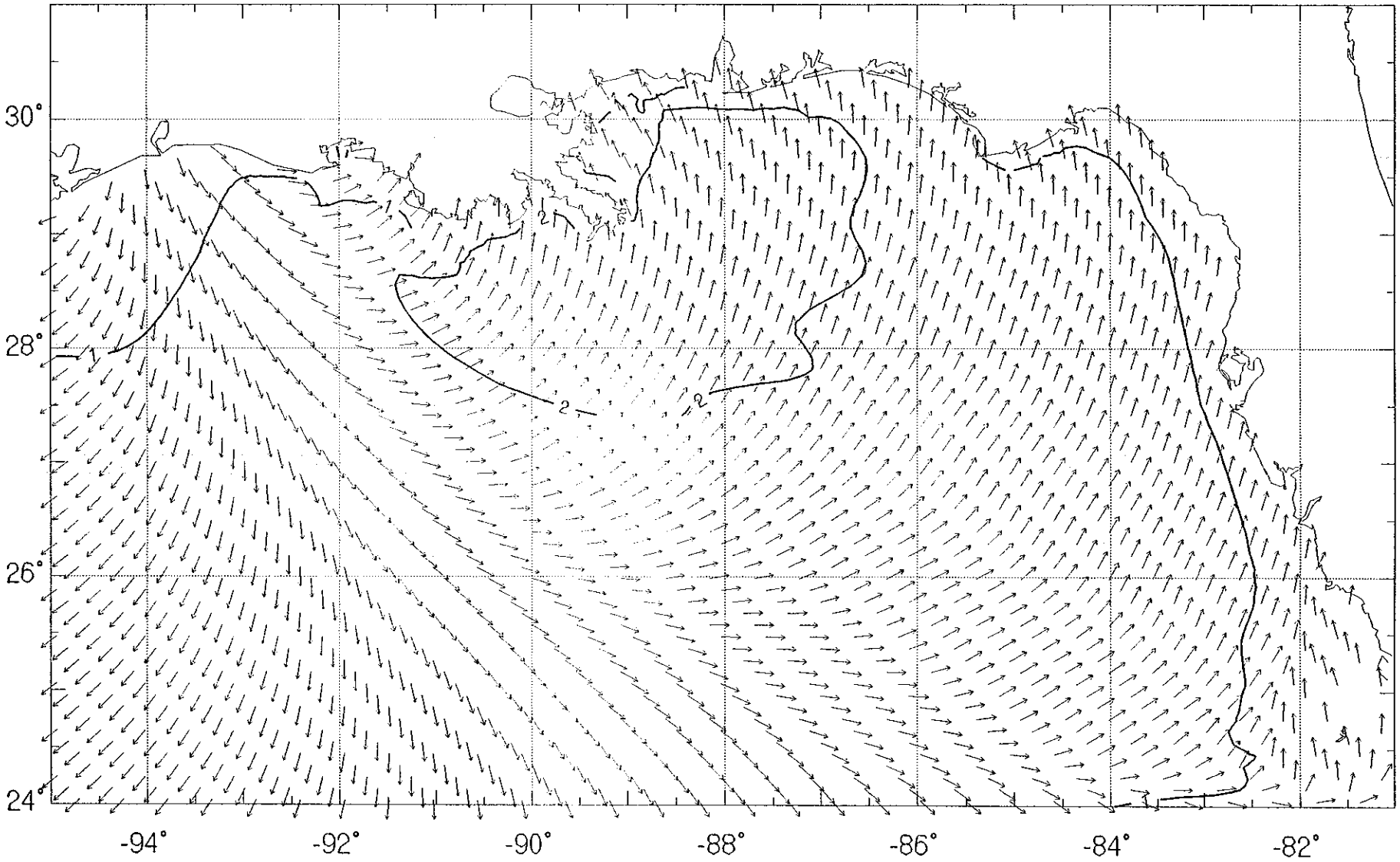

Significant Wave Height
with Vector Mean Direction

92082621

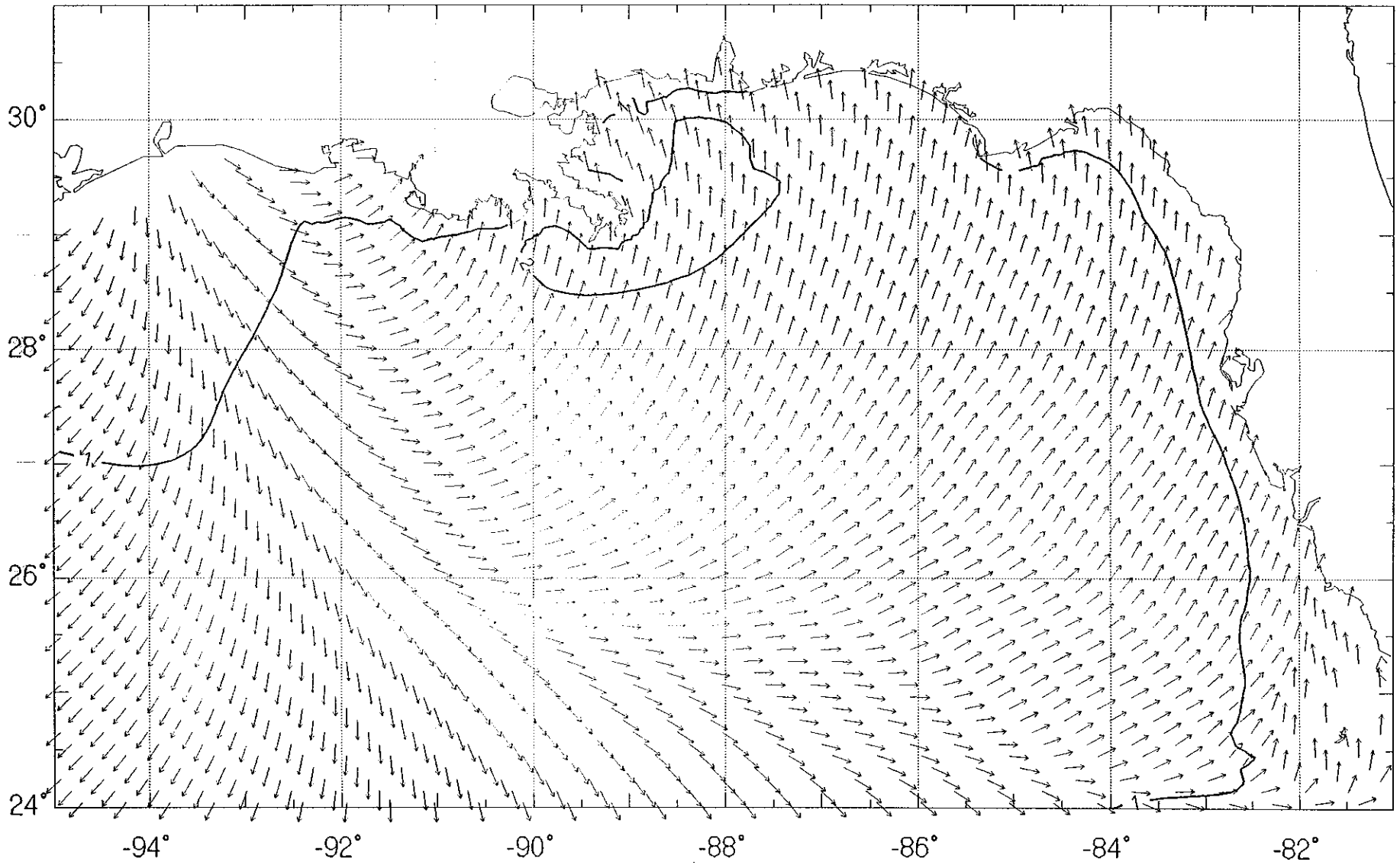

Significant Wave Height
with Vector Mean Direction

92082700

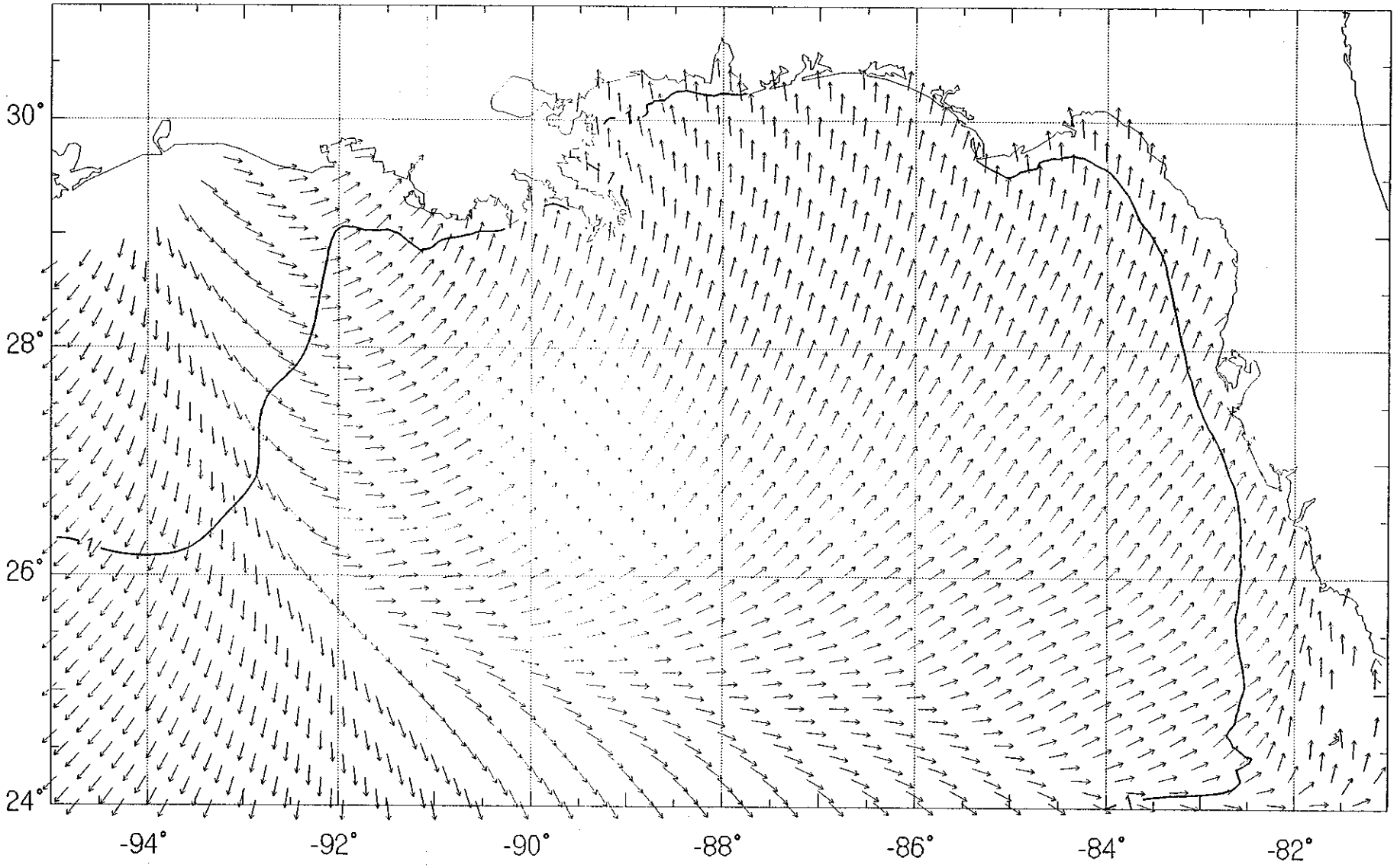

Appendix G.

Observed surface currents at hourly intervals during the passage of Hurricane Andrew indicated as plotteed vectors (see scale at top) at the measurrement sites. The track of the center of Andrew is shown and the position of the center at the time of the map is indicated by a cross. The circle surrounding the cross is the approximate radius of maximum wind.

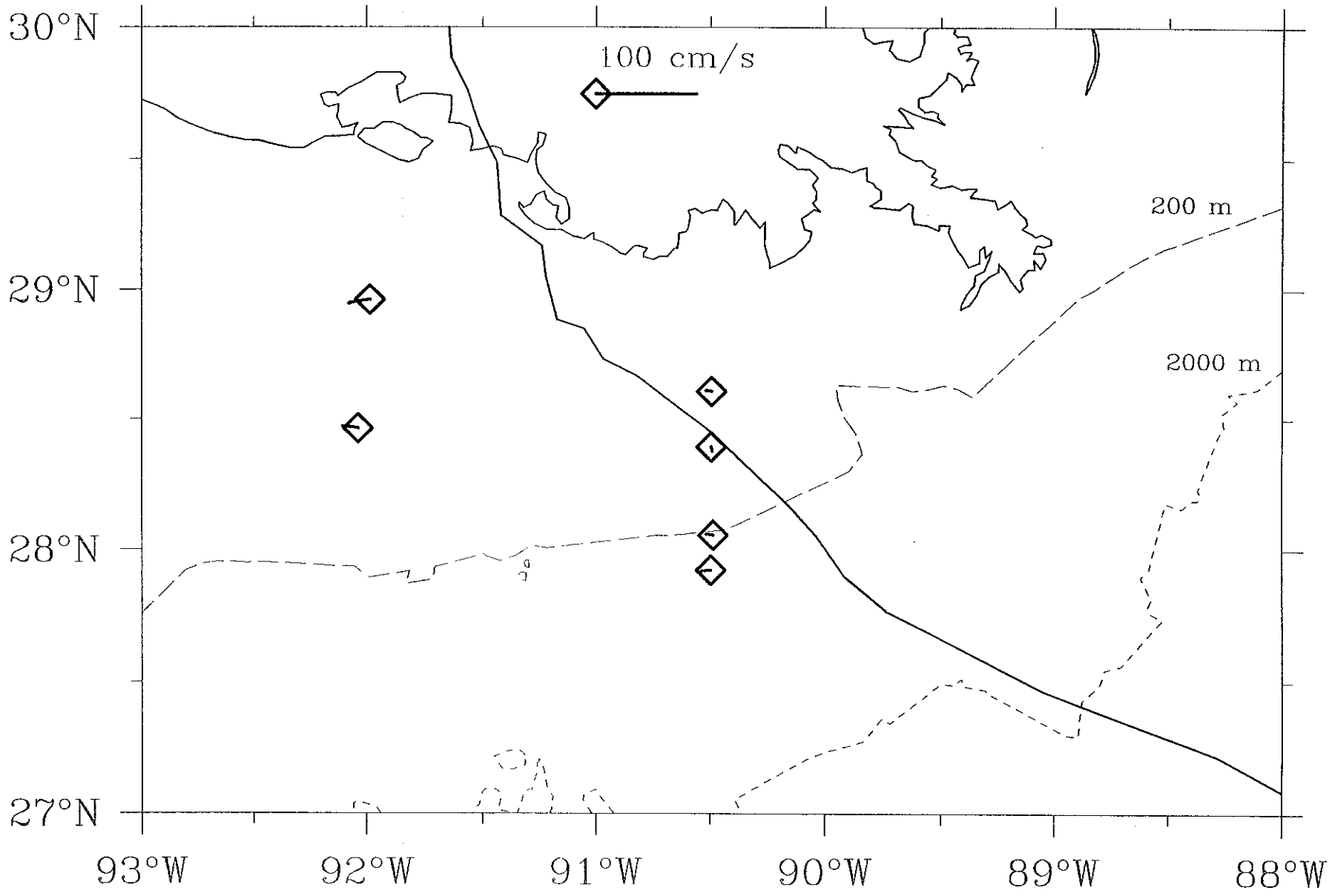

Observed Surface Currents: August-25-00:00 GMT

Frame 00

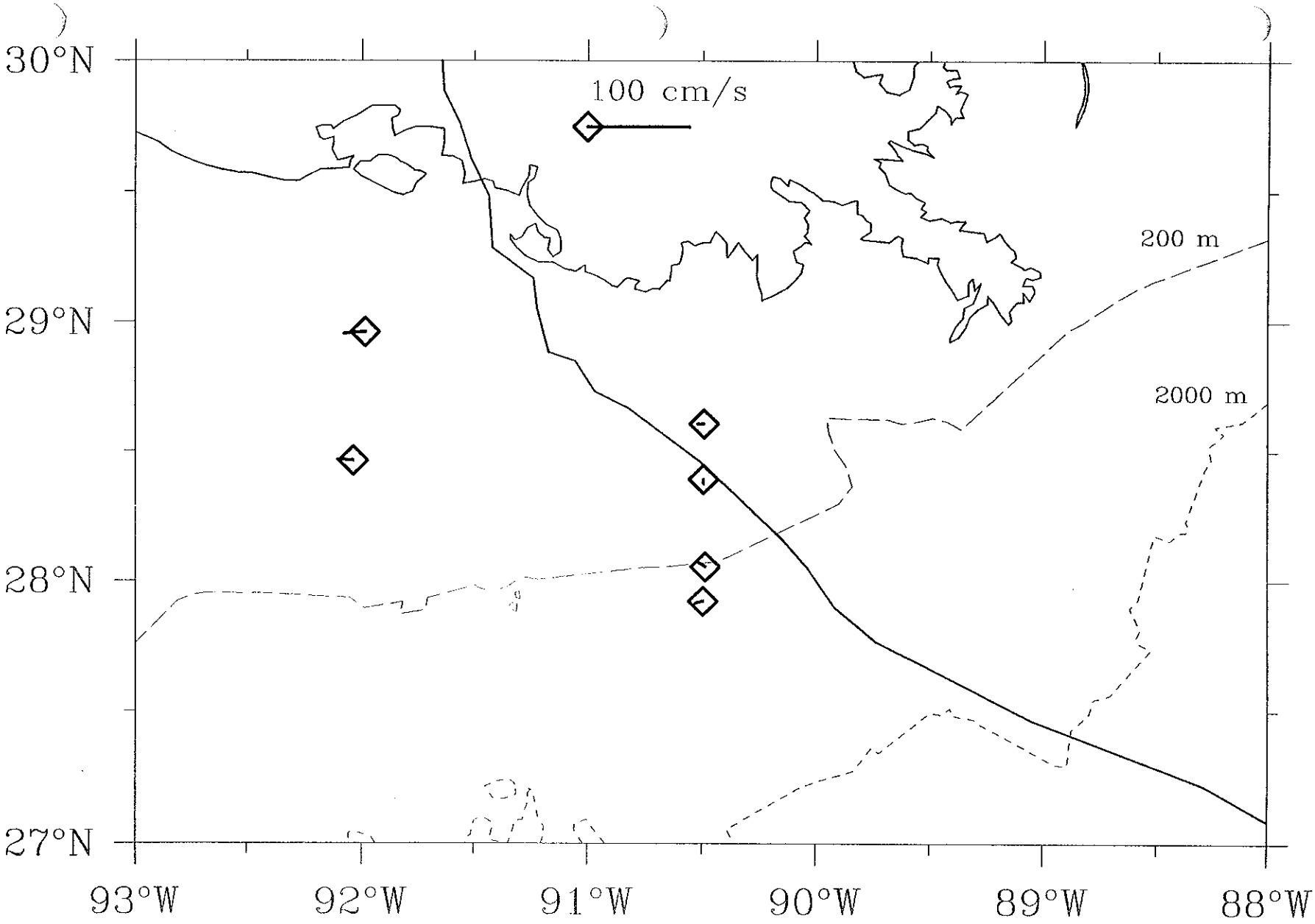

Observed Surface Currents: August-25-00:30 GMT

Frame 001

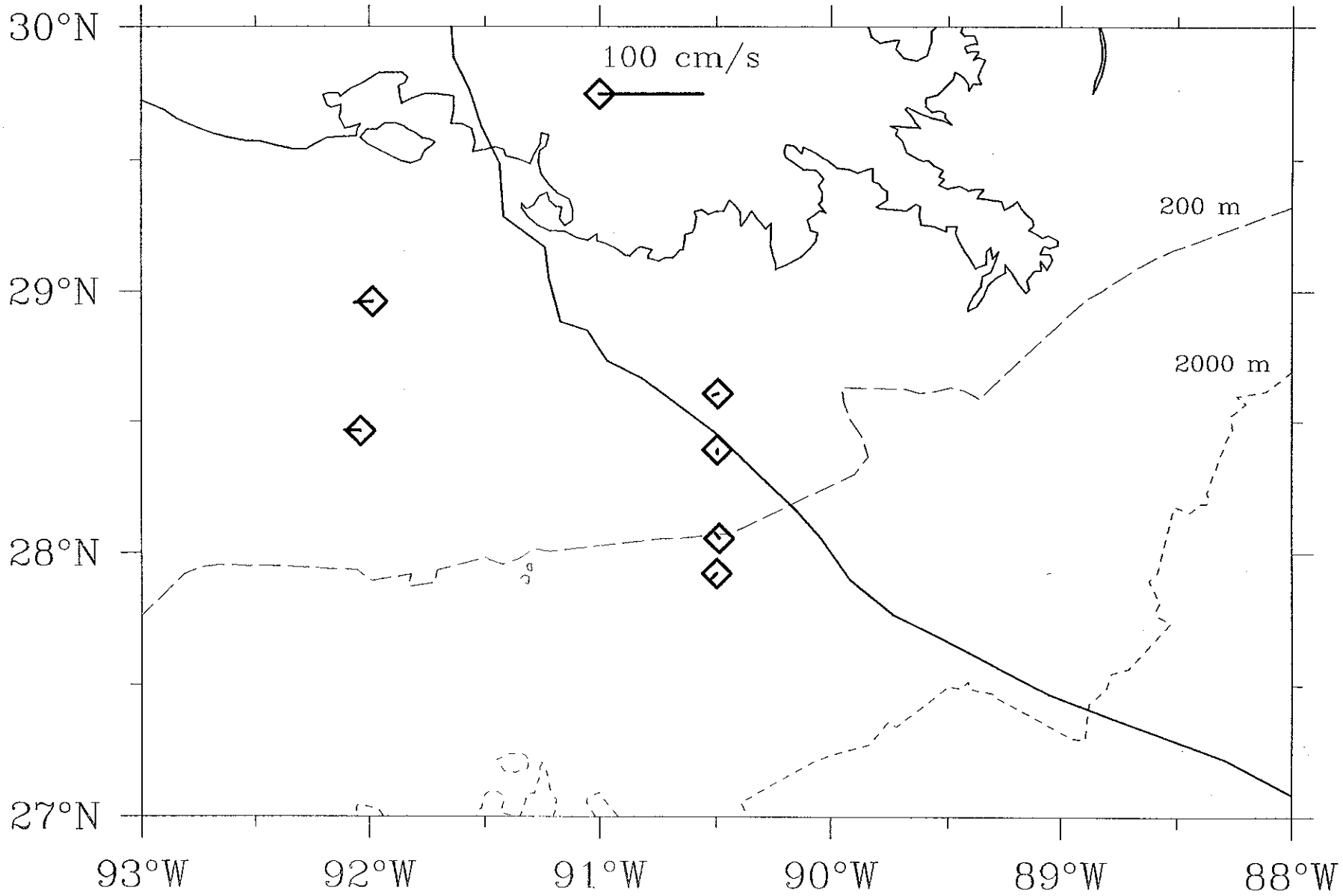

Observed Surface Currents: August-25-01:00 GMT

Frame 002

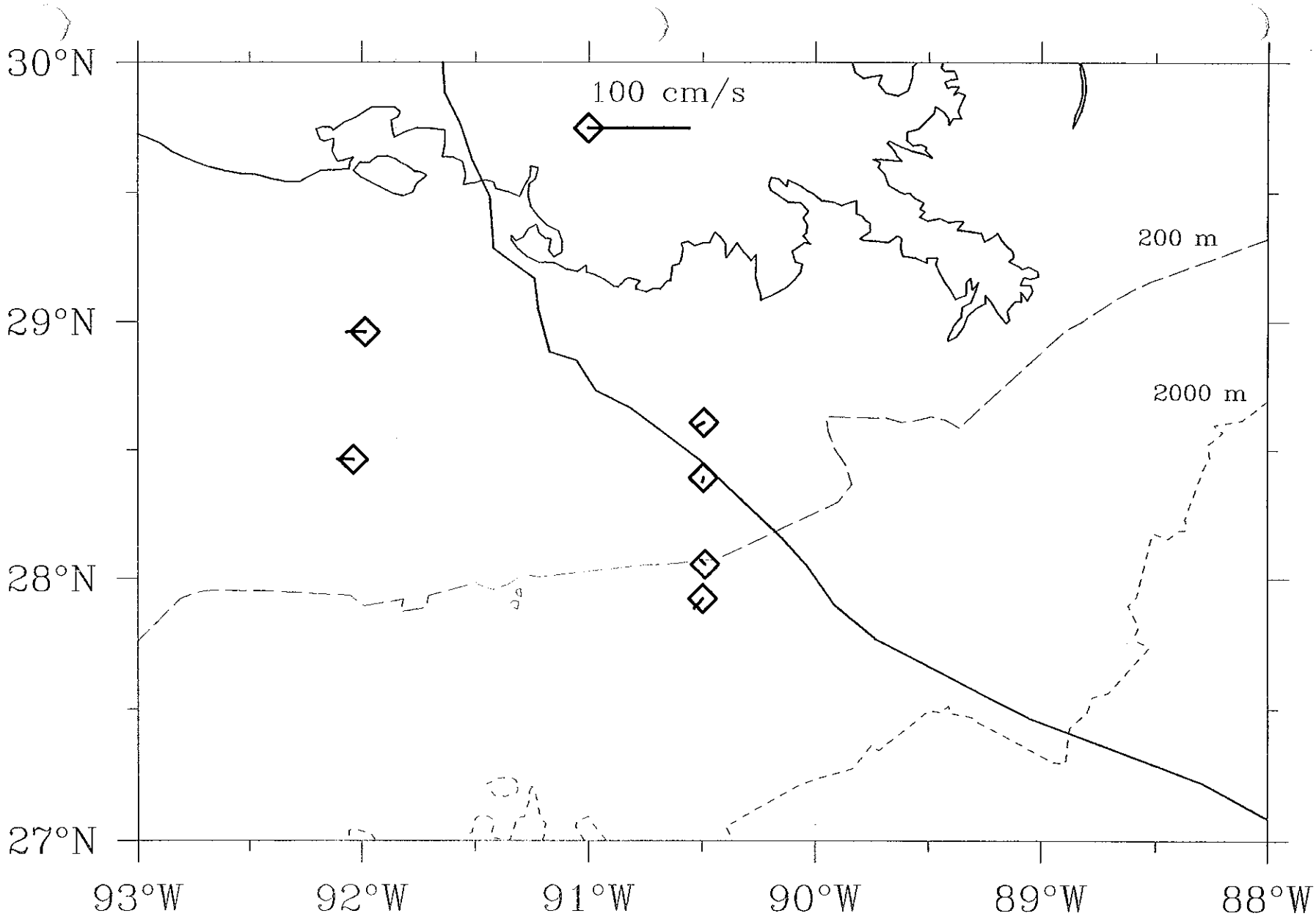

Observed Surface Currents: August-25-01:30 GMT

Frame 003

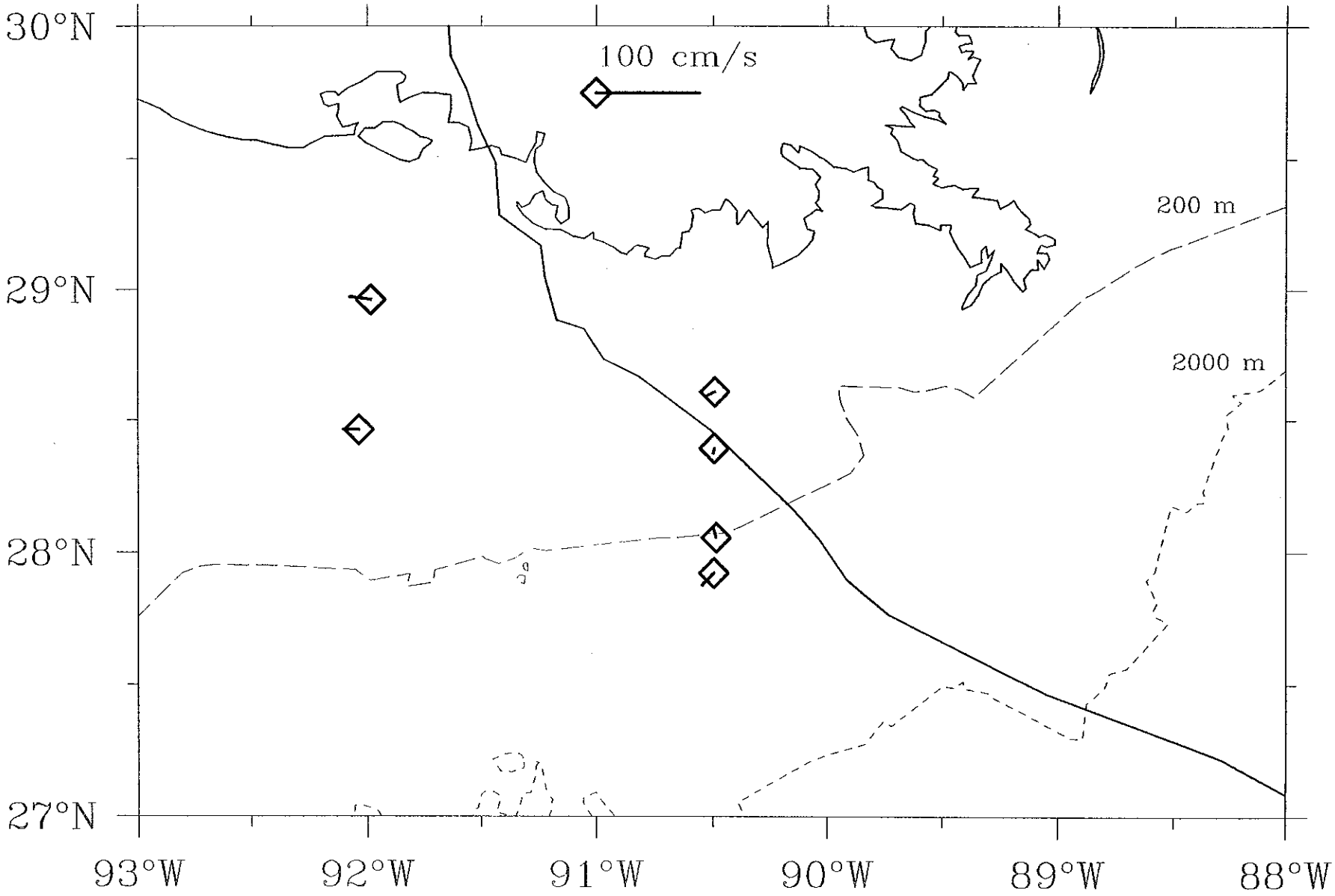

Observed Surface Currents: August-25-02:00 GMT

Frame 00

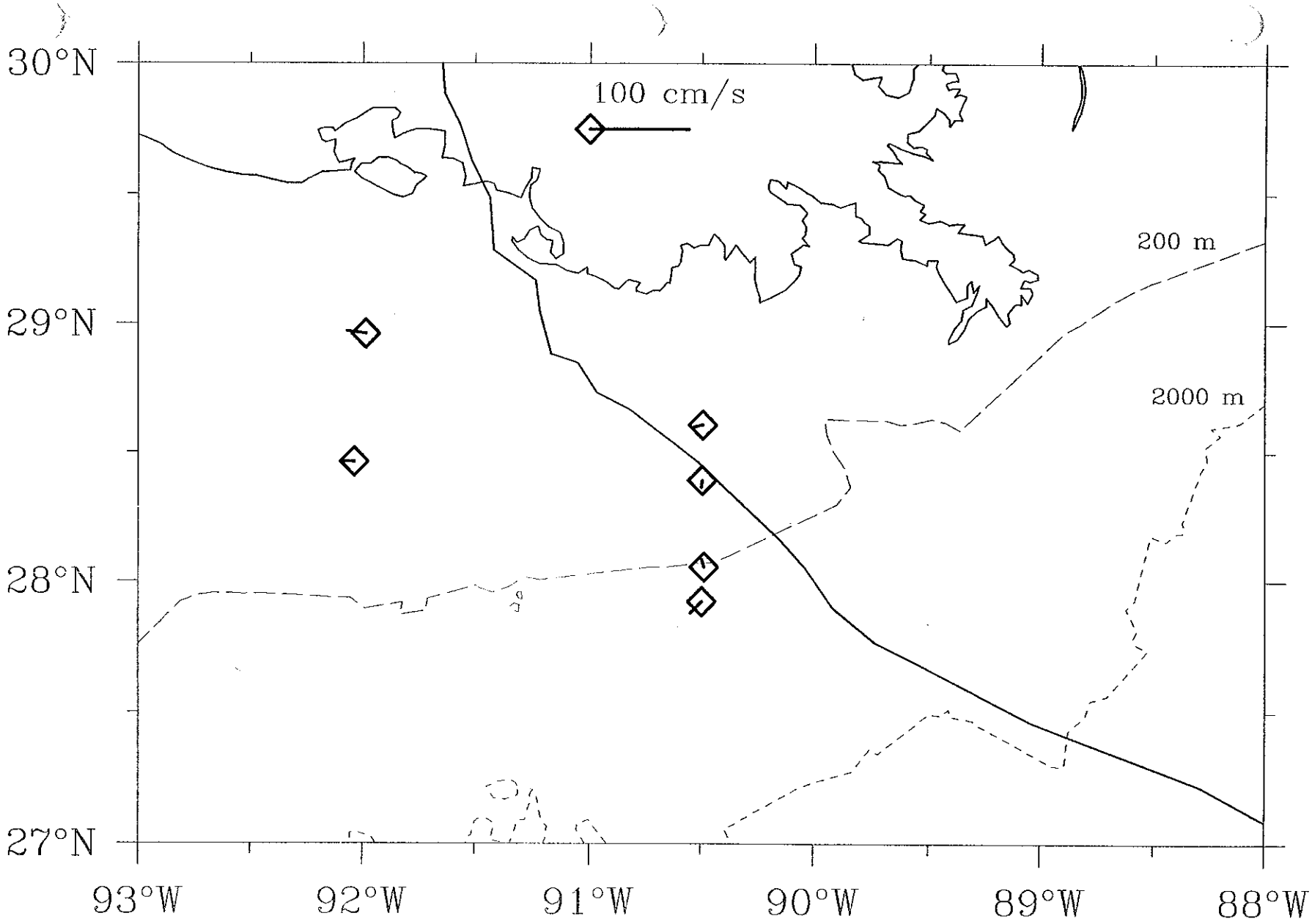

Observed Surface Currents: August-25-02:30 GMT

Frame 005

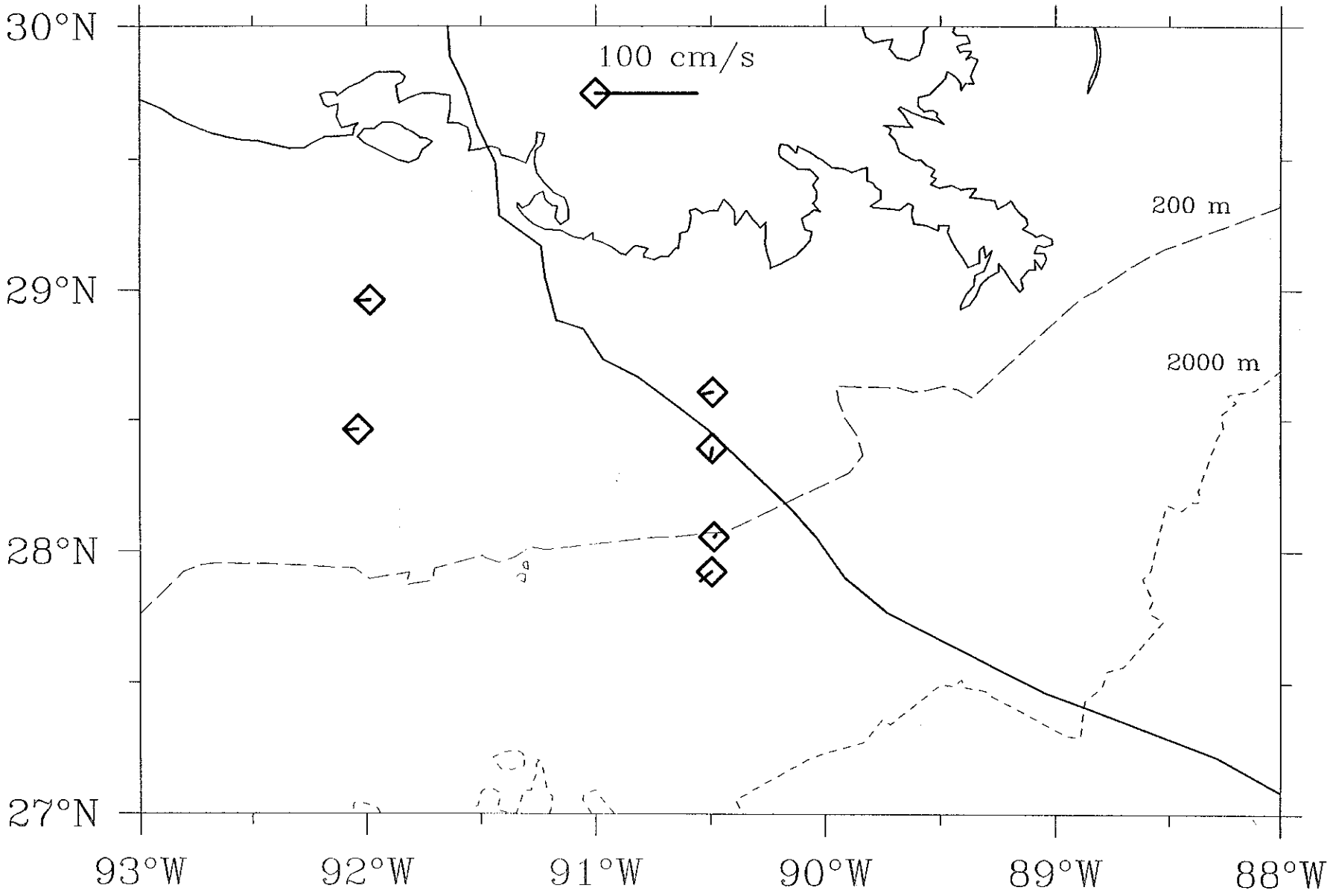

Observed Surface Currents: August-25-03:00 GMT

Frame 006

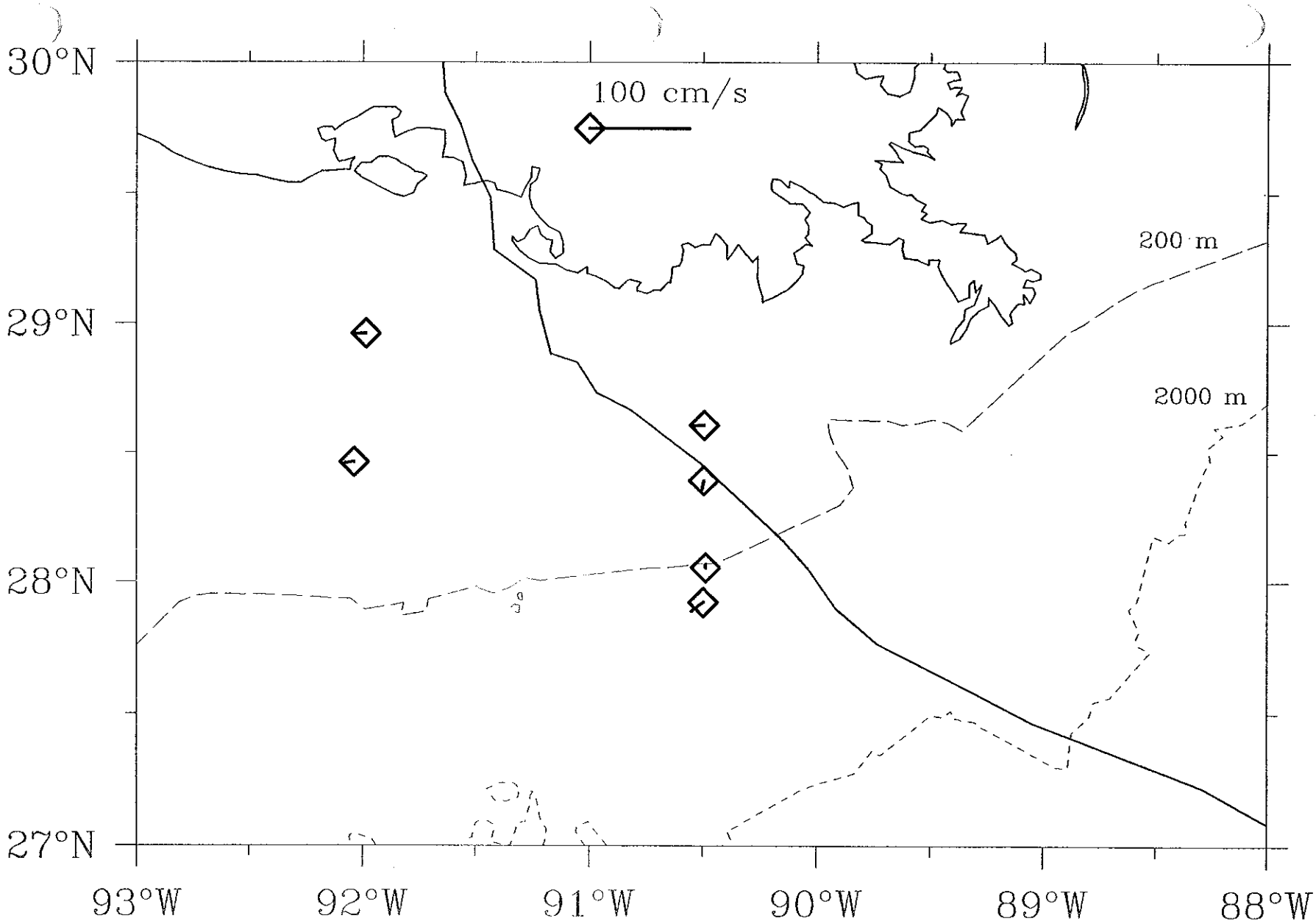

Observed Surface Currents: August-25-03:30 GMT

Frame 007

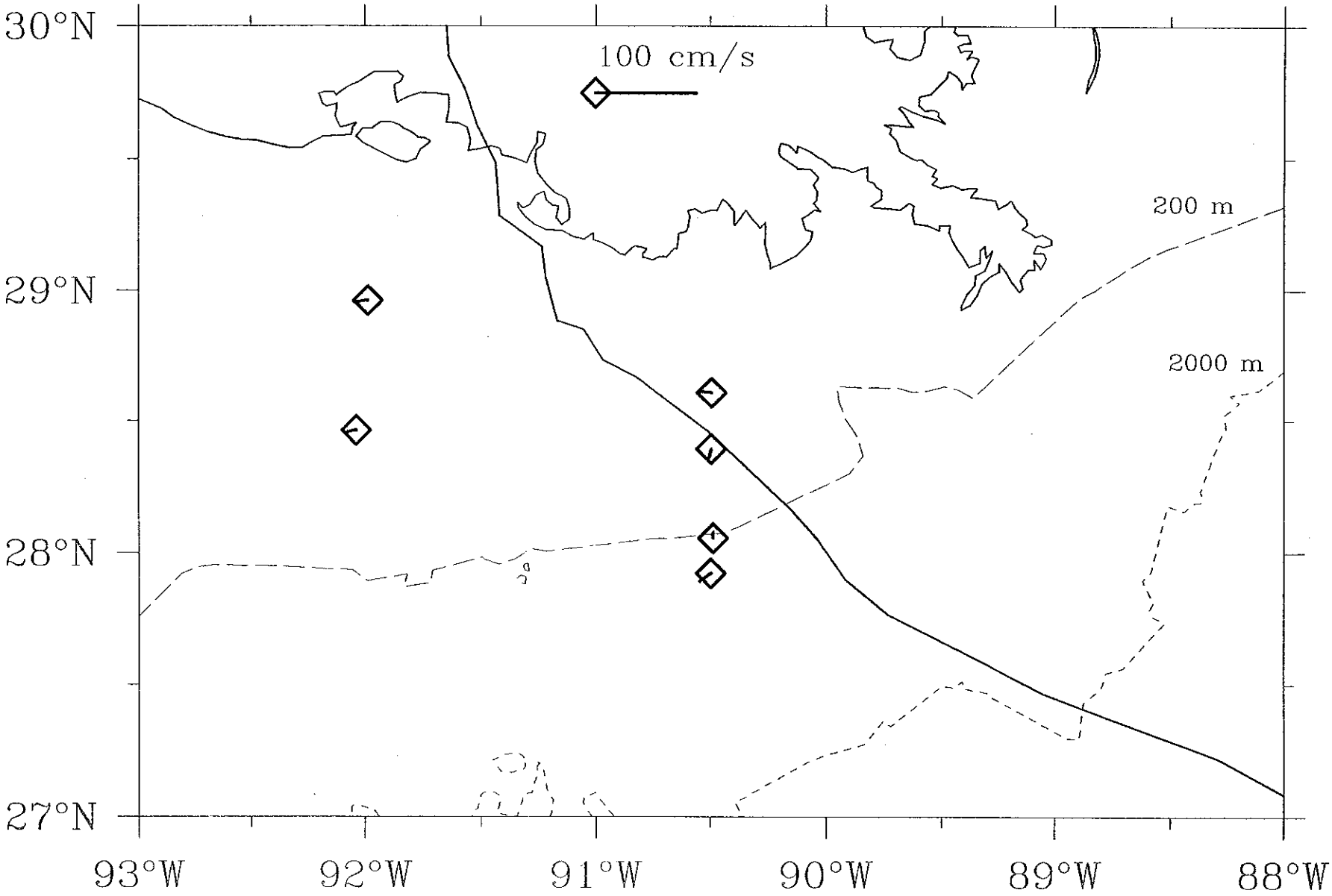

Observed Surface Currents: August-25-04:00 GMT

Frame 008

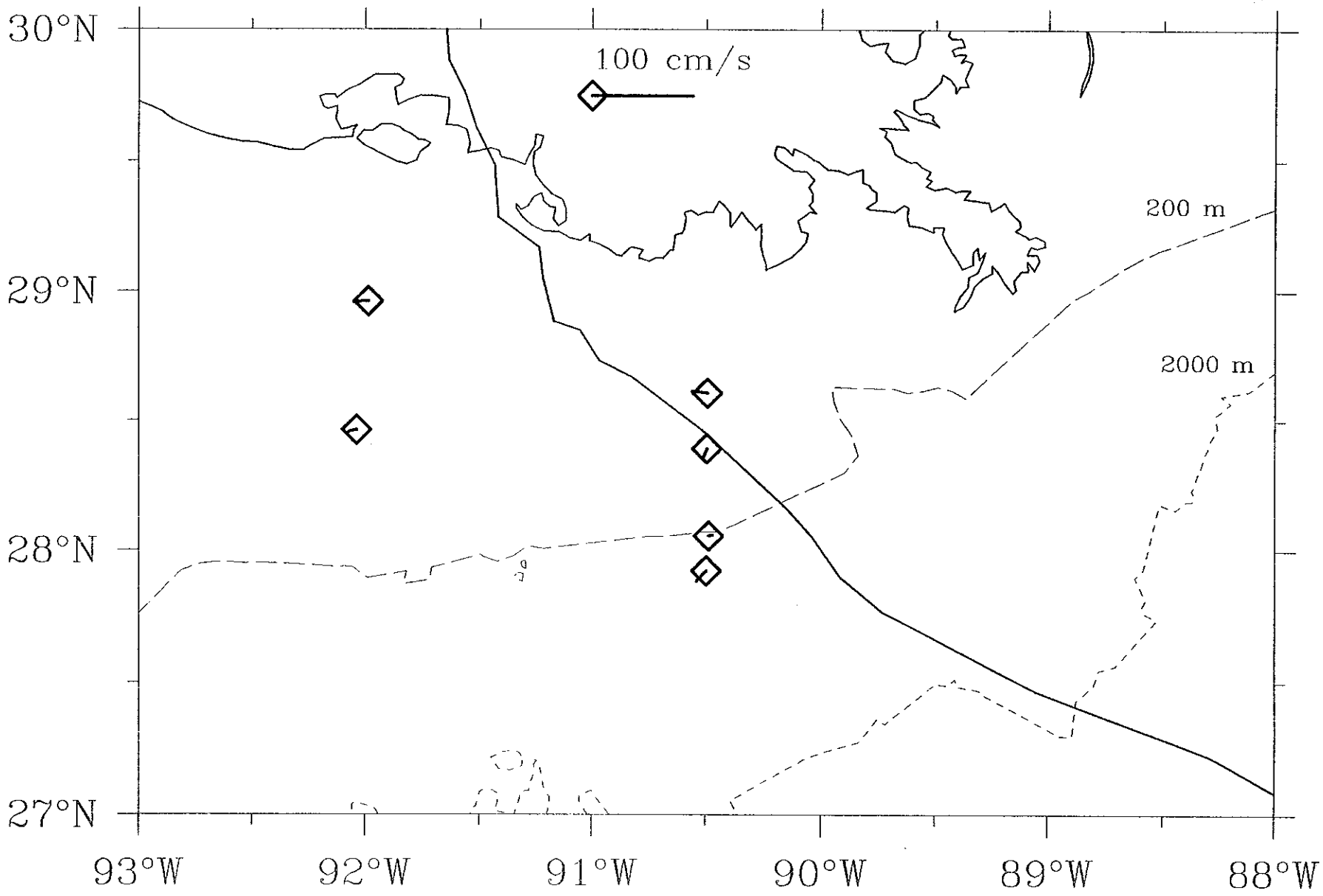

Observed Surface Currents: August-25-04:30 GMT

Frame 009

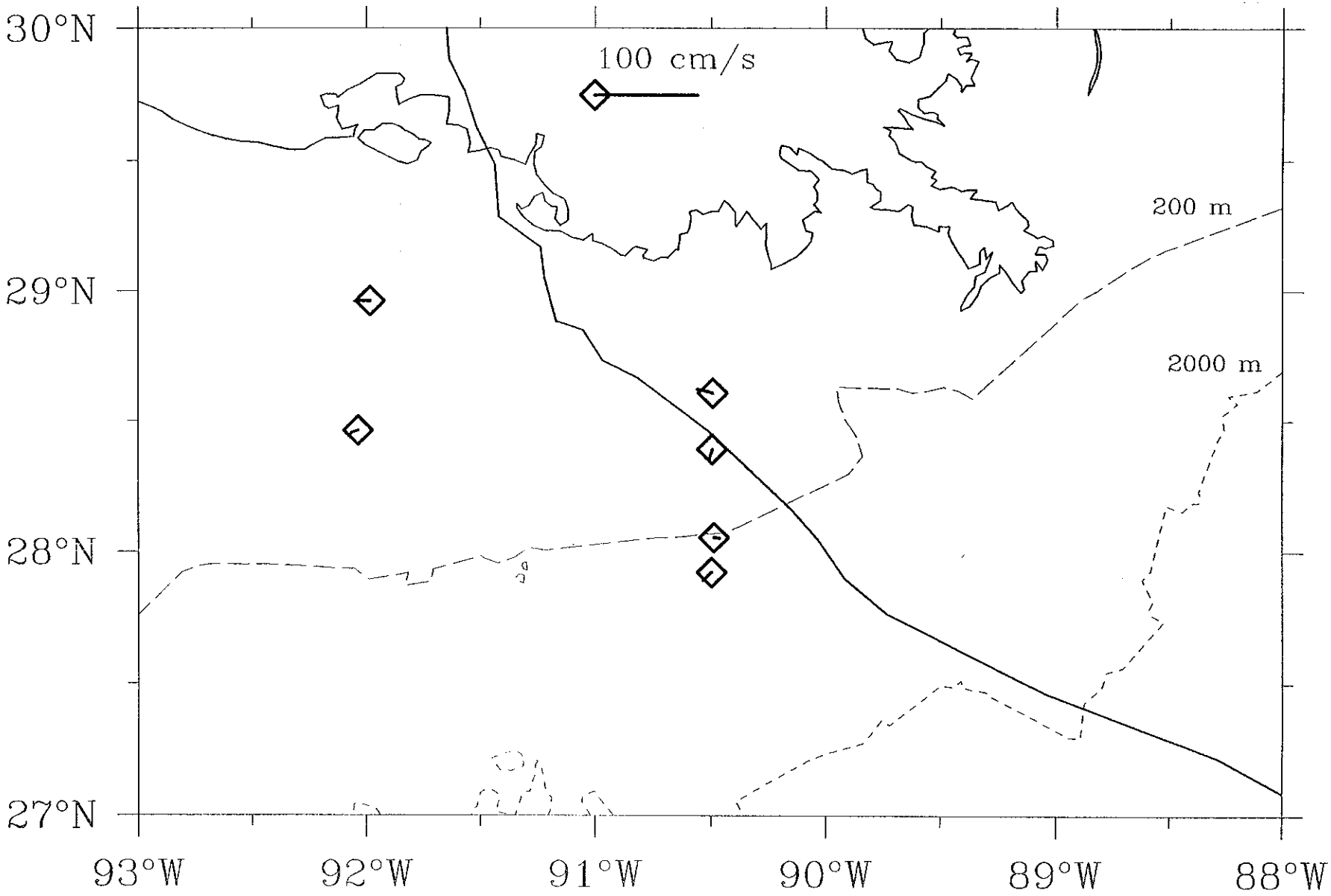

Observed Surface Currents: August–25–05:00 GMT

Frame 010

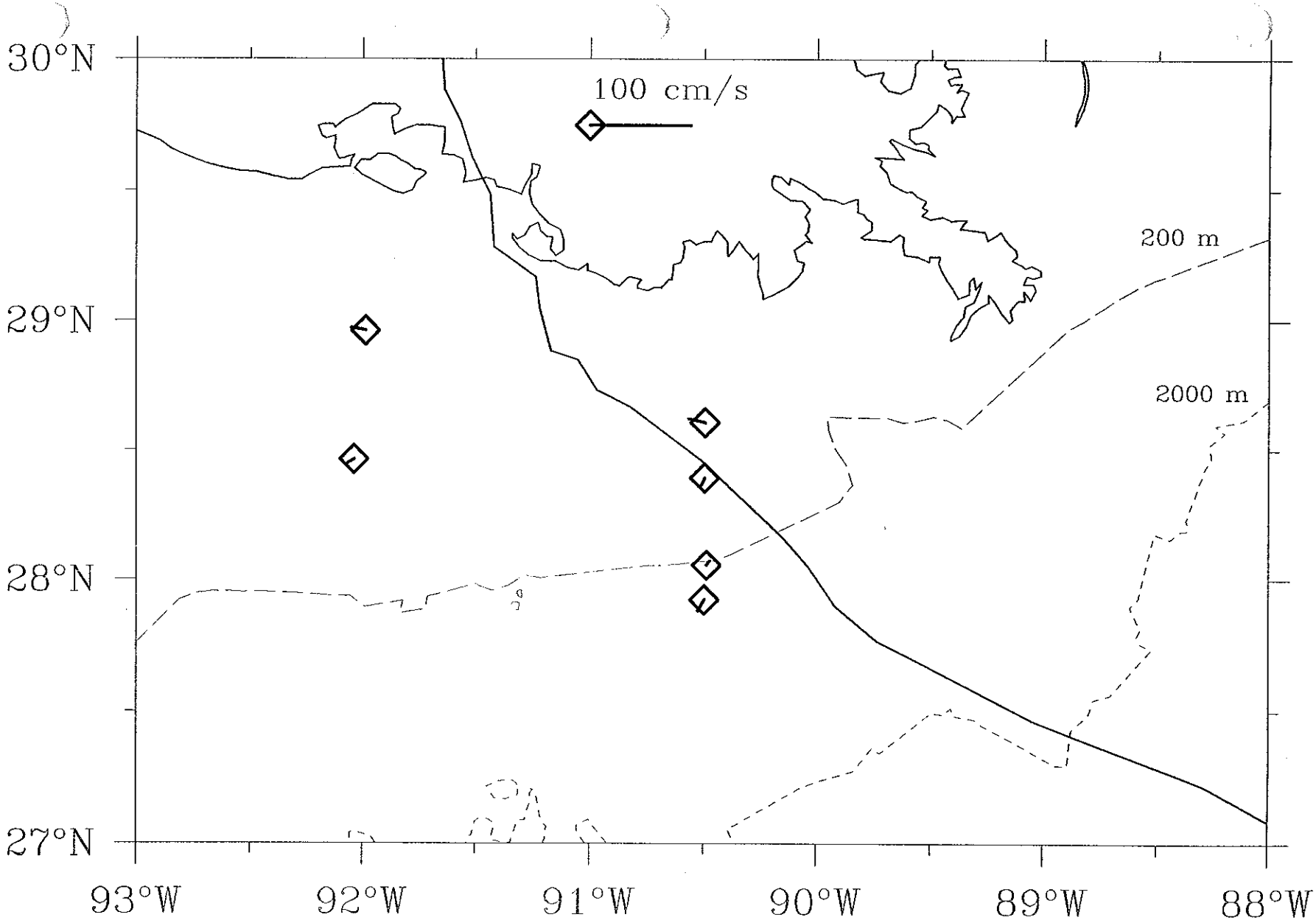

Observed Surface Currents: August-25-05:30 GMT

Frame 011

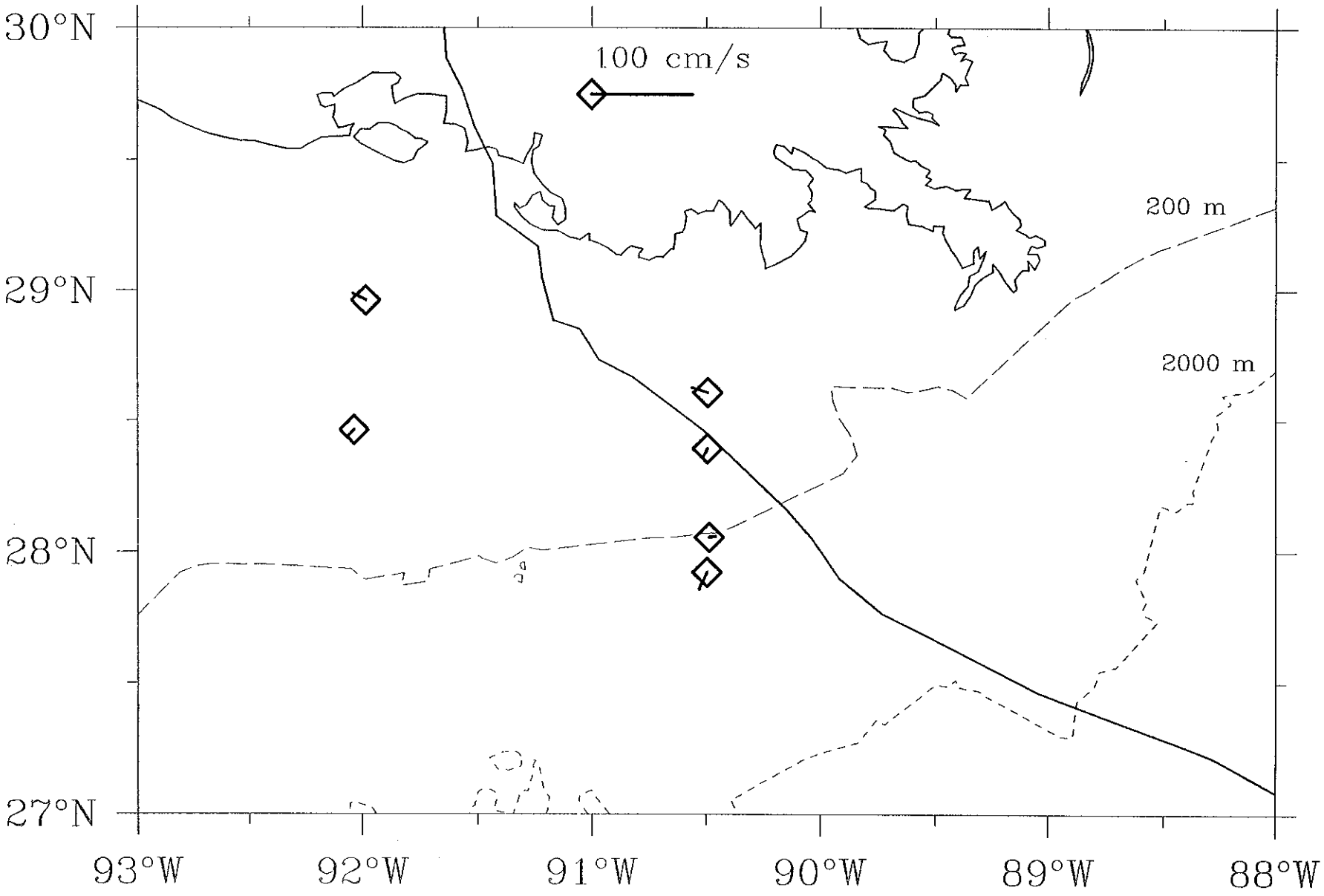

Observed Surface Currents: August-25-06:00 GMT

Frame 01

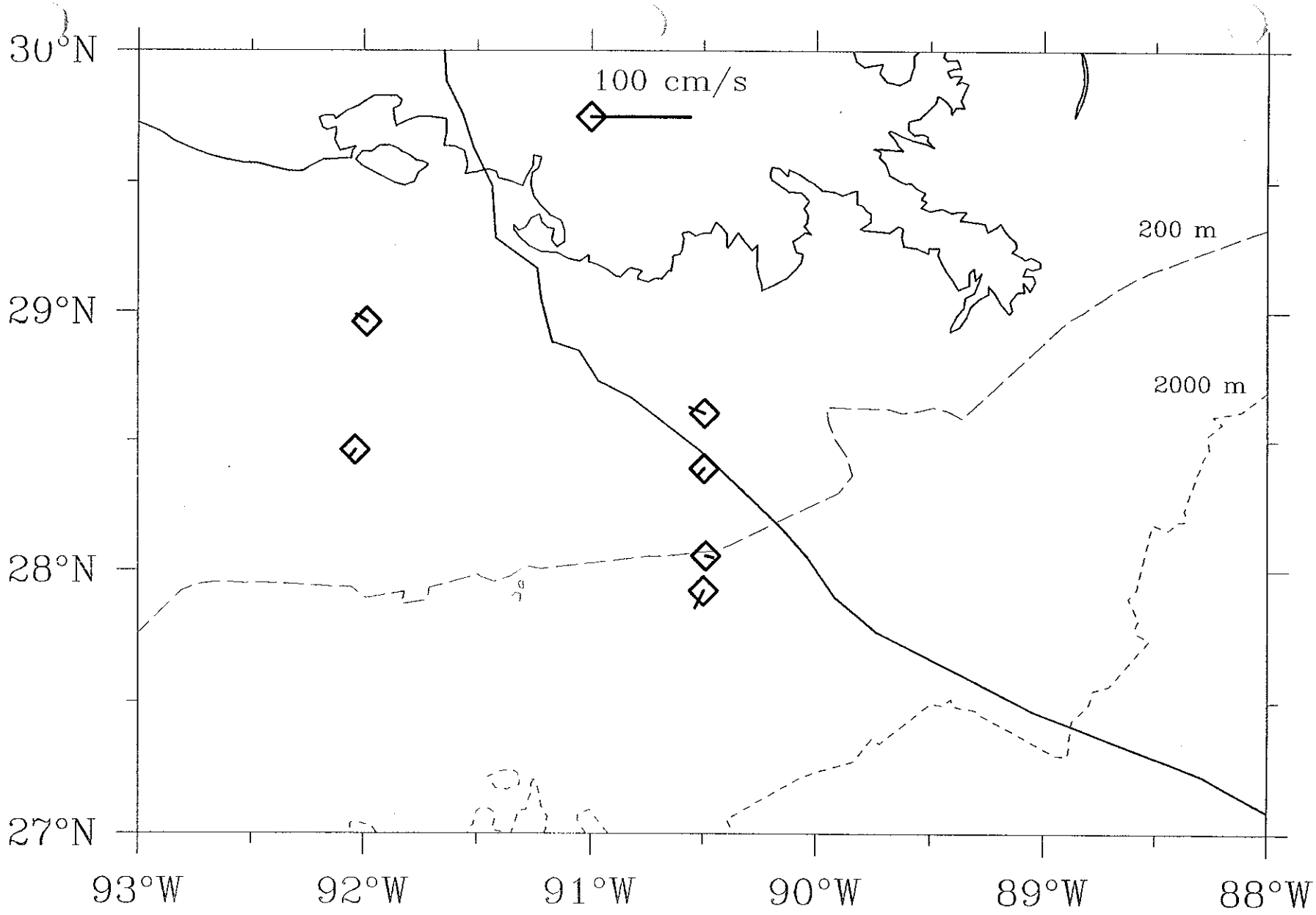

Observed Surface Currents: August-25-06:30 GMT

Frame 013

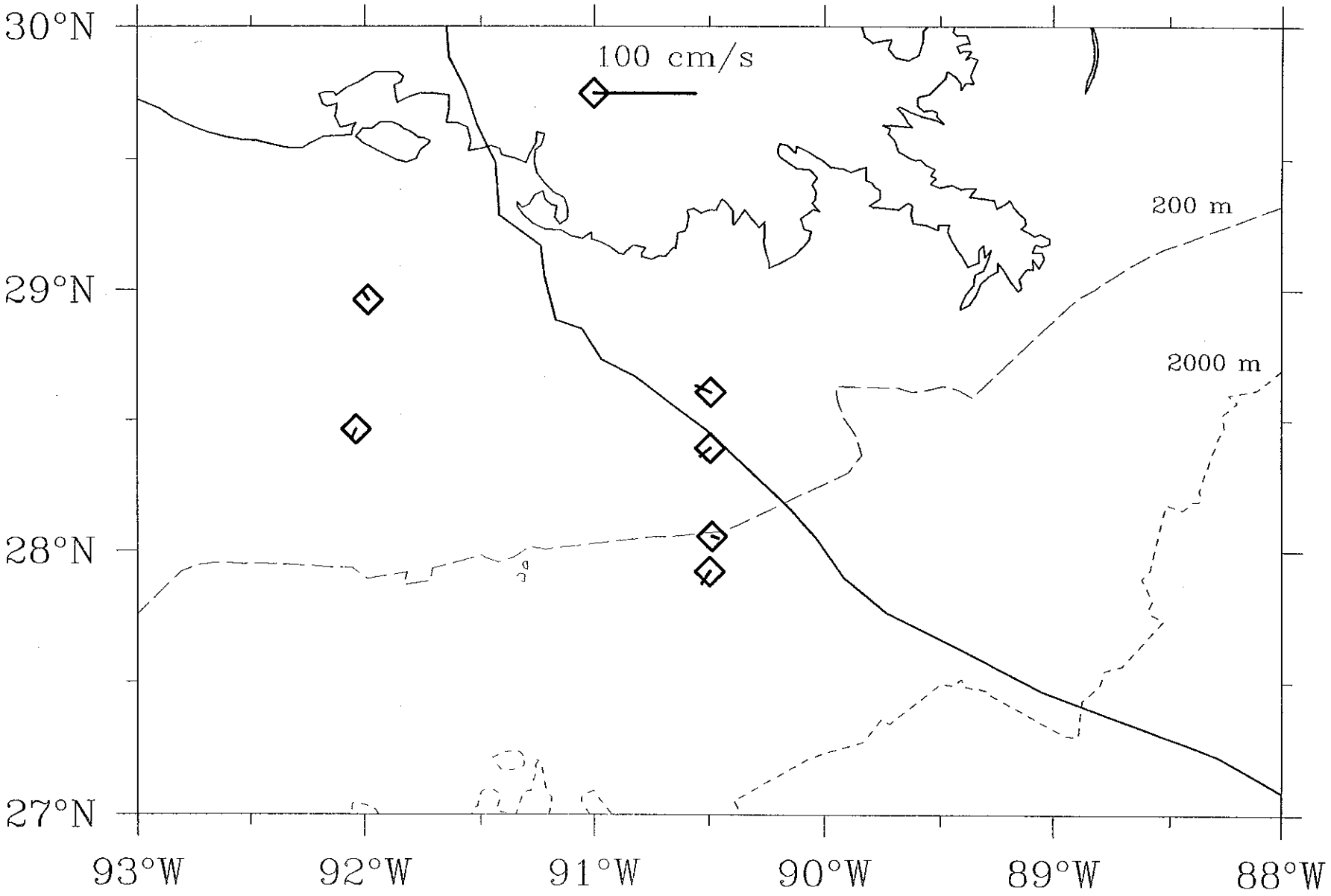

Observed Surface Currents: August–25–07:00 GMT

Frame 01

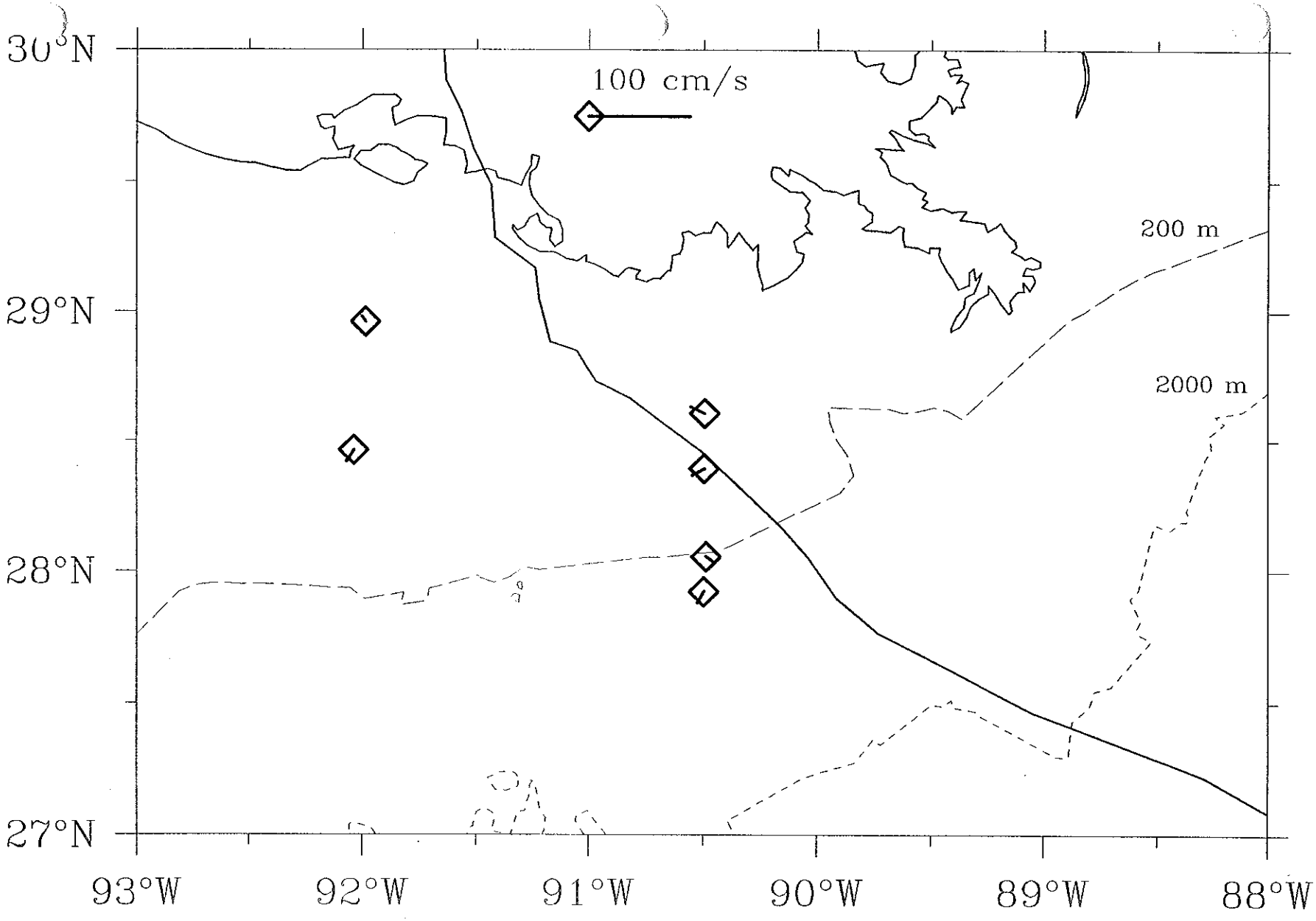

Observed Surface Currents: August–25–07:30 GMT

Frame 015

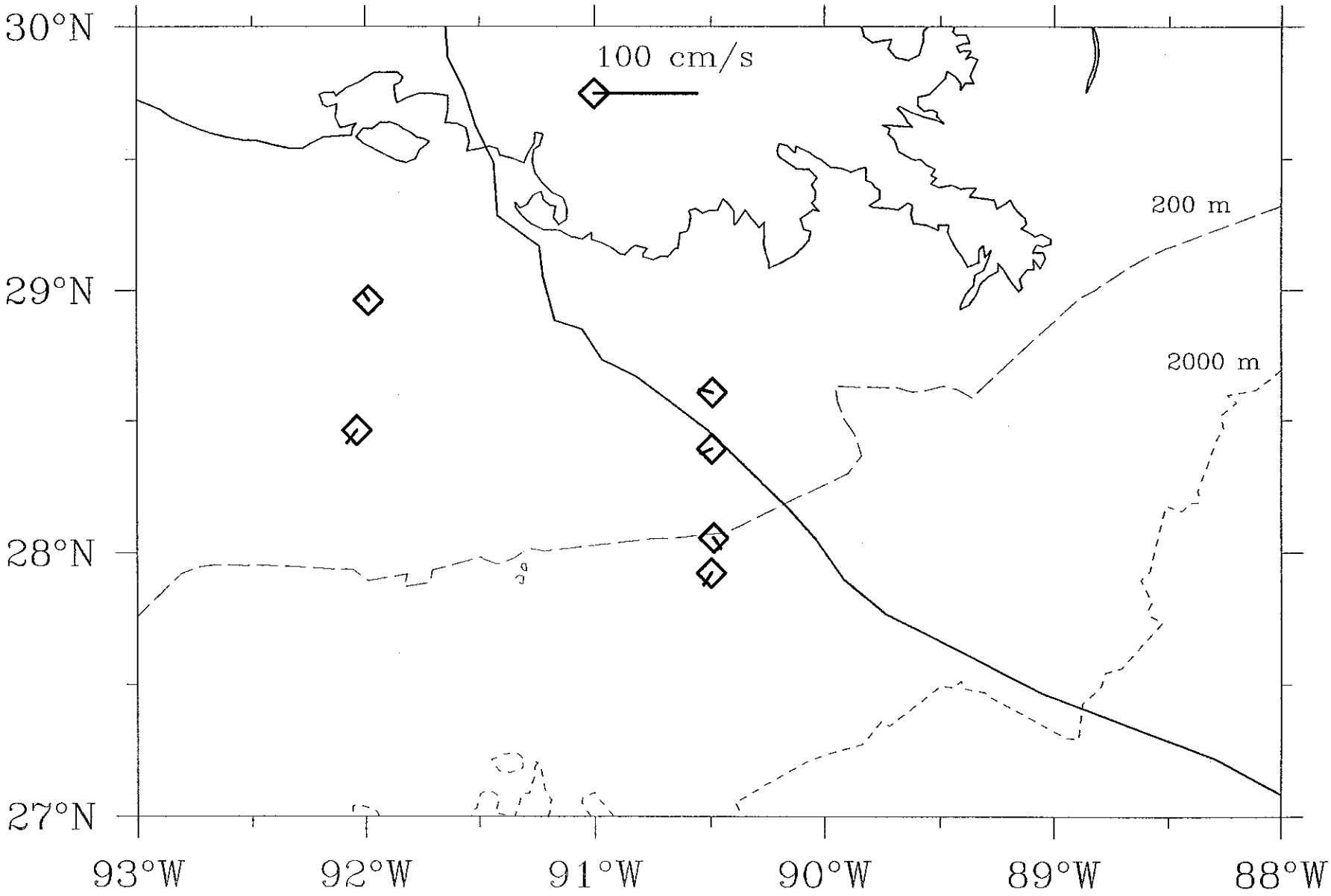

Observed Surface Currents: August-25-08:00 GMT

Frame 01

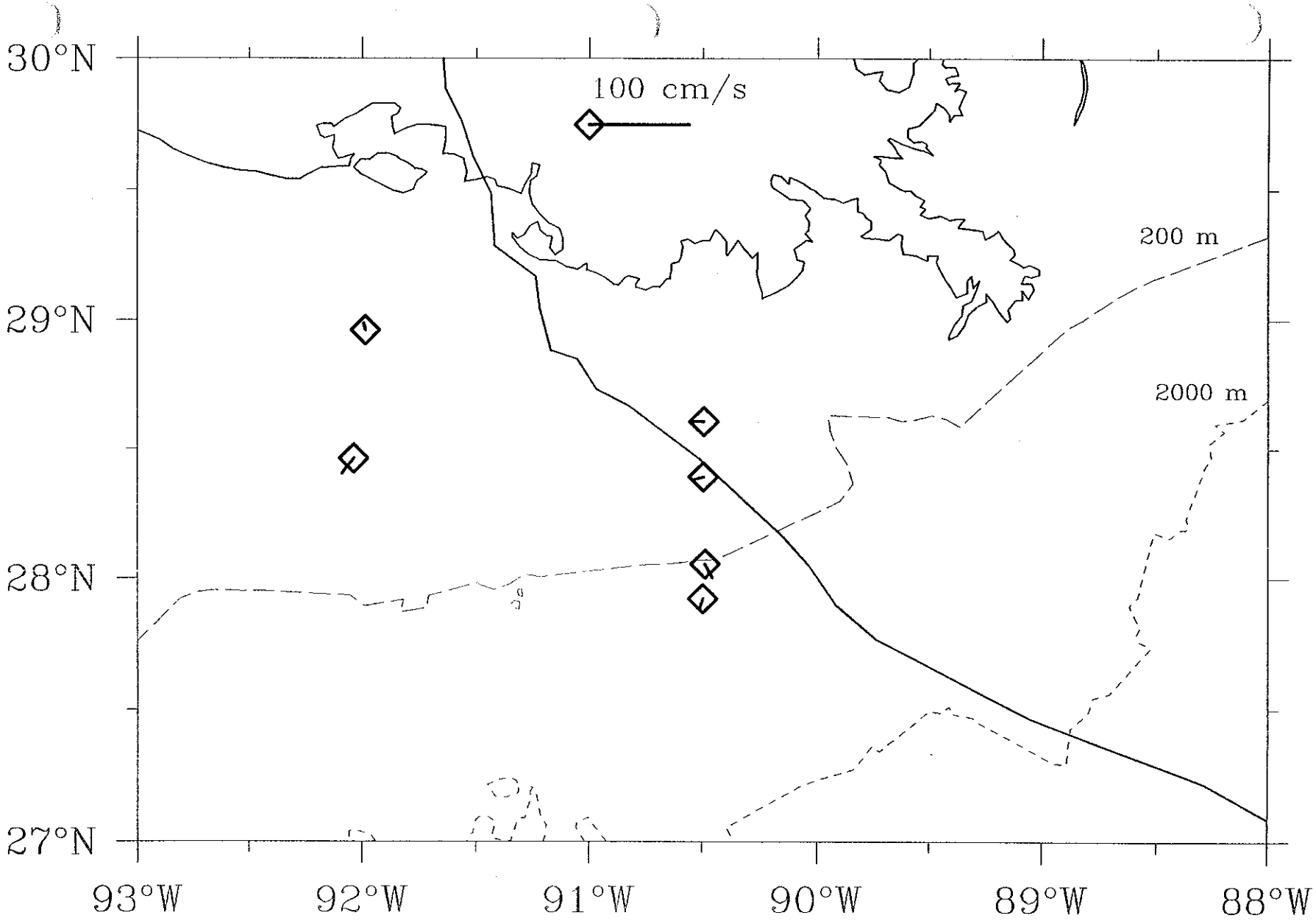

Observed Surface Currents: August-25-08:30 GMT

Frame 017

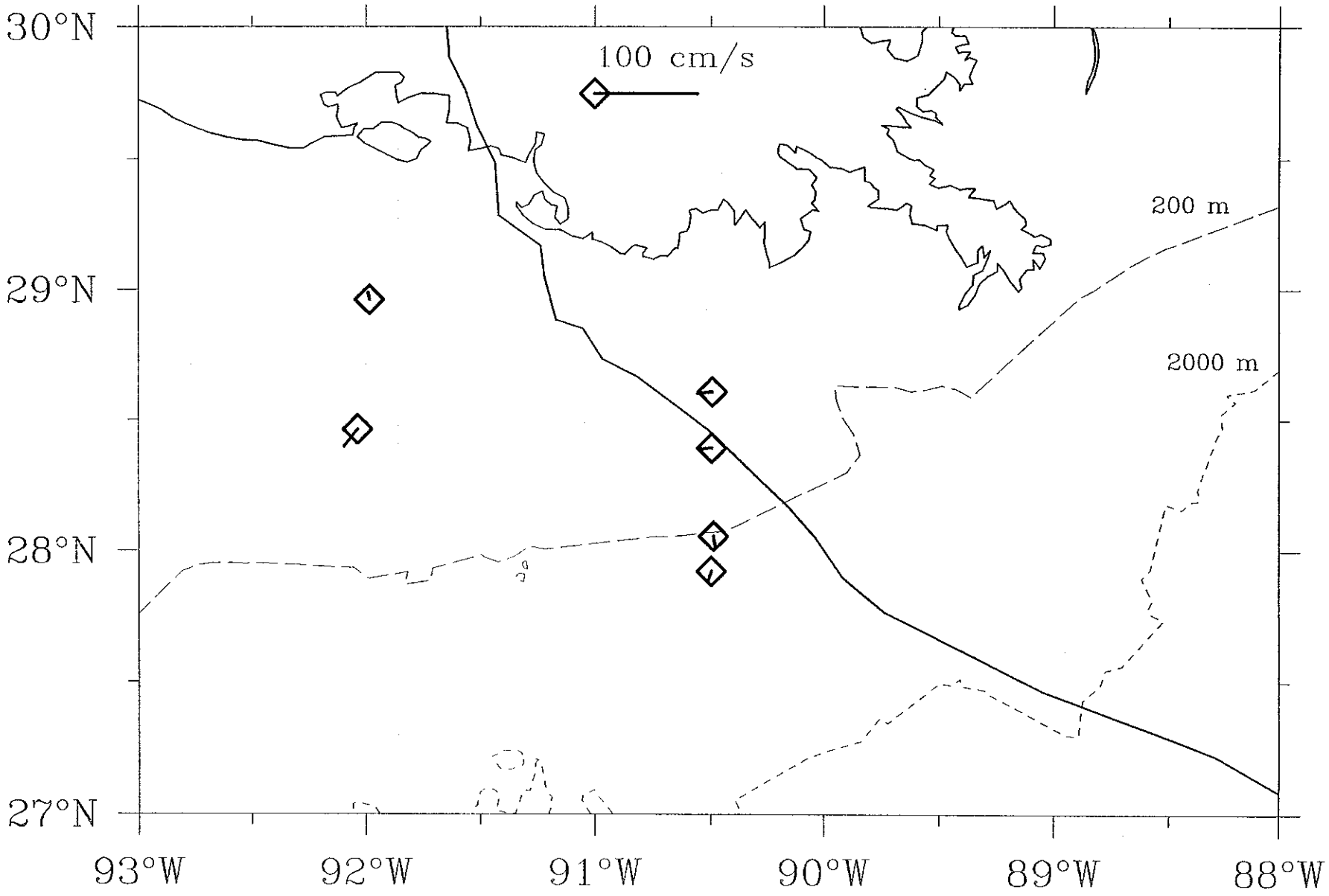

Observed Surface Currents: August–25–09:00 GMT

Frame 013

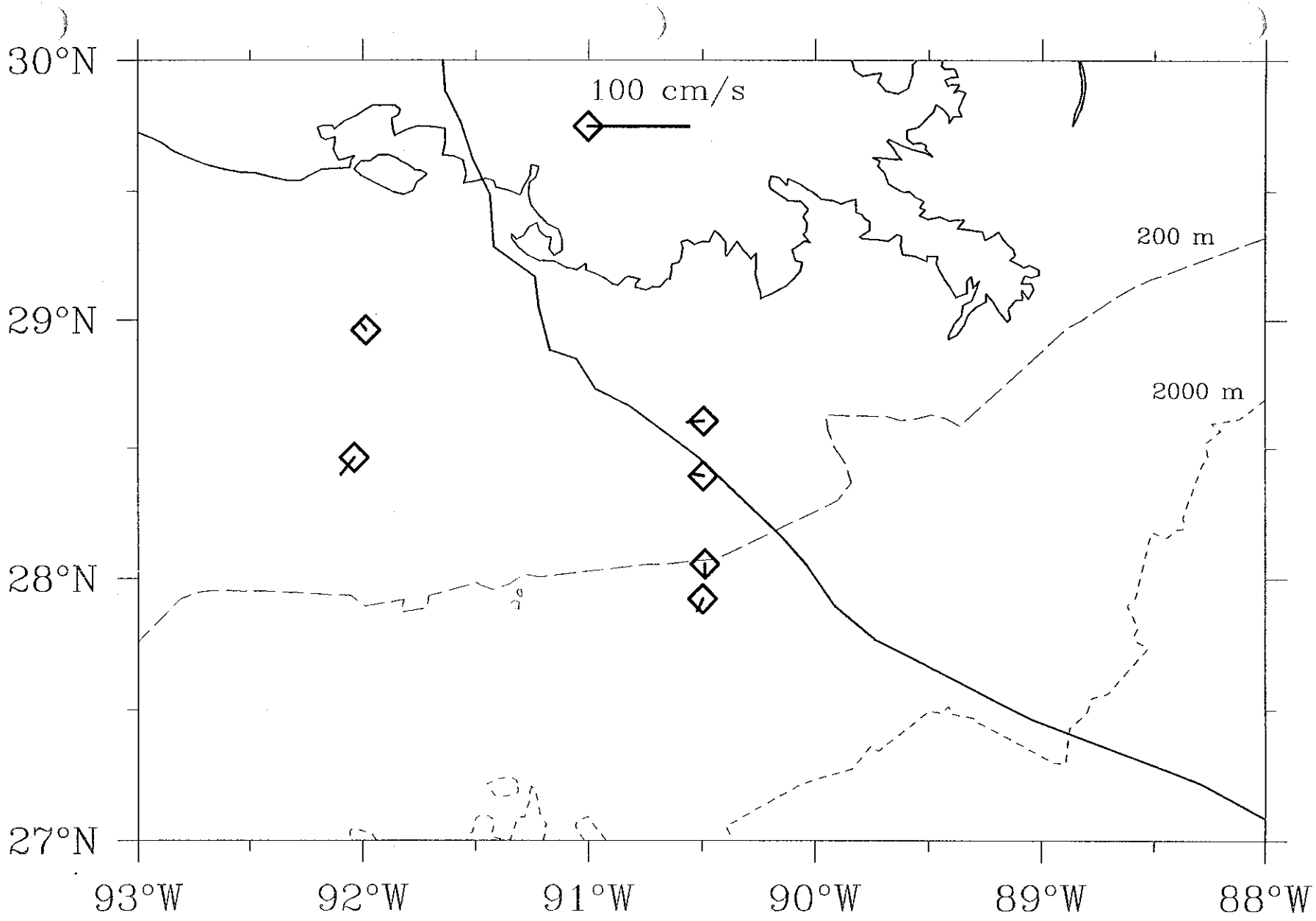

Observed Surface Currents: August-25-09:30 GMT

Frame 019

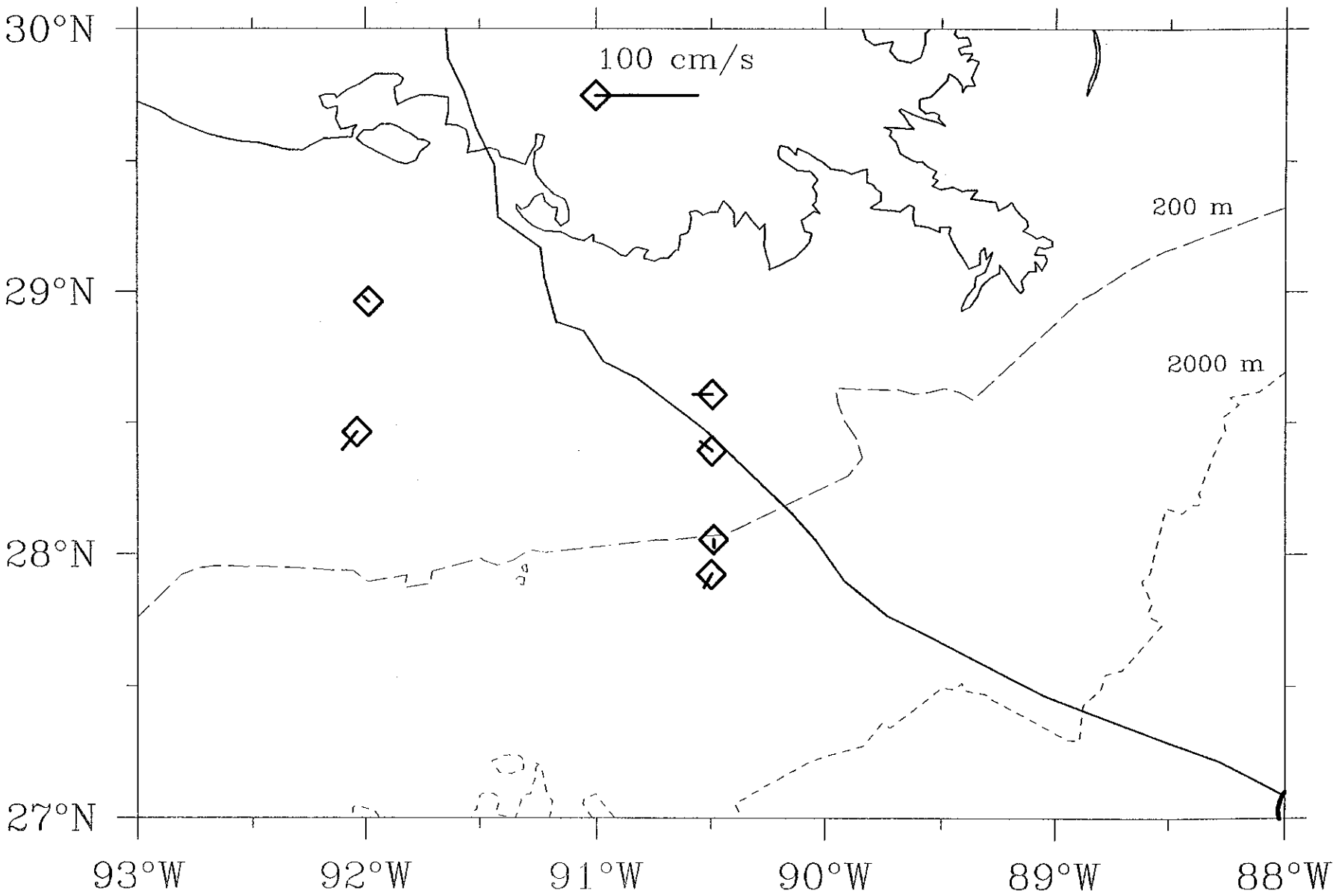

Observed Surface Currents: August-25-10:00 GMT

Frame 020

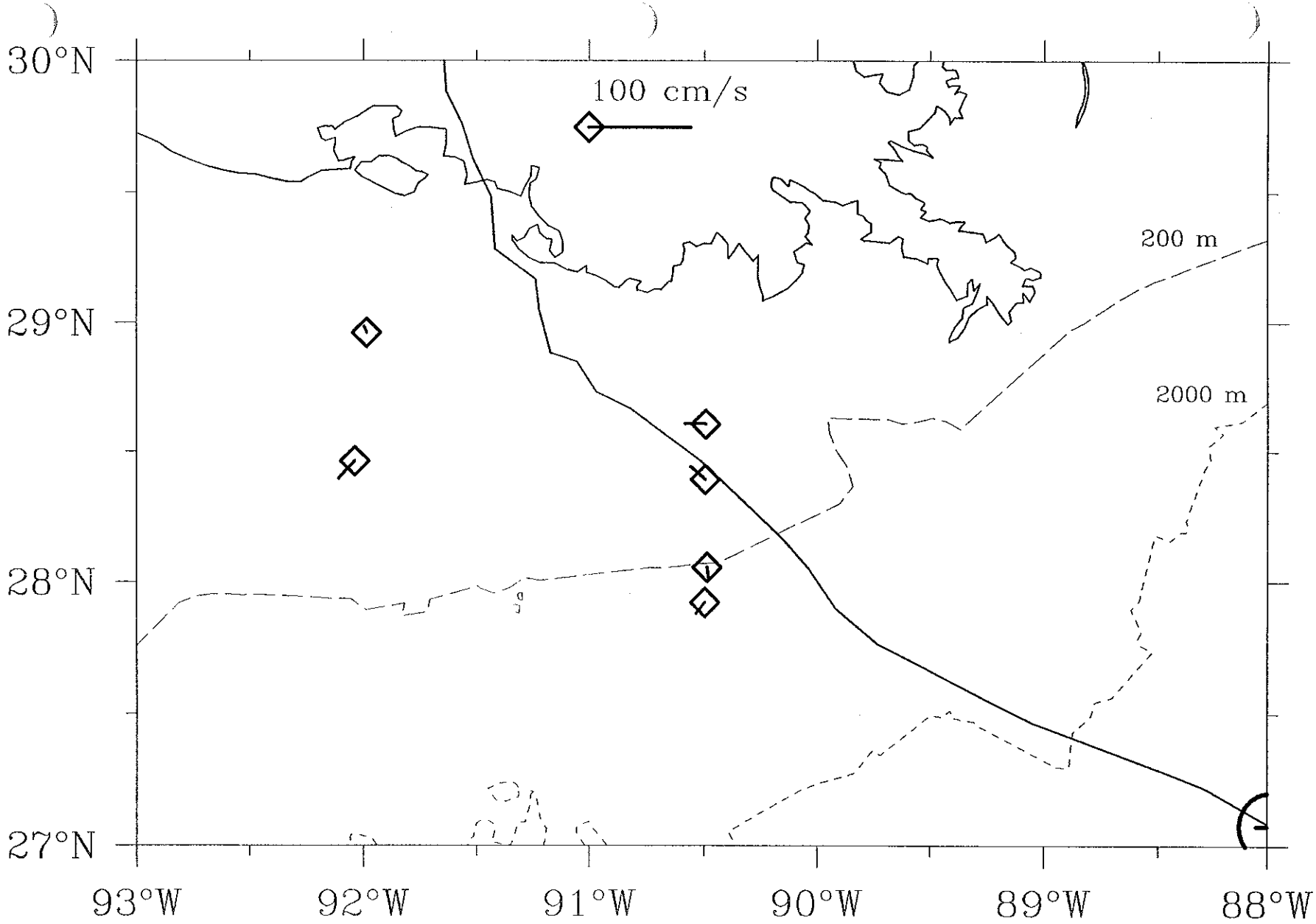

Observed Surface Currents: August-25-10:30 GMT

Frame 021

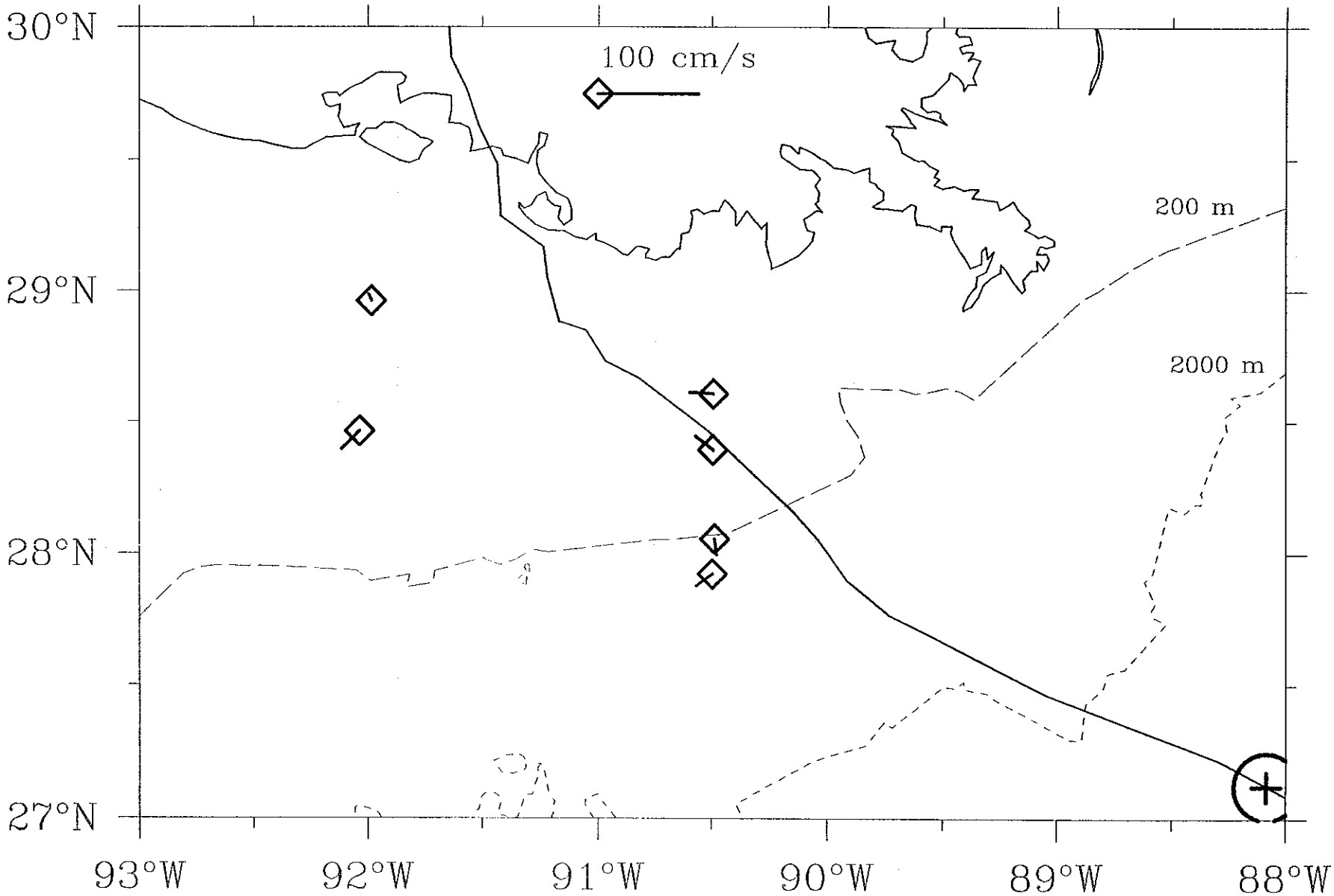

Observed Surface Currents: August-25-11:00 GMT

Frame 022

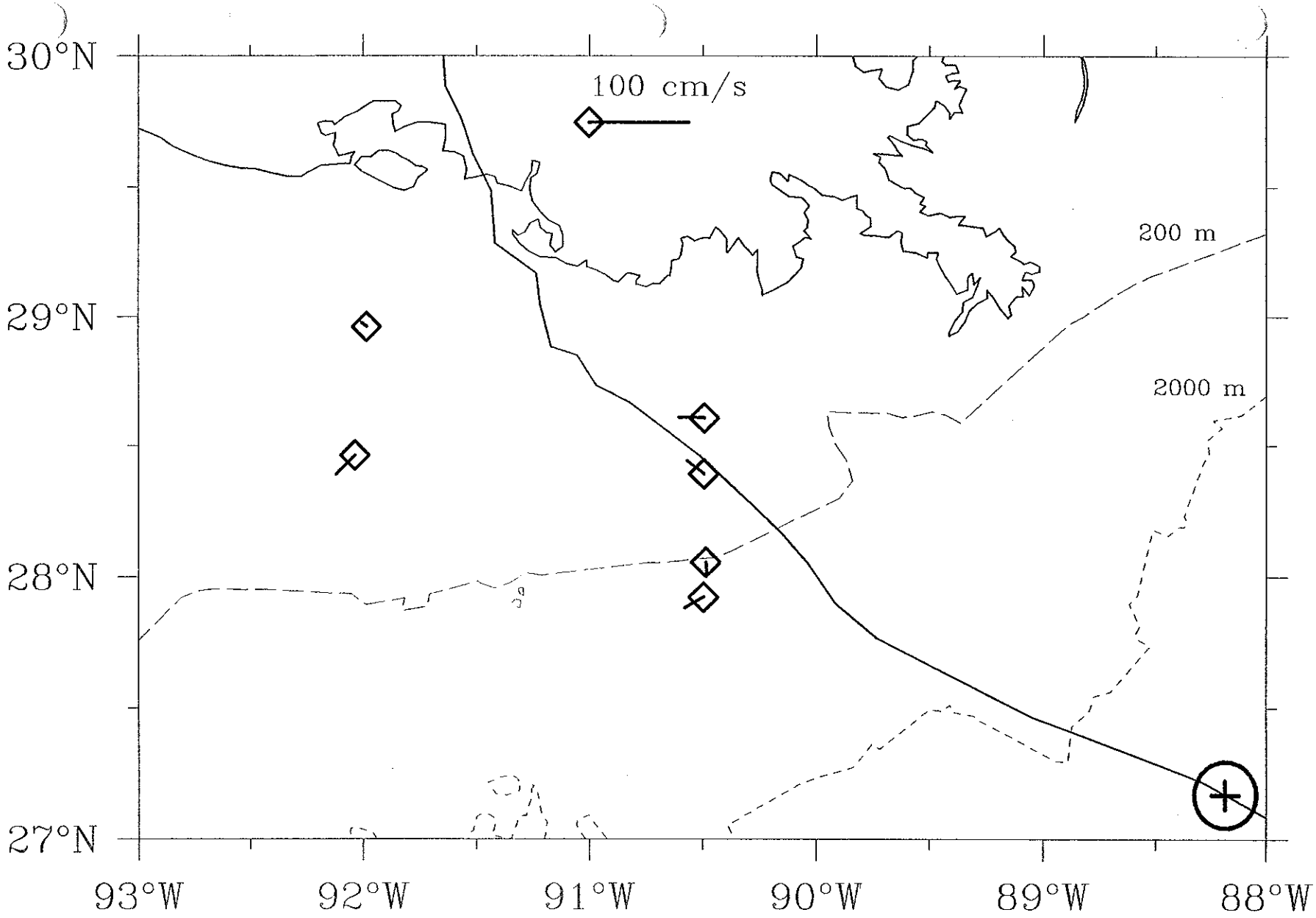

Observed Surface Currents: August-25-11:30 GMT

Frame 023

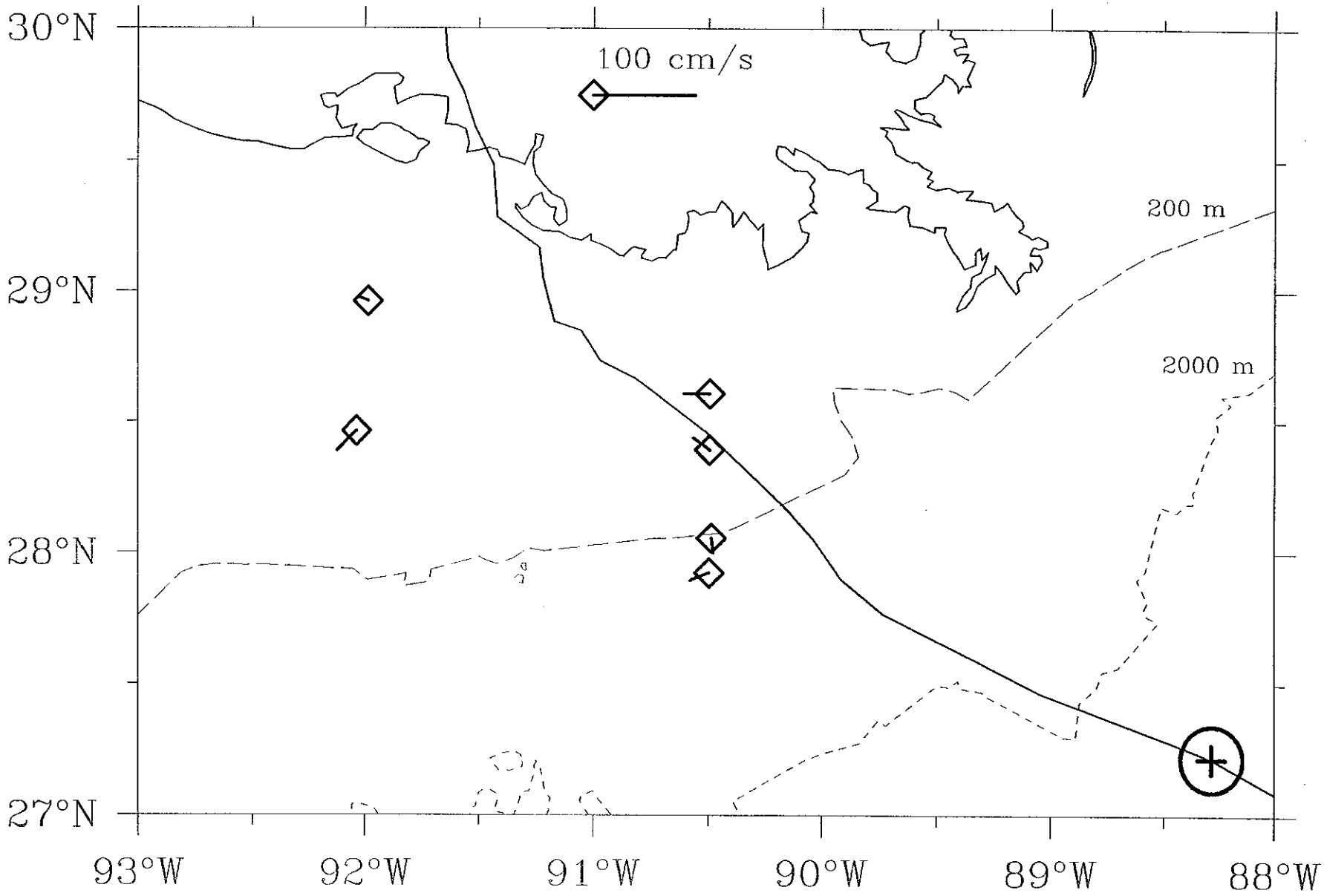

Observed Surface Currents: August-25-12:00 GMT

Frame 021

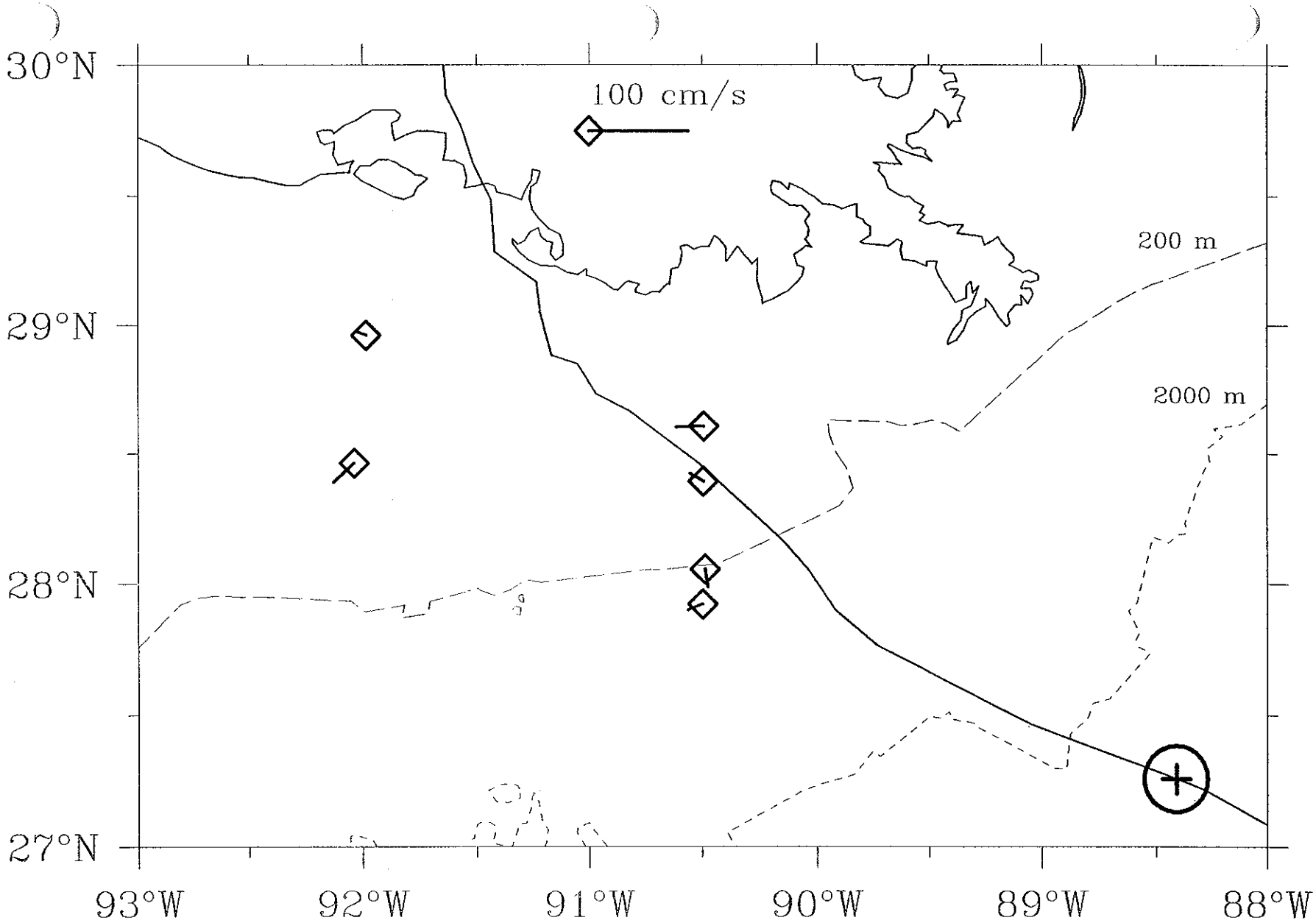

Observed Surface Currents: August-25-12:30 GMT

Frame 025

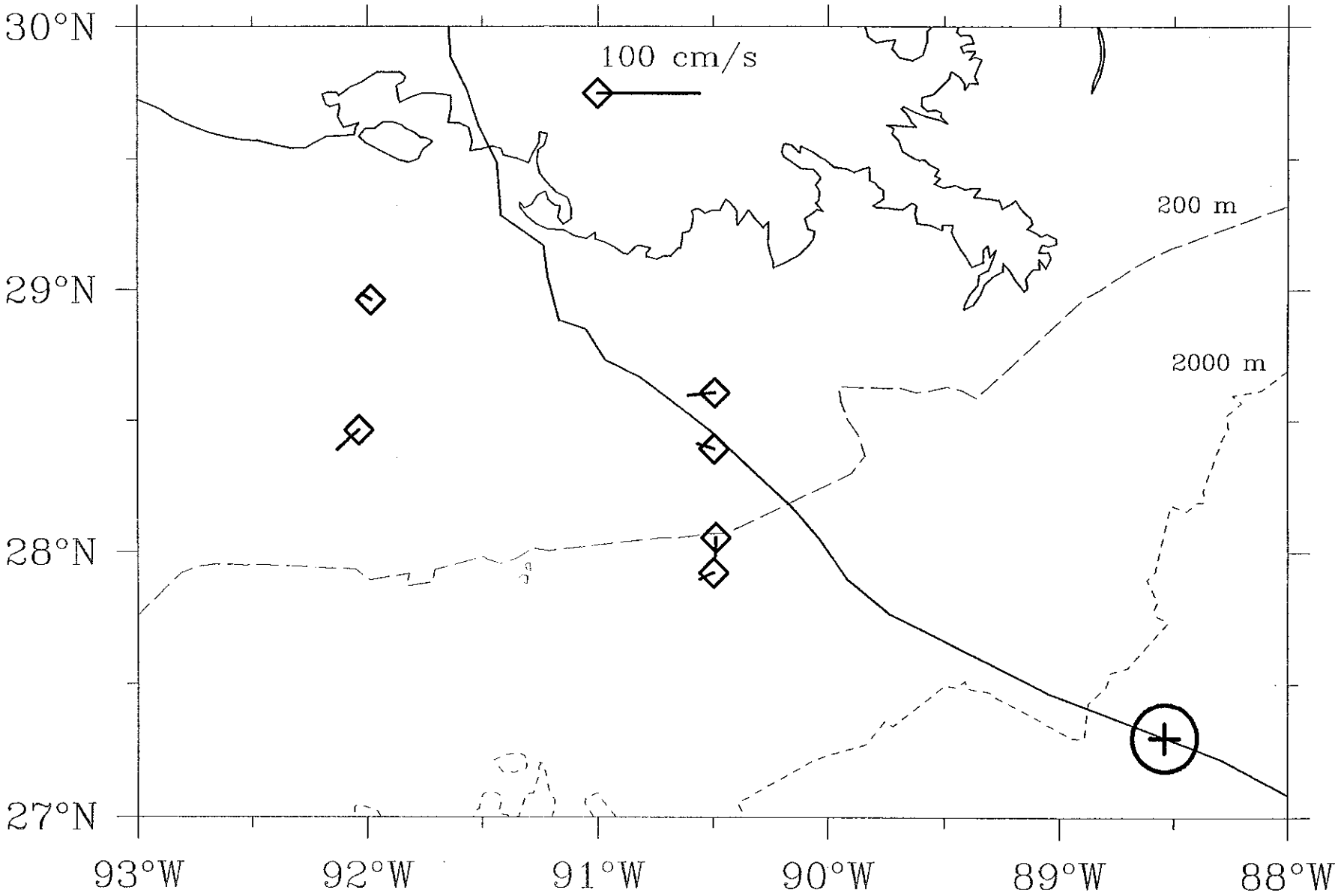

Observed Surface Currents: August-25-13:00 GMT

Frame 026

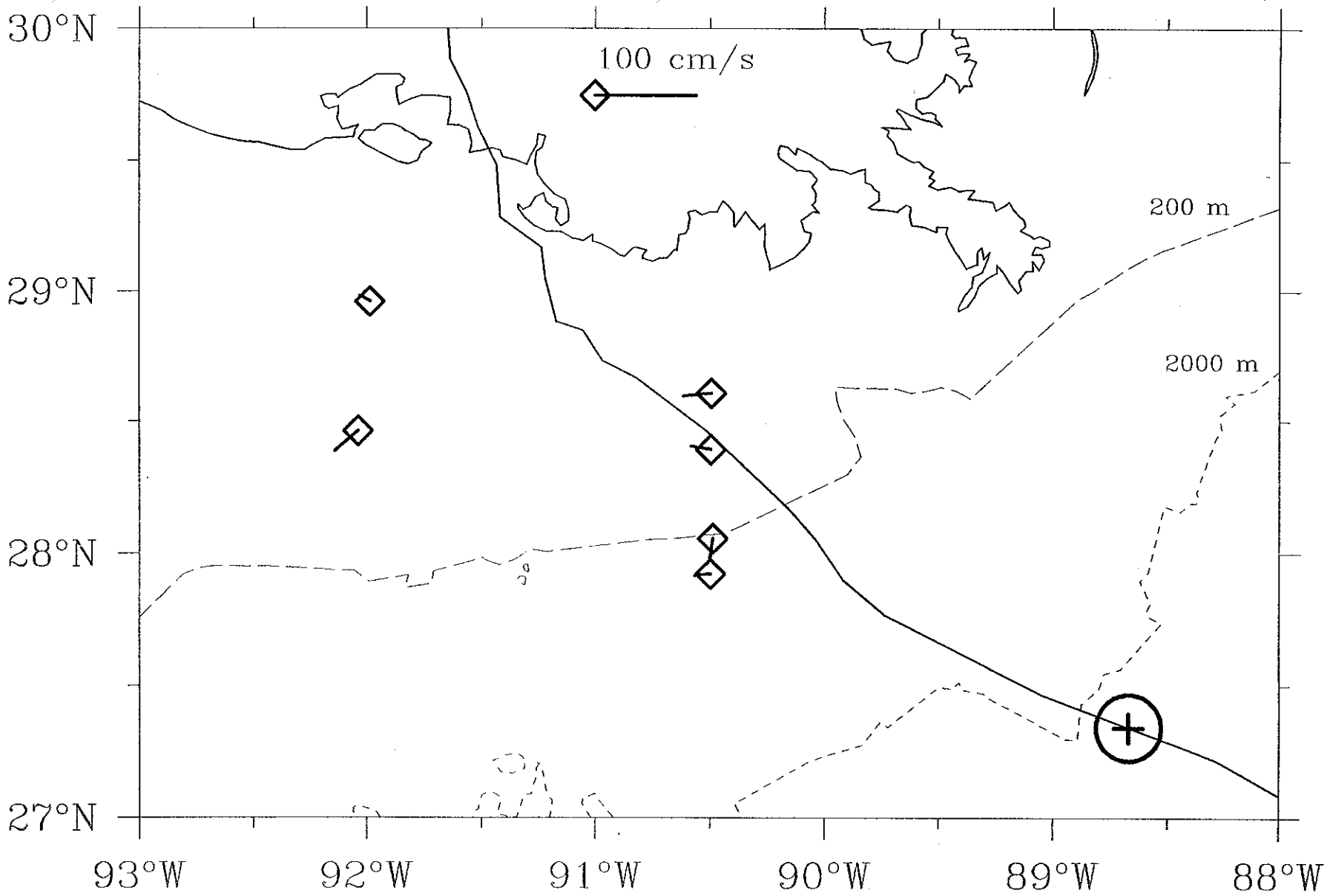

Observed Surface Currents: August-25-13:30 GMT

Frame 027

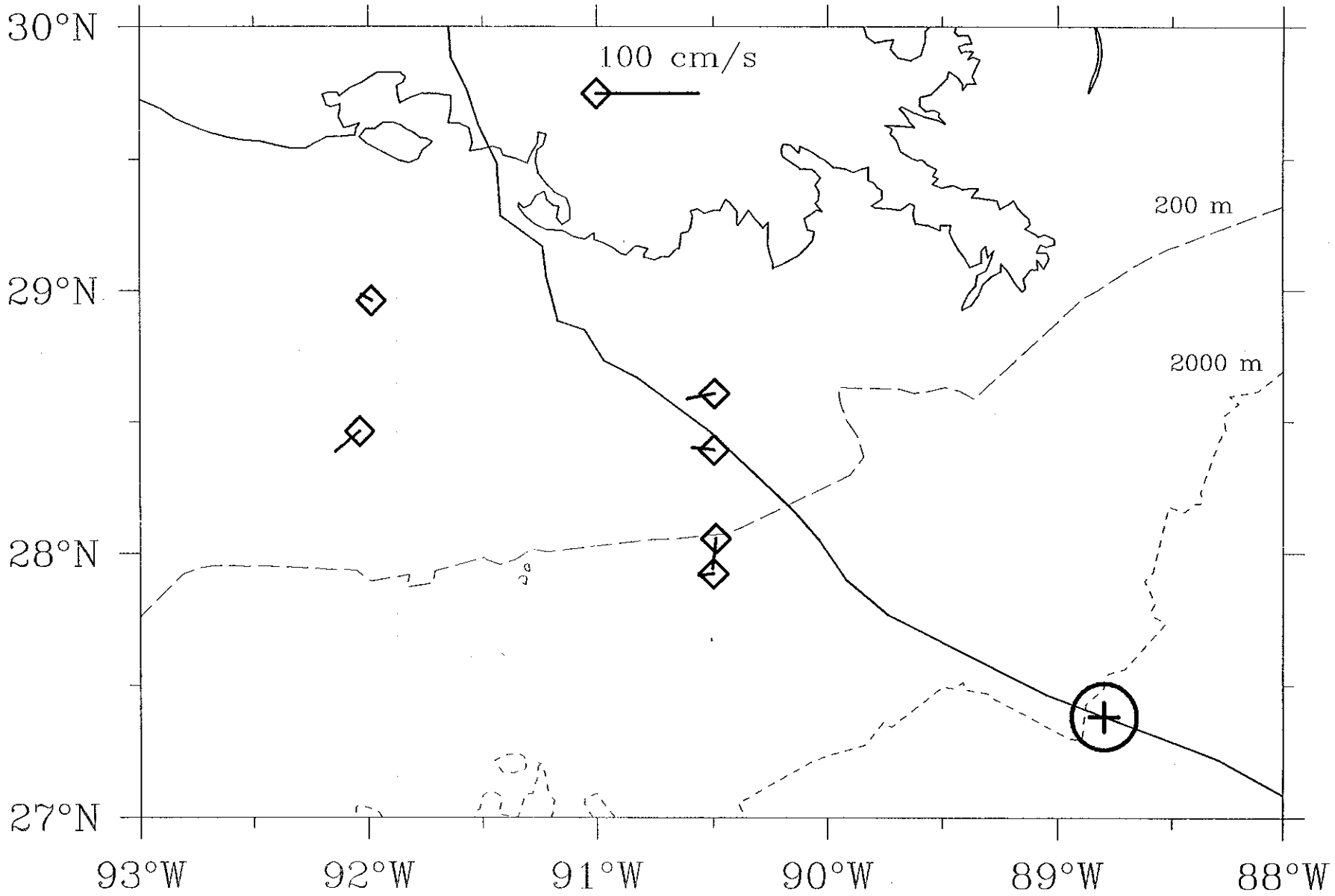

Observed Surface Currents: August-25-14:00 GMT

Frame 028

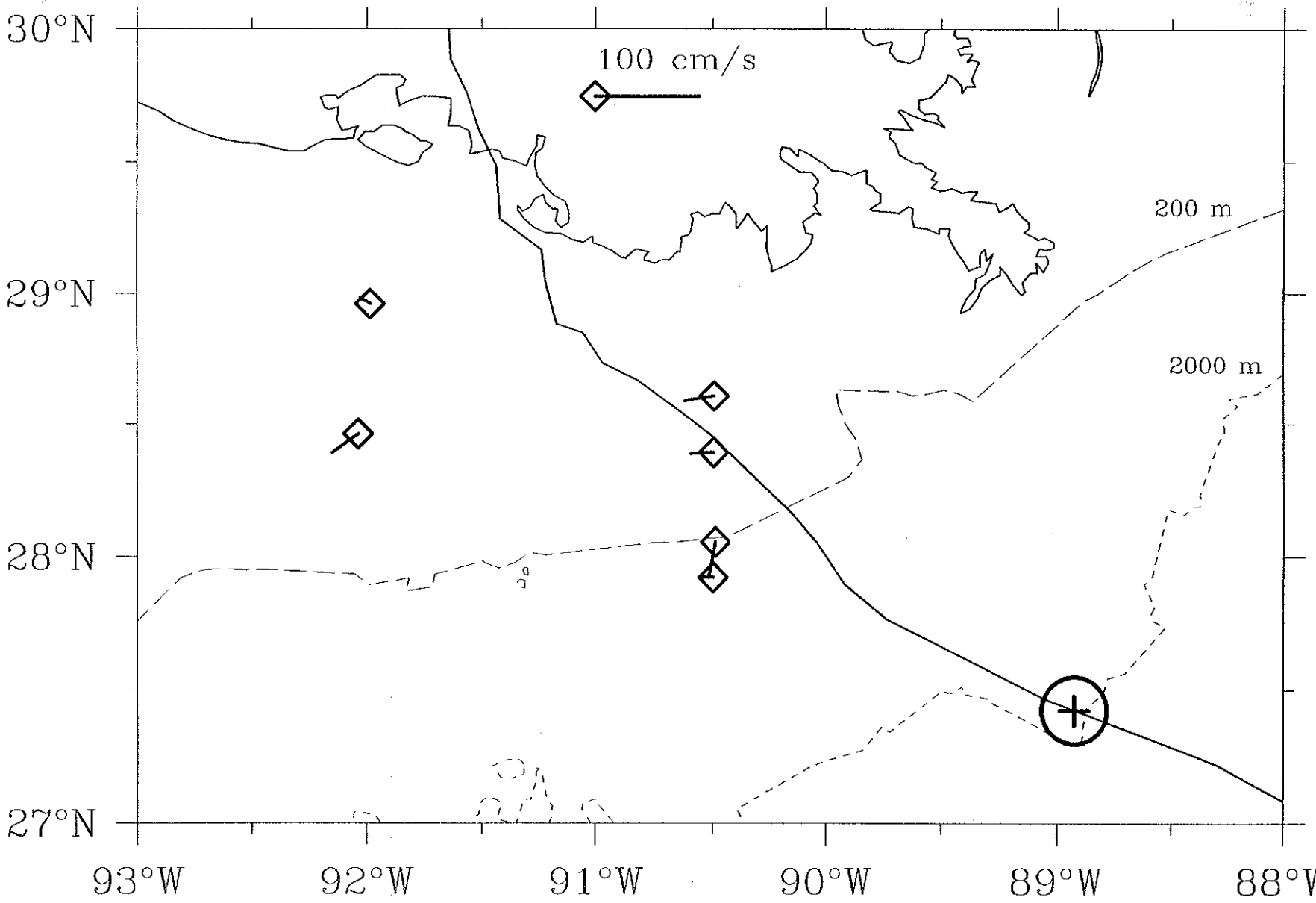

Observed Surface Currents: August-25-14:30 GMT

Frame 029

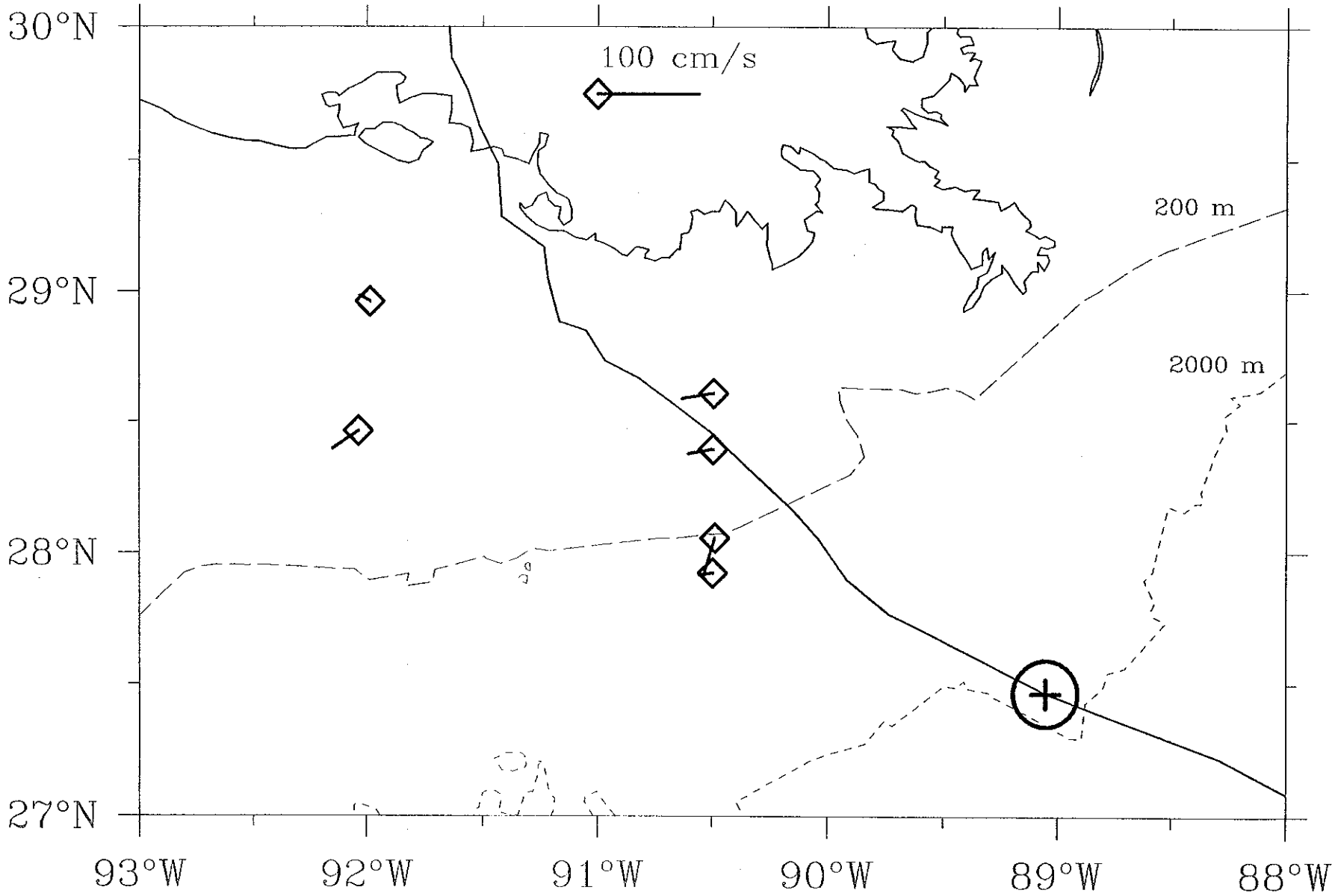

Observed Surface Currents: August-25-15:00 GMT

Frame 030

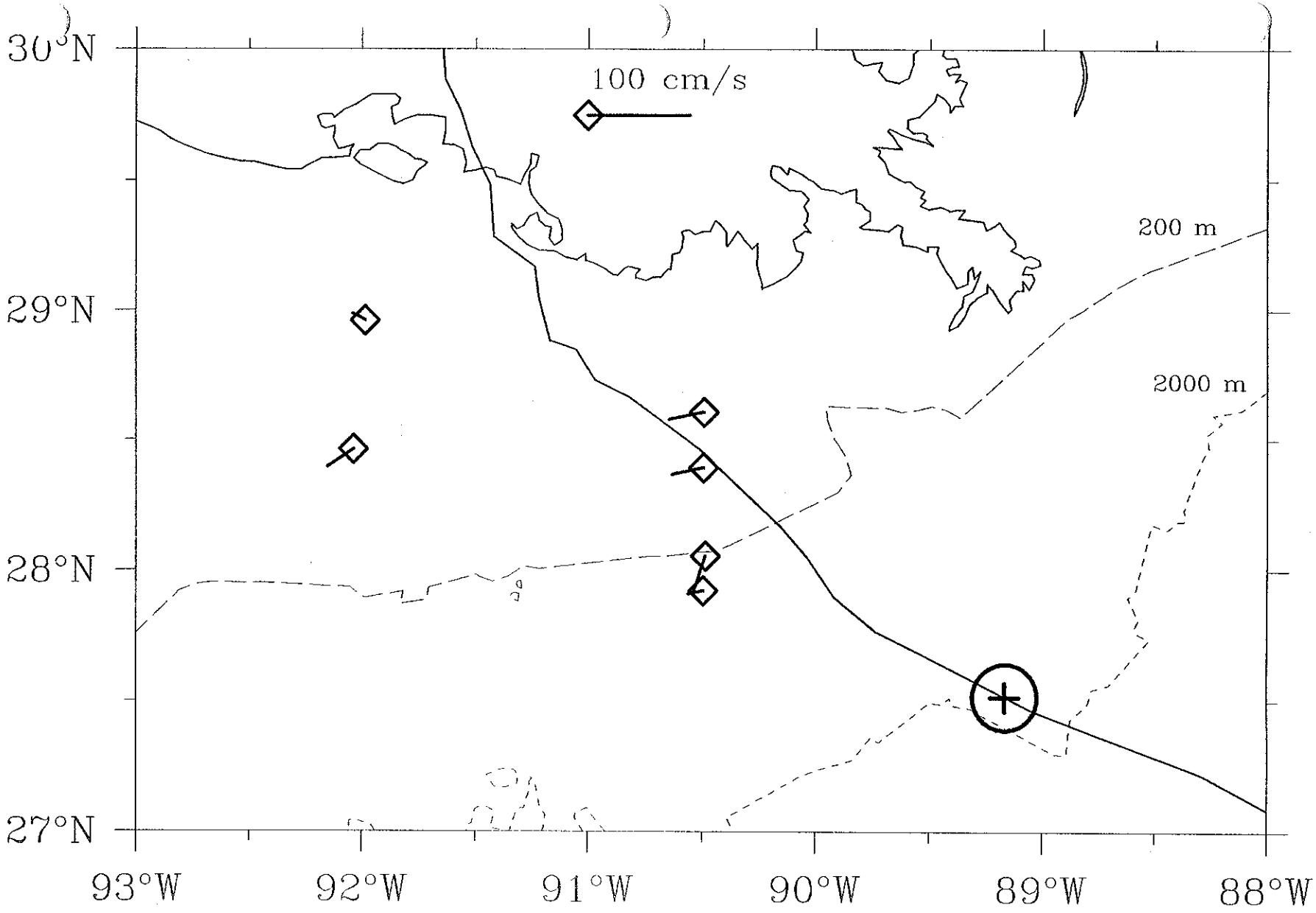

Observed Surface Currents: August-25-15:30 GMT

Frame 031

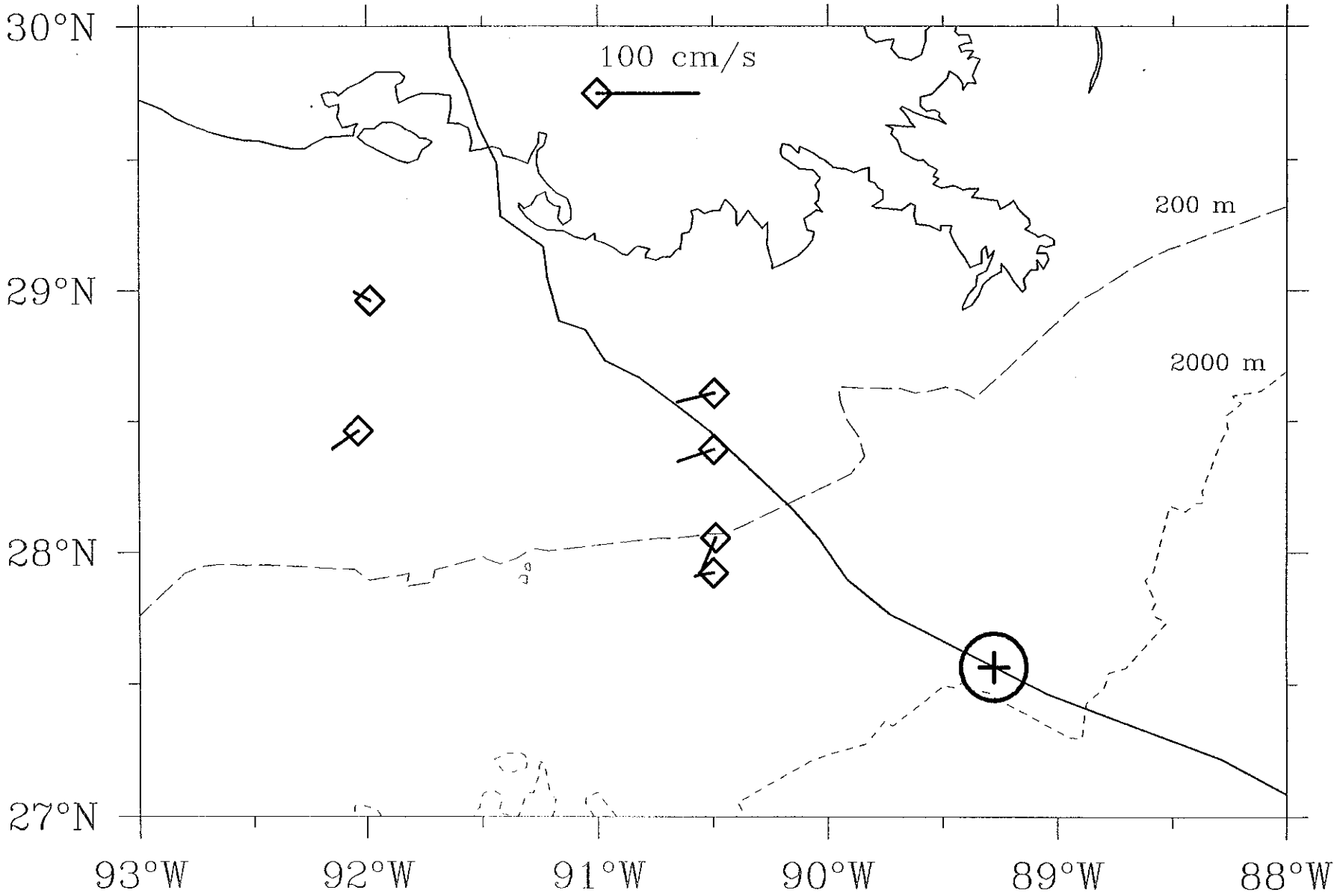

Observed Surface Currents: August–25–16:00 GMT

Frame 032

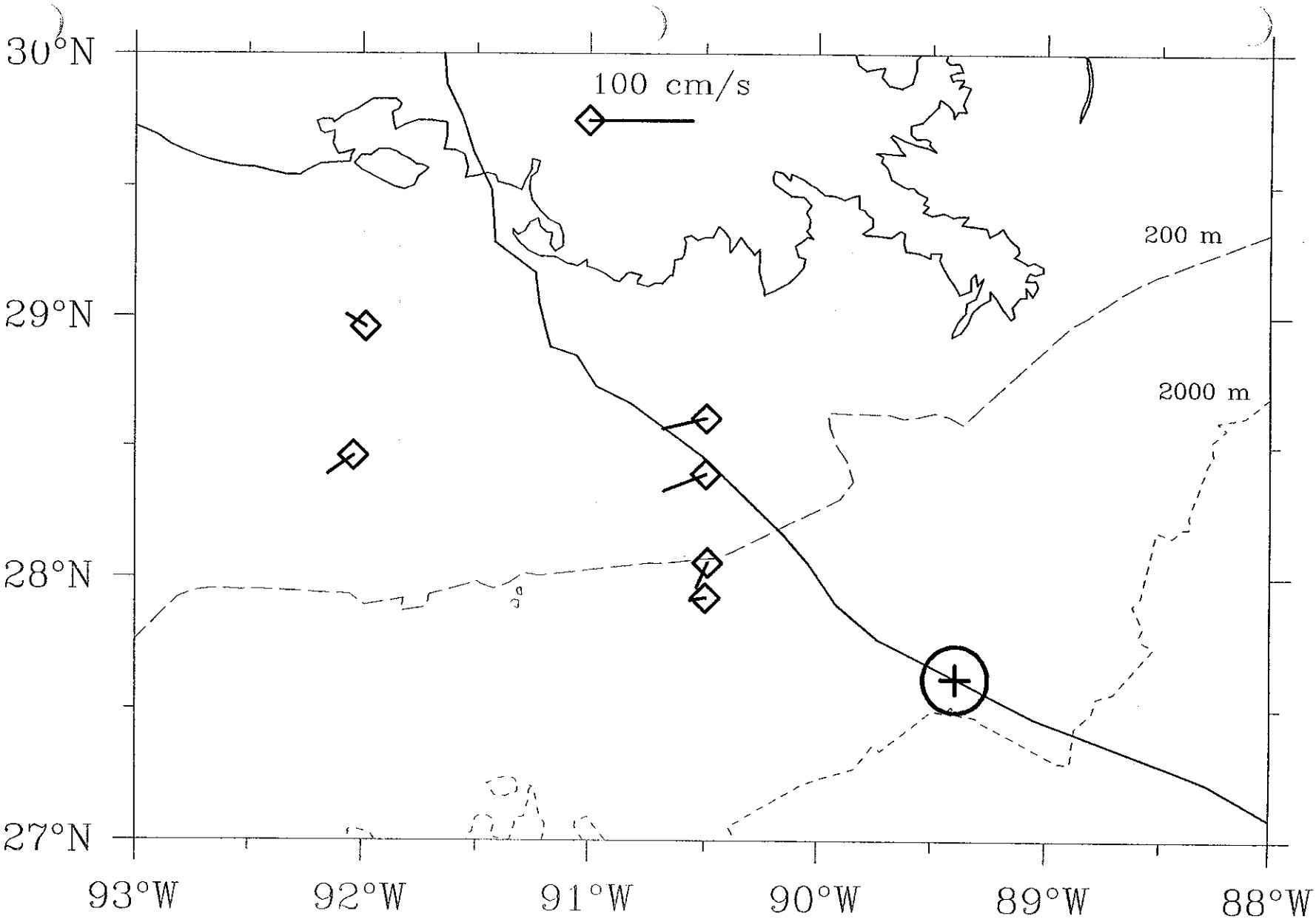

Observed Surface Currents: August-25-16:30 GMT

Frame 033

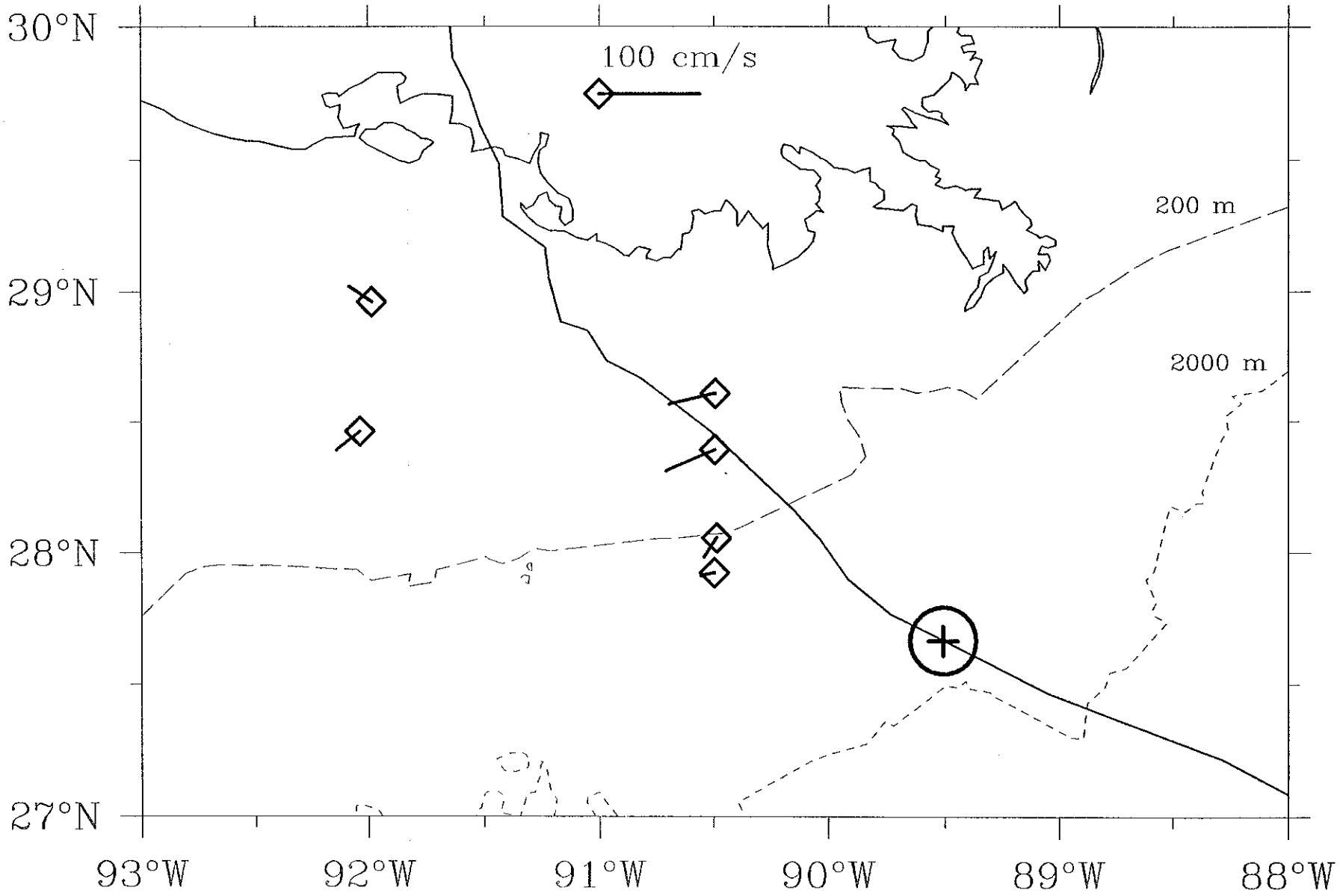

Observed Surface Currents: August-25-17:00 GMT

Frame 0?1

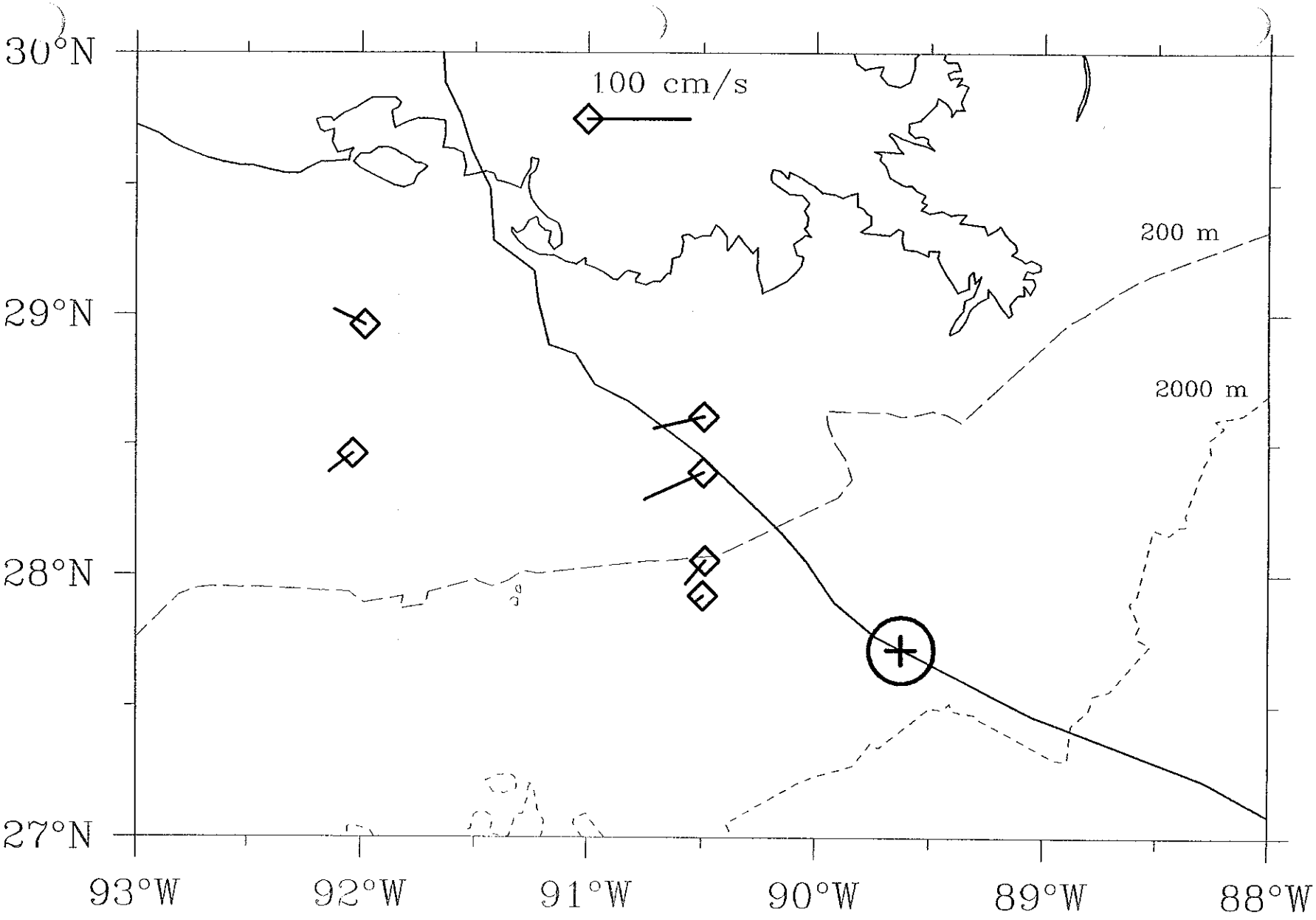

Observed Surface Currents: August–25–17:30 GMT

Frame 035

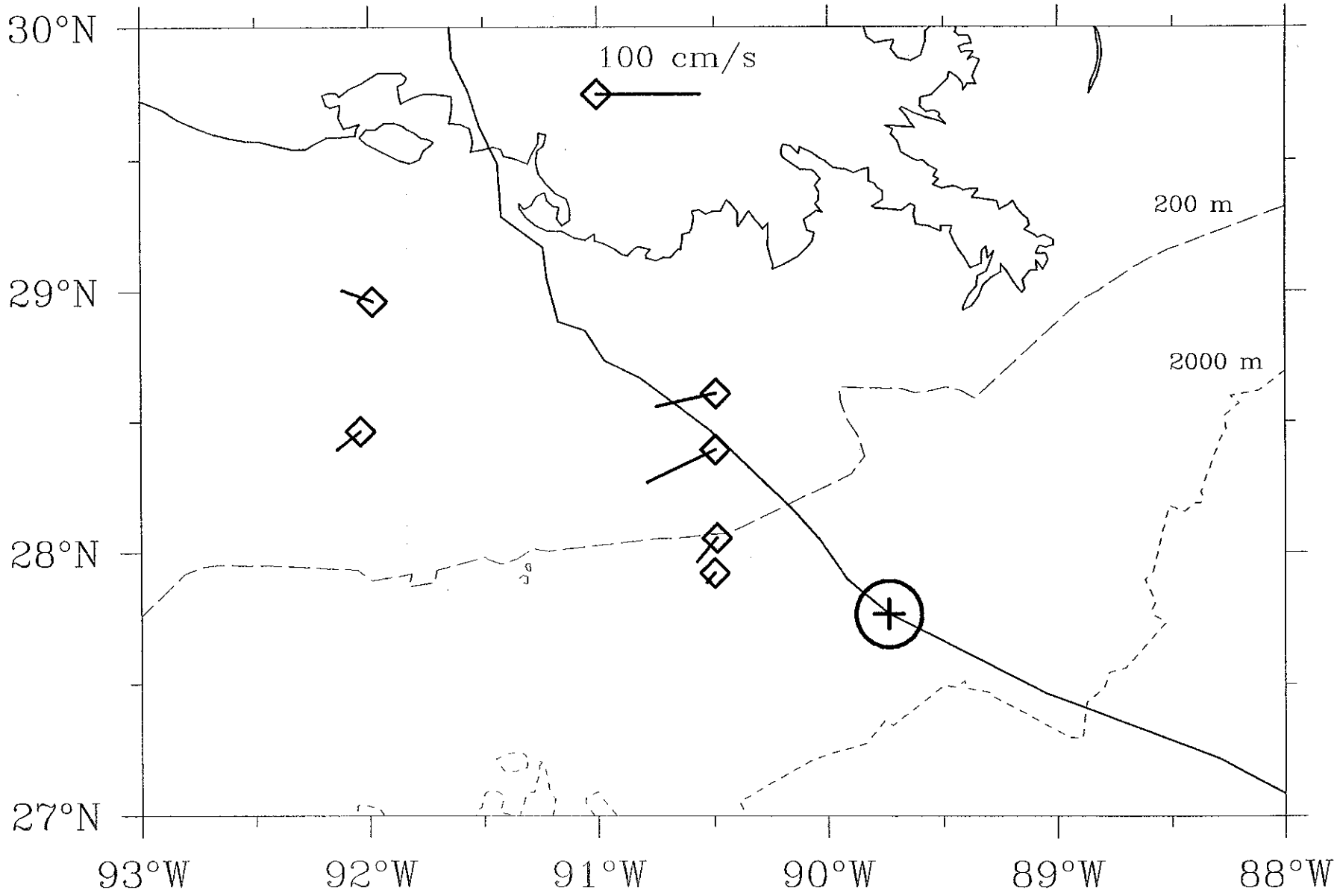

Observed Surface Currents: August-25-18:00 GMT

Frame 0??

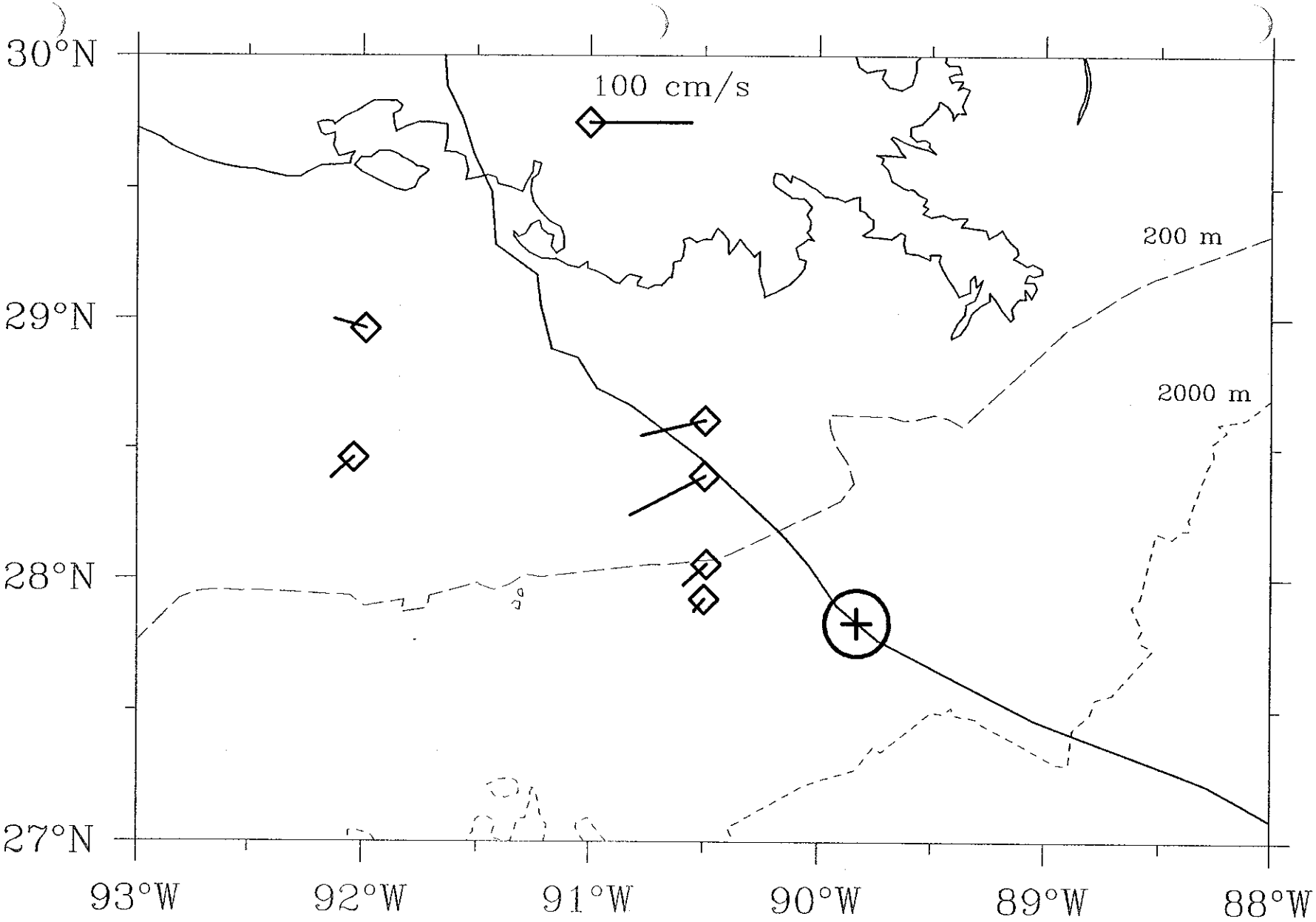

Observed Surface Currents: August-25-18:30 GMT

Frame 037

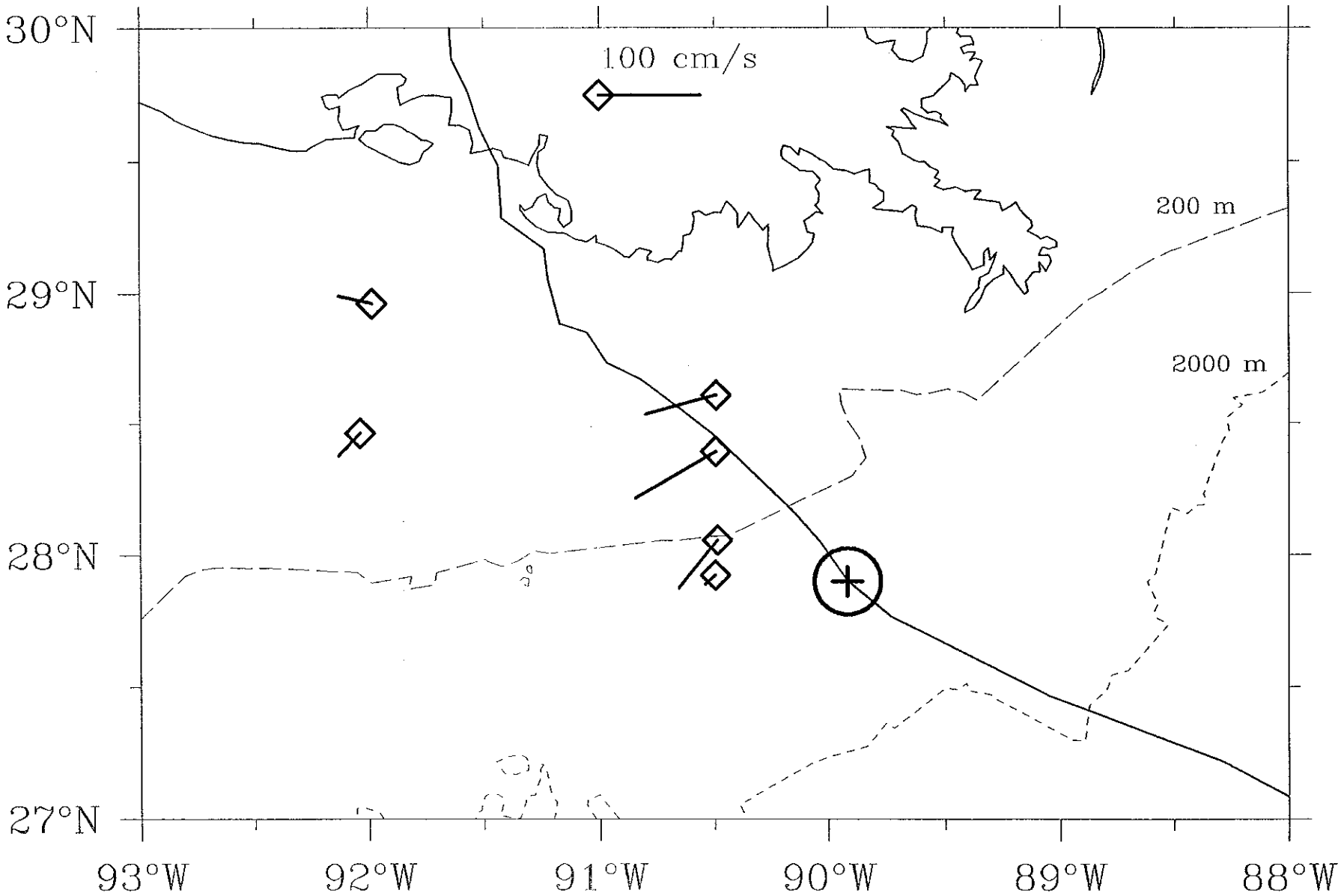

Observed Surface Currents: August-25-19:00 GMT

Frame 028

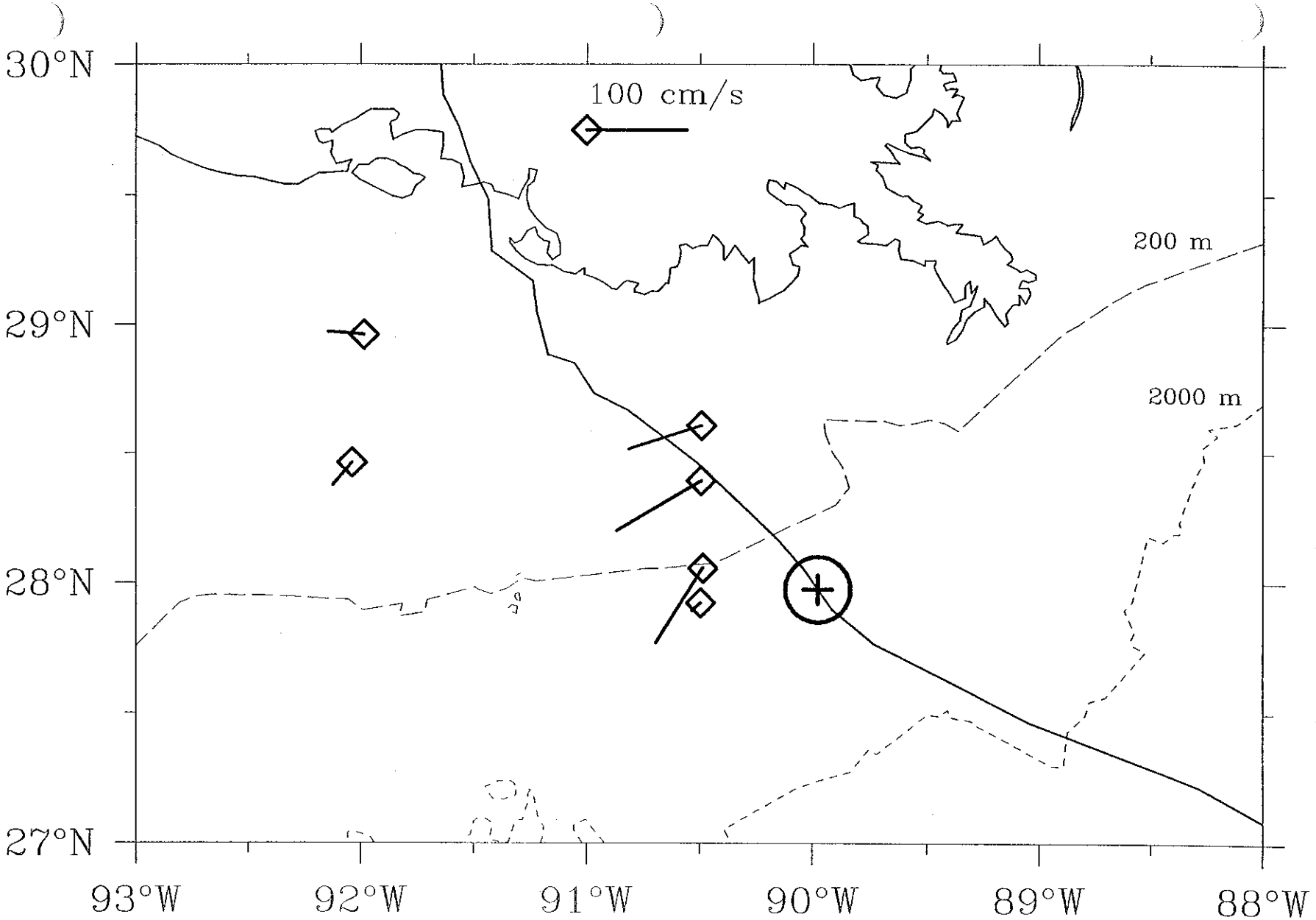

Observed Surface Currents: August-25-19:30 GMT

Frame 039

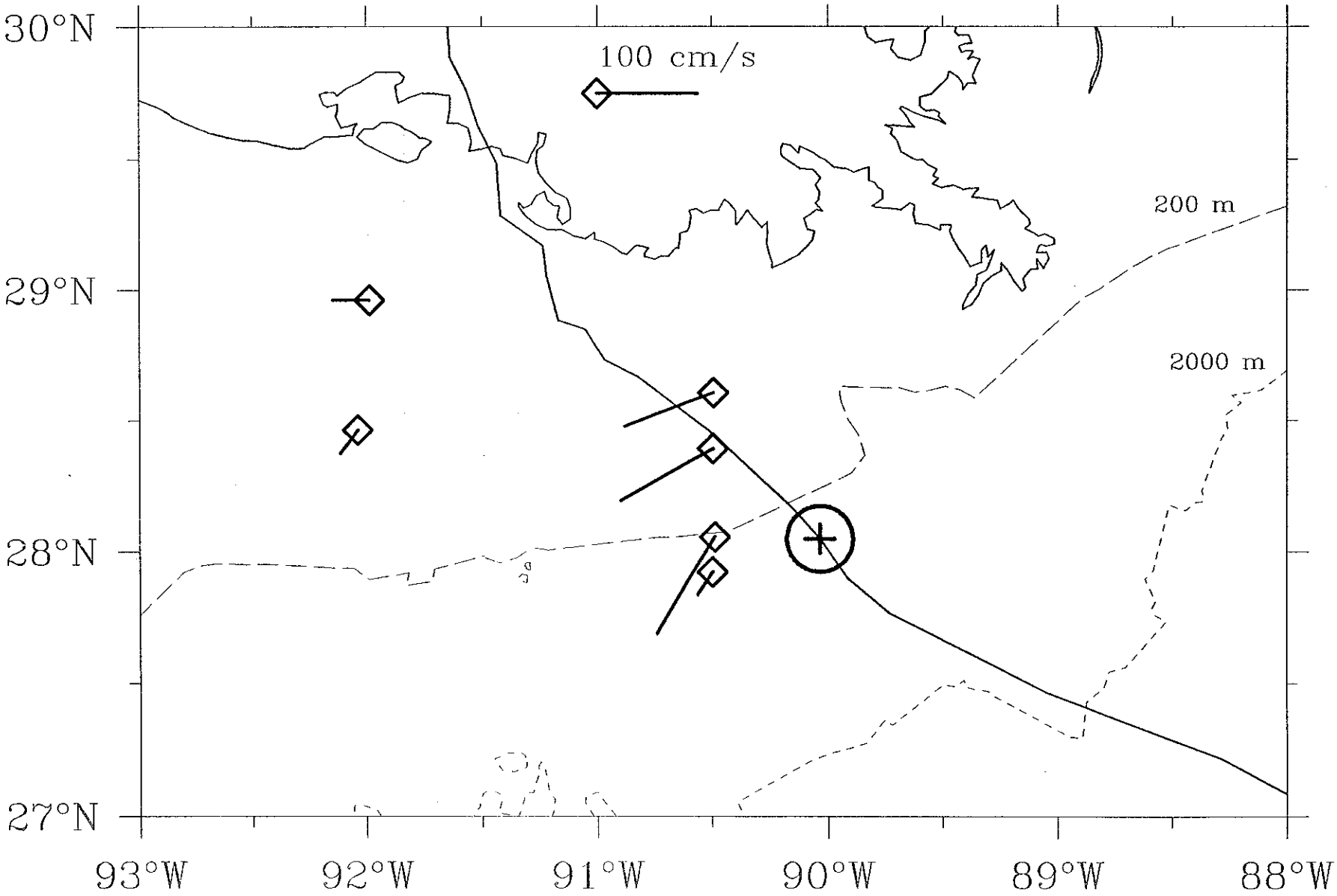

Observed Surface Currents: August-25-20:00 GMT

Frame 040

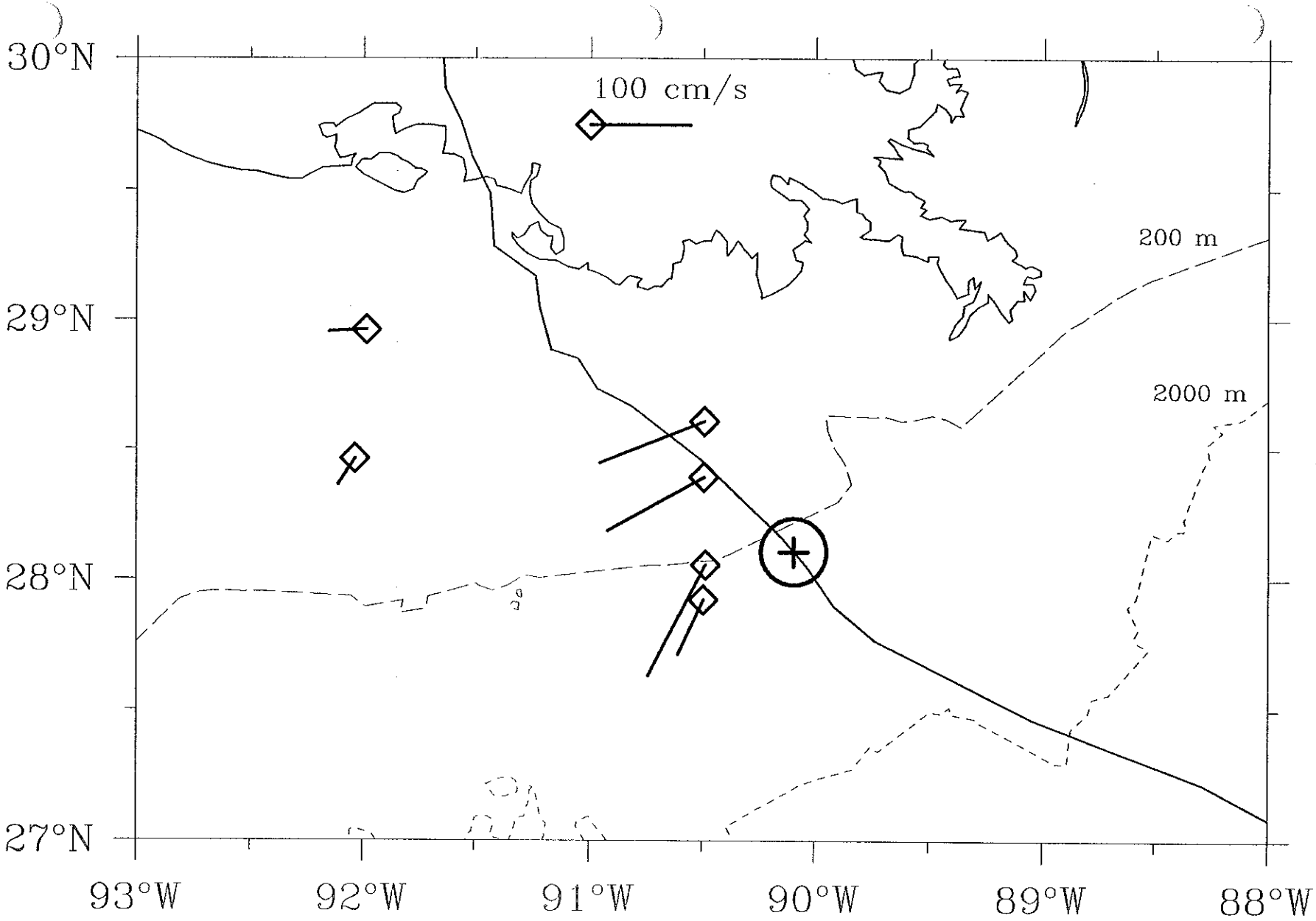

Observed Surface Currents: August-25-20:30 GMT

Frame 041

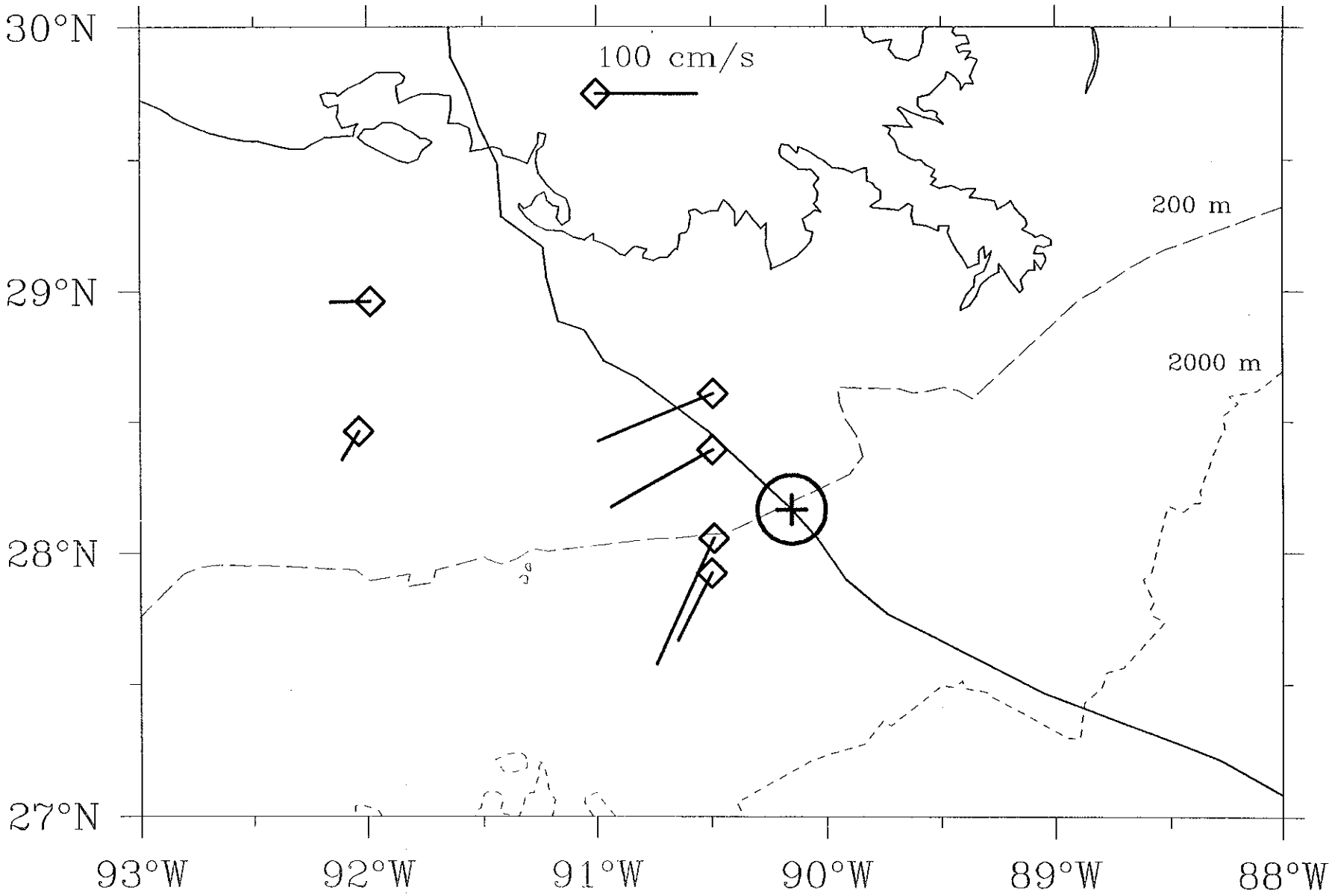

Observed Surface Currents: August-25-21:00 GMT

Frame 043

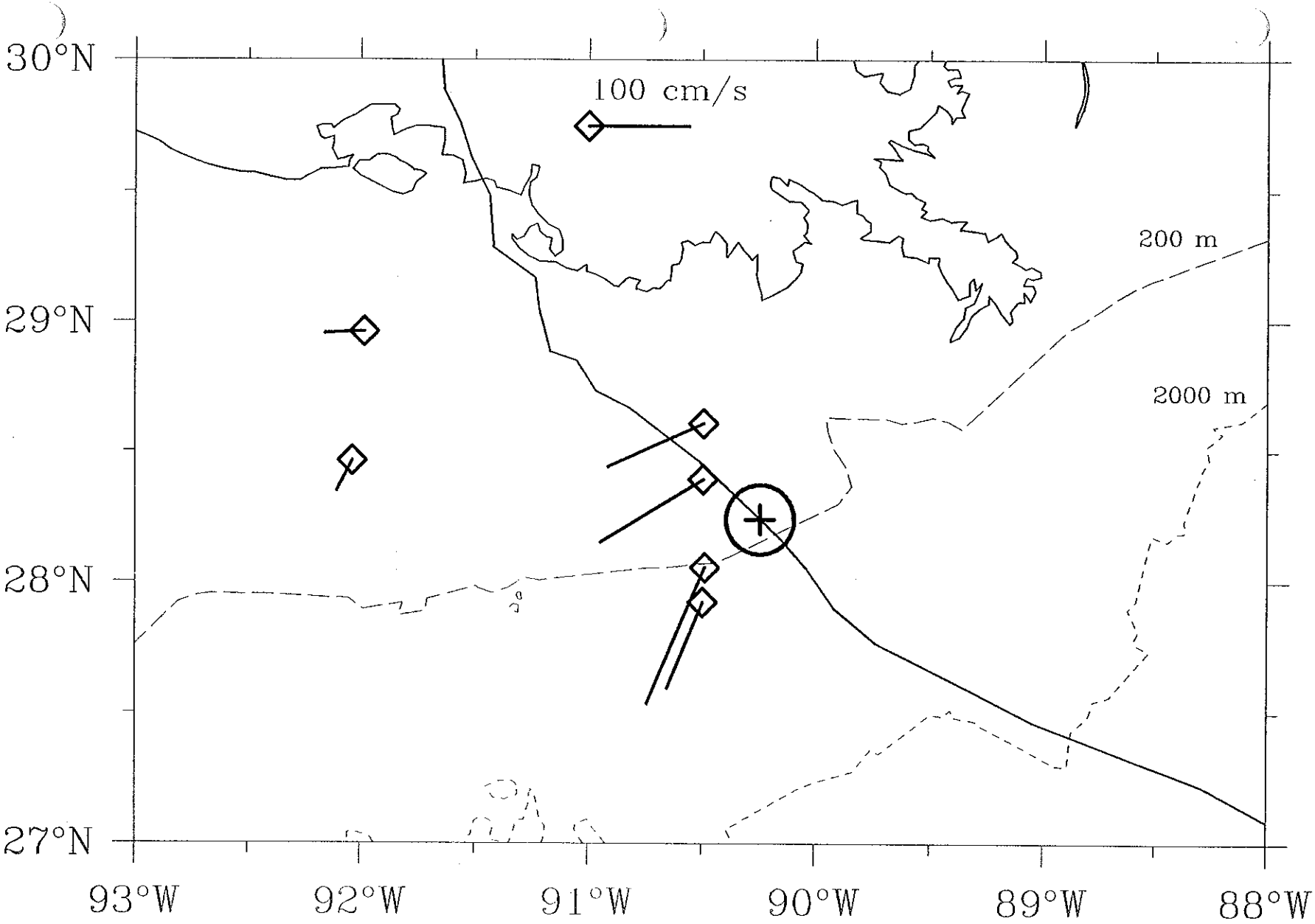

Observed Surface Currents: August-25-21:30 GMT

Frame 043

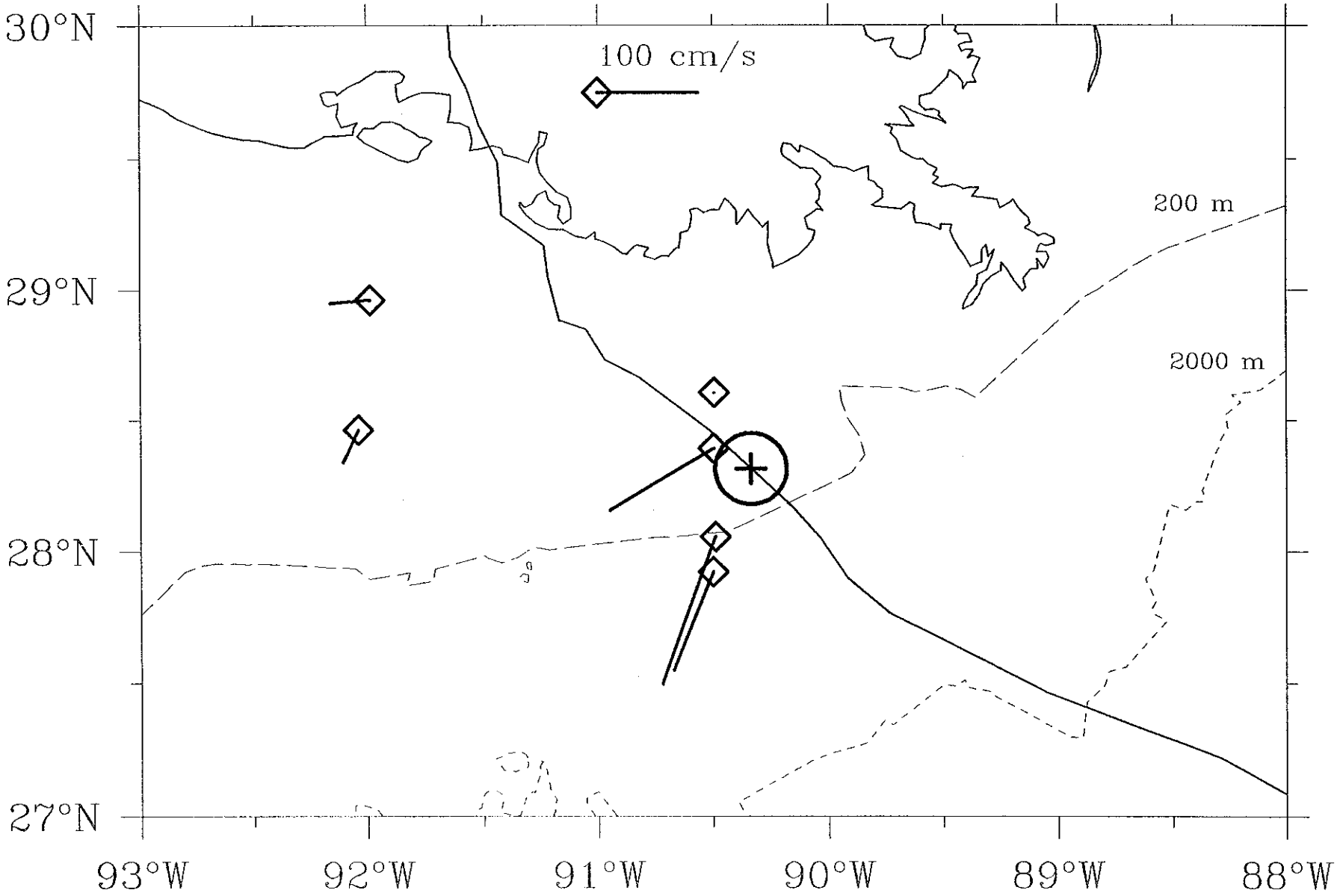

Observed Surface Currents: August-25-22:00 GMT

Frame 044

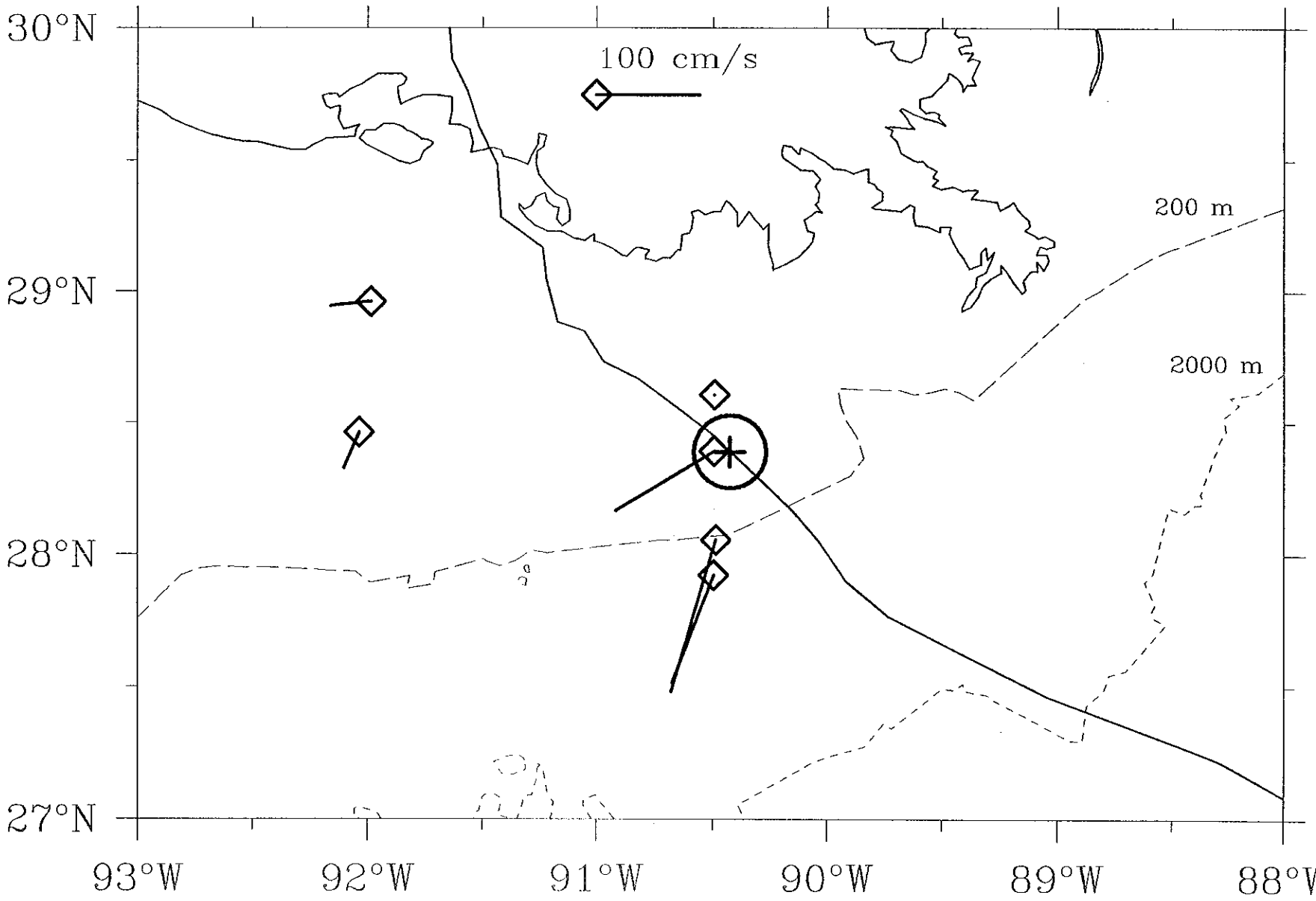

Observed Surface Currents: August-25-22:30 GMT

Frame 045

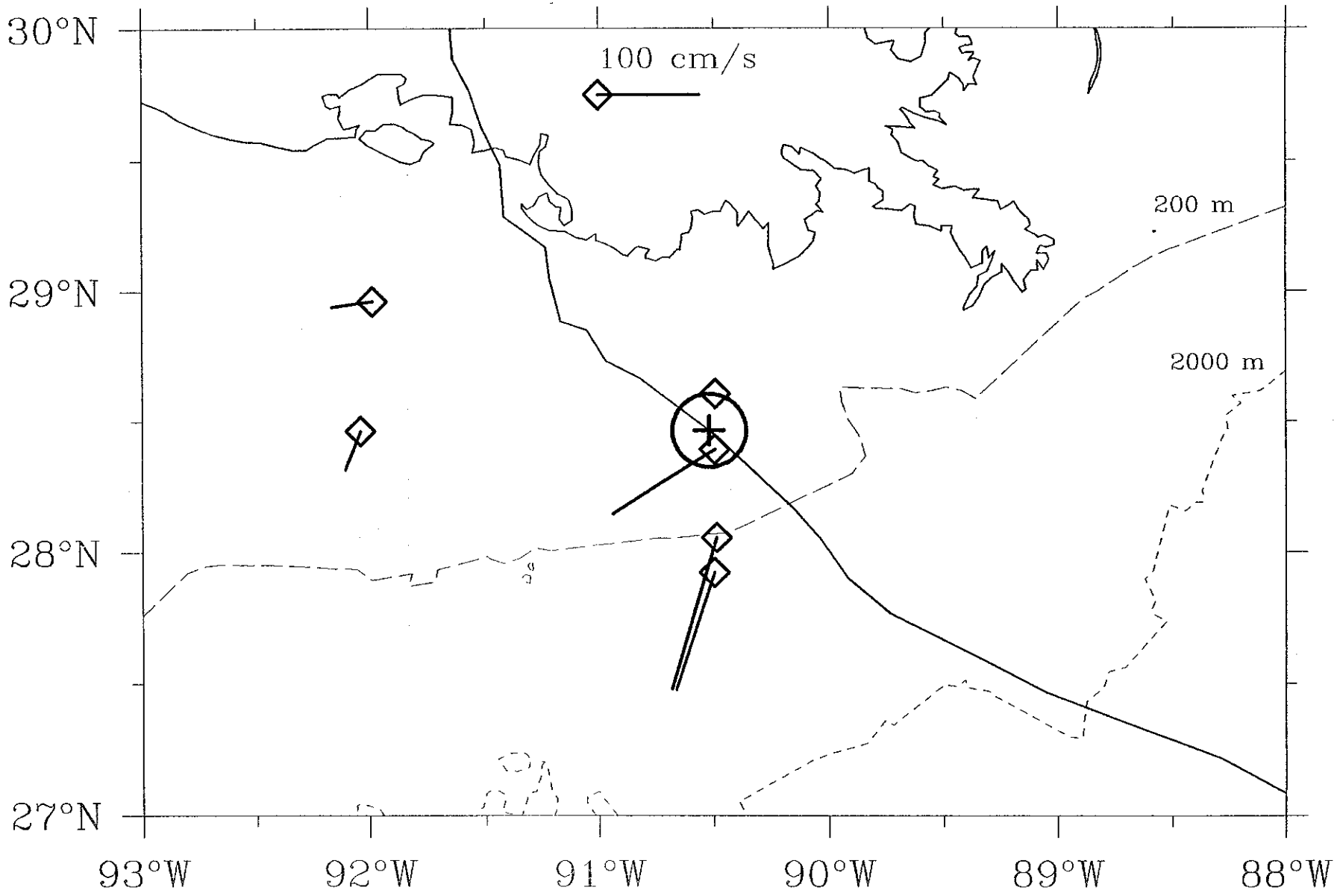

Observed Surface Currents: August-25-23:00 GMT

Frame 0

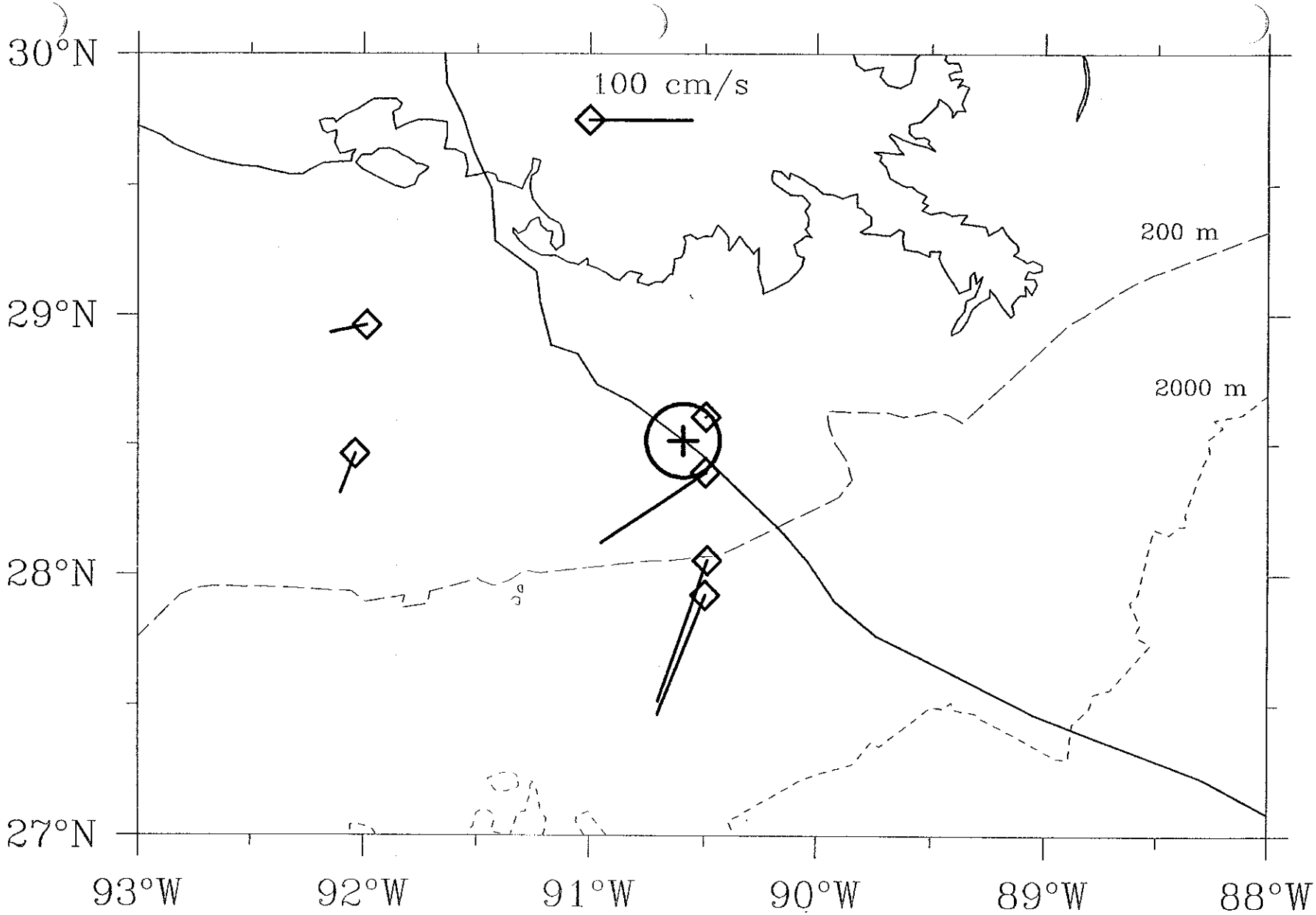

Observed Surface Currents: August-25-23:30 GMT

Frame 047

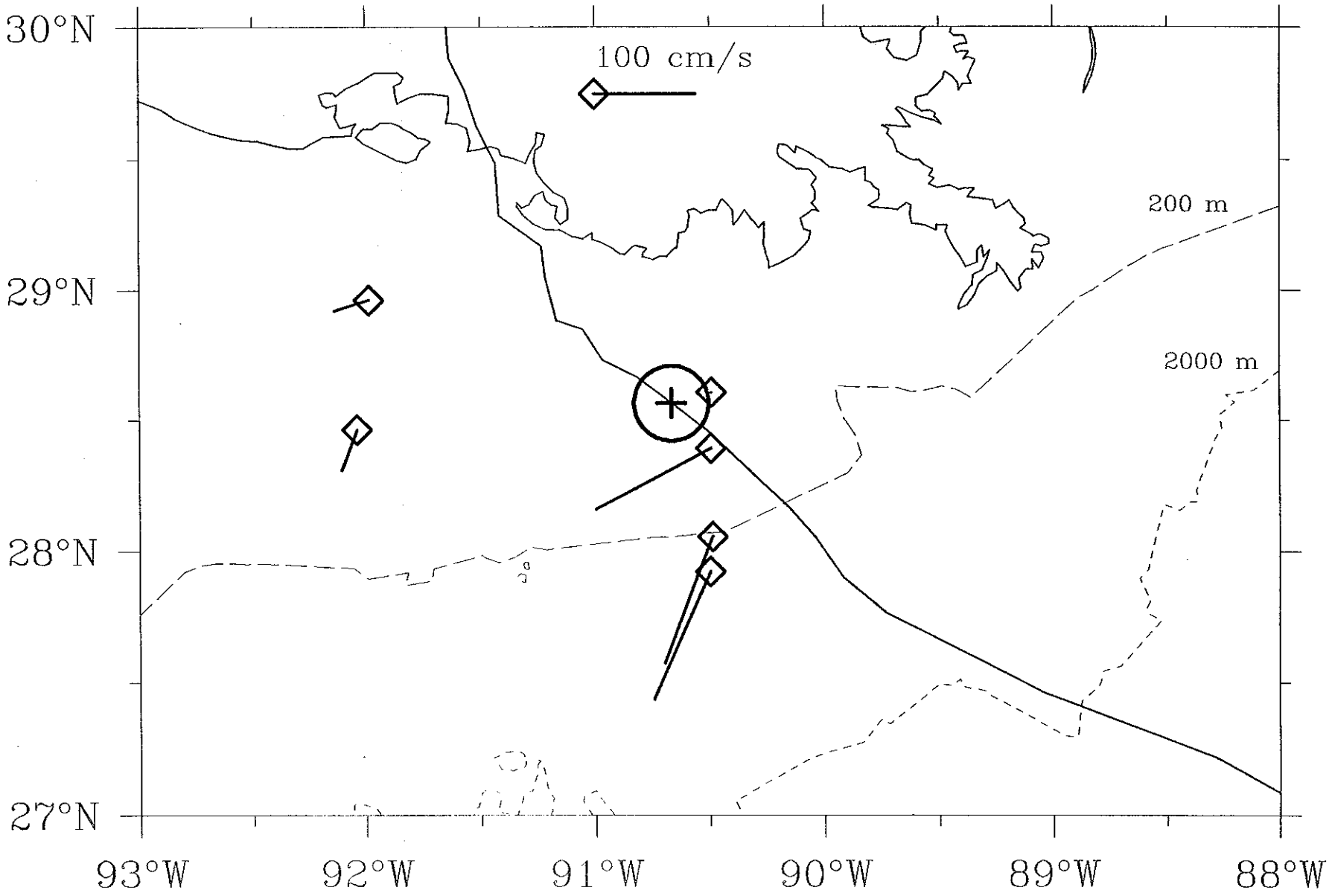

Observed Surface Currents: August-26-00:00 GMT

Frame 048

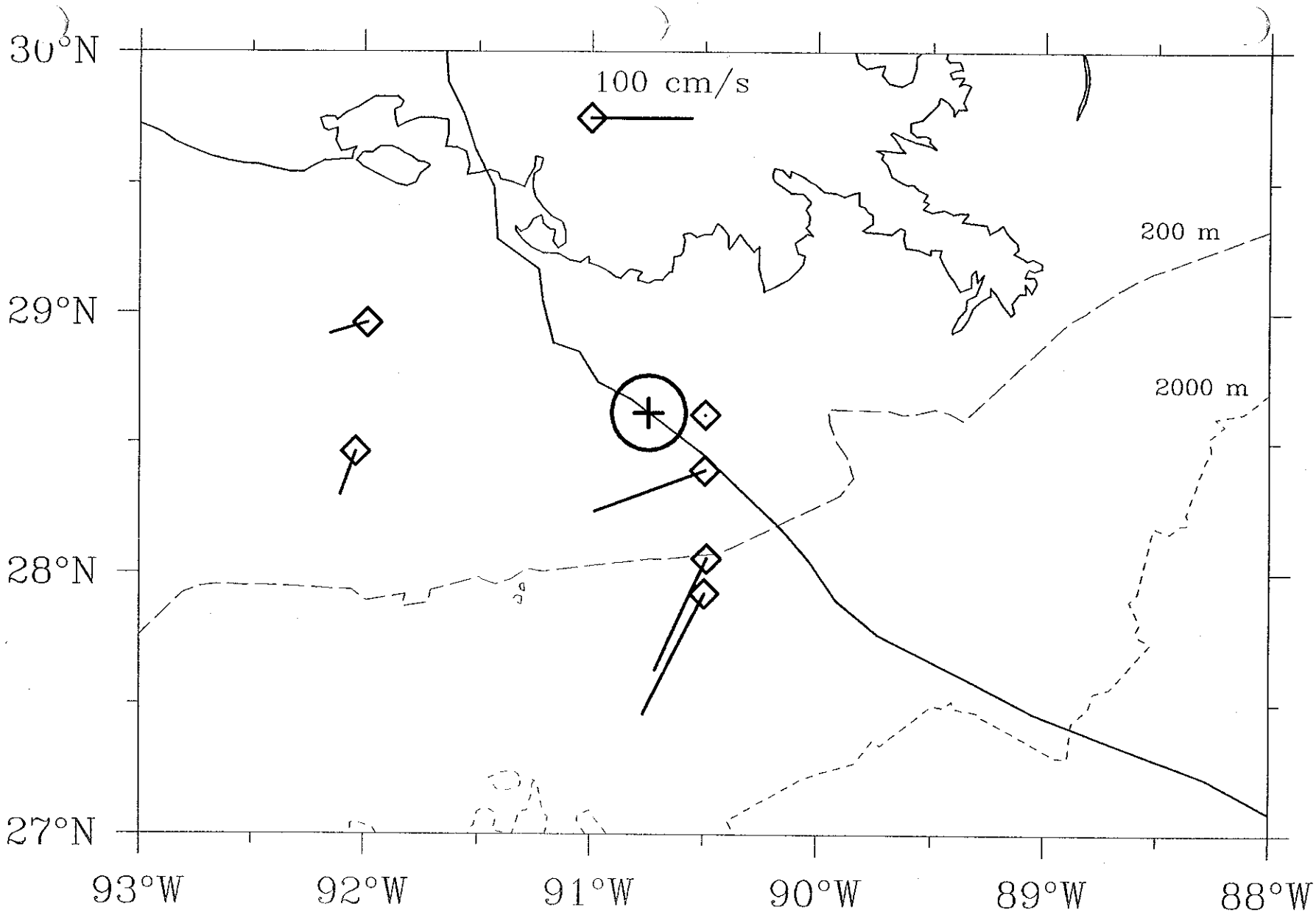

Observed Surface Currents: August-26-00:30 GMT

Frame 049

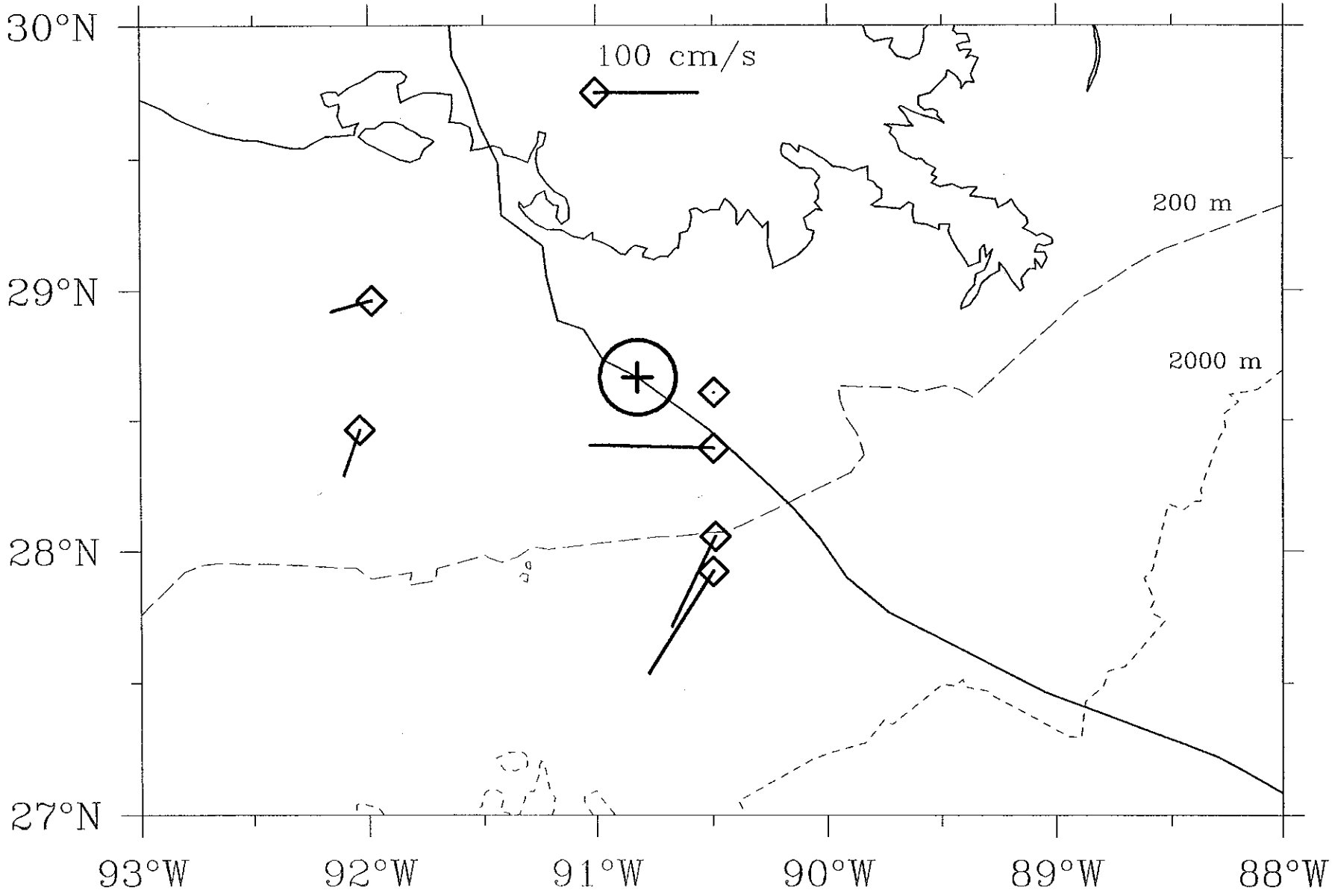

Observed Surface Currents: August-26-01:00 GMT

Frame 052

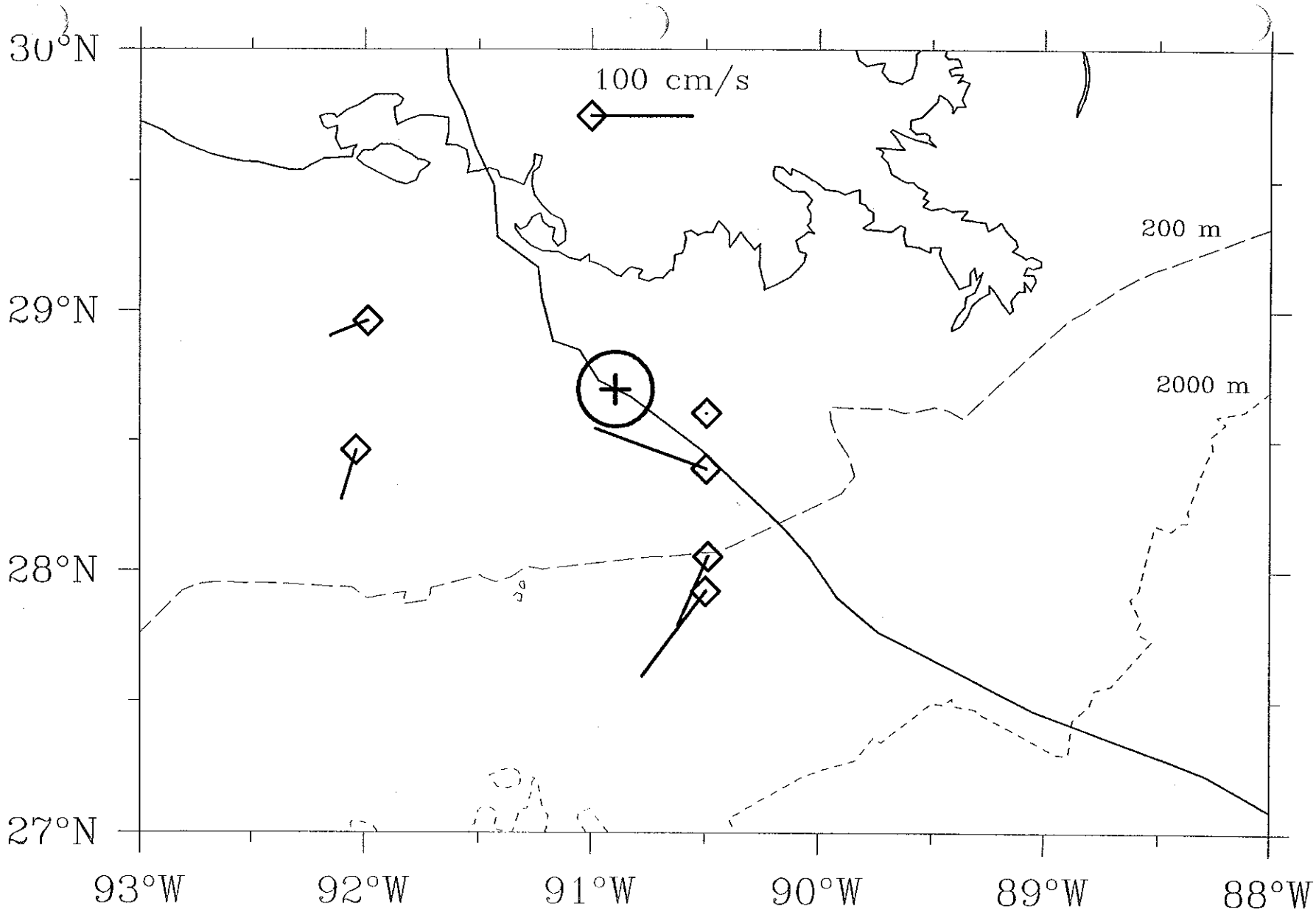

Observed Surface Currents: August-26-01:30 GMT

Frame 051

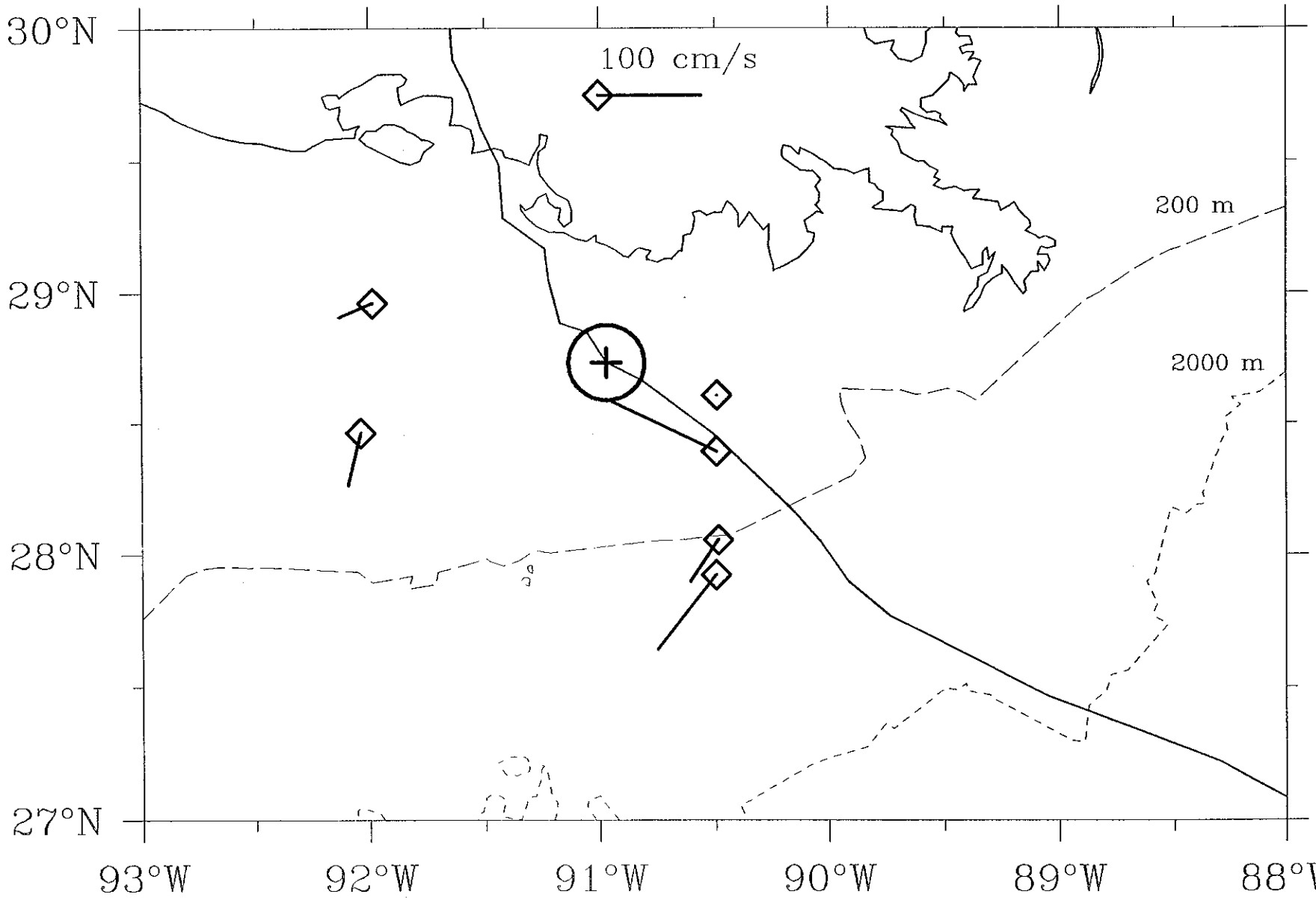

Observed Surface Currents: August-26-02:00 GMT

Frame 0[illegible]

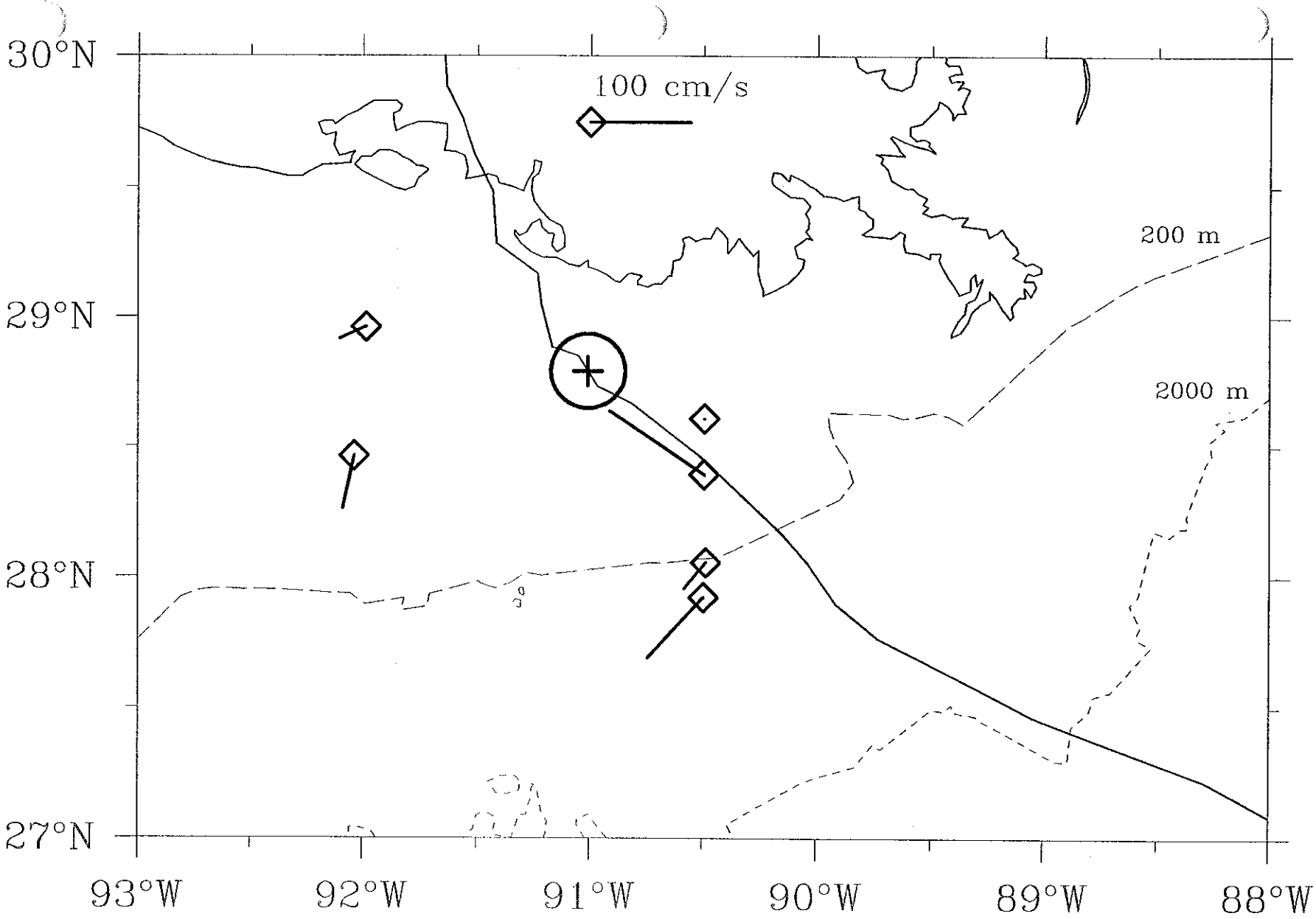

Observed Surface Currents: August-26-02:30 GMT

Frame 053

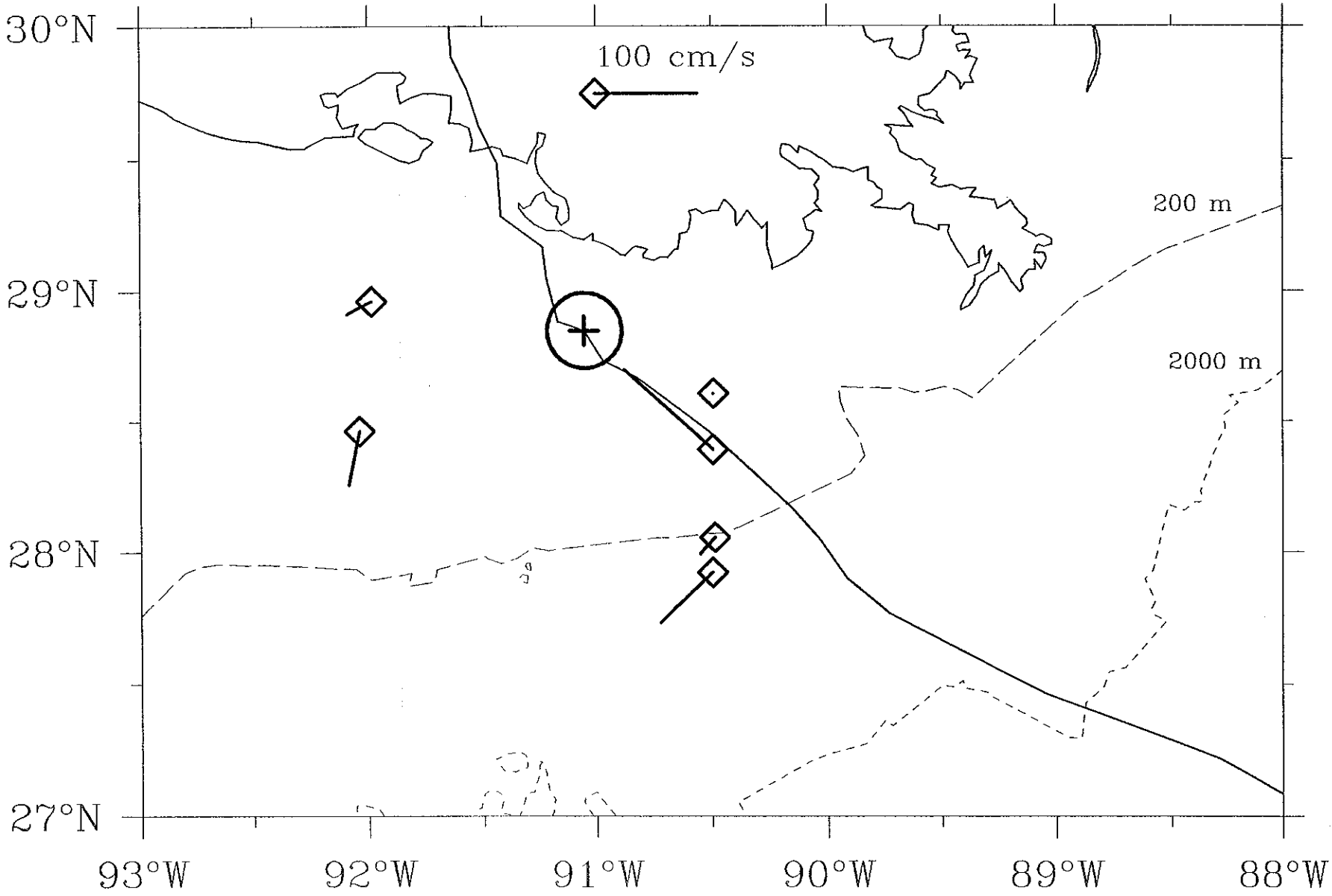

Observed Surface Currents: August-26-03:00 GMT

Frame 071

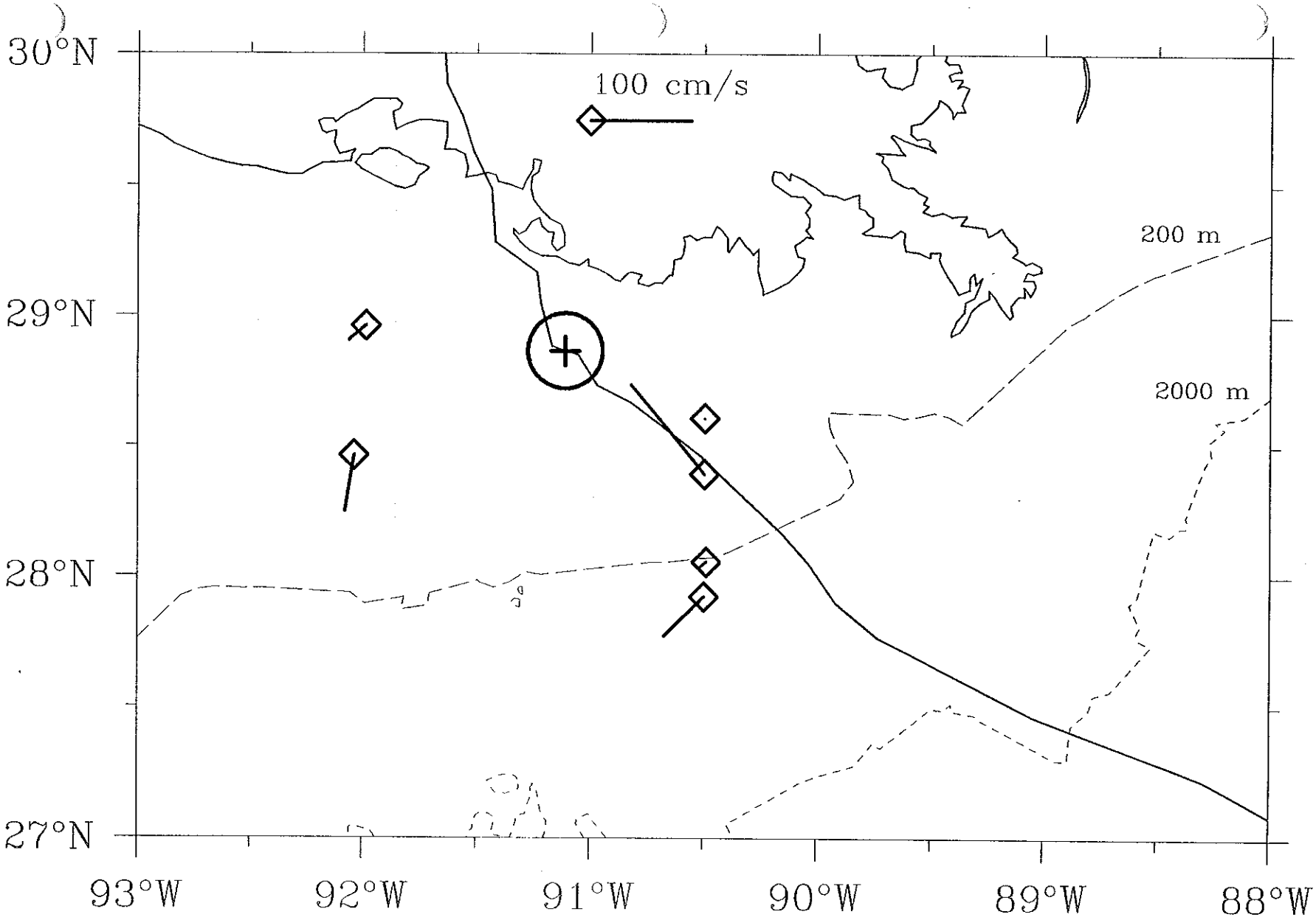

Observed Surface Currents: August-26-03:30 GMT

Frame 055

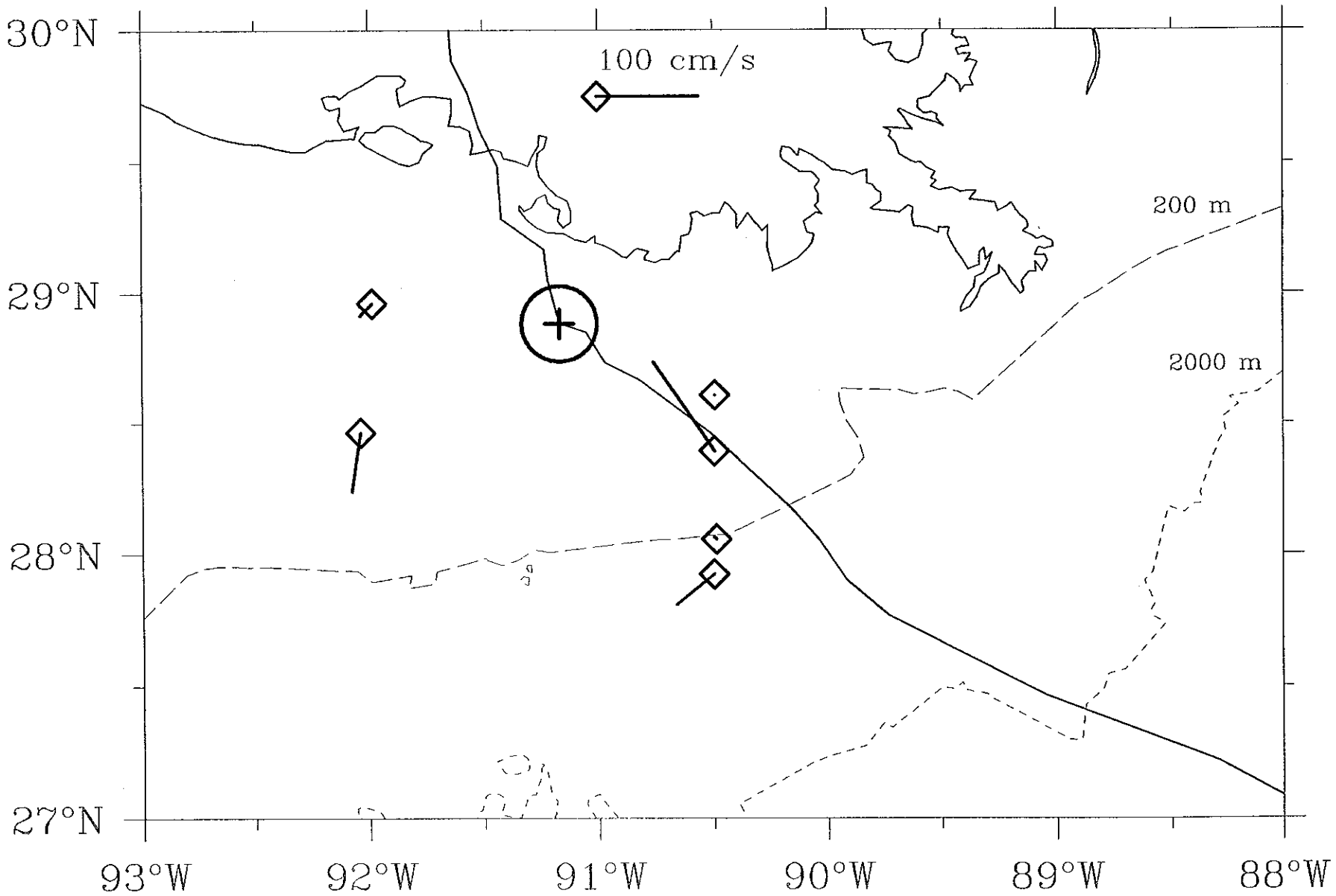

Observed Surface Currents: August-26-04:00 GMT

Frame 056

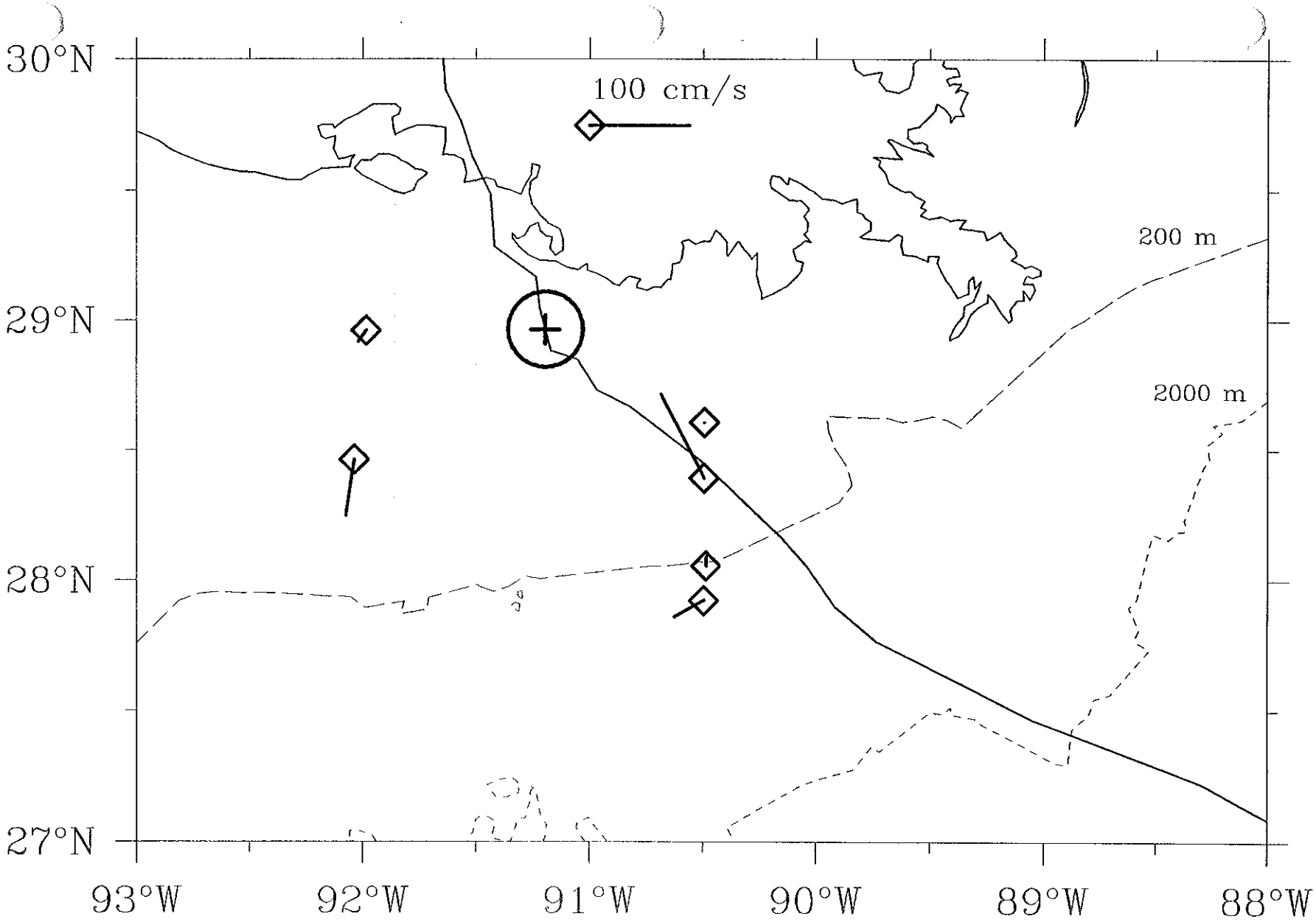

Observed Surface Currents: August-26-04:30 GMT

Frame 057

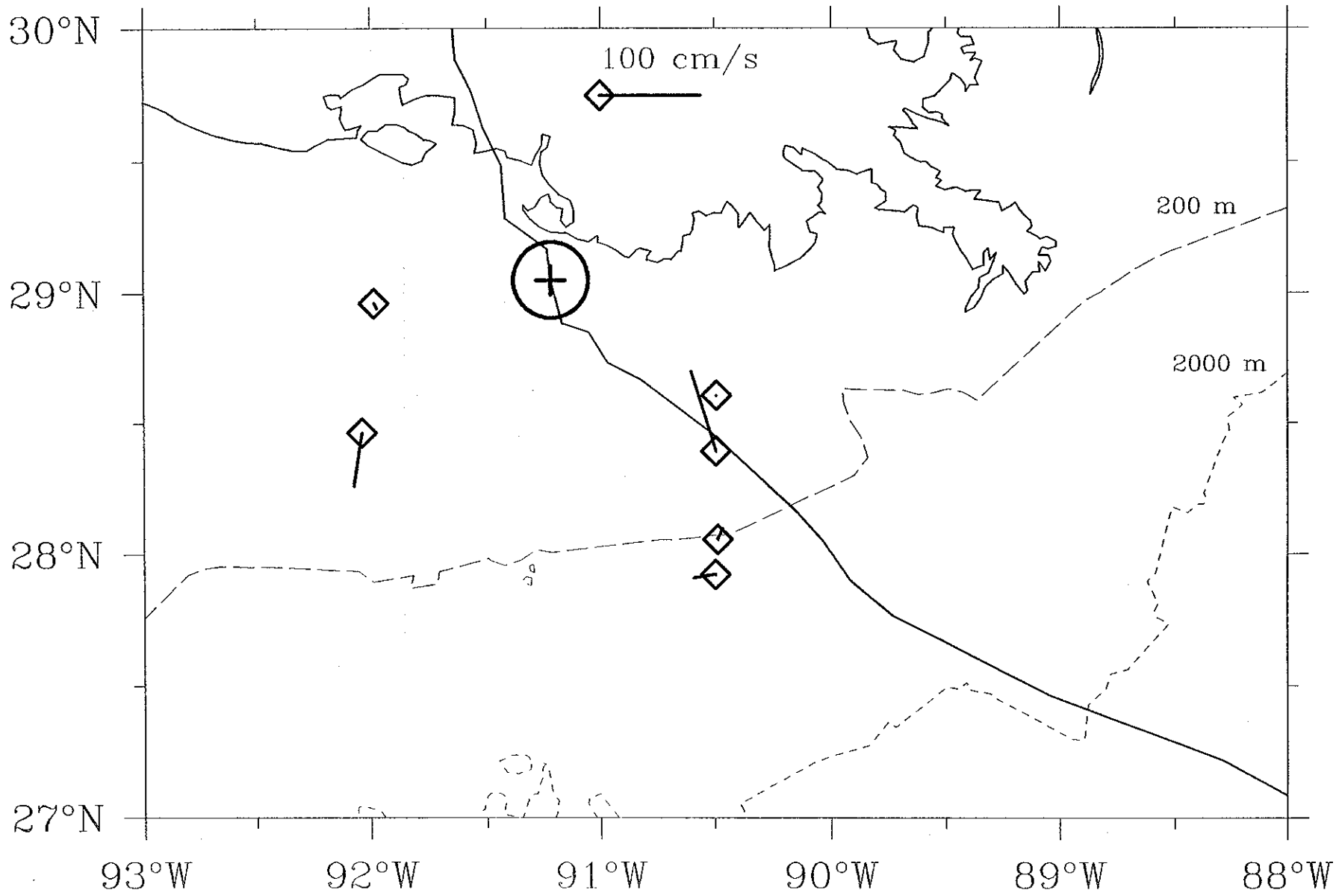

Observed Surface Currents: August-26-05:00 GMT

Frame 059

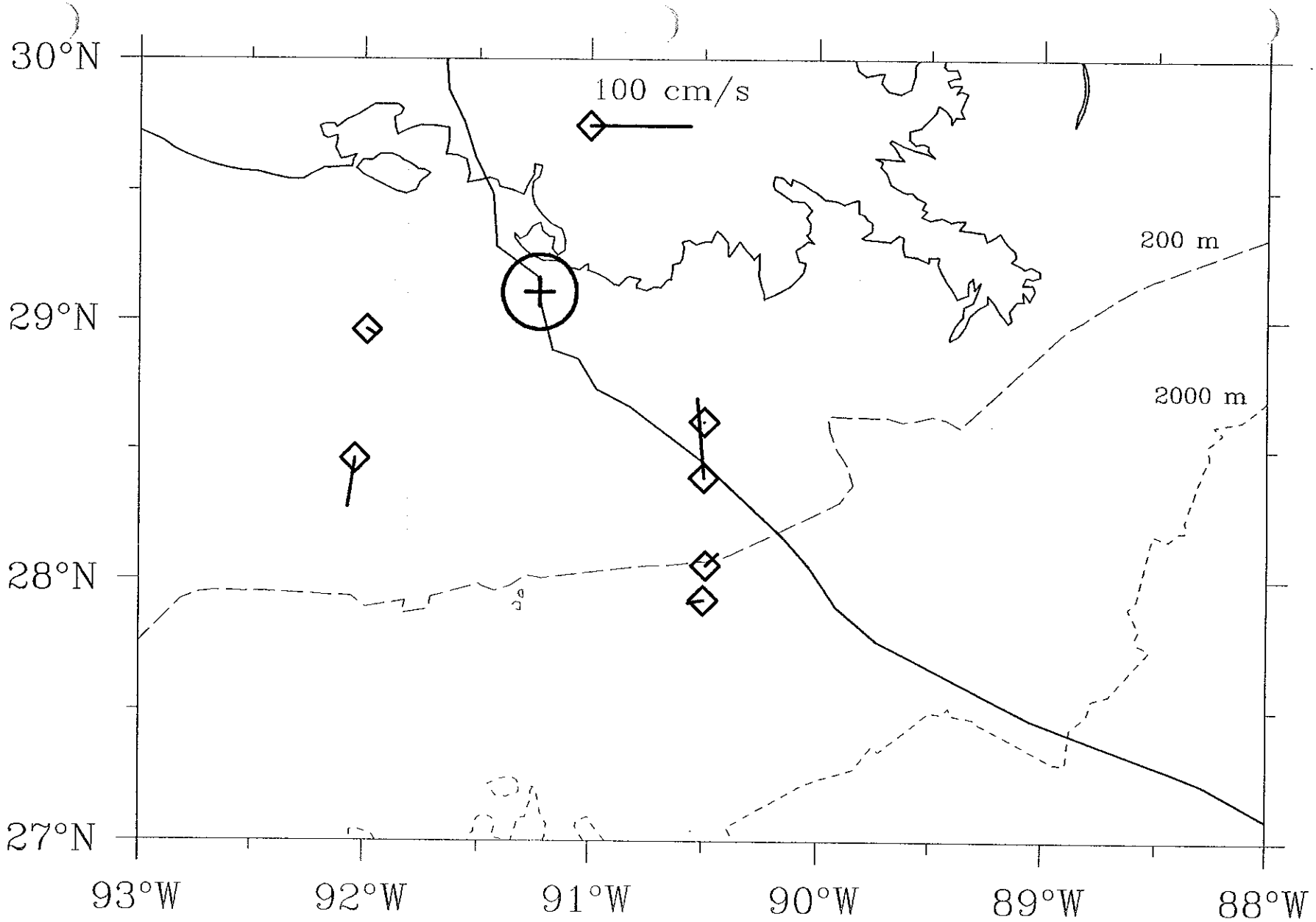

Observed Surface Currents: August-26-05:30 GMT

Frame 059

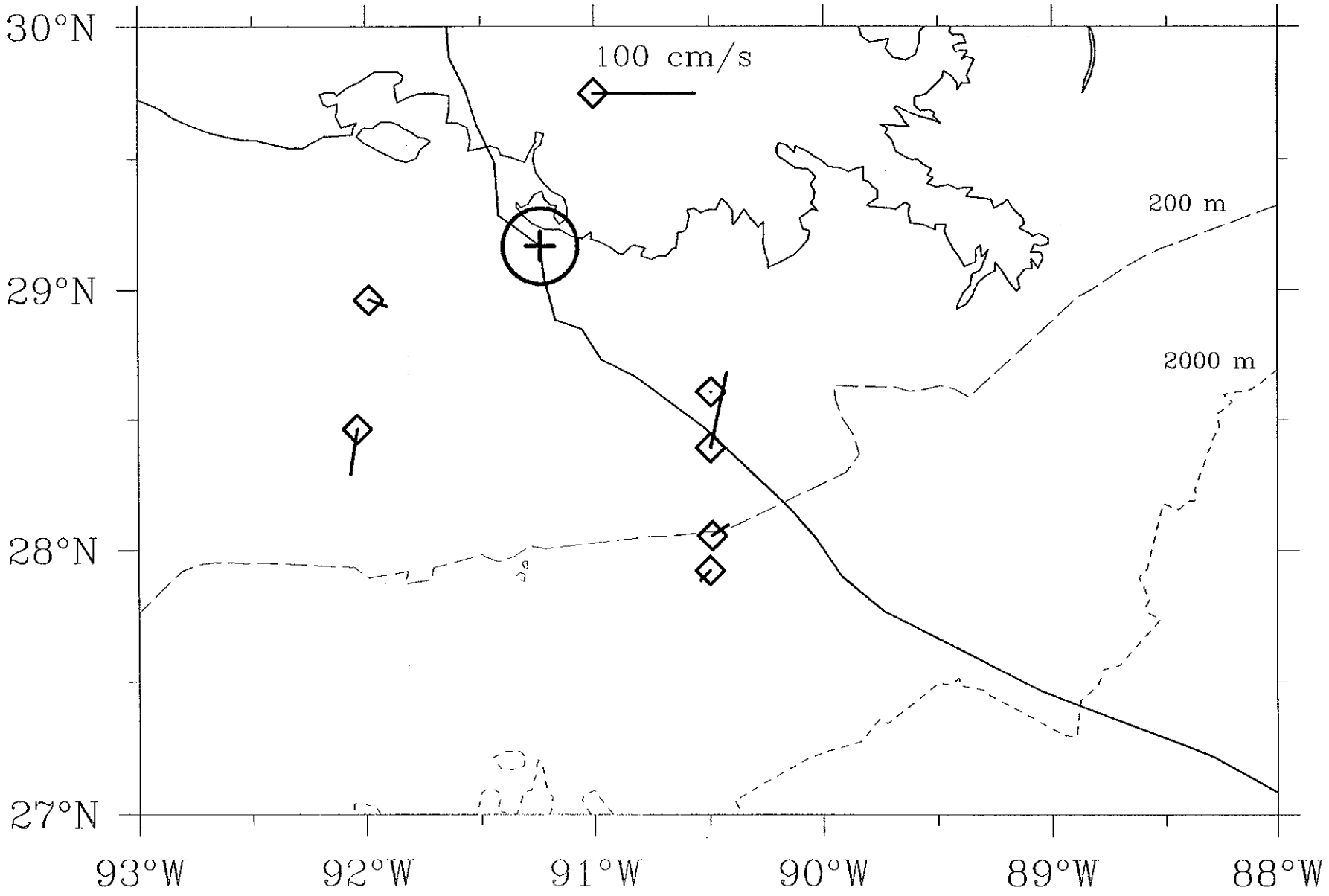

Observed Surface Currents: August-26-06:00 GMT

Frame 06

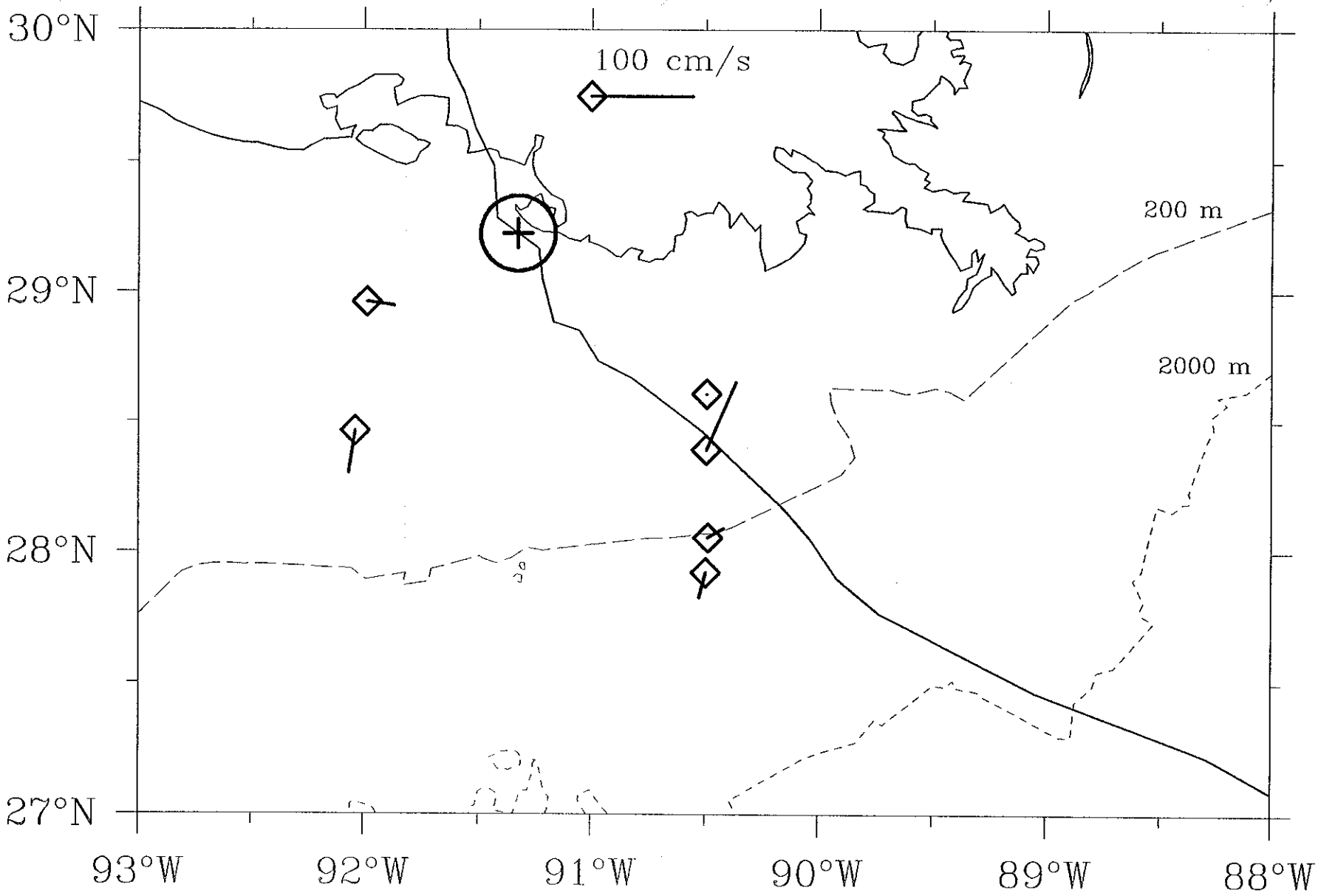

Observed Surface Currents: August-26-06:30 GMT

Frame 061

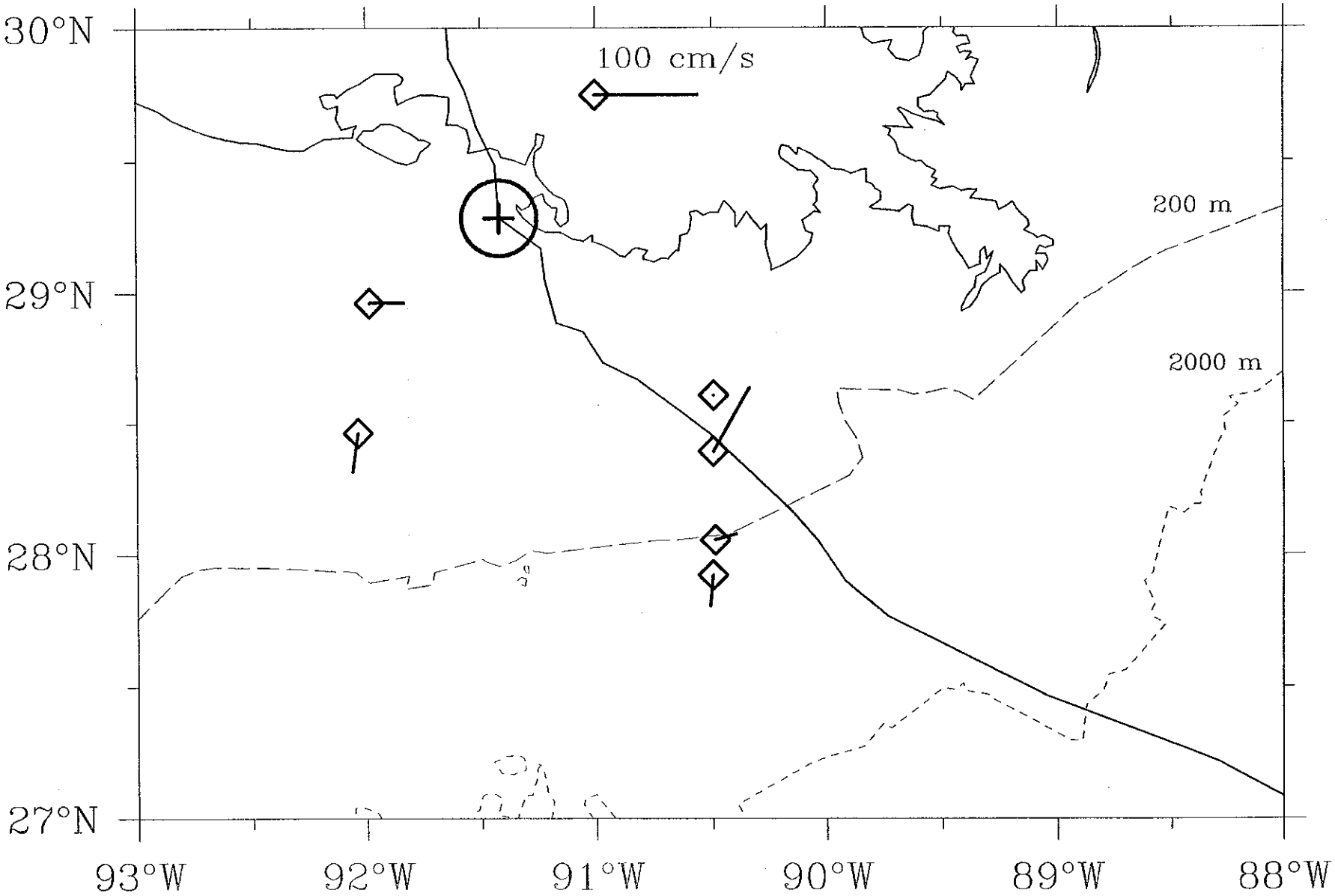

Observed Surface Currents: August-26-07:00 GMT

Frame 062

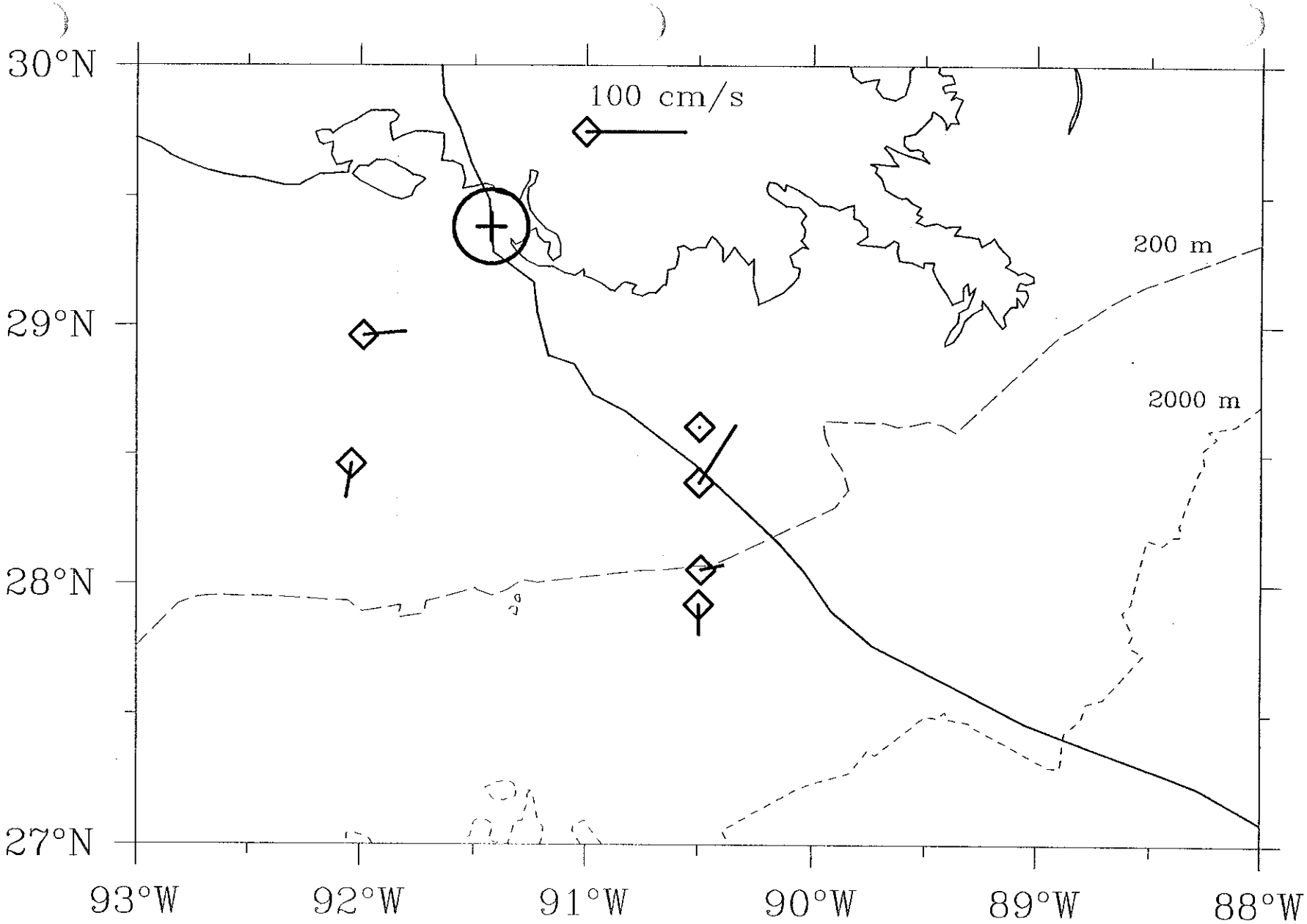

Observed Surface Currents: August-26-07:30 GMT

Frame 063

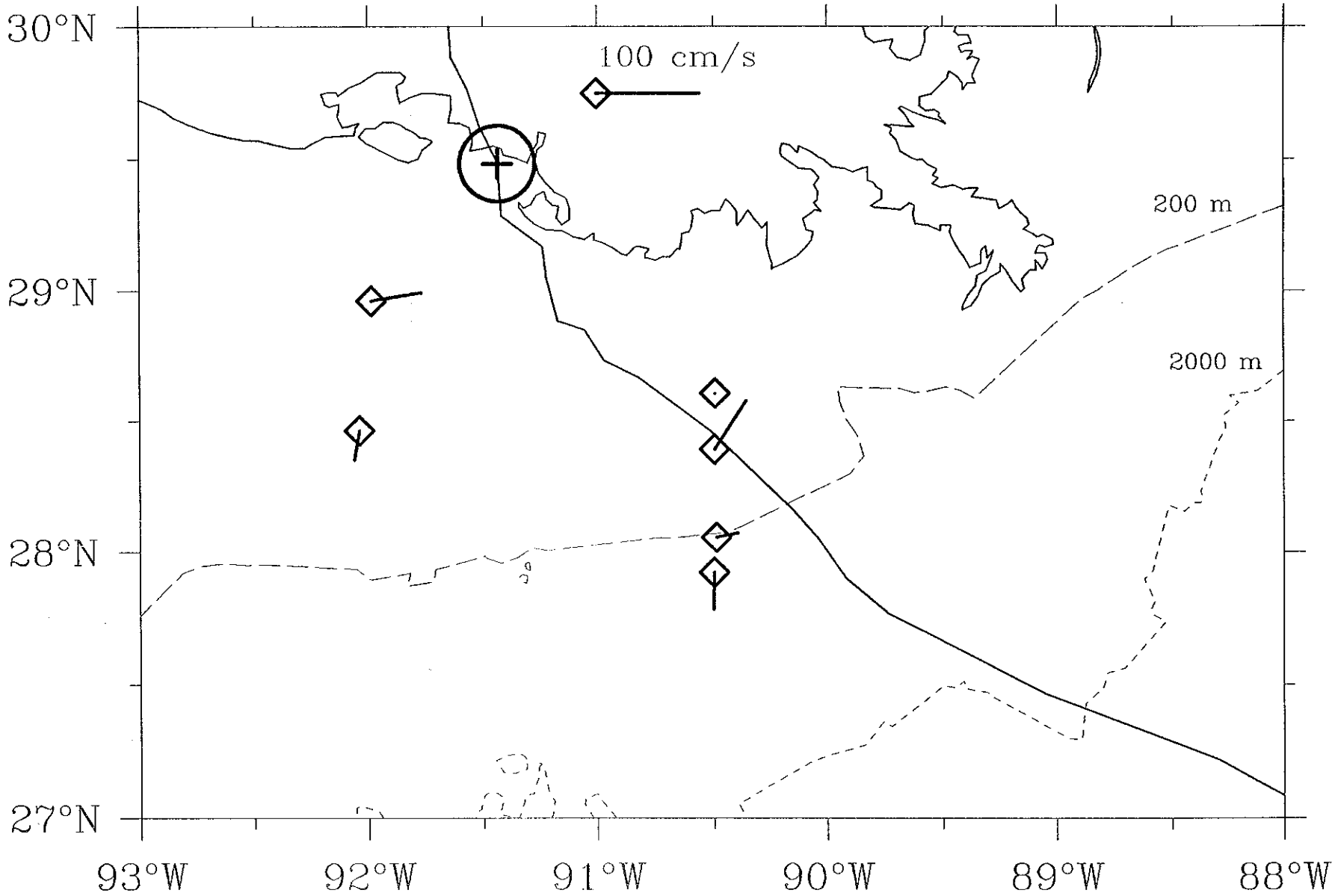

Observed Surface Currents: August-26-08:00 GMT

Frame 064

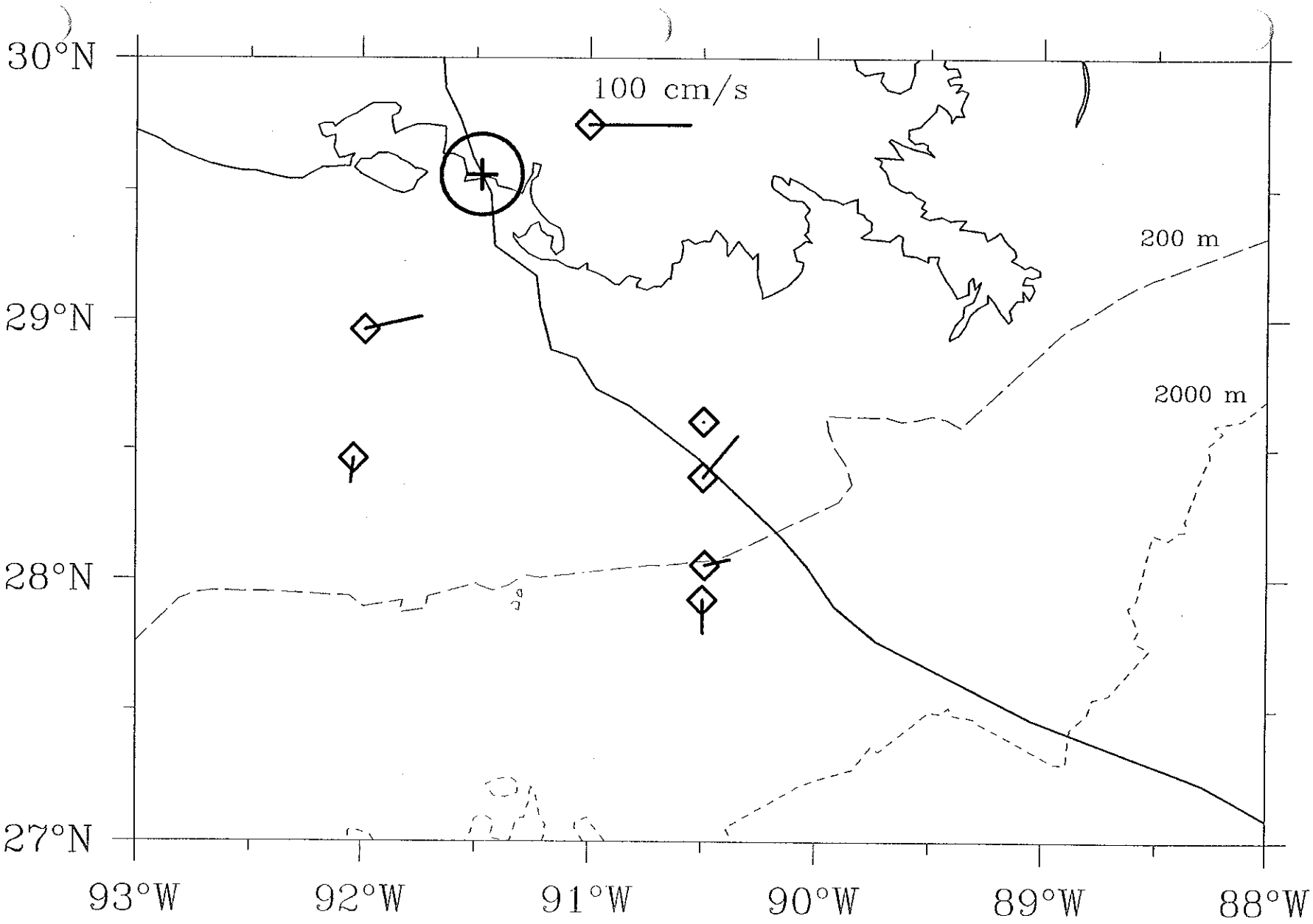

Observed Surface Currents: August-26-08:30 GMT

Frame 065

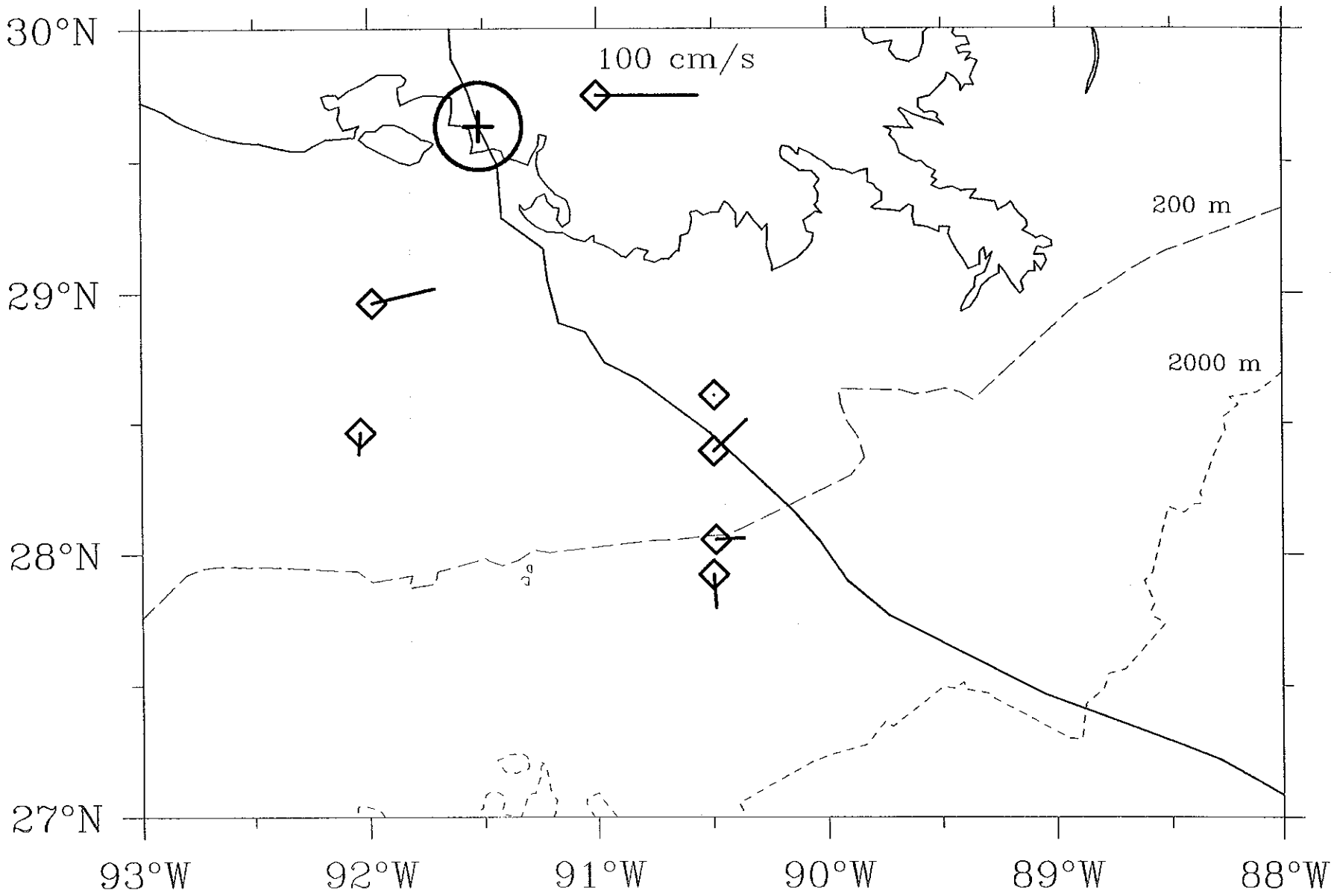

Observed Surface Currents: August–26–09:00 GMT

Frame 063

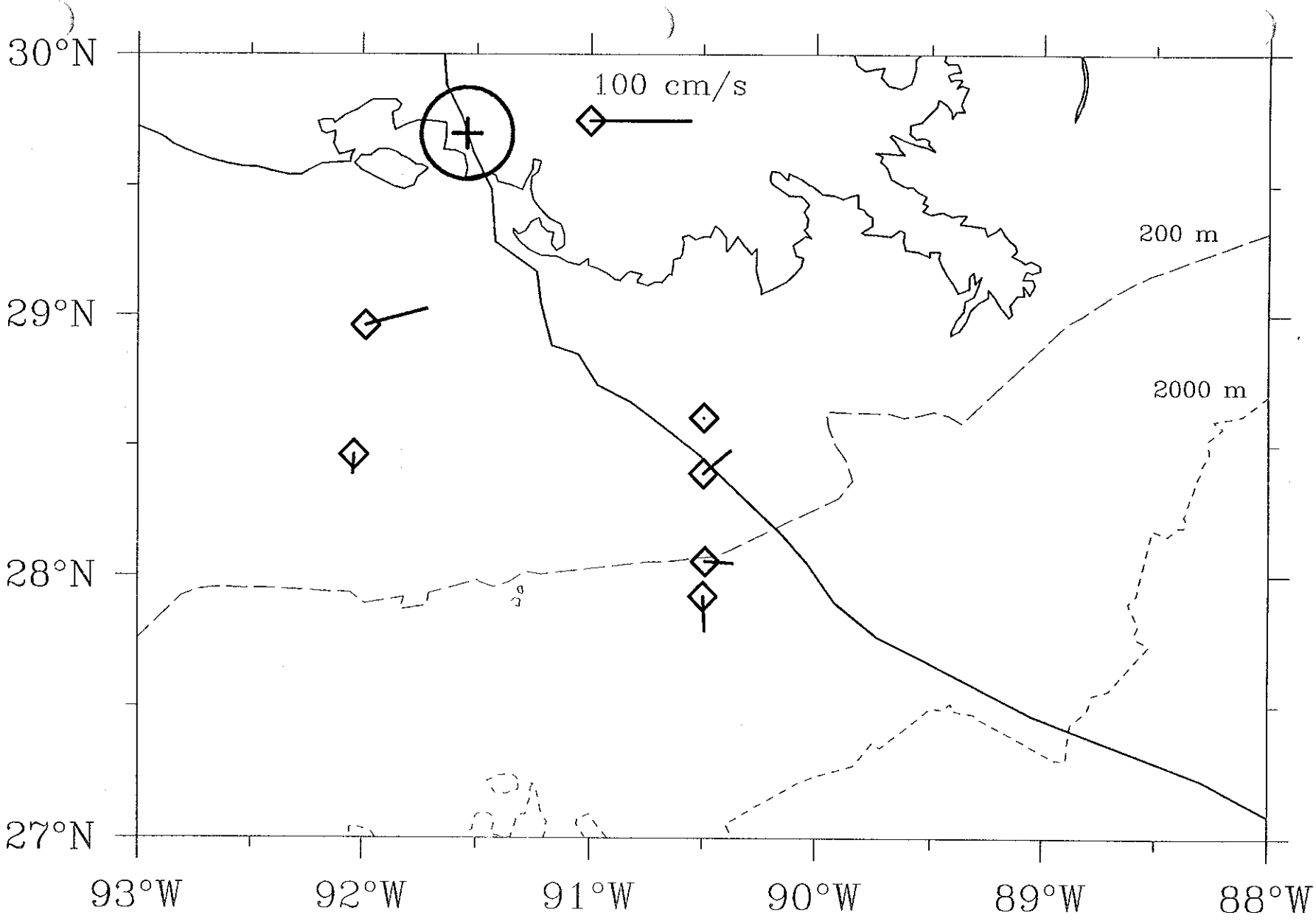

Observed Surface Currents: August-26-09:30 GMT

Frame 067

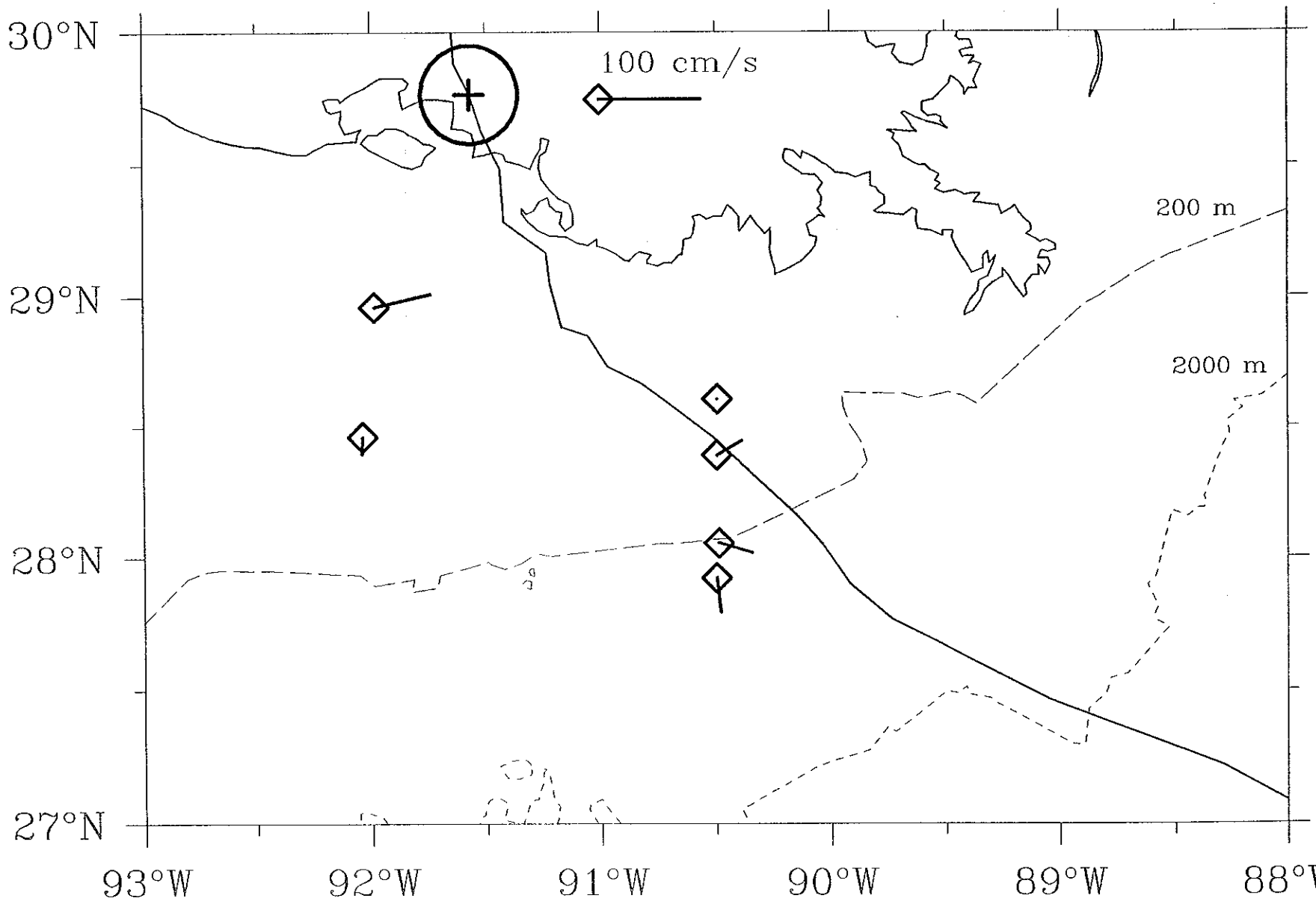

Observed Surface Currents: August–26–10:00 GMT

Frame 0[illegible]

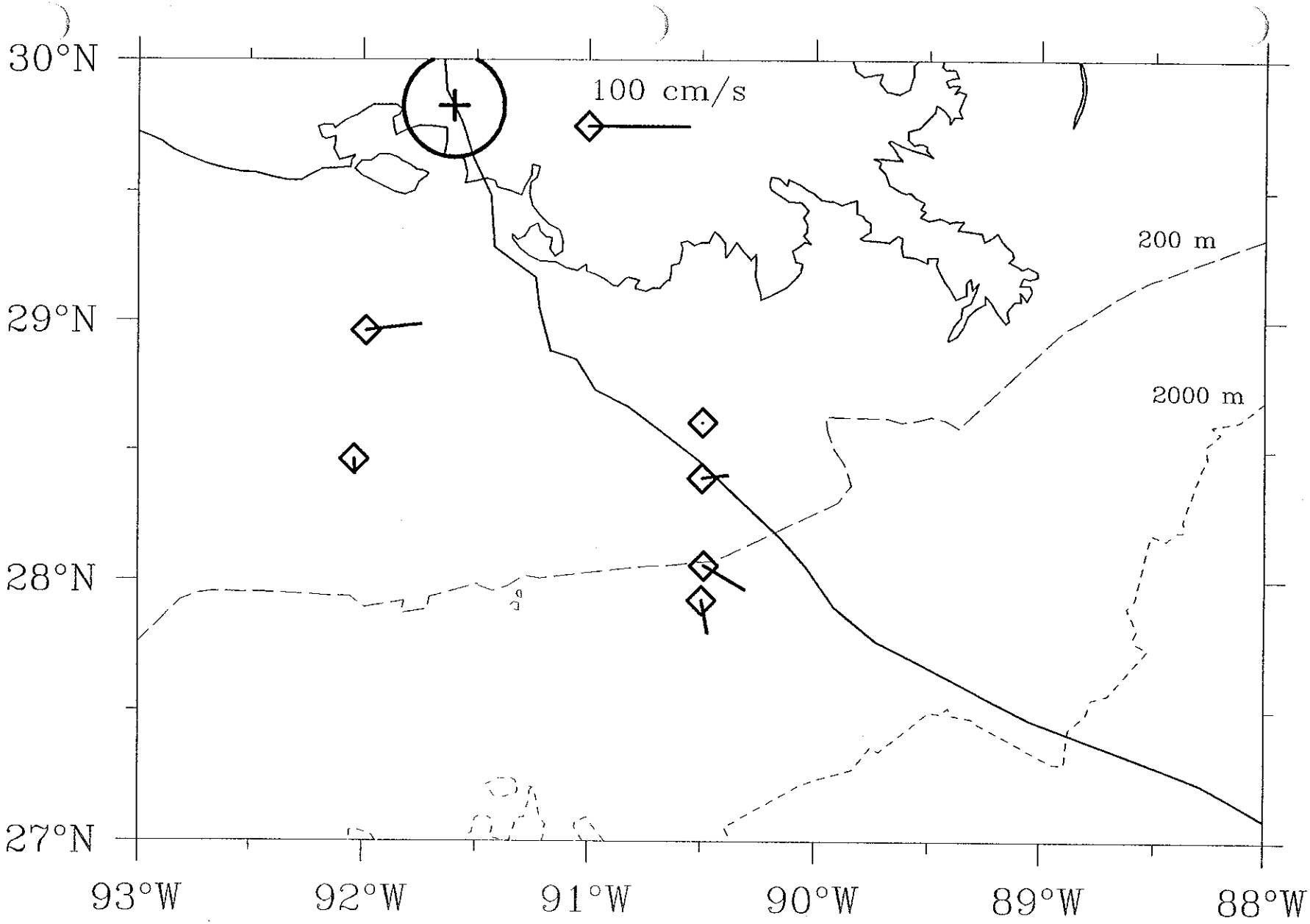

Observed Surface Currents: August-26-10:30 GMT

Frame 069

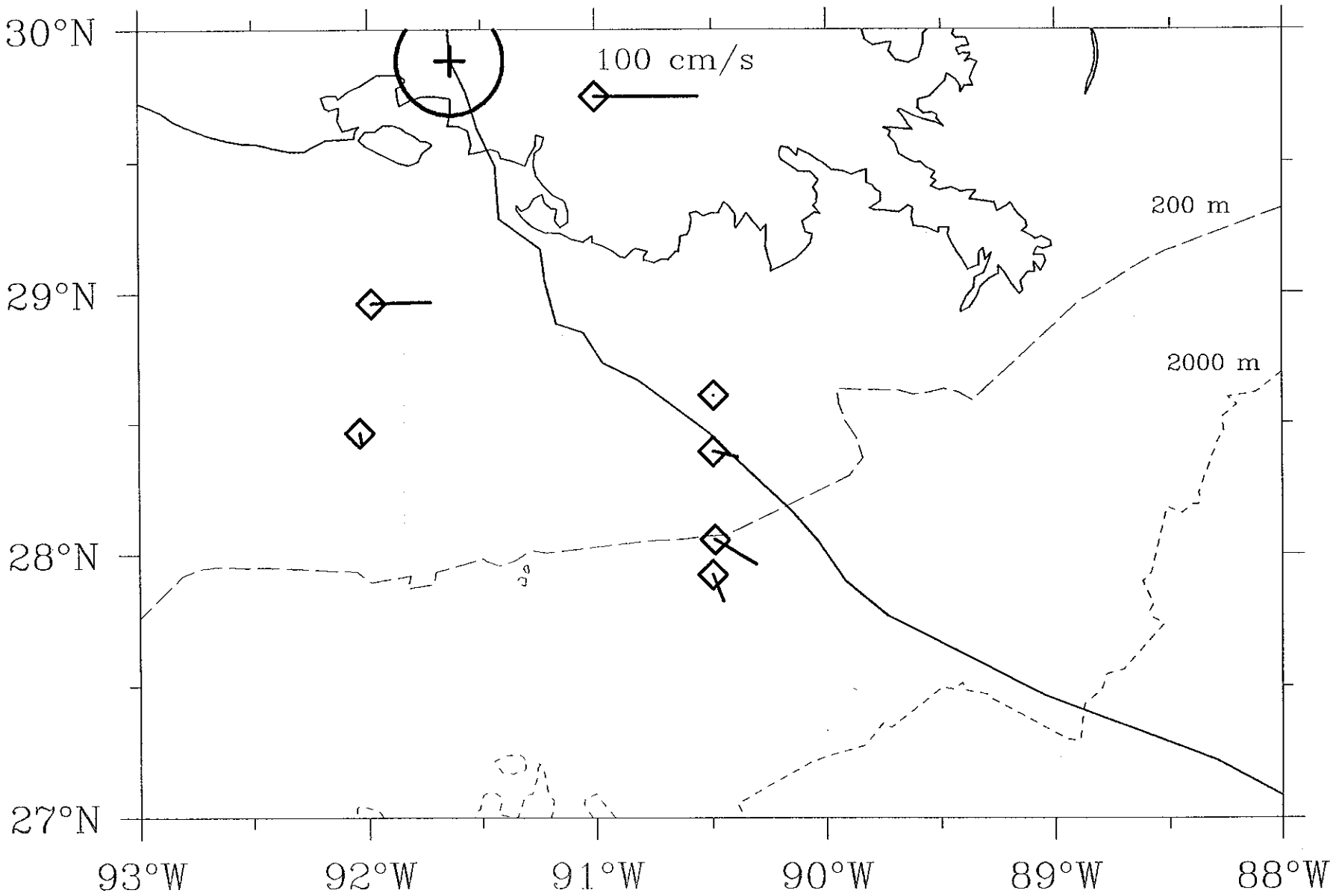

Observed Surface Currents: August-26-11:00 GMT

Frame 0

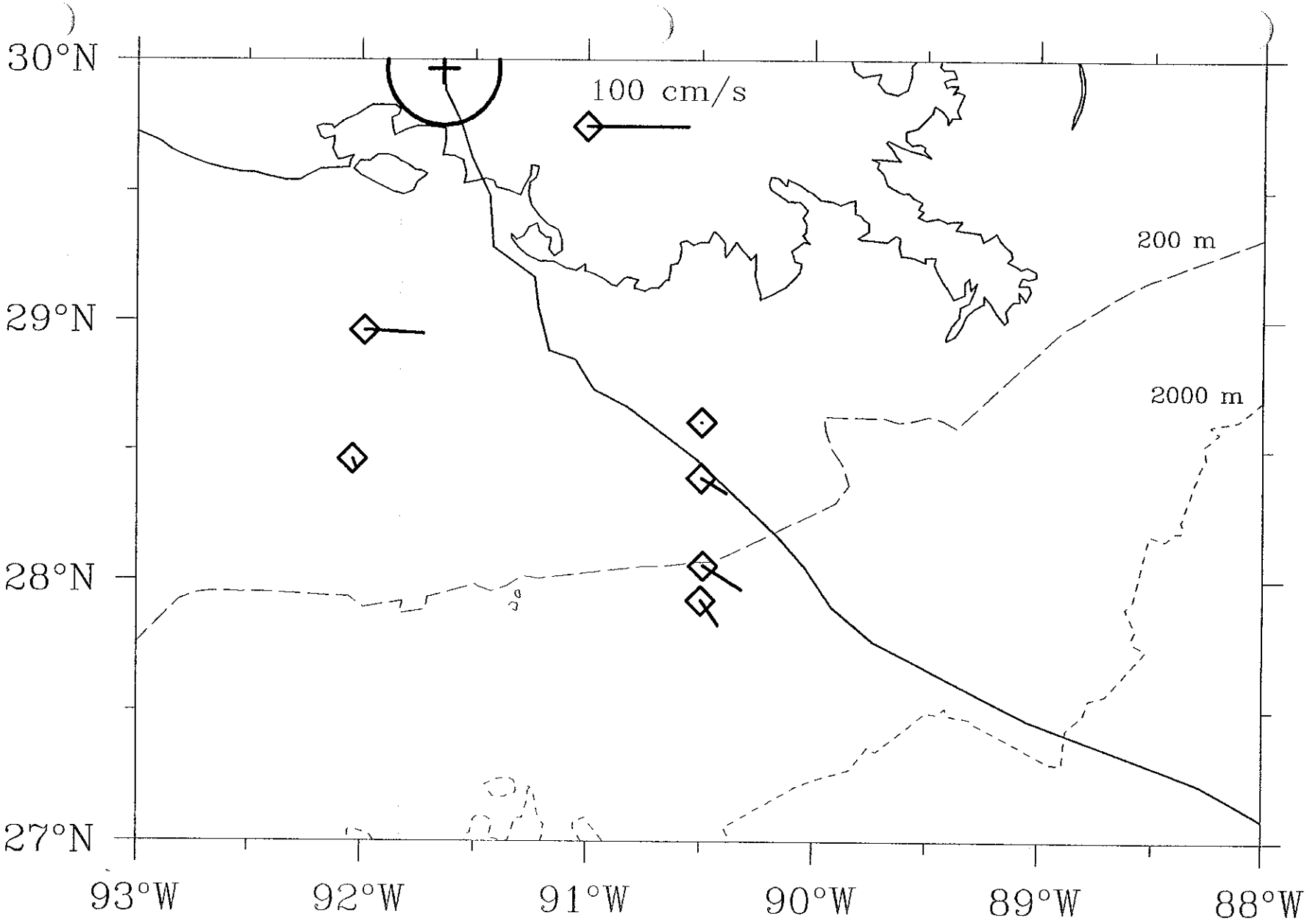

Observed Surface Currents: August-26-11:30 GMT

Frame 071

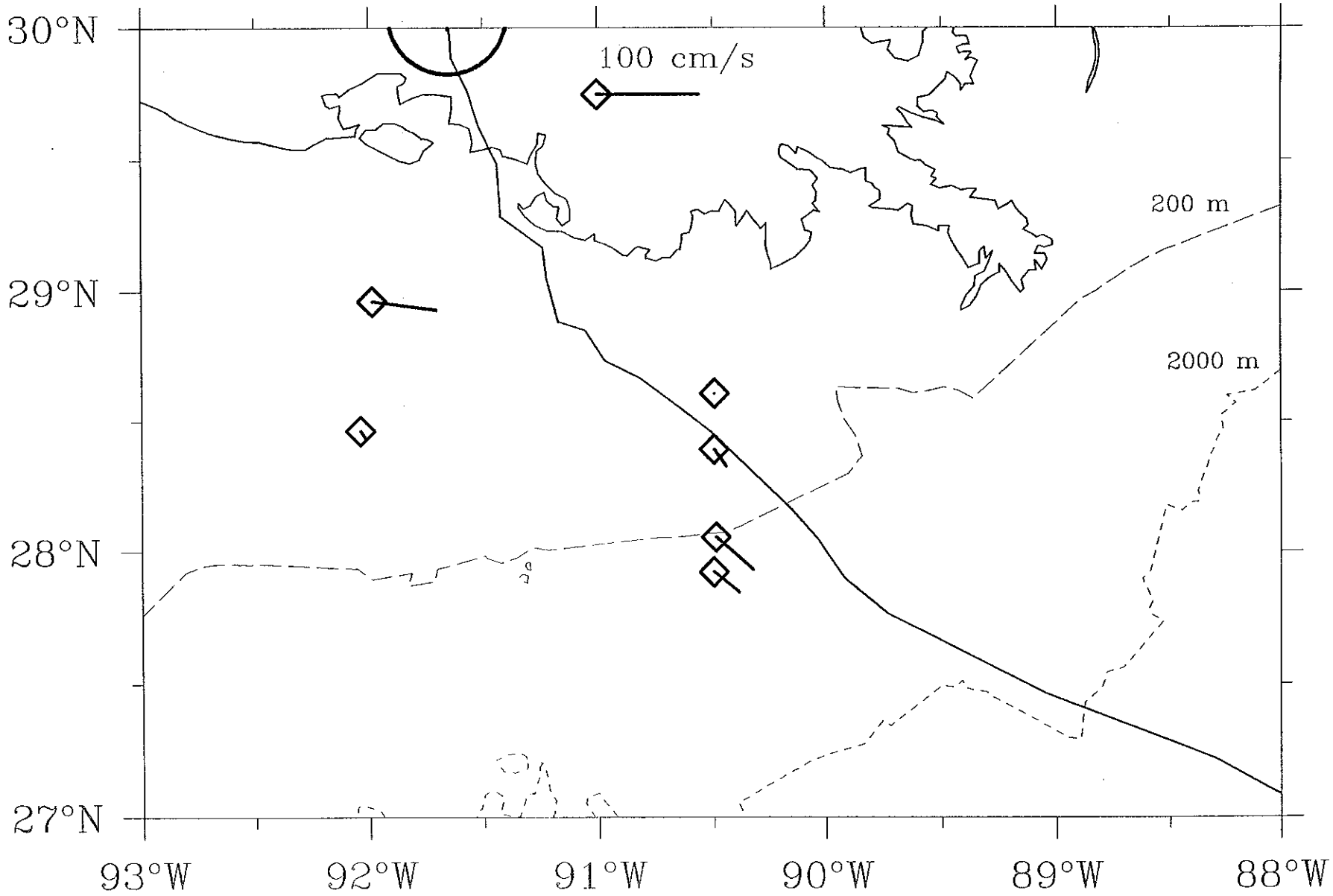

Observed Surface Currents: August-26-12:00 GMT

Frame 0[illegible]

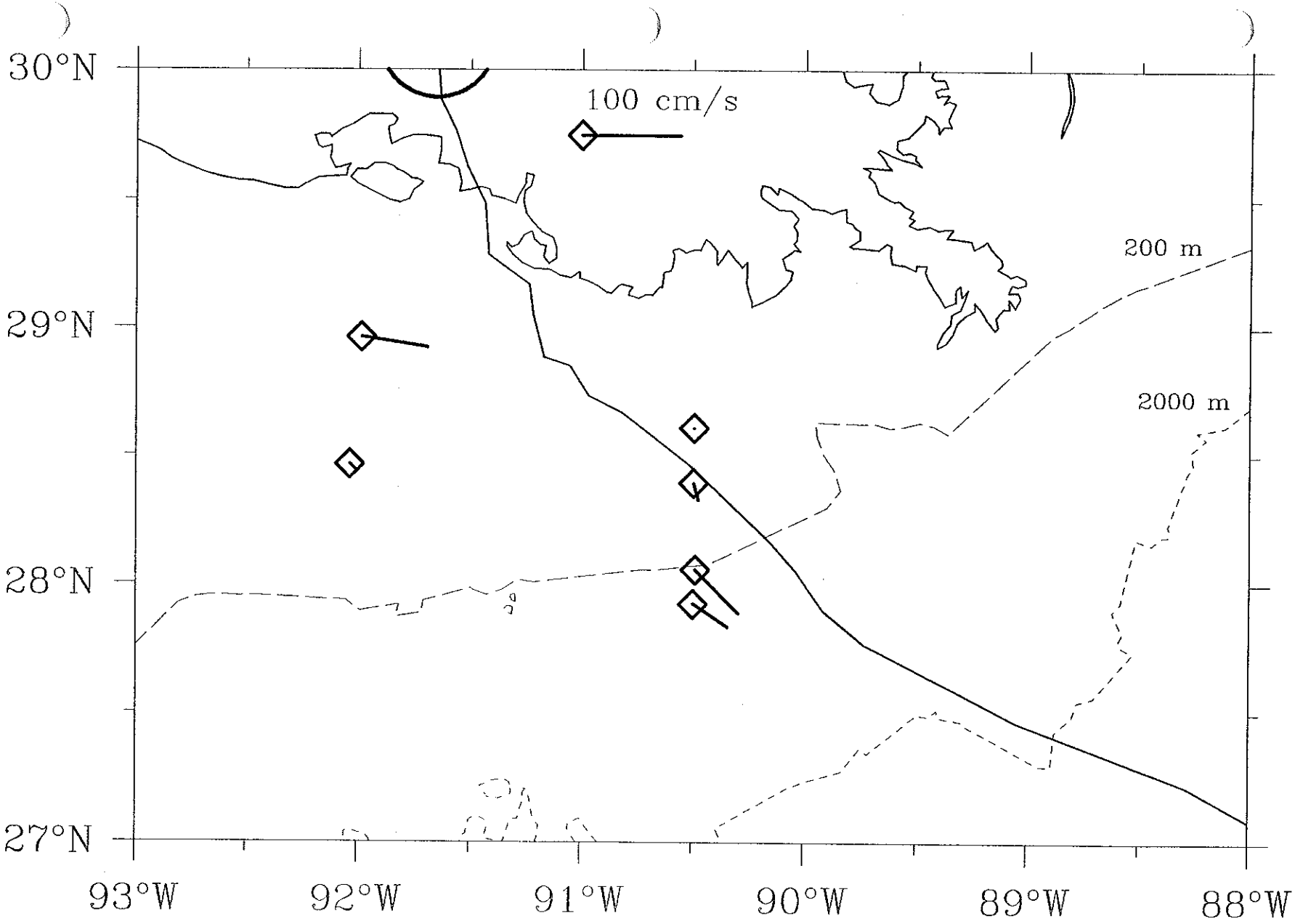

Observed Surface Currents: August-26-12:30 GMT

Frame 073

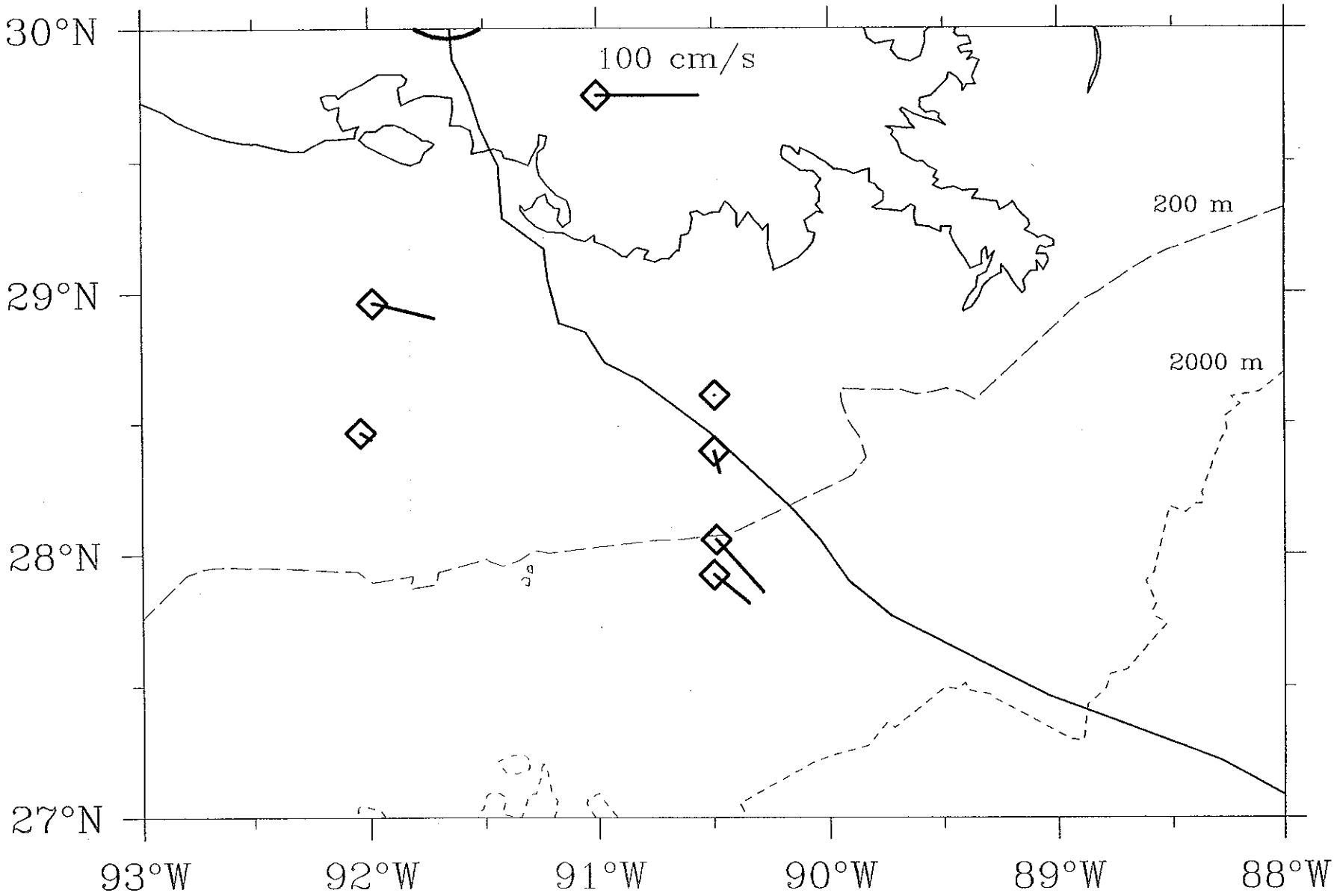

Observed Surface Currents: August-26-13:00 GMT

Frame 074

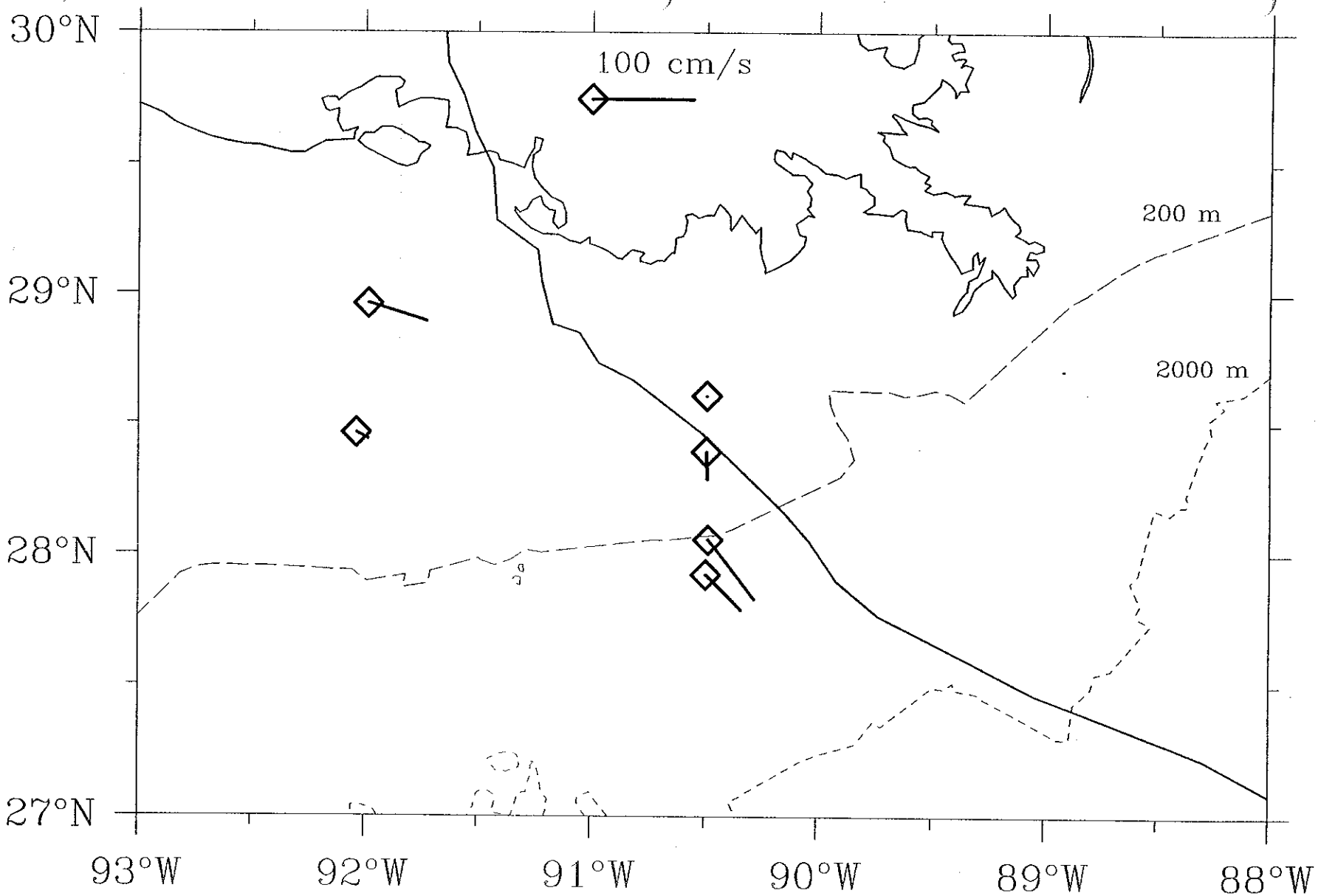

Observed Surface Currents: August-26-13:30 GMT

Frame 075

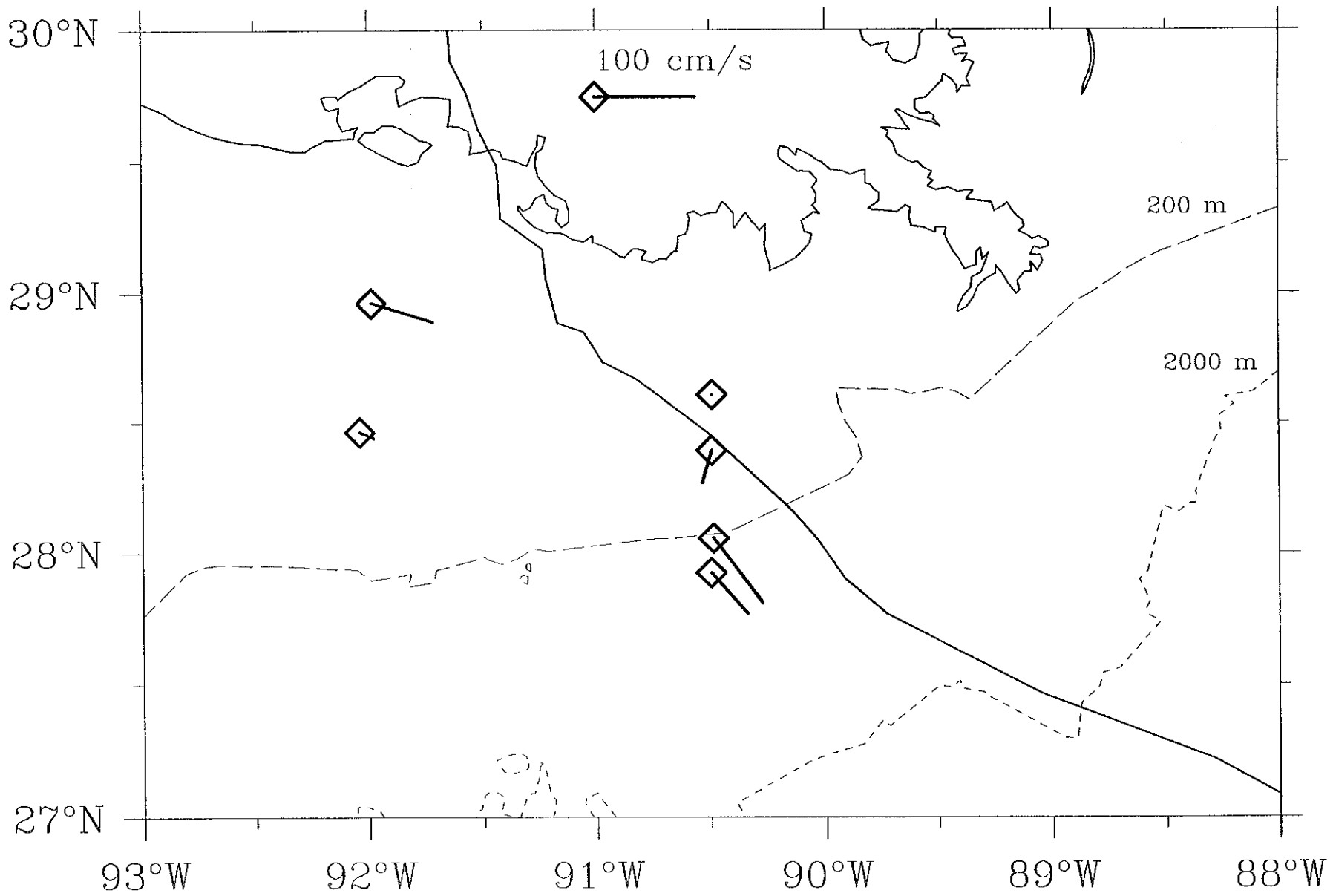

Observed Surface Currents: August-26-14:00 GMT

Frame 07

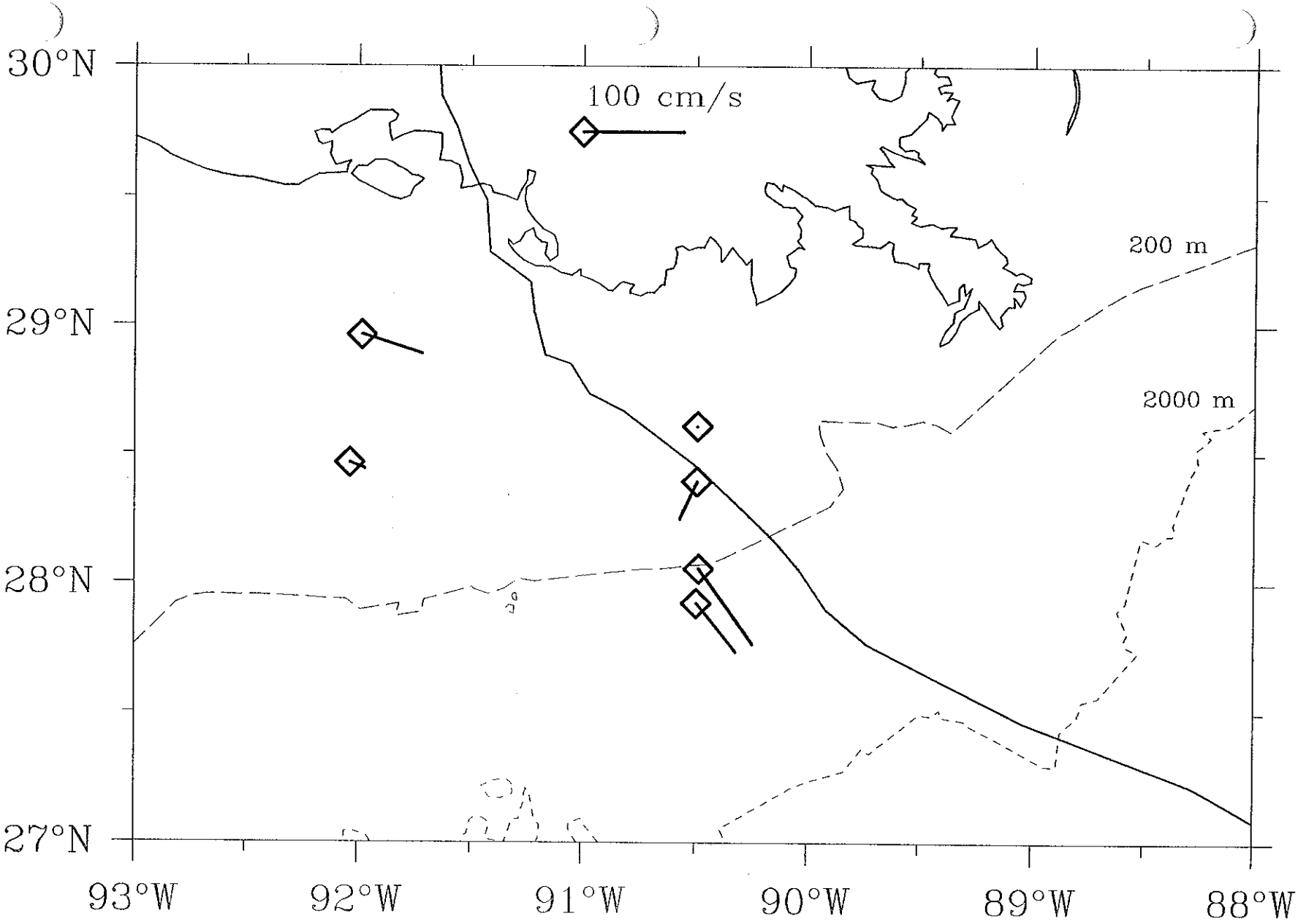

Observed Surface Currents: August-26-14:30 GMT

Frame 077

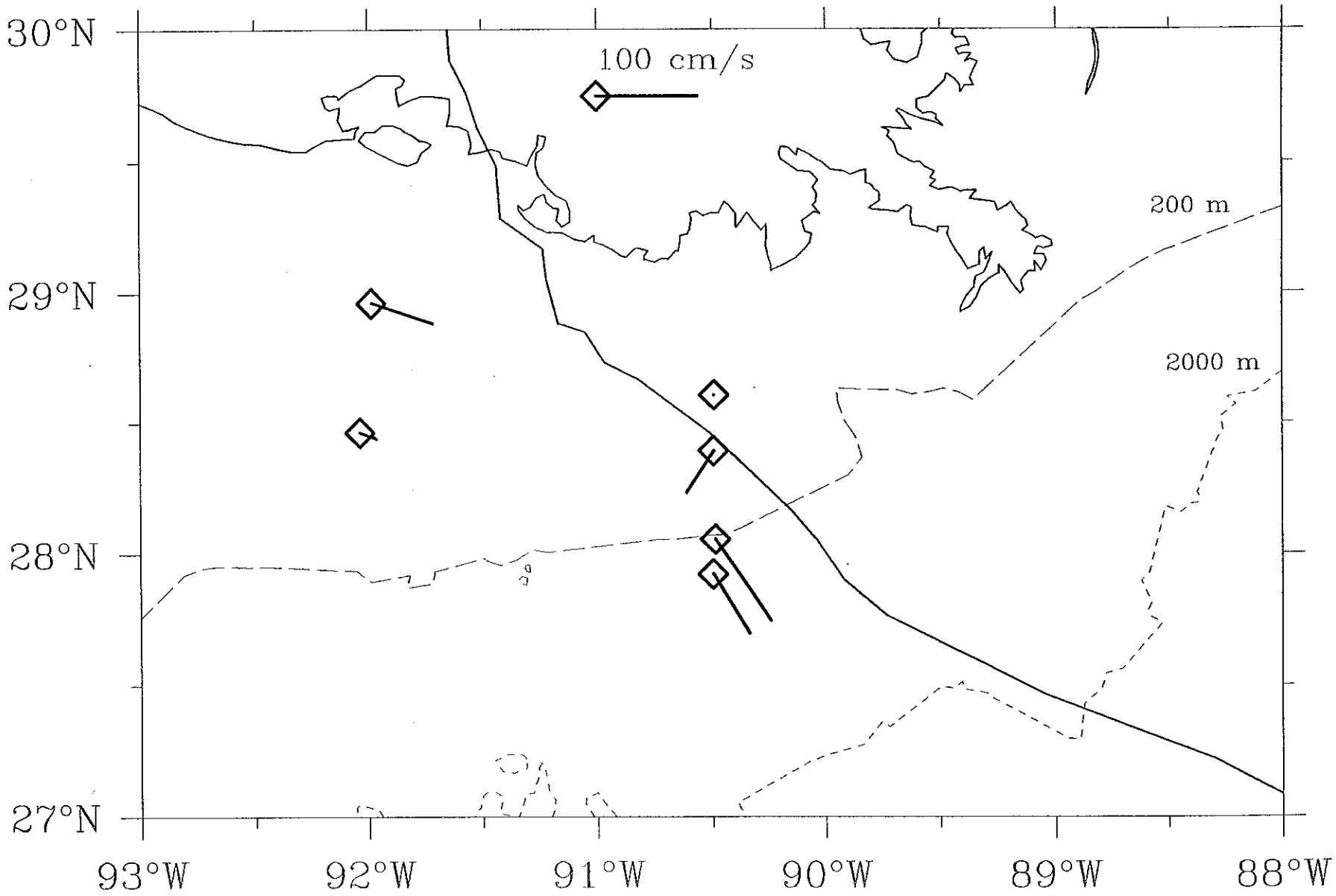

Observed Surface Currents: August-26-15:00 GMT

Frame 07°

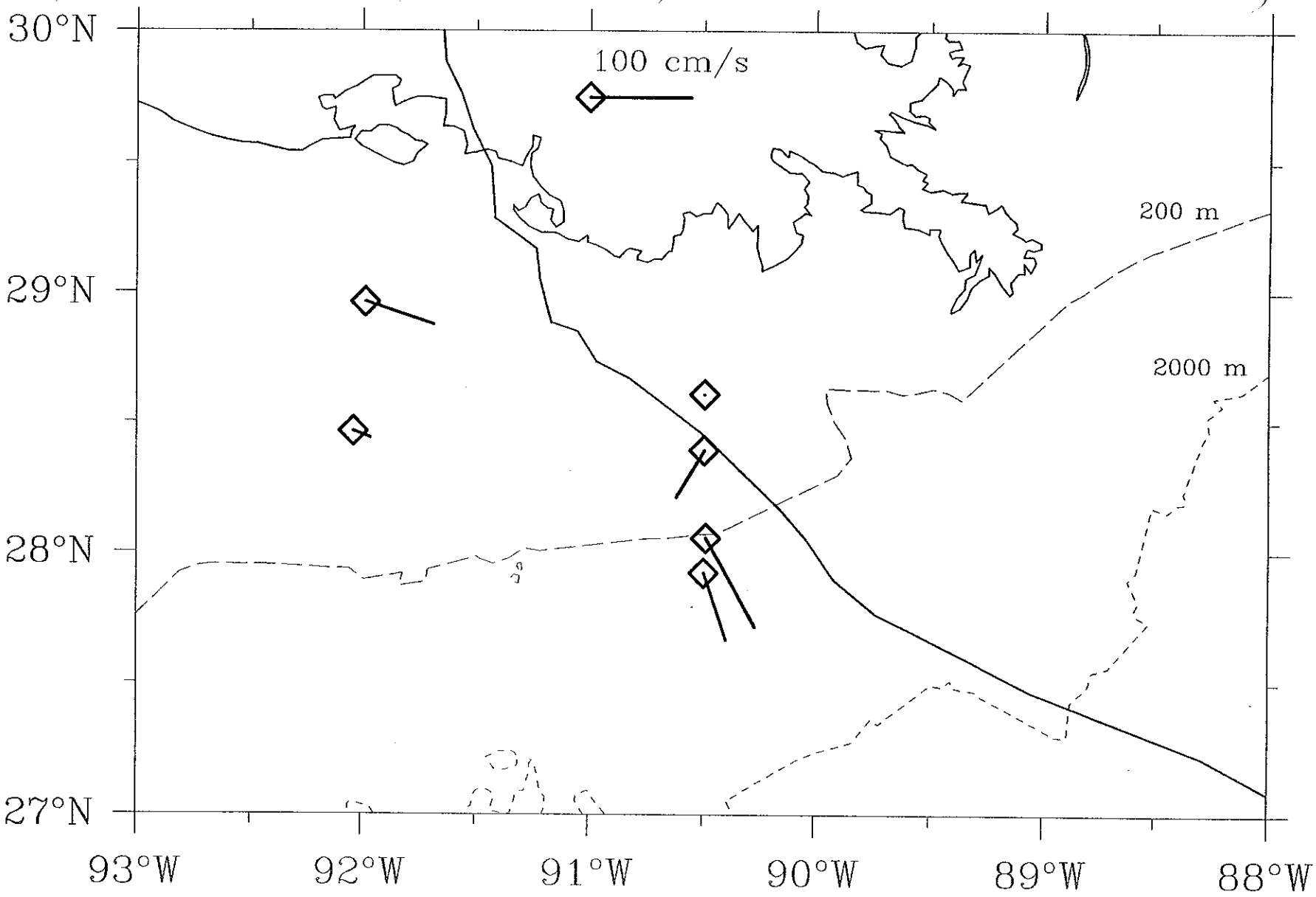

Observed Surface Currents: August-26-15:30 GMT

Frame 079

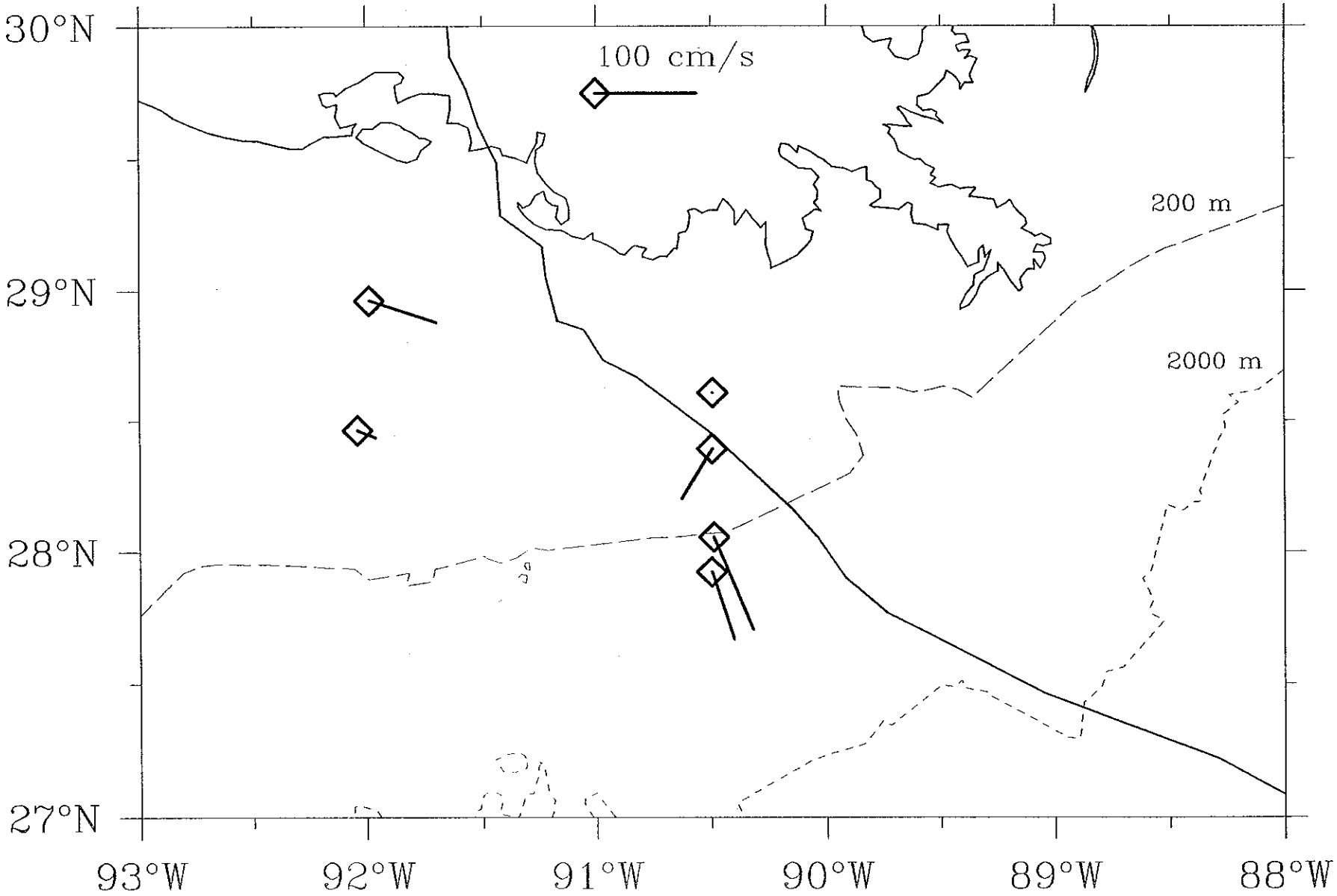

Observed Surface Currents: August-26-16:00 GMT

Frame 080

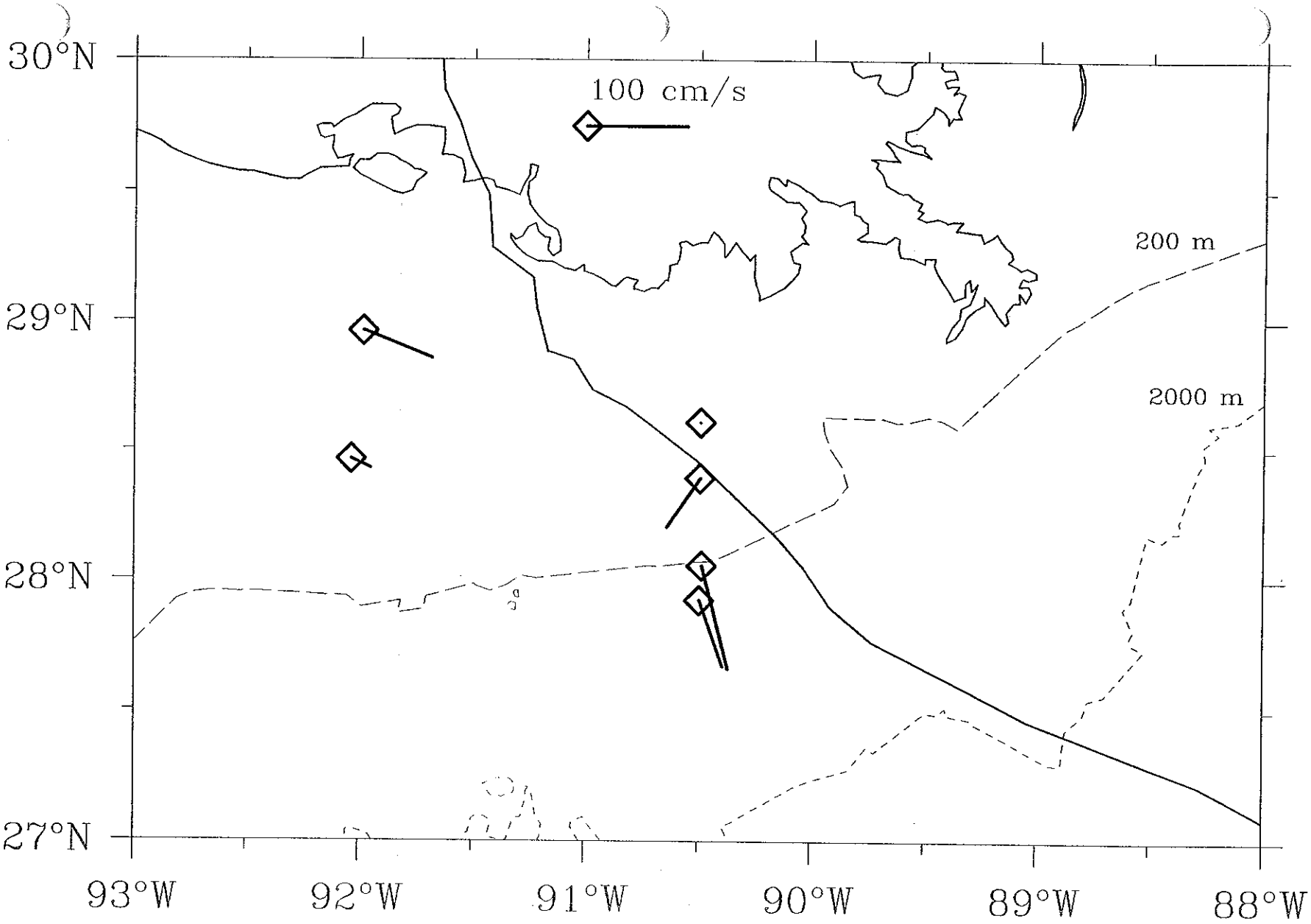

Observed Surface Currents: August-26-16:30 GMT

Frame 081

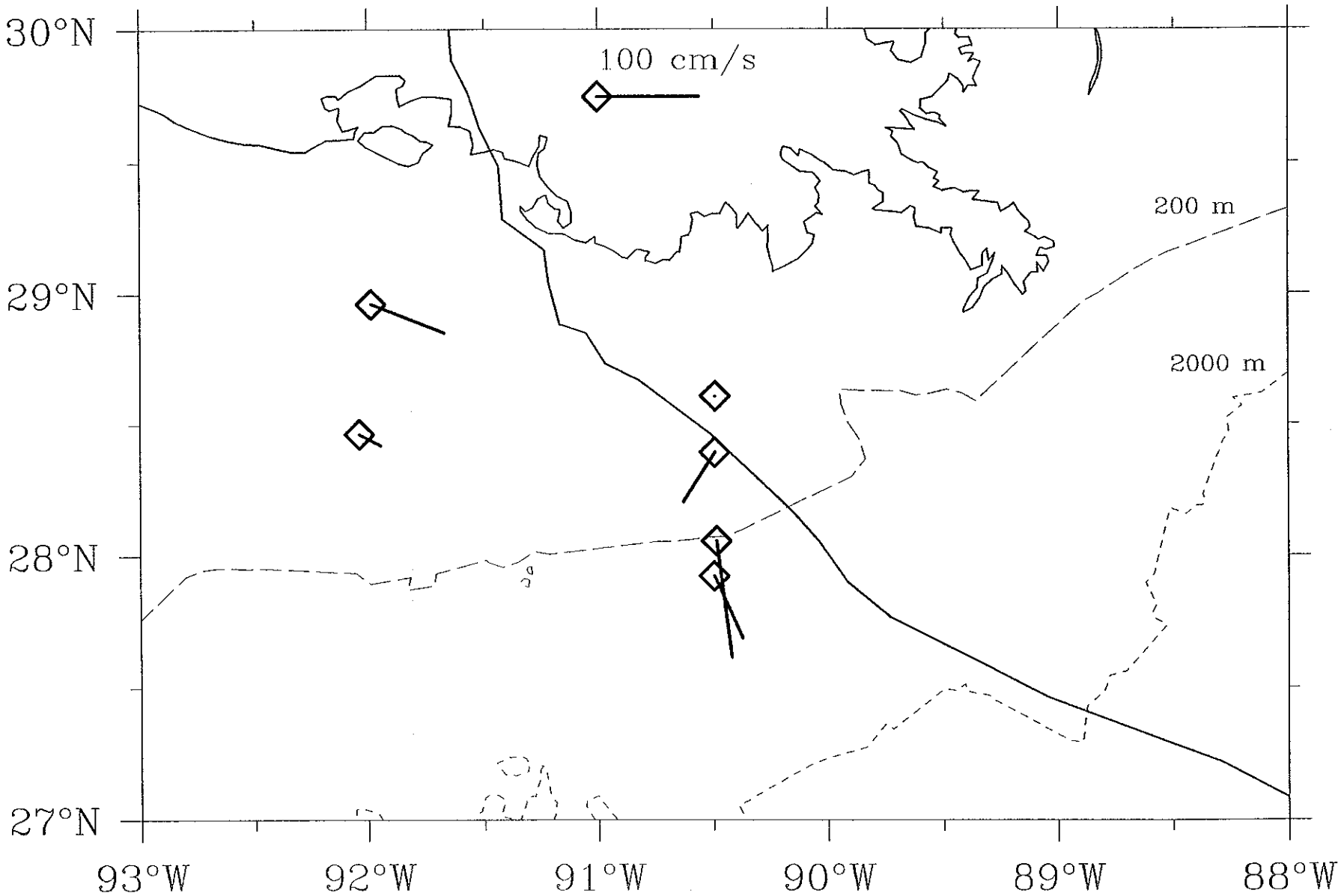

Observed Surface Currents: August-26-17:00 GMT

Frame 082

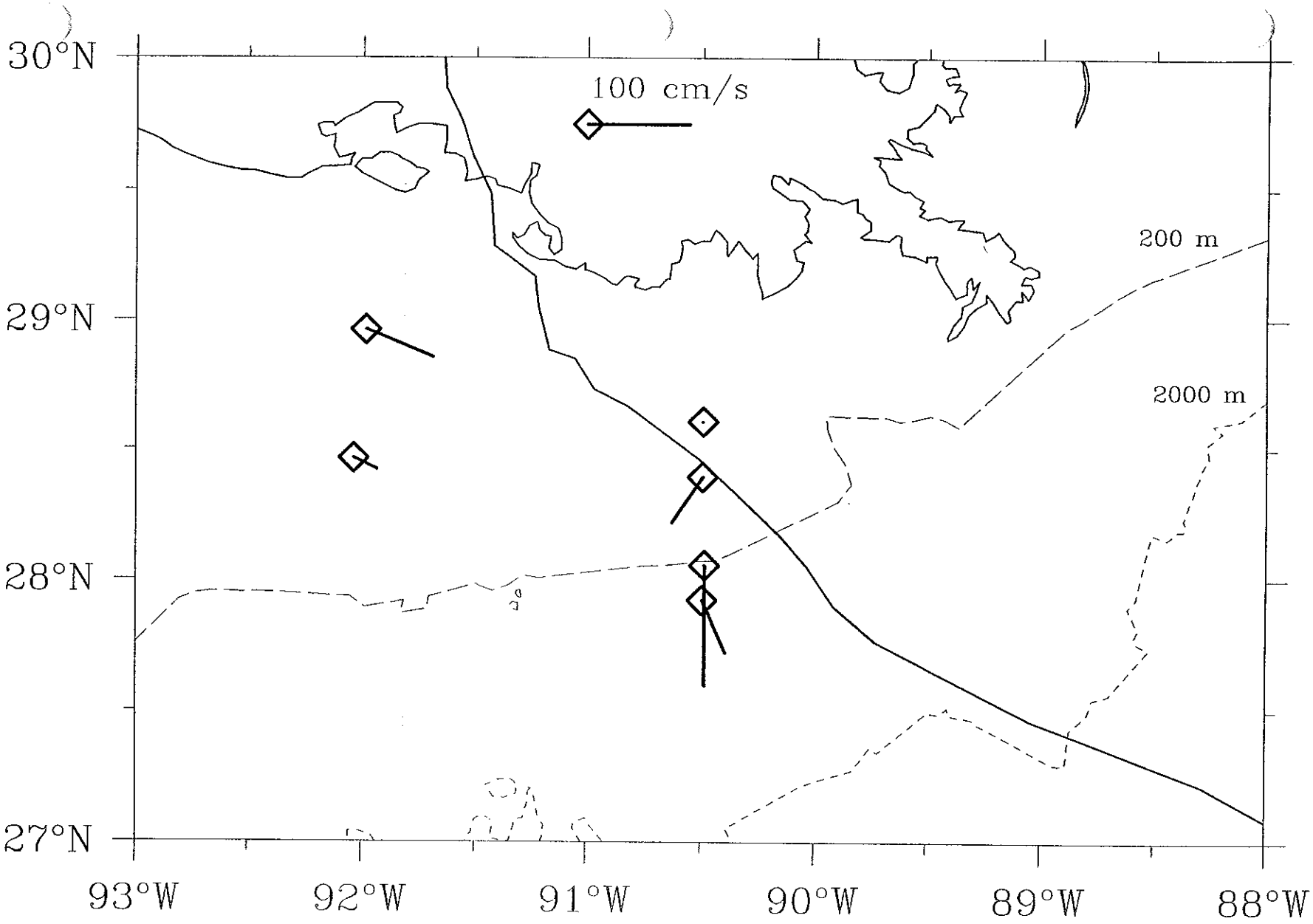

Observed Surface Currents: August-26-17:30 GMT

Frame 083

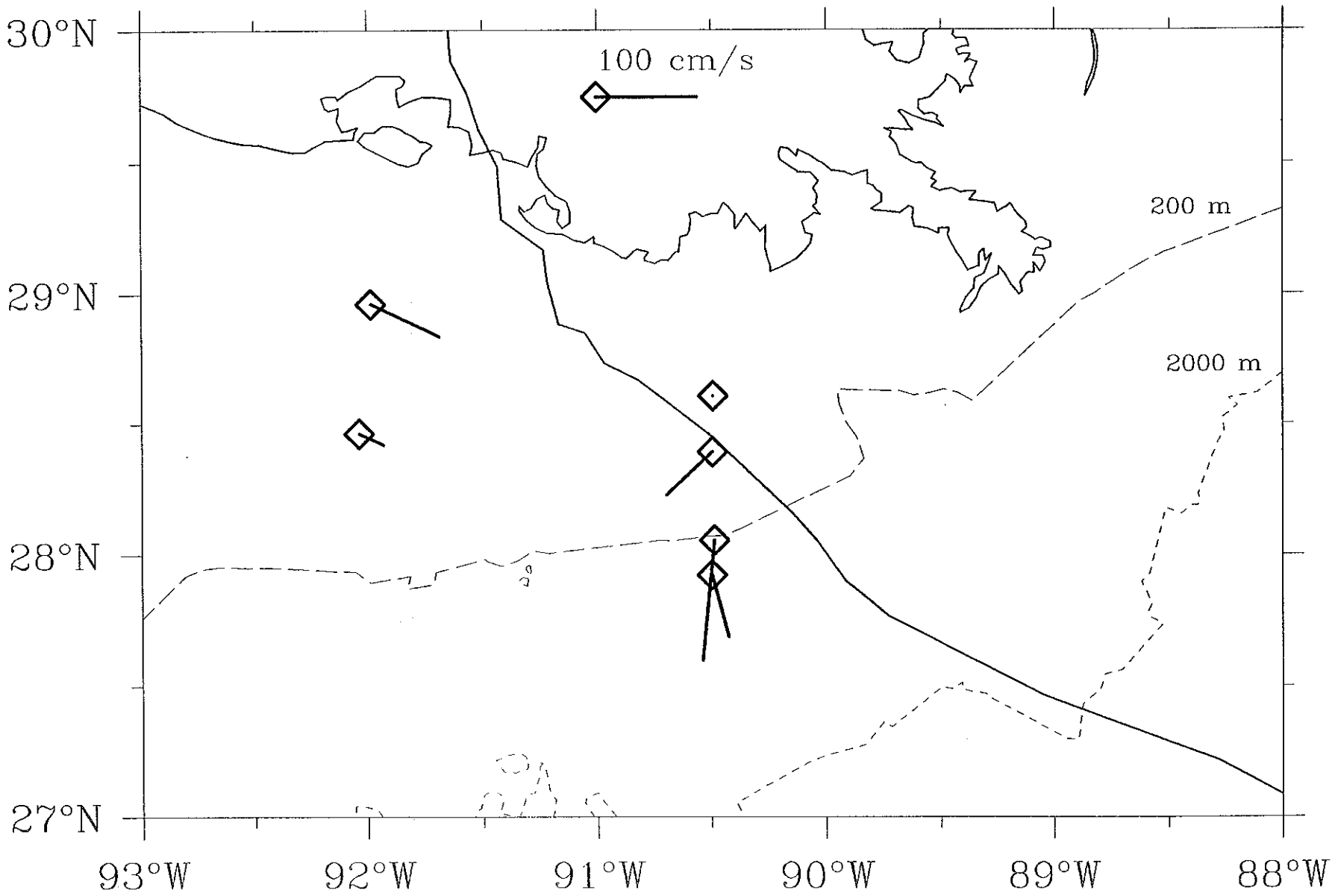

Observed Surface Currents: August–26–18:00 GMT

Frame 08

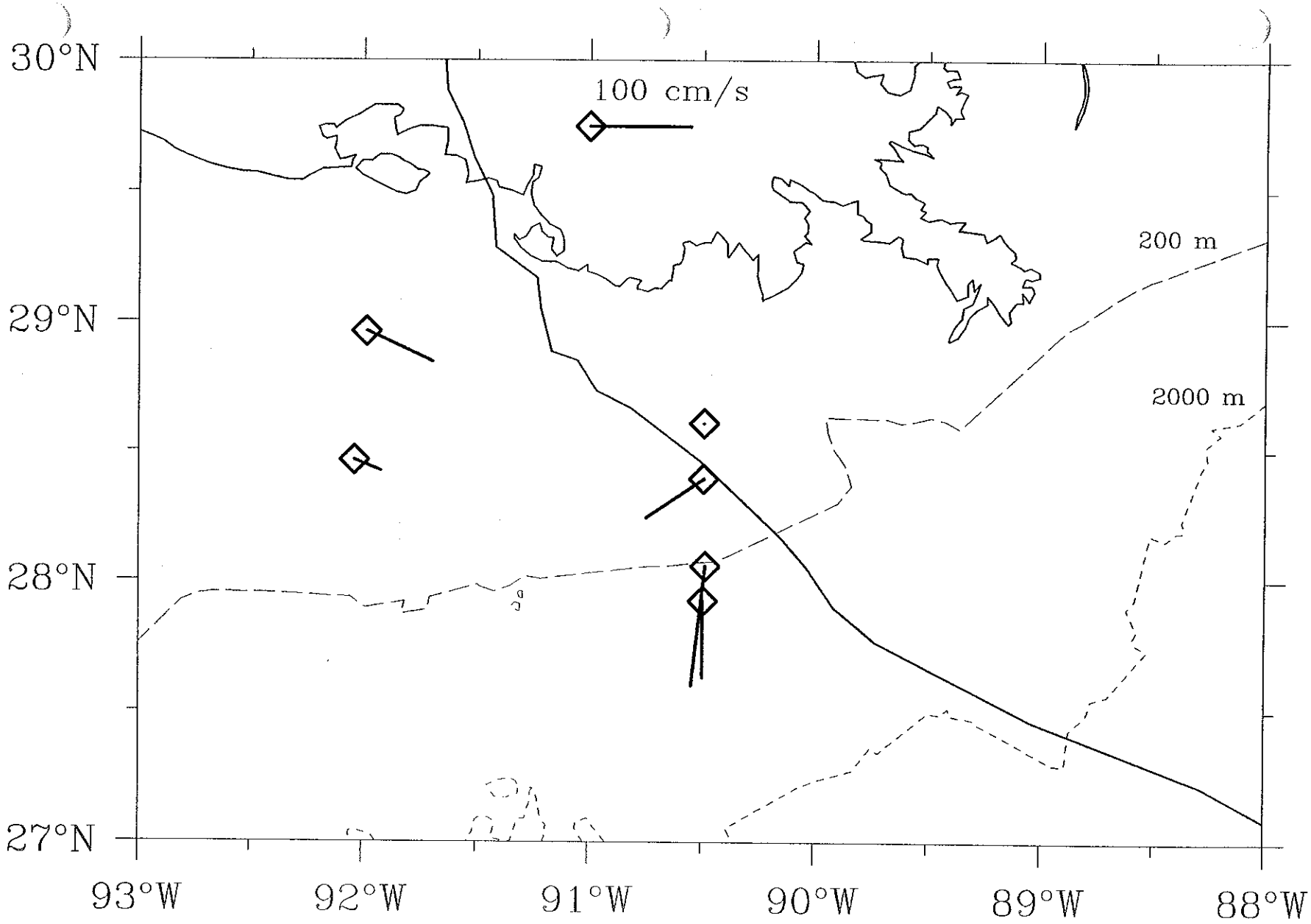

Observed Surface Currents: August-26-18:30 GMT

Frame 085

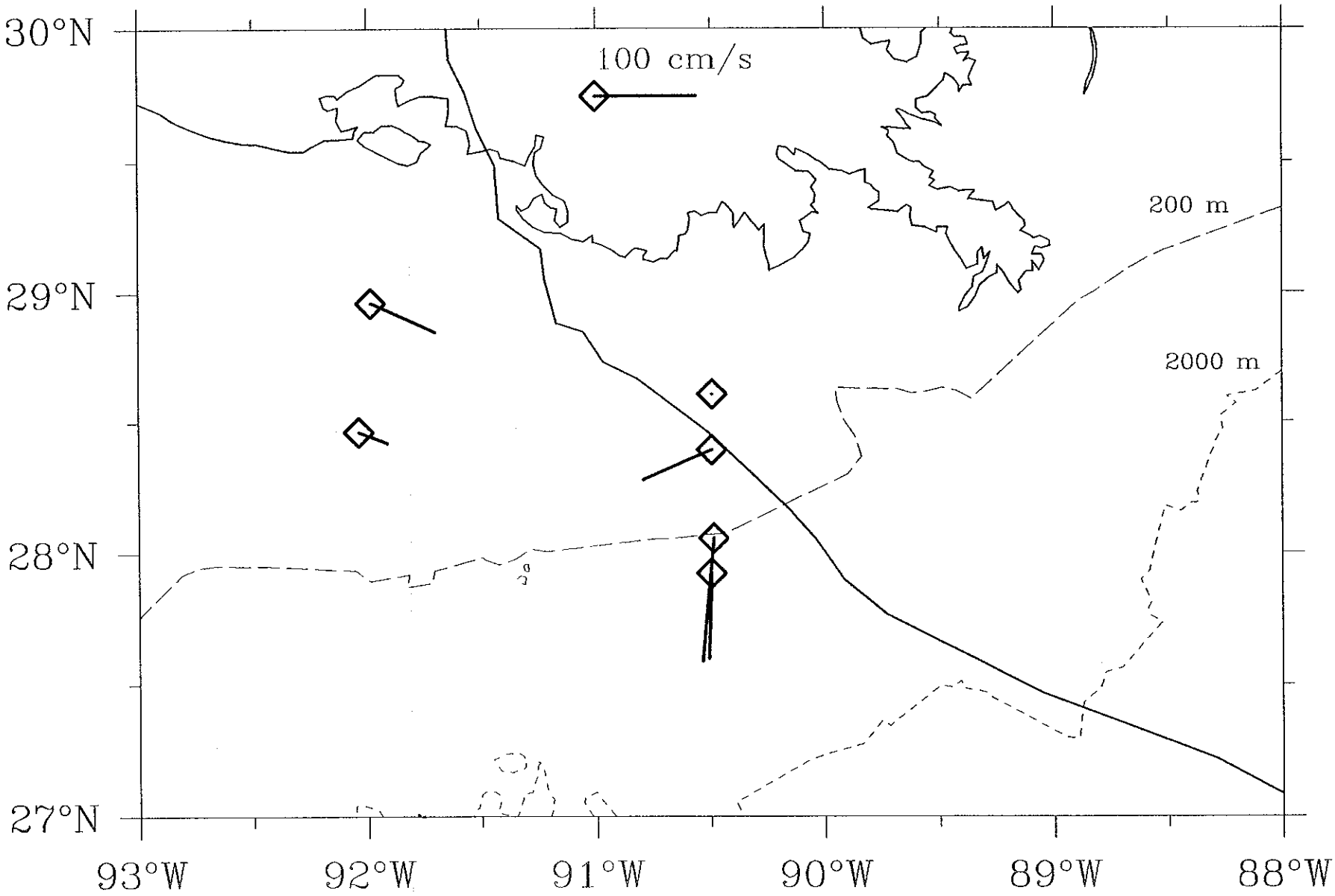

Observed Surface Currents: August-26-19:00 GMT

Frame 08

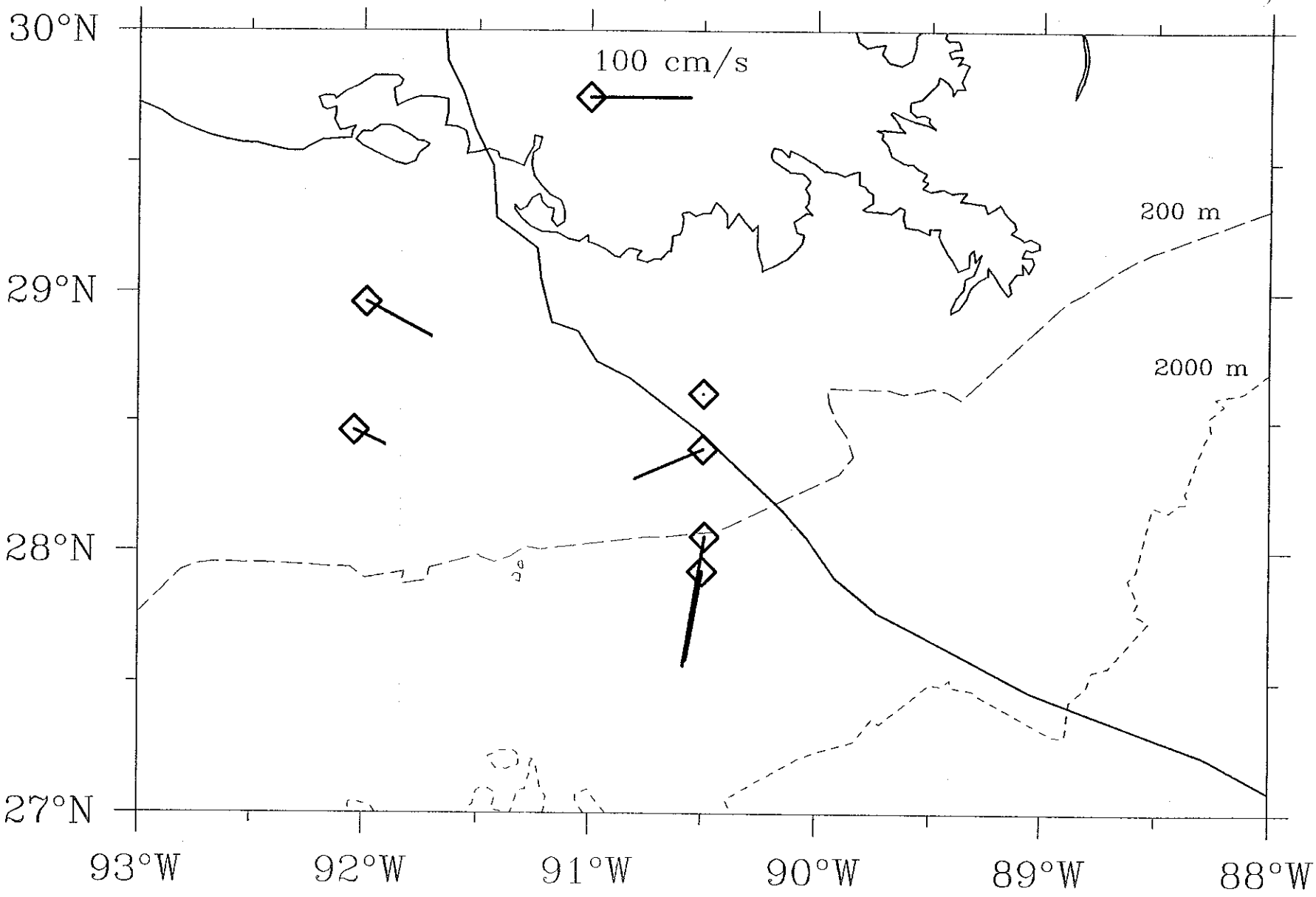

Observed Surface Currents: August-26-19:30 GMT

Frame 087

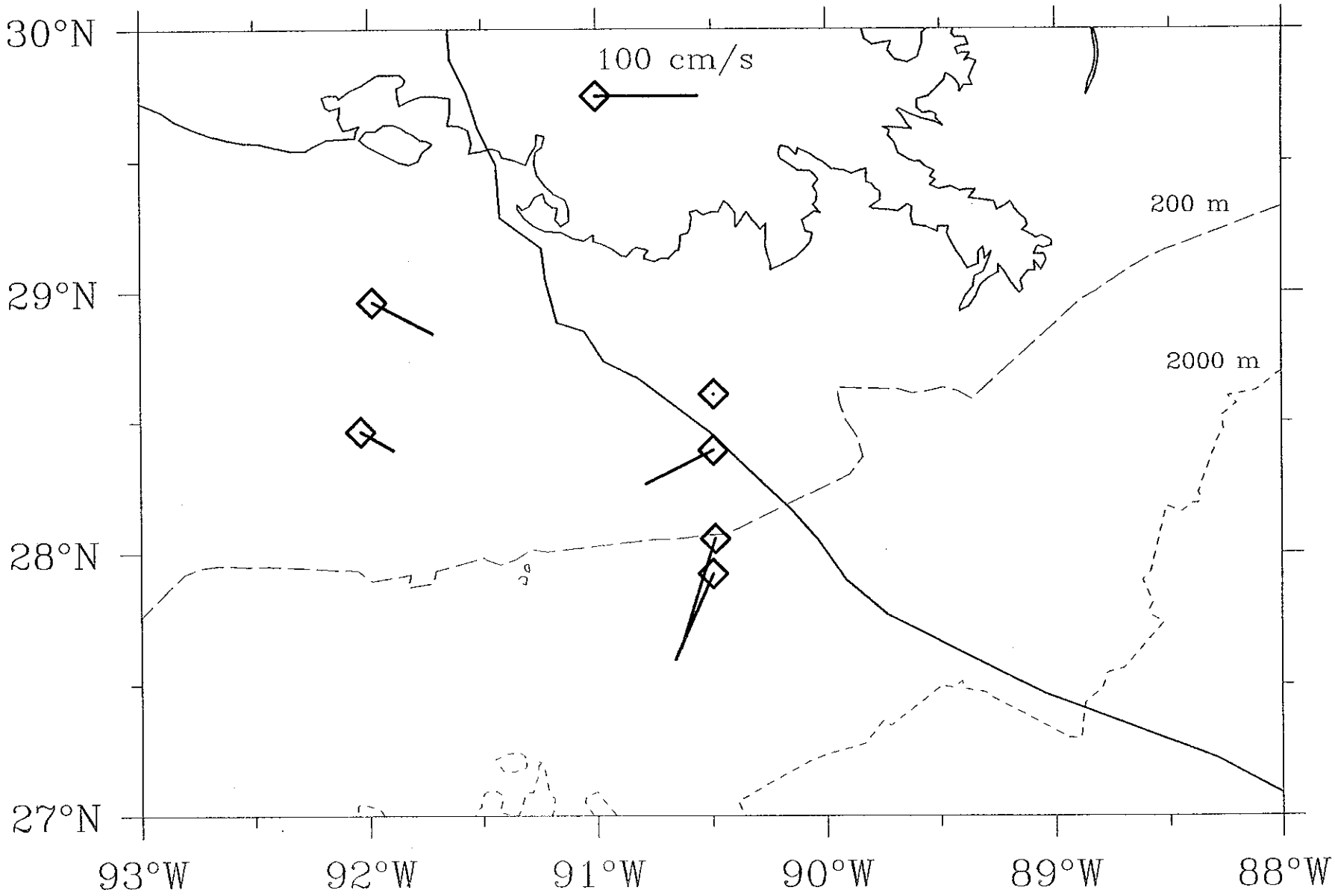

Observed Surface Currents: August-26-20:00 GMT

Frame 0[illegible]

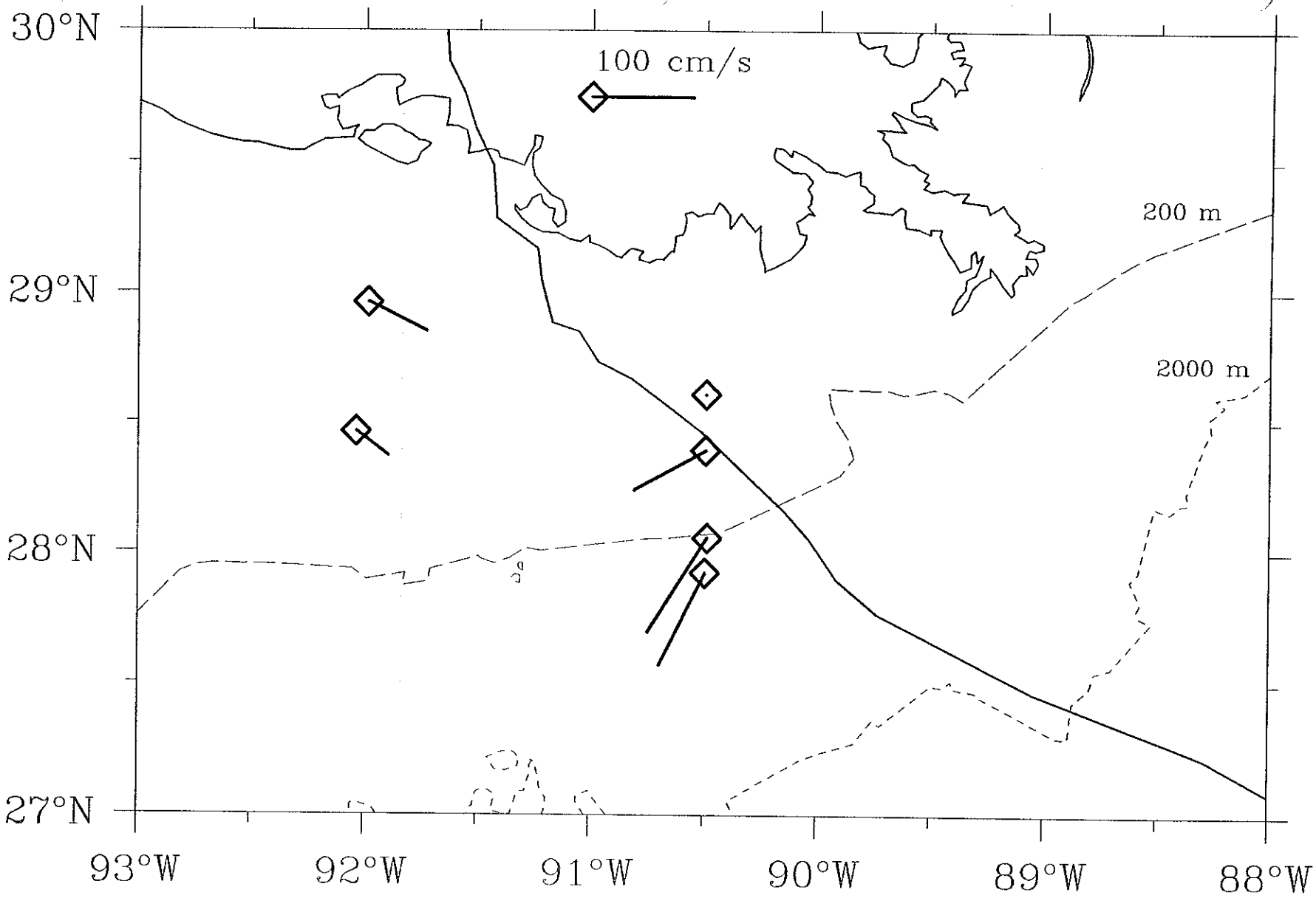

Observed Surface Currents: August-26-20:30 GMT

Frame 089

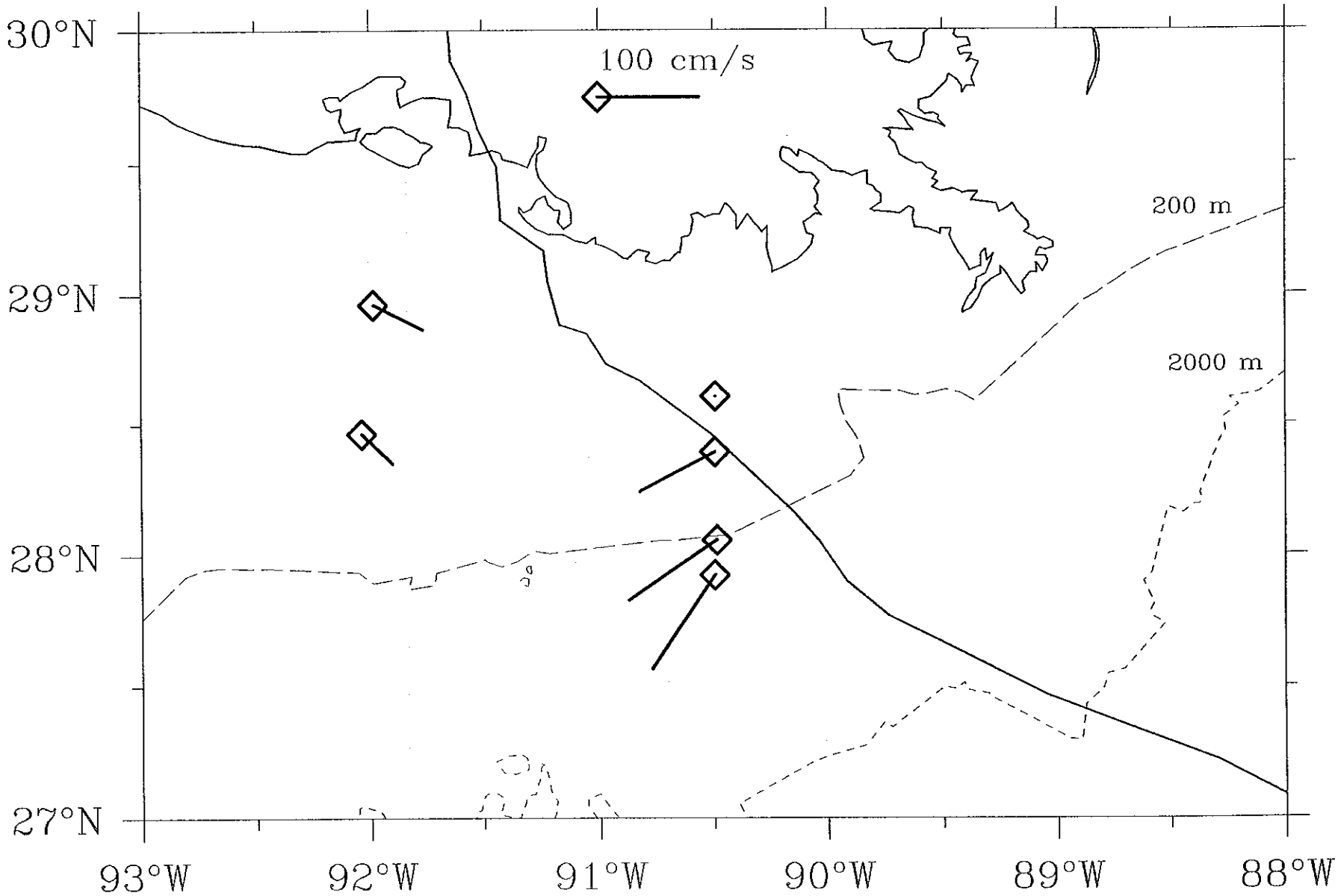

Observed Surface Currents: August-26-21:00 GMT

Frame 090

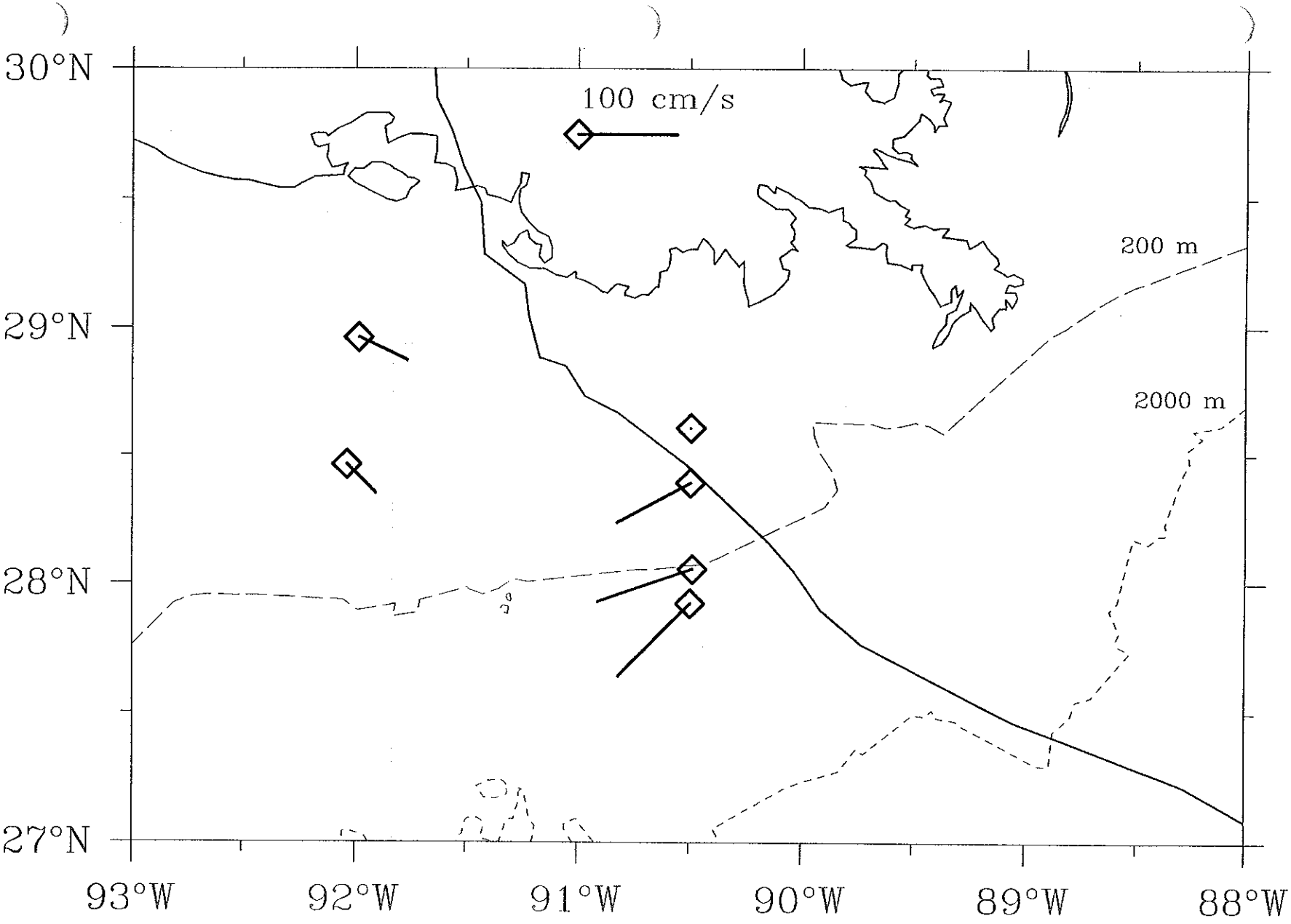

Observed Surface Currents: August-26-21:30 GMT

Frame 091

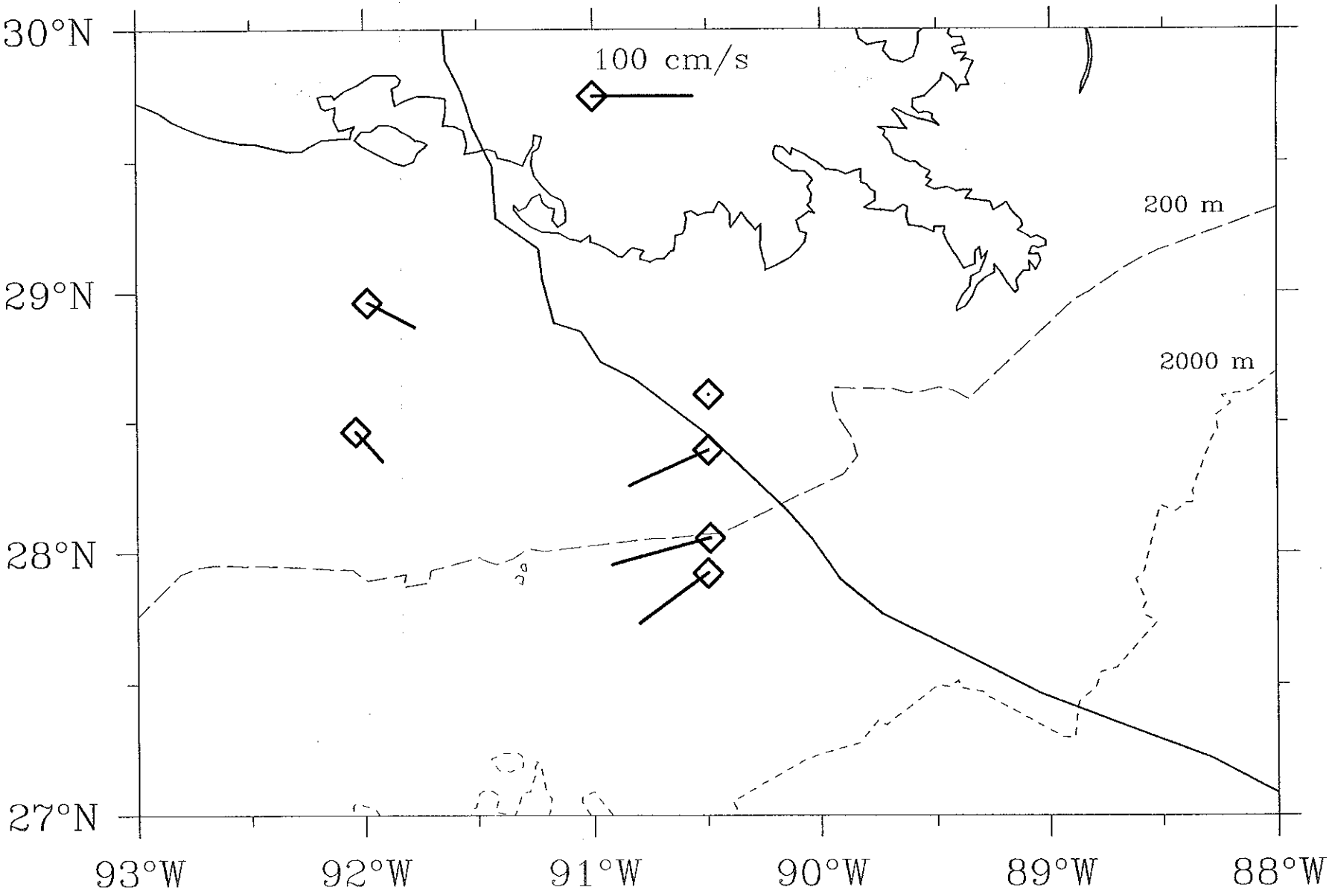

Observed Surface Currents: August-26-22:00 GMT

Frame 003

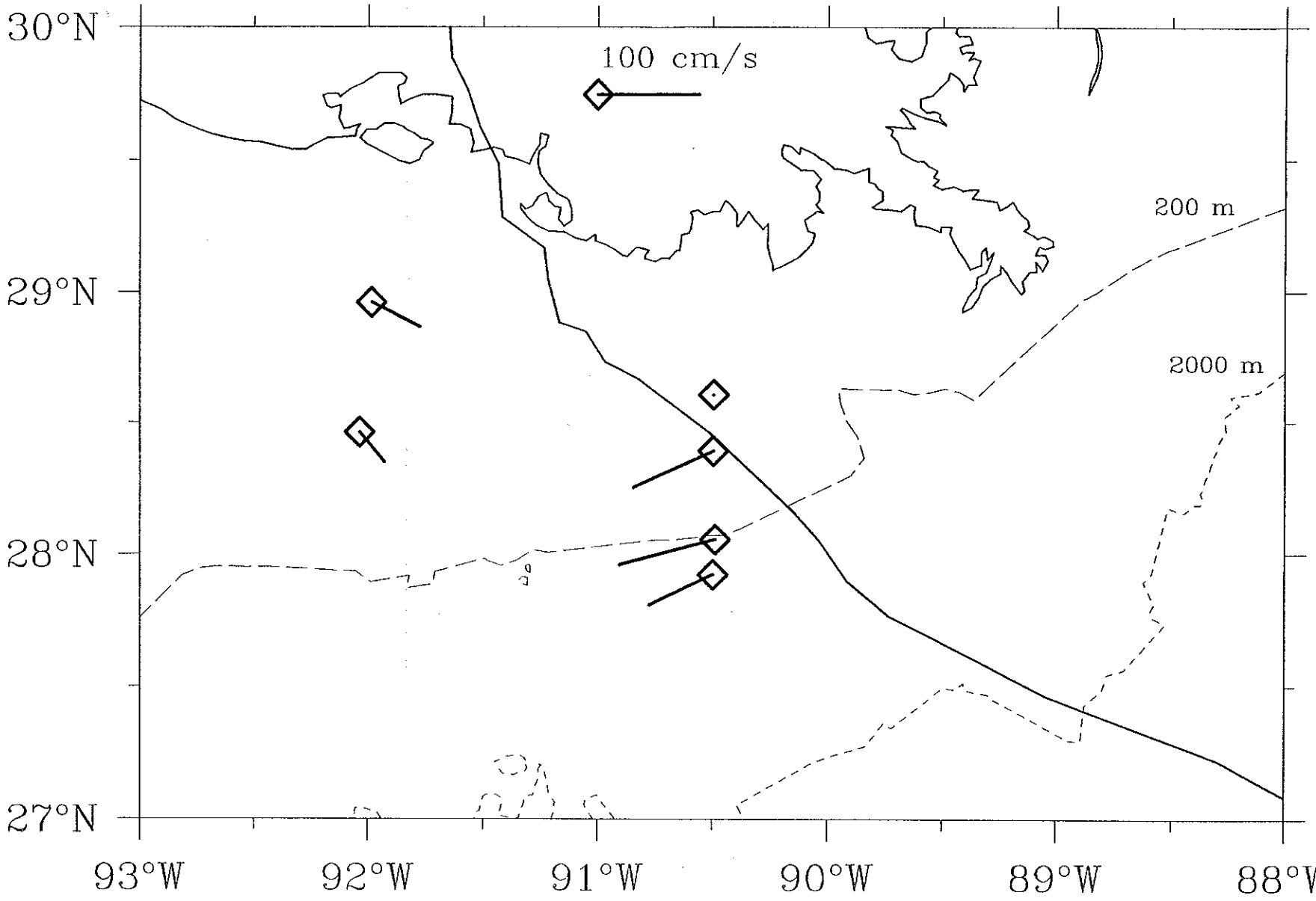

Observed Surface Currents: August-26-22:30 GMT

Frame 093

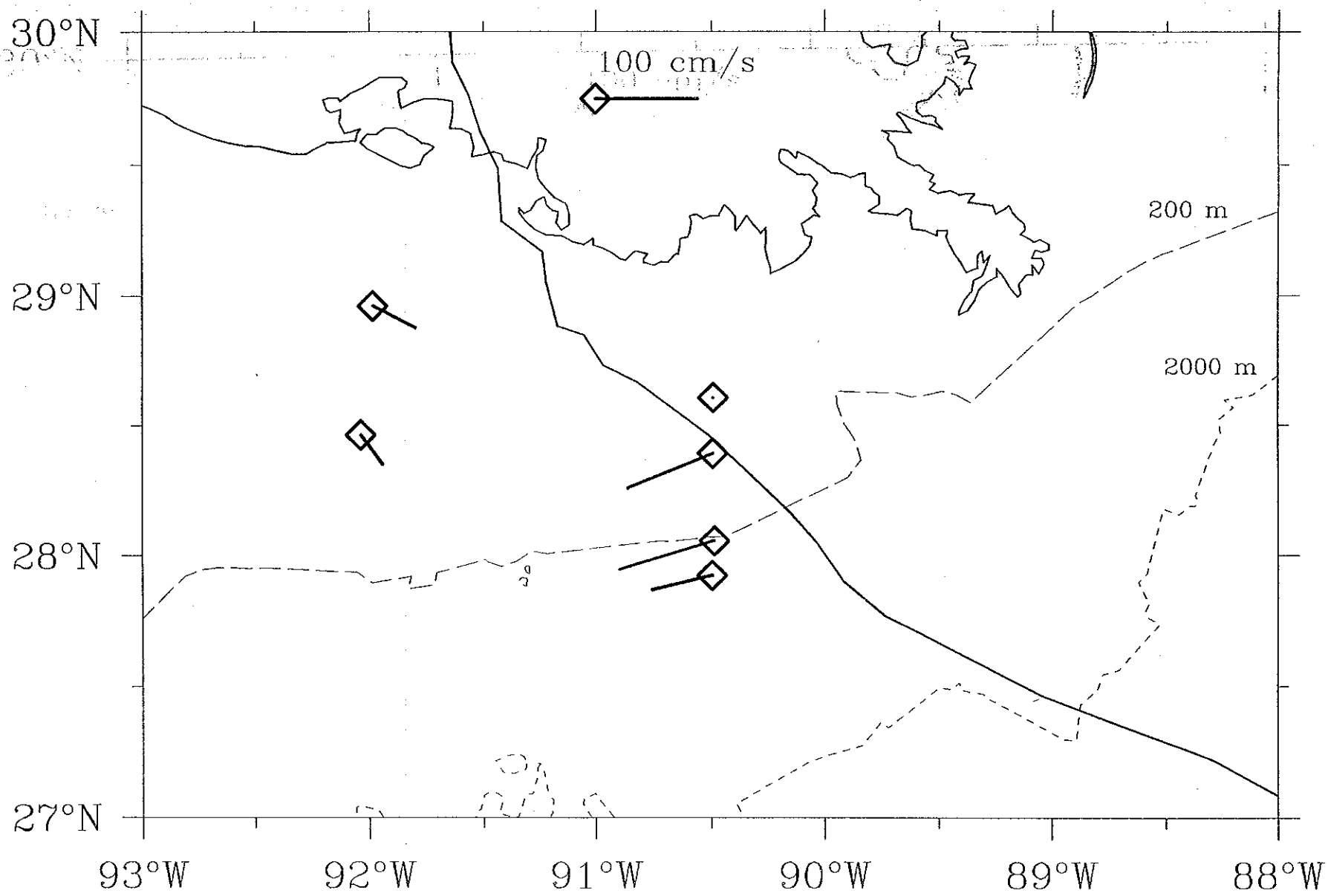

Observed Surface Currents: August-26-23:00 GMT

Frame 094

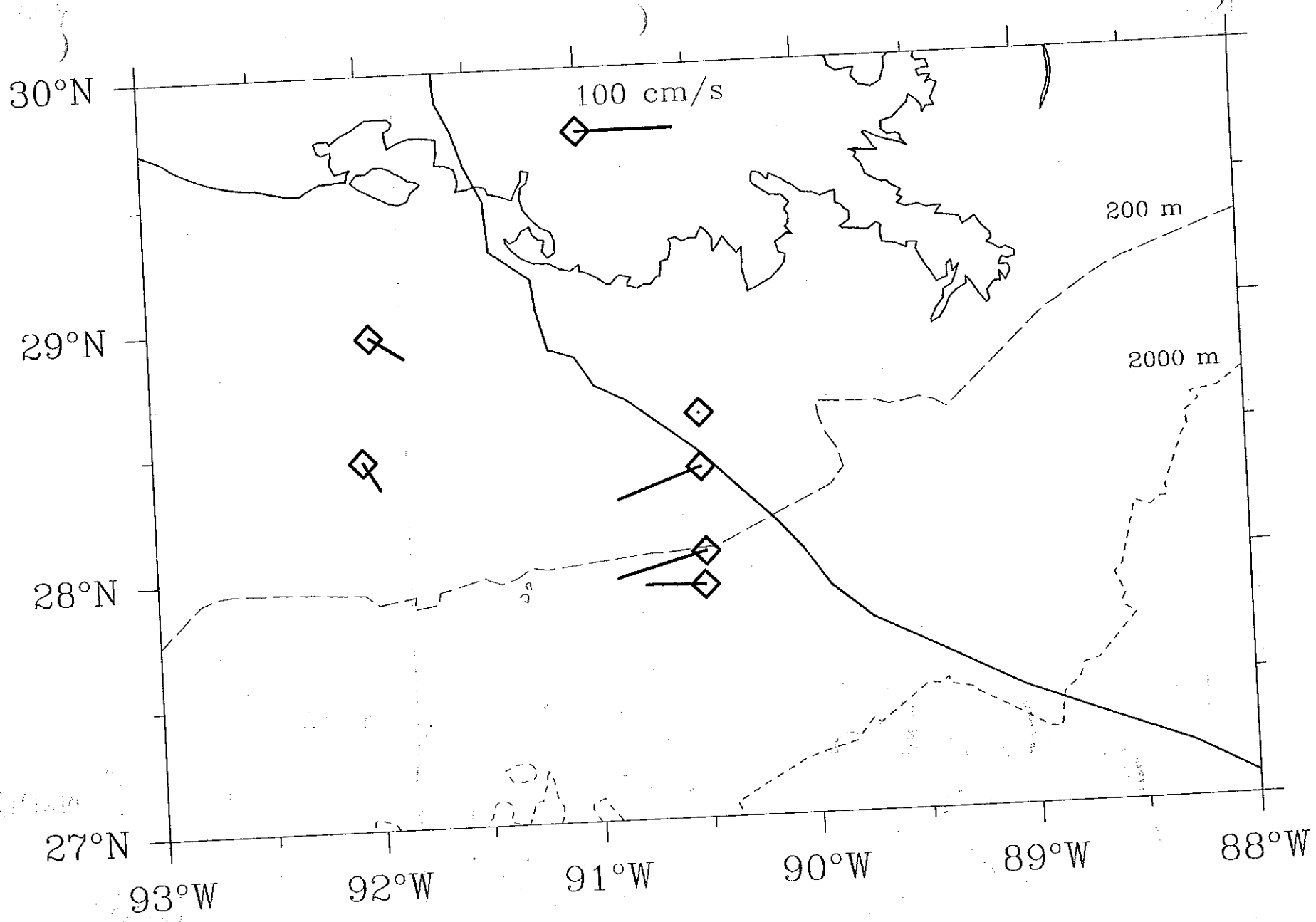

Observed Surface Currents: August-26-23:30 GMT

Frame 095

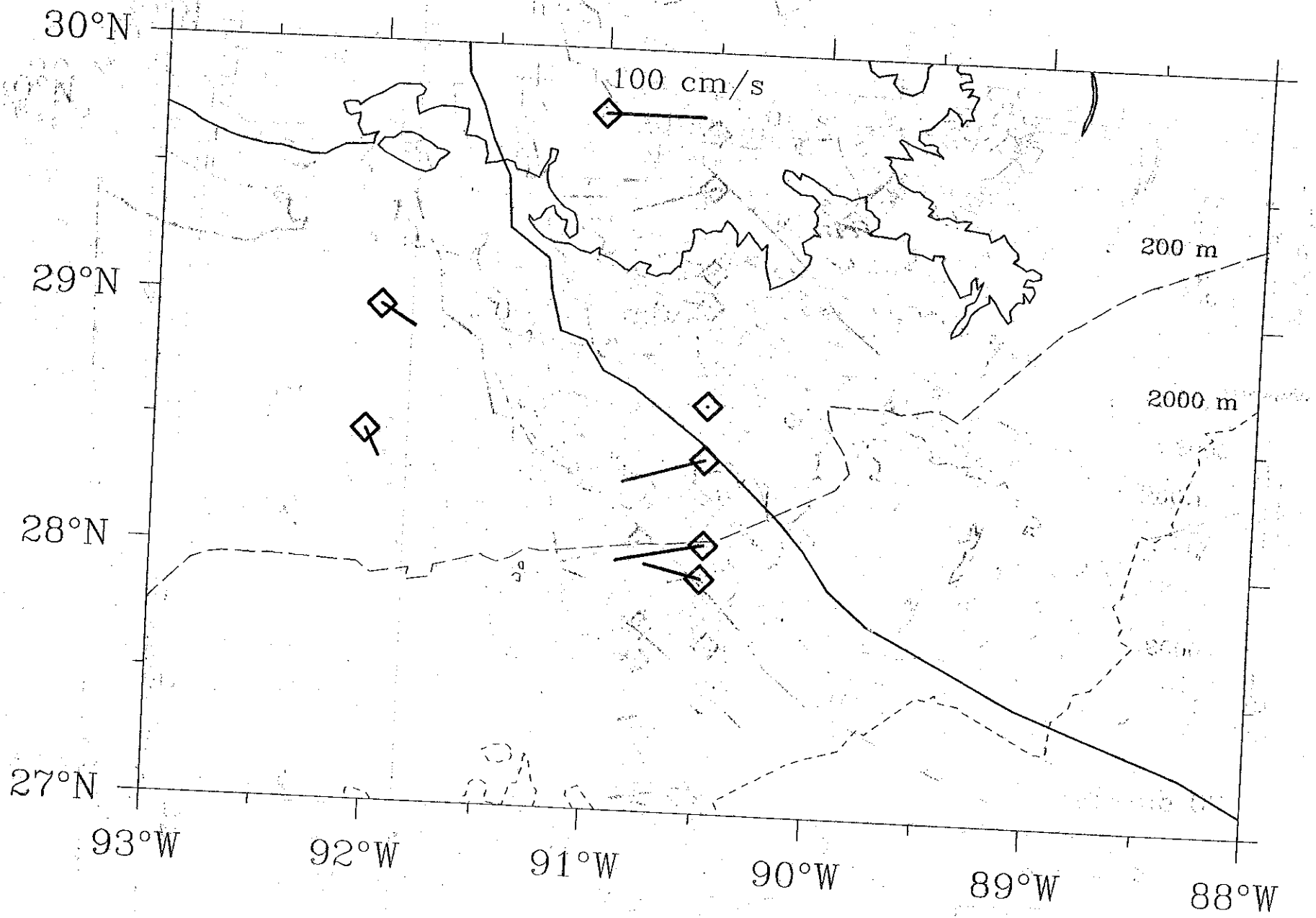

Observed Surface Currents: August-27-00:00 GMT

Frame 0